STATE OF CALIFORNIA • DEPARTMENT OF TRANSPORTATION

TECHNICAL REPORT DOCUMENTATION PAGE

TR0003 (REV 10/98)

ADA Notice

For individuals with sensory disabilities, this document is available in alternate formats. For alternate format information, contact the Forms Management Unit at (916) 445-1233, TTY 711, or write to Records and Forms Management, 1120 N Street, MS-89, Sacramento, CA 95814.

1. REPORT NUMBER	2. GOVERNMENT ASSOCIATION NUMBER	3. RECIPIENT'S CATALOG NUMBER
CA15-2316		

4. TITLE AND SUBTITLE

Shear Resistance of End Panels in Steel and Steel-Concrete Composite Girders

5. REPORT DATE

March 2015

6. PERFORMING ORGANIZATION CODE

7. AUTHOR

Dong-Won Kim and Chia-Ming Uang

8. PERFORMING ORGANIZATION REPORT NO.

SSRP-15/02

9. PERFORMING ORGANIZATION NAME AND ADDRESS

Department of Structural Engineering
Jacobs School of Engineering
University of California, San Diego
La Jolla, California 92093-0085

10. WORK UNIT NUMBER

11. CONTRACT OR GRANT NUMBER

65A0473

12. SPONSORING AGENCY AND ADDRESS

California Department of Transportation
Division of Research, Innovation, and System Information
P.O. Box 942873
Sacramento, CA 94273-0001

13. TYPE OF REPORT AND PERIOD COVERED

Final Report
June 1, 2012 - March 31, 2015

14. SPONSORING AGENCY CODE

15. SUPPLEMENTARY NOTES

Prepared in cooperation with the State of California Department of Transportation

16. ABSTRACT

Plate girders, usually characterized by having very deep sections, have been widely used for long-span structures and bridges. US design provisions (AASHTO Specifications for bridge design and AISC Specifications for building design) allow the designer to include the contribution of tension-field action after web buckling in calculating the ultimate shear strength of interior panels, but not exterior panels, because it is believed that no effective anchor mechanism exists to resist the horizontal component of the tension-field force. This has had a negative impact on the evaluation and load rating of existing bridges. This conservatism often requires unnecessary rehabilitation of existing steel girder bridges which have provided satisfactory service in the past half-century. Testing of two large-size steel plate girders and two steel-concrete composite plate girders was carried out in Phase 1 of this research to investigate the shear resistance of end panels. Test results demonstrated a much higher shear resistance than that predicted by code provisions in the steel girders. Tension-field action was observed in all specimens. The concrete slab in the composite specimens also contributed to the shear resistance, although to a lesser extent. Nonlinear finite element analyses were conducted to correlate the test results. Results from a parametric study strongly supported the behaviors observed from testing and confirmed the existence of partial tension-field action in the end panels. Based on the failure mode observed from both testing and finite element simulation, an analytical model was developed to simulate the collapse mechanism. Plastic analysis was used to derive a predictive shear strength equation. This equation is similar in format to that used in AASHTO Specifications for interior panels but includes a parameter α to account for the contribution of partial tension-field action. A resistance factor for the proposed shear strength equation was also derived. Based on a strut-and-tie model, the contribution from the concrete slab was also presented. For Phase 2 test program, another two steel plate girders and two steel-concrete composite plate girders with larger width-to-depth ratios and a small depth-to-thickness ratio were fabricated and tested. Testing showed the same failure mode as that observed from Phase 1 test program and confirmed the accuracy of the proposed equation. However, the concrete component of the shear equation developed in Phase 1 underestimates the shear resistance of Phase 2 composite specimens that had closely spaced shear connectors. A modification was made to the proposed equation to account for this spacing effect. Rehabilitation of end panels by using a common scheme, first proposed by Basler and has been adopted in Eurocode 3, was found unconservative. Two rehabilitation schemes were proposed and the effectiveness was verified by finite element simulation. Additionally, the effects of longitudinal stiffeners, small flange areas, large width-depth ratios, noncompact web, and unequatl top and bottom flanges were investigated by finite element analysis and the results confirmed that the proposed equation also gives a reasonable correlation with the analysis results.

17. KEY WORDS	18. DISTRIBUTION STATEMENT
Shear Strength, End Panels, Steel Girder, Composite Girder, Tension-Field Action, Post-Buckling Strength, Rehabilitation	No restrictions. This document is available to the public through the National Technical Information Service, Springfield, VA, 22161.

19. SECURITY CLASSIFICATION *(of this report)*	20. NUMBER OF PAGES	21. COST OF REPORT CHARGED
Unclassified	396	

DISCLAIMER STATEMENT

This document is disseminated in the interest of information exchange. The contents of this report reflect the views of the authors who are responsible for the facts and accuracy of the data presented herein. The contents do not necessarily reflect the official views or policies of the State of California or the Federal Highway Administration. This publication does not constitute a standard, specification or regulation. This report does not constitute an endorsement by the Department of any product described herein.

For individuals with sensory disabilities, this document is available in alternate formats. For information, call (916) 654-8899, TTY 711, or write to California Department of Transportation, Division of Research, Innovation and System Information, MS-83, P.O. Box 942873, Sacramento, CA 94273-0001.

STRUCTURAL SYSTEMS

RESEARCH PROJECT

Report No.
SSRP-15/02

Shear Resistance of End Panels in Steel and Steel-Concrete Composite Plate Girders

by

Dong-Won Kim

Chia-Ming Uang

Final Report to California Department of Transportation

March 2015

Department of Structural Engineering
University of California, San Diego
La Jolla, California 92093-0085

University of California, San Diego
Department of Structural Engineering
Structural Systems Research Project

Report No. SSRP-15/02

SHEAR RESISTANCE OF END PANELS IN STEEL AND STEEL-CONCRETE COMPOSITE PLATE GIRDERS

by

Dong-Won Kim
Postdoctoral Researcher

Chia-Ming Uang
Professor

Final Report to California Department of Transportation

Department of Structural Engineering
University of California, San Diego
La Jolla, California 92093-0085

March 2015

DISCLAIMER

This document is disseminated in the interest of information exchange. The contents of this report reflect the views of the authors who are responsible for the facts and accuracy of the data presented herein. The contents do not necessarily reflect the official views or policies of the State of California or the Federal Highway Administration. This publication does not constitute a standard, specification or regulation. This report does not constitute an endorsement by the California Department of Transportation of any product described herein.

For individuals with sensory disabilities, this document is available in Braille, large print, audiocassette, or compact disk. To obtain a copy of this document in one of these alternate formats, please contact: the Division of Research and Innovation, MS-83, California Department of Transportation, P.O. Box 942873, Sacramento, CA 94273-0001.

ACKNOWLEDGEMENTS

The California Department of Transportation (Caltrans) funded this work under Contract #65A0473. We would like to thank Drs. Charles Sikorsky (project manager), George Huang, and Lian Duan at Caltrans for their guidance and advice.

The testing was conducted in the Charles Lee Powell Structures Laboratories at the University of California, San Diego. Technical assistance from Dr. Christopher Latham and Paul Greco is much appreciated.

ABSTRACT

Plate girders, usually characterized by having very deep sections, have been widely used for long-span structures and bridges. US design provisions (AASHTO Specifications for bridge design and AISC Specifications for building design) allow the designer to include the contribution of tension-field action after web buckling in calculating the ultimate shear strength of interior panels, but not exterior panels, because it is believed that no effective anchor mechanism exists to resist the horizontal component of the tension-field force. This has had a negative impact on the evaluation and load rating of existing bridges. This conservatism often requires unnecessary rehabilitation of existing steel girder bridges which have provided satisfactory service in the past half-century.

Testing of two large-size steel plate girders and two steel-concrete composite plate girders was carried out in Phase 1 of this research to investigate the shear resistance of end panels. Test results demonstrated a much higher shear resistance than that predicted by code provisions in the steel girders. Tension-field action was observed in all specimens. The concrete slab in the composite specimens also contributed to the shear resistance, although to a lesser extent.

Nonlinear finite element analyses were conducted to correlate the test results. Results from a parametric study strongly supported the behaviors observed from testing and confirmed the existence of partial tension-field action in the end panels. Based on the failure mode observed from both testing and finite element simulation, an analytical model was developed to simulate the collapse mechanism. Plastic analysis was used to derive a predictive shear strength equation. This equation is similar in format to that used in AASHTO Specifications for interior panels but includes a parameter α to account for the contribution of partial tension-field action. A resistance factor for the proposed shear strength equation was also derived. Based on a strut-and-tie model, the contribution from the concrete slab was also presented.

For Phase 2 test program, another two steel plate girders and two steel-concrete composite plate girders with larger width-to-depth ratios and a small depth-to-thickness ratio were fabricated and tested. Testing showed the same failure mode as that observed

from Phase 1 test program and confirmed the accuracy of the proposed equation. However, the concrete component of the shear equation developed in Phase 1 underestimates the shear resistance of Phase 2 composite specimens that had closely spaced shear connectors. A modification was made to the proposed equation to account for this spacing effect.

Rehabilitation of end panels by using a common scheme, first proposed by Basler and has been adopted in Eurocode 3, was found unconservative. Two rehabilitation schemes were proposed and the effectiveness was verified by finite element simulation. Additionally, the effects of longitudinal stiffeners, small flange areas, large width-depth ratios, noncompact web, and unequatl top and bottom flanges were investigated by finite element analysis and the results confirmed that the proposed equation also gives a reasonable correlation with the analysis results.

TABLE OF CONTENTS

LIST OF FIGURES

LIST OF TABLES

1. INTRODUCTION

1.1 Plate Girders

Typically in building construction, hot-rolled W-shape or I-shape members are used as beams. However, for longer spans in which flexural demands are greater, such as in bridges, deeper beam sections are required. Since hot-rolled shapes are not economical in such circumstances, beams built-up from steel plates, which are commonly referred to as plate girders, have been used for long-span structures.

Since plate girders typically have very deep sections, the web of a plate girder is very slender. The slender web causes an instability problem under shear loading. To remediate this issue, the web of the plate girder is typically reinforced with transverse stiffeners and occasionally longitudinal stiffeners to increase its shear buckling strength. Figure 1.1 shows the typical structural configuration of a steel plate girder. As shown in the figure, the web is stiffened with transverse stiffeners. Transverse stiffeners that are located at the supports are called bearing stiffeners, and should be double-sided. Those located away from the supports are called intermediate stiffeners, which can be either one-sided or double-sided. A panel is defined as a region of the girder web that is surrounded by girder flanges and transverse stiffeners. The panel nearest to the support is referred to as an end panel or an exterior panel, while the remaining panels are referred to as interior panels. Also, some portion of the web is typically extended out beyond the bearing stiffeners and is referred to as the extended web (e in Figure 1.1). Figure 1.2 shows a sample steel girder bridge which was built in 1967. The bridge comprises welded steel plate girders, which act compositely with a concrete slab through headed shear studs. Many transverse stiffeners were used to increase the web shear strength. Therefore, the design strategy for plate girders is to determine an optimal combination of plate size and thickness, and stiffener spacing.

1.2 Shear Load-Carrying Mechanism of Stiffened Steel Plate Girder

Unlike flexural buckling for columns and lateral-torsional buckling for beams, the stiffened web panels of steel girders can carry more shear load after exceeding the shear

buckling strength. A web in shear is initially in a pure shear stress state. The shear stresses present are equivalent to two principal stresses (one in tension and one in compression) that are inclined at 45º to the shear stresses [see Figure 1.3(a)]. This shear-transfer mechanism prior to web buckling is referred to as "beam action". When the elastic shear buckling strength of the panel is reached, the panel buckles along the panel diagonal while showing out-of-plane deformation.

After elastic shear buckling occurs, the principal compressive stresses do not increase any further, and the principal tensile stresses continue to increase and approach the panel yield strength as further buckling occurs along the panel diagonal. This diagonally buckled portion in the panel functions as a tension tie member, while the transverse stiffeners serve as compression strut members in a Pratt truss [see Figure 1.3 (b)]. This shear transfer mechanism resembling a truss system provides additional post-buckling strength. The inclined tensile membrane stress (or tension-field stress) of the panel is referred to as "tension-field action".

Therefore, the ultimate shear strength of a plate girder consists of two components: the "beam action" shear strength (or shear buckling strength) and the "tension-field action" shear strength (or post-buckling strength).

1.3 Tension-Field Action in Interior Panels

1.3.1 General

The source of the post-buckling strength was first observed by Wilson (1886). The first tension-field action theory for web panels was developed by Wagner (1931) and his work was extended by Kuhn (1956) for aircraft design. Basler (1961a) developed the first mathematical model to quantify the post-buckling shear resistance due to tension-field action of plate girders for structural engineering applications.

1.3.2 Basler's Theory

Basler assumed that the tension-field action can develop if the boundaries can provide enough resistance to the tension-field force. Since tension-field action takes place in the web diagonally [see Figure 1.3 (b)], the boundaries that comprise the girder flanges and the transverse stiffeners of neighboring panels should resist the horizontal

and vertical component of the diagonal tension-field force. Basler also assumed that the flanges are too flexible to resist the vertical force induced by the tension-field force, so tension-field action cannot take place along the flanges. Instead, vertical component of the tension-field force can be resolved by the transverse stiffeners, while the horizontal component is resisted by the neighboring panels. Thus, the boundary along the transverse stiffeners can effectively resist all forces induced by tension-field force.

For an interior panel, the resulting tension band based on this assumption is shown in Figure 1.4(a). The inclination of the yield band is defined by the angle of θ, which was chosen to maximize the web shear strength. To evaluate the post-buckling strength due to tension-field action, Basler first cut a section horizontally at mid-depth and vertically at the middle of the panels so that the diagonal tensile stress lied over the free-body (see Figure 1.5). From the free-body diagram, taking the horizontal force equilibrium and moment equilibrium at point "O" gives

$$\sum F_x = 0:$$

$$\Delta F_f = \sigma_t t_w d_o \sin\theta\cos\theta = \frac{d_o}{2}\sigma_t t_w \sin 2\theta \tag{1.1}$$

$$\sum M_O = 0:$$

$$\Delta F_f = \frac{d_o}{D} V_{tf} \tag{1.2}$$

$\sin 2\theta$ in Eq. (1.1) is equal to $\dfrac{1}{\sqrt{1+(d_o/D)^2}}$. The shear strength due to tension-field action can be determined by substituting Eq. (1.2) into Eq. (1.1).

$$V_{tf} = \frac{\sigma_t (D t_w)}{2}\left[\frac{1}{\sqrt{1+(d_o/D)^2}}\right] \tag{1.3}$$

Basler also derived the tension-field stress (σ_t) by assuming that the superposition of the buckling stress and the inclined membrane tensile stress satisfies the yield condition. A two-dimensional view of the element in a state of pure shear is shown in Figure 1.6(a). The same state of plane stress can be described on any other coordinate system, such as x'-y' in Figure 1.6 (b). This x'-y' coordinate system is generated from the x-y coordinate system by a counterclockwise rotation of θ. By

cutting along the dashed line in Figure 1.6 (a) and drawing the free-body diagram of the wedge-shape, the stress components in the rotated coordinate system can be determined. The stresses must first be multiplied by the areas of the sides of the triangular element to obtain forces. For convenience, the hypotenuse is taken to be of unit length, and the element thickness is assumed to be unity. The resulting free-body is shown in Figure 1.7(a). Taking horizontal and vertical equilibriums of the free-body gives two equations:

$$\sum F_x = 0;$$

$$-\sigma'_y \sin\theta - \tau' \cos\theta + \tau_{cr} \cos\theta = 0 \tag{1.4}$$

$$\sum F_y = 0;$$

$$\sigma'_y \cos\theta - \tau' \sin\theta - \tau_{cr} \sin\theta = 0 \tag{1.5}$$

Solving simultaneous Eqs. (1.4) and (1.5) gives

$$\begin{aligned} \sigma'_y &= \tau_{cr} \sin 2\theta \\ \tau' &= \tau_{cr} \cos 2\theta \end{aligned} \tag{1.6}$$

By substituting (θ +90°) into σ'_y, normal stress σ'_x becomes $-\tau_{cr} \sin 2\theta$. After shear buckling occurs, membrane tension-field stress develops as shown in Figure 1.7 (b). Superposition of the two stress conditions in the direction of y' yields

$$\begin{aligned} \sigma'_x &= -\tau_{cr} \sin 2\theta \\ \sigma'_y &= \tau_{cr} \sin 2\theta + \sigma_t \\ \tau' &= \tau_{cr} \cos 2\theta \end{aligned} \tag{1.7}$$

In a two-dimensional plane stress state, von Mises yield condition can be defined as

$$\sigma_M^2 = F_{yw}^2 = (\sigma'_x)^2 + (\sigma'_y)^2 - (\sigma'_x)(\sigma'_y) + 3(\tau')^2 \tag{1.8}$$

where F_{yw} is web yield stress. Substituting Eq. (1.7) into Eq. (1.8) gives the tension-field stress

$$\sigma_t = -\frac{3}{2}\tau_{cr} \sin 2\theta + \sqrt{F_{yw}^2 + \tau_{cr}^2 \left[\left(\frac{3}{2} \sin 2\theta \right)^2 - 3 \right]} \tag{1.9}$$

To simplify the solution, Basler assumed a linear approximation of the von Mises yield condition on the ellipse between points A and B (see Figure 1.8). The equation of the straight line is $\sigma_1 = F_{yw} + \sigma_2\left(\sqrt{3}-1\right)$. Also, assuming $\theta = 45°$, $\sigma_x^{'}$ and $\sigma_y^{'}$ in Eq. (1.7) become principal stresses $\sigma_1 = \tau_{cr} + \sigma_t$, and $\sigma_2 = -\tau_{cr}$, respectively. Therefore, as an approximated form of the yield condition, the simple solution for the tension-field stress is

$$\sigma_t = F_{yw}\left(1 - \frac{\tau_{cr}}{\tau_y}\right) \tag{1.10}$$

where τ_y is shear yield stress ($= F_{yw}/\sqrt{3}$) Substituting Eq. (1.10) into Eq. (1.3), the post-buckling strength due to tension-field action is

$$V_{tf} = \frac{F_{yw} D t_w}{2} \frac{\left(1 - \frac{\tau_{cr}}{\tau_y}\right)}{\sqrt{1 + (d_o / D)^2}} = V_p \frac{0.87(1-C)}{\sqrt{1 + (d_o / D)^2}} \tag{1.11}$$

where $V_p = \frac{F_{yw} D t_w}{\sqrt{3}}$, $C = \frac{\tau_{cr}}{\tau_y}$, and $\tau_y = \frac{F_{yw}}{\sqrt{3}}$. Eq. (1.11) is currently adopted in the AASHTO Specifications (2014) for calculating the shear strength of interior panels. The AISC Specifications (2010) also has a similar form, but with τ_y approximated as $0.6F_{yw}$.

1.3.3 Brief Review of Various Tension-Field Theories

After Basler's theory was developed, a number of researchers have proposed alternate tension-field stress models for predicting the ultimate shear strength of the web. Most of the works addressing tension-field action were summarized in Ajam (1986) and SSRC (2010). Figure 1.4 presents the various tension-field models.

Basler (1960, 1961a, 1961b), Takeuchi (1964), Rockey and Skaloud (1972), Herzog (1974), and Porter et. al. (1975) assumed that a diagonal tension-field develops in a limited portion of the web. Fujii (1968, 1971), Chern and Ostapenko (1969) and Komatsu (1971) assumed that a diagonal tension-field develops in a much larger region

in the web panel, but the intensity of the diagonal tension varies across the perpendicular direction of the tension diagonal (Yoo and Lee, 2006).

Takeuchi (1964) first considered the effect of flange out-of-plane stiffness on the web yield band. He assumed that the tension-field stress extends to the distances c_1 and c_2 along the top and bottom flanges, respectively. These distances were also assumed to be proportional to the moment of inertia of the flanges. Although his model could not provide a good correlation with the test results, the flange stiffness effects were considered in all other researchers' models afterwards. Therefore, all models in Figure 1.4 except Basler's model show that plastic hinges develop on both flanges, and the diagonal tension-field action acts on both flanges and sides of the transverse stiffeners.

Chern and Ostapenko (1969), Rockey and Skaloud (1972), and Porter et al. assumed that a portion of the web interacts with the flanges and was included in computing the plastic moments of the flanges. Therefore, a T-shaped flange section including a portion of the web was used to determine the flange plastic moment.

Only Porter et al. (1975) assumed that the tension-field stress angle is different from the angle of the tension-field zone. In this model, the inclined angle of the tension-field stress was assumed to be two-third of the angle of the panel diagonal with respect to the flange. The ultimate shear strength was then determined by iteration.

Hoglund first developed his theory in 1971 (Hoglund, 1971) for the girders with bearing stiffeners at the supports only, and later (1997) extended his theory to include girders with intermediate stiffeners. As shown in Figure 1.4(i), Hoglund replaced the web by a system of tension and compression bars that intersected one another perpendicularly. The inclination of the bars changed as the load increased. It was observed that the compression bars carried a constant stress which was equal to the shear buckling stress, while the stress in the tension bars increased as the angle between the tension bars and the flanges decreased (Ajam, 1986). He also considered the shear contribution of the flanges and formulated an empirical solution for the ultimate shear strength of the panel. His solution was adopted by Eurocode 3 (2006).

Lee and Woo (1998, 1999) conducted a number of finite-element analyses varying the web depth-to-thickness ratio and the web width-to-depth ratio. Based on the findings, they suggested a simple empirical solution for the ultimate shear strength.

They also demonstrated the accuracy of the empirical solution through an experimental study.

Note that all studies summarized in this section are for interior panels.

1.4 US Plate Girder Shear Design Practice

1.4.1 General

Since both US design methods [AASHTO Specifications (2014) for bridge design and AISC Specifications (2010) for building design] adopt Basler's theory, tension-field action is only allowed for interior panels whose boundaries comprise the flanges and intermediate stiffeners of neighboring panels. Since end panels do not have a neighboring panel adjacent to the bearing stiffener pair, they do not qualify for tension-field action.

1.4.2 Interior Panels

Based on AASHTO Specifications (2014), the nominal shear resistance (V_n) of a stiffened interior web panel is given by

$$V_n = V_p\left[C + \frac{0.87(1-C)}{\sqrt{1+(d_0/D)^2}}\right] \qquad \text{for } \frac{2Dt_w}{(b_{fc}t_{fc}+b_{ft}t_{ft})} \le 2.5 \tag{1.12}$$

$$V_n = V_p\left[C + \frac{0.87(1-C)}{\sqrt{1+(d_0/D)^2}+(d_0/D)}\right] \qquad \text{for } \frac{2Dt_w}{(b_{fc}t_{fc}+b_{ft}t_{ft})} > 2.5 \tag{1.13}$$

$$V_p = \frac{1}{\sqrt{3}}F_{yw}Dt_w = 0.58F_{yw}Dt_w \tag{1.14}$$

where

d_0 = transverse stiffener spacing (in.),

D = web depth (clear distance between flanges, in.),

t_w = web thickness (in.),

b_{fc} = width of compression flange (in.),

b_{ft} = width of tension flange (in.),

t_{fc} = thickness of compression flange (in.),

t_{ft} = thickness of tension flange (in.),

F_{yw} = web yield stress (ksi),

V_p = plastic shear force or shear yield strength (kips), and

C = ratio of the shear buckling strength to the shear yield strength.

The shear buckling strength to shear yield strength ratio, C, can be determined as follows:

$$C = 1.0 \qquad \text{if} \quad \frac{D}{t_w} \le 1.12\sqrt{\frac{Ek}{F_{yw}}} \tag{1.15}$$

$$C = \frac{1.12}{D/t_w}\sqrt{\frac{Ek}{F_{yw}}} \qquad \text{if} \quad 1.12\sqrt{\frac{Ek}{F_{yw}}} \le \frac{D}{t_w} \le 1.40\sqrt{\frac{Ek}{F_{yw}}} \tag{1.16}$$

$$C = \frac{1.57}{(D/t_w)^2}\left(\frac{Ek}{F_{yw}}\right) \qquad \text{if} \quad \frac{D}{t_w} > 1.40\sqrt{\frac{Ek}{F_{yw}}} \tag{1.17}$$

where

E = modulus of elasticitity of steel

k = shear buckling coefficient $\left(= 5 + \frac{5}{(d_0/D)^2}\right)$

Note that the shear buckling coefficient (k) is a simplification of two exact equations based on simply supported boundary conditions. The exact solutions for k is given by (Timoshenko and Gere, 1961)

$$k_{exact} = \begin{cases} 4 + \dfrac{5.34}{(d_0/D)^2} & \text{for } \dfrac{d_0}{D} < 1 \\ 5.34 + \dfrac{4}{(d_0/D)^2} & \text{for } \dfrac{d_0}{D} \ge 1 \end{cases} \tag{1.18}$$

1.5 End Panels

The first and second terms on the right-hand side of Eq. (1.12) are the shear strength components due to beam action and tension-field action, respectively. Since an end panel does not have a neighboring panel beyond the support to anchor the horizontal component of the tension-field action, the AASHTO Specifications (2014) only considers the beam action in computing its nominal shear resistance:

$$V_n = CV_p \tag{1.19}$$

The constant C should be calculated based on Eqs. (1.15) through (1.17). In addition, AASHTO limits the width-to-depth ratio (d_0 / D) of the end panel to 1.5.

1.6 Statement of Problem

Based on Basler's tension-field action theory, design shear strength equations were first introduced in the 11th Edition of the AASHTO Standard Specifications (1973). In the Specifications (11th Edition), shear capacities of both interior and end panels were the same. Later, the shear capacity of end panels was reduced in AASHTO 12th Edition (1977). In AASHTO Interim Specifications (1986), the current format of the end panel shear strength equations was introduced.

Since the maximum shear occurs at the support, the end web panel may become the controlling component for steel girder design, evaluation and load rating (AASHTO 2011). AASHTO LRFD Specifications (7th Edition, 2014) does not provide any provisions to allow the end web panel to be designed for tension-field action. As a result, many steel girder bridges in which the end shear controls have a rating factor below 1.0. Rating factors less than 1.0 require that the bridges must be strengthened or vehicular loading on the bridge must be restricted.

However, Basler (1961a), whose equation became the basis of shear design for plate girders in AASHTO Specifications (2014), pointed out that a partial tension-field action may occur in the end panel because some amount of horizontal force can be anchored by the bearing stiffeners and the extended web portion. But since the degree of post-buckling strength was uncertain, he conservatively ignored it.

There may be another source of increase in shear strength at the end panel: concrete deck shear strength. Plate girders in bridges are almost always used in conjunction with concrete slabs, which are able to resist some amount of shear. However, the contribution of concrete deck is not considered for the shear strength design in AASHTO Specifications (2014).

The current AASHTO Specifications may be too conservative in the shear design of plate girder end panels. This is especially true for the rating of existing steel plate girder bridges. Among others, California Department of Transportation (Caltrans) has identified many existing steel girder bridges that require retrofit based on the current ASHTO method, although these bridges have performed well in the past few decades. To avoid unnecessary retrofit, it is necessary to develop more accurate and practical shear design equations for the end panel that include the potential contributions from both tension-field action and the concrete slab.

1.7 Shear Resistance in End Panels

Huslid and Rockey (1979) experimentally and analytically studied end panel behavior. With a total of 8 specimens, they conducted 13 tests by repairing the specimens. Although the specimen sizes were very small (the ultimate panel shear strength achieved from the testing varied from 4.8 kips to 13.7 kips), the test results showed the contribution of tension-field action in the end panels. Figure 1.9 shows their tension-field model to predict the ultimate shear strength for the end panels. Their analytical model was extended by a study of the interior panels conducted by Porter et al. (1975). The study found that the tension-field stress angle differed from the angle of the tension band, and that the inclined angle of the tension-field stress must be determined to maximize the shear strength. With their model, an iterative method was necessary to determine the ultimate shear strength.

Safar (2013) conducted a nonlinear finite element parametric study with 64 plate girder end panels. The parameters included configurations of bearing stiffeners (e.g., having no bearing stiffeners, a one-sided bearing stiffener, one pair of bearing stiffeners, and two pairs of bearing stiffeners), flange thickness-to-web thickness ratio, web depth-

to-thickness ratio, and web width-to-depth ratio. Based on the numerical results, an empirical solution was suggested for the ultimate end panel shear strength.

In current European design methods, the basic design concept is similar to that of the US. However, there are two major differences in the Eurocode 3 (CEN 2006) design procedure. First, Eurocode 3 provides the plate girder shear strength as a summation of the contributions from the web and flanges. Secondly, Eurocode 3 considers a partial post-buckling strength in the end panel. Figure 1.10(a) shows the rigid end post at the support, which has an additional pair of stiffeners at the end of the girder to generate the tension-field action; and the panel with the rigid end post is treated as an interior panel. Figure 1.10(b) shows the non-rigid end post at the support that is treated as an end panel as in US design practice. But since the end post and bearing stiffeners at the support have a limited ability to serve as an anchor for the horizontal component of the tension-field force, Eurocode 3 accounts for its partial post-buckling strength which is less than that of the interior panel.

First, consider the shear resistance of the girder web. The non-dimensional web slenderness ratio, $\overline{\lambda}_w$, for the end panel is defined in Eurocode 3 as

$$\overline{\lambda}_w = \frac{D}{37.4\varepsilon t_w \sqrt{k_{exact}}} \tag{1.20}$$

where $\varepsilon = \sqrt{235/F_y}$, F_y is the yield stress (MPa), and k_{exact} is presented in Eq. (1.18). Based on $\overline{\lambda}_w$, a reduction factor for the shear resistance of the web χ_w is determined (see Table 1.1 and Figure 1.11) for both rigid end posts (interior panels) and non-rigid end posts (end panels). In the table, η is the coefficient that considers the increase of shear resistance at smaller web depth-to-thickness ratios. It is recommended that η=1.2 for steel grades of S235 ($F_y = 235$ MPa = 34.1 ksi) to S460 ($F_y = 460$ MPa = 66.7 ksi) and η=1.0 for steel grades over S460. Then, the shear strength contribution from the web ($V_{bw,Rd}$) is given by

$$V_{bw,Rd} = \frac{\chi_w F_{yw} D t_w}{\sqrt{3}\gamma_{M1}} \tag{1.21}$$

where γ_{M1} is a factor for the partial resistance to instability which may be chosen in the range 1.0 to 1.10.

Next, consider the shear resistance from the flanges. Eurocode 3 includes the contribution of the flanges to the shear resistance. When the flange resistance is not completely utilized in resisting the bending moment ($M_{Ed} < M_{f,Rd}$), the contribution from the flanges should be obtained as follows:

$$V_{bf,Rd} = \frac{b_f t_f^2 F_{yf}}{c\gamma_{M1}} \left[1 - \left(\frac{M_{Ed}}{M_{f,Rd}} \right)^2 \right] \tag{1.22}$$

where b_f is the effective flange width taken as no greater than $15\varepsilon t_f$ on each side of the web, t_f is the flange thickness, F_{yf} is the flange yield stress, M_{Ed} is the design bending moment in a web panel, and $M_{f,Rd}$ is the moment of resistance of the cross section consisting of the effective area of the flanges only, and c is the width of the portion of the web between the plastic hinges, which is approximated by

$$c = d_0 \left(0.25 + \frac{1.6 b_f t_f^2 F_{yf}}{t_w D^2 F_{yw}} \right) \tag{1.23}$$

By summing up the shear resistances contributed from the web and flanges, the design shear resistance of a panel $V_{b,Rd}$ is given by

$$V_{b,Rd} = V_{bw,Rd} + V_{bf,Rd} \le \frac{\eta F_{yw} D t_w}{\sqrt{3}\gamma_{M1}} \tag{1.24}$$

The last term in Eq. (1.24) represents the shear yield strength.

1.8 Steel-Concrete Composite Plate Girder

There were no studies that directly address the shear strength of the end panels of steel-concrete composite plate girders. All available literature on composite plate girders addressed the behavior of interior panels in composite plate girders.

Allison et al. (1982) conducted an experimental study to investigate the contribution of the concrete slab on the post-buckling strength of the steel web under combined shear and negative bending. One steel plate girder specimen and five steel-

concrete composite plate girder specimens were tested. All specimens had transversely stiffened webs and a web depth-to-thickness ratio of 130. Also, the ratios of steel girder depth-to-slab thickness were 4.6 and 9.2. Test results showed that the increase in shear strength of the interior panels due to the concrete slab varied from 2.8% to 6.6%.

Shanmugam and Baskar (2003) experimentally tested a total of six specimens with a web width-to-depth ratio of 1.5. Among them, two specimens were bare steel plate girders with web depth-to-thickness ratios of 250 and 150. Among four composite girders, two composite girders had a reinforced concrete slab, and the other two composite girders had a reinforced concrete slab with shear links. The ratio of girder depth-to-slab thickness was 5 for all composite girders. The test results showed that the increase of shear strength in the interior panels due to the concrete slab without and with shear links was 76% and 122% for the web depth-to-thickness ratio of 250 and 40% and 68% for the ratio of 150, respectively.

Nie et al. (2004) tested a total of sixteen simply supported steel-concrete composite specimens and two plain steel girders. Test results shows that the concrete slab resisted 33% ~ 56% of the total ultimate shear. Based on the test results, an empirical solution based on an additive formula of the shear strengths of the concrete slab and steel girder was suggested for calculating the shear strength of the composite girder.

Liang et al. (2005) suggested that the contributions of the concrete slab and composite action should be incorporated into the vertical shear strength in design codes. A numerical study was carried out to quantify the contributions of the concrete slab and composite action. They showed that the ultimate shear strength of the composite girder is a function of the degree of shear connection and proposed an empirical solution.

Darehshouri et al. (2012) suggested an analytical model to predict the ultimate shear strength of steel-concrete composite girders. Full composite action was assumed in this model. The virtual work method was used to determine the post-buckling strength for the steel girder. The plastic hinges were assumed to form in the flanges. The top flange and concrete slab were assumed to be a composite flange with an increased top flange flexural strength, resulting in the plastic hinge in top flange being located further away from the intersection of the top flange and the transverse stiffeners. The optimum value of the angle of the tension-field stress was determined by trial and

error to give the maximum value of shear strength. The concrete slab was separated into two regions along its width to determine its shear strength: the first region of the slab had the same width as the top flange of the steel girder and the second region was the remaining slab width. A strut-tie model was used to determine the shear strength in the first region, while the ACI (2005) equation for beam shear strength was used for the second region. Note that they considered the full slab width as effective in resisting shear. The ultimate shear strength of the composite girders was an additive formula of the shear strengths of the concrete slab and steel beam.

1.9 Scope and Objectives

The main objective of this study is to investigate the shear behaviors of end panels in steel plate girders experimentally and analytically. Specifically, the aim is to explore the contributions from the tension-field action and the composite action of the concrete slab; both of which are ignored in the current design specifications. Design equations that include these effects and are practical for potential code adoption are to be proposed.

1.10 Organization of Report

This report begins with a general introduction and literature review of plate girders, shear load transfer mechanism, and shear design philosophy for both interior and end (exterior) panels. Since the test program consisted of two phases, this report summarizes the research results of each pahse separately.

Phase 1

A total of four specimens (two steel and two steel-concrete composite girders) were fabricated and tested in Phase 1. Chapters 2 and 3 describe the experimental test program and results, while Chapters 4 and 5 discuss the finite element analysis results including a correlation study with the test results, and parametric studies to identify factors affecting the shear strength of end panels. Chapter 6 presents an analytical work to develop practical shear design provisions for the end panels. Chapter 7 discusses rehabilitation schemes of end panels and proposes an effective scheme.

Phase 2

Additional four specimens with different panel width-to-depth ratios and depth-to-thickness ratio were tested in Pahse 2. Chapter 8 presents the experimental test program and results. Chapter 9 provides the finite element analysis results of the Phase 2 test specimens and compares the test results with the predicted shear strengths to verify the adequacy of the proposed shear strength equation.

Chapter 10 provides additional finite element analysis results for the effects of longitudinal stiffeners, small flange areas, noncompact web, and unequal top and bottom flanges. Chapter 11 presents the development of resistance factor based on the large-scale test specimens from this research program (Phases 1 and 2) and the small-scale test specimens from the literature. Chapter 12 summarizes and concludes the findings of these studies.

Table 1.1: Eurocode 3 Shear Resistance Reduction Factor (χ_w) of Web

$\overline{\lambda}_w$	Rigid End Post (Interior Panel)	Non-Rigid End Post (End Panel)
$\overline{\lambda}_w < 0.83/\eta$	η	η
$0.83/\eta \le \overline{\lambda}_w < 1.08$	$\frac{0.83}{\overline{\lambda}_w}$	$\frac{0.83}{\overline{\lambda}_w}$
$\overline{\lambda}_w \ge 1.08$	$\frac{1.37}{0.7+\overline{\lambda}_w}$	$\frac{0.83}{\overline{\lambda}_w}$

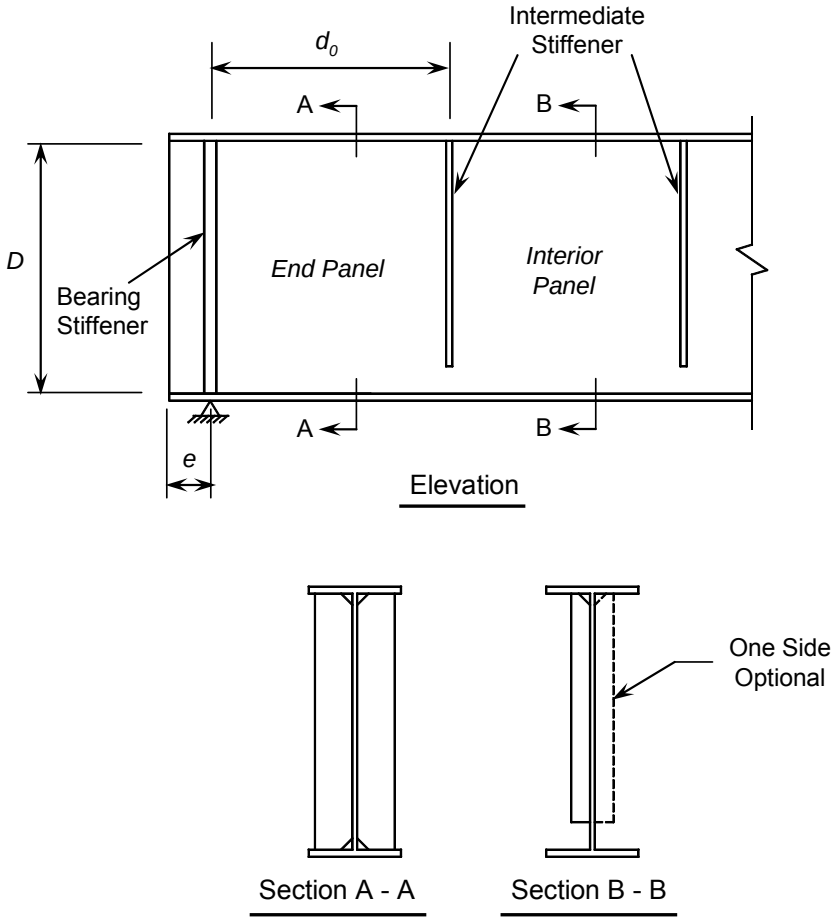

Figure 1.1: Typical Configuration of Steel Plate Girder

Figure 1.2: Typical Plate Girder (Caltrans Br. No. 50-0316)

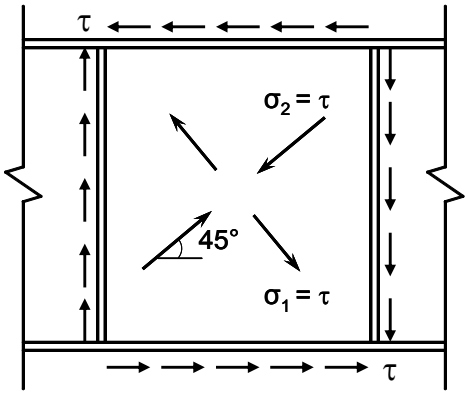

(a) Before Buckling

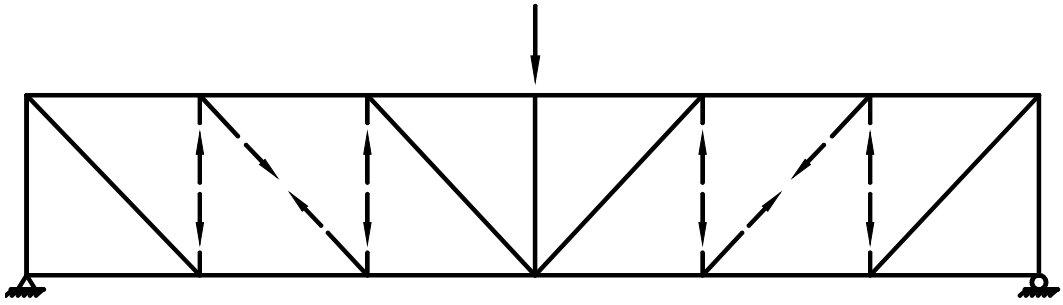

Pratt Truss

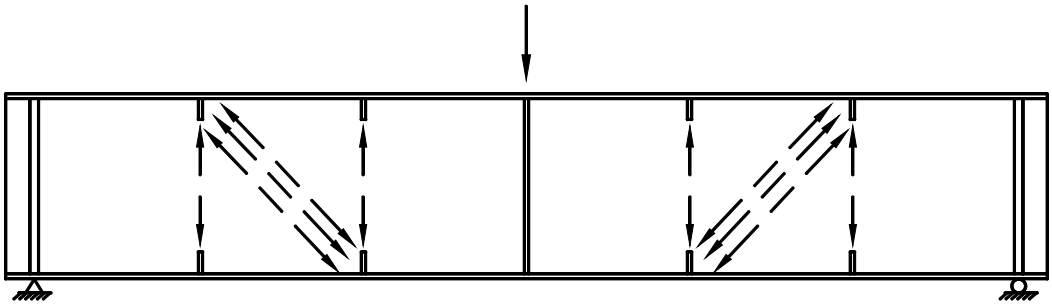

Plate Girder

(b) After Buckling (adapted from Yen and Basler, 1962)

Figure 1.3: Plate Girder Shear Load-Carrying Mechanism

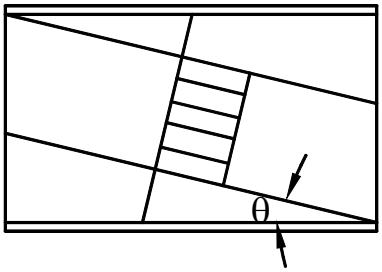

(a) Basler (1961a)

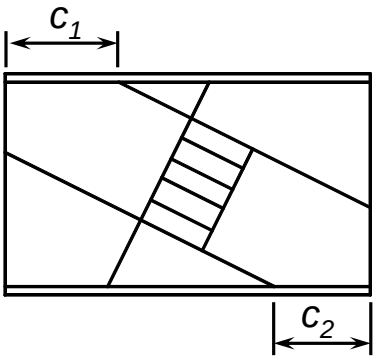

(b) Takeuchi (1964)

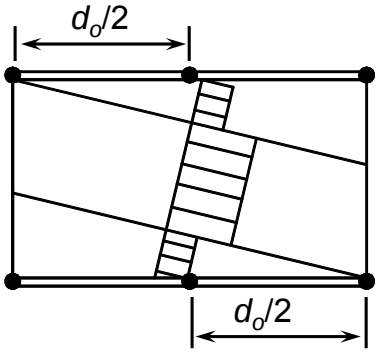

(c) Fujii

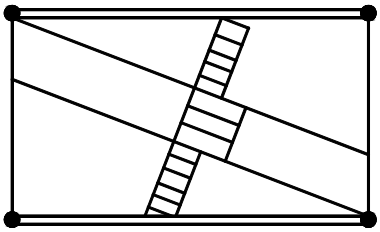

(d) Chern and Ostapenko (1969)

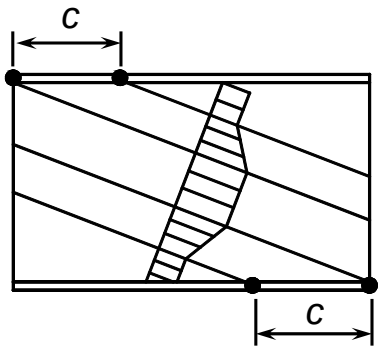

(e) Komatsu (1971)

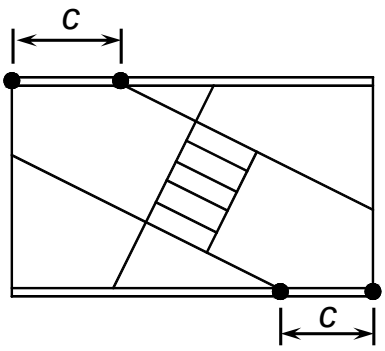

(f) Rockey and Skaloud (1972)

Figure 1.4: Various Tension-Field Models for Interior Panels

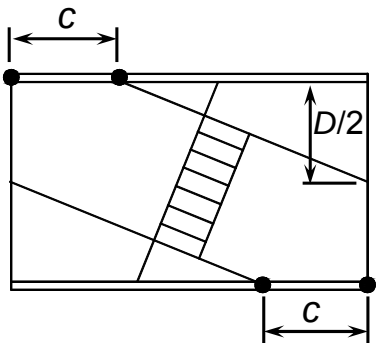

(g) Herzog (1974)

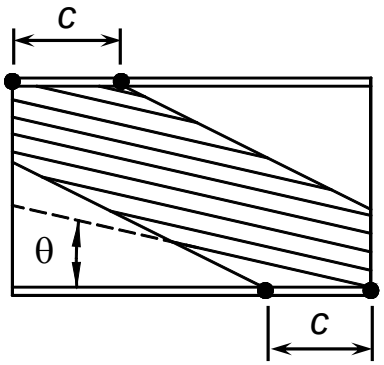

(h) Porter et al. (1975)

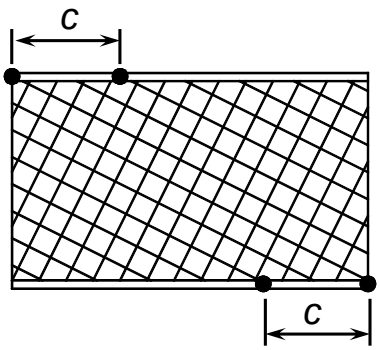

(i) Hoglund (1997)

Figure 1.4: Various Tension-Field Models for Interior Panels (continued)

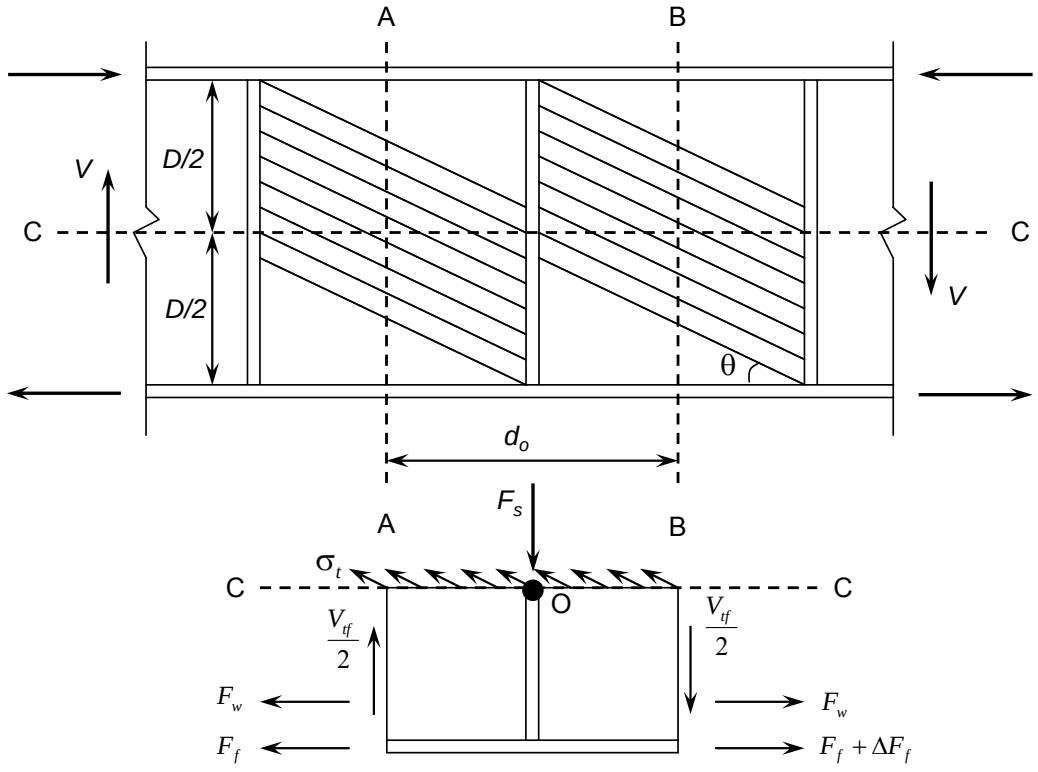

Figure 1.5: Free-Body Diagram from Basler (adapted from Basler, 1961a)

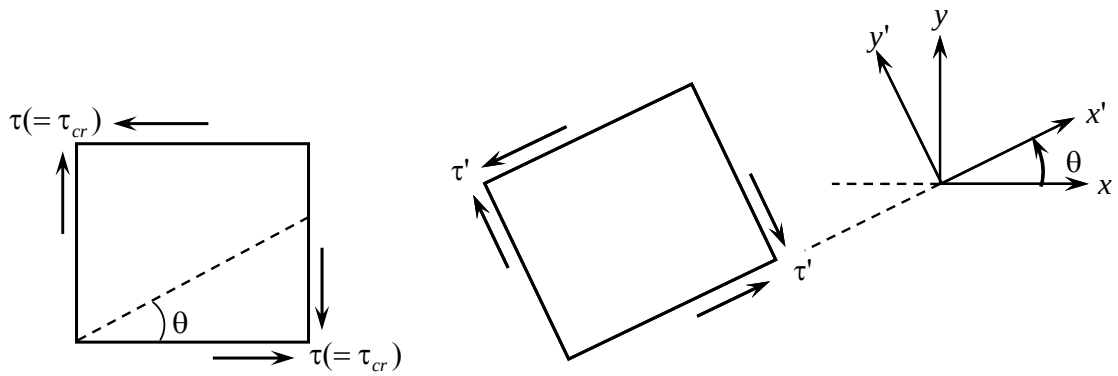

(a) Original Coordinate System (b) Rotated Coordinate System

Figure 1.6: Plane Stress in Pure Shear

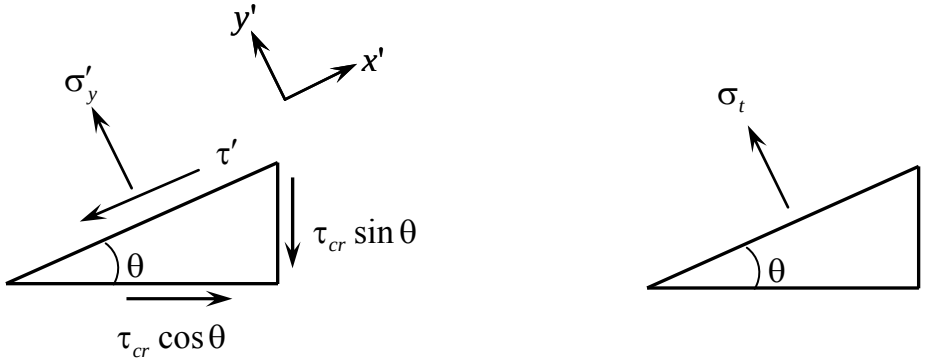

(a) due to shear buckling stress (b) due to membrane tensile stress

Figure 1.7: State of Stresses due to Shear Buckling and Tension-Field Action

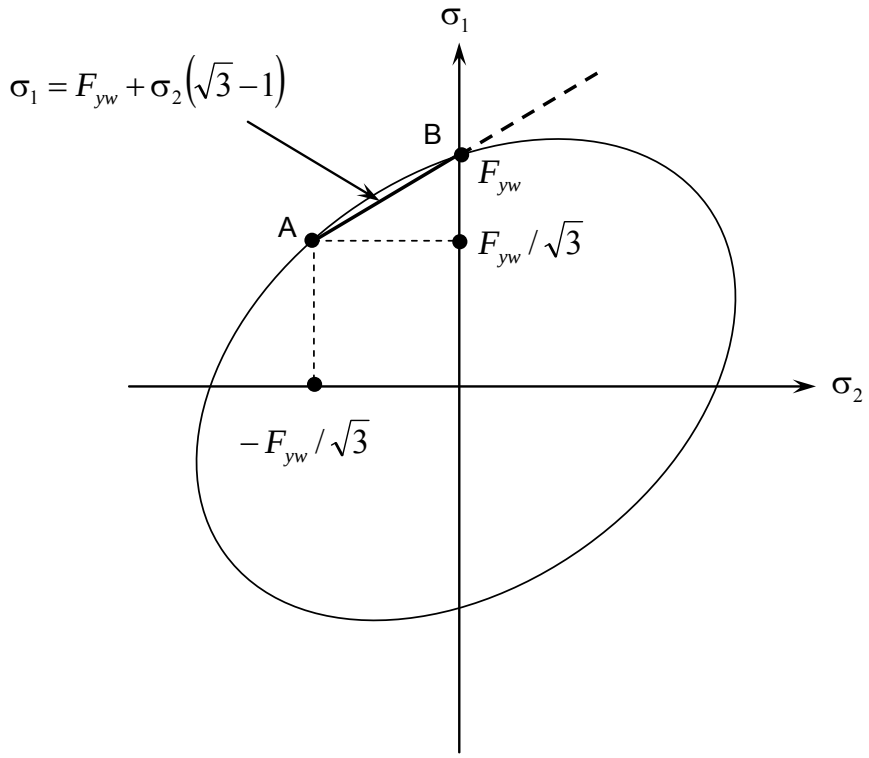

Figure 1.8: Von Mises Yield Condition (adapted from Basler, 1961a)

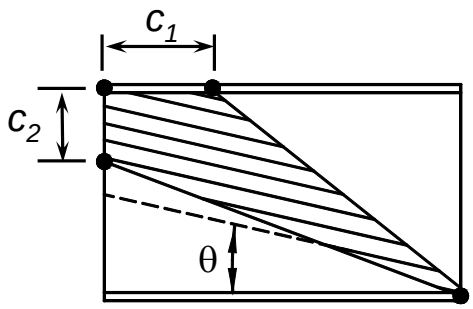

Figure 1.9: End Panel Tension-Field Model (adapted from Huslid and Rockey, 1979)

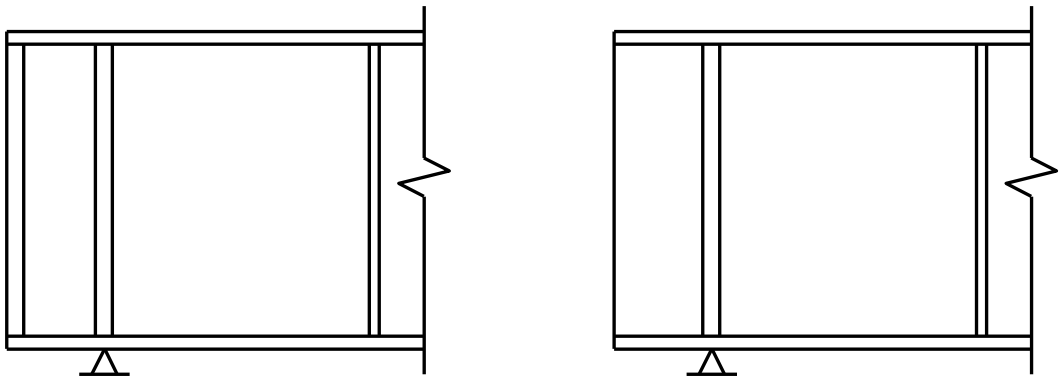

(a) Rigid End Post (b) Non-Rigid End Post

Figure 1.10: Different End Supports for Plate Girders

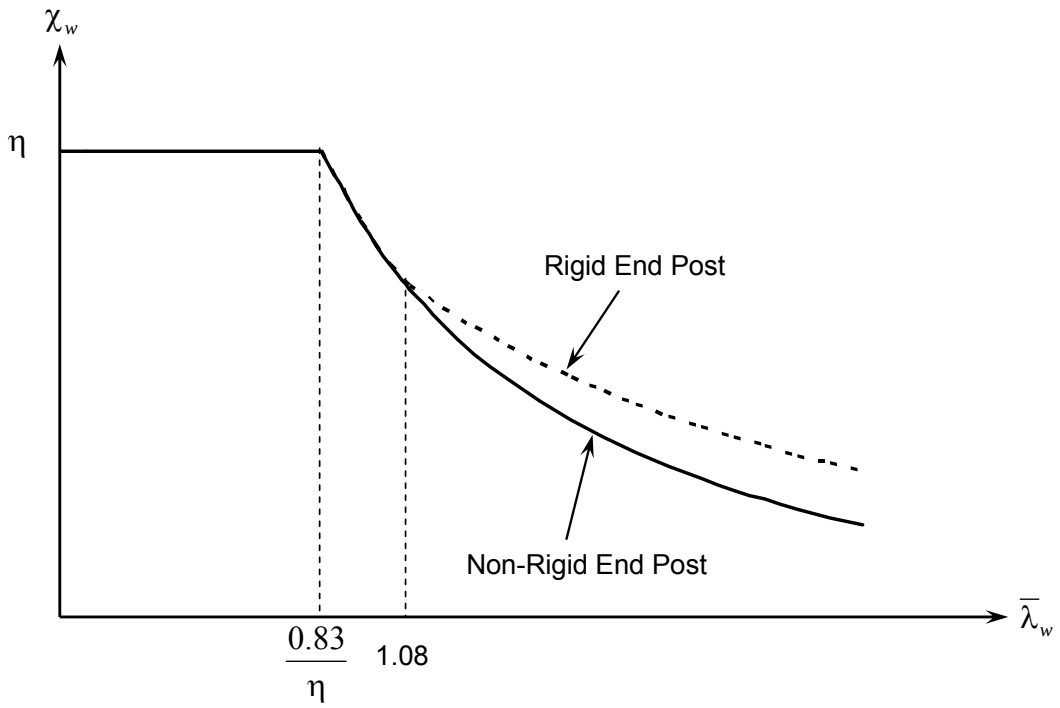

Figure 1.11: Eurocode 3 Shear Resistance Factor (χ_w) of Web

2. TEST PROGRAM (PHASE 1)

2.1 General

The primary objective of the testing program is to determine the ultimate shear resistance of the end panels of steel-concrete composite plate girders. In Phase 1 test program, a total of four test specimens were fabricated by a certified commercial fabricator and were designated as Specimens SG1, SG2, CG1 and CG2. The notation "SG," which stands for "Steel Girder," represents a steel girder without a concrete slab. The notation "CG," which stands for "Composite Girder", represents a steel girder with a concrete slab. Specimens SG1 and SG2 were tested first, then Specimens CG1 and CG2, which were nominally identical to the first two specimens, were subsequently tested to study the effects of the presence of a concrete slab.

2.2 Configuration and Fabrication of Test Specimens

2.2.1 Steel Girder Specimens (SG1 and SG2)

Table 2.1 shows the dimensions of two sample steel bridge girders provided by the California Department of Transportation (Caltrans) for Phase 1 test program. Table 2.2 shows the specimens dimensions used in Phase 1 testing. Depth-to-thickness ratio of 210 and 280 were used for Specimens SG1 and SG2, respectively. A panel width-to-depth ratio of 0.5 was used for both Specimen SG1 and SG2. The actual plate thicknesses of the specimens were measured and are summarized in Table 2.3.

For testing purpose, the sample girder dimensions from Caltrans were slightly modified. The width and thickness of the plates used for the top and bottom flanges of each girder were identical. In consideration for the capacities of the laboratory actuators, the sample girders were scaled down by 2/3 and 1/2 for Specimens SG1 and SG2, respectively.

Figure 2.1 shows the configuration of the test specimens. Flexural effects were minimized by designating a short span in order to study the shear behavior of the specimens.

2.2.2 Steel-Concrete Composite Girder Specimens (CG1 and CG2)

The girders of Specimens CG1 and CG2 were nominally identical to those of Specimens SG1 and SG2, respectively. Additionally, headed shear studs were welded to the top flanges of Specimens CG1 and CG2 to incorporate a concrete slab. A total slab thickness (t_c) and haunch depth (d_h) are shown in Table 2.2. Figure 2.2 and Figure 2.3 show the size of the shear studs, the geometry of concrete slab, and the steel reinforcement layout for Specimens CG1 and CG2, respectively.

Figure 2.4 shows the construction procedure of the concrete slab. First, formwork for the slab was built and reinforcements were placed. Concrete was then poured for Specimens CG1 and CG2 at the same time. A needle vibrator was used to compact the concrete during pouring. Then, the concrete was covered by plastic sheets to reduce the surface evaporation of water during curing.

2.3 Material Properties

2.3.1 Structural Steel Plates

ASTM A709 Grade 50 steel was specified for the flanges and web of the specimens, while ASTM A36 steel was specified for the bearing and intermediate transverse stiffeners to match those of the sample girders provided by Caltrans. Tensile coupons were cut from the same plates for material testing. The standard tensile coupon test results are shown in Figure 2.5. Average values of the measured mechanical properties of the component plates are summarized in Table 2.4.

2.3.2 Reinforcement and Concrete

Grade 40 reinforcement (No. 3 and No. 4 for Specimen CG1, and No. 3 for Specimen CG2) with a minimum yield strength of 40 ksi and a minimum ultimate strength of 70 ksi was used. Although No. 2 reinforcement bars were specified for the upper longitudinal direction in the concrete slab of Specimen CG2, No. 2 wires were used instead due to availability issues. Three samples of each size of reinforcement were tested. The tensile stress versus strain curves are shown in Figure 2.6. The average values of the measured mechanical properties are also summarized in Table 2.5.

A design concrete compressive strength of 4,000 psi with 3/8 in. river aggregate was specified for the concrete slab. A slump test was performed before casting the concrete; the measured slump was 3.5 in. A total of 18 cylinders were cast and cured under the same conditions as the test specimens to obtain the compressive and split tensile strengths of the concrete. Each three-cylinder set was tested for compressive strength on the 7^{th}, 14^{th}, 22^{nd} (day of testing for Specimen CG1), and 30^{th} day (day of testing for Specimen CG2), while another three-cylinder set was tested for spliting tensile strength on the day of testing for each composite specimen. Table 2.6 summarizes the average values of compressive and splitting tensile strengths from testing. Figure 2.7 plots the relationship between concrete compressive strength and curing time.

2.3.3 Shear Studs

Type B headed shear stud connectors made from ASTM A108 material with a minimum yield strength of 51 ksi and a minimum ultimate strength of 65 ksi was used for the interconnection of steel girder and concrete slab.

2.4 Initial Geometrical Imperfections

Initial geometrical imperfections of the steel girders were measured before testing. Figure 2.8 shows the measurement locations, and Figure 2.9 plots the measured imperfections. The measured web minimum and maximum imperfection values of each panel are also summarized in Table 2.7.

2.5 Test Setup and Loading Procedure

The overall configuration of the test setup is shown in Figure 2.10 for Specimens SG1 and SG2, and Figure 2.11 for Specimens CG1 and CG2. Each specimen was simply supported and monotonically loaded by two 500-kip hydraulic actuators. Figure 2.12 shows a close-up of the support detail. The load was applied to the top flange through a W36×302 loading beam at mid-span of the specimen, as shown in Figure 2.13. To easily detect yielding and buckling of the specimen, whitewash and 2 in. grid lines were applied to the web of the specimen. Testing was initially conducted in a load-control mode up to 90% of the nominal shear strength per AASHTO Specifications

(2014). Thereafter, testing was conducted in a displacement-control mode with a small increment of mid-span deflection until failure occurred.

Figure 2.14 shows the lateral bracing system. To avoid any unexpected failure mode, L6×4×½ lateral bracing was bolted to one side of the web at two locations along the girder length as shown in Figure 2.1. The other side of the lateral bracing was bolted to a WT6×85 connection piece that was bolted to a W18×97 support column. To accommodate the vertical deflection of the plate girder, the hole on the WT6×85 connection piece was slotted vertically; two bolts at this location were finger tightened.

2.6 Instrumentation

Test specimens were instrumented with a combination of displacement transducers, strain gage rosettes, and uni-axial strain gages to measure global and local responses at specific locations. Most displacement transducers measured the deformation of the flanges, web, and bearing stiffeners. One displacement transducer measured vertical displacement at the mid-span of each specimen and was used as the feedback sensor for actuator control. Strain gage rosettes measured the principal strains on the web panel, while uni-axial strain gages monitored the strains of flanges and bearing stiffeners. Load cells mounted on the actuators measured applied load. The instrumentation plan for each specimen is provided in Appendix A.

Table 2.1: Sample Caltrans Steel Bridge Girder Dimensions

Bridge No.	Section			Width-Depth Ratio, d_0/D	Depth-Thickness Ratio, D/t_w
	Top Flange (in.)	Web (in.)	Bottom Flange (in.)		
56-0571	20×1	83×3/8	24×1-1/8	0.58	221
39-0164L	28×1-1/4	106×3/8	28×1-1/4	0.45	283

Table 2.2: Specimen Dimensions

Spec. No.	Width-Depth Ratio, d_0/D	Depth-Thickness Ratio, D/t_w	Web Depth, D (in.)	Top and Bottom Flanges		Total Slab Thickness (t_c)/ Haunch Depth (d_h) (in.)	Scale Factor
				Thickness, t_f (in.)	Width, b_f (in.)		
SG1	0.5	210	52.5	0.75	16.0	No Slab	2/3
CG1						8.0 / 3.0	
SG2	0.5	280	52.5	0.625	14.0	No Slab	1/2
CG2						6.0 / 2.0	

Table 2.3: Steel Plate Thicknesses

Specimen No.	Component	Nominal Thickness (in.)	Measured Thickness (in.)
SG1 / CG1	Flanges	0.75	0.755
	Web	0.25	0.247
SG2 / CG2	Flanges	0.625	0.620
	Web	0.1875	0.183
SG1 / CG1 SG2 / CG2	Bearing Stiffener	1	1.009
	Intermediate Stiffener	0.5	0.496

Table 2.4: Average Mechanical Properties of Steel Plates

Specimen No.	Steel Grade	Component / Heat Number	Yield Stress (ksi)	Tensile Strength (ksi)	Elongation (%)
SG1, CG1	A709 Gr.50	Flanges / W9I542	57.8 (54.0)[a]	79.7 (75.0)	39.2[b] (26)[c]
		Web / NW7384	60.3 (58.5)	76.9 (74.5)	32.2[b] (24)[c]
SG2, CG2		Flanges / NW5341	51.5 (54.0)	71.9 (71.5)	39.2[b] (25.5)[c]
		Web / W2K713	57.4 (61.0)	80.0 (79.0)	29.2[b] (24)[c]
SG1, CG1, SG2, CG2	A36	Bearing Stiffener / NW8339	41.1 (41.9)	69.2 (67.5)	38.4[b] (33)[b]
		Intermediate Stiffener / E3B184	47.6 (49.0)	68.0 (66.0)	39.7[b] (28)[c]

Note:

a. Values in parentheses are based on Certified Mill Test Reports, others from tensile coupon tests at UCSD.

b. Elongation is based on 2 in. gage length.

c. Elongation is based on 8 in. gage length.

Table 2.5: Average Mechanical Properties of Steel Reinforcements

Bar Size	Yield Stress (ksi)	Tensile Strength (ksi)
No. 2	60.8	71.0
No. 3	48.5	69.0
No. 4	47.8	69.7

Table 2.6: Average Mechanical Properties of Concrete

Curing Period (Days)	Compressive Strength, f'_c (ksi)	Splitting Tensile Strength, f_t (ksi)
7	4.1	NA
14	4.7	NA
22 (Testing of CG1)	5.0	0.47
30 (Testing of CG2)	5.4	0.43

Table 2.7: Measured Initial Web Imperfections (in.)

Measured Initial Imperfections		Specimen No.			
		SG1	SG2	CG1	CG2
Panel 1	Min.	-0.109	-0.2	-0.203	-0.125
	Max.	0.016	0	0.109	0.125
Panel 2	Min.	-0.141	-0.25	-0.266	-0.047
	Max.	0.078	0.25	0.109	0.266
Panel 3	Min.	-0.156	-0.35	-0.156	-0.109
	Max.	0.031	0.15	0.094	0.141
Panel 4	Min.	-0.078	-0.25	-0.172	-0.125
	Max.	0.109	0.15	0.078	0.125

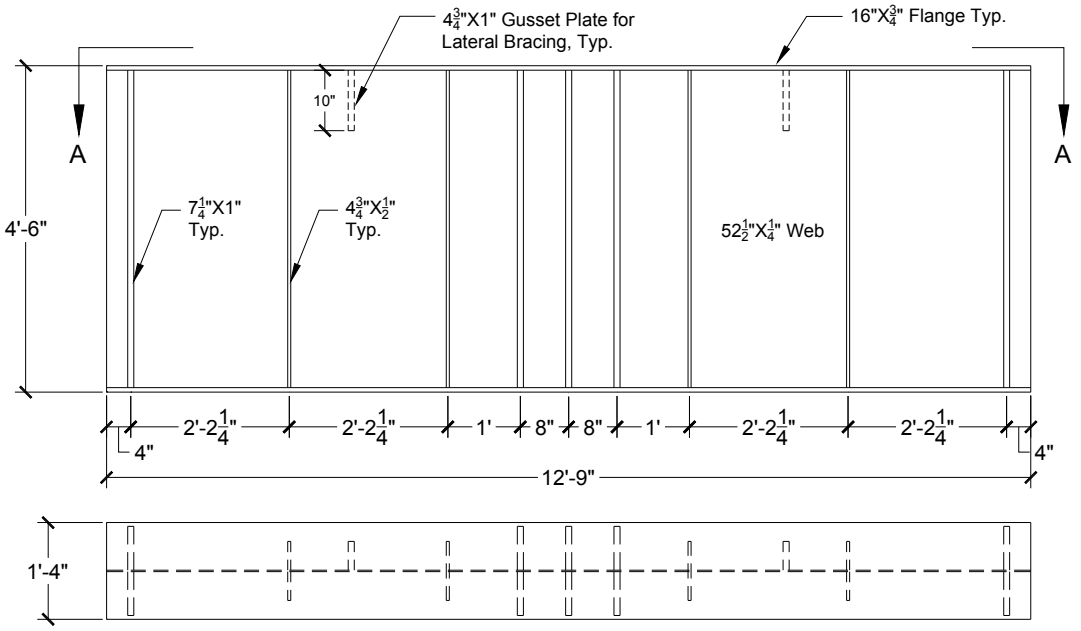

View A - A

(a) Specimen SG1

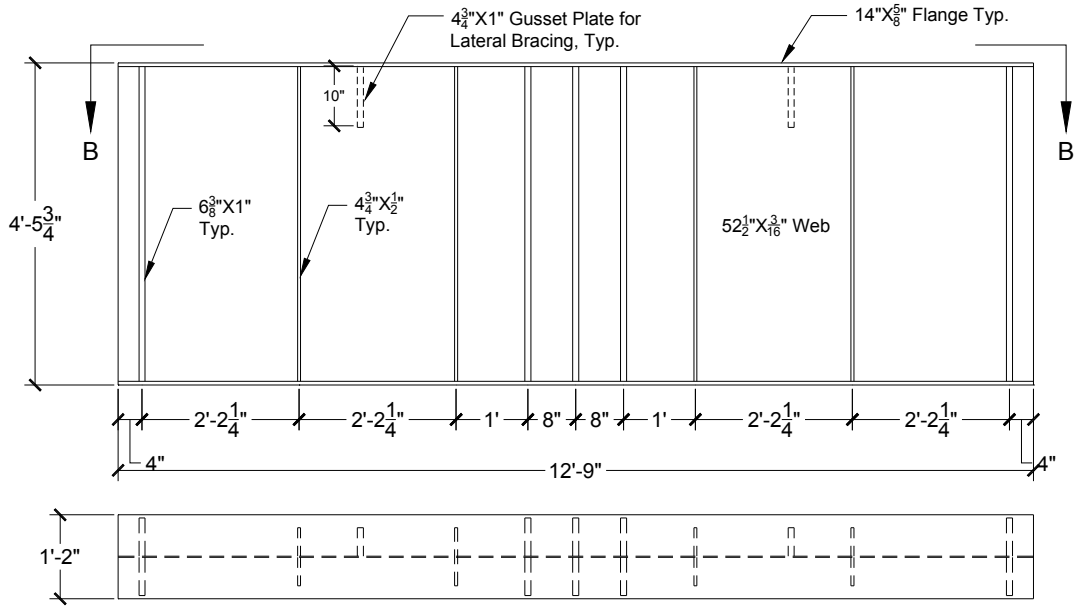

View B - B

(b) Specimen SG2

Figure 2.1: Configuration of Steel Girder Test Specimens

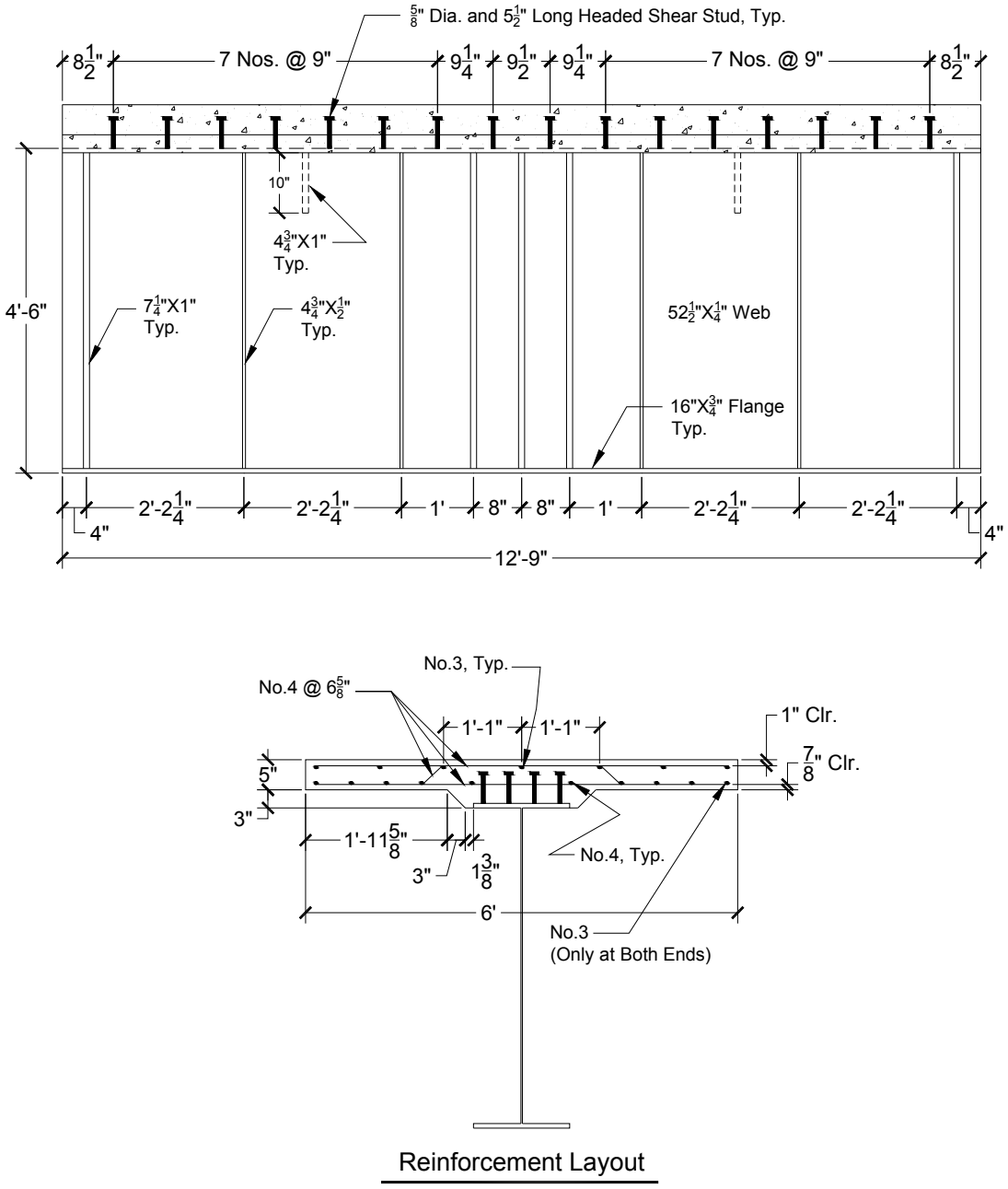

Figure 2.2: Specimen CG1: Configuration of Composite Girder Test Specimens

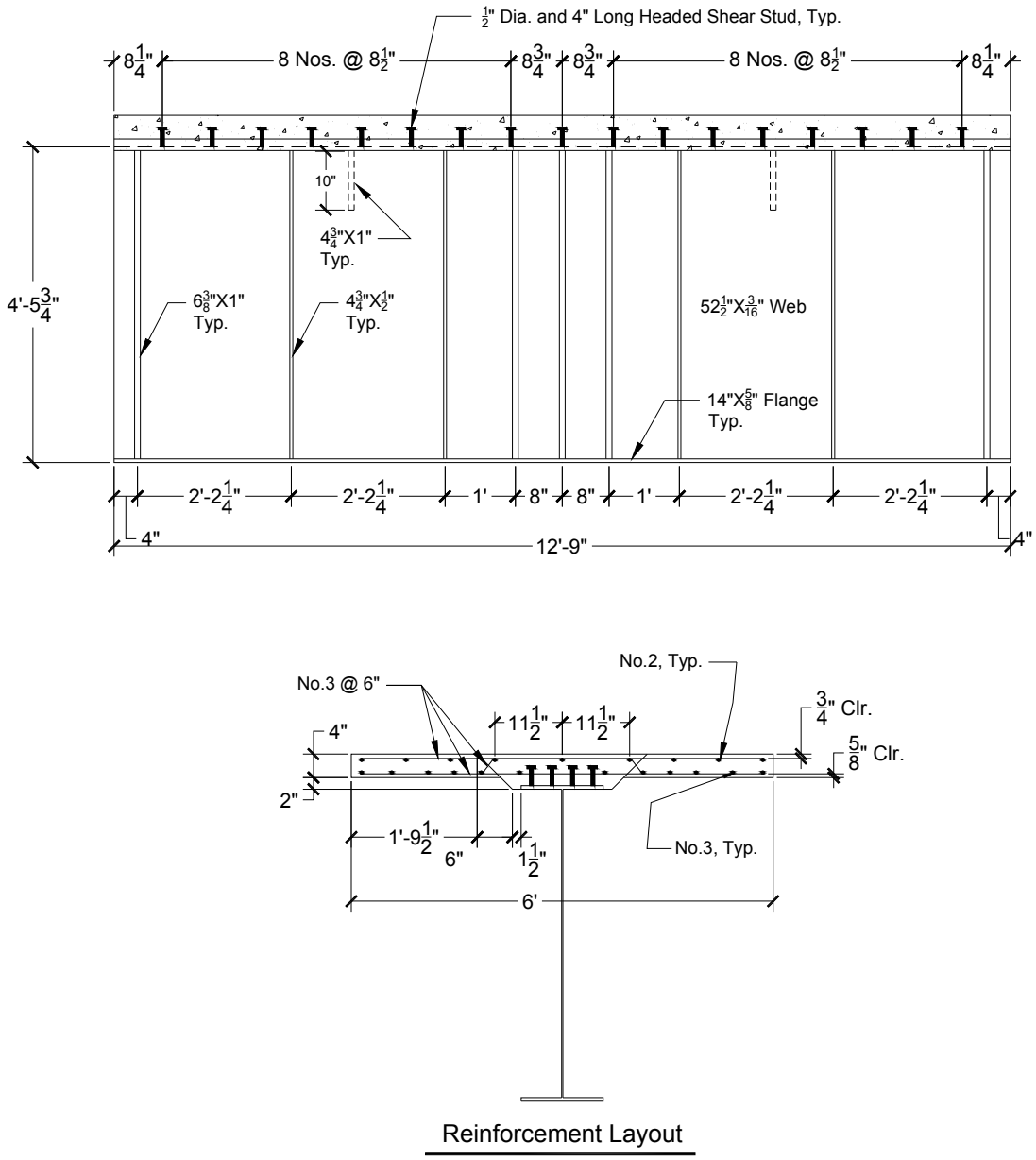

Figure 2.3: Specimen CG2: Configuration of Composite Girder Test Specimens

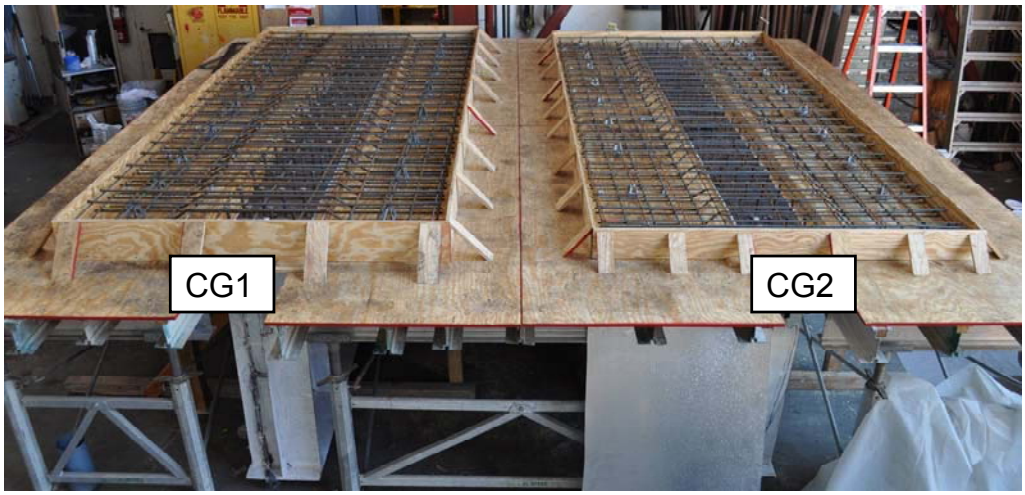

(a) Reinforcement Layout

(b) Pouring Concrete

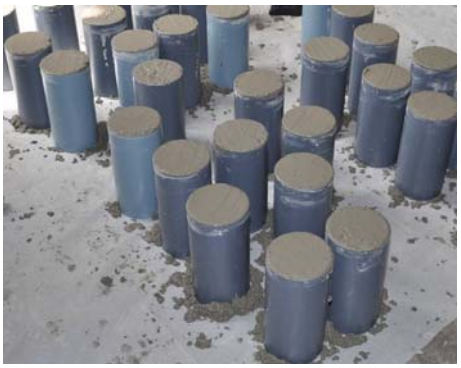

(c) Concrete Cylinders

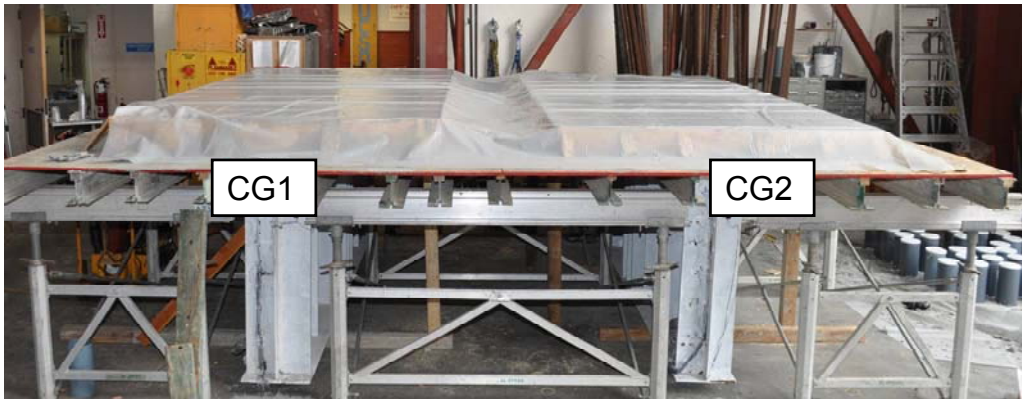

(d) Curing

Figure 2.4: Concrete Slab Construction

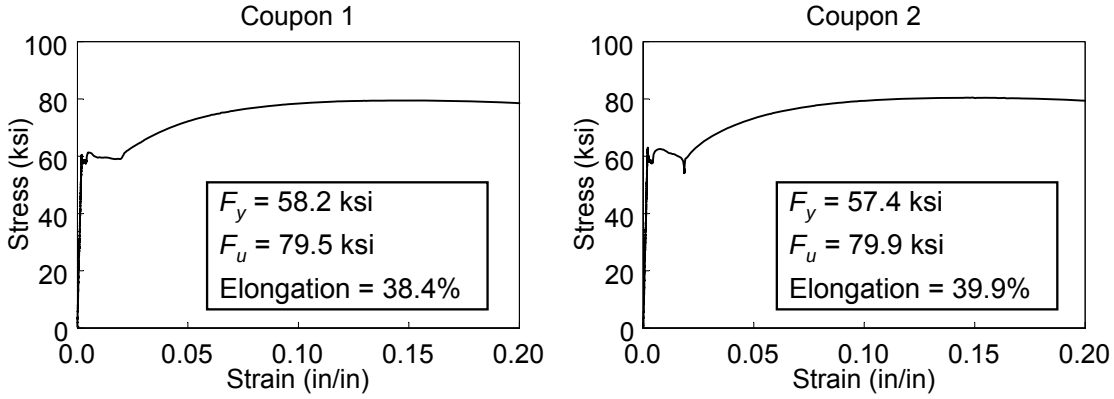

(a) Specimen SG1 Flange

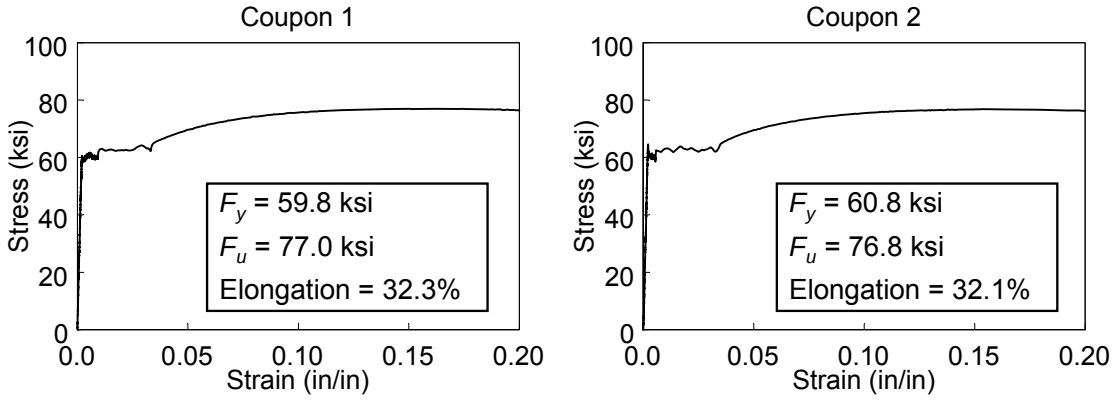

(b) Specimen SG1 Web

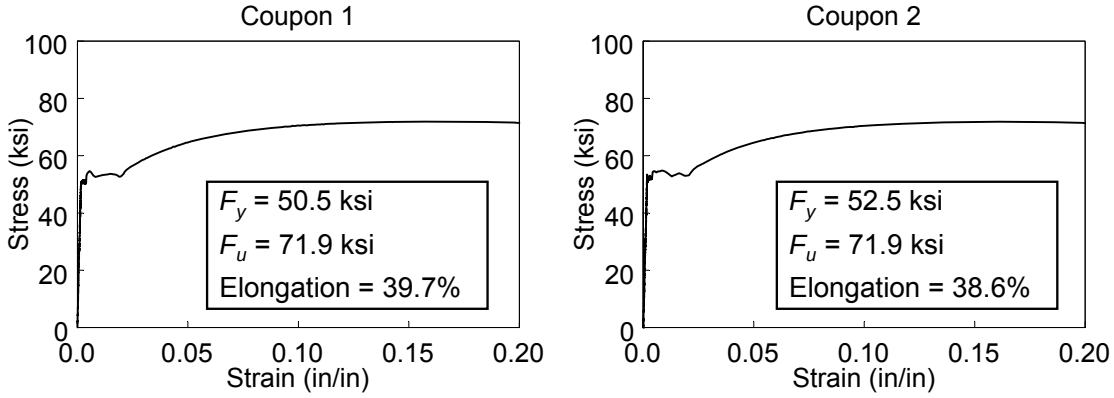

(c) Specimen SG2 Flange

Figure 2.5: Steel Plate Stress versus Strain Curves

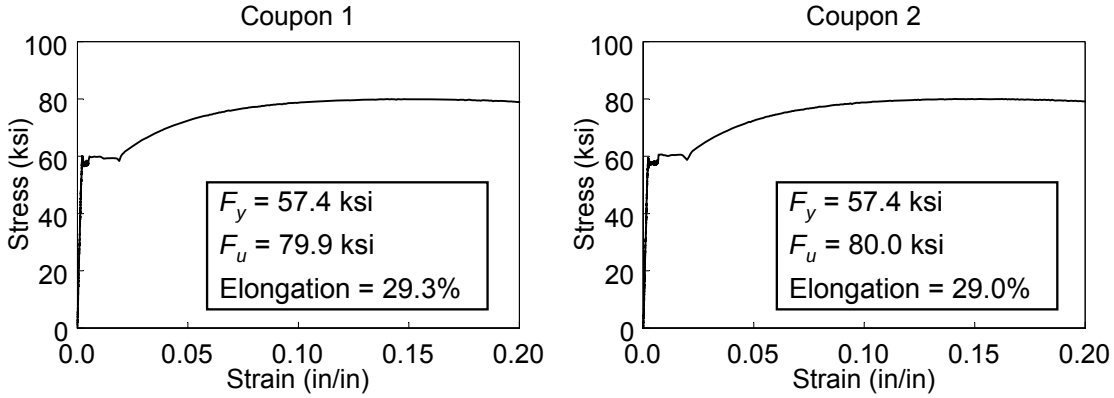

(d) Specimen SG2 Web

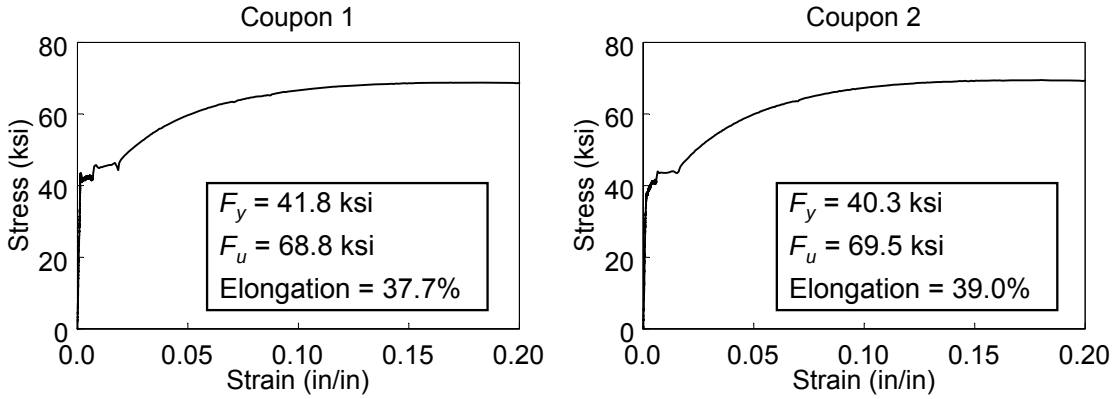

(e) Bearing Stiffener

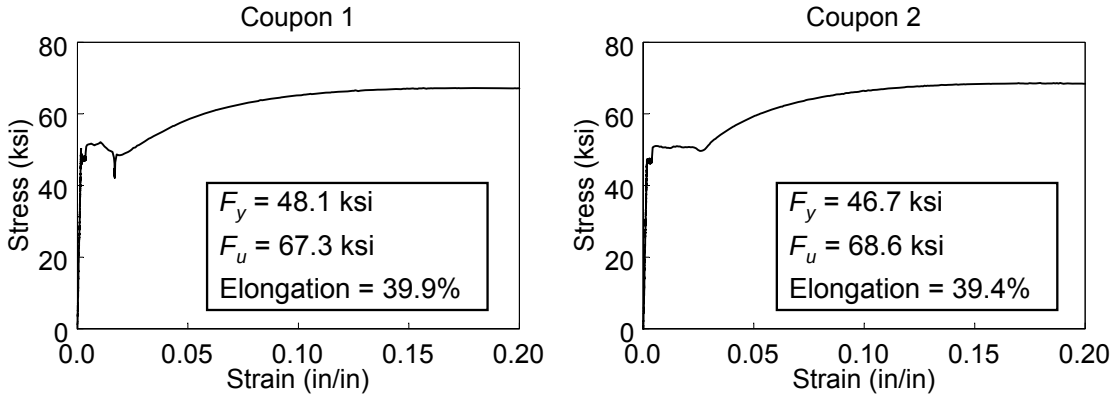

(f) Intermediate Stiffener

Figure 2.5: Steel Plate Stress versus Strain Curves (continued)

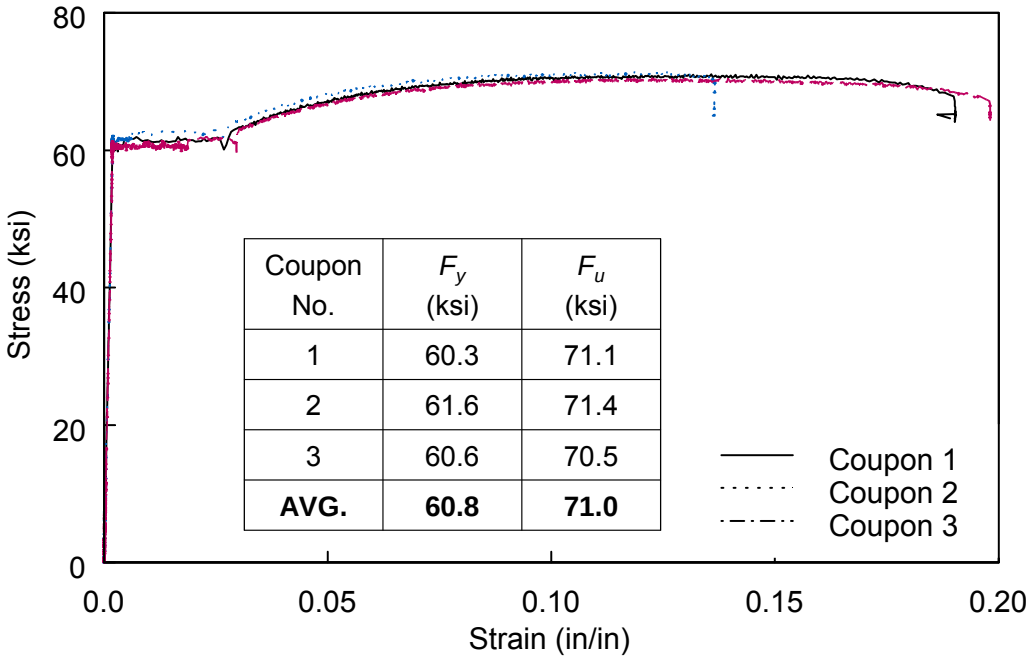

Coupon No.	F_y (ksi)	F_u (ksi)
1	60.3	71.1
2	61.6	71.4
3	60.6	70.5
AVG.	**60.8**	**71.0**

(a) No. 2 Reinforcement

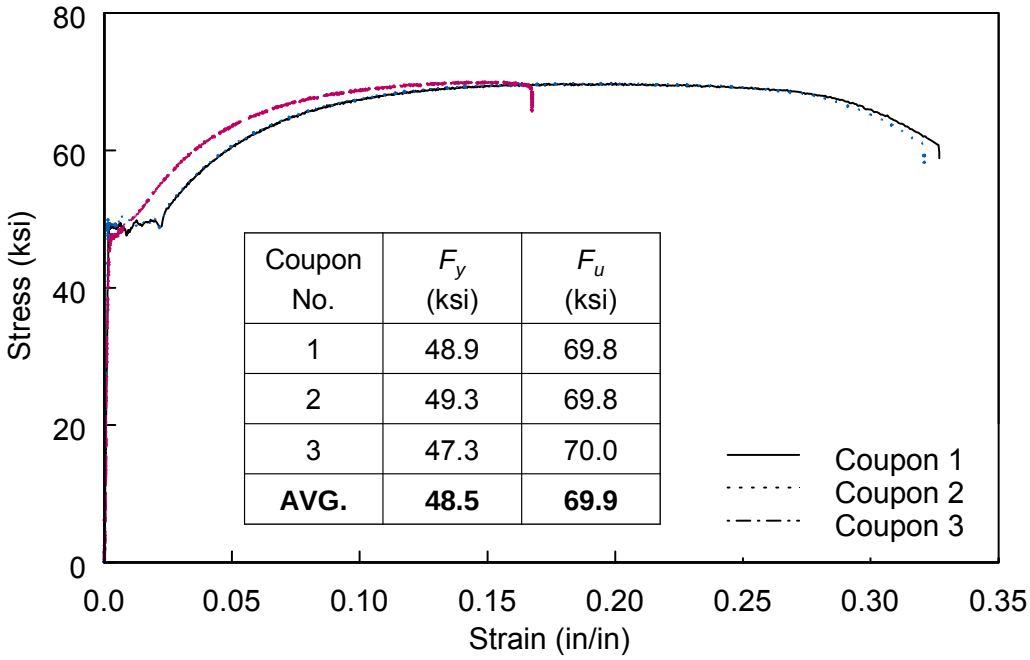

Coupon No.	F_y (ksi)	F_u (ksi)
1	48.9	69.8
2	49.3	69.8
3	47.3	70.0
AVG.	**48.5**	**69.9**

(b) No. 3 Reinforcement

Figure 2.6: Steel Reinforcement Stress versus Strain Curves

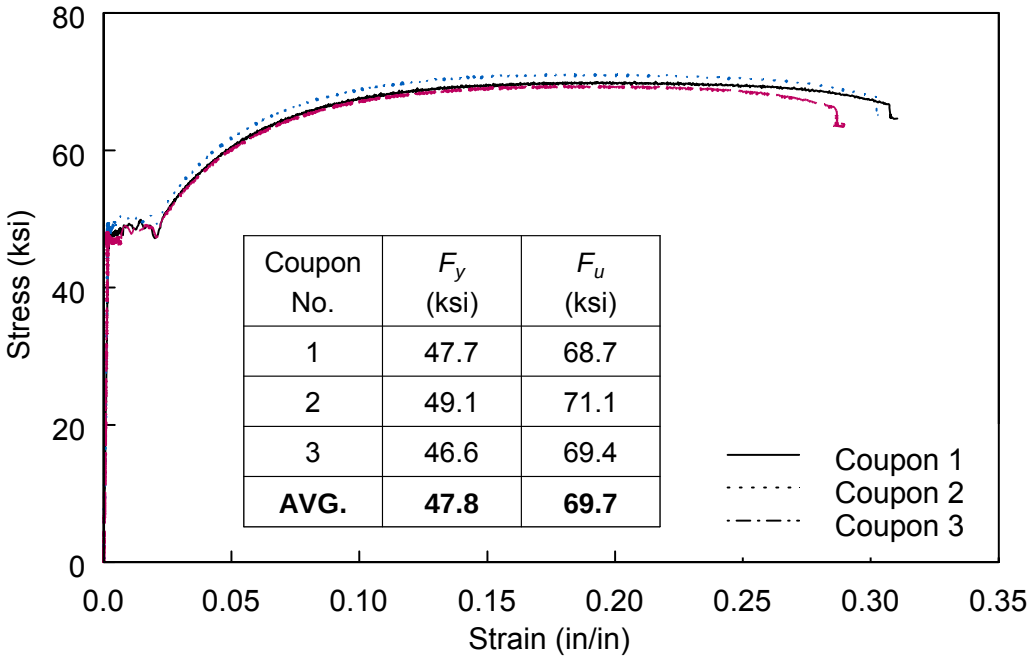

Coupon No.	F_y (ksi)	F_u (ksi)
1	47.7	68.7
2	49.1	71.1
3	46.6	69.4
AVG.	**47.8**	**69.7**

(c) No. 4 Reinforcement

Figure 2.6: Steel Reinforcement Stress versus Strain Curves (continued)

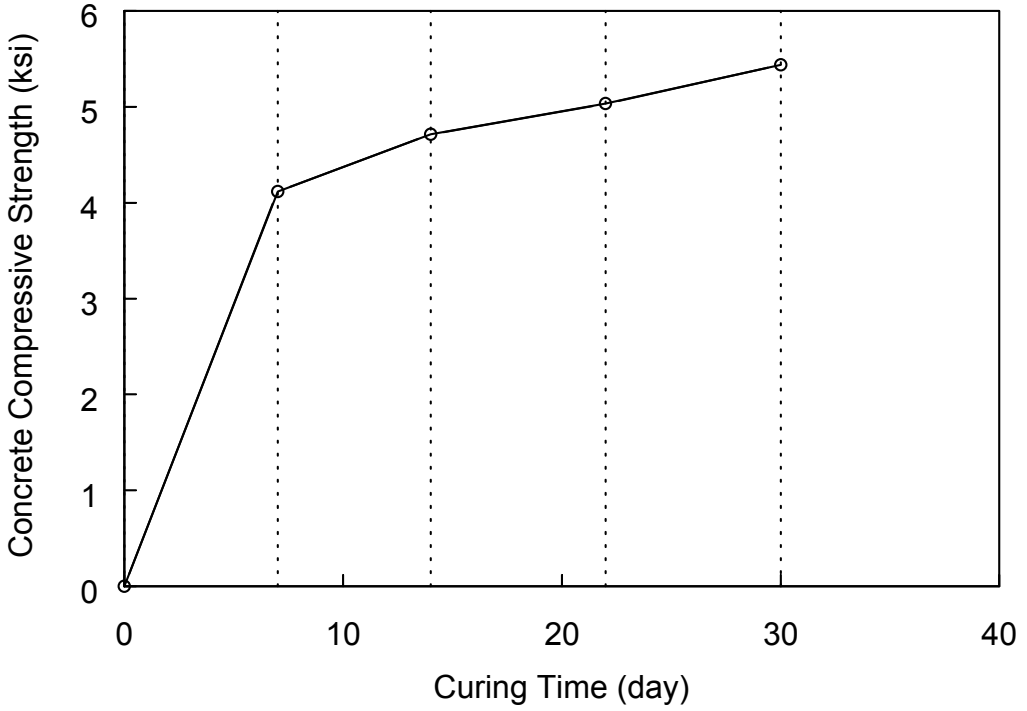

Figure 2.7: Concrete Cylinder Compressive Strength versus Curing Time

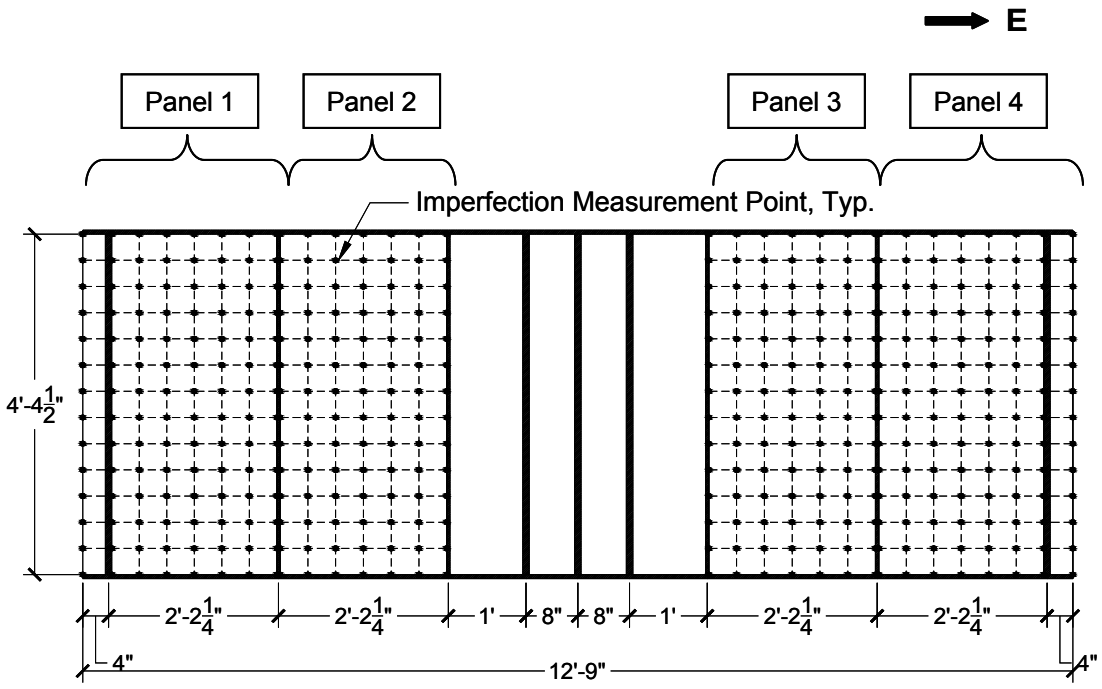

Figure 2.8: Measured Locations for Elevation ical Imperfections of Steel Girders

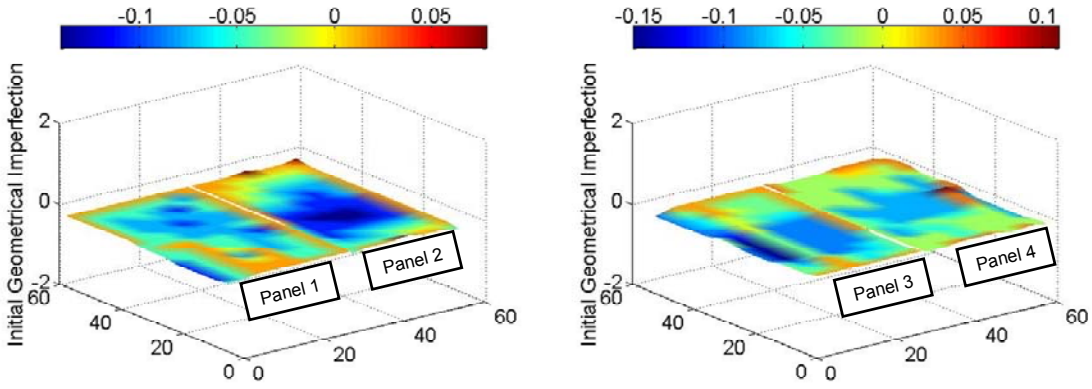

(a) SG1

Figure 2.9: Initial Geometrical Imperfection Measurements

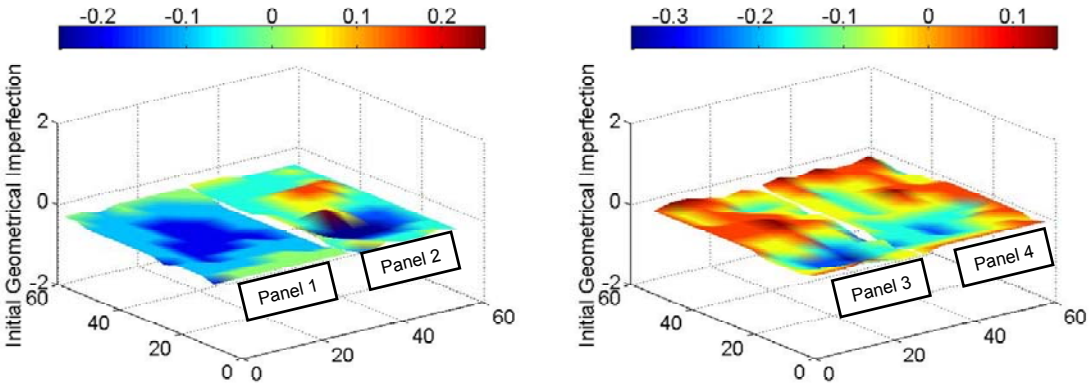

(b) SG2

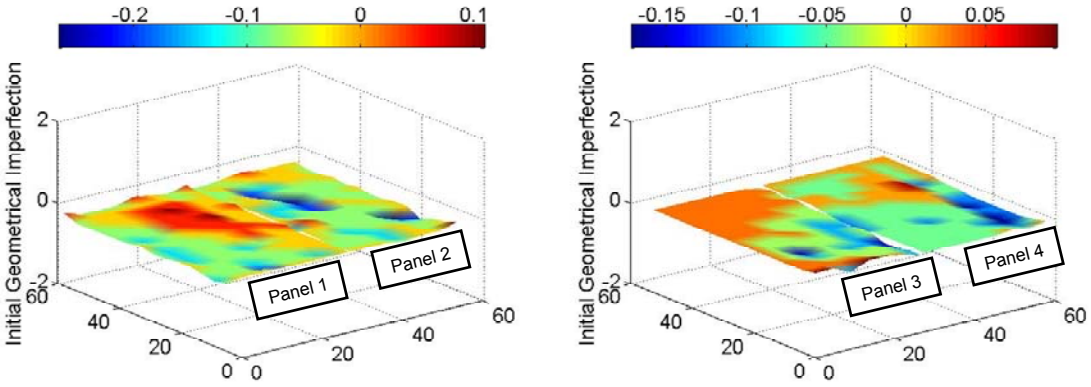

(c) CG1

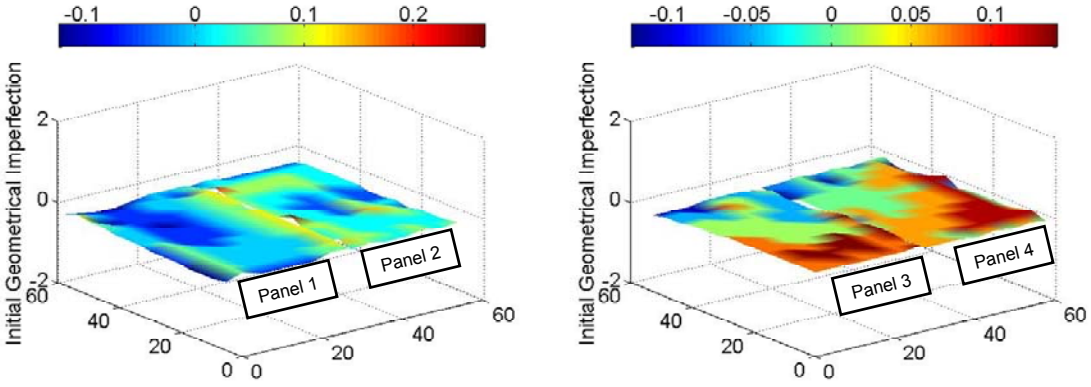

(d) CG2

Figure 2.9: Initial Geometrical Imperfection Measurements (continued)

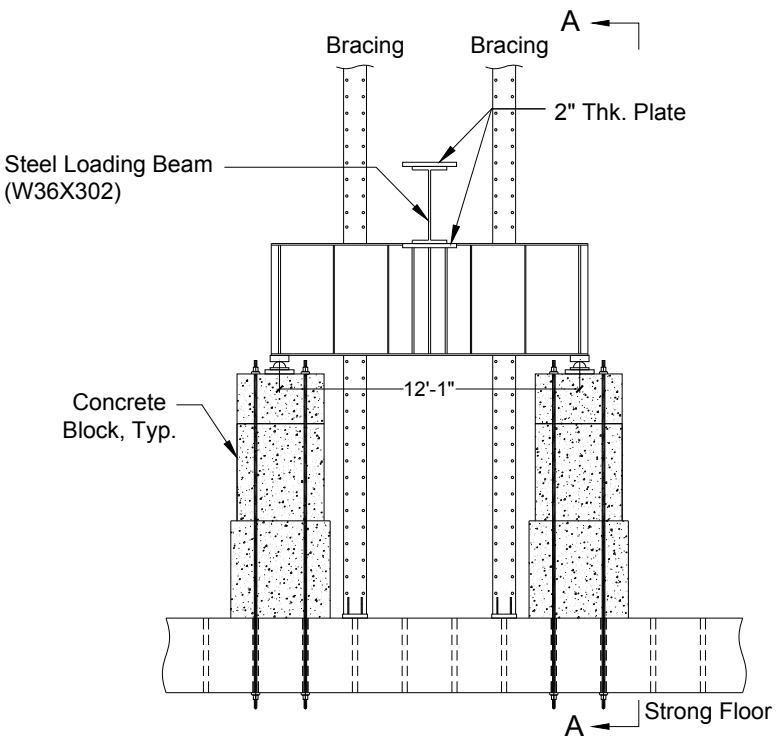

(a) Elevation

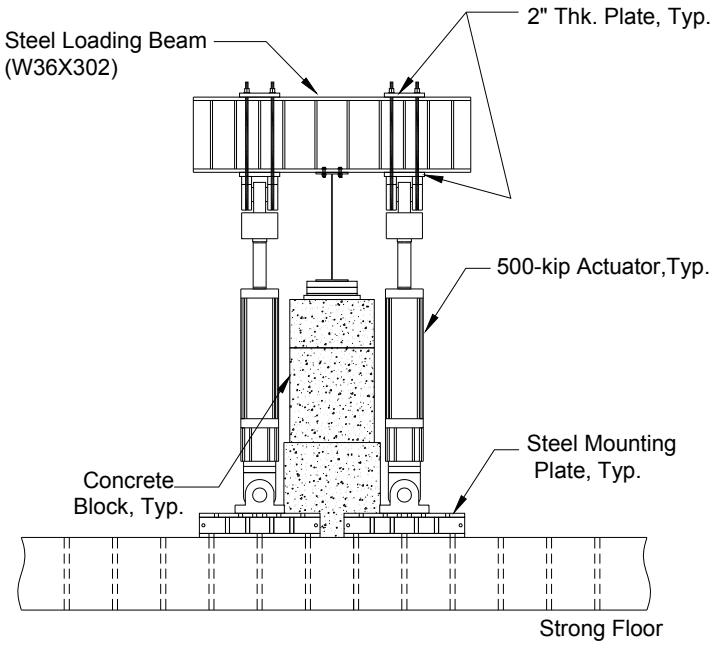

(b) View A - A

Figure 2.10: Test Setup: Specimens SG1 and SG2

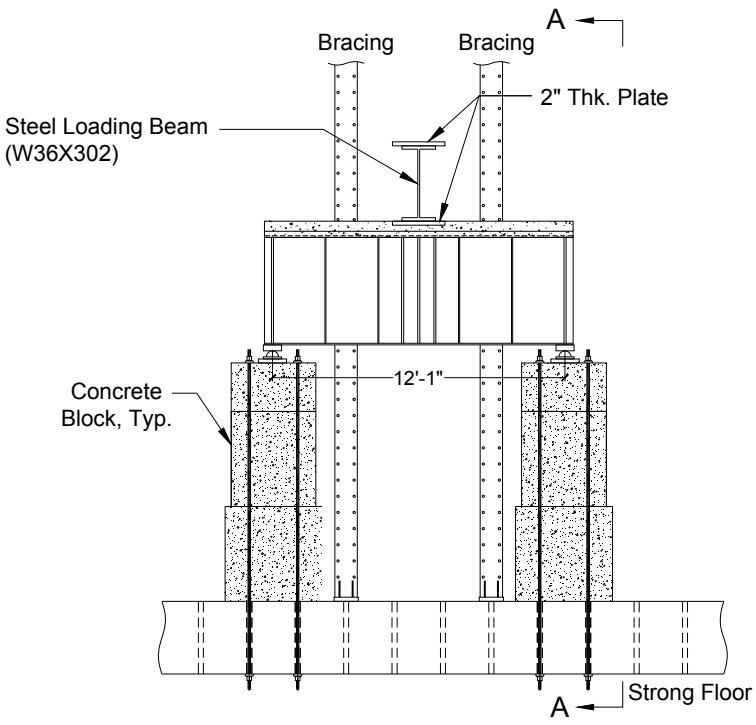

(a) Elevation

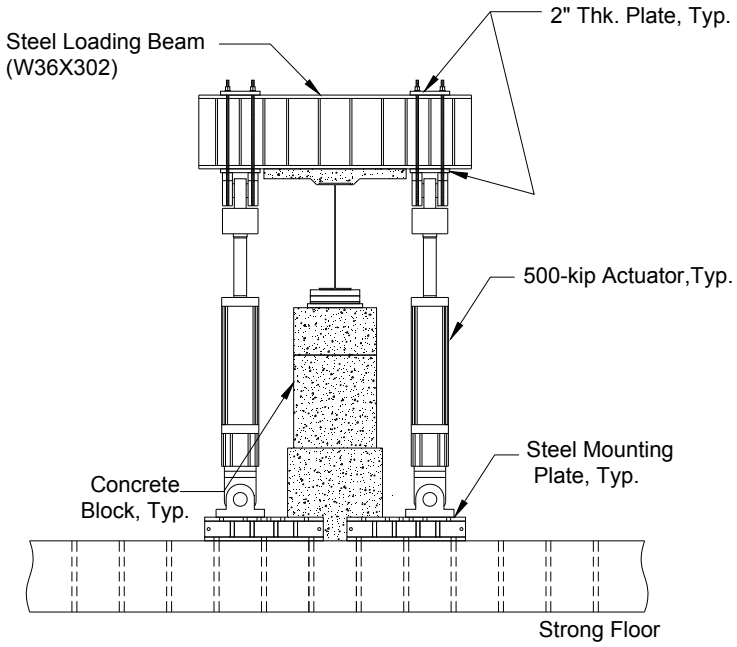

(b) View A - A

Figure 2.11: Test Setup: Specimens CG1 and CG2

Figure 2.12: Support Detail

Figure 2.13: Steel Loading Beam

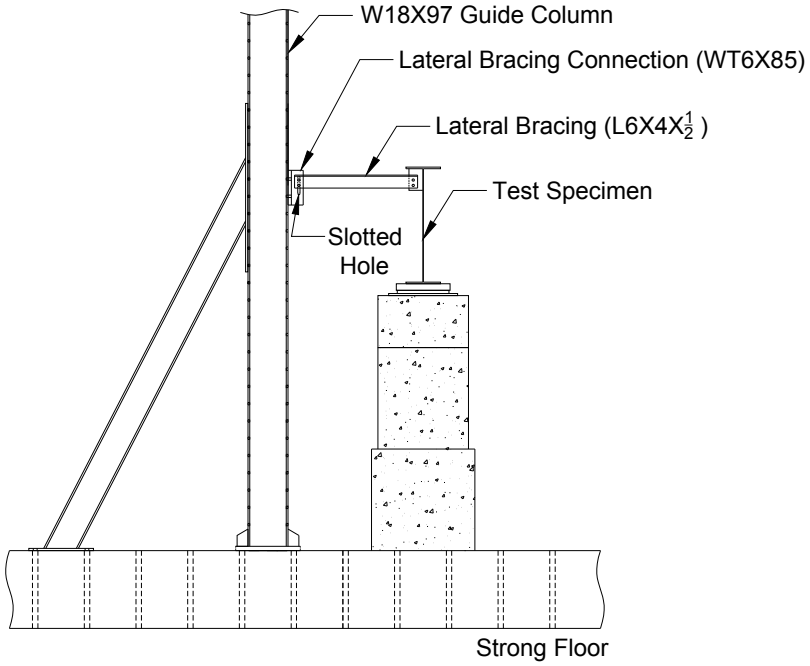

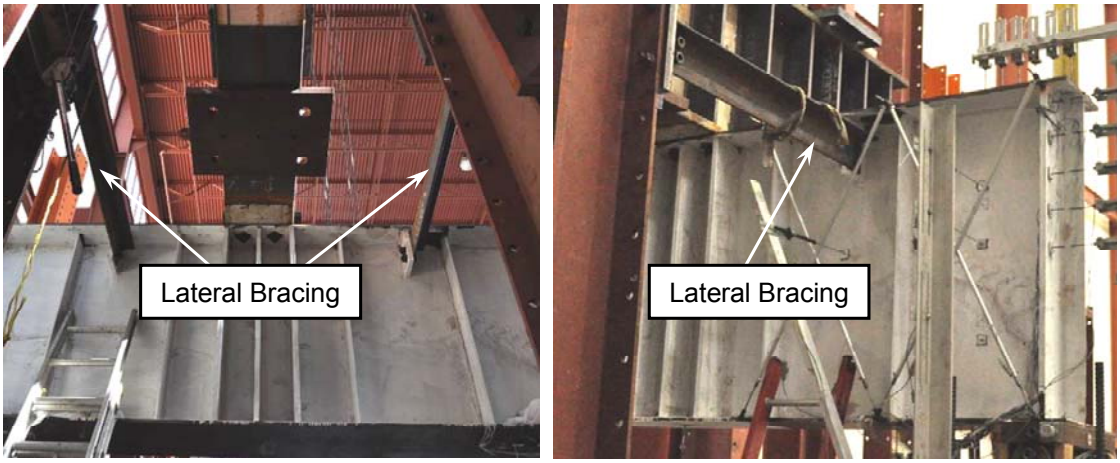

Figure 2.14: Test Setup: Beam Lateral Bracing

3. TEST RESULTS (PHASE 1)

3.1 Specimen SG1

Figure 3.1 shows the test setup prior to testing. The relationship between the applied load and mid-span deflection is shown in Figure 3.2. The theoretical stiffness was computed by using Timoshenko beam theory. The mid-span deflection of simply supported beams can be determined by combinating the deformations due to flexure and shear as follows (see Figure 3.3).

$$\Delta = \Delta_f + \Delta_s = \frac{PL^3}{48EI} + \frac{P}{2GA_s}\left(\frac{L}{2}\right) \tag{3.1}$$

where

P = applied load (kips),

L = beam length (in.),

E = modulus of elasticitity (ksi),

I = moment of inertia (in.^{4}),

G = shear modulus (ksi), and

A_s = shear area (in.^{2}).

The theoretical stiffness computed from Eq. (3.1) is also plotted in Figure 3.2. It matches well with the stiffness computed from test data.

Figure 3.4 shows the test specimen at event *A*, which corresponds with the AASHTO nominal shear strength for end panels. Minor web buckling was visible at both end panels. When the maximum applied load was reached (event *B*), web buckling became significant and minor yielding at both end panels was observed, as evidenced by the flaking of the whitewash (see Figure 3.5 and Figure 3.6). After maximum load was achieved, the strength degraded slowly and plastic hinges formed in the bearing stiffeners and both flanges of the west end panel. The deformed shape at event *C* is shown in Figure 3.7. The front and back sides of the west end panel after the specimen was unloaded and intrumetation removed are shown in Figure 3.8. The observed plastic hinges are also marked in the figure.

3.2 Specimen SG2

A plot of the applied load versus mid-span deflection is shown in Figure 3.9. The stiffness from the test started to deviate from the theoretical stiffness when the AASHTO nominal shear strength (event *A*) was exceeded.

In this specimen, minor web buckling was observed in all four panels at event *A* (see Figure 3.10). At maximum load (event *B*), yielding in both end panels was observed (see Figure 3.11). A close-up view of both end panels at event *B* in Figure 3.12 shows web local buckling. After achieving the maximum load, the strength degradation was gradual as the displacement was increased. The west end panel failed in this specimen and the deformed shape with plastic hinges on boundary members at event *C* is shown in Figure 3.13. At the completion of testing, failure modes included plastic hinges on the boundary members and yielding and web buckling on the front and back sides of west end panel as shown in Figure 3.14. As seen in Figure 3.15, the failure modes of both Specimens SG1 and SG2 are very similar.

3.3 Specimen CG1

Specimen CG1 was nominally identical to Specimen SG1, except that it incorporated a concrete slab. Figure 3.16 shows the relationship between applied load and mid-span deflection. To calculate the theoretical stiffness of the steel-concrete composite specimen, the moment of inertia (I) in Eq. (3.1) was replaced by the effective moment of inertia (I_{eff}) to account for the effects of partial composite beam action (AISC 2010).

$$I_{eff} = I_s + \sqrt{\frac{\sum Q_n}{C_f}}\left(I_{tr} - I_s\right) \tag{3.2}$$

where

$\sum Q_n$ = summation of the stud strength for partial composite action (= 639 kips),

C_f = horizontal force for full composite action (= 1,807 kips),

I_{tr} = transformed section moment of inertia (= 42,408 in.^{4}), and

I_s = moment of inertia of the bare steel beam (= 20,029 in.^{4}).

The theoretical stiffness thus calculated is also shown in Figure 3.16.

Specimen CG1 showed similar behavior to Specimens SG1 and SG2. At event *A*, minor web buckling developed in the west end panel. Then yielding in the end panels was observed at a mid-span deflection of 0.2 in. (see Figure 3.17 and Figure 3.18). At that point, the recorded applied load was 632 kips, which is very close to the maximum applied load (= 630.5 kips) for Specimen SG1. After that point, the stiffness softened and further loading resulted in flexural cracks on the concrete haunch at event *B* [Figure 3.19(a)]. This flexural crack caused a small drop in the applied load. It was also observed that a shear crack occurred near bearing stiffeners [Figure 3.19(b)]. As the mid-span deflection increased, the cracks widened and the number of cracks increased. The crack patterns are summarized in Figure 3.19. The failure mode of the specimen at the maximum deflection (= 1.8 in., event *C*) is shown in Figure 3.20. At the completion of testing, concrete spalling at the top surface of the concrete slab above the end panel is shown in Figure 3.21(a). Figure 3.21(b) and Figure 3.21(c) show significant yielding in the web along the panel diagonal and plastic hinges developed in the flanges and bearing stiffeners.

3.4 Specimen CG2

Specimen CG2 was nominally identical to Specimen SG2, except that CG2 incorporated a concrete slab. Figure 3.22 shows the relationship between applied load and mid-span deflection.

At event *A*, web buckling was visible in all four panels (see Figure 3.23). Yielding in both end panels was observed when the maximum load was achieved (event *B*). The yielding pattern is shown in Figure 3.24. At this point, one flexural crack in the concrete appeared near the middle of the end panel, and one shear crack appeared near the bearing stiffeners. Figure 3.25 shows the concrete crack patterns observed during the test. Figure 3.26 shows the failure mode of the specimen at event *C*. Figure 3.27 shows the front and back sides of the west end panel at the completion of testing. Plastic hinges that developed in flanges and bearing stiffeners are also marked in the figure.

3.5 Recorded Response

Figure 3.28 shows the locations of the displacement transducers that measured the web out-of-plane deformations of each specimen. L2, L3, and L4 were installed on the back side of the east end panel, while L7, L8, L9 were placed on the back side of the west end panel. Figure 3.29 shows the web out-of-plane deformation of Specimen SG1. The expected buckling load predicted per AASHTO Specifications (2014) is also presented in the figure. In the figure, displacements recorded by L2 in the east end panel and L7 to L9 in the west end panel start changing in slope near the predicted buckling strength, and the web out-of-plane deformations rapidly increased. This indicates that the buckling strength predicted by AASHTO Specifications is reasonable. In Specimen SG2, similar responses are observed in the east end panel, but not in the west end panel (see Figure 3.30). Figure 3.31 and Figure 3.32 show the web out-of-plane deformation of Specimens CG1 and CG2.

Figure 3.33 shows the locations and orientations of the strain gage rosettes for all specimens except Specimen SG1. Specimen SG1 had the same arrangement of the rosettes only in the west panel (see Appendix A for the locations of the rosettes in the east panel). All strain gage rosettes were installed on the back side of the panel web. From the rosette data, principal strains and directions were computed. Figure 3.34 plots the principal tensile strains across the panel diagonal of both east and west end panels at the ultimate load (Event *B*). The horizontal reference line in the figure represents the strain value corresponding to the tension-field stress (σ_t) calculated by using Eq. (1.10). The ratio of the shear buckling strength to shear yield strength ($C = \tau_{cr} / \tau_y$) in Eq. (1.10) is determined by Eqs. (1.15) to (1.17).

The tensile principal strains recorded from five middle strain gage rosettes in each panel (R05 to R09 in the east end panel and R18 to R22 in the west end panel) are close to or beyond the strain. Table 3.2 and Table 3.3 summarize the principal tensile directions of five middle strain gage rosettes of each section at ultimate load (Event *B*). The recorded principal angles varied but most of them were within ± 10° of 63.4°, which is the angle of the panel diagonal with respect to the flange. More principal strain plots associated with different displacement levels are presented in Appendix B. Recorded

response plots from both displacement transducers and uni-axial strain gages are also shown in Appendix B.

3.6 Comparison of Test Results

3.6.1 Failure Mechanism

Coincidentally, all specimens failed in the west end panel and showed similar behaviors. Minor web buckling occurred after the shear buckling strength was achieved. Subsequent yielding in the web appeared. After the ultimate strength was reached, significant yielding occurred along the diagonal of the web panel, and was accompanied by the development of plastic hinges in both flanges and bearing stiffeners. Shear cracks also appeared in the concrete slab for composite specimens.

After completing the tests, plastic hinge locations in the top flange and bearing stiffeners for each test specimen were measured and are summarized in Figure 3.35. For the composite specimens, a portion of the concrete slab was cut out to investigate shear crack propagation (see Figure 3.36). The measured shear crack angles with respect to the concrete slab were 17° and 14° for CG1 andCG2, respectively (see Figure 3.37).

3.6.2 Comparison with AASHTO Shear Strength

Table 3.1 summarizes the end panel shear strengths based on both AASHTO Specifications (2014) and experimental results. The shear overstrengths for each specimen, which is defined as the ratio of the experimental strength to the AASHTO nominal strength, are listed in the last column of the table. It is clear that AASHTO Specifications (2014), which ignores tension-field action in end panels, underestimates the shear strength of the end panels considerably.

Figure 3.38 shows the relationship between the normalized ultimate shear strength and the web depth-to-thickness ratio. In the plot, based on the actual web yield stress from the coupon tests, two AASHTO nominal strength curves are presented: one that excludes tension-field action for end panels, and another that includes tension-field action for interior panels. Experimental shear strengths were found to be between the AASHTO strengths with and without tension-field action. Therefore, this concludes that partial tension-field action develops in the end panels.

3.6.3 Contribution of Concrete Slab

In current AASHTO Specifications (2014), the composite action provided by the concrete slab is ignored in evaluating the shear strength. Specimens CG1 and CG2 showed a higher shear capacity than their counterparts (SG1 and SG2), respectively. The increase in shear strength due to the contribution from concrete slab is about 12% in both composite specimens.

Table 3.1: Comparison of End Panel Shear Strengths

Specimen No.	Web Depth-Thickness Ratio	AASHTO Predicted Nominal Strength (kips)	Experimental Shear Strength (kips)	Shear Overstrength
SG1	210	196.5	315.3	1.60
CG1			352.6	1.79
SG2	280	82.9	190.3	2.30
CG2			212.1	2.56

Table 3.2: Prinicipal Strain Direction at Ultimate Load (Steel Plate Girders)

Specimen No.		Rosette Number	Panel Diagonal Angle (degree)	Principal Tensile Strain Angle (degree)
SG1	West Panel 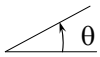	R18	63	44
		R19		52
		R20		54
		R21		47
		R22		10
SG2	East Panel 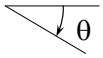	R09		39
		R08		3
		R07		57
		R06		62
		R05		61
	West Panel 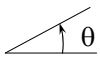	R18		74
		R19		51
		R20		60
		R21		62
		R22		56

Table 3.3: Prinicipal Strain Direction at Ultimate Load (Composite Plate Girders)

Specimen No.		Rosette Number	Panel Diagonal Angle (degree)	Principal Tensile Strain Angle (degree)
CG1	East Panel 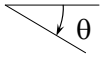	R09	63	51
		R08		67
		R07		76
		R06		61
		R05		58.
	West Panel 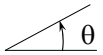	R17		59
		R19		45
		R20		57
		R21		74
		R22		60
CG2	East Panel 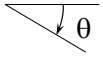	R09		74
		R08		38
		R07		58
		R06		59
		R05		55
	West Panel 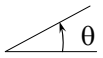	R18		46
		R19		59
		R20		70
		R21		65
		R22		79

Figure 3.1: Specimen SG1: Test Setup

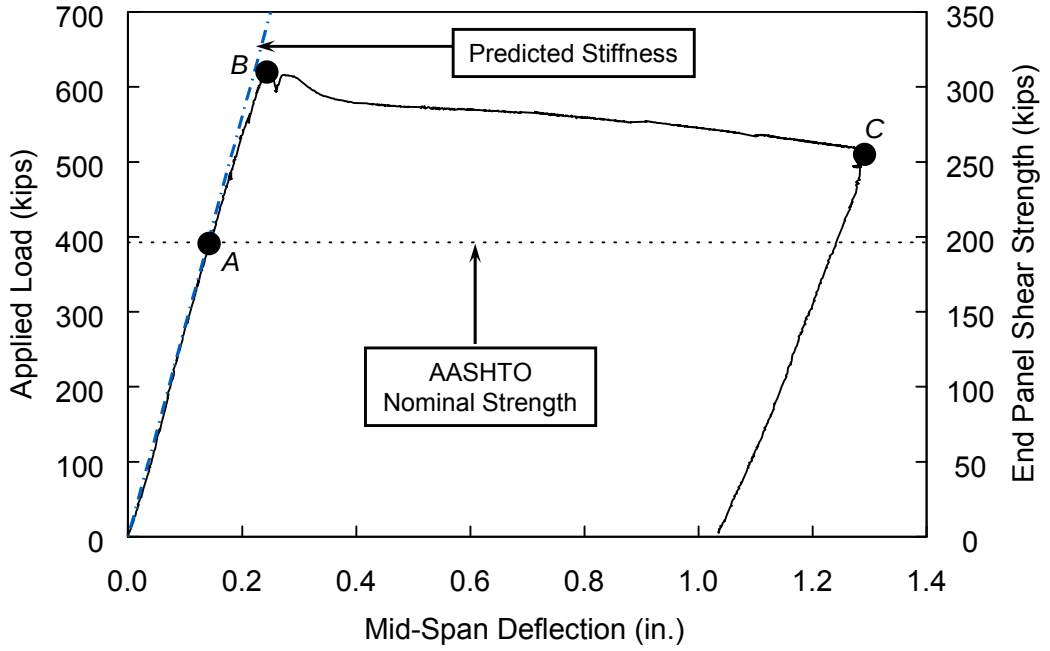

Figure 3.2: Specimen SG1: Applied Load versus Mid-Span Deflection

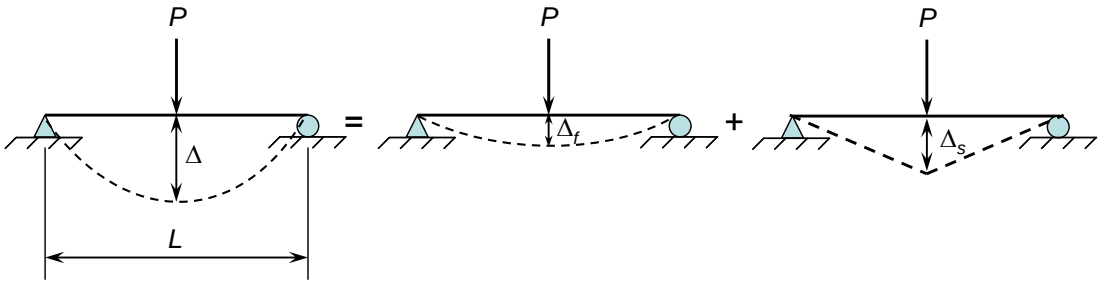

Figure 3.3: Elastic Timoshenko Beam Deformation

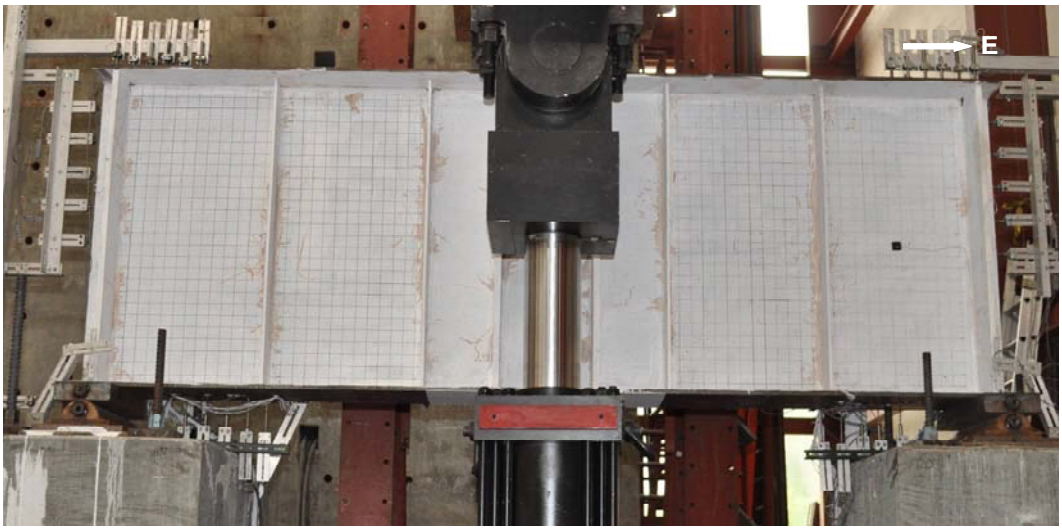

Figure 3.4: Specimen SG1: Deformed Shape at Event *A*

Figure 3.5: Specimen SG1: Web Local Buckling at Event *B*

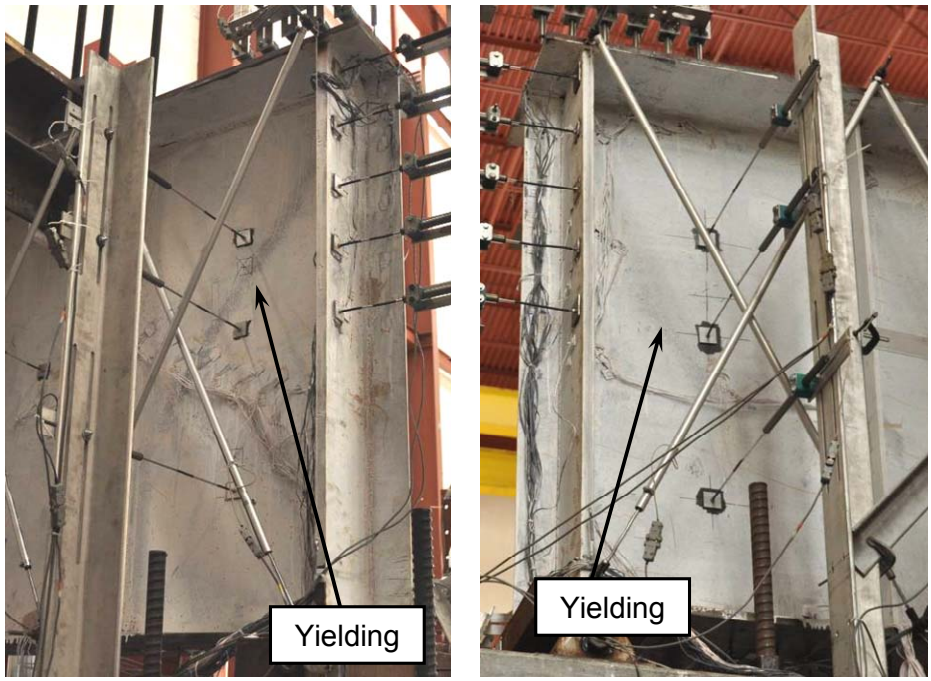

(a) West End Panel (b) East End Panel

Figure 3.6: Specimen SG1: Yielding Patterns at Event *B* (Back Side)

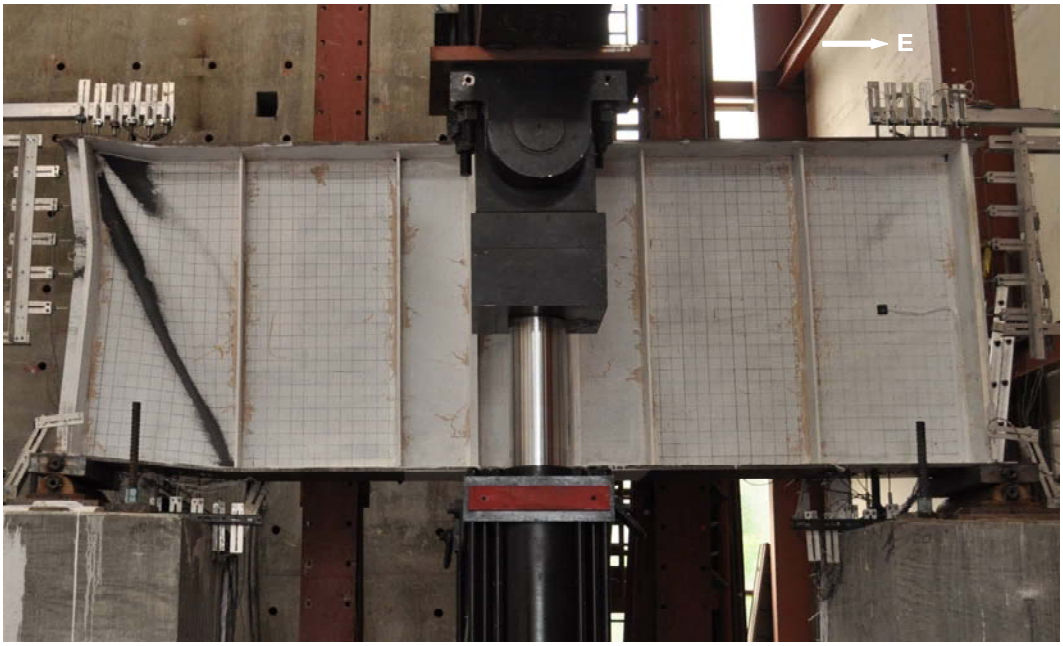

Figure 3.7: Specimen SG1: Failure Mode at Event *C*

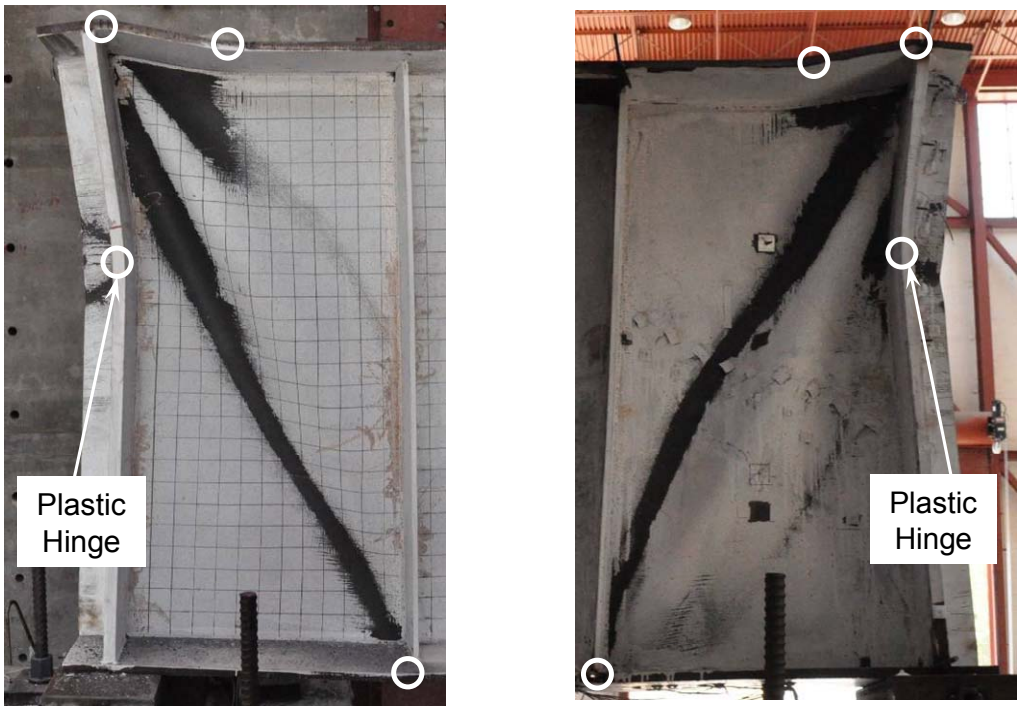

(a) Front Side (b) Back Side

Figure 3.8: Specimen SG1: Failure Mode after Completion of Test (West End Panel)

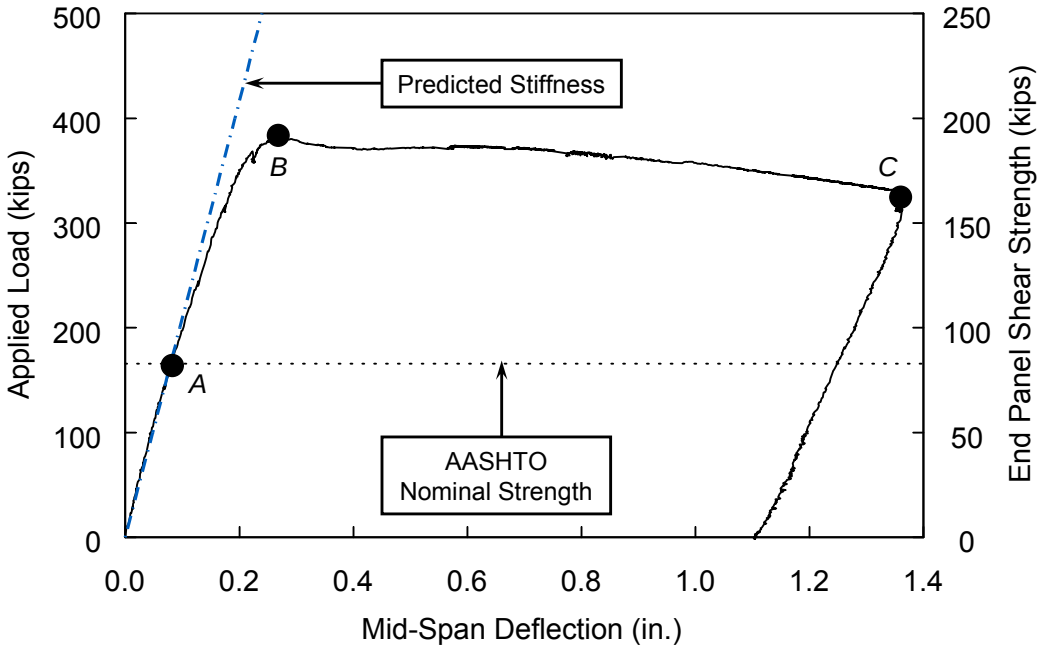

Figure 3.9: Specimen SG2: Applied Load versus Mid-Span Deflection

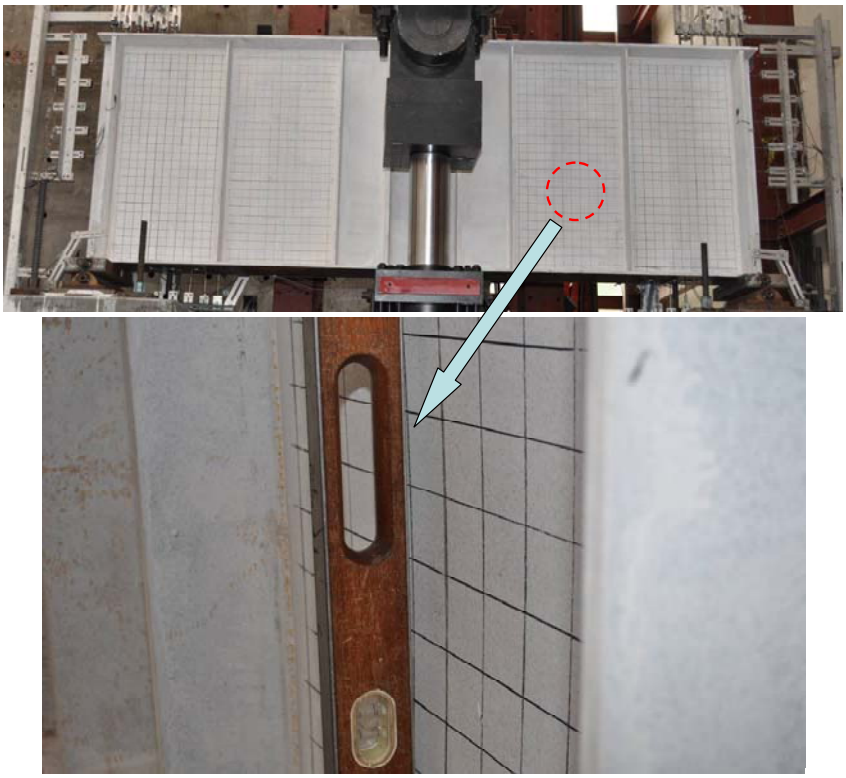

Figure 3.10: Specimen SG2: Minor Web Local Buckling at Event *A*

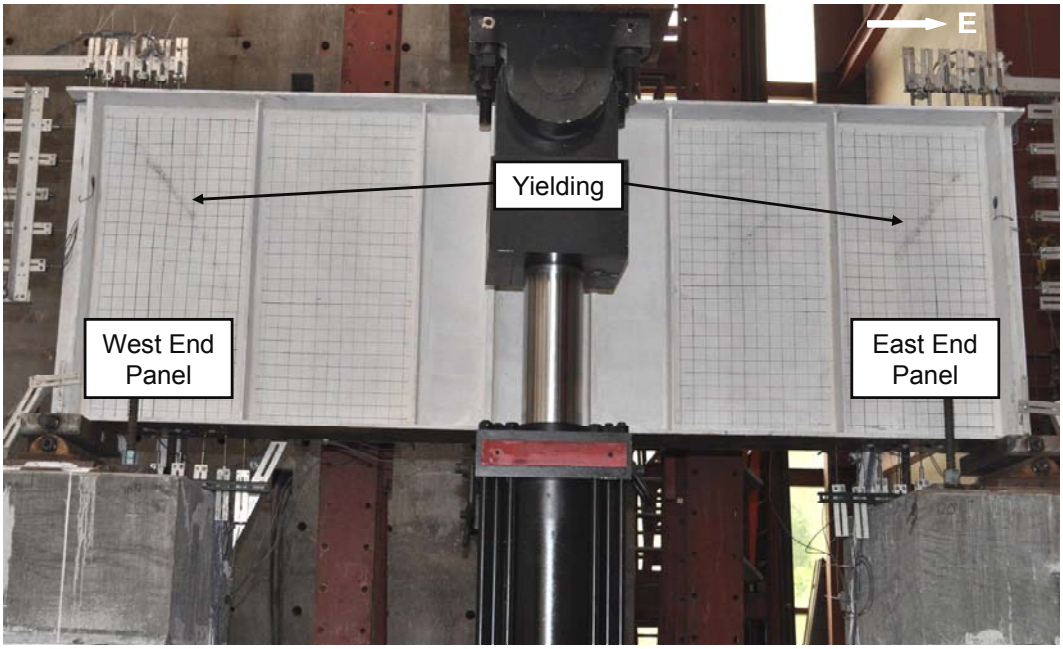

Figure 3.11: Specimen SG2: Yielding Pattern at Event *B*

(a) West End Panel (b) East End Panel

Figure 3.12: Specimen SG2: Web Local Buckling at Event *B*

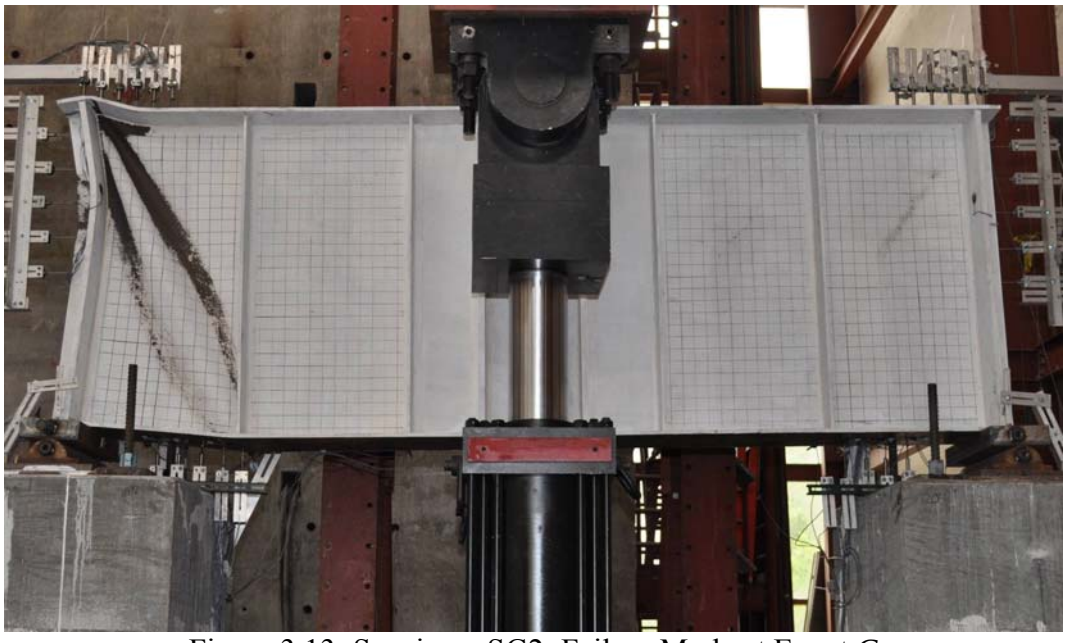

Figure 3.13: Specimen SG2: Failure Mode at Event *C*

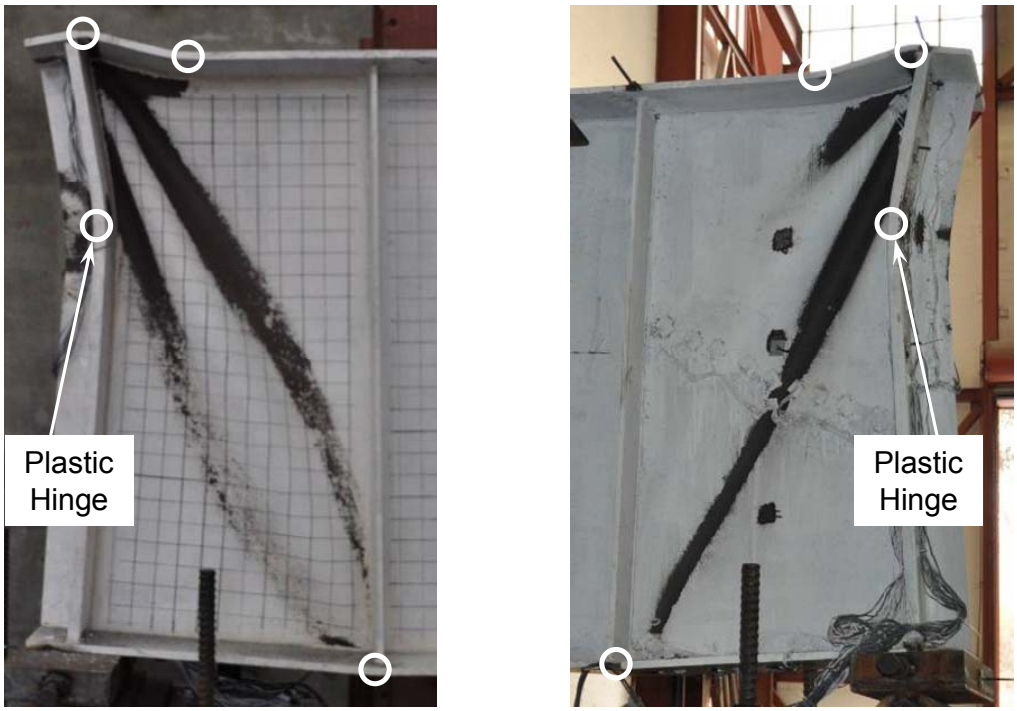

(a) Front Side (b) Back Side

Figure 3.14: Specimen SG2: Failure Mode after Completion of Test (West End Panel)

Figure 3.15: Failure Modes of SG1 and SG2

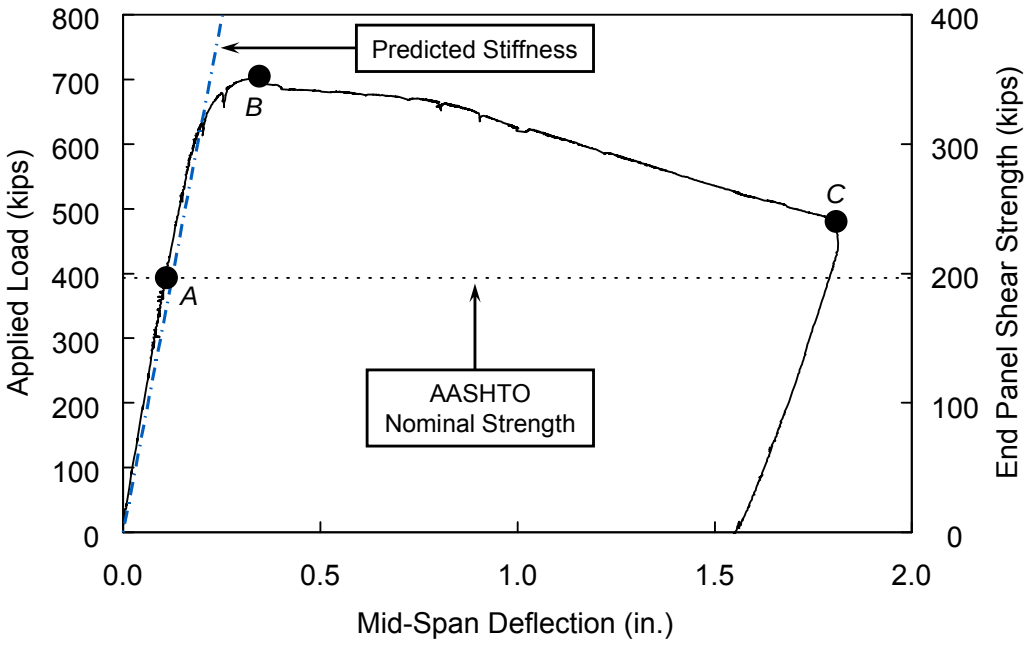

Figure 3.16: Specimen CG1: Applied Load versus Mid-Span Deflection

Figure 3.17: Specimen CG1: Web Yielding and Local Buckling at Δ=0.2 in.

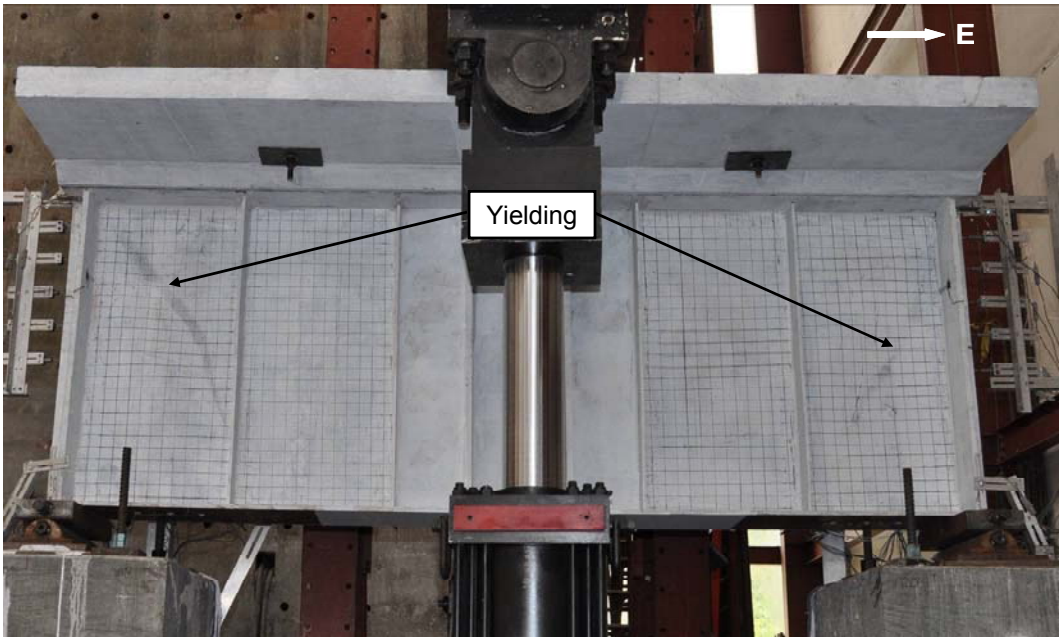

(a) Front View

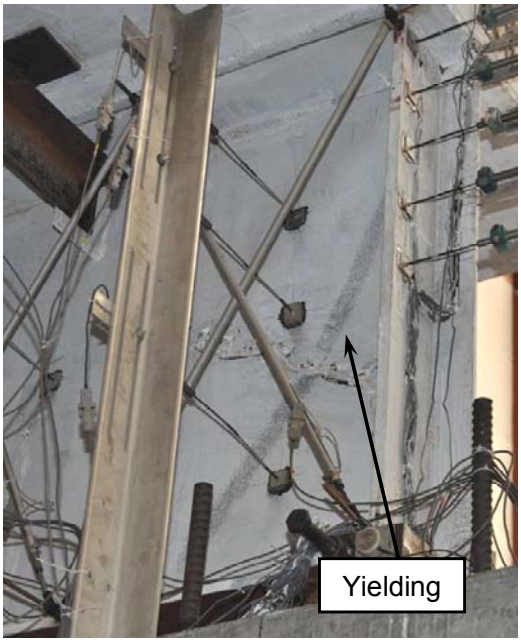

(b) West End Panel

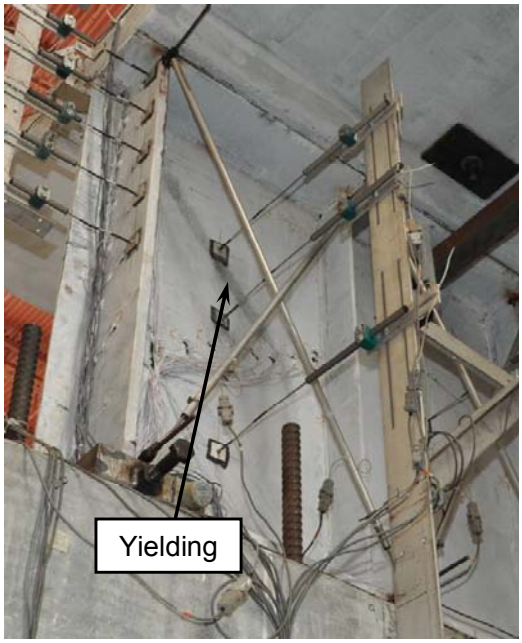

(c) East End Panel

Figure 3.18: Specimen CG1: Yielding Patterns at Event *B* (Back Side)

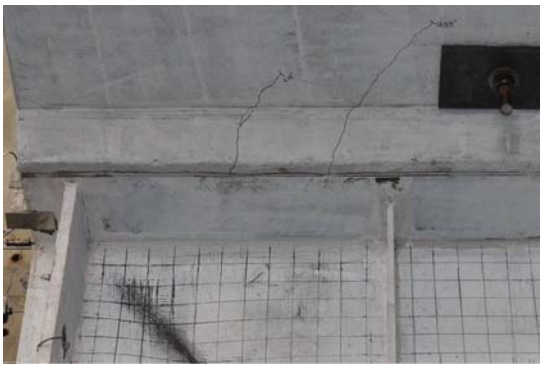

(a) at Δ=0.35 in. (Event *B*)

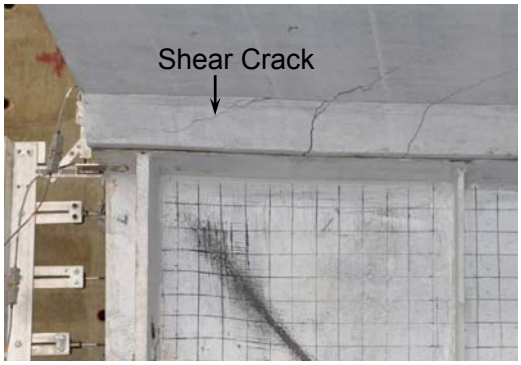

(b) at Δ=0.5 in.

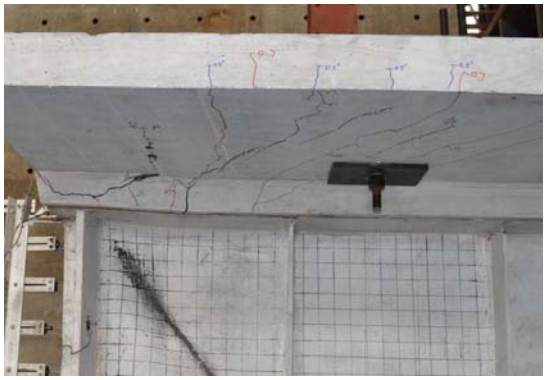

(c) at Δ=0.7 in.

(d) at Δ=1.0 in.

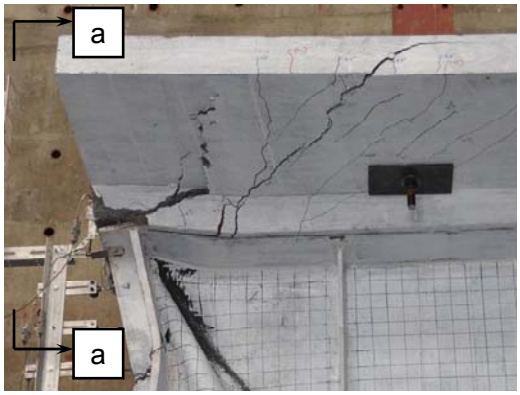

(e) at Δ=1.8 in.

(f) View a - a

Figure 3.19: Specimen CG1: Propagation Concrete Slab Cracks

Figure 3.20: Specimen CG1: Failure Mode at Event *C*

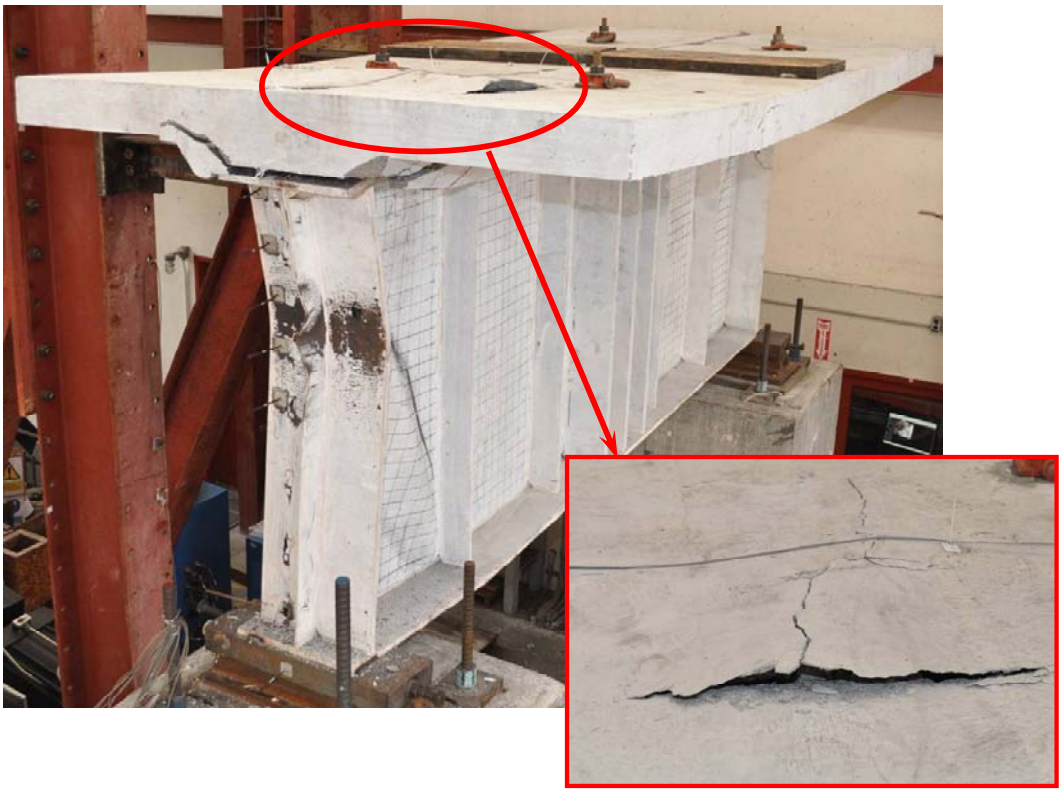

(a) Concrete Spalling

Figure 3.21: Specimen CG1: Failure Mode after Completion of Test

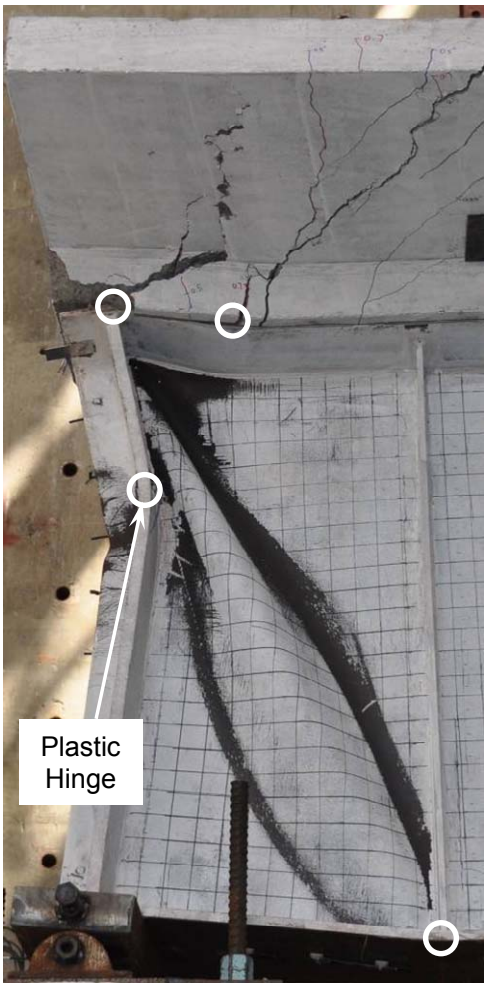

(b) Front Side of West End Panel

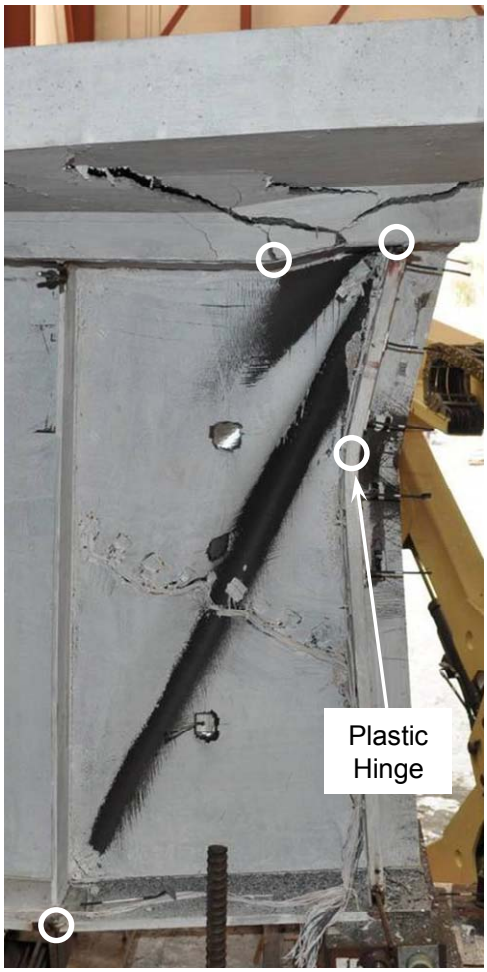

(c) Back Side of West End Panel

Figure 3.21: Specimen CG1: Failure Mode after Completion of Test (continued)

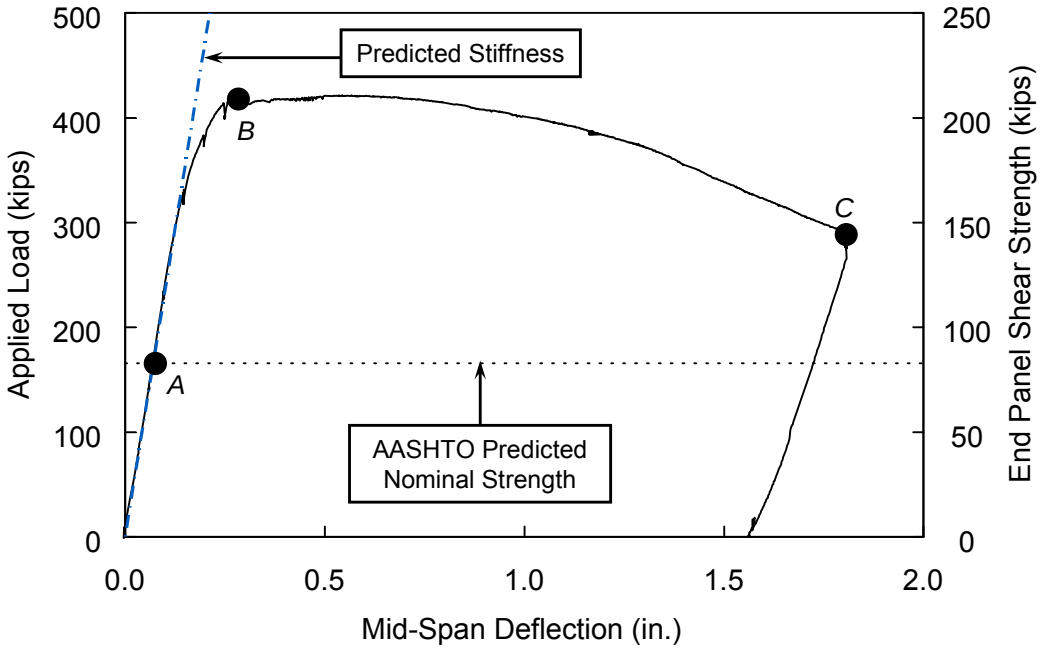

Figure 3.22: Specimen CG2: Applied Load versus Mid-Span Deflection

(a) West End Panel

Figure 3.23: Specimen CG2: Web Local Buckling at Event *A*

(b) East End Panel

Figure 3.23: Specimen CG2: Web Local Buckling at Event *A* (continued)

Figure 3.24: Specimen CG2: Yielding Pattern at Event *B*

(a) at Δ=0.3 in. (Event *B*)

(b) at Δ=0.5 in.

(c) at Δ=0.8 in.

(d) at Δ=1.0 in.

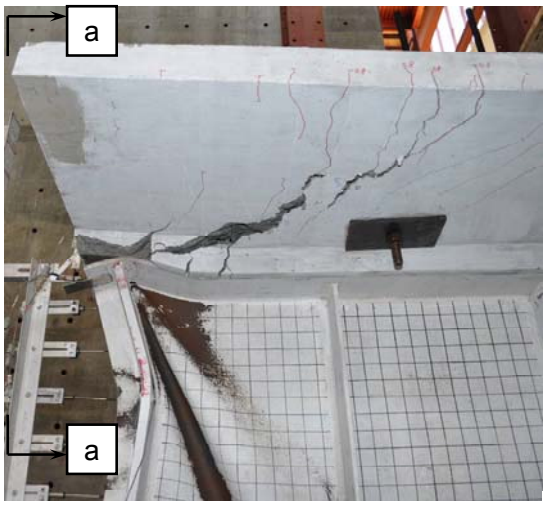

(e) at Δ=1.8 in.

(f) View a - a

Figure 3.25: Specimen CG2: Concrete Slab Crack Propagation

Figure 3.26: Specimen CG2: Failure Mode at Event *C*

(a) Front Side (b) Back Side

Figure 3.27: Specimen CG2: Failure Mode after Completion of Test (West End Panel)

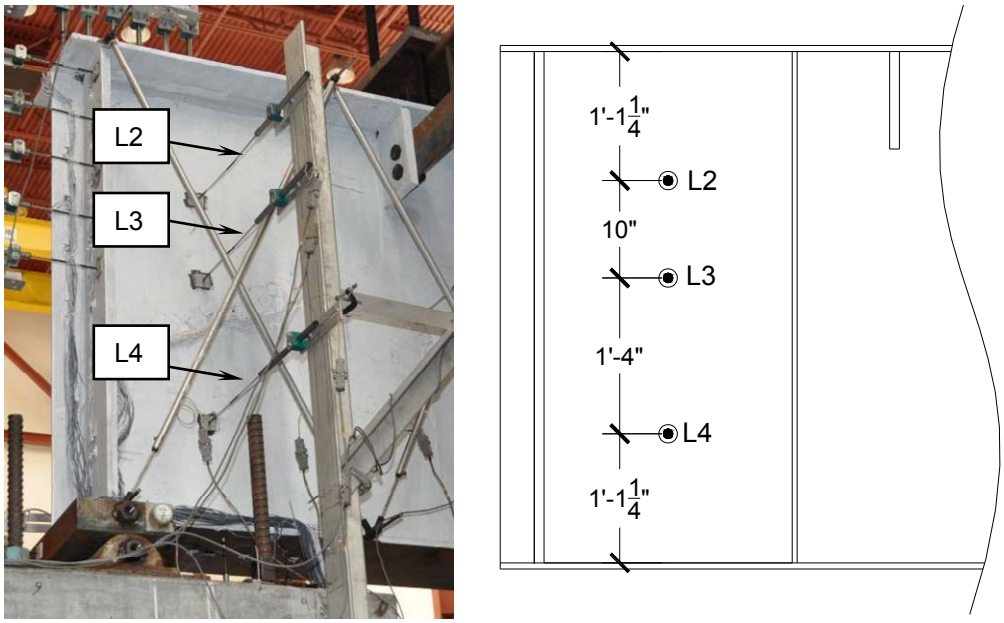

(a) East End Panel

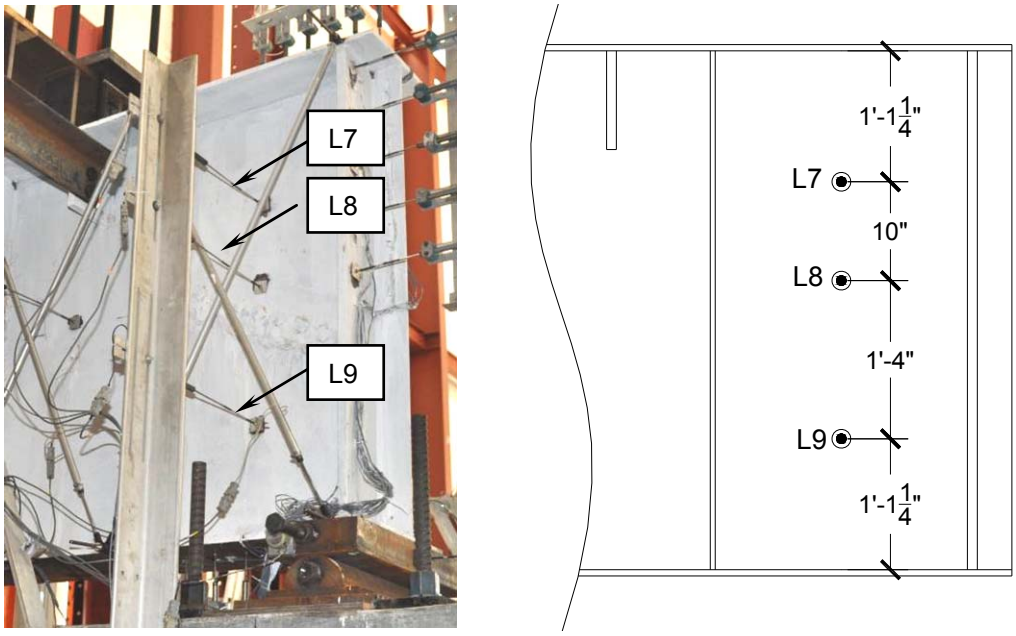

(b) West End Panel

Figure 3.28: Typical Locations of Displacement Transducers (Back Side)

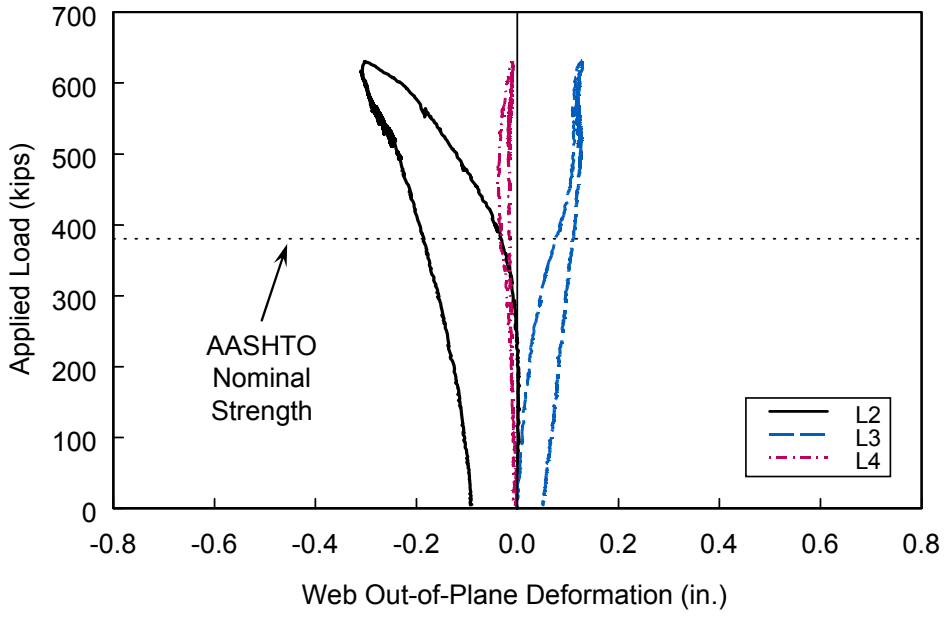

(a) East End Panel

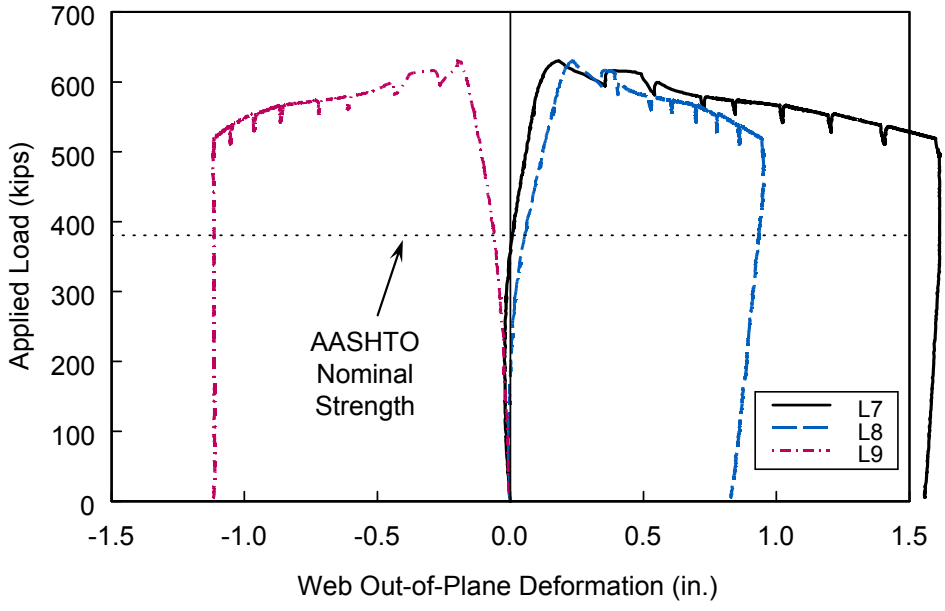

(b) West End Panel

Figure 3.29: Specimen SG1: Web Out-of-Plane Deformation

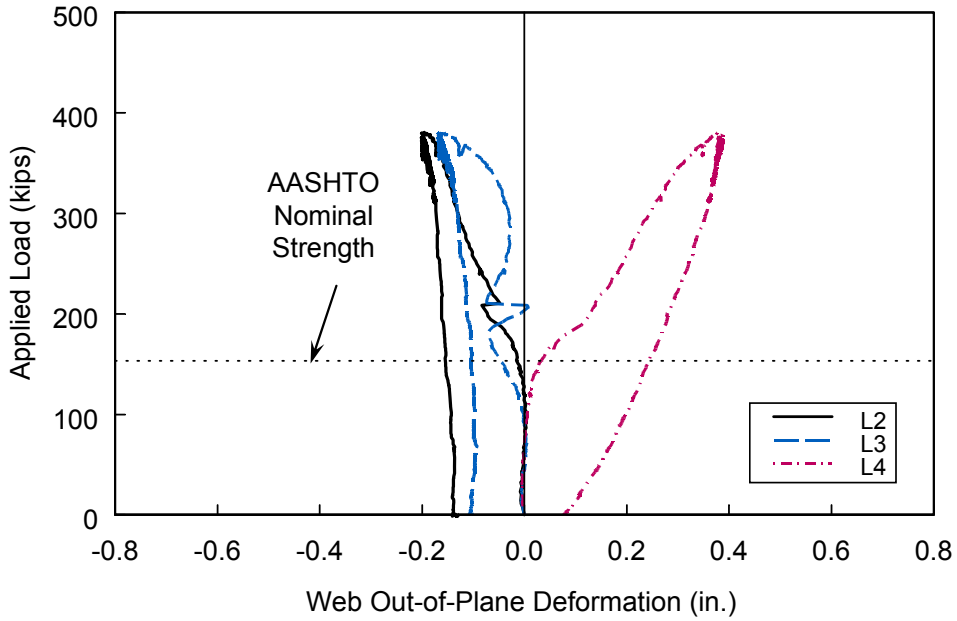

(a) East End Panel

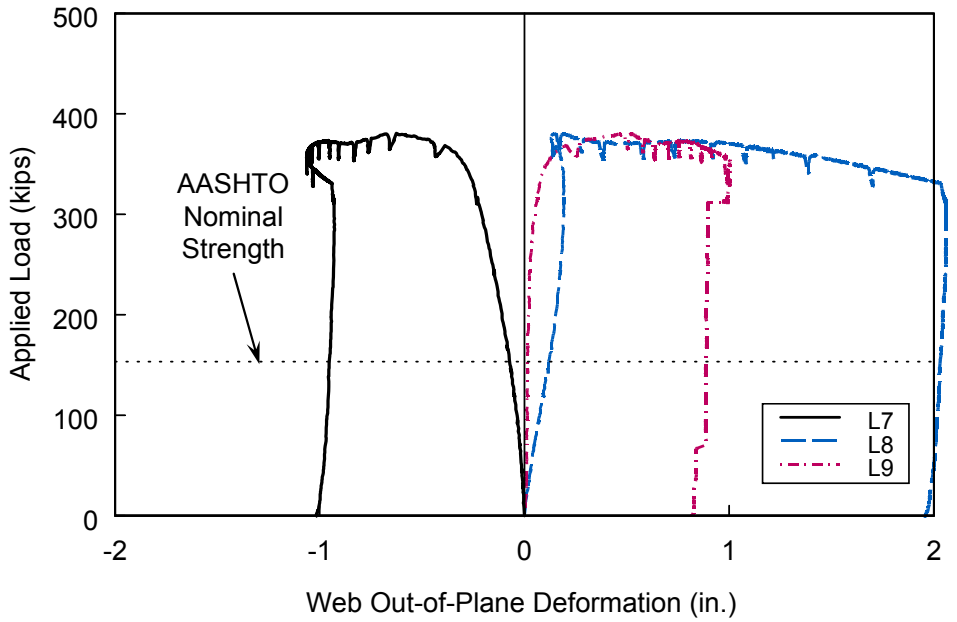

(b) West End Panel

Figure 3.30: Specimen SG2: Web Out-of-Plane Deformation

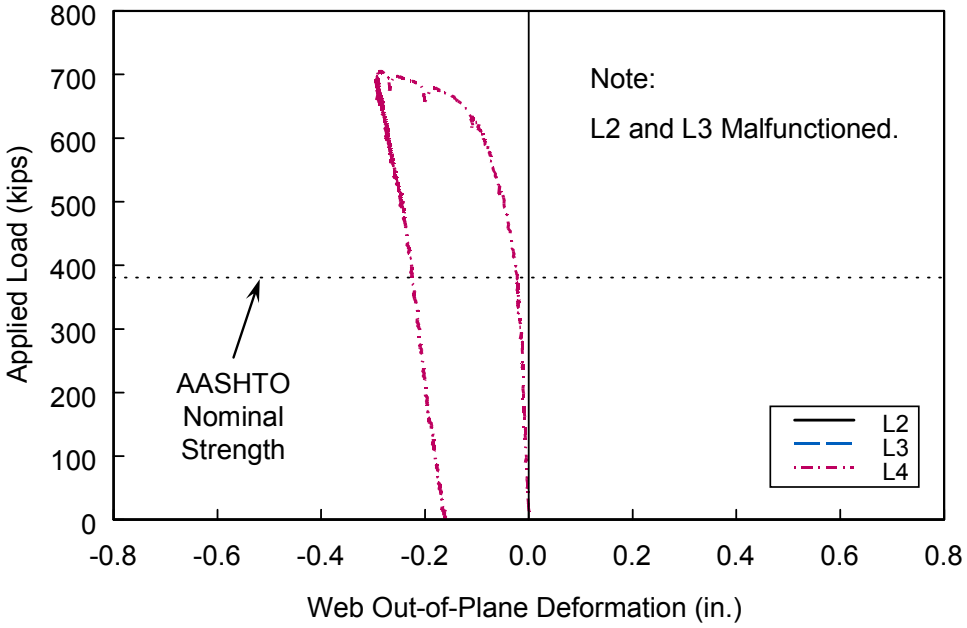

(a) East End Panel

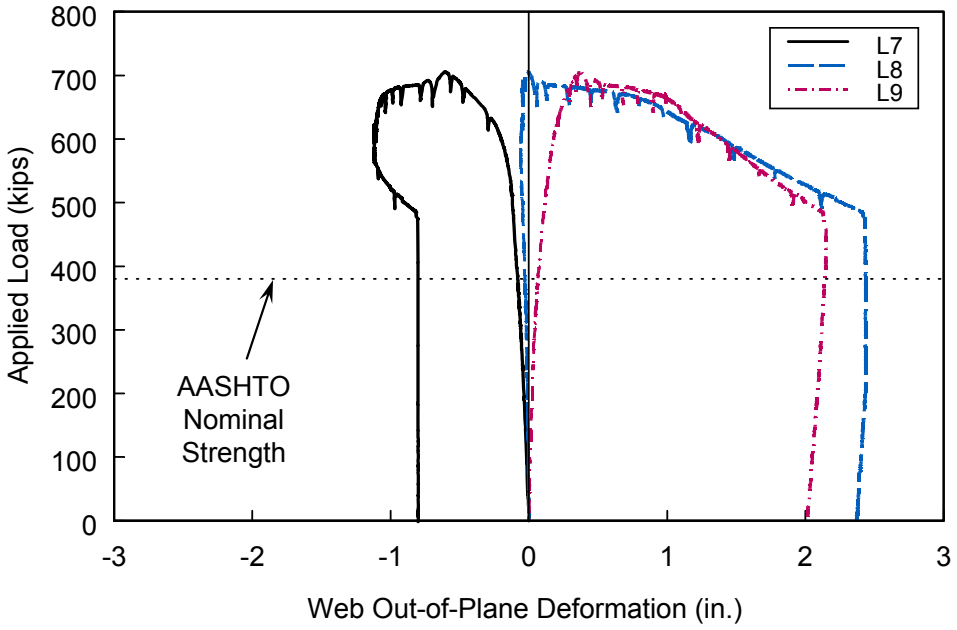

(b) West End Panel

Figure 3.31: Specimen CG1: Web Out-of-Plane Deformation

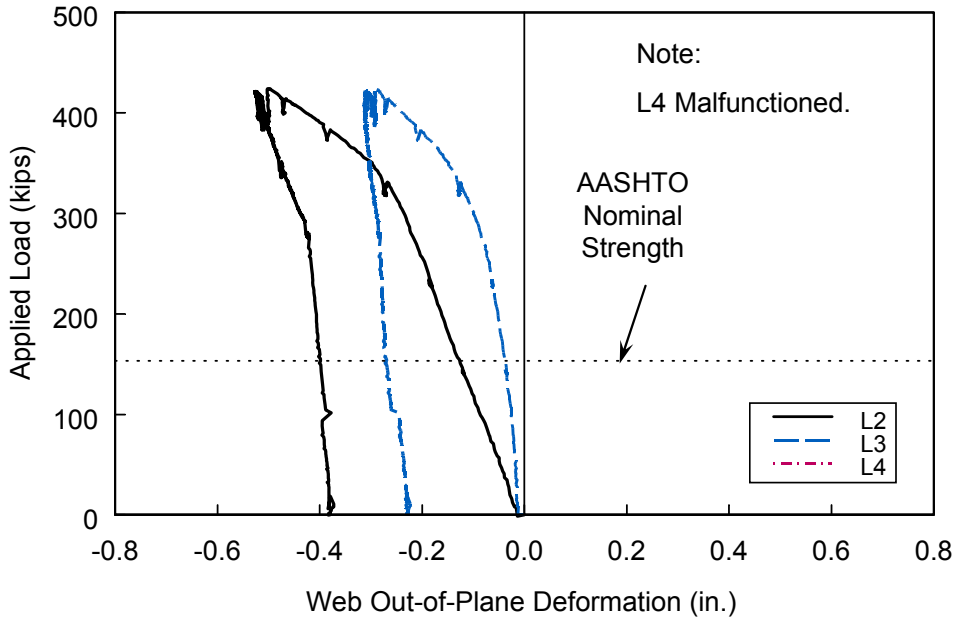

(a) East End Panel

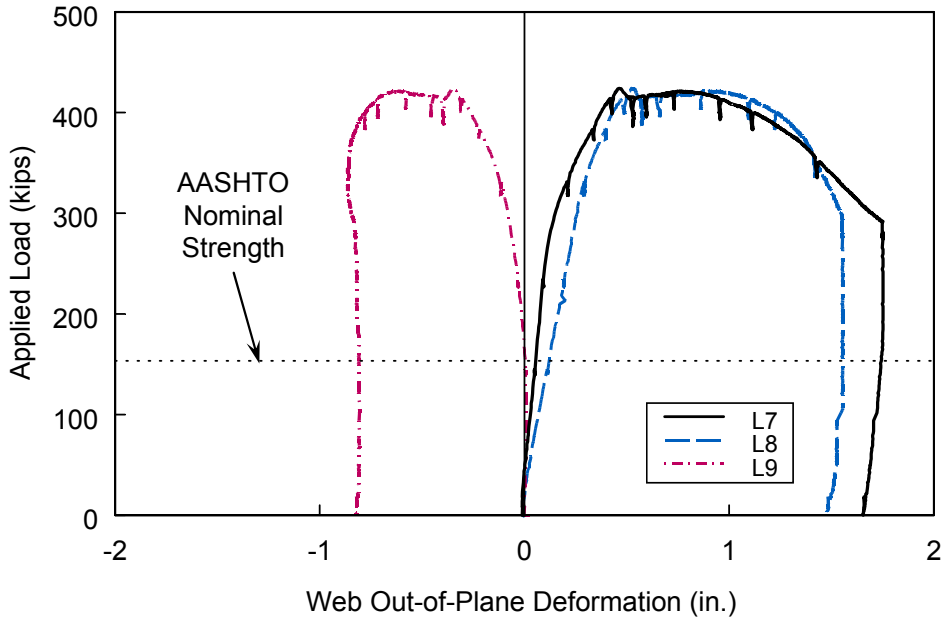

(b) West End Panel

Figure 3.32: Specimen CG2: Web Out-of-Plane Deformation

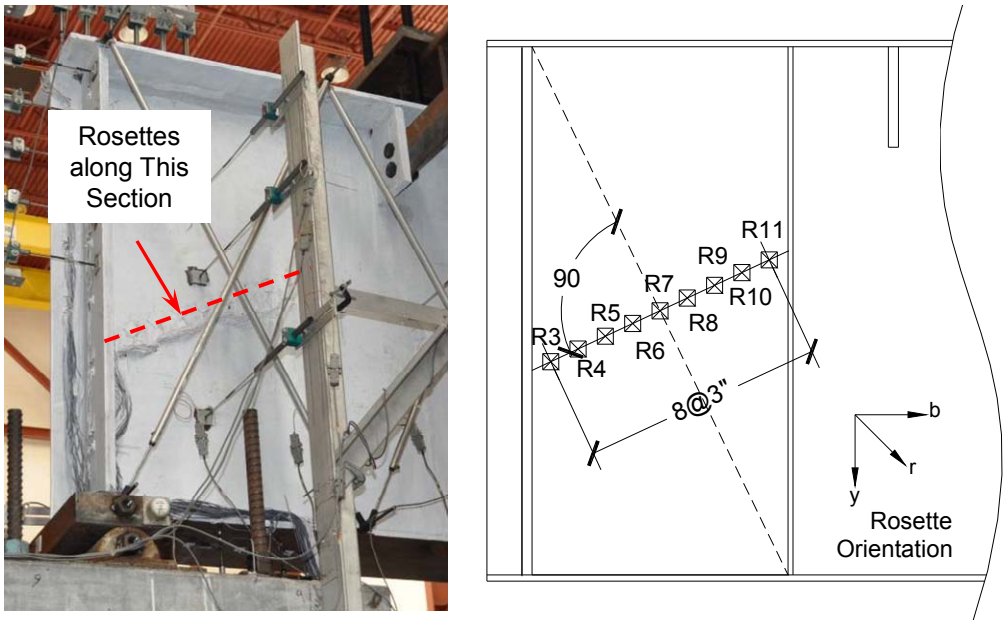

(a) East End Panel

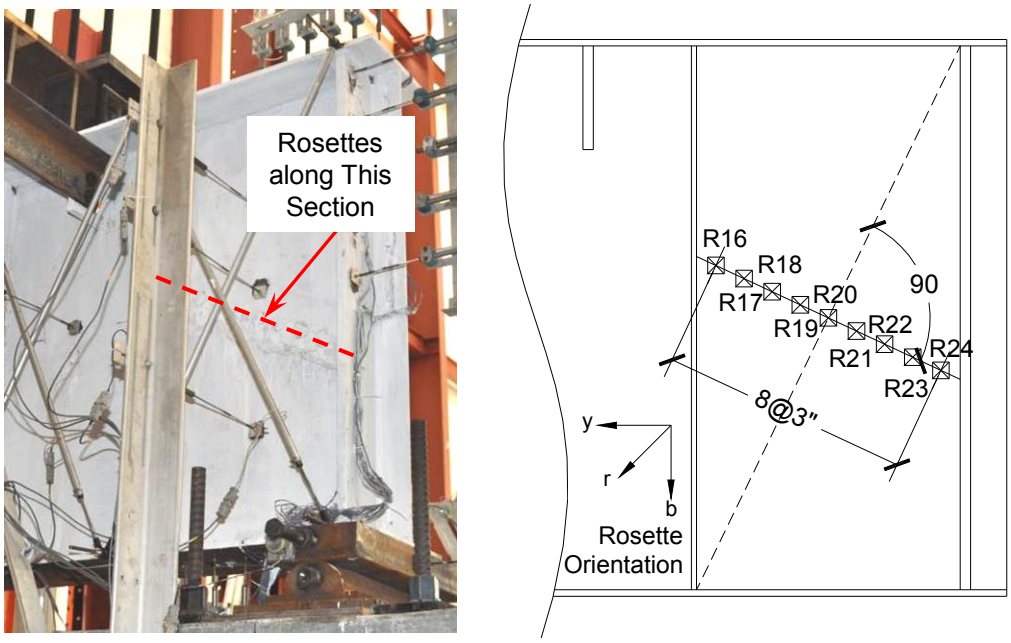

(b) West End Panel

Figure 3.33: Typical Locations of Strain Rosettes in End Panels (Back Side)

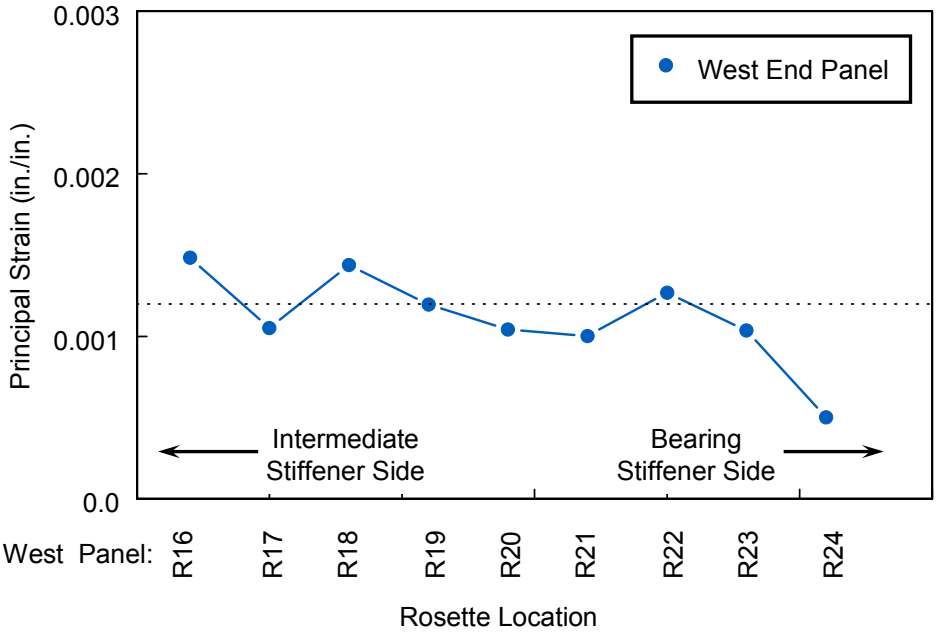

(a) Specimen SG1

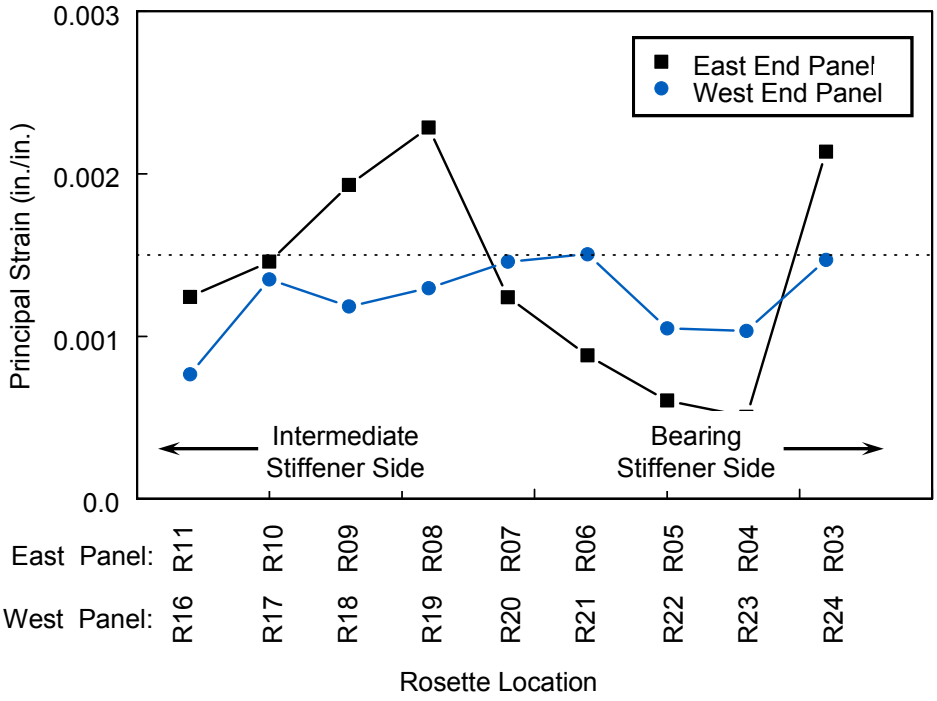

(b) Specimen SG2

Figure 3.34: Principal Strains across Panel Diagonals at Maximum Load

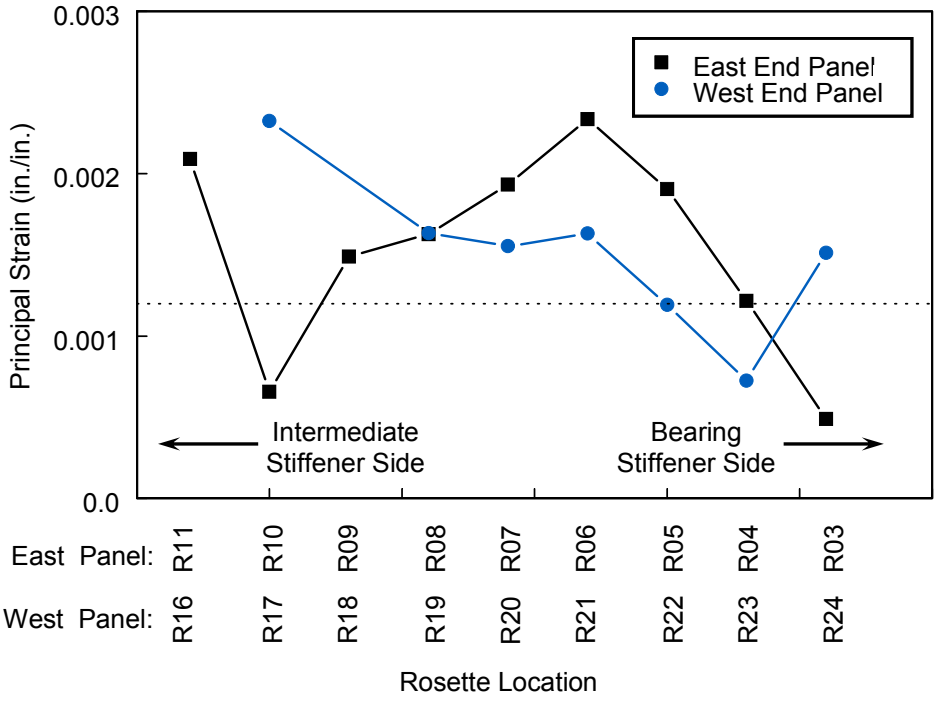

(c) Specimen CG1

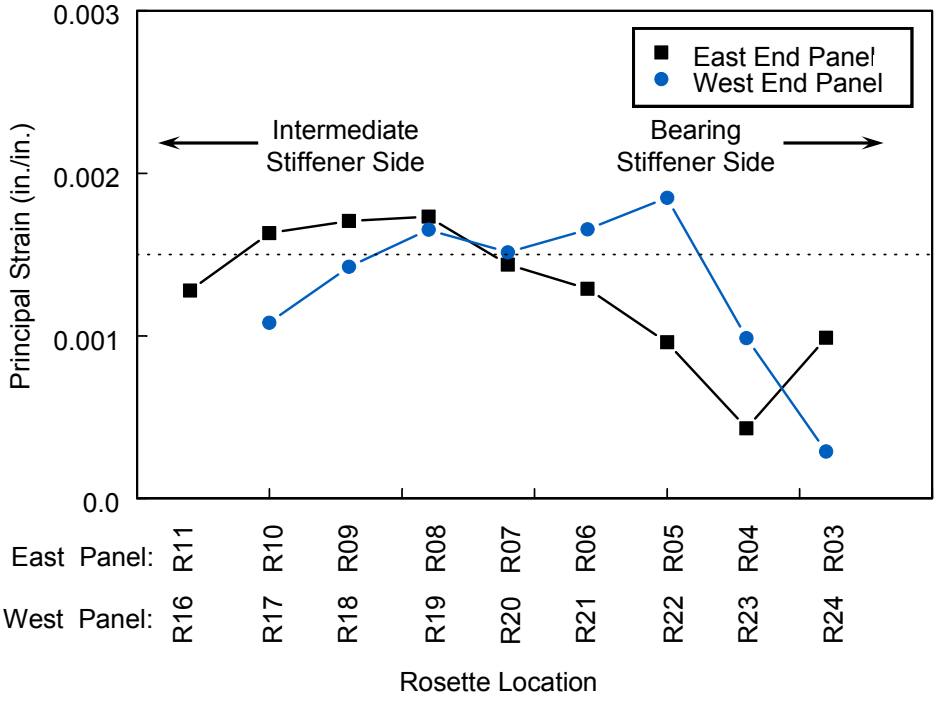

(d) Specimen CG2

Figure 3.34: Principal Strains across Panel Diagonals at Maximum Load (continued)

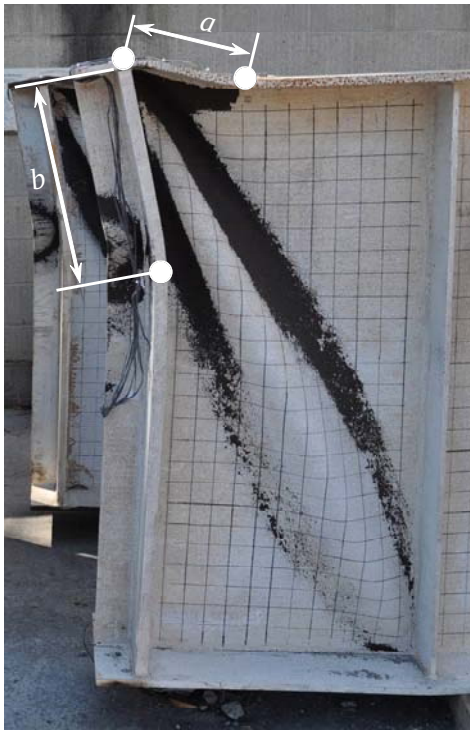

Specimen No.	*a* (in.)	*b* (in.)
SG1	10.5	18.125
CG1	10.0	18.0
SG2	9.125	14.75
CG2	9.375	14.75

Figure 3.35: Measured Plastic Hinge Locations

Figure 3.36: Specimen CG2: Concrete Shear Crack Propagation

(a) Specimen CG1

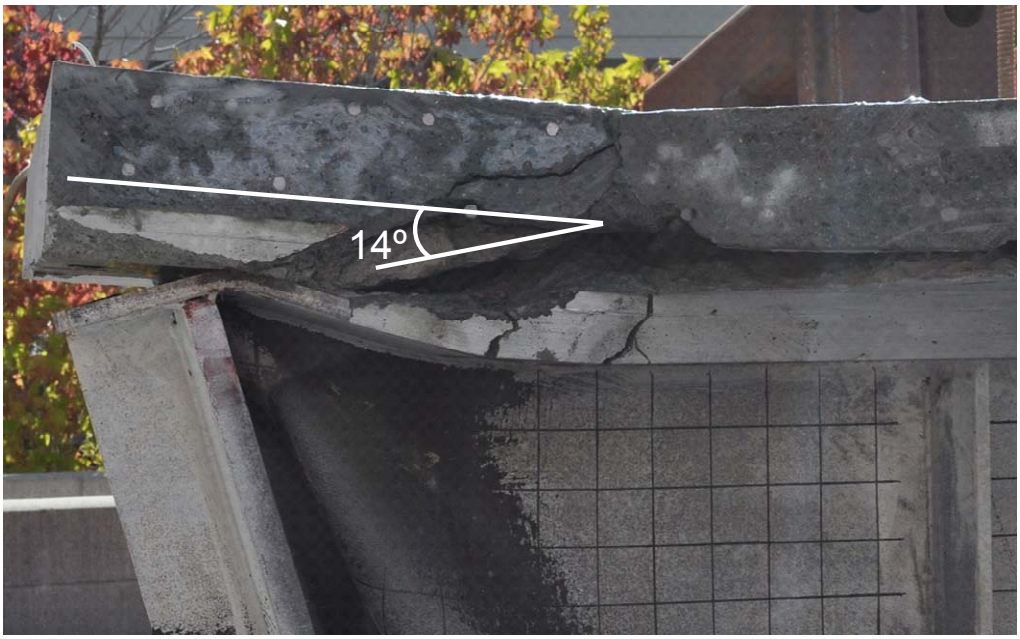

(b) Specimen CG2

Figure 3.37: Measured Concrete Shear Crack Angles

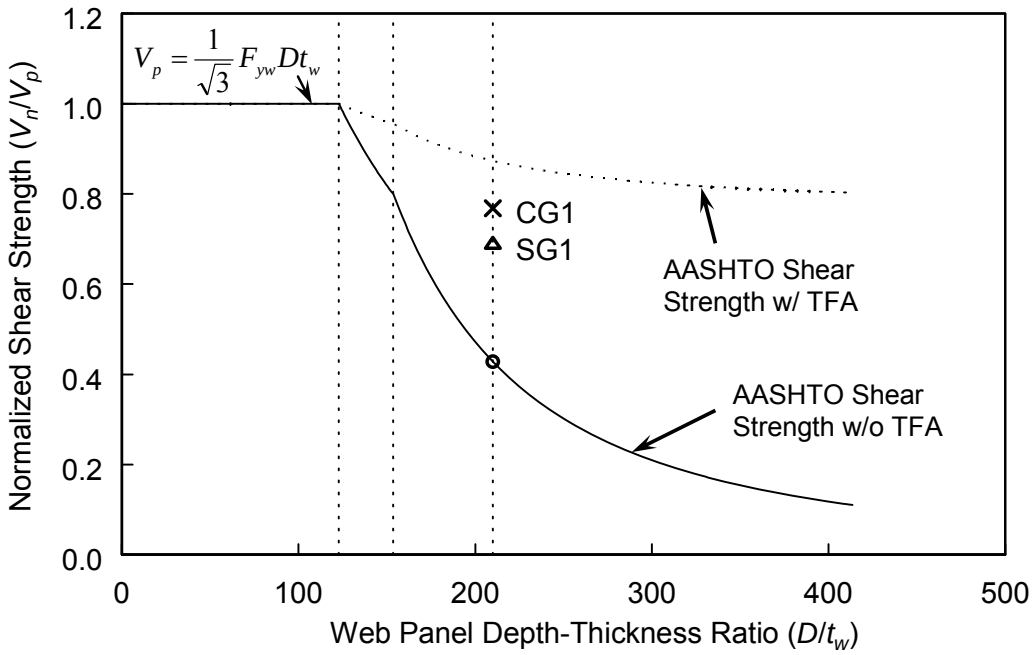

(a) Specimens SG1 and CG1

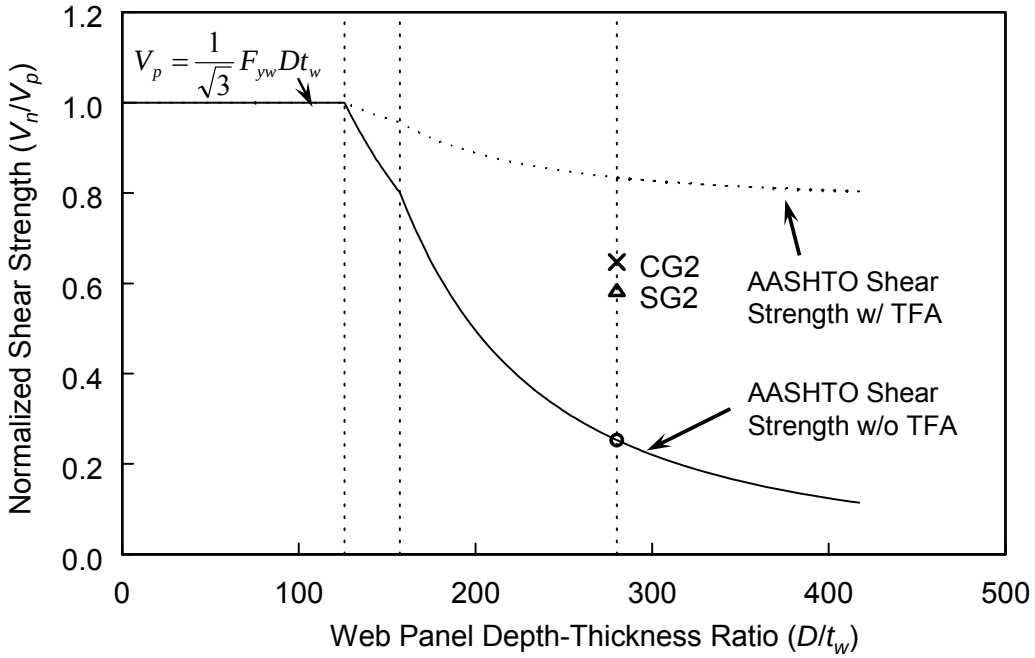

(b) Specimens SG2 and CG2

Figure 3.38: Comparison between Test Results and AASHTO Nominal Shear Strengths

4. NONLINEAR FINITE ELEMENT ANALYSIS OF TEST SPECIMENS (PHASE 1)

4.1 General

Nonlinear finite element analyses on the shear behavior of plate girders have been carried out by a number of researchers (Marsh et al. 1988, Baskar et al. 2002, Liang et al. 2005, Real et at. 2007, and Alinia et al. 2009a and 2009b). The analysis results from these studies have shown reasonable agreement with the test results. In this study, the commercial finite element analysis software package, ABAQUS 6.11 (2011), was used to correlate the test results presented in Chapter 3.

4.2 Steel Plate Girder Specimens (SG1 and SG2)

4.2.1 Finite Element Models

Figure 4.1 shows the typical finite element model. Standard 3-D shell elements (S4R) were used to model both steel plate girder specimens (SG1 and SG2). The S4R element is a four-node quadrilateral shell element with reduced integration and is suitable for both thin and thick shells. A simply supported boundary condition was used, and the lateral bracing was simulated by preventing the lateral movement of the bracing locations from the experiments. Also, the measured plate thicknesses shown in Table 2.3 were used in the finite element models.

The load was applied to one node at mid-span of the top flange width, while the other nodes on the loading surface were constrained to the controlled node by using the kinematic coupling option for all six degrees of freedom.

4.2.2 Material Stress-Strain Characteristics

Typical steel properties (modulus of elasticity of 29,000 ksi and Poisson's ratio of 0.3) were used to describe the elastic material characteristics, while the yield stress and plastic strain extracted from the coupon test results were used to define the plastic behavior. Since ABAQUS is designed to input true plastic stress and strain, the

engineering stress and strain measured from the coupon tests were converted to the true stress and strain by using Eqs. (4.1) and (4.2).

$$\sigma_T = \sigma(1+\varepsilon) \tag{4.1}$$

$$\varepsilon_T = \ln(1+\varepsilon) \tag{4.2}$$

where σ and σ_T are engineering and true stresses, respectively, while ε and ε_T are engineering and true strains, respectively.

4.2.3 Residual Stresses and Geometric Imperfections

Residual stresses were not considered in this study because a number of research studies revealed that residual stresses had a small or negligible effect on the shear behavior of I-shaped girders (Horne and Grayson 1983, Stanway et al. 1993).

Initial geometrical imperfections were incorporated in this study. To apply the initial imperfections, elastic buckling analysis was first conducted. Then, the first buckling mode shape profile was applied as the initial geometry of the model. It was noted in Chapter 2 that initial imperfections were measured at several locations prior to testing; the measured absolute maximum magnitudes of the initial imperfections were 0.16 in. for SG1, 0.35 in. for SG2, and 0.27 in. for CG1 and CG2. Thus, the magnitude of $D/210$, which is equal to 0.25 in., was adopted and used in all numerical models.

The chosen value of maximum imperfection was also compared with the geometric tolerance specified in AWS (2000). AWS Section 5.23.6.2 specifies that the maximum variation be $d_0/80$ (0.33 in. for the specimens) when the depth-to-thicknes ratio is greater than 150 ($D/t_w \geq 150$) and intermediate stiffeners on both sides of the web are used. Therefore, the selected magnitude of imperfection is within the tolerance set by AWS and is a reasonable representative magnitude for this study.

4.2.4 Correlation between Test Results and FEA Predictions

Figure 4.2 shows the deformed shape of Specimens SG1 and SG2 from both testing and finite element analysis. The corresponding load-deflection curves are compared in Figure 4.3. As shown in Figure 4.2 and Figure 4.3, the finite element analysis results closely resembled the behavior of the specimens during testing. The

ratios of ultimate shear strength from finite element analysis to that from experimental testing are 1.01 and 1.02 for Specimens SG1 and SG2, respectively (see Table 4.1).

Figure 4.4 compares the plastic hinge locations formed in the top flange and bearing stiffeners. Plastic hinge locations for SG1 and SG2 from experimental testing and finite element analysis are summarized in the corresponding table.

4.2.5 Simulated Strains

Figure 4.5(a) marks Events *A*, *B*, and *C* on the plot of the applied load versus mid-span deflection for discussion of the simulated flexural strains of the flanges and bearing stiffeners from the finite element analysis of Model SG1. Event *A* represents the state at maximum load, and Events *B* and *C* are the points when the strength has degraded. Interestingly, all boundary members (flanges and bearing stiffeners) remained elastic at maximum load [see Figure 4.5(b) through (d)] for Specimen SG1. Immediately after maximum load was reached, the top flange near the bearing stiffeners reached the yield strain, accompanied with significant buckling of the web. Then, the strains at the expected plastic hinge locations rapidly increased with little loss in shear resistance at Events *B* and *C*. Similar behavior was observed in the bearing stiffeners shown in Figure 4.5(d). After maximum load was reached, the strains at the expected plastic hinge locations increased rapidly. Figure 4.5(c) shows the strain profile of the bottom flange. After maximum load was achieved, the tensile strain at the point of intersection between the intermediate stiffeners and the bottom flange rapidly increased and reached the yield strain at Event *B*. In addition, the compressive strain also increased at a distance away from the intersection point but still remained in the elastic range.

Figure 4.6 shows the principal tensile strains, which all exceed the strain value corresponding to the tension-field stress in the web. The principal strain directions are also shown in the figure. A reference line along the panel diagonal was drawn and two parallel lines passing through the plastic hinges in the top flange and bearing stiffeners were also drawn. Interestingly, the principal tensile strains were mostly in the shaded area. Therefore, the shaded zone can be treated as the tension-field zone. Also, the figure shows that the directions of principal strains are close to that of the panel diagonal.

Similar strain profiles were observed in Model SG2, as shown in Figure 4.7 and Figure 4.8. However, the strains of the top flange at the intersection with the bearing stiffeners exceeded the yield strain at maximum load (Event *A*).

4.3 Steel-Concrete Composite Plate Girder Specimens (CG1 and CG2)

4.3.1 Finite Element Models

Figure 4.9 shows the typical finite element model for Models CG1 and CG2. Standard 3-D shell elements (S4R) were used for modeling the steel girder. The concrete slab was modeled with eight-node linear brick elements (C3D8R). The steel reinforcement and shear studs were modeled with two-node linear beam elements (B31). These beam elements were bonded with the concrete slab by using the "EMBEDDED" constraint option in ABAQUS.

Surface-to-surface interaction techniques were also used to properly connect the surfaces between the two different material surfaces: the steel girder flange and the concrete slab. The steel girder flange surface was selected as the master surface, while the concrete slab surface was selected as the slave surface. Then, the hard contact property was applied for the surface-to-surface interaction to prevent penetration of the surfaces, while allowing separation between the surfaces. Through these interaction techniques, slippage between the steel and concrete surfaces was modelled. Boundary conditions and lateral bracing also simulated the test conditions.

4.3.2 Material Stress-Strain Characteristics

A stress-strain curve of concrete in compression shows an almost linear elastic behavior up to the initial yield stress, which can be taken as 30~40% of the concrete peak stress ($f_c^{'}$), then the curve becomes nonlinear up to the peak stress. Beyond the peak stress, strain softening takes place until failure occurs by crushing of the concrete. Based on these material behaviors, many approaches, including those by Kent and Park (1971), Popovics (1973), Thorenfeldt et al. (1987), Tsai (1988), and Karthik and Mander (2011), predict the stress-strain relationship of unconfined (plain) concrete. Among them, Karthik and Mander's model (2011) was adopted to simulate concrete behavior in compression for unconfined concrete. Figure 4.10 shows Karthik and Mander's

compressive stress-strain curve of concrete. As shown in the figure, the constitutive model consists of three branches; an initial power curve up to the peak stress, followed by a bilinear relation in the post-peak region. Based on a predicted stress-strain relation of normal-weight concrete (Collins and Mitchell, 1994), Karthik and Mander expressed the peak strain as

$$\varepsilon_{c0} = 0.0015 + f_c^{'}(\text{psi})/10^7 \tag{4.3}$$

The ultimate stress and strain were defined as $f_{c1} = 1.74$ ksi and $\varepsilon_{c1} = 0.0036$, respectively. They also specified the failure strain as

$$\varepsilon_{sp} = 0.012 - 7\times10^{-7}\, f_c^{'}(\text{psi}) \tag{4.4}$$

With these parameters, stress of the unconfined concrete as a function of strain can be expressed as follows:

$$f_c = Kf_c^{'}\left(1-|1-x|\right)^n \qquad \text{for} \quad 0 \le x < 1 \tag{4.5}$$

$$f_c = Kf_c^{'} - \left(\frac{Kf_c^{'} - f_{c1}}{x_u - 1}\right)(x-1) \qquad \text{for} \quad 1 \le x < x_u \tag{4.6}$$

$$f_c = f_{c1}\left(\frac{x - x_f}{x_u - x_f}\right) \qquad \text{for} \quad x_u \le x < x_f \tag{4.7}$$

where x is the normalized strain $(= \varepsilon_c / \varepsilon_{c0})$, $x_u = \varepsilon_{c1}/\varepsilon_{c0}$, $x_f = \varepsilon_{sp}/\varepsilon_{c0}$, $K = 1$, $n = E_c\varepsilon_{c0}/f_c^{'}$, and E_c is the Young's Modulus of concrete.

With Karthik and Mander's model, concrete behavior in compression can be inputted into ABAQUS. First, typical concrete material properties (Young's Modulus, E_c, and Poisson's ratio of 0.2) were used to describe elastic material characteristics. It was assumed that first yielding occurs at 40% of the concrete peak stress. Then, the Concrete Damage Plasticity model available in the material library of ABAQUS was used to simulate the nonlinear behavior.

Also, tension stiffening behavior was modeled in the analysis. There are three methods in ABAQUS to model the tension stiffening behaviors: defining cracking strain, defining cracking displacement, and defining fracture energy. Since the tension stiffening approach using a stress-strain relationship usually causes an undesirable mesh sensitivity problem, the fracture energy approach is widely used to mitigate this problem.

The fracture energy is the energy required to propagate a tensile crack of unit area. With the fracture energy (G_f) approach, the brittle behavior of the concrete is characterized by a stress-displacement response that is independent of the mesh size (ABAQUS Manual, 2011) rather than a stress-strain response. Figure 4.11 shows the relationship between the post-failure stress and fracture energy. As shown in the figure, it was assumed that the stress decreases linearly after cracking and hence the failure displacement as a function of fracture energy is

$$u_{to} = 2G_f / f_{to} \tag{4.8}$$

CEB/FIP Model Code (CEB/FIP, 2010) which is the European design code for concrete structures provides a simple equation to calculate the fracture energy:

$$G_f = 73 f_{cm}^{0.18} \tag{4.9}$$

where f_{cm} is the mean compressive strength ($= f_c^{'} + \Delta f$) and $\Delta f = 8$ MPa. The fracture energy for ordinary normal weight concrete in Eq. (4.9) has units of N/m. The mean compressive strengths from the concrete cylinder tests (described in Chapter 2) conducted for Specimens CG1 and CG2 were used to calculate the fracture energy.

Coupon test results were used to simulate the relationship between the stress and strain for the steel girders and reinforcement. A bilinear response was assumed for the shear studs, which have a nominal yield strength of 51 ksi.

4.3.3 Correlation between Test Results and FEA Predictions

The correlation between the predicted and experimental responses for the steel-concrete composite girder specimens is provided in Figure 4.12. The finite element analysis was able to predict the maximum load. However, the analysis diverged and was terminated when it was in the degradation branch. Model CG1, as shown in Figure 4.12(a), only showed a 1-kip load drop after the peak before the analysis was stopped. This type of convergence issue has been observed and addressed by Baskar et al. (2002) for finite element analysis of steel-concrete composite girders using ABAQUS. The convergence issue mainly comes from the concrete, which is a brittle material. Once the concrete fails in tension, the analysis might have to be aborted. These convergence issues can be overcome by increasing the fracture energy value or increasing the failure

displacement shown in Figure 4.11. However, the increase of fracture energy results in an increase of the ultimate load. Therefore, it is desirable to avoid modifying the tensile behavior of concrete. Since the nonlinear finite element analysis successively achieved the ultimate load in this study, no modification to the tensile behavior of the concrete was made. The ratios of ultimate shear strengths obtained form finite element analyses to those of the experiments are 1.03 and 1.06 for Specimens CG1 and CG2, respectively (see Table 4.1).

4.3.4 Simulated Strains

Figure 4.13 shows the principal tensile strains, which all exceed the strain value corresponding to the tension-field stress in the web of Model CG1. As with steel girder specimens like Model SG1, the yield band in the web of the composite girder specimens can be approximated by the shaded area. The magnitude and directions of the strains are also similar to those of the steel girders. Figure 4.14(a) shows all principal compressive strains in the concrete slab. The simulated compressive strains indicate that the compressive stresses flow from the base of the first stud to the head of the second stud. Figure 4.14(b) plots the compressive strains that exceed 0.002, which is the peak strain corresponding to the peak stress ($f_c^{'}$). Figure 4.14(c) shows the principal tensile strains that exceed the cracking strain of concrete. Since most elements between the shear studs reached the concrete cracking strain, it implies that there is high cracking potential between the shear studs.

A similar behavior of Model CG2 was observed and principal tensile strains in the web and principal compressive strains in the concrete slab are shown in Figure 4.15 and Figure 4.16, respectively. Figure 4.17 shows that the compressive stresses that flow from the base of the first stud to the head of the second stud are within the flange width of steel girders. This indicates that the effective width for shear strength evaluation is much smaller than that for bending.

Table 4.1: Shear Strength Comparison between FEM and Experiments

Specimen No.	Panel Shear Strength, V (kips)		V_{FEM} / V_{TEST}
	FEM Result (V_{FEM})	Test Result (V_{TEST})	
SG1	318.8	315.3	1.01
SG2	194.5	190.3	1.02
CG1	363.6	352.6	1.03
CG2	225.2	212.1	1.06

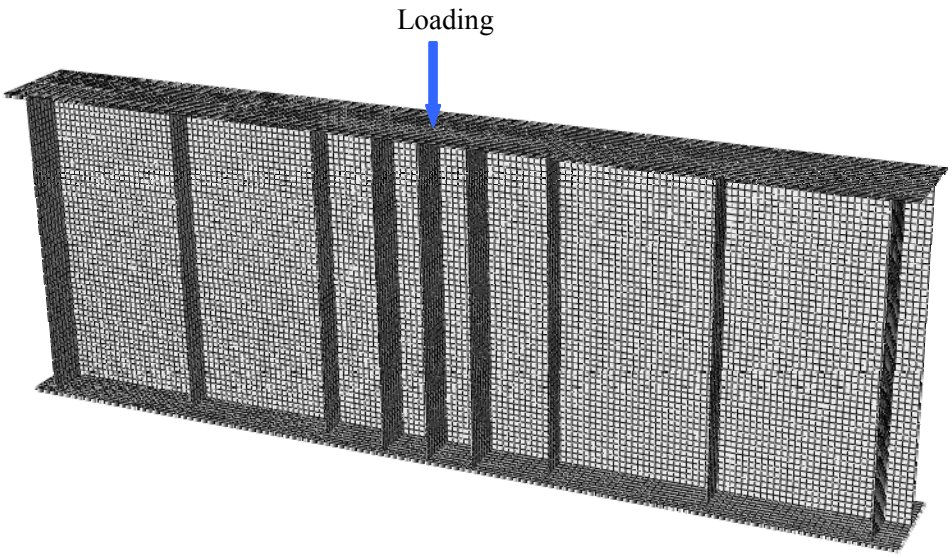

Figure 4.1: Specimen SG1: Typical Finite Element Model and Mesh

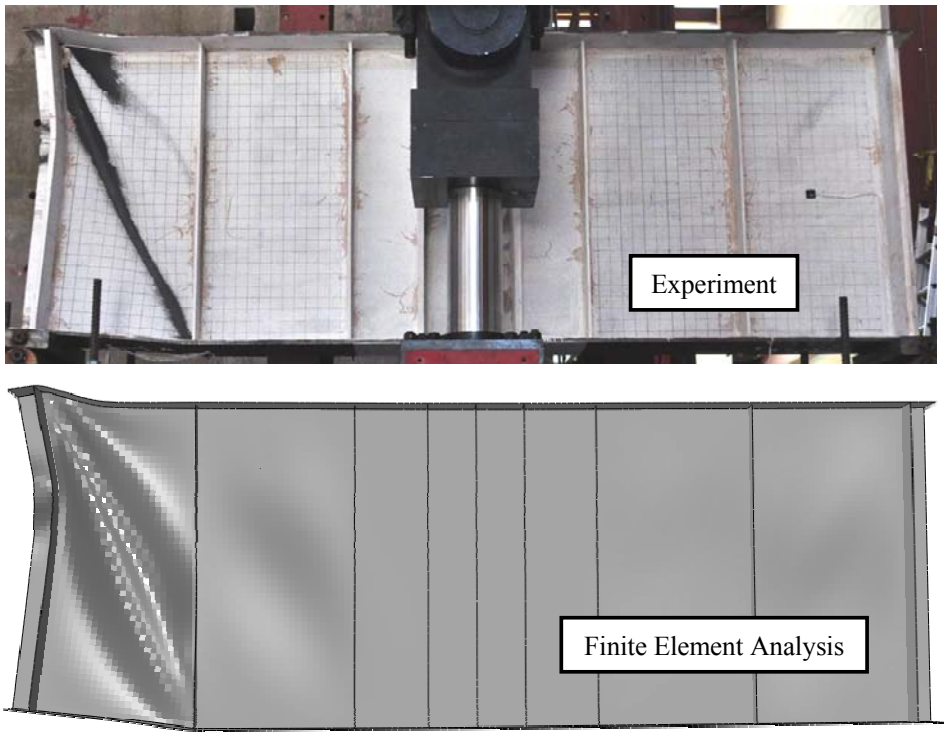

(a) Specimen SG1

Figure 4.2: Comparison of Deformed Shape

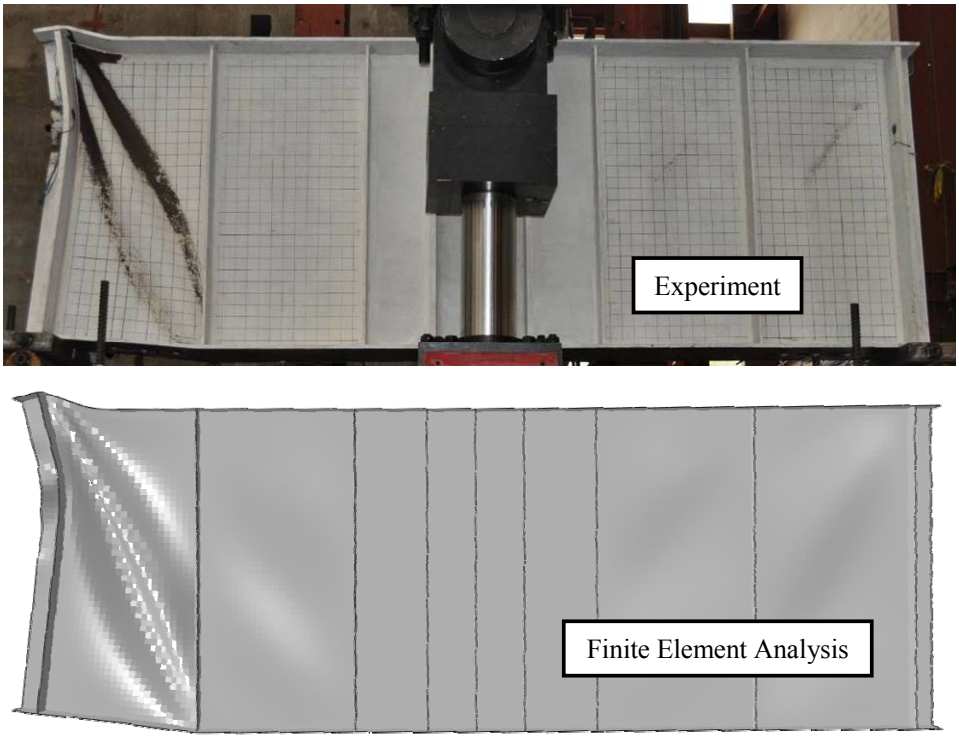

(b) Specimen SG2

Figure 4.2: Comparison of Deformed Shape (continued)

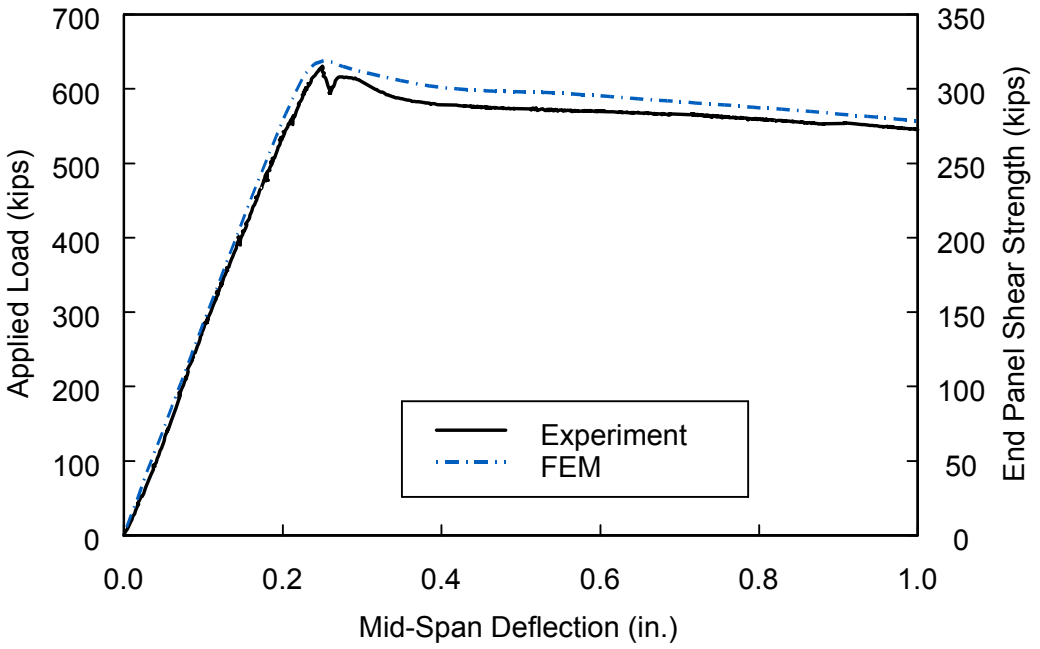

(a) Specimen SG1

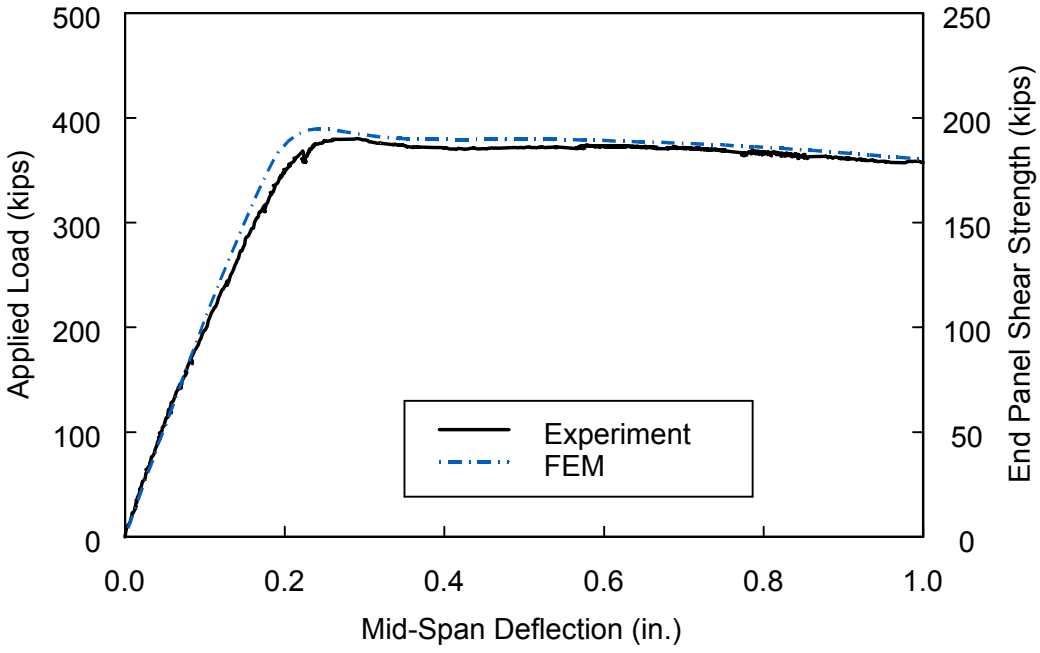

(b) Specimen SG2

Figure 4.3: Correlation between Test Results and FEM Analyses

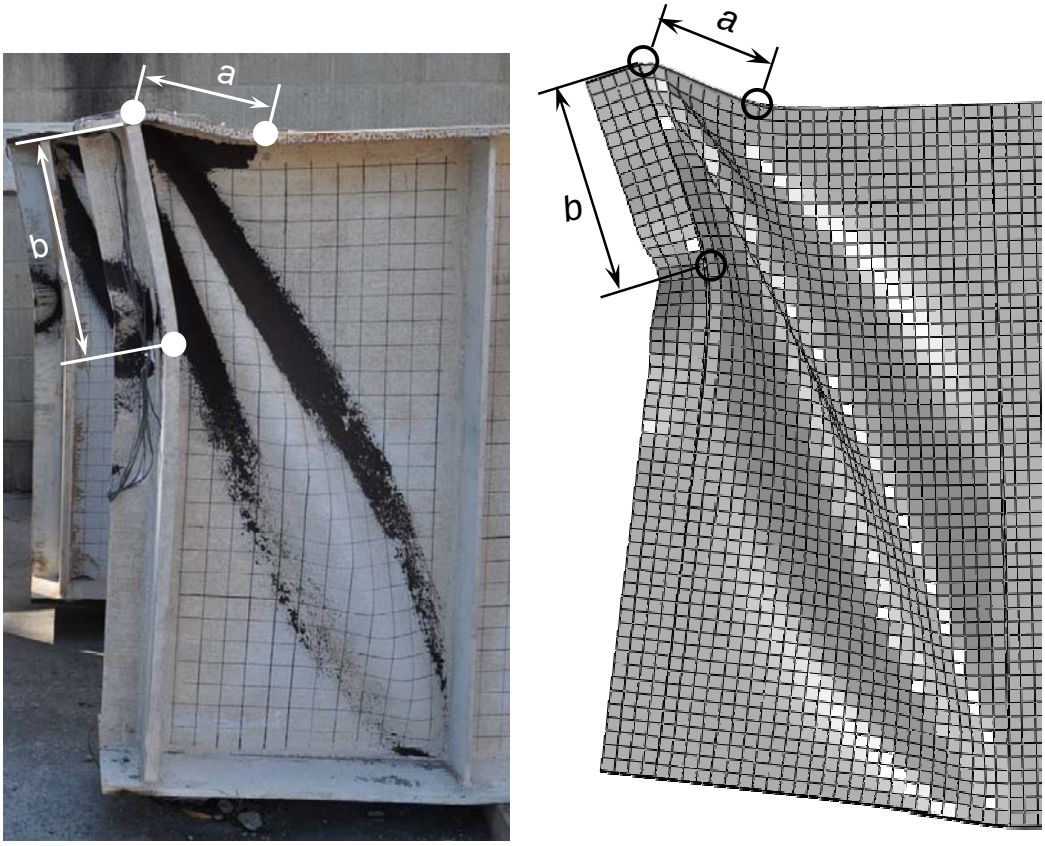

Specimen No.	*a* (in.)		*b* (in.)	
	Test	FEM	Test	FEM
SG1	10.5	10.1	18.1	18.3
SG2	9.1	8.1	14.8	15.7

Figure 4.4: Comparison of Plastic Hinge Locations

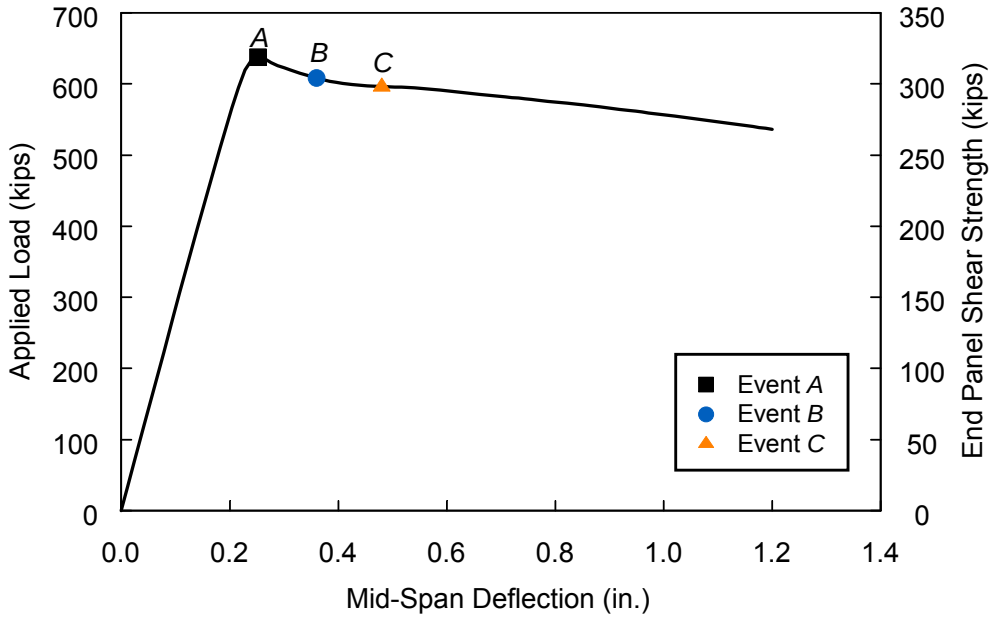

(a) Load versus Mid-Span Deflection

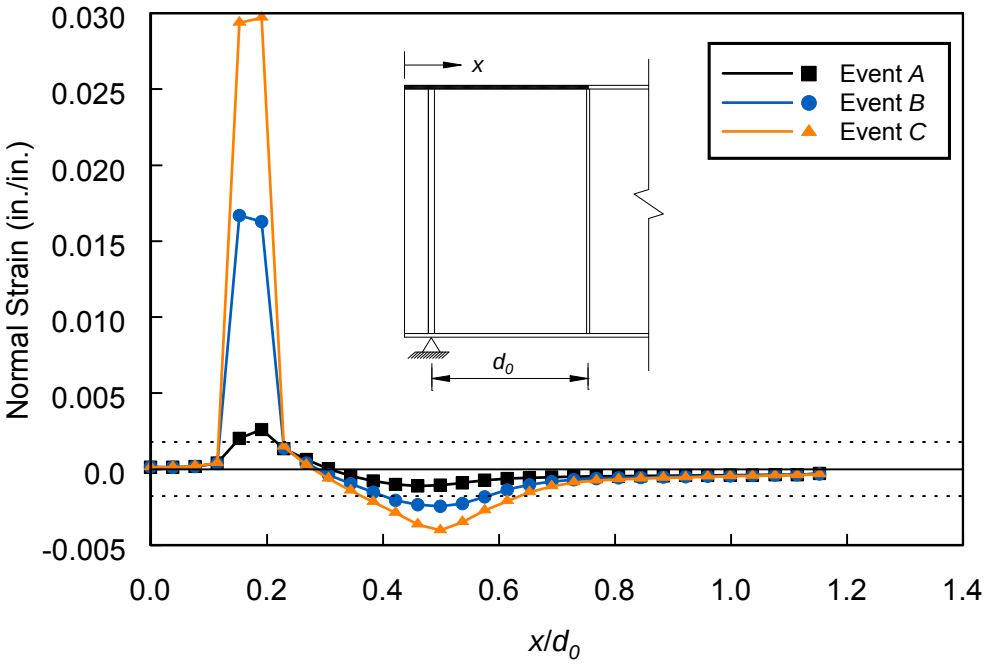

(b) Normal Strain Profiles on Top Flange

Figure 4.5: SG1: Strain Profiles

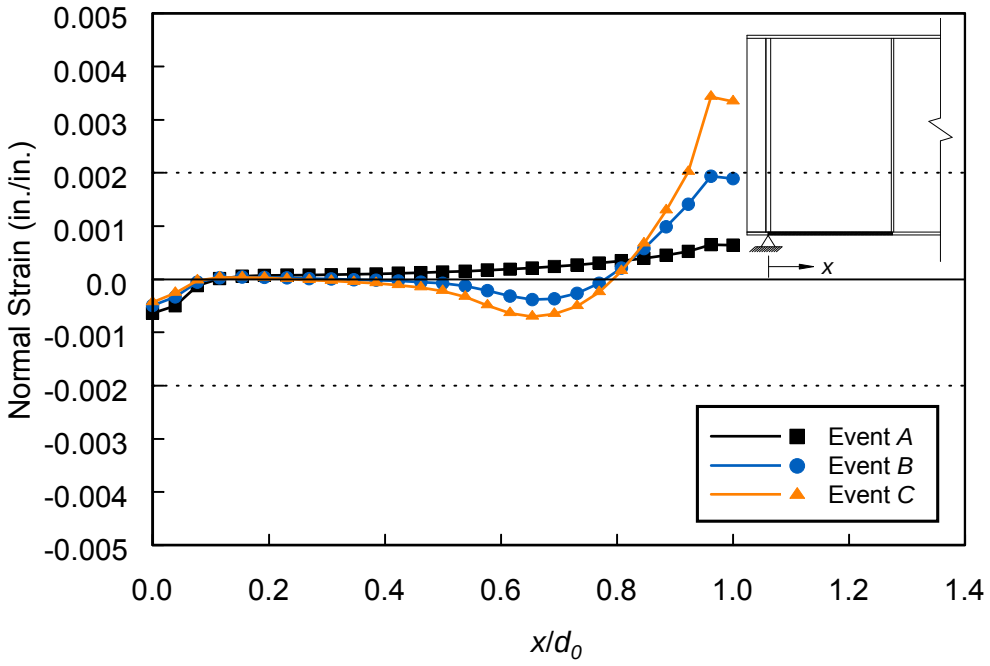

(c) Normal Strain Profiles on Bottom Flange

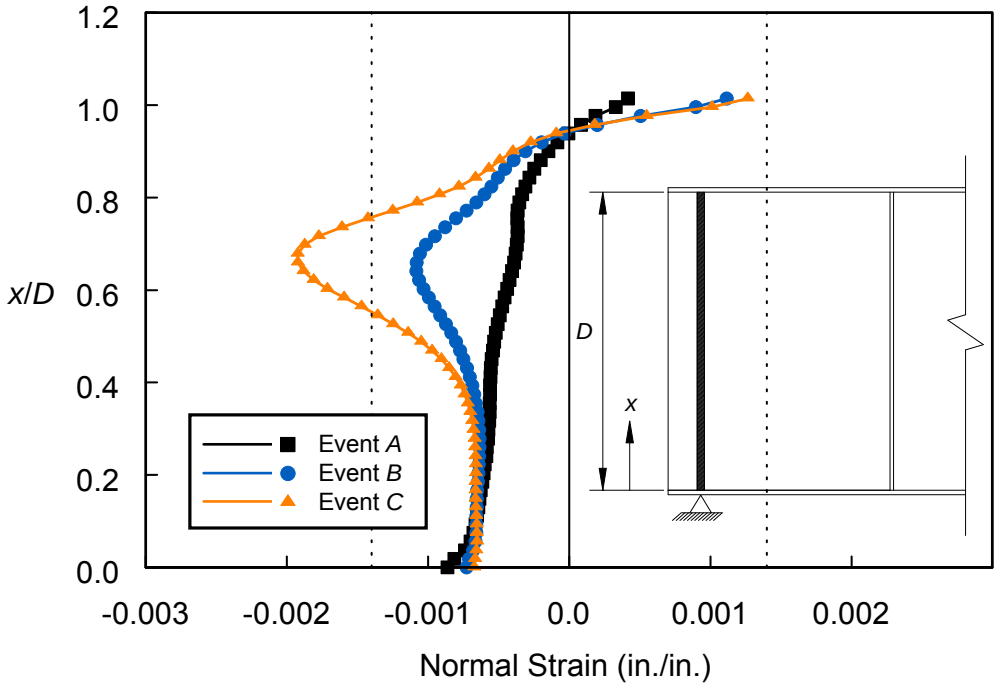

(d) Normal Strain Profiles along Height of Bearing Stiffener

Figure 4.5: SG1: Strain Profiles (continued)

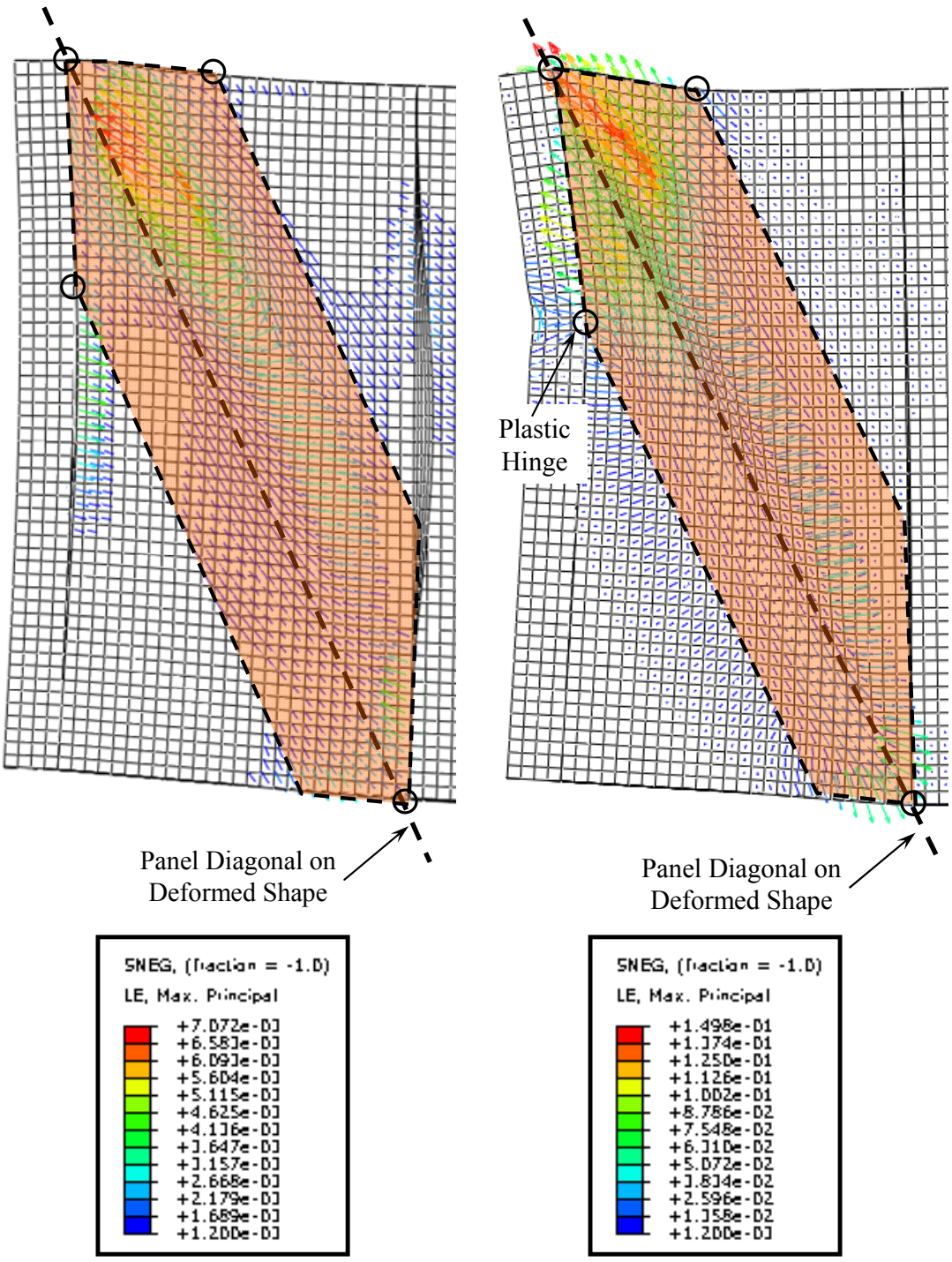

(a) at Maximum Load (b) at End of Analysis (Δ=1.2 in.)

Figure 4.6: SG1: Principal Tensile Strains

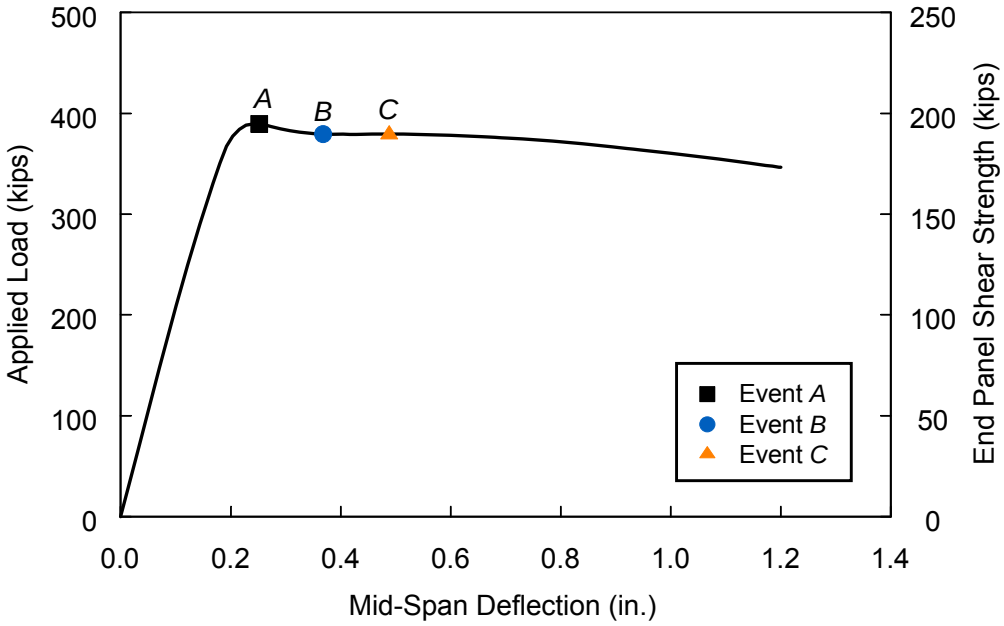

(a) Load versus Displacement

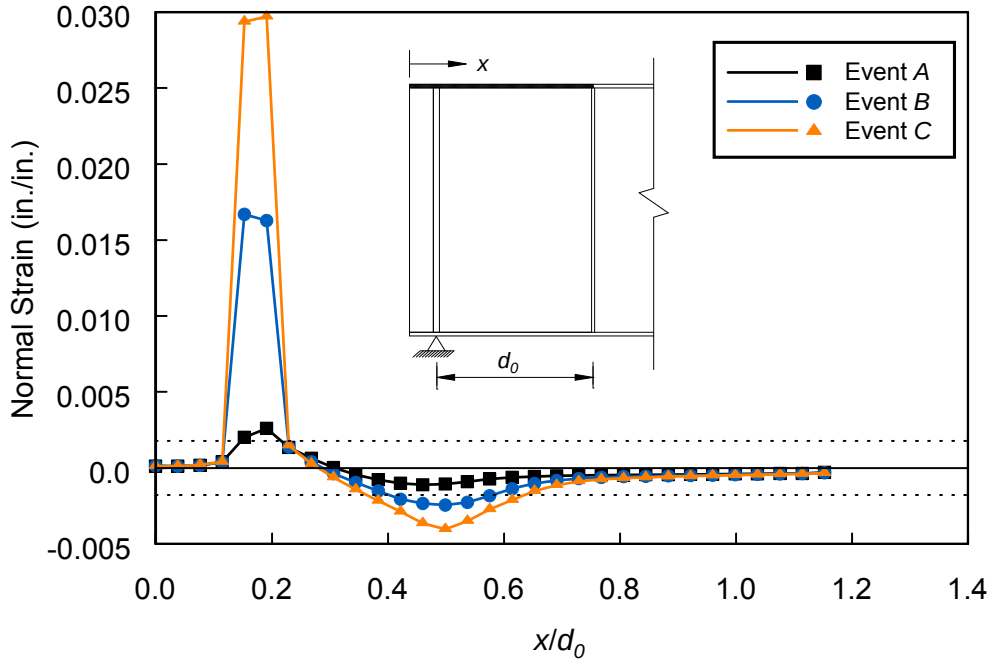

(b) Normal Strain Profiles on Top Flange

Figure 4.7: SG2: Strain Profiles

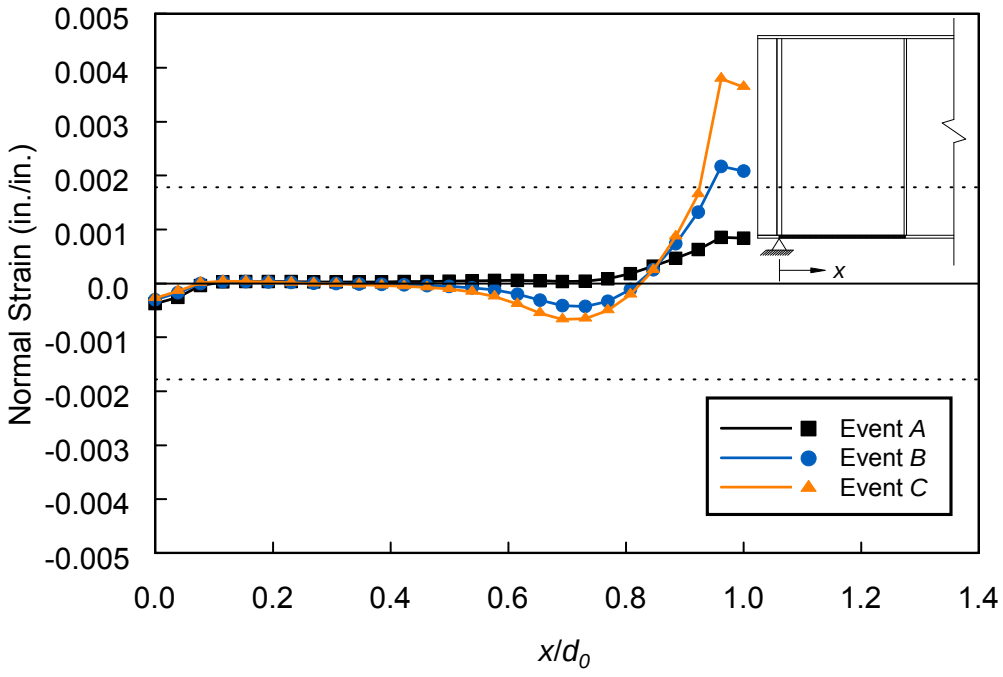

(c) Normal Strain Profiles on Bottom Flange

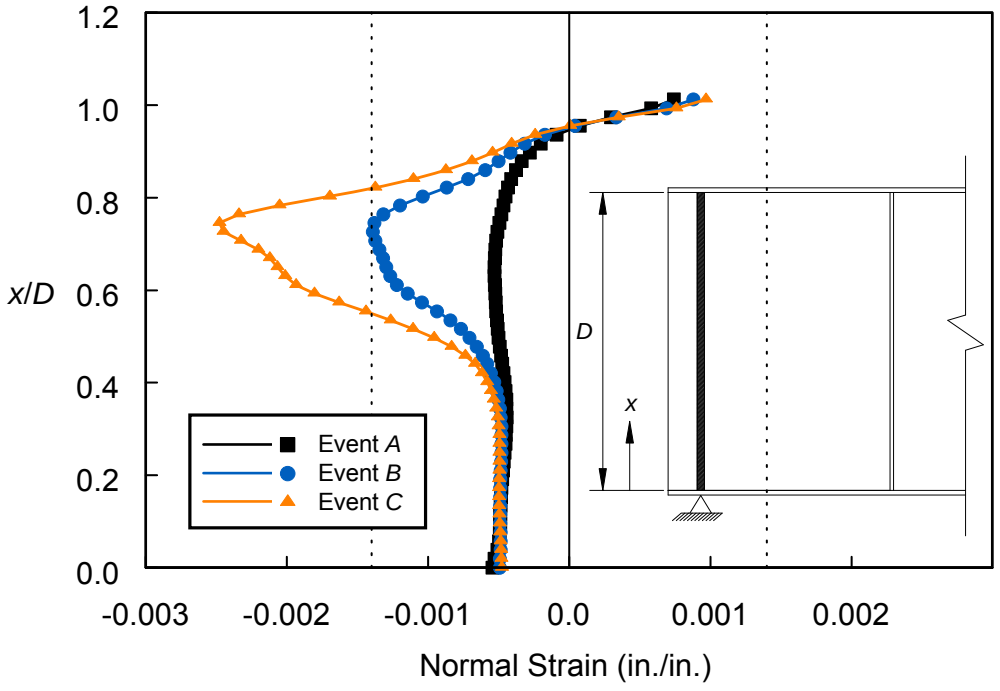

(d) Normal Strain Profiles along Height of Bearing Stiffener

Figure 4.7: SG2: Strain Profiles (continued)

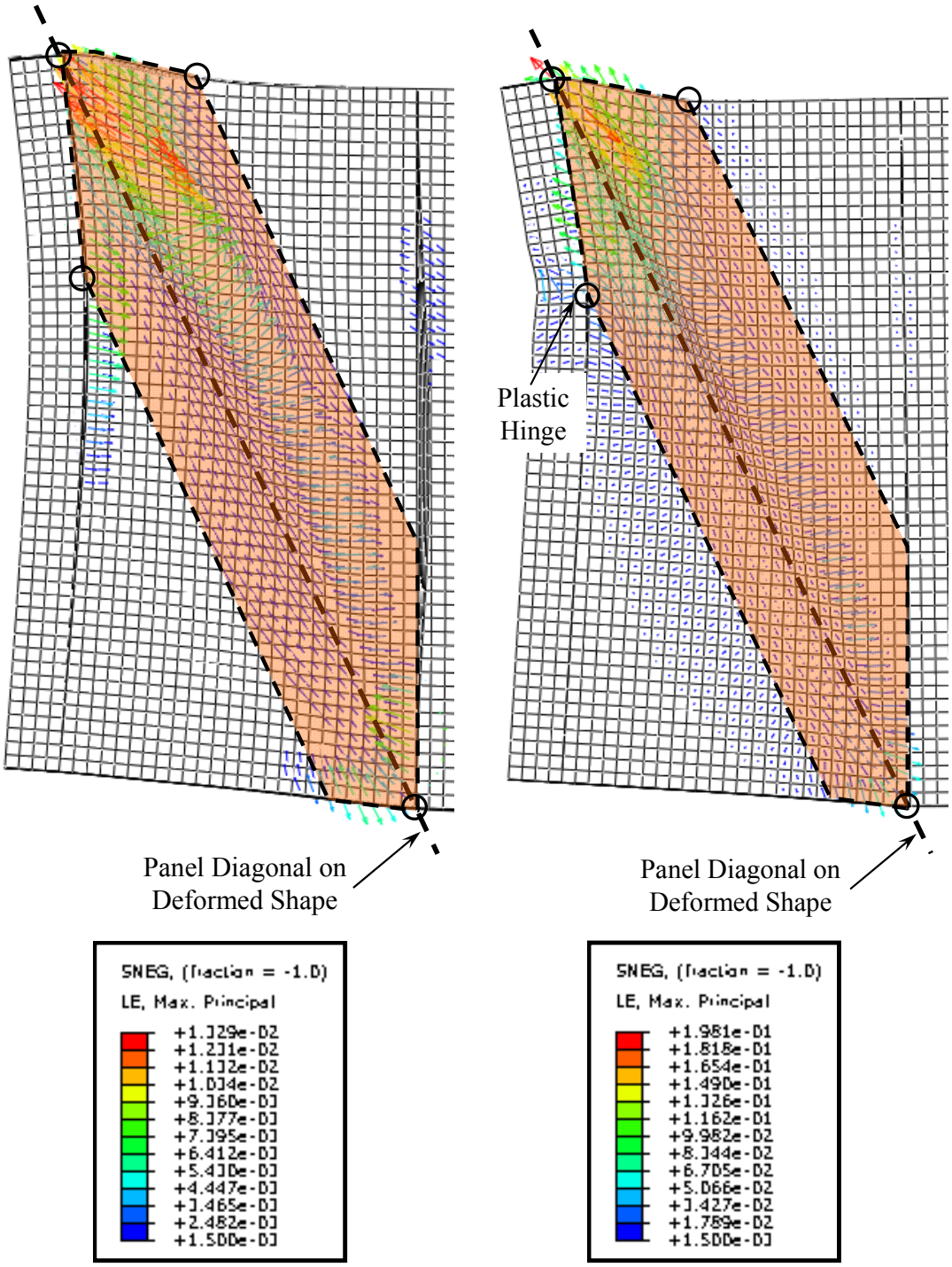

(a) at Maximum Load (b) at End of Analysis (Δ=1.2 in.)

Figure 4.8: SG2: Principal Tensile Strains

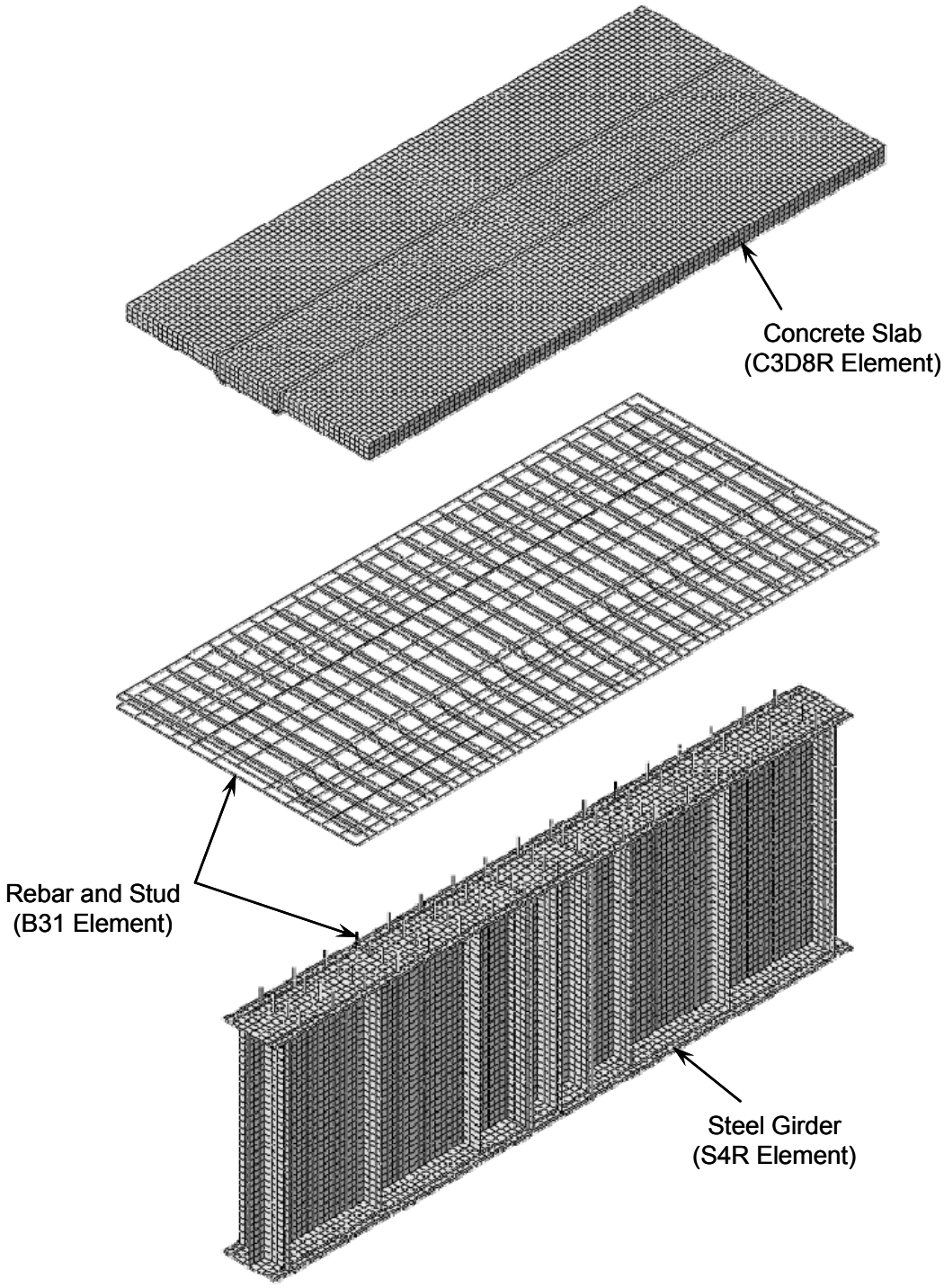

Figure 4.9: Specimen CG2: Typical Finite Element Model and Mesh

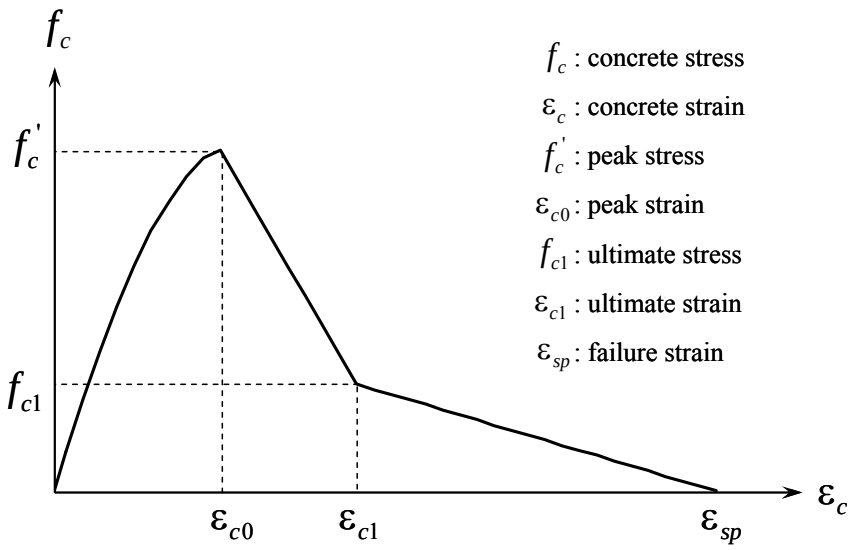

Figure 4.10: Typical Concrete Stress-Strain Curve in Compression

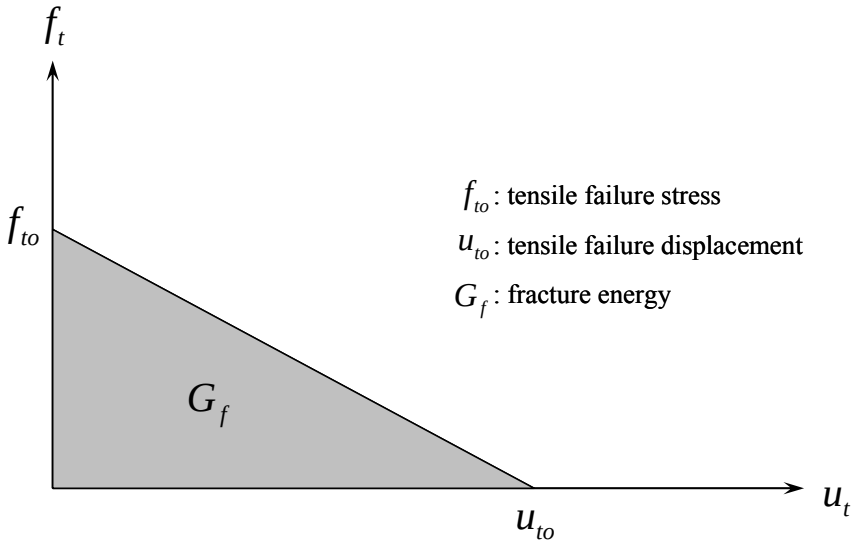

Figure 4.11: Relationship between Post-Failure Stress and Fracture Energy

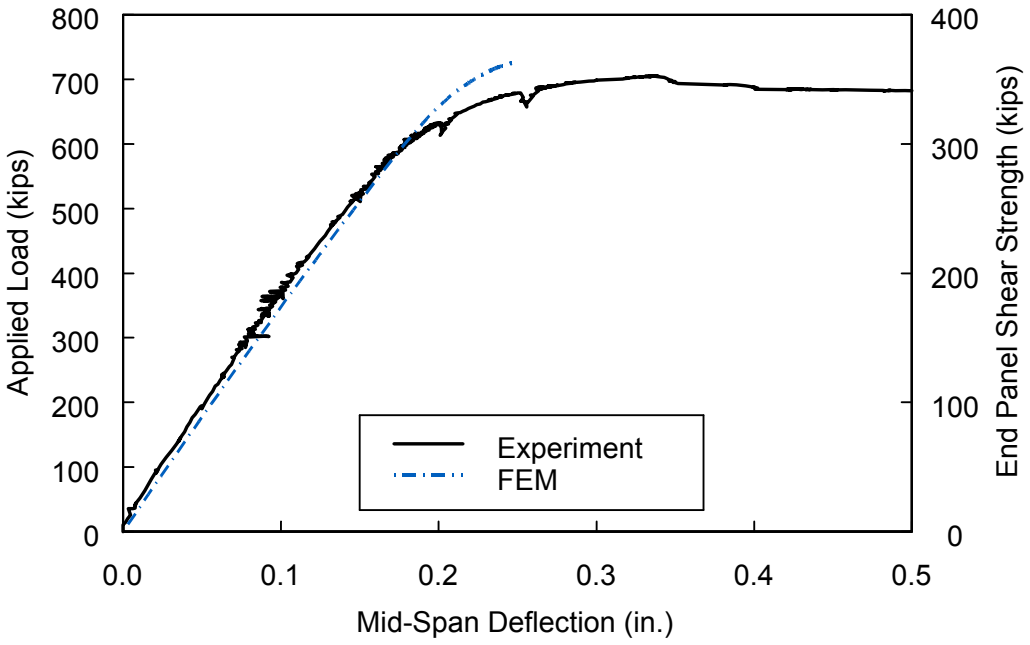

(a) Specimen CG1

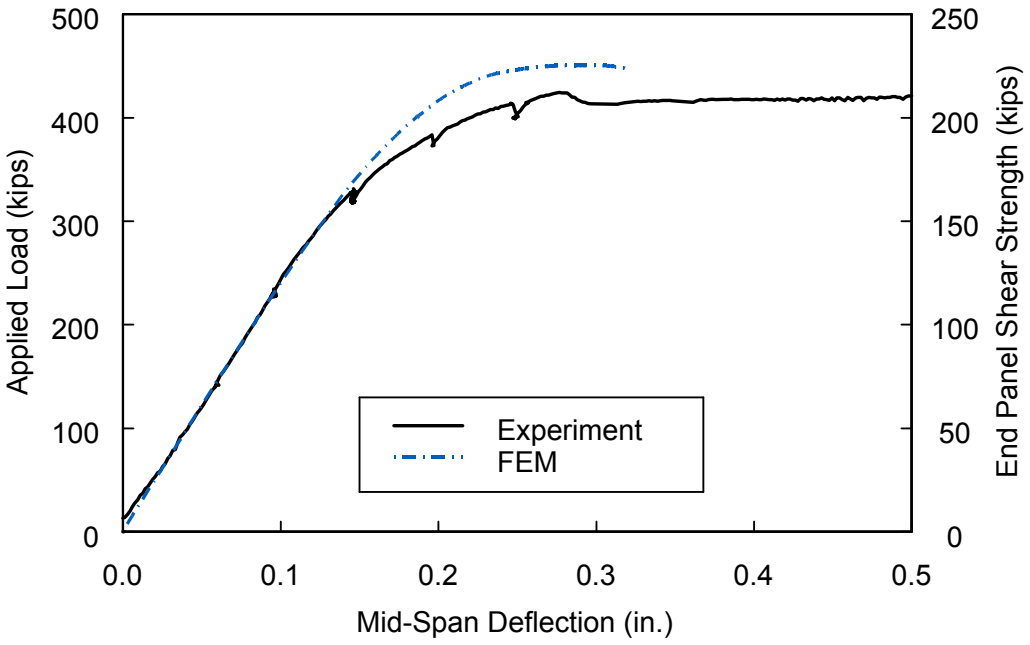

(b) Specimen CG2

Figure 4.12: Correlation between Test Results and FEM Analyses

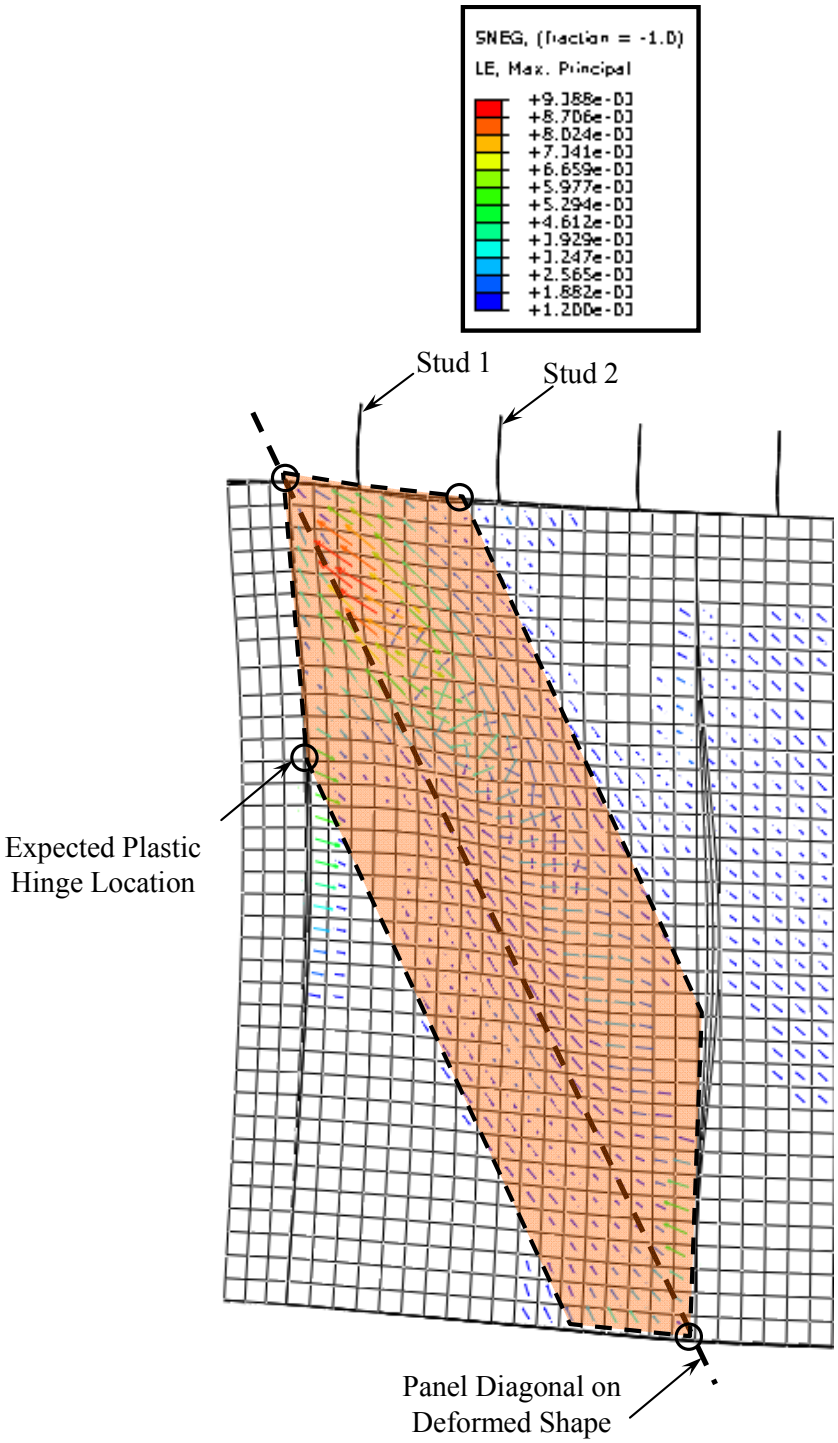

Figure 4.13: CG1: Principal Tensile Strains (Δ=0.25 in.)

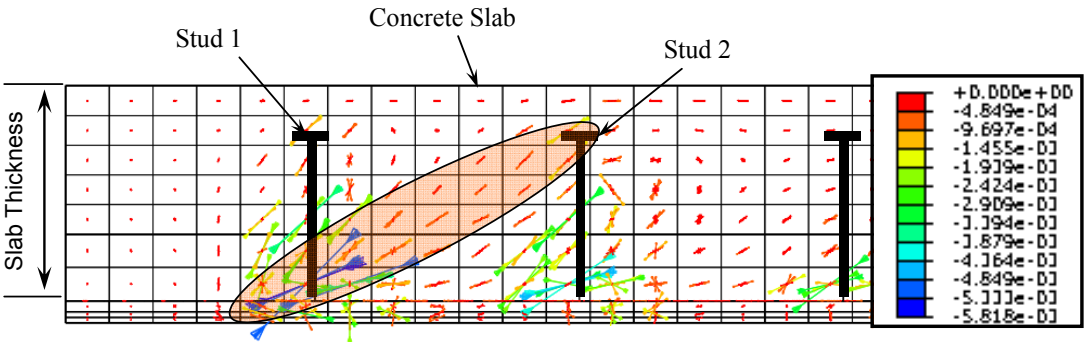

(a) Principal Compressive Strains (Range from 0 to 0.0058)

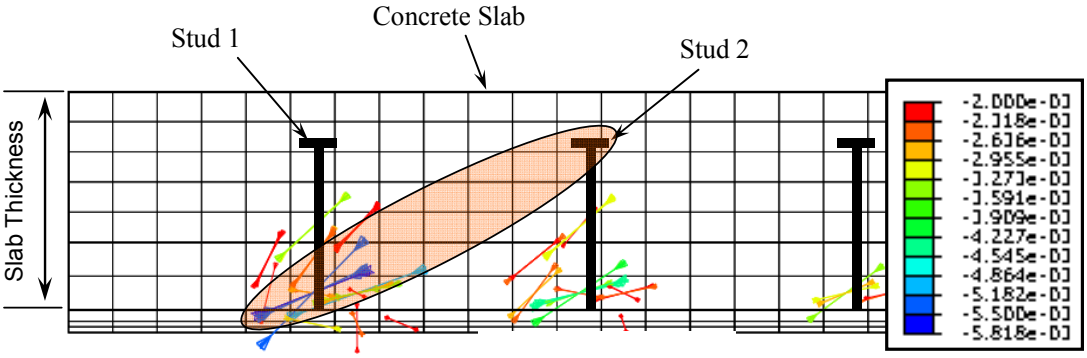

(b) Principal Compressive Strains (Range from 0.002 to 0.0058)

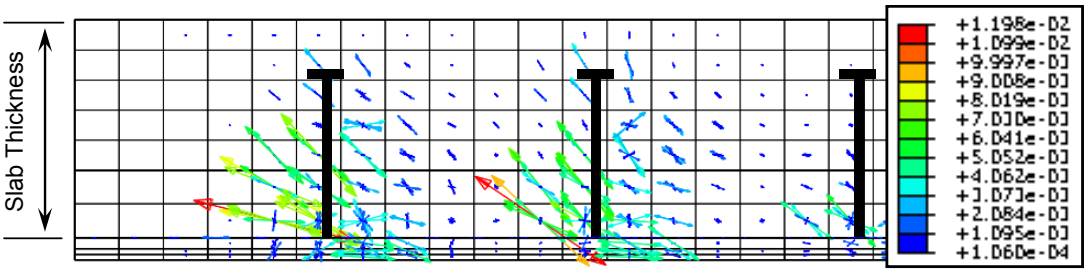

(c) Principal Tensile Strains

Figure 4.14: CG1: Principal Strains in Concrete Slab

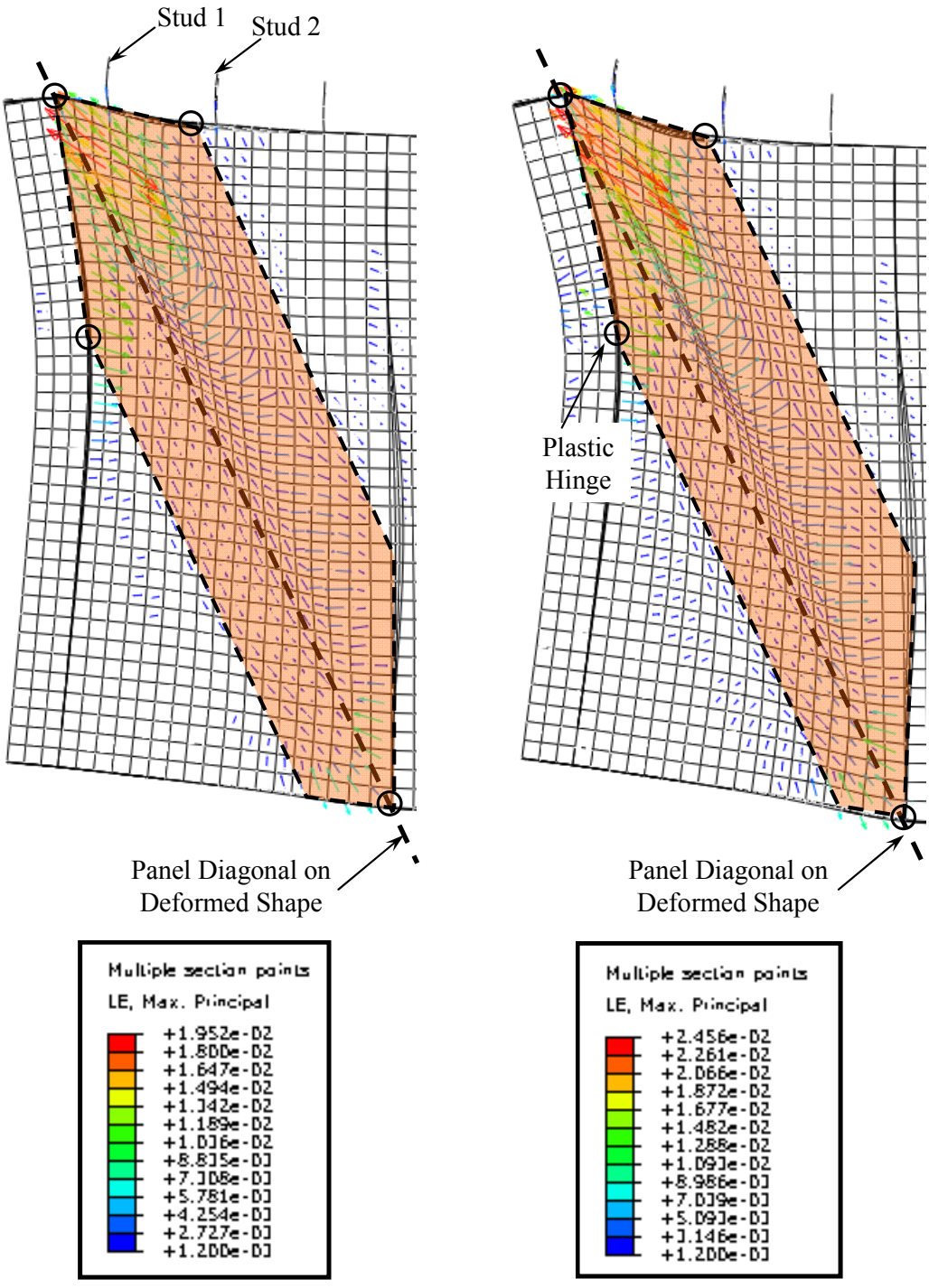

(a) at Maximum Load (b) at End of Analysis (Δ=0.31 in.)

Figure 4.15: CG2: Principal Tensile Strains

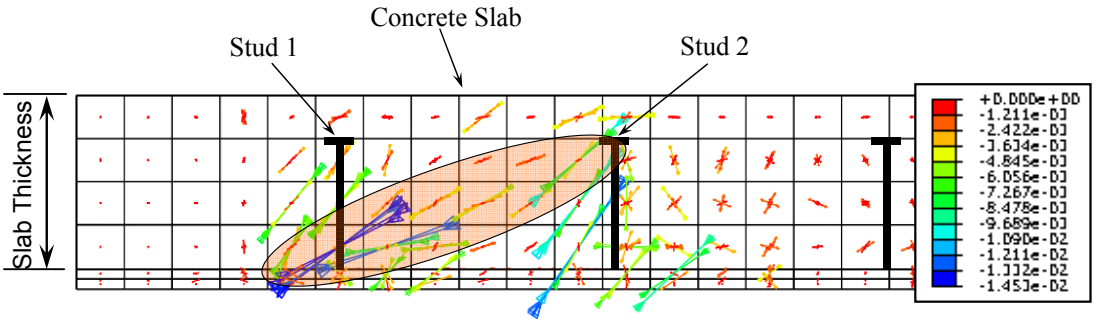

(a) Principal Compressive Strains (Range from 0 to 0.0145)

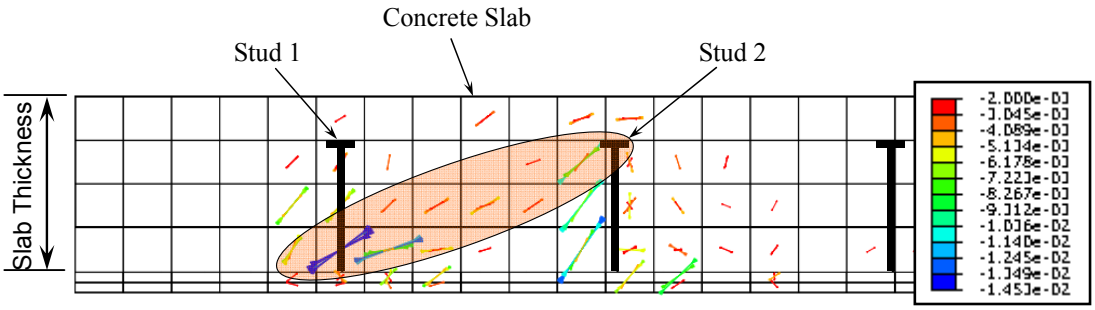

(b) Principal Compressive Strains (Range from 0.002 to 0.0145)

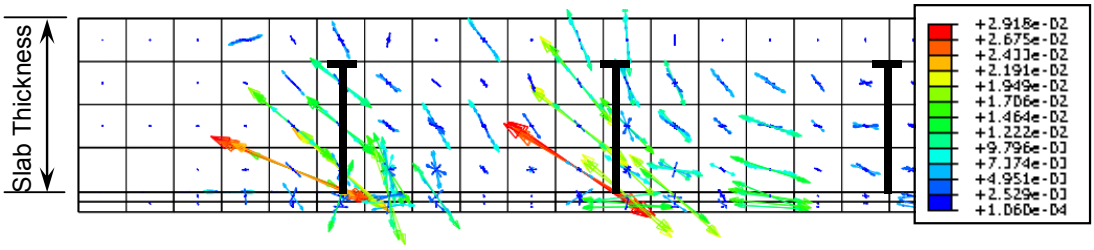

(c) Principal Tensile Strains

Figure 4.16: CG2: Principal Strains in Concrete Slab

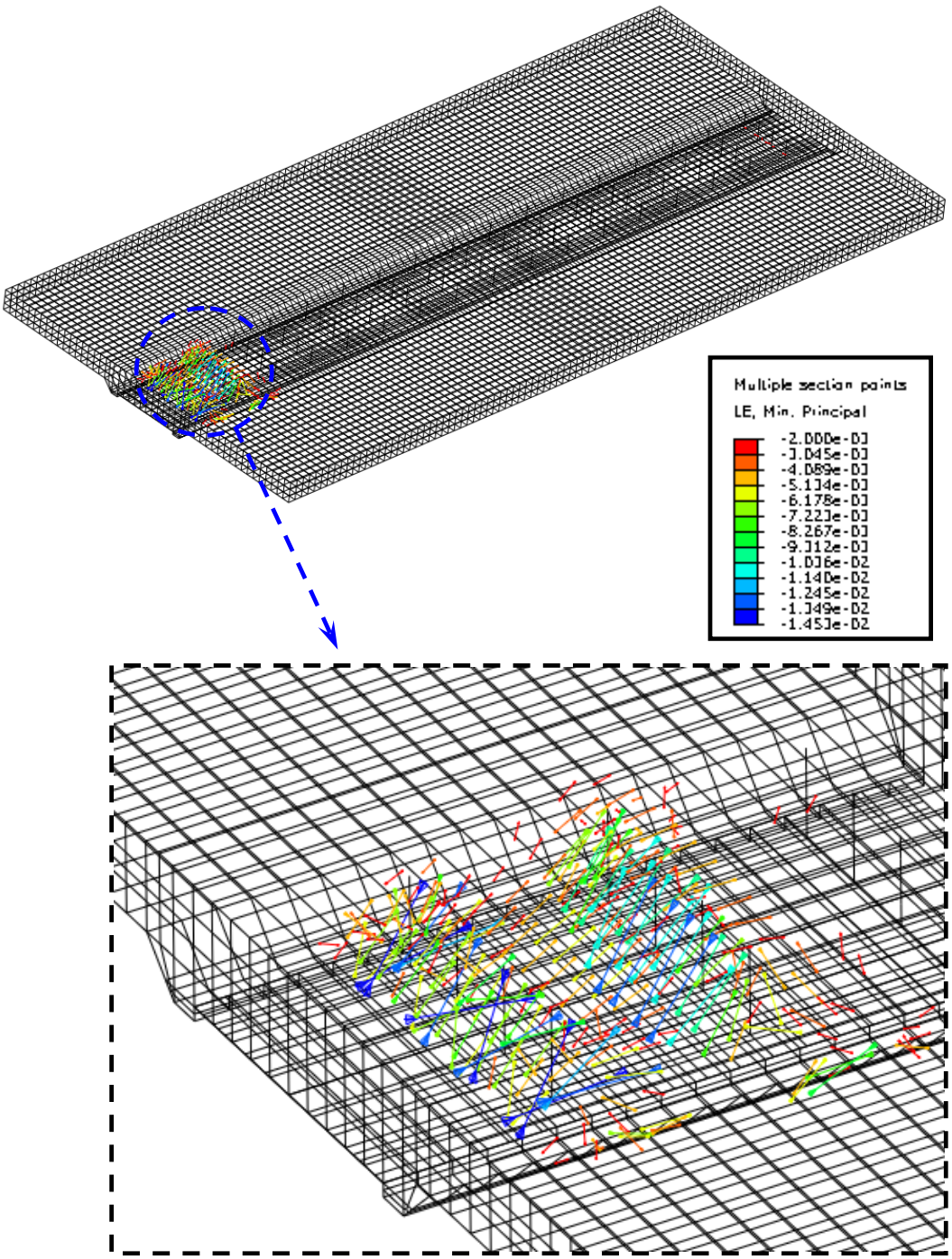

Figure 4.17: CG2: Concrete Slab Effective Shear Width

5. FACTORS AFFECTING SHEAR RESISTANCE OF END PANELS: A PARAMETRIC STUDY (PHASE 1)

5.1 General

In Chapter 4, finite element analyses were carried out to study the behavior of the plate girder end panels, and to correlate the behavior with that observed during testing. However, the shear resistance of the plate girder end panel may be affected by several parameters, including flange and bearing stiffener thicknesses, panel depth-to-thickness ratio, and panel width-to-depth ratio. Finite element analyses were performed in this chapter in order to study the effects of these parameters. Also, the findings from this parametric study will be used to develop an analytical model in Chapter 6 for the prediction of end panel shear strength.

5.2 Steel Plate Girders

5.2.1 Introduction

A total of 99 models (63 variation models from Model SG1 and 36 variation models from Model SG2) were analyzed. The parameters in this study were flange thickness (t_f), bearing stiffener thickness (t_b), width-to-depth ratio (d_0 / D), and depth-to-thickness ratio (D/t_w). The main objective of this study was to identify variables that affect the panel shear strength and plastic hinge locations in the top flange and bearing stiffeners. Material properties from the test specimens were used in the finite element models. Also, the nominal plate thicknesses of the test specimens were used for all finite element models. Figure 5.1 shows a typical finite element model used in this parametric study. To evaluate the effect of panel width-to-depth ratio, the girder length had to be increased, and the increased length may cause an unexpected failure mode like flexural failure. To avoid this failure mode, only two end panels were used in the study. To confirm similar behaviors between the models with 4 panels and 2 panels, the behavior of the steel plate girder Model SG1 with 4 panels (see Figure 4.1) and 2 panels are compared in Figure 5.2. As expected, the initial stiffness of the model with 2 panels

is stiffer than the one with 4 panels. However, the maximum shear strengths of two cases are almost the same. The maximum loads achieved from the finite element analyses are 637.5 and 638.7 kips for the model with 4 and 2 panels, respectively [see Figure 5.2(a)]. The plastic hinge locations are also almost the same between the two models, as shown in Figure 5.2(b). A minor discrepancy between the two might be due to having slightly different mesh sizes.

5.2.2 Effect of Flange and Bearing Stiffener Thicknesses

Figure 5.3(a-c) and Figure 5.4(a-c) show the effect of the flange and bearing stiffener thicknesses. The end panel shear capacity increases as the flanges or bearing stiffeners increase in thickness. Additionally the plastic hinges at the top flange and bearing stiffeners tend to form further away from the intersection of the top flange and the bearing stiffeners as thicknesses are increased. This may be due to the fact that the increased thicknesses of the boundary members (flanges and bearing stiffeners) result in higher flexural strengths of these members to resist higher tension-field forces before they fail. According to Basler's equation [see Eq. (1.10)] to calculate the tension-field stress, the magnitude of the web tension-field stress remains the same if the same material and geometry of the web panels are used. Therefore, to increase the tension-field force, the width of the tension-band should be increased to fail the boundary members. As a result, the plastic hinges will form further away from the intersection of the top flange and bearing stiffeners. Table 5.1(a-c) and Table 5.2(a-c) summarize the plastic hinge locations identified from the analyses.

5.2.3 Effect of Panel Depth-to-Thickness and Width-to-Depth Ratios

Figure 5.3(d) plots the variation of the end panel shear strength with respect to the width-to-depth ratio and depth-to-thickness ratio. The panel depth, flange size, and bearing stiffener size corresponded to those in Model SG1, but the panel width and web thickness were varied. Since AASHTO Specifications (2014) limits the end panel width-to-depth ratio to 1.5, panel width-to-depth ratios of 0.5, 1.0, and 1.5 were consiered. The panel depth-to-thickness ratio also varied from 180 to 320.

Table 5.3 and Figure 5.5 show that when the panel width-to-depth ratio is constant, the depth-to-thickness ratio has a minor effect on the plastic hinge locations.

For example, when the depth-to-thickness ratio increased from 180 to 320 with a constant width-to-depth ratio of 0.5, the plastic hinge locations shifted only by 1 in. Also, for the same increase in depth-to-thickness ratio with a constant width-to-depth ratio of 1.5, the plastic hinges formed at the same locations, regardless of the depth-to-thickness ratio. This observation deserves special attention. In Basler's equation [see Eq. (1.10)] to calculate the tension-field stress, the tension-field stress is a function of the ratio of panel buckling stress to the yield stress. Since both web yield stress, F_{yw}, and shear yield stress, τ_y, are constant, the only variable to determine the tension-field stress is the buckling stress, τ_{cr}. When the panel depth-to-thickness ratio is increased, the buckling stress of the web panel is decreased, and the tension-field stress increases. With a higher tension-field stress, boundary members need to resist a higher out-of-plane force (vertical force for flanges and horizontal force for bearing stiffeners) induced by the tension-field stress. Therefore, per Basler's theory, the boundary members should fail by forming plastic hinges closer to the intersection of the top flange and bearing stiffeners.

However, the results from the parametric study do not support this. Since the plastic hinge locations remain about the same, it suggests that there must be another source which increases the out-of-plane flexural strength of the boundary members. That is, when the tension-field stress increases, flexural strengths of the boundary members must also increase to be consistent with observations made from the parametric study. One way to increase the flexural strength of the boundary members is to allocate a small portion of the web to act together with flanges and bearing stiffeners. This issue is further discussed in Section 6.7.

5.2.4 Effect of Web End Extension, *e*

Figure 5.4(d) shows the effect of extending the web beyond the support. The results, including the ultimate shear strength and plastic hinge locations, are summarized in Table 5.4. When the web extension, *e*, increases, the distance to the plastic hinge location (*b*) increases, while the plastic hinge remains at the same location in the flange. Because the web extension together with the bearing stiffeners can resist a higher horizontal component of the tension-field force, the shear strength also increases. In this parametric study, at a width-to-depth ratio of 0.5, the shear strength was about 7%

greater when the web extension is 8 in. (e = 8 in.) than when there was no web extension. When the width-to-depth ratios were 1.0 and 1.5, the shear strengths increased by about 8% and 6%, respectively.

5.3 Steel-Concrete Composite Plate Girders

5.3.1 Introduction

To study the contribution of the concrete slab on the ultimate shear strength in the end panels of steel-concrete composite girders, a parametric study was performed. Model CG2 was adopted as a base model for finite element analysis. Then two parameters, concrete slab width and shear stud location, were varied to investigate thier effects on the shear strength.

5.3.2 Effect of Concrete Slab Width

Both Models CG1 and CG2 had a 6-ft wide concrete slab. In the nonlinear finite element analysis in Chapter 4, it was observed that the effective width of the concrete slab for shear resistance was close to the flange width of the steel girder (see Figure 4.17). This observation contradicted a previous research study (Darehshouri et al. 2012) which concluded that the entire slab width is effective. To better understand this issue, the concrete slab width was varied from 2 to 8 ft. The ultimate shear strengths are summarized in Table 5.5. Figure 5.6 indicates that the concrete slab width has a very minor effect on the ultimate shear strength of steel-concrete composite girders. This confirms that, for calculating the shear strength of end panels, the effective concrete slab width should be close to the steel girder flange width.

5.3.3 Effect of Shear Stud Location

Figure 4.14 and Figure 4.16 show that the compressive stresses in the concrete flow between the shear studs under shear loading. The most critical section is the diagonal direction between stud 1 and stud 2. To confirm the load-carrying mechanism in the concrete slab, stud 2 was placed at varying distances away from stud 1. The total number of shear studs was maintained to keep the same degree of composite action.

Figure 5.7 plots the effect of the distance between end studs on the shear strength of end panels. The ultimate shear strength increases slightly as the distance between

two consecutive studs decreases. Figure 5.8 confirms the load-transfer mechanism between two end studs, regardless of the distance between them. This observation will be used in Section 6.9 for the development of a model that considers the contribution of the concrete slab to the shear strength of end panels.

Table 5.1: Summary of Model SG1 Parametric Study ($D/t_w = 210$)

(a) $d_0/D = 0.5$

t_b	$t_f = 0.5$ in. ($2t_w$)			$t_f = 0.75$ in. ($3t_w$)			$t_f = 1.0$ in. ($4t_w$)			$t_f = 1.5$ in. ($6t_w$)		
	Ultimate Strength (kips)	a (in.)	b (in.)	Ultimate Strength (kips)	a (in.)	b (in.)	Ultimate Strength (kips)	a (in.)	b (in.)	Ultimate Strength (kips)	a (in.)	b (in.)
0.5 in. ($2t_w$)	312.2	8.2	15.6	316.9	10.3	17.6	323.0	12.2	18.6	336.5	13.1	19.6
0.75 in. ($3t_w$)	315.7	8.2	15.6	321.8	10.3	17.6	328.2	13.1	19.6	344.3	13.1	20.6
1.0 in. ($4t_w$)	316.8	8.2	15.6	324.3*	10.3*	17.6*	331.9	14.1	20.6	362.8	16.2	21.6
1.5 in. ($6t_w$)	318.2	9.2	17.6	328.1	10.3	19.6	347.0	14.1	21.6	410.1	20.2	26.6

* Model SG1

Table 5.1: Summary of Model SG1 Parametric Study ($D/t_w = 210$, continued)

(b) $d_0/D = 1.0$

t_b	$t_f = 0.5$ in. ($2t_w$)			$t_f = 0.75$ in. ($3t_w$)			$t_f = 1.0$ in. ($4t_w$)			$t_f = 1.5$ in. ($6t_w$)		
	Ultimate Strength (kips)	*a* (in.)	*b* (in.)	Ultimate Strength (kips)	*a* (in.)	*b* (in.)	Ultimate Strength (kips)	*a* (in.)	*b* (in.)	Ultimate Strength (kips)	*a* (in.)	*b* (in.)
0.5 in. ($2t_w$)	226.3	10.1	9	231.9	12.1	11.8	241.1	14.1	11.8	251.0	16.2	11.8
0.75 in. ($3t_w$)	228.3	10.1	10	234.7	12.1	12.7	247.1	14.1	14.6	259.2	16.2	14.6
1.0 in. ($4t_w$)	228.2	10.1	12.7	238.2	12.1	13.6	252.2	14.1	15.6	275.0	18.2	16.6
1.5 in. ($6t_w$)	230.6	10.1	14.6	243.7	13.1	15.6	259.5	14.1	16.6	305.4	21.2	19.6

Table 5.1: Summary of Model SG1 Parametric Study ($D/t_w = 210$, continued)

(c) $d_0/D = 1.5$

t_b	$t_f = 0.5$ in. ($2t_w$)			$t_f = 0.75$ in. ($3t_w$)			$t_f = 1.0$ in. ($4t_w$)			$t_f = 1.5$ in. ($6t_w$)		
	Ultimate Strength (kips)	*a* (in.)	*b* (in.)	Ultimate Strength (kips)	*a* (in.)	*b* (in.)	Ultimate Strength (kips)	*a* (in.)	*b* (in.)	Ultimate Strength (kips)	*a* (in.)	*b* (in.)
0.5 in. ($2t_w$)	197.9	12.1	10.0	203.3	15.1	11.1	211.6	16.2	11.1	220.4	18.2	11.1
0.75 in. ($3t_w$)	199.1	12.1	11.1	205.3	15.1	12.1	215.7	16.2	13.1	226.0	18.2	13.1
1.0 in. ($4t_w$)	199.4	12.1	12.1	207.8	15.1	13.1	219.1	16.2	15.1	232.7	21.2	15.1
1.5 in. ($6t_w$)	200.9	12.1	14.1	211.6	15.1	14.1	223.7	18.2	16.1	249.1	23.2	17.1

Table 5.2: Summary of Model SG2 Parametric Study ($D/t_w = 280$)

(a) $d_0/D = 0.5$

t_b	$t_f = 0.5625$ in. ($3t_w$)			$t_f = 0.75$ in. ($4t_w$)			$t_f = 1.125$ in. ($6t_w$)		
	Ultimate Strength (kips)	*a* (in.)	*b* (in.)	Ultimate Strength (kips)	*a* (in.)	*b* (in.)	Ultimate Strength (kips)	*a* (in.)	*b* (in.)
0.5625 in. ($3t_w$)	195.1	8.2	15.0	202.3	9.2	16.0	216.3	11.3	16.0
0.75 in. ($4t_w$)	197.2	8.2	16.0	204.9	10.3	17.0	229.6	13.3	18.0
1.125 in. ($6t_w$)	199.6	9.2	17.0	210.4	10.3	18.0	253.2	15.3	21.0

* Model SG2

(b) $d_0/D = 1.0$

t_b	$t_f = 0.5625$ in. ($3t_w$)			$t_f = 0.75$ in. ($4t_w$)			$t_f = 1.125$ in. ($6t_w$)		
	Ultimate Strength (kips)	*a* (in.)	*b* (in.)	Ultimate Strength (kips)	*a* (in.)	*b* (in.)	Ultimate Strength (kips)	*a* (in.)	*b* (in.)
0.5625 in. ($3t_w$)	141.9	10.1	10.0	150.4.	12.1	11.0	164.6	15.1	12.0
0.75 in. ($4t_w$)	143.9	10.1	11.0	153.1	12.1	12.0	173.6	16.2	14.0
1.125 in. ($6t_w$)	147.2	10.1	13.0	157.4	13.1	13.0	187.5	17.2	16.0

Table 5.2: Summary of Model SG2 Parametric Study (D/t_w = 280, continued)

(c) d_0/D = 1.5

t_b	t_f = 0.5625 in. ($3t_w$)			t_f = 0.75 in. ($4t_w$)			t_f = 1.125 in. ($6t_w$)		
	Ultimate Strength (kips)	*a* (in.)	*b* (in.)	Ultimate Strength (kips)	*a* (in.)	*b* (in.)	Ultimate Strength (kips)	*a* (in.)	*b* (in.)
0.5625 in. ($3t_w$)	123.1	12.9	10.0	130.2	14.9	11.0	138.0	18.8	11.0
0.75 in. ($4t_w$)	124.4	12.9	11.0	132.0	14.9	12.0	143.3	18.8	13.0
1.125 in. ($6t_w$)	126.5	12.9	12.0	134.5	14.9	13.0	151.5	19.8	15.0

Table 5.3: Summary of Model SG1 Parametric Study
(t_f = 0.75 in. and t_b = 1.0 in.)

D/t_w	d_0/D = 0.5			d_0/D = 1.0			d_0/D = 1.5		
	Ultimate Strength (kips)	*a* (in.)	*b* (in.)	Ultimate Strength (kips)	*a* (in.)	*b* (in.)	Ultimate Strength (kips)	*a* (in.)	*b* (in.)
180	407.0	10.3	17.6	302.7	12.1	13.6	266.0	15.1	13.1
210	324.3	10.3	17.6	238.2	12.1	13.6	207.8	15.1	13.1
240	267.1	10.3	17.6	199.8	12.1	13.6	172.9	15.1	13.1
280	219.7	10.3	18.6	164.9	12.1	13.6	141.3	15.1	13.1
320	192.6	11.2	18.6	144.2	13.1	13.6	119.5	15.1	13.1

Table 5.4: Summary of Model SG2 Parametric Study
(t_f = 0.5625 in. and t_b = 1.0 in.)

e	d_0/D = 0.5			d_0/D = 1.0			d_0/D = 1.5		
	Ultimate Strength (kips)	*a* (in.)	*b* (in.)	Ultimate Strength (kips)	*a* (in.)	*b* (in.)	Ultimate Strength (kips)	*a* (in.)	*b* (in.)
0 in.	196.7	8.2	14.0	143.1	10.1	11.0	124.4	12.9	11.0
4 in.	201.4*	8.2*	15.0*	149.2	10.1	12.0	128.4	12.9	12.0
8 in.	210.2	8.2	16.0	154.2	10.1	12.0	132.3	12.9	12.0

Table 5.5: Effect of Concrete Slab Width

Concrete Width (ft)	Shear Strength (kips)
8	227.1
6	225.2
5	223.4
4	221.6
3	219.1
2	218.5

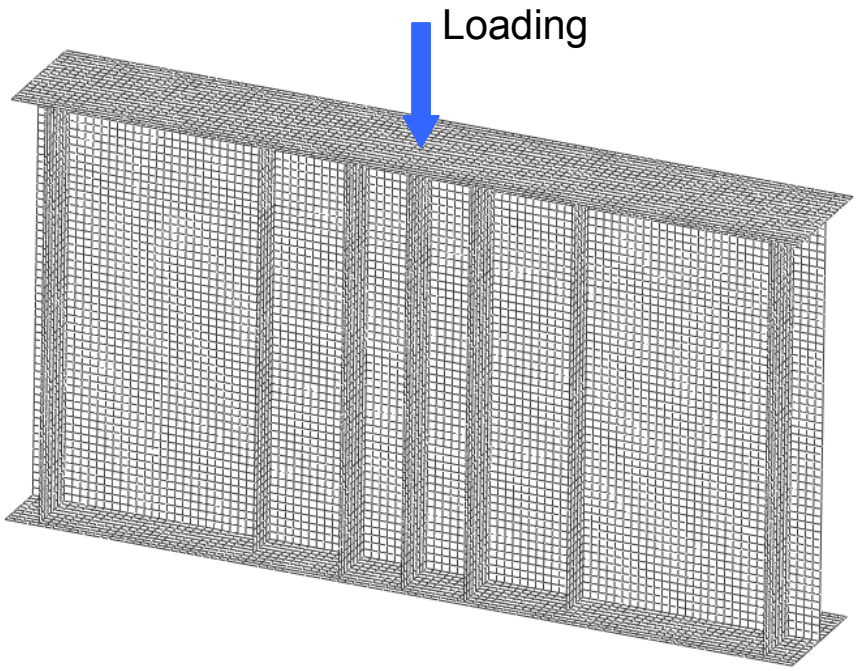

Figure 5.1: Typical Finite Element Model (2 Panels)

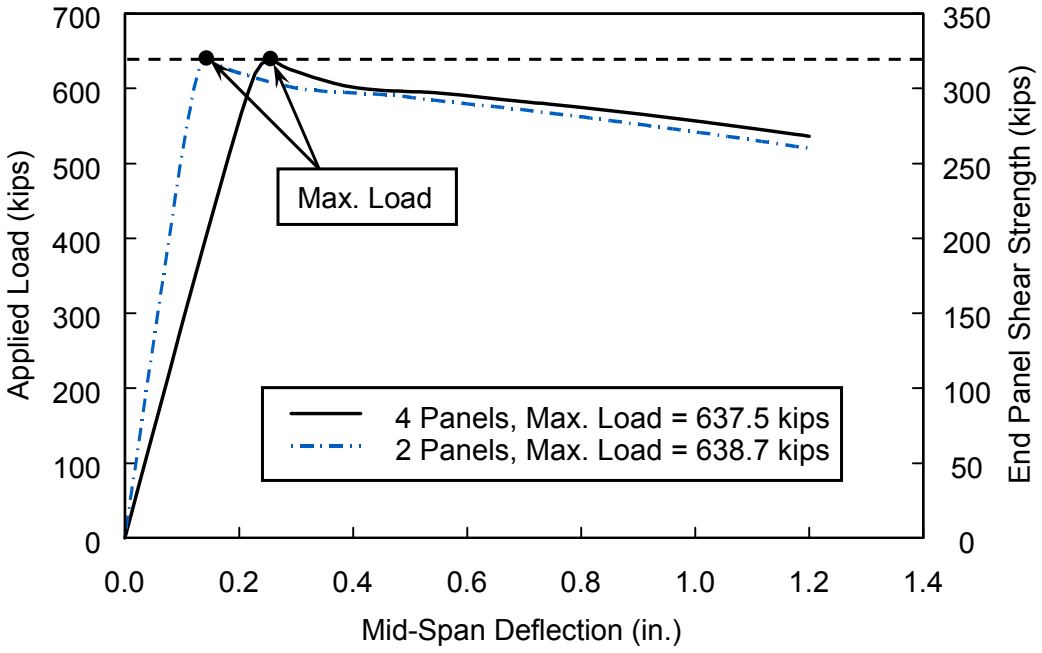

(a) Global Response

Figure 5.2: Model SG1: Comparison of 4 Panels and 2 Panels

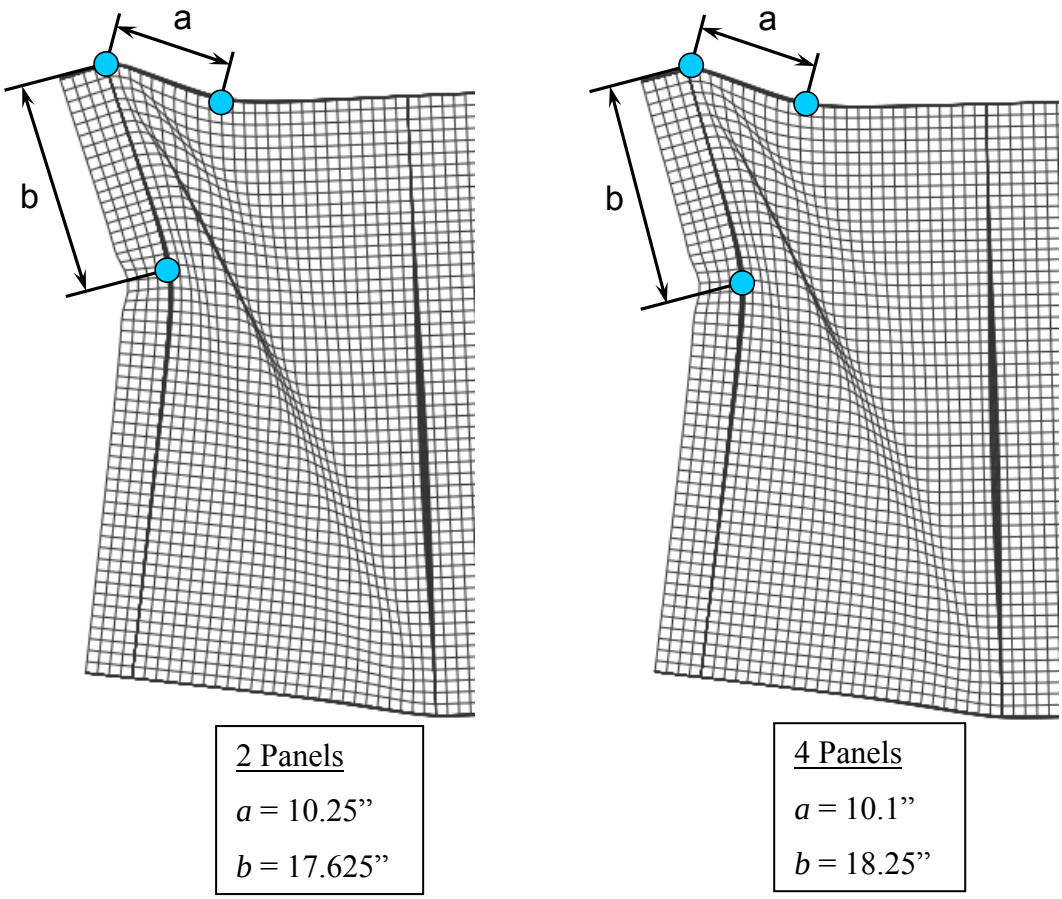

(b) Plastic Hinge Locations

Figure 5.2: Model SG1: Comparison of 4 Panels and 2 Panels (continued)

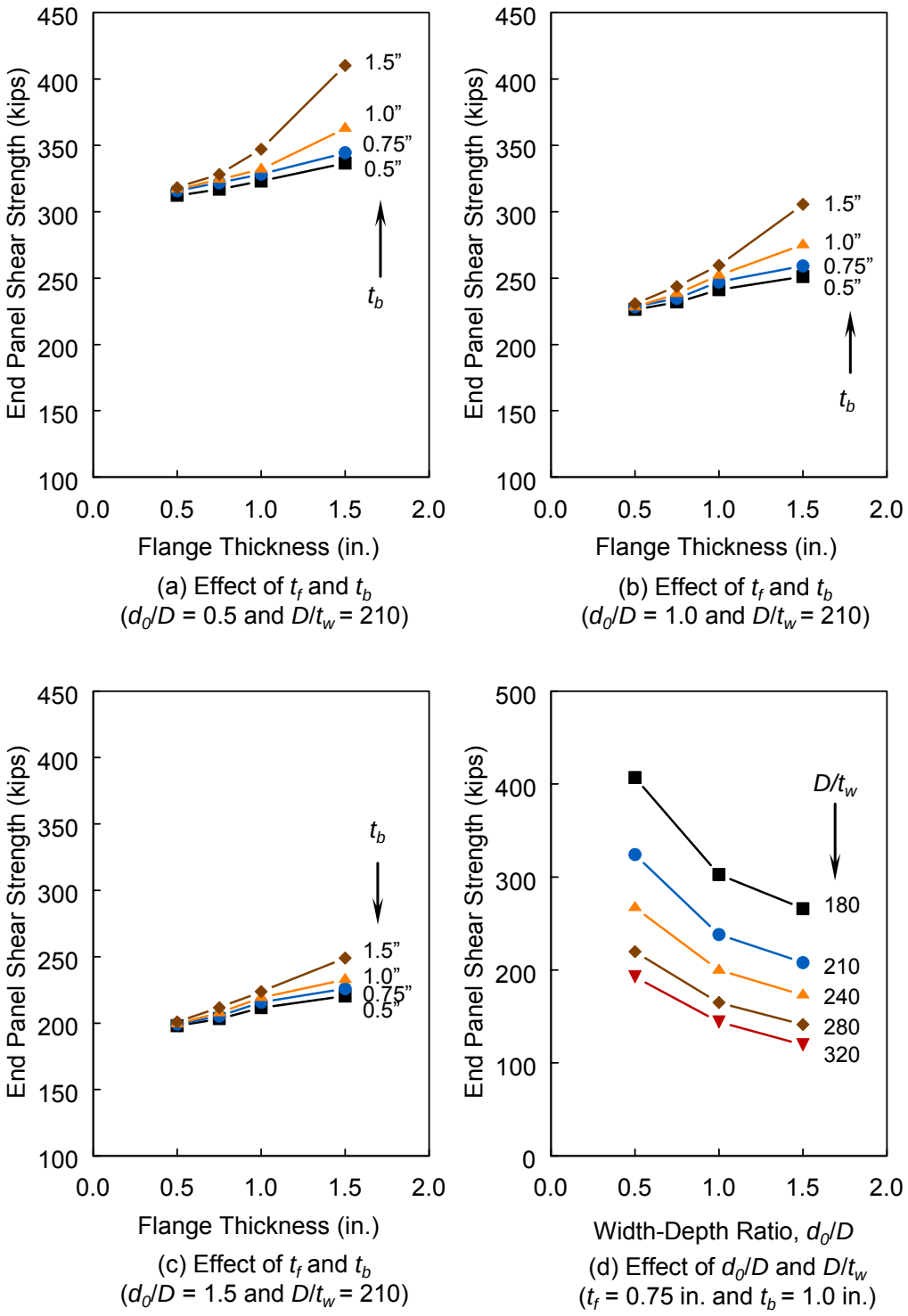

Figure 5.3: Model SG1: Summary of Parametric Study

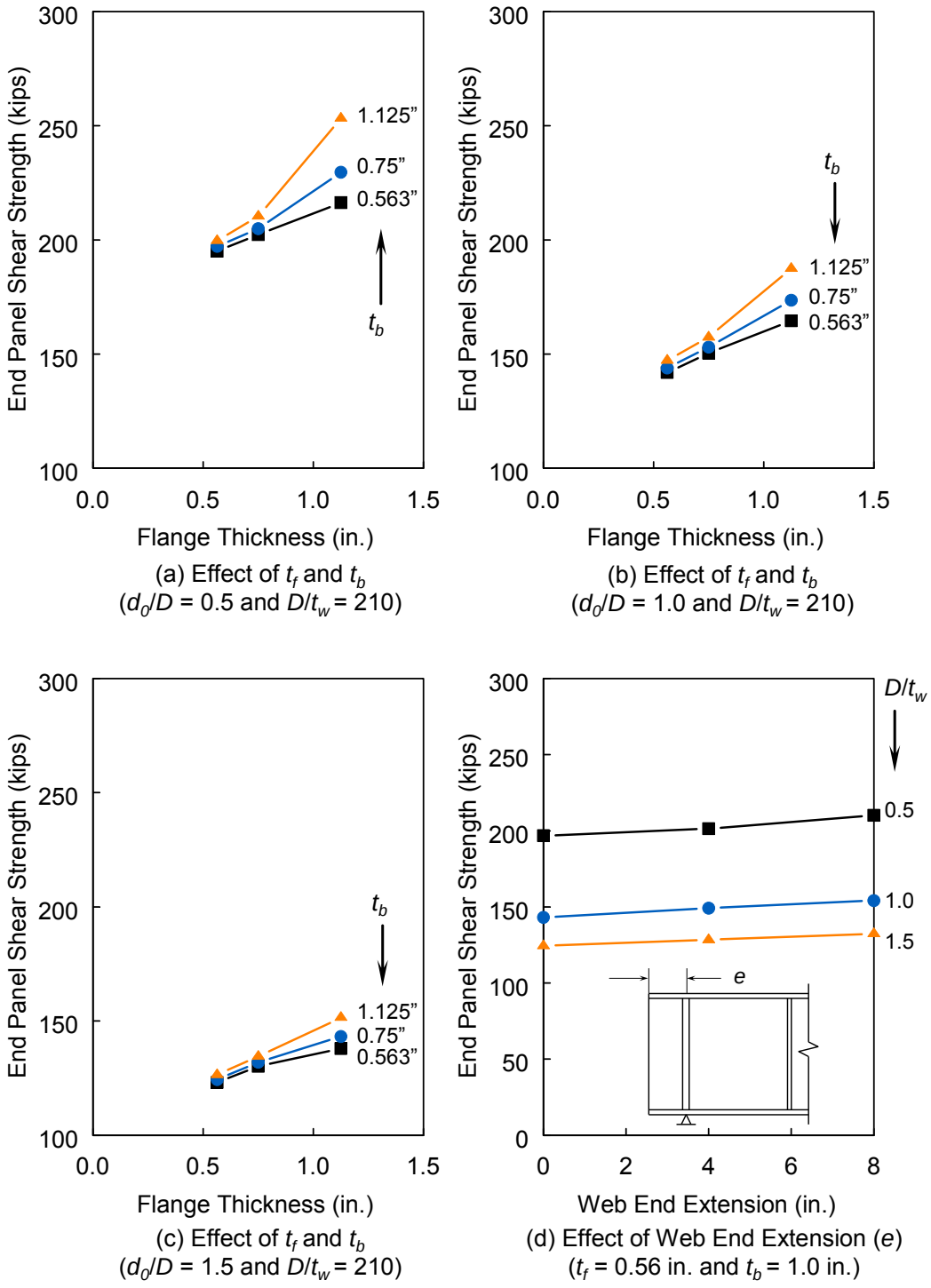

Figure 5.4: Model SG2: Summary of Parametric Study

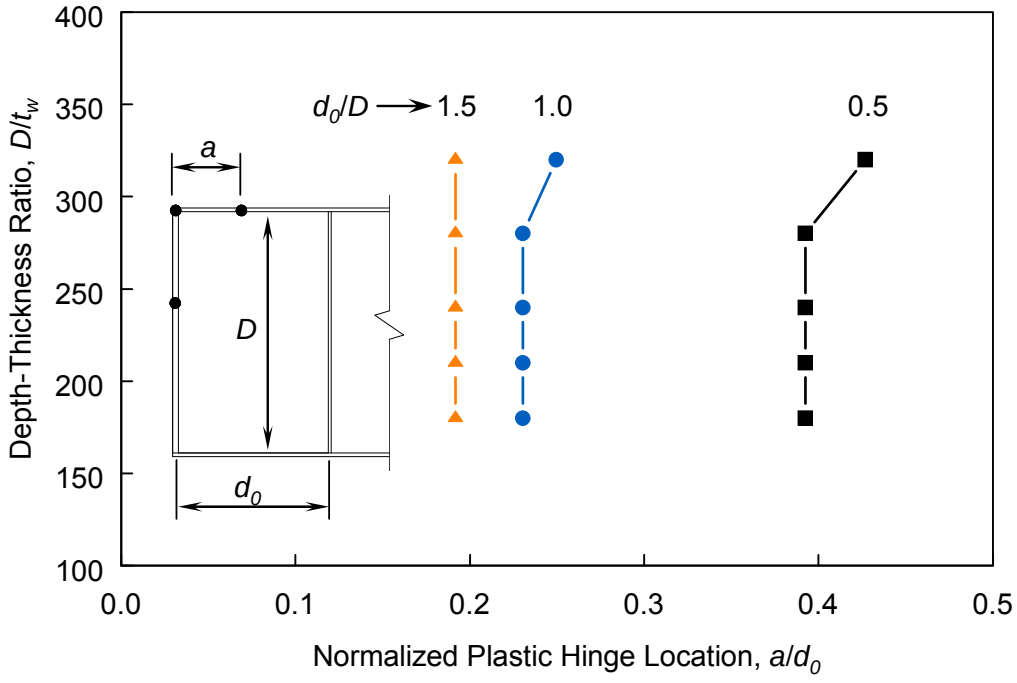

(a) Normalized Plastic Hinge Location, a/d_0

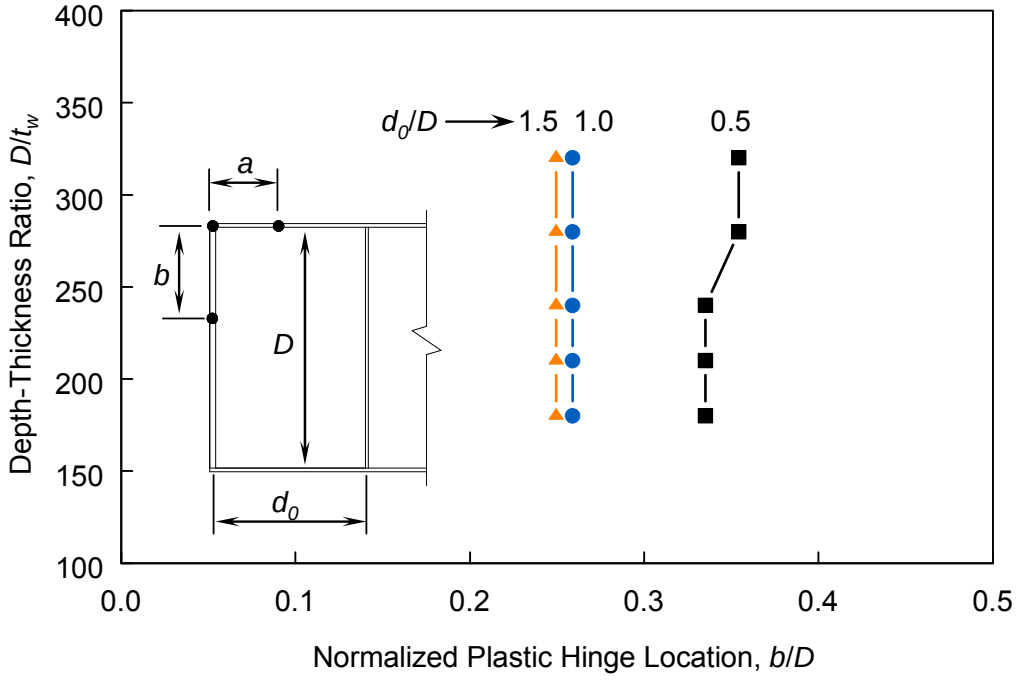

(b) Normalized Plastic Hinge Location, b/D

Figure 5.5: Effect of d_0/D and D/t_w on Plastic Hinge Location

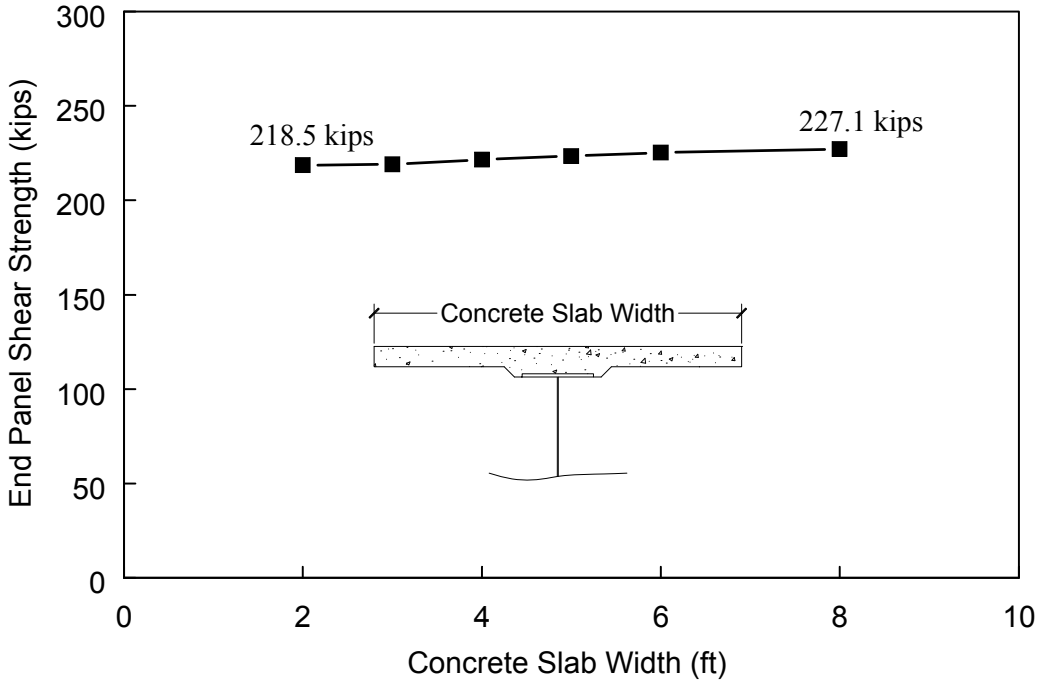

Figure 5.6: Model CG2: Effect of Concrete Slab Width

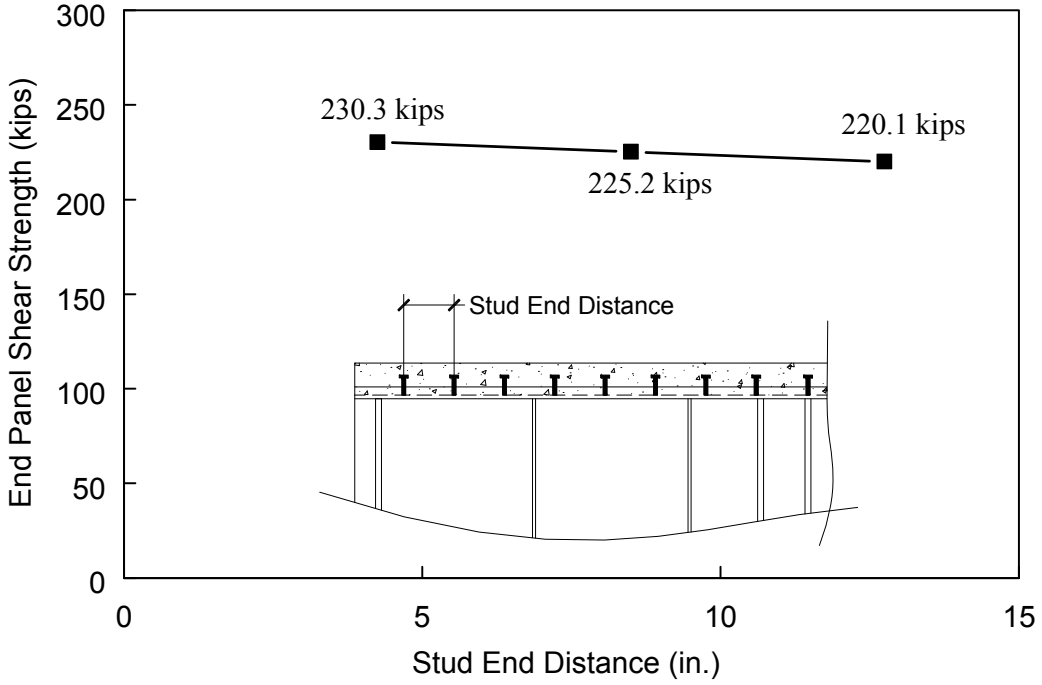

Figure 5.7: Model CG2: Effect of Stud End Distance

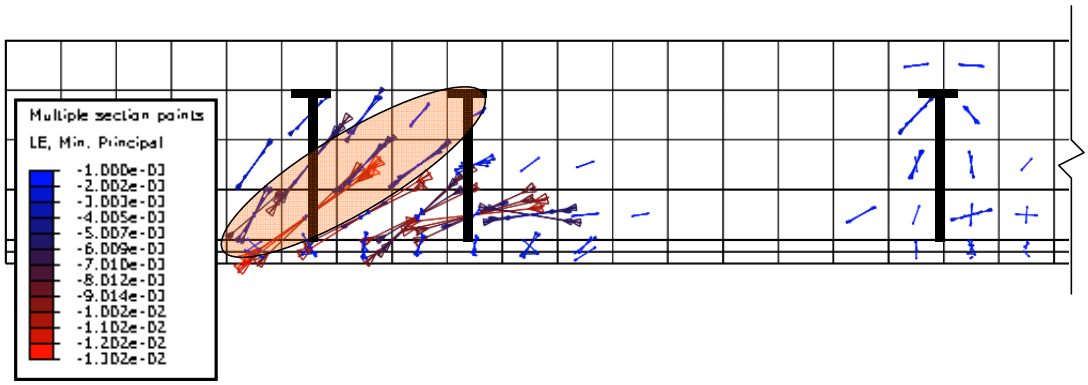

(a) Stud End Distance = 4.25 in.

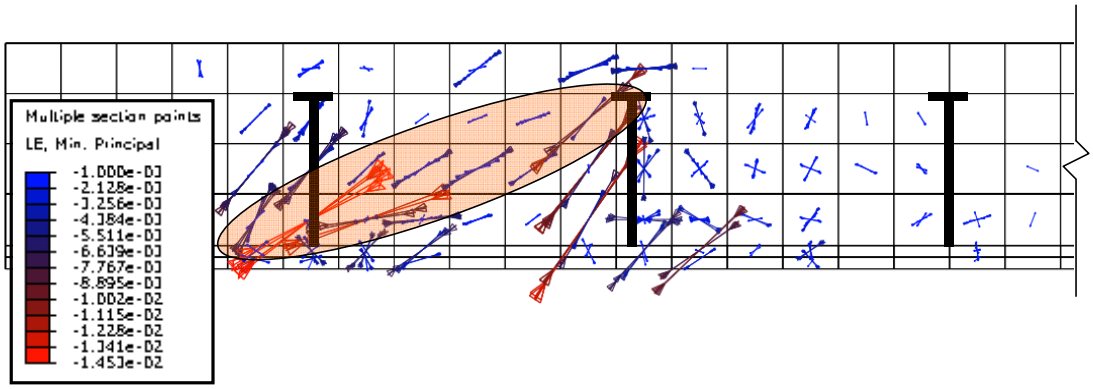

(b) Stud End Distance = 8.5 in.

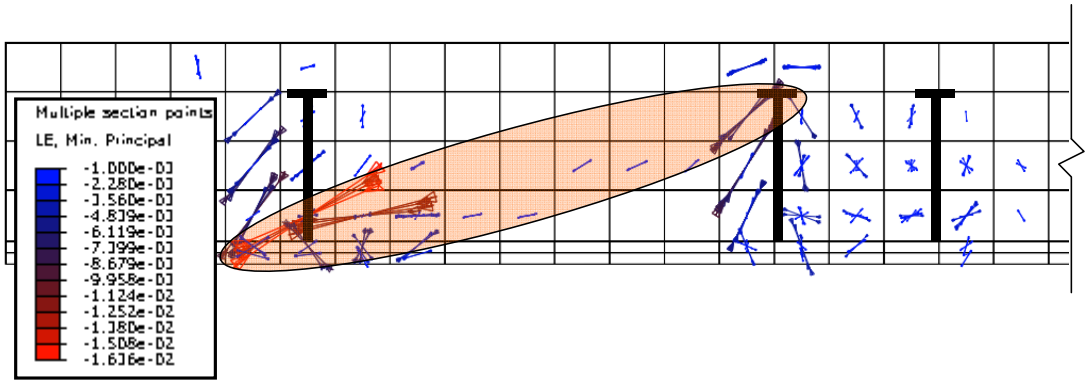

(c) Stud End Distance = 12.75 in.

Figure 5.8: Specimen CG2: Direction of Compressive Principal Strain

6. SHEAR RESISTANCE OF END PANELS: DERIVATION OF PREDICTIVE EQUATIONS

6.1 General

Current US design practices (AASHTO and AISC Specifications) ignore the tension-field action in the plate girder end panels due to the lack of an effective anchoring mechanism for the horizontal component of the tension-field force. However, Basler (1961a) indicated that the bearing stiffeners and the web portion extending beyond the support would provide some amount of bending rigidity to anchor the horizontal component of tension-field force. This concept is reflected in Eurocode 3 (2006) and post-buckling strength due to this partial tension-field action is accounted for in the design strength of end panels.

Test results also showed that ignoring tension-field action in the end panel is too conservative. In this chapter, an analytical study was conducted to provide a simple model to calculate the ultimate shear strength of the end panel. In the end panel region, it is assumed that both the top and bottom flanges have the same dimensions and steel grade.

The shear strength of a steel plate girder is provided by the following two contributions: (a) the beam action shear V_{cr}, and (b) the post-buckling shear due to the tension-field action shear V_{ps}.

$$V_s = V_{cr} + V_{ps} \tag{6.1}$$

The beam action shear strength is the web panel buckling strength:

$$V_{cr} = \tau_{cr} A_w \tag{6.2}$$

where the elastic shear buckling stress, τ_{cr}, is

$$\tau_{cr} = k\left[\frac{\pi^2 E}{12(1-\nu^2)}\left(\frac{t_w}{D}\right)^2\right] \tag{6.3}$$

$$A_w = Dt_w \tag{6.4}$$

The coefficient *k* in Eq. (6.3) is the elastic shear buckling coefficient [see Eq. (1.18)].

6.2 Failure Modes

Unlike interior panels, end panels do not have an adjacent panel beyond the support, which results in a deficiency in anchoring the horizontal component of tension-field force. Therefore, the failure modes are highly dependent on the flexural strength of the pair of bearing stiffeners to resist this horizontal force. When tension-field action occurs in the slender web, the post-buckling strength is dependent on the width, *s*, of the tension-field zone. Therefore, it is important that this width be determined accurately.

Figure 6.1 shows three possible failure modes of an end panel. The first mode involves failure of the top and bottom flanges. This occurs when very rigid bearing stiffeners are used and do not fail. A total of four plastic hinges in this failure mode are formed: two at the top flange and two at the bottom flange (see Failure Mode 1 in Figure 6.1). This failure mode is the same as for interior panels, because the vertical boundaries are rigid enough to serve as an anchor like the adjacent web panels of the interior panel. As a result, the horizontal boundaries (top and bottom flanges) have to fail. With this type of failure mode, the width of tension band is large to achieve the full tension-field action as in interior panels.

The second failure mode is the failure of the flanges and bearing stiffeners. This is most typical of real-life plate girder end panels where non-rigid bearing stiffeners are used. This failure mode involves four plastic hinges, with one plastic hinge forming in the bearing stiffeners instead of in the bottom flange. Due to the formation of the plastic hinge in the bearing stiffeners, the tension band is narrower than the first failure mode and, hence, only a partial tension-field action can be developed. Referring to Failure Mode 2 in Figure 6.1(c), a' in the bottom flange has to be less than the dimension a in Figure 6.1(b) so that a plastic hinge cannot occur in the bottom flange.

The third failure mode in Figure 6.1(d) is a combination of the first and second failure modes and requires five plastic hinges. However, the tension band width may be close to that of the first failure mode due to the formation of two plastic hinges at the bottom flange. Assuming that a plastic hinge in the bottom flange forms at the same location as in the first failure mode, this failure mode may provide almost the same post-buckling shear capacity as the first failure mode (i.e., interior panel failure mode) due to the same tension band width.

Since the second failure mode is representative of typical steel end panels, it is the focus of this study.

6.3 Tension Band Width, s

Figure 6.2 shows an assumed tension band width overlapped on the failure mode of the end panel of Specimen SG2. The assumed tension band is defined by first drawing the panel diagonal line (*AF*) with an inclination angle of θ. Then parallel lines (*BE* and *GJ*) are made, where *A*, *B*, *F*, and *J* correspond to the four plastic hinge locations in Figure 6.1(c).

Assume that a uniform tension-field stress σ_t develops across the tension band width. Given the location of plastic hinges defined by *a* and *b*, the tension band width, *s*, can be determined by using the panel geometry as:

$$s = a\sin\theta + b\cos\theta \tag{6.5}$$

where

$$\sin\theta = \frac{D}{\sqrt{d_0^2 + D^2}} \tag{6.6a}$$

$$\cos\theta = \frac{d_0}{\sqrt{d_0^2 + D^2}} \tag{6.6b}$$

Considering Eqs. (6.6a) and (6.6b), $\sin\theta$ and $\cos\theta$ can be expressed in one equation.

$$\sin\theta = \frac{D}{d_0}\cos\theta \tag{6.7}$$

6.4 Post-Buckling Strength: A Plastic Mechanism Approach

Porter et al. (1975), Huslid and Rockey (1979), and Darehshouri et al. (2012) used plastic mechanism analysis to develop their tension-field theories. Since the plastic analysis provides an upper bound solution, it requires finding a solution which minimizes the post-buckling shear strength (V_{ps}) of the end panel. Figure 6.3 shows the failure mechanism of an end panel. The shaded area in the web represents the yielding zone due to the tension-field action. By excluding the web plate, the tension-field stresses in the shaded area were considered as external loads that act on the boundary members as

shown in Figure 6.4(a). Applying the virtual work principle, a virtual vertical displacement δ is applied at support *H*, which results in rotations at the four plastic hinge locations shown in Figure 6.3.

Internal Work

The internal virtual work is

$$W_I = M_{pA}(\theta_B + \theta_A) + M_{pB}(\theta_B) + M_{pJ}(\theta_F + \theta_A) + M_{pF}(\theta_F) \tag{6.8}$$

where M_{pB} and M_{pF} equal the flange plastic moment ($=M_{pf}$), M_{pJ} is the plastic moment of a pair of bearing stiffeners ($=M_{pb}$), and M_{pA} is the minimum of M_{pf} and M_{pb} ($=M_{pm}$). Also, the rotations at the plastic hinges can be expressed as a function of the virtual displacement δ.

$$\begin{aligned} \theta_B &= \frac{\delta}{a} \\ \theta_F &= \frac{\delta}{d_0} \\ \theta_A &= \frac{(D-b)\theta_F}{b} = \frac{(D-b)\delta}{bd_0} \end{aligned} \tag{6.9}$$

Substituting Eq. (6.9) into Eq. (6.8), the internal work is rewritten as:

$$W_I = \left(M_{pf} + M_{pm}\right)\frac{\delta}{a} + \left(M_{pb} + M_{pm}\right)\frac{(D-b)\delta}{bd_0} + \left(M_{pf} + M_{pb}\right)\frac{\delta}{d_0} \tag{6.10}$$

External Work

Since the web plate is excluded in the free-body in Figure 6.4(a), the tension-field stresses acting on the boundary members are considered as external loads. The diagonal tension stresses are decomposed into horizontal and vertical components as shown in Figure 6.4(b). Vertical shear V_{ps} with an applied vertical displacement δ creates external virtual work.

(1) Member *AB*

Considering a rotation θ_B at B, member AB with a vertical distributed load ($\sigma_t t_w \sin^2\theta$ in Figure 6.5) experiences an average upward movement of $a\theta_B/2$, thus producing a negative work of $-a\sigma_t t_w \sin^2\theta(a\theta_B/2)$. Since there is no horizontal movement on member AB, the horizontal component of the tension-field stresses produces no work.

$$W_{E(AB)} = -a\sigma_t t_w \sin^2\theta\left(\frac{a\theta_B}{2}\right) \tag{6.11}$$

(2) Member *AJ*

Similarly, member *AJ* experiences a vertical movement of δ and an average horizontal movement of $b\theta_A/2$. The horizontal and vertical movements together with horizontal and vertical distributed loads generate the following external work:

$$W_{E(AJ)} = b\sigma_t t_w \cos^2\theta\left(\frac{b\theta_A}{2}\right) - b\sigma_t t_w \sin\theta\cos\theta(\delta) \tag{6.12}$$

Member *GF*

The length of member *GF* can be calculated by using the panel geometry.

$$L_{GF} = d_0 - \frac{(D-b)}{\tan\theta} = d_0 - \frac{(D-b)}{(D/d_0)} = \frac{bd_0}{D} \tag{6.13}$$

The member *GF* undergoes an average vertical upward movement of $(bd_0/D)\theta_F/2$ but no horizontal movement. This vertical movement results in the following external work:

$$W_{E(GF)} = \frac{bd_0}{D}\sigma_t t_w \sin^2\theta\left[\frac{(bd_0/D)\theta_F}{2}\right] = \frac{\sigma_t t_w b^2\cos^2\theta}{2}\theta_F \tag{6.14}$$

Since member *EF* does not have any virtual movement, the load acting on the member does not produce work (see Figure 6.3). Therefore, the total external work is

$$\begin{aligned} W_E &= V_{ps}(\delta) + W_{E(AB)} + W_{E(AJ)} + W_{E(GF)} \\ &= V_{ps}(\delta) - \left(\frac{a\sigma_t t_w \sin^2\theta}{2}\right)\delta + \left(\frac{b\sigma_t t_w \cos^2\theta(D-b)}{2d_0}\right)\delta - b\sigma_t t_w \sin\theta\cos\theta(\delta) \\ &\quad + \frac{\sigma_t t_w b^2\cos^2\theta}{2d_0}\delta \end{aligned} \tag{6.15}$$

Equate Eq. (6.10) with Eq. (6.15) to solve the post-buckling shear strength:

$$V_{ps} = \frac{\left(M_{pf} + M_{pm}\right)}{a} + \frac{(D-b)\left(M_{pb} + M_{pm}\right)}{bd_0} + \frac{\left(M_{pf} + M_{pb}\right)}{d_0} + \left(\frac{a\sigma_t t_w \sin^2\theta}{2}\right) - \left(\frac{b\sigma_t t_w \cos^2\theta (D-b)}{2d_0}\right) + b\sigma_t t_w \sin\theta\cos\theta - \frac{\sigma_t t_w b^2 \cos^2\theta}{2d_0} \tag{6.16}$$

6.5 Plastic Hinge Locations in Boundary Members

It is seen from Eq. (6.16) that the post-buckling strength is a function of plastic hinge locations defined by *a* and *b*. These two variables can be computed by using the static equilibrium of the free-bodies of flange member *AB* and bearing stiffener member *AJ* shown in Figure 6.5. Due to the formation of the plastic hinges, the member end moments are known. However, the axial and shear forces are still indeterminate. Therefore, two shear ratio parameters (γ for flange shear ratio and κ for bearing stiffener shear ratio) are introduced in the free-bodies of members *AB* and *AJ*. Internal axial forces of these members then can be established by static equilibrium.

By considering the moment equilibrium at *A* of each member from Figure 6.5(b), the plastic hinge distances can be determined as follows:

$$a = \sqrt{\frac{2(M_{pf} + M_{pm})}{\sigma_t t_w (1-2\gamma)\sin^2\theta}} \tag{6.17a}$$

$$b = \sqrt{\frac{2(M_{pb} + M_{pm})}{\sigma_t t_w (1-2\kappa)\cos^2\theta}} \tag{6.17b}$$

If γ or κ is greater than 0.5, *a* or *b* will have an imaginary number. Therefore, both γ and κ must be less than 0.5.

Substituting Eq. (6.17) into Eq. (6.16), the post-buckling strength V_{ps} is expressed with two independent variables, γ and κ. Based on the upper bound theory in plastic analysis (Neal, 1985), γ and κ should be chosen to minimize the post-buckling strength V_{ps}:

$$\frac{\partial V_{ps}}{\partial \gamma} = 0 \tag{6.18a}$$

$$\frac{\partial V_{ps}}{\partial \kappa} = 0 \tag{6.18b}$$

Theoretically, the two variables of γ and κ can be determined by solving the simultaneous equations in Eq. (6.18). However, it is very complex to derive the closed-form solution of γ and κ. Therefore, it was decided to establish the values of γ and κ numerically.

Both Models SG1 and SG2 were used for this case study. By varying the γ and κ values in Eq. (6.17a) and (6.17b), the values of a and b can be determined. Substituting these two values into Eq. (6.16) gives the post-buckling strength. Figure 6.6 shows the effect of the shear ratio parameters. It is seen that the post-buckling strength of the end panel becomes minimal when both γ and κ approach zero.

Setting both γ and κ to zero in Eq. (6.17), the plastic hinge location parameters are

$$a = \sqrt{\frac{2(M_{pf} + M_{pm})}{\sigma_t t_w \sin^2 \theta}} \tag{6.19a}$$

$$b = \sqrt{\frac{2(M_{pb} + M_{pm})}{\sigma_t t_w \cos^2 \theta}} \tag{6.19b}$$

Substituting Eq. (6.19) into Eq. (6.16), the post buckling strength V_{ps} is reduced to:

$$V_{ps} = \sigma_t t_w \sin\theta(a\sin\theta + b\cos\theta) + \frac{M_{pf} + M_{pb}}{d_0} - \frac{\sigma_t t_w b^2}{2d_0}\cos^2\theta \tag{6.20}$$

The free-body diagrams of the end panel boundary members due to the tension-field action are summarized in Figure 6.7.

Summing up the beam action shear buckling strength and post-buckling strength ($V_{cr}+V_{ps}$) gives the ultimate shear strength of the end panel.

$$V_s = \sigma_t t_w \sin\theta(a\sin\theta + b\cos\theta) + \frac{M_{pf} + M_{pb}}{d_0} - \frac{\sigma_t t_w b^2}{2d_0}\cos^2\theta + \tau_{cr} D t_w \tag{6.21}$$

6.6 Simplification

Depending on the relative plastic moment values of the girder flange and bearing stiffener pair, Eq. (6.21) can be further simplified as follows.

Case 1: $M_{pf} \le M_{pb}$ (weak flange)

In this case, M_{pm} is equal to M_{pf}. Then, $\left(M_{pf} + M_{pb}\right)$ in Eq. (6.19b) becomes

$$M_{pf} + M_{pb} = \frac{b^2}{2}\sigma_t t_w \cos^2\theta \tag{6.22}$$

Dividing by d_0 on both sides, Eq. (6.22) can be rewritten as

$$\frac{\left(M_{pf} + M_{pb}\right)}{d_o} = \frac{b^2}{2d_o}\sigma_t t_w \cos^2\theta^2 \tag{6.23}$$

It is readily shown that the second and third terms on right hand side of Eq. (6.21) cancel out, and the ultimate shear strength is reduced to

$$V_s = \sigma_t t_w \sin\theta(a\sin\theta + b\cos\theta) + \tau_{cr} D t_w \tag{6.24}$$

Case 2: $M_{pf} > M_{pb}$ (weak bearing stiffeners)

In this case, M_{pm} is equal to M_{pb}. Then, by using Eq. (6.19a), $\left(M_{pf} + M_{pb}\right)$ is

$$M_{pf} + M_{pb} = \frac{a^2}{2}\sigma_t t_w \sin^2\theta \tag{6.25}$$

Substituting Eq. (6.25) into Eq. (6.21), the ultimate shear strength becomes

$$V_s = \sigma_t t_w \sin\theta(a\sin\theta + b\cos\theta) + \frac{\sigma_t t_w (a^2\sin^2\theta - b^2\cos^2\theta)}{2d_0} + \tau_{cr} D t_w \tag{6.26}$$

Eq. (6.26) consists of three terms; the first term is the post-buckling strength due to tension-field action in the web, the second is the shear resistance from the bottom flange (see Figure 6.7), and the last is the web shear buckling strength.

Generally the flange shear strength is very small compared to the web shear strength. To evaluate the contribution of the flange to the ultimate shear strength, a total of 99 cases including Models SG1 and SG2 and the results from a parametric study which are summarized in Chapter 5 were used. Figure 6.8 shows that the bottom flange contribution increases with plastic moment of the flange. But the contribution is only a

few percent and can be ignored for practical reasons. By ignoring the contribution of the flange, Eq. (6.26) reduces to (6.24).

Eq. (6.24) can be further simplified. Substituting Eq. (6.6) into Eq. (6.24), the ultimate shear strength is expressed as:

$$V_s = \sigma_t t_w \left(\frac{a + b(d_0 / D)}{1 + (d_0 / D)^2} \right) + \tau_{cr} D t_w \tag{6.27}$$

Note that Basler (1961a) suggested a simplified tension-field stress (σ_t).

$$\sigma_t = F_{yw} \left(1 - \frac{\tau_{cr}}{\tau_{yw}} \right) = F_{yw}(1 - C) \tag{6.28}$$

where $C = \tau_{cr} / \tau_{yw}$. Substituting Eq. (6.28) into Eq. (6.19), *a* and *b* become:

$$a = \frac{1}{\sin\theta} \sqrt{\frac{2(M_{pf} + M_{pm})}{\sigma_t t_w}} = \frac{\sqrt{d_0^2 + D^2}}{D} \sqrt{\frac{2(M_{pf} + M_{pm})}{\sigma_t t_w}} \tag{6.29a}$$

$$b = \frac{1}{\cos\theta} \sqrt{\frac{2(M_{pb} + M_{pm})}{\sigma_t t_w}} = \frac{\sqrt{d_0^2 + D^2}}{d_0} \sqrt{\frac{2(M_{pb} + M_{pm})}{\sigma_t t_w}} \tag{6.29b}$$

Substituting Eq. (6.29) into the numerator in Eq. (6.27),

$$\begin{aligned} a + b\left(\frac{d_0}{D}\right) &= \frac{\sqrt{d_0^2 + D^2}}{D} \sqrt{\frac{2(M_{pf} + M_{pm})}{\sigma_t t_w}} + \frac{\sqrt{d_0^2 + D^2}}{D} \sqrt{\frac{2(M_{pb} + M_{pm})}{\sigma_t t_w}} \\ &= \frac{\sqrt{d_0^2 + D^2}}{D} \left[\frac{\sqrt{2(M_{pf} + M_{pm})} + \sqrt{2(M_{pb} + M_{pm})}}{\sqrt{\sigma_t t_w}} \right] \\ &= \frac{\sqrt{1 + (d_0 / D)^2}}{\sqrt{t_w F_{yw}(1 - C)}} \left[\sqrt{2(M_{pf} + M_{pm})} + \sqrt{2(M_{pb} + M_{pm})} \right] \end{aligned} \tag{6.30}$$

Also, the beam-action shear buckling strength can be rewritten as:

$$V_{cr} = \tau_{cr} D t_w = \left(\frac{\tau_{cr}}{\tau_{yw}} \right) \tau_{yw} D t_w = 0.58 F_{yw} D t_w C \tag{6.31}$$

Substituting Eqs. (6.28), (6.30), and (6.31) into Eq. (6.27), the ultimate shear strength is

$$
\begin{aligned}
V_s &= \frac{F_{yw}(1-C)t_w}{1+(d_0/D)^2}\frac{\sqrt{1+(d_0/D)^2}}{\sqrt{t_w F_{yw}(1-C)}}\left[\sqrt{2(M_{pf}+M_{pm})}+\sqrt{2(M_{pb}+M_{pm})}\right]+V_{cr} \\
&= \frac{F_{yw}(1-C)t_w}{\sqrt{1+(d_0/D)^2}}\frac{D\left[\sqrt{2(M_{pf}+M_{pm})}+\sqrt{2(M_{pb}+M_{pm})}\right]}{D\sqrt{t_w F_{yw}(1-C)}}+0.58F_{yw}Dt_wC \\
&= 0.58F_{yw}Dt_w\left[C+\frac{0.87(1-C)}{\sqrt{1+(d_0/D)^2}}\left(\frac{\sqrt{2(M_{pf}+M_{pm})}+\sqrt{2(M_{pb}+M_{pm})}}{0.58(0.87)D\sqrt{t_w F_{yw}(1-C)}}\right)\right] \\
&= 0.58F_{yw}Dt_w\left[C+\frac{0.87(1-C)}{\sqrt{1+(d_0/D)^2}}\left(\frac{2.8\left(\sqrt{M_{pf}+M_{pm}}+\sqrt{M_{pb}+M_{pm}}\right)}{D\sqrt{t_w F_{yw}(1-C)}}\right)\right]
\end{aligned}
\tag{6.32}
$$

The above expression can be rewritten in the following form:

$$
V_s = V_p\left[C+\alpha\frac{0.87(1-C)}{\sqrt{1+(d_0/D)^2}}\right] \tag{6.33}
$$

where

$$
V_p = 0.58F_{yw}Dt_w \tag{6.34}
$$

$$
C = \frac{\tau_{cr}}{\tau_{yw}} \tag{6.35}
$$

$$
\alpha = \frac{2.8\left(\sqrt{M_{pf}+M_{pm}}+\sqrt{M_{pb}+M_{pm}}\right)}{D\sqrt{t_w F_{yw}(1-C)}} \le 1.0 \tag{6.36}
$$

Note that Eq. (6.33) has the same format as that used in 2014 AASHTO Specifications for calculating the shear resistance of interior panels, except that it contains one additional parameter α to consider the partial tension-field action. The parameter (α) accounts for the flexural strength of the boundary members (top flange and bearing stiffeners). When tension-field action exists, the end panel shear strength will be generally less than that of an interior panel with the same dimensions. Therefore, α should be no larger than 1.0. Eq. (6.33) is written in a format which is applicable to both interior and end panels. At one extreme when both the flange and bearing stiffeners offer little flexural strength, α approaches zero and only the beam action contributes to the shear strength. As the other extreme when both the flange and bearing stiffeners offer large flexural strengths, α approaches 1.0, which is equivalent to the

development of full tension-field action as in an interior panel. The value of α will be less than 1.0 for end panels in typical steel plate girder bridges.

6.7 Effective Depth of End Panel Boundary Members

The post-buckling strength depends on the plastic hinge location parameters, *a* and *b*. These two parameters are a function of the plastic moment capacities of the flanges (M_{pf}) and bearing stiffener pair (M_{pb}) as well as the tension-field stress (σ_t) as shown in Eq. (6.29). As observed in Section 5.2.3, varying the depth-to-thickness ratio (D/t_w) while keeping the panel width-to-depth ratio (d_0/D) constant had virtually no effect on the plastic hinge locations in the top flange and bearing stiffener pair. Since the tension-field stress is a function of D/t_w [see Eq. (6.28)], the above observation implies that some portion of the web would act together with the boundary members (see Section 5.2.3).

Past researchers investigating the shear strength of interior panels (Chern and Ostapenko 1969, Rockey and Skaloud 1972, and Porter et al. 1975) also assumed that the flanges act with an effective web depth. Figure 6.9 shows the same concept applied to the end panel. When the web experiences inelastic buckling in a panel of low depth-to-thickness ratio, only a small portion of the web area can act with the flange, and this portion can be ignored conservatively. However, when the web is very slender (high D/t_w ratio) and experiences elastic buckling, a larger portion of the web area will be effective and should be considered to determine the moment capacities of the flange (M_{pf}) and bearing stiffeners (M_{pb}). Eqs. (6.37) and (6.38) are the effective depths of the web suggested by past researchers for interior panels.

$$d_e^{CO} = 12.5 t_w \left(0.8 - \frac{\tau_{cr}}{\tau_{yw}} \right) \qquad \text{by Chern and Ostapenko (1969)} \qquad (6.37)$$

$$d_e^{RS} = 30 t_w \left(1 - 2\frac{\tau_{cr}}{\tau_{yw}} \right) \qquad \text{by Rockey and Skaloud (1972) and Porter et al. (1975)} \qquad (6.38)$$

Both equations assume that the effective web depth is proportional to the shear buckling stress normalized by the shear yield stress. Since the terms in the parentheses must remain positive, Eqs. (6.37) and (6.38) imply that inelastic buckling occurs when τ_{cr}

exceeds $0.8\tau_{yw}$ and $0.5\tau_{yw}$, respectively (see Figure 6.10). Note that Basler (1961a) and US design codes (both 2014 AASHTO Specifications and 2010 AISC Specifications) specify that inelastic buckling occurs when the plate shear buckling stress τ_{cr} exceeds $0.8\tau_{yw}$. Therefore, when elastic buckling occurs, a T-section of the flange and a T- or cruciform-section (when the web extends beyond the support by a distance *e*) of the bearing stiffener pair should be included to compute the plastic section modulus, Z_x (see Figure 6.9 and Figure 6.11). Then the plastic moment capacities are computed as follows.

$$M_{pf} = Z_{xf} F_{yf} \tag{6.39}$$

$$M_{pb} = Z_{xb} F_{yb} \tag{6.40}$$

where Z_{xf} and Z_{xb} are the effective plastic section moduli of the flange and bearing stiffener pair, and F_{yf} and F_{yb} are the yield strengths of the flange and bearing stiffeners, respectively.

To evaluate the accuracy of Eqs. (6.37) and (6.38), a parametric study with 99 cases including Models SG1 and SG2 (reported in Chapter 5) was conducted. For each case, a_p and b_p are the plastic hinge location parameters predicted by either Eq. (6.37) or (6.38). These values were then compared with those (a_i and b_i) directly identified from nonlinear finite element analyses. Figure 6.12(a) and Figure 6.13(a) show the correlation with the Chern-Ostapenko model, which on average, this model underpredicts both *a* and *b*. Figure 6.12(b) and Figure 6.13(b) show the correlation with the Rockey-Skaloud model, which tends to overpredict the *a* and *b* values. The actual effective depth of the web falls between these two models.

As a trial to fit the data, two suggested effective depth equations are plotted in Figure 6.14(a). In the figure, the two straight lines intersect at the point of 0.379 on the horizontal axis (C = 0.421). As shown in Figure 6.14(b), one straight line, defined by Eq. (6.37), was drawn from 0 to the intersection point to be consistent with US practice of inelastic buckling criteria, and another straight line, defined by Eq. (6.38), was drawn

beyond the intersection point. The combined lines can be expressed as a power function using a regression.

$$d_e = \omega_1 t_w (0.8 - C)^{\omega_2} = \omega_1 t_w \left(0.8 - \frac{\tau_{cr}}{\tau_{yw}} \right)^{\omega_2} \tag{6.41}$$

The variables of ω_1 and ω_2 in Eq. (6.41) from the regression are 34.1 and 1.6, respectively. The power curve is also plotted in Figure 6.14(b). Those values (ω_1 and ω_2) are rounded off to the nearest integers of 35 and 2. Figure 6.14(c) shows the power curve that is calibrated with and lies between the two straight lines defined by Eqs. (6.37) and (6.38). As a result, it is proposed that Eq. (6.42) be used to determine the effective web depth.

$$d_e = 35 t_w \left(0.8 - \frac{\tau_{cr}}{\tau_{yw}} \right)^2 \qquad \text{for } \frac{\tau_{cr}}{\tau_{yw}} \le 0.8 \tag{6.42a}$$

$$d_e = 0 \qquad \text{for } \frac{\tau_{cr}}{\tau_{yw}} > 0.8 \tag{6.42b}$$

By using the proposed formula for effective depth, the identified and predicted plastic hinge locations are shown in Figure 6.12(c) for the plastic hinge in the flange and in Figure 6.13(c) for that in the bearing stiffener pair (see Table 5.1 through Table 5.4 for the identified plastic hinge locations). From the figures, the proposed equation is capable of reasonably estimating the plastic hinge locations. In addition, the average ratios (a_p / a_i, and b_p / b_i) calculated by the proposed Eq. (6.42) are 0.960 and 1.009, respectively, with standard deviations of 0.102 and 0.148, respectively.

6.8 Validation of Shear Strength Formula

The end panel shear strengths predicted by Eq. (6.33) are compared with available test results. Table 6.1 and Table 6.2 provide plate sizes and material properties of the test specimens, while Table 6.3 summarizes the ultimate shear strength from testing and nominal shear strengths from Eq. (6.33), AASHTO Specifications (2014), and Eurocode 3. The tables include two tested specimens (SG1 and SG2) in this test program and EPS series which were tested by Huslid and Rockey (1979). Figure 6.15 compares three

predicted shear strengths, which are normalized by the shear strengths from testing. The predicted-to-test ratio varies from 0.837 to 1.116, and the average ratio is 0.972 with a standard deviation of 0.078, while the average AASHTO-to-test and Eurocode-to-test ratios are 0.283 and 0.722 with the standard deviations of 0.122 and 0.147, respectively. The predictions provided by the proposed model are significantly better than those from AASHTO Specifications and Eurocode 3.

To further validate Eq. (6.33), the parametric study results from the finite element analyses described in Chapter 5 are also compared with the predicted values (see Figure 6.16 and Figure 6.17). The shear strengths predicted by Eq. (6.33) correlate very well with the results from finite element analyses. Table 6.4 and Table 6.5 summarize the results from nonlinear finite element analyses and predicted shear strengths for SG1 and SG2 model series, respectively.

Figure 6.18 compares the shear strength for 114 cases (15 from test results and 99 from FEM). The horizontal axis is the predicted shear strength from Eq. (6.33), and the vertical axis is the shear strength from testing or finite element analysis. The mean ratio of predicted shear strength to the test (or FEM) is 0.965 with a standard deviation of 0.058. Therefore, it can be concluded that Eq. (6.33) provides a highly accurate prediction of the ultimate shear strength of end panel.

Figure 6.19 visualizes the results. The black bars correspond to the end panel shear strength predicted by AASHTO Specifications, which is equal to beam-action buckling shear strength. The horizontally-hatched bars represent the predicted post-buckling strength due to the tension-field action in the end panel. Comparison of these two quantities highlights the contribution to the ultimate shear strength of end panels predicted by Eq. (6.33), relative to that predicted by AASHTO. Shear strengths obtained through testing or finite element analysis are also shown in the figure. Eq. (6.33) very closely matches or slightly underestimates the ultimate shear strengths from testing and finite element analysis. For comparison purposes, predicted shear strengths per Eurocode 3 are also provided in the figure. Eurocode 3 generally tends to underestimate the ultimate shear strengths of the end panel more conservatively than the ones predicted by Eq. (6.33), but it significantly overestimates the ultimate shear strengths when thick flanges with small width-to-depth ratios were used.

6.9 Shear Resistance of Steel-Concrete Composite Girder End Panel

By providing shear connectors between the concrete slab and steel plate girder, composite action will increase the flexural strength of the plate girder. The shear connectors, which are welded to the plate girder top flange and are embedded in the reinforced concrete slab, accommodate longitudinal (or horizontal) shear force to minimize the slip. The degree of composite action depends on the strength and the number of shear stud connectors used.

Experimental test results showed that the plastic hinge locations in the top flange and bearing stiffeners of the composite girder specimens (CG1 and CG2) are practically the same as in the steel girder specimens (SG1 and SG2), as shown in Figure 3.35. Therefore, the ultimate shear strength of the composite plate girder end panel can be determined by using the superposition of the shear strengths of the steel girder and concrete slab.

$$V_n = V_s + V_c \tag{6.43}$$

where V_s is computed by using Eq. (6.33). The testing of the two composite girders exhibited diagonal shear cracks as the primary failure mode in the concrete slab. Based on the observation of the shear cracks from testing and the findings of the compressive stress flow in the concrete slab from nonlinear finite element analysis, it is assumed that one shear crack (upper shear crack) starts from the plastic hinge location *A* (see Figure 6.20 and Figure 6.21) on the steel girder flange, and the other shear crack (lower shear crack) starts from the base of the shear stud nearest to the bearing stiffeners (see Figure 6.20 and Figure 6.21). Then, the cracks propagate to the heads of the second and third nearest studs from the girder end. The assumed crack patterns are compared with the test results in Figure 6.20 and Figure 6.21 for CG1 and CG2, respectively. The assumed crack angles are very close to those from the test results. Based on these failure modes, a strut-tie model was used to evaluate the shear capacity of the concrete slab. The concrete between the two shear cracks shown in Figure 6.20 and Figure 6.21 serves as a compression strut. Figure 6.22 shows the failure mode of concrete slab from Specimen CG1. The compression strut resulted in crushing of the concrete slab.

Based on ACI 318 (2008), the nominal compressive strength (f_{ns}) of a compressive strut is determined by multiplying the effective compressive strength of the concrete (f_{ce}) by the cross-sectional area of the strut (A_{cs}).

$$f_{ns} = f_{ce} A_{cs} \tag{6.44}$$

where

f_{ce} = $0.85\beta_s f_c^{'}$,

β_s = { 1.0 for a strut with a uniform cross-section,
0.75 for a bottle shape strut with sufficient transverse reinforcement,

$f_c^{'}$ = concrete compressive strength, and

A_{cs} = cross-sectional area perpendicular to the axis of the strut at one end.

Two different angles of the shear cracks will create a bottle shape of the strut and, therefore, 0.75 equals β_s. Figure 6.23 shows an analytical model based on these assumptions for the load transfer mechanism in concrete. The strut angle can be determined as

$$\phi = \tan^{-1}\left(\frac{h_s}{S_h}\right) \tag{6.45}$$

The diagonal compressive strut force can be decomposed into the horizontal and vertical components. The vertical force is resisted by the bearing stiffener pair, and the horizontal force is anchored by the shear studs which are welded onto the flange. Therefore, the effective strut width (b_{st}) can be assumed as the distance between the studs as shown in Figure 6.24.

The cross-sectional area of the compressive strut is determined by multiplying the effective strut width (b_{st}) by the compressive strut depth (d_{st}) at the end of the strut, which has the smallest cross-sectional area. The strut depth and area can be determined as

$$d_{st} = S_{h1} \sin\phi \tag{6.46}$$

$$A_{cs} = b_{st} d_{st} = b_{st} S_{h1} \sin\phi \tag{6.47}$$

Taking the vertical component of the inclined compressive strut force, the concrete shear strength is

$$V_c = f_{ns} \sin\phi = 0.85\beta_s f_c^{'} A_{cs} \sin\phi = 0.85(0.75) f_c^{'} b_{st} S_{h1} \sin^2\phi \qquad (6.48)$$

The shear strengths calculated in this manner are 32.7 kips and 17.8 kips for CG1 and CG2, respectively (see Table 6.6). Adding the shear strength contribution from the steel girder, the ultimate shear strength of the composite girder end panel can be determined by using Eq. (6.43).

Table 6.6 compares the predicted shear strengths with test results. The ratios of the predicted strength to that from testing are 1.026 and 0.975 for CG1 and CG2, respectively.

Table 6.1: Plate Girder Test Specimen Dimensions

Spec. No.	D (in.)	d_0 (in.)	t_w (in.)	b_f (in.)	t_f (in.)	t_b (in.)	b_b (in.)	e (in.)
SG1	52.5	26.25	0.247	16	0.75	1.01	14.75	4
SG2	52.5	26.25	0.183	14	0.62	1.01	12.94	4
EPS1-1	18.5	27.76	0.064	4	0.25	0.24	3.94	0
EPS1-2	18.5	27.76	0.065	4	0.25	0.49	3.94	0
EPS4-3	18.5	27.76	0.065	4	0.59	0.59	3.94	0
EPS2-4	18.5	27.76	0.065	4	0.25	0.39	3.94	0
EPS2-5	18.5	27.76	0.065	4	0.25	0.59	3.94	0
EPS3-6	18.5	27.76	0.065	4	0.59	0.24	3.94	0
EPS3-7	18.5	27.76	0.066	4	0.59	0.5	3.94	0
EPS5-8	18.5	27.83	0.063	4	0.24	0.48	3.93	0
EPS5-9	18.5	27.79	0.063	4	0.24	0.48	3.93	0
EPS6-10	18.5	27.81	0.063	4	0.24	0.59	3.94	0
EPS7-11	18.5	18.55	0.039	4	0.24	0.47	3.94	0
EPS7-12	18.5	23.14	0.039	4	0.24	0.48	3.94	0
EPS8-13	18.5	27.64	0.039	4	0.24	0.40	3.91	0

Note: SG series from this study and EPS series from Huslid and Rockey (1979).

Table 6.2: Material Properties and Identified Plastic Hinge Locations from Tests

Spec. No.	F_{yw} (ksi)	F_{yf} (ksi)	F_{yb} (ksi)	a (in.)	b (in.)
SG1	60.3	57.8	41.1	10.5	18.1
SG2	57.4	51.5	41.1	9.1	14.8
EPS1-1	27.1	45.4	45.0	8.5	3.2
EPS1-2	27.3	45.7	40.6	7.4	6.0
EPS4-3	28.5	34.7	35.1	10.2	7.2
EPS2-4	28.2	46.1	34.3	5.7	5.2
EPS2-5	29.4	45.7	34.3	5.6	6.6
EPS3-6	29.7	34.0	44.7	9.1	5.1
EPS3-7	28.2	34.3	36.1	8.5	8.4
EPS5-8	24.5	31.7	37.7	5.4	5.8
EPS5-9	25.5	31.8	37.7	6.2	5.2
EPS6-10	26.0	30.7	34.4	5.6	6.0
EPS7-11	25.3	31.2	35.8	5.4	7.1
EPS7-12	26.5	31.6	34.6	5.8	6.2
EPS8-13	24.0	29.9	38.4	6.3	6.1

Table 6.3: End Panel Shear Strength Comparison between Prediction and Experiment Results

Spec. No.	Shear Strength, V_s (kips)				Prediction / Test	AASHTO / Test	Eurocode / Test
	Test	Predic-tion	AAS-HTO	Euro-code			
SG1	315.3	328.9	190.2	326.1	1.04	0.60	1.03
SG2	190.3	188.5	76.6	178.6	0.99	0.40	0.94
EPS1-1	8.4	8.4	2.7	5.9	0.99	0.32	0.71
EPS1-2	9.0	9.7	2.9	6.1	1.08	0.32	0.68
EPS4-3	12.9	13.2	2.8	10.1	1.02	0.22	0.78
EPS2-4	8.9	9.2	2.9	6.3	1.04	0.32	0.71
EPS2-5	9.2	10.3	2.9	6.5	1.12	0.31	0.71
EPS3-6	11.6	10.2	2.9	10.5	0.88	0.25	0.91
EPS3-7	13.7	12.3	2.9	10.1	0.89	0.21	0.74
EPS5-8	8.2	7.9	2.6	5.6	0.96	0.31	0.68
EPS5-9	8.6	8.1	2.6	5.8	0.94	0.30	0.68
EPS6-10	8.9	8.5	2.6	5.9	0.954	0.29	0.66
EPS7-11	7.1	5.9	0.8	3.4	0.84	0.12	0.49
EPS7-12	5.6	5.4	0.7	3.2	0.97	0.13	0.57
EPS8-13	4.8	4.3	0.6	2.6	0.88	0.13	0.55
Average					0.97	0.28	0.72
Standard Deviation					0.08	0.12	0.15
Range (min./max.)					0.84/1.12	0.12/0.60	0.49/1.03

Table 6.4: Model SG1 Series: End Panel Shear Strength Comparison between Prediction and Design Codes
(Based on $F_{yw} = 60.3\,\text{ksi}$, $F_{yf} = 57.8\,\text{ksi}$, $F_{yb} = 41.1\,\text{ksi}$, $b_f = 16\,\text{in.}$, $b_b = 14.75\,\text{in.}$, and $e = 4\,\text{in.}$)

Model No	D (in.)	d_0 (in.)	t_w (in.)	t_f (in.)	t_b (in.)	Shear Strength, V_s (kips)				Prediction / FEM	AASHTO / FEM	Eurocode / FEM
						FEM	Preidic-tion	AAS-HTO	Euro-code			
SG1-1	52.75	26.25	0.250	0.5	0.5	312.2	294.9	197.0	284.2	0.95	0.63	0.91
SG1-2					0.75	315.7	300.9	197.0	284.2	0.95	0.62	0.90
SG1-3					1.0	316.8	308.4	197.0	284.2	0.97	0.62	0.90
SG1-4					1.5	318.2	325.9	197.0	284.1	1.02	0.62	0.89
SG1-5	52.5			0.75	0.5	316.9	318.2	196.5	330.9	1.00	0.62	1.04
SG1-6					0.75	321.8	327.2	196.5	330.7	1.02	0.61	1.03
SG1-7*					1.0	324.3	333.8	196.5	330.7	1.03	0.61	1.03
SG1-8					1.5	328.1	350.0	196.5	330.6	1.07	0.60	1.01
SG1-9	52.25			1.0	0.5	323.0	328.0	195.9	379.7	1.02	0.61	1.18
SG1-10					0.75	328.2	342.8	195.9	379.6	1.04	0.60	1.16
SG1-11					1.0	331.9	360.8	195.9	379.5	1.09	0.59	1.14
SG1-12					1.5	347.0	376.1	195.9	379.1	1.08	0.57	1.09
SG1-13	51.75			1.5	0.5	336.5	350.3	194.8	493.1	1.04	0.58	1.47
SG1-14					0.75	3443	363.9	194.8	492.9	1.06	0.57	1.43
SG1-15					1.0	362.8	380.5	194.8	492.5	1.05	0.54	1.36
SG1-16					1.5	410.1	419.7	194.8	491.4	1.02	0.48	1.20
SG1-17	52.75	52.50		0.5	0.5	226.3	207.4	78.6	168.4	0.92	0.34	0.74
SG1-18					0.75	228.3	212.1	78.6	168.4	0.93	0.34	0.74
SG1-19					1.0	228.2	218.1	78.6	168.4	0.96	0.34	0.74
SG1-20					1.5	230.6	232.8	78.6	168.3	1.01	0.34	0.73
SG1-21	52.5			0.75	0.5	231.9	220.4	78.6	191.2	0.95	0.34	0.83

* Model SG1

Table 6.4: Model SG1 Series: End Panel Shear Strength Comparison between Prediction and Design Codes (continued)

Model No	D (in.)	d_0 (in.)	t_w (in.)	t_f (in.)	t_b (in.)	Shear Strength, V_s (kips)				Prediction / FEM	AASHTO / FEM	Eurocode / FEM
						FEM	Preidic -tion	AAS-HTO	Euro-code			
SG1-22	52.5	52.50	0.250	0.75	0.75	234.7	232.3	78.6	191.1	0.99	0.34	0.81
SG1-23					1.0	238.2	237.8	78.6	191.0	1.00	0.33	0.80
SG1-24					1.5	243.7	251.5	78.6	190.8	1.03	0.32	0.78
SG1-25	52.25			1.0	0.5	241.1	228.5	78.6	215.7	0.95	0.33	0.90
SG1-26					0.75	247.1	241.1	78.6	215.5	0.98	0.32	0.87
SG1-27					1.0	252.2	256.6	78.6	215.3	1.02	0.31	0.85
SG1-28					1.5	259.5	273.4	78.6	215.1	1.05	0.30	0.83
SG1-29	51.75			1.5	0.5	251.0	247.7	78.6	273.0	0.99	0.31	1.09
SG1-30					0.75	259.2	259.5	78.6	272.7	1.00	0.30	1.05
SG1-31					1.0	275.0	274.1	78.6	272.2	1.00	0.29	0.99
SG1-32					1.5	305.4	309.0	78.6	271.1	1.01	0.26	0.89
SG1-33	52.75	78.75		0.5	0.5	197.9	169.4	56.7	143.5	0.86	0.29	0.73
SG1-34					0.75	199.1	173.0	56.7	143.4	0.87	0.29	0.72
SG1-35					1.0	199.4	177.6	56.7	143.4	0.89	0.28	0.72
SG1-36					1.5	200.9	189.0	56.7	143.4	0.94	0.28	0.71
SG1-37	52.5			0.75	0.5	203.3	177.9	56.8	158.2	0.88	0.28	0.78
SG1-38					0.75	205.3	188.0	56.8	158.2	0.92	0.28	0.77
SG1-39					1.0	207.8	192.6	56.8	158.0	0.93	0.27	0.76
SG1-40					1.5	211.6	203.2	56.8	157.9	0.96	0.27	0.75
SG1-41	52.25			1.0	0.5	211.6	184.1	56.9	174.6	0.87	0.27	0.83
SG1-42					0.75	215.7	193.9	56.9	174.4	0.90	0.26	0.81
SG1-43					1.0	219.0	206.0	56.9	174.2	0.94	0.26	0.80
SG1-44					1.5	223.7	220.2	56.9	174.0	0.99	0.25	0.78

Table 6.4: Model SG1 Series: End Panel Shear Strength Comparison between Prediction and Design Codes (continued)

Model No	D (in.)	d_0 (in.)	t_w (in.)	t_f (in.)	t_b (in.)	Shear Strength, V_s (kips)				Prediction / FEM	AASHTO / FEM	Eurocode / FEM
						FEM	Preidic-tion	AAS-HTO	Euro-code			
SG1-45	51.75	78.75	0.250	1.5	0.5	220.4	199.0	57.1	213.0	0.90	0.26	0.97
SG1-46					0.75	226.0	208.2	57.1	212.7	0.92	0.25	0.94
SG1-47					1.0	232.7	219.5	57.1	212.5	0.94	0.25	0.91
SG1-48					1.5	249.1	247.0	57.1	211.8	0.99	0.23	0.85
SG1-49	52.5	26.25	0.292	0.75	1.0	407.0	435.6	312.0	423.5	1.07	0.77	1.04
SG1-50		52.5				302.7	293.1	124.8	246.0	0.97	0.41	0.82
SG1-51		78.75				266.0	240.3	90.1	205.1	0.90	0.34	0.77
SG1-52		26.25	0.250			324.3	333.8	196.5	330.7	1.03	0.61	1.02
SG1-53		52.5				238.2	237.8	78.6	191.0	1.00	0.33	0.80
SG1-54		78.75				207.8	192.6	56.8	158.0	0.93	0.27	0.76
SG1-55		26.25	0.219			267.1	273.5	131.6	270.0	1.02	0.49	1.01
SG1-56		52.5				199.8	200.2	52.7	154.7	1.00	0.26	0.77
SG1-57		78.75				172.9	160.5	38.0	126.9	0.93	0.22	0.73
SG1-58		26.25	0.188			219.7	223.3	82.9	216.8	1.02	0.38	0.99
SG1-59		52.5				164.9	166.1	33.2	123.0	1.01	0.20	0.75
SG1-60		78.75				141.3	132.1	23.9	99.5	0.93	0.17	0.70
SG1-61		26.25	0.164			192.6	190.6	55.5	181.8	0.99	0.29	0.94
SG1-62		52.5				144.2	143.1	22.2	102.1	0.99	0.15	0.71
SG1-63		78.75				119.5	113.2	16.0	81.6	0.95	0.13	0.68
							Average			0.978	0.38	0.90
							Standard Deviation			0.06	0.15	0.18
							Range (min./max.)			0.86/1.09	0.13/0.77	0.68/1.47

Table 6.5: Model SG2 Series: End Panel Shear Strength Comparison between Prediction and Design Codes
(Based on $F_{yw} = 57.4\,\text{ksi}$, $F_{yf} = 51.5\,\text{ksi}$, $F_{yb} = 41.1\,\text{ksi}$, $b_f = 14\,\text{in.}$, and $b_b = 12.94\,\text{in.}$)

Model No	D (in.)	d_0 (in.)	e (in.)	t_w (in.)	t_f (in.)	t_b (in.)	Shear Strength, V_s (kips)				Prediction / FEM	AASHTO / FEM	Eurocode / FEM
							FEM	Preidic-tion	AAS-HTO	Euro-code			
SG2-64	52.69	26.25	4	0.188	0.563	0.563	195.1	179.9	83.1	179.3	0.92	0.43	0.92
SG2-65						0.750	197.2	184.0	83.1	179.3	0.93	0.42	0.91
SG2-66						1.125	199.6	194.3	83.1	179.2	0.97	0.42	0.90
SG2-67	52.50				0.750	0.563	202.3	195.7	82.9	203.1	0.97	0.41	1.00
SG2-68						0.750	204.9	200.4	82.9	203.0	0.98	0.41	0.99
SG2-69						1.125	210.4	209.9	82.9	202.9	1.00	0.39	0.96
SG2-70	52.13				1.125	0.563	216.3	208.3	82.5	261.2	0.96	0.38	1.21
SG2-71						0.750	229.6	218.6	82.5	260.9	0.95	0.36	1.14
SG2-72						1.125	253.2	243.7	82.5	260.4	0.96	0.33	1.03
SG2-73	52.69	52.5			0.563	0.563	141.9	131.2	34.5	107.2	0.92	0.24	0.76
SG2-74						0.750	143.9	134.4	34.5	107.2	0.93	0.24	0.75
SG2-75						1.125	147.2	142.6	34.5	107.1	0.97	0.23	0.73
SG2-76	52.50				0.750	0.563	150.4	142.0	34.5	119.5	0.94	0.23	0.80
SG2-77						0.750	153.1	147.1	34.5	119.4	0.96	0.23	0.78
SG2-78						1.125	157.4	154.8	34.5	118.7	0.98	0.22	0.76
SG2-79	52.13				1.125	0.563	164.6	152.1	34.5	149.6	0.92	0.21	0.91
SG2-80						0.750	173.6	160.5	34.5	149.3	0.92	0.20	0.86
SG2-81						1.125	187.5	181.1	34.5	148.9	0.97	0.18	0.80
SG2-82	52.69	78.75			0.563	0.563	123.1	104.8	23.9	87.2	0.85	0.19	0.71
SG2-83						0.750	124.4	107.3	23.9	87.2	0.86	0.19	0.70
SG2-84						1.125	126.5	113.6	23.9	87.1	0.90	0.19	0.69
SG2-85	52.50				0.750	0.563	130.2	112.8	23.9	95.0	0.87	0.18	0.73

Table 6.5: Model SG2 Series: End Panel Shear Strength Comparison between Prediction and Design Codes (continued)

Model No	D (in.)	d_0 (in.)	e (in.)	t_w (in.)	t_f (in.)	t_b (in.)	Shear Strength, V_s (kips)				Prediction / FEM	AASHTO / FEM	Eurocode / FEM
							FEM	Preidic-tion	AAS-HTO	Euro-code			
SG2-86	52.50	78.75	4	0.188	0.750	0.750	132.0	117.1	23.9	95.0	0.89	0.18	0.72
SG2-87						1.125	134.5	123.1	23.9	94.9	0.92	0.18	0.71
SG2-88	52.13				1.125	0.563	138.0	120.6	24.0	114.5	0.87	0.17	0.83
SG2-89						0.750	143.3	127.2	24.0	114.4	0.89	0.17	0.80
SG2-90						1.125	151.5	143.4	24.0	114.0	0.95	0.16	0.75
SG2-91	52.63	26.25	0		0.625	1.0	196.7	189.0	83.0	189.9	0.96	0.42	0.97
SG2-92*			4				201.4	195.5	83.0	202.4	0.97	0.41	1.01
SG2-93			8				210.2	212.1	83.0	213.4	1.01	0.40	1.02
SG2-94		52.5	0				143.1	138.3	33.2	144.6	0.97	0.23	1.01
SG2-95			4				149.2	143.4	33.2	150.3	0.96	0.22	1.01
SG2-96			8				154.2	156.7	33.2	155.9	1.02	0.22	1.01
SG2-97		78.75	0				124.4	110.3	23.9	138.2	0.89	0.19	1.11
SG2-98			4				128.4	114.2	23.9	142.2	0.89	0.19	1.11
SG2-99			8				132.3	124.7	23.9	146.1	0.94	0.18	1.10
								Average			0.94	0.27	0.89
								Standard Deviation			0.042	0.097	0.15
								Range (min./max.)			0.85/1.02	0.16/0.43	0.69/1.21

* Model SG2

Table 6.6: Composite Girder Shear Strength Prediction

Specimen No.	f_c' (ksi)	h_s (in.)	S_h (in.)	S_{h1} (in.)	ϕ (degree)	A_{cs} (in.^{2})	V_c (kips)	V_s (kips)	V_n (kips)	V_{TEST} (kips)	$\frac{V_n}{V_{TEST}}$
CG1	5.0	5.5	13.5	4.5	22.2	21.6	26.0	328.9	354.9	352.6	1.01
CG2	5.4	4.0	12.75	4.25	17.4	13.4	13.8	188.5	202.3	212.1	0.95

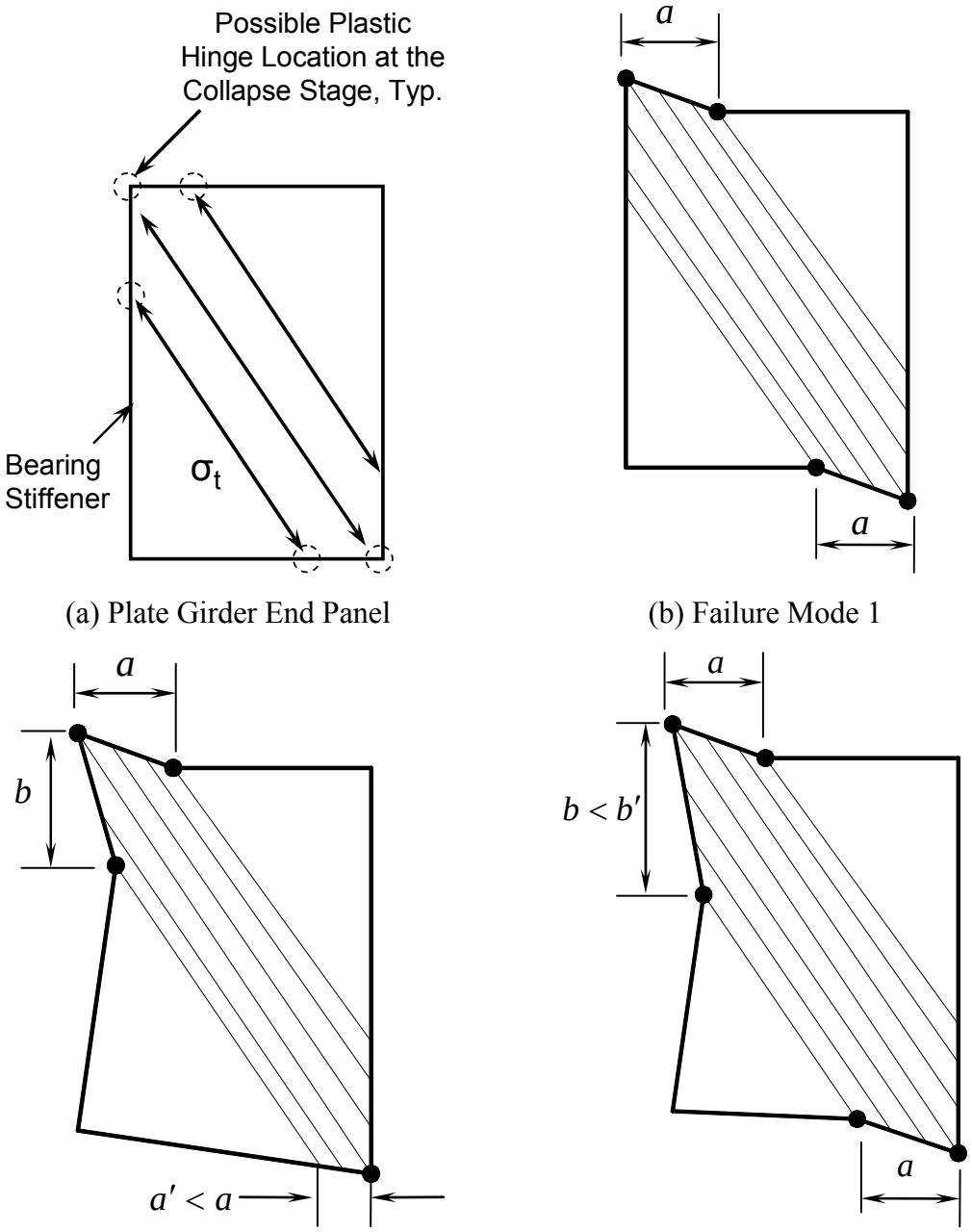

(a) Plate Girder End Panel

(b) Failure Mode 1

(c) Failure Mode 2

(d) Failure Mode 3

Figure 6.1: Failure Modes

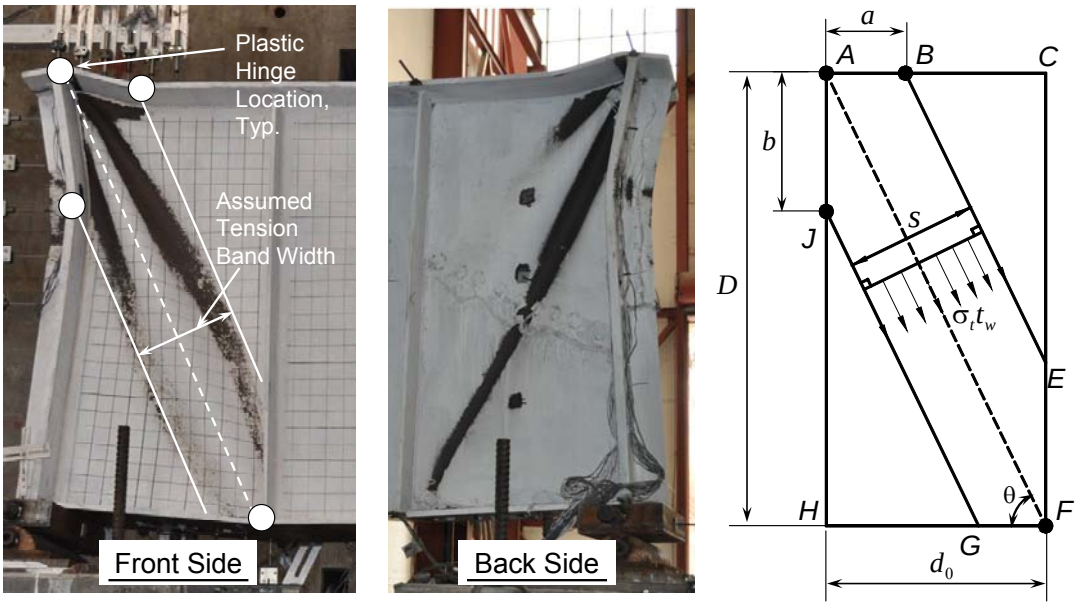

Figure 6.2: Tension-Field Band Width

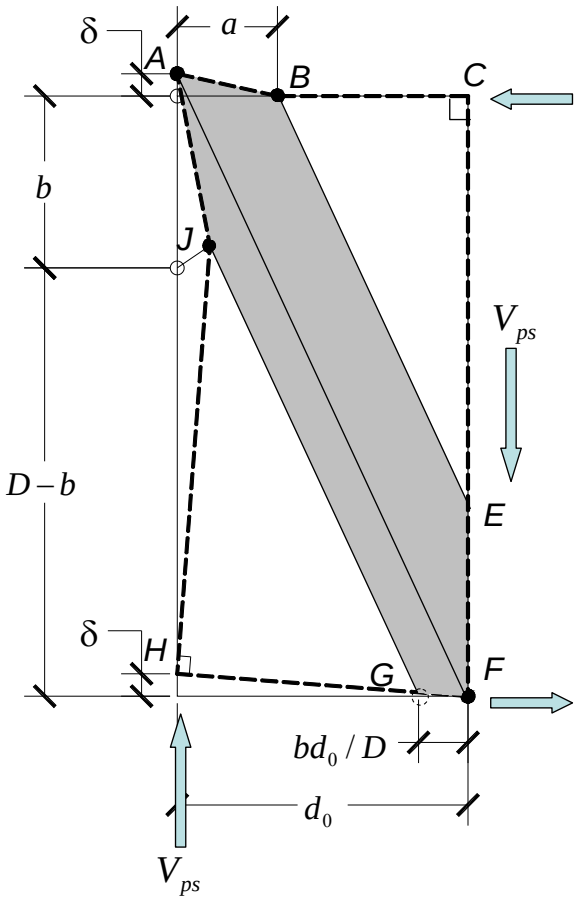

(a) Assumed Collapse Mechanism

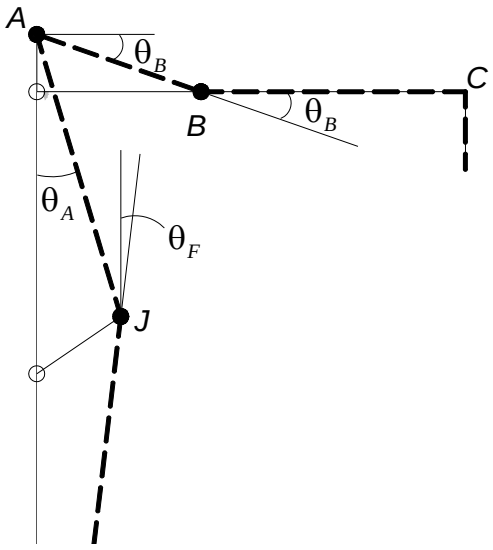

(b) Kinematics (Upper Left Corner)

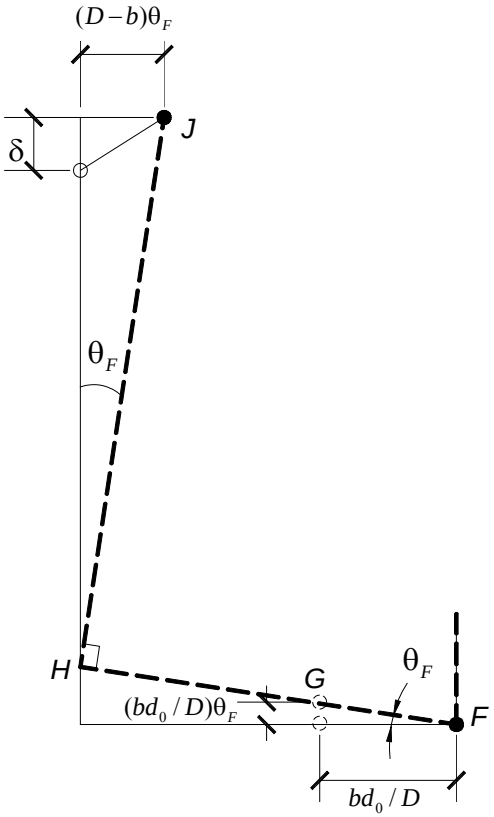

(c) Kinematics (Lower Portion)

Figure 6.3: Assumed End Panel Collapse Mechanism

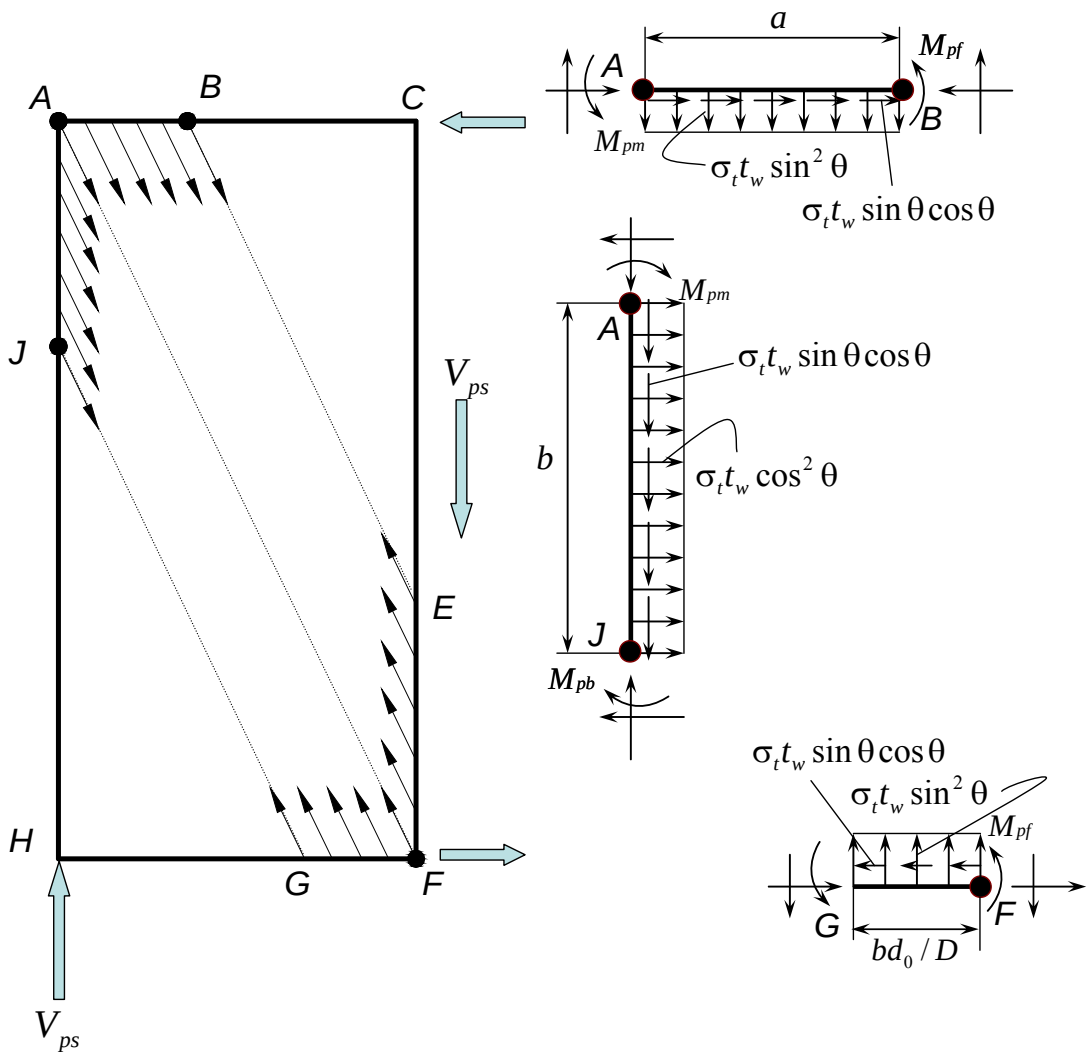

(a) Free-Body of End Panel

(b) Free Bodies of Boundary Member Segments

Figure 6.4: Free-Body Diagram of End Panel with Web Excluded

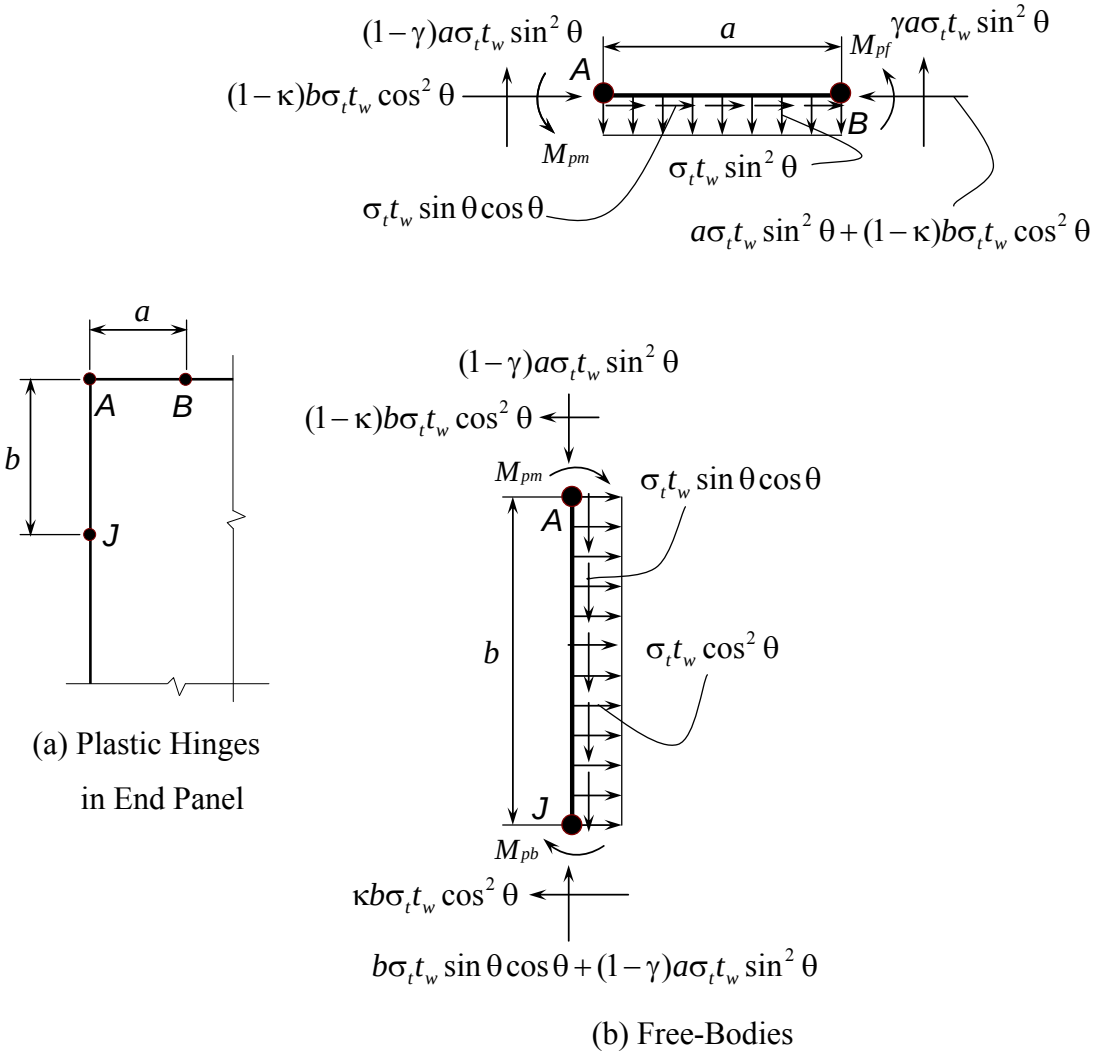

Figure 6.5: Free-Body Diagram of Boundary Members between Plastic Hinges

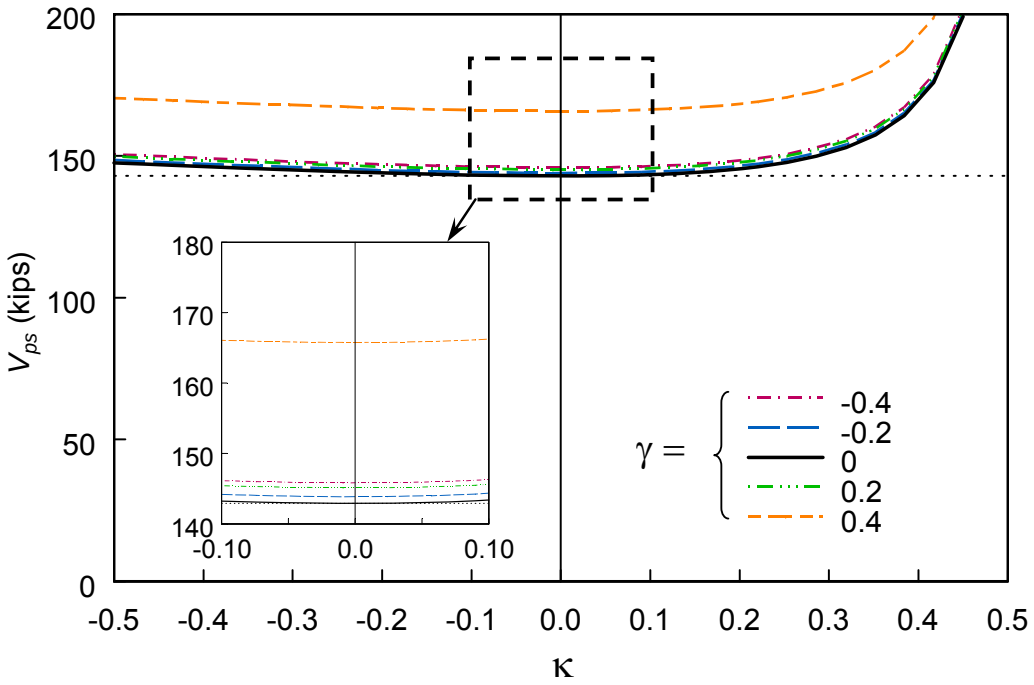

(a) Model SG1

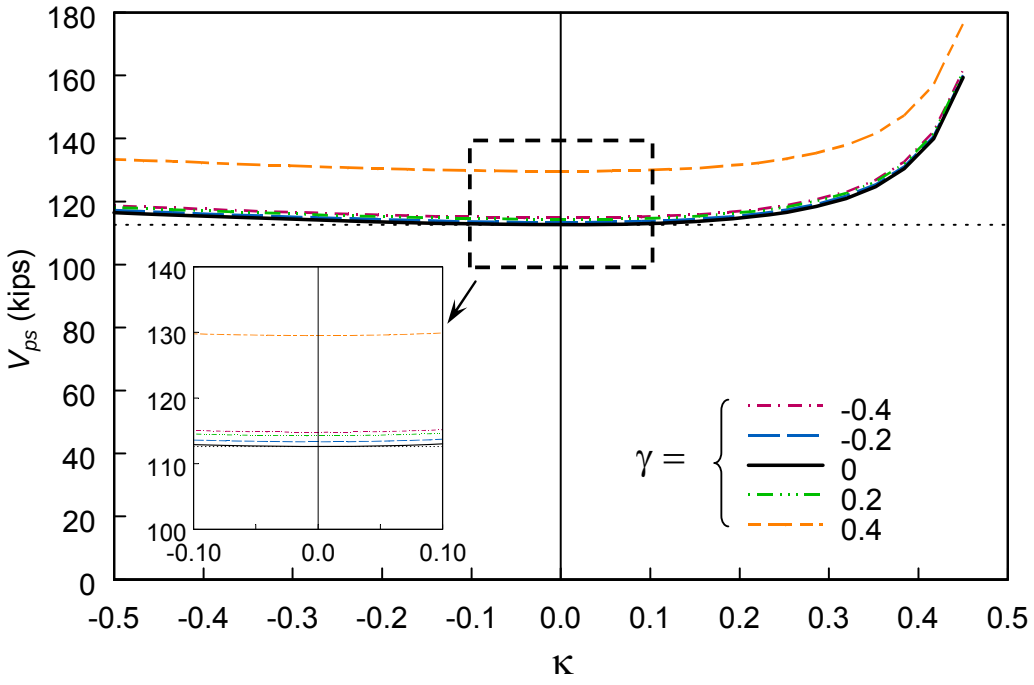

(b) Model SG2

Figure 6.6: Effect of Shear Ratio Parameters

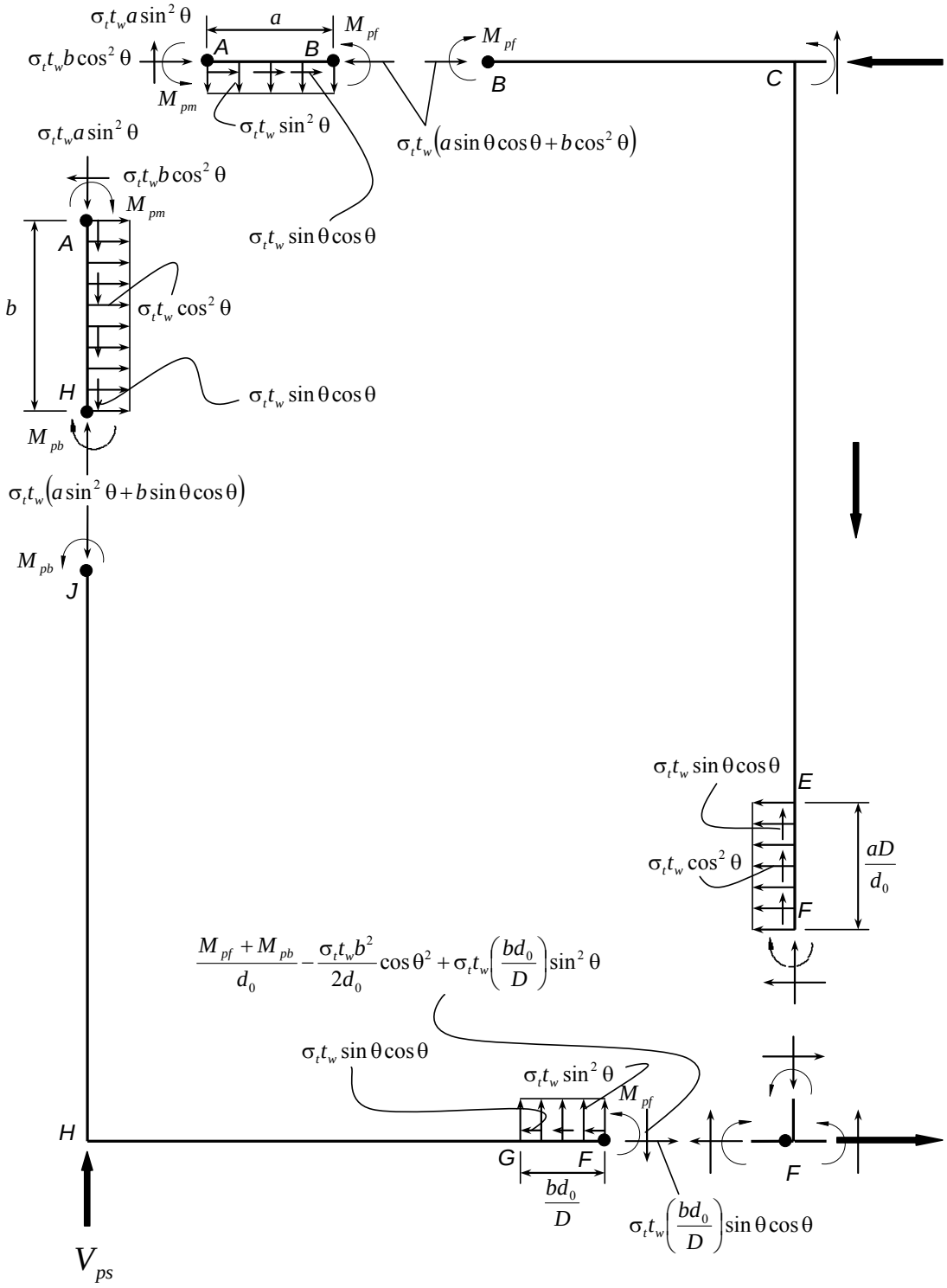

Figure 6.7: Free-Body of End Panel Due to Tension-Field Action

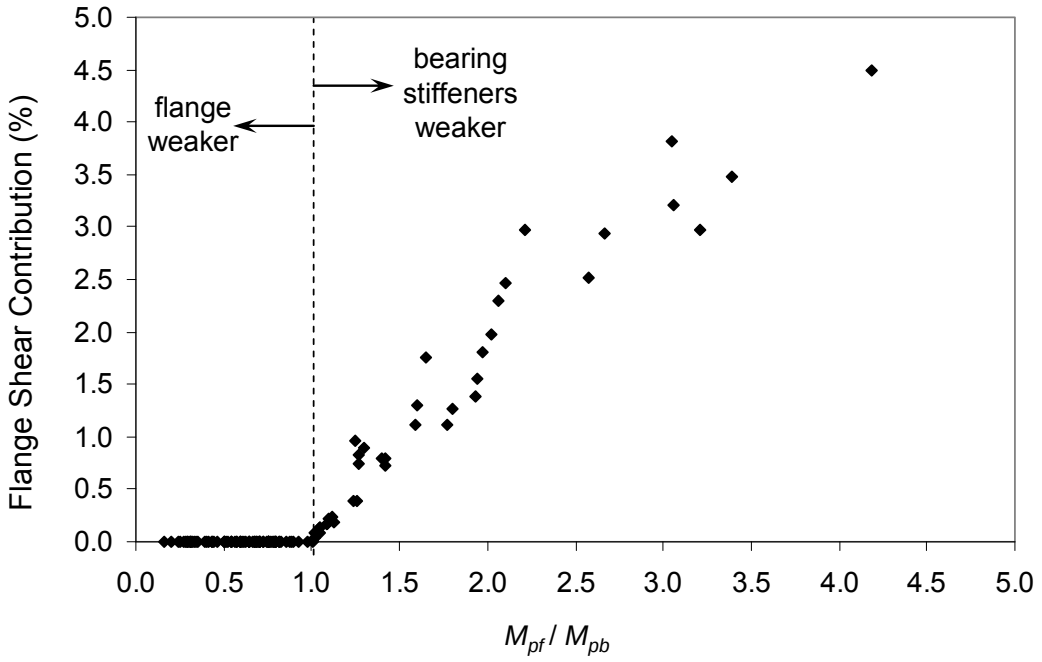

Figure 6.8: Flange Shear Contribution

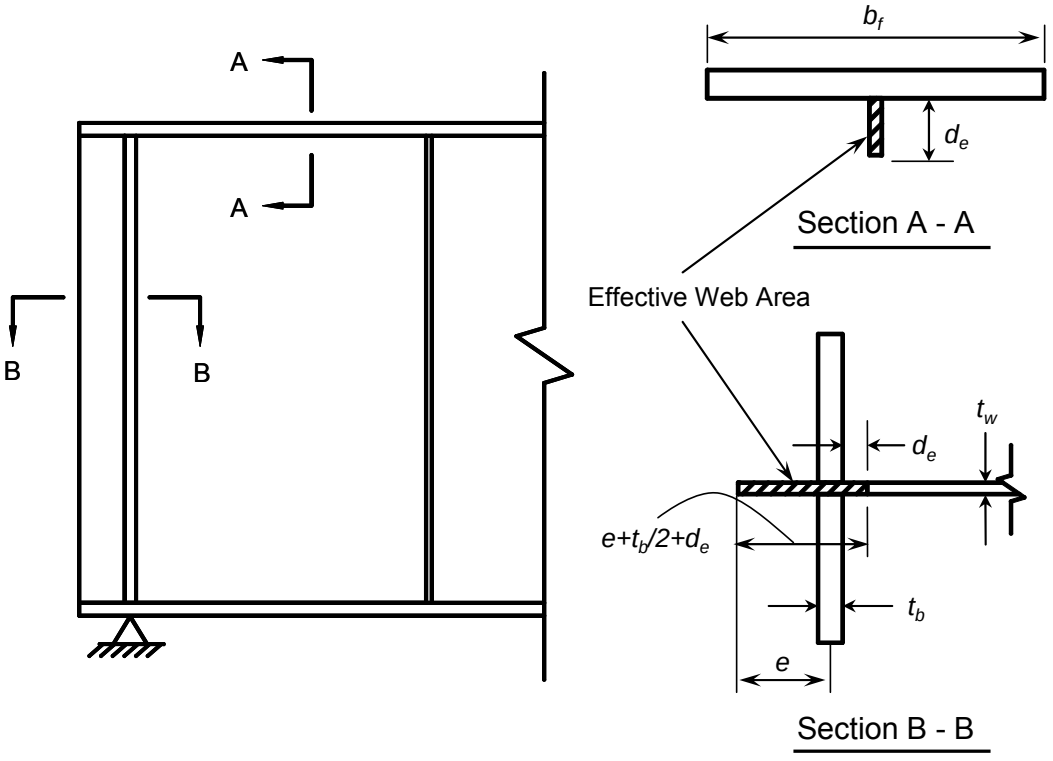

Figure 6.9: Effective Web Depth, d_e

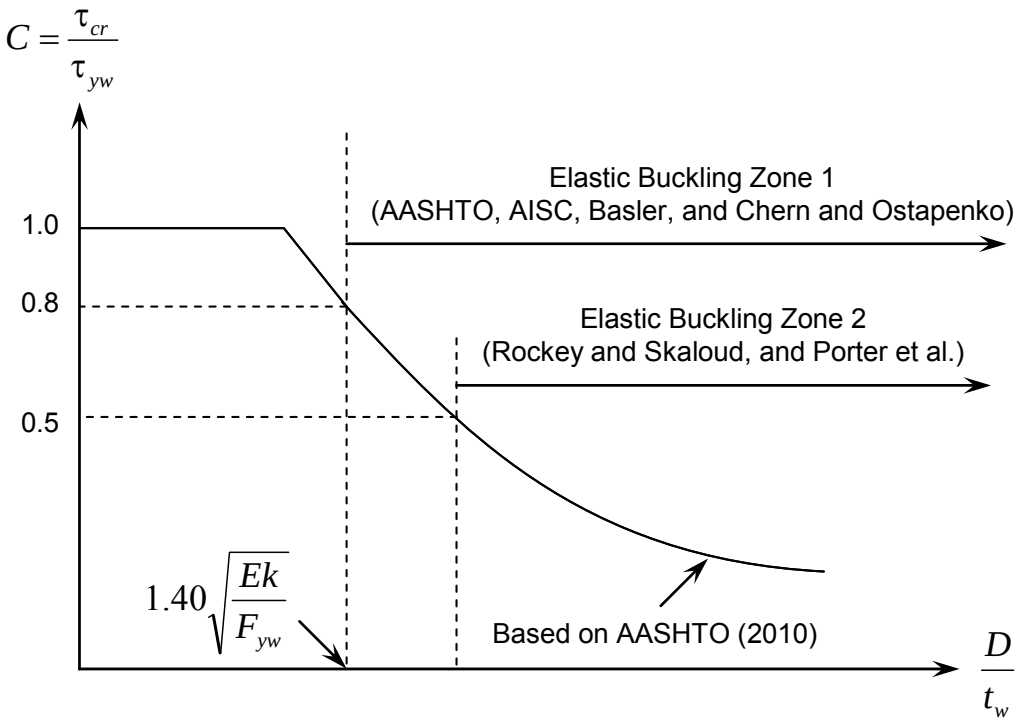

Figure 6.10: Relationship between C and D/t_w

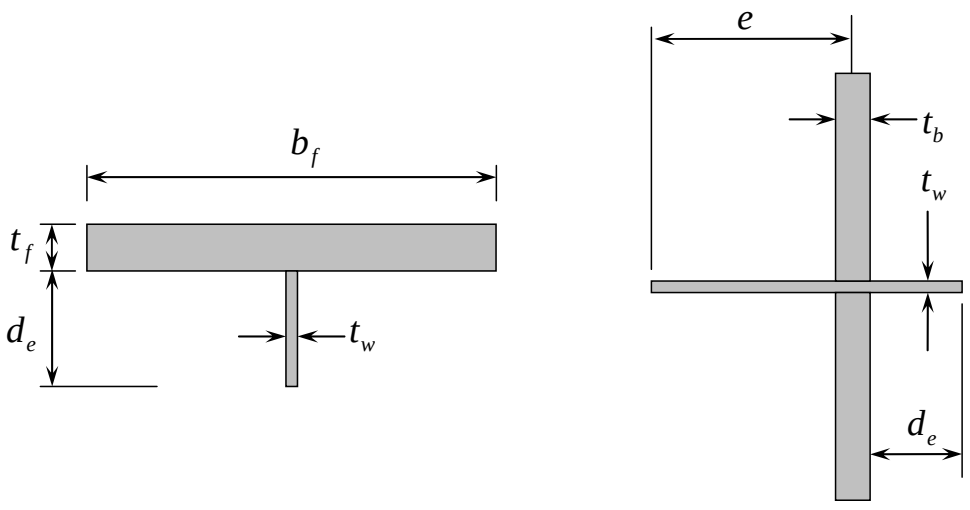

(a) Girder Flange (b) Bearing Stiffeners

Figure 6.11: Effective Sections of Boundary Members

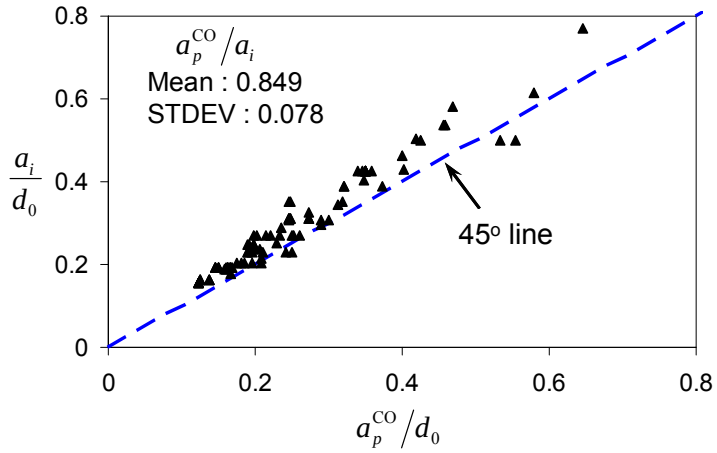

(a) from Chern and Ostapenko (1969) [Eq. (6.37)]

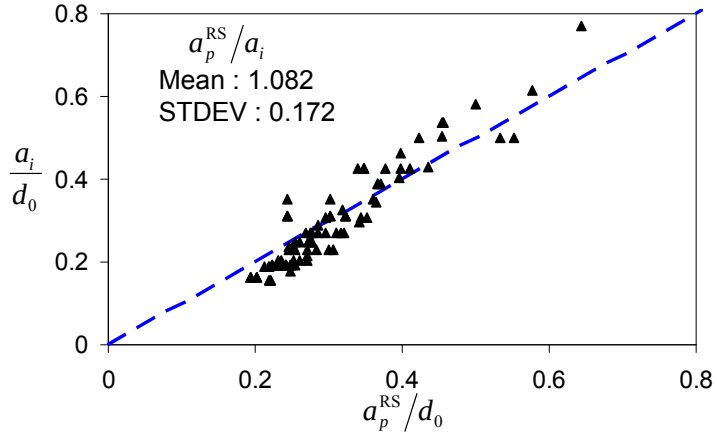

(b) from Rockey and Skaloud (1972) [Eq. (6.38)]

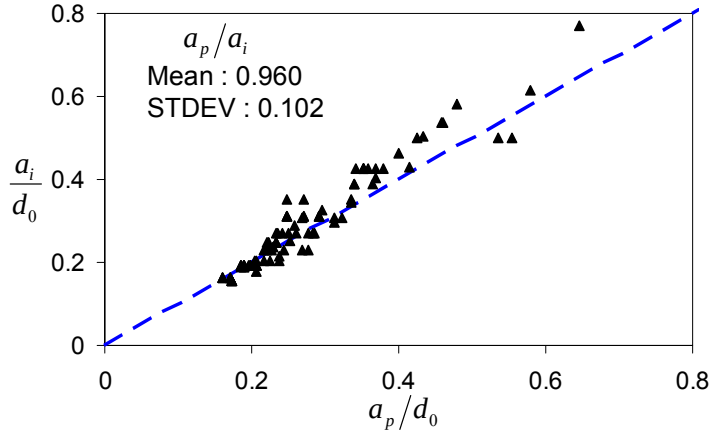

(c) from Proposed [Eq. (6.42)]

Figure 6.12: Comparison of Plastic Hinge Location *a* in Top Flange

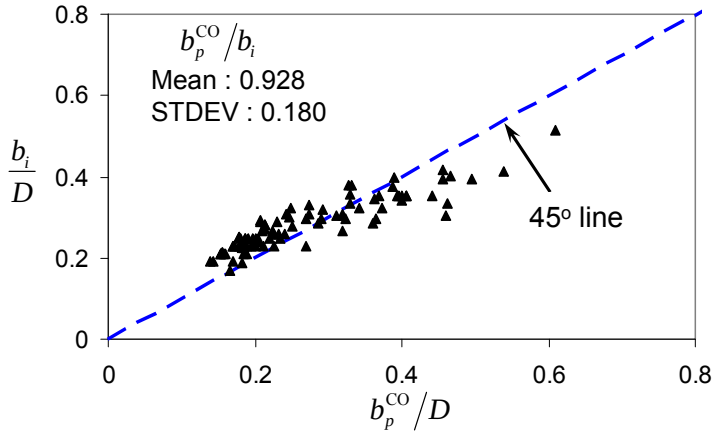

(a) from Chern and Ostapenko (1969) [Eq. (6.37)]

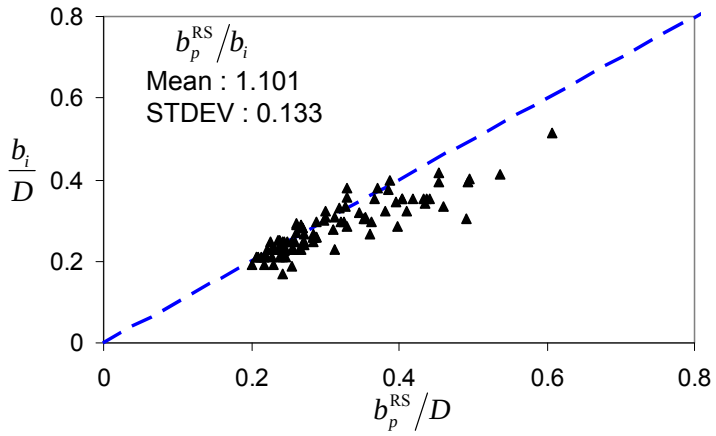

(b) from Rockey and Skaloud (1972) [Eq. (6.38)]

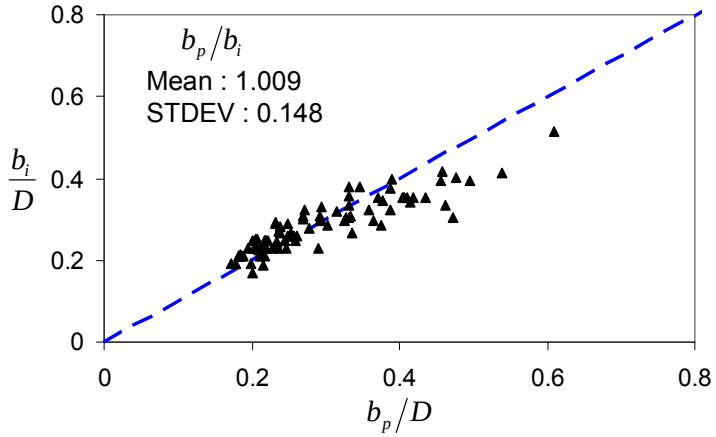

(c) from Suggestion [Eq. (6.42)]

Figure 6.13: Comparison of Plastic Hinge Location *b* in Bearing Stiffeners

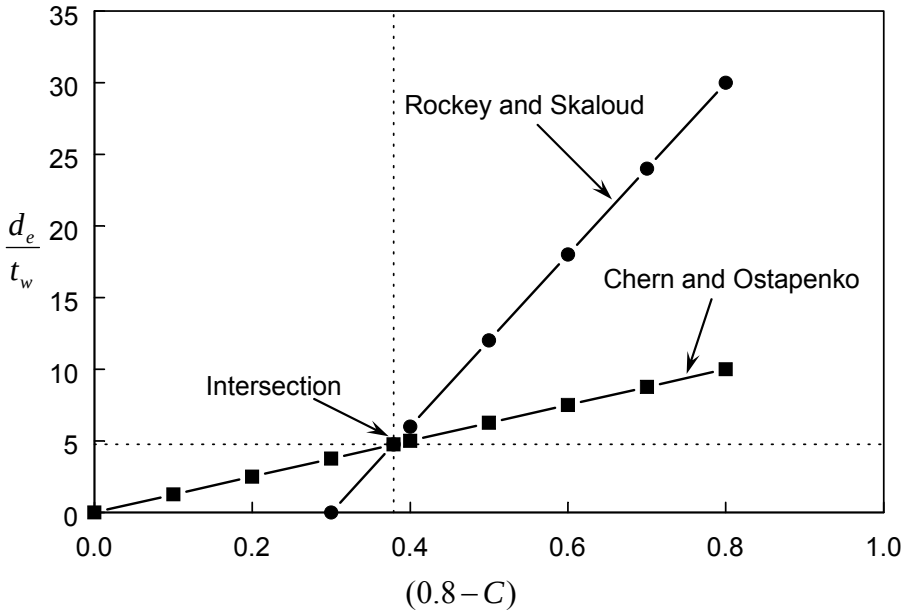

(a) Effective Web Depth from Eqs. (6.37) and (6.38)

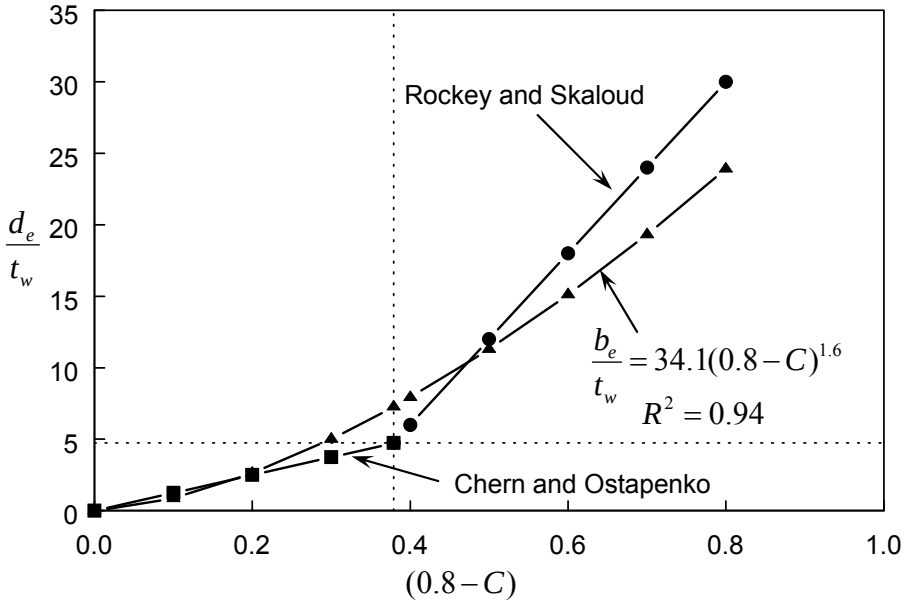

(b) Regression

Figure 6.14: Comparison of Effective Web Depth, d_e

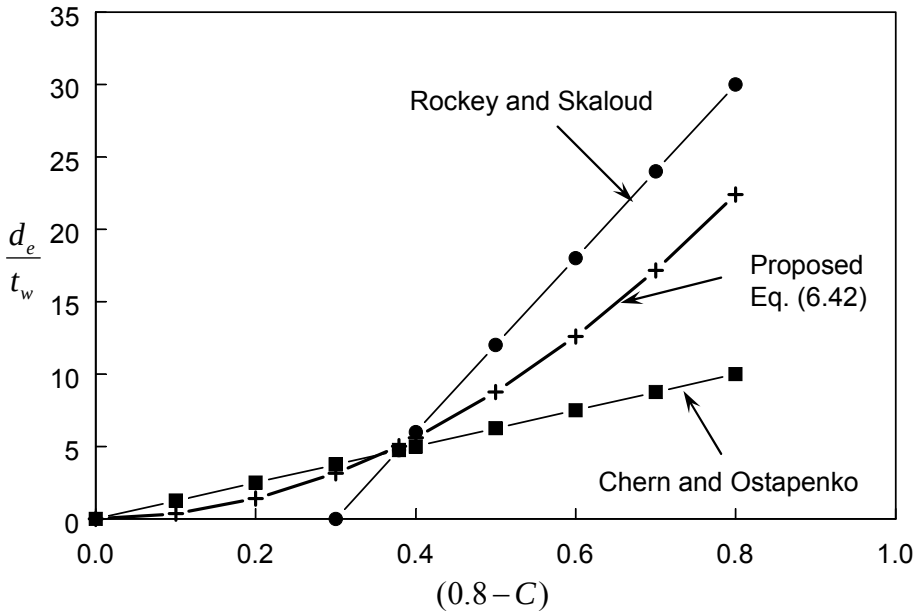

(c) Suggested Effective Web Depth

Figure 6.14: Comparison of Effective Web Depth, d_e (continued)

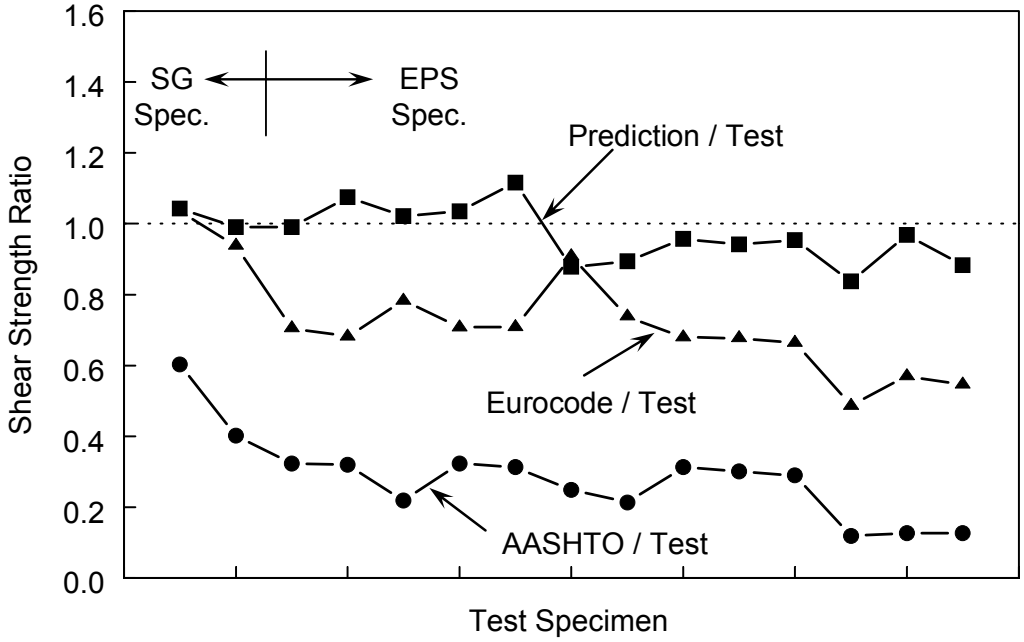

Figure 6.15: Comparison of End Panel Shear Strengths (Test Specimens)

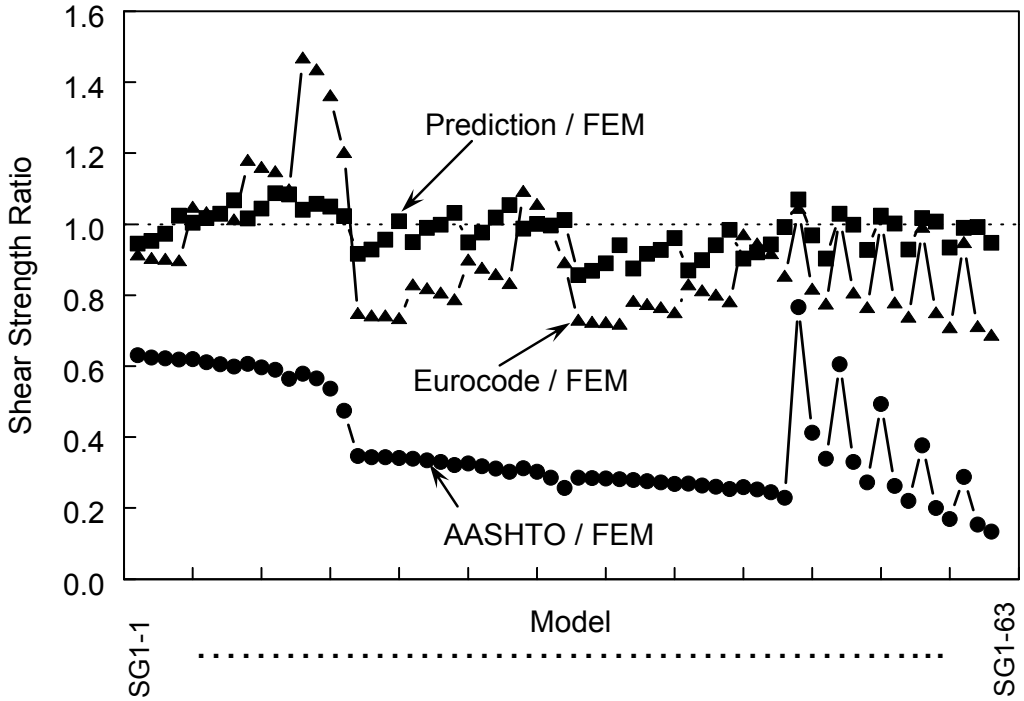

Figure 6.16: Comparison of End Panel Shear Strengths
(SG1 Models from Parametric Study)

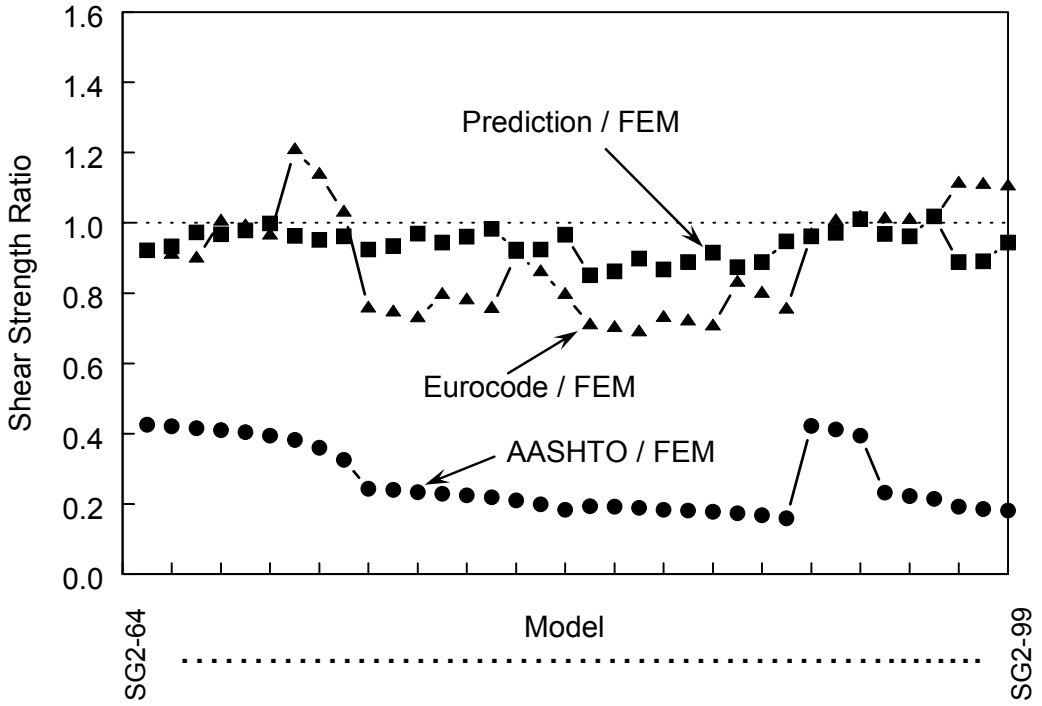

Figure 6.17: Comparison of End Panel Shear Strengths
(SG2 Models from Parametric Study)

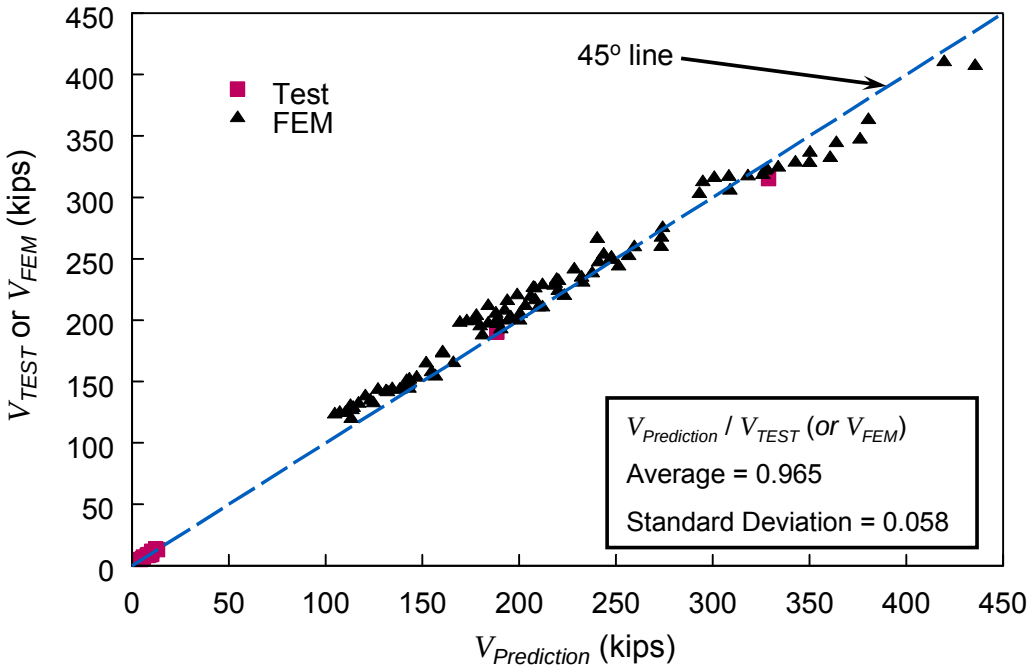

Figure 6.18: Comparison of End Panel Shear Strengths

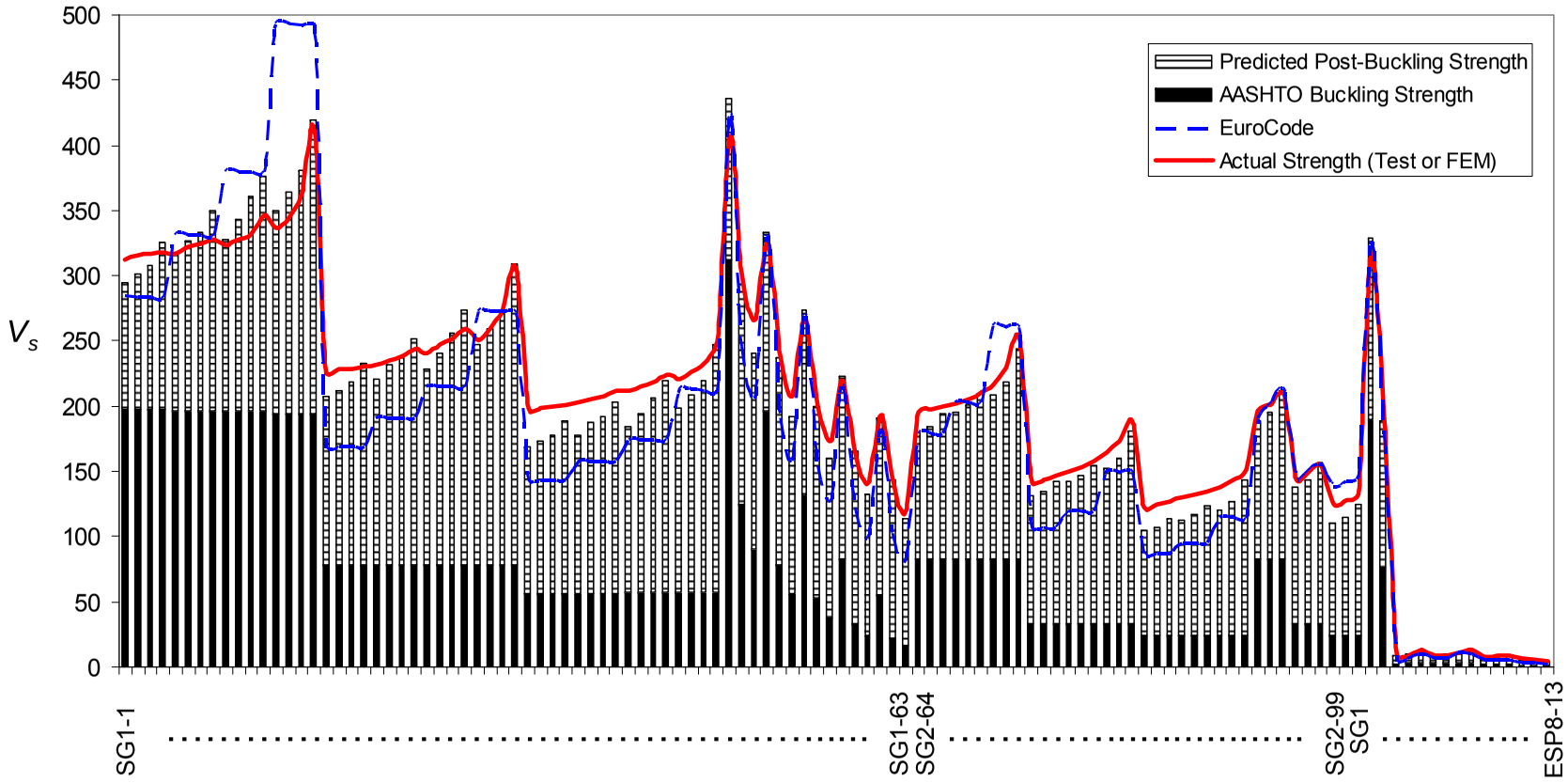

Figure 6.19: Comparison of End Panel Shear Strengths

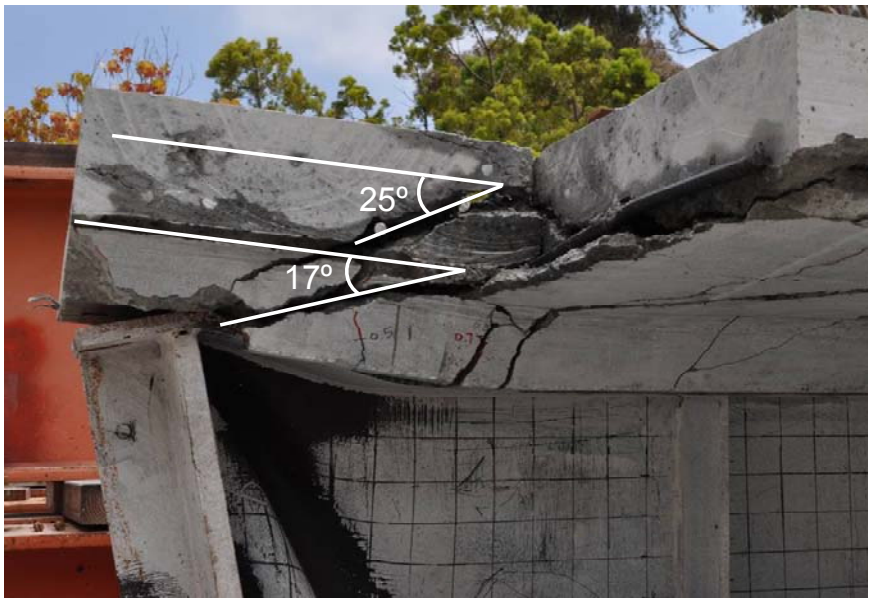

(a) Test Specimen

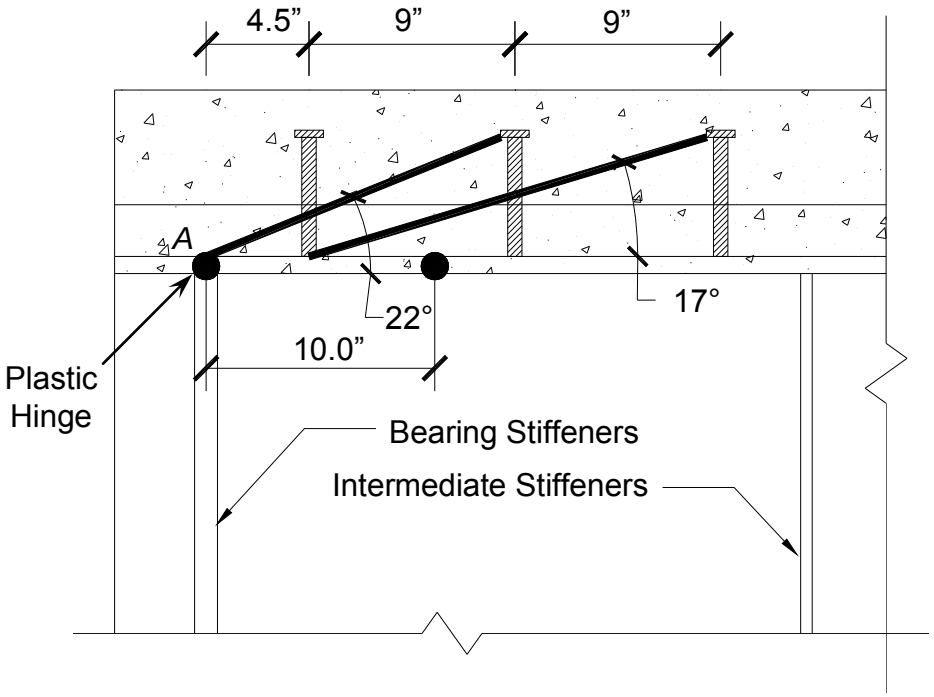

(b) Assumed Crack Pattern

Figure 6.20: CG1: Shear Crack Comparison in Concrete Slab

(a) Test Specimen

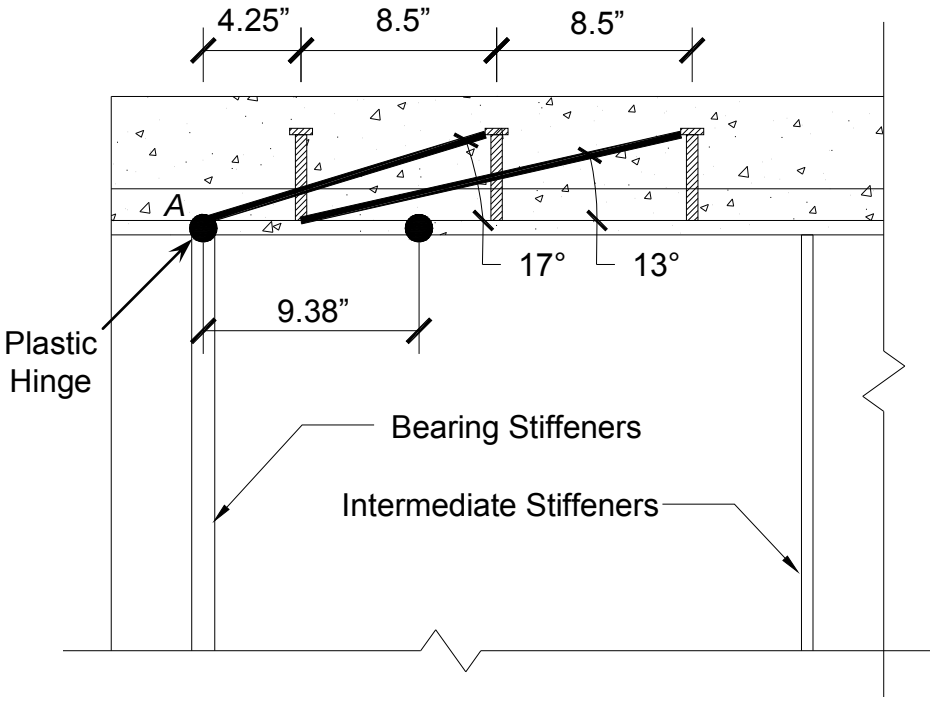

(b) Assumed Crack Pattern

Figure 6.21: CG2: Shear Crack Comparison in Concrete Slab

(a) Side View

(b) Top View

Figure 6.22: Specimen CG1: Concrete Crushing

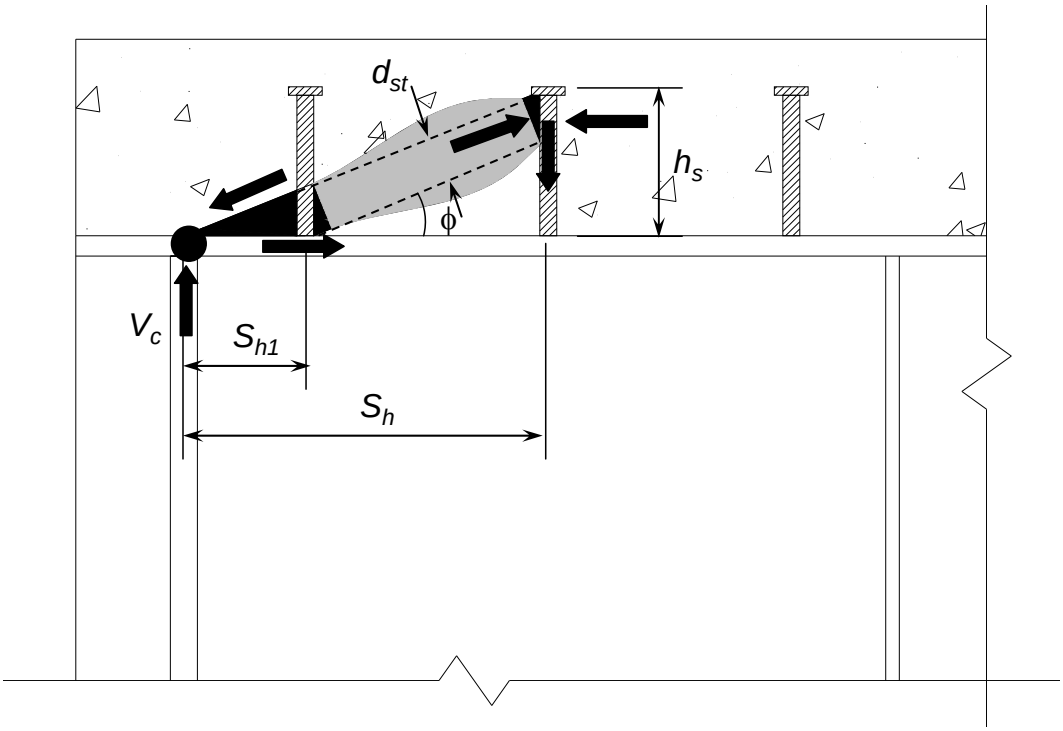

Figure 6.23: Analytical Model for Load Transfer Mechanism in Concrete Slab

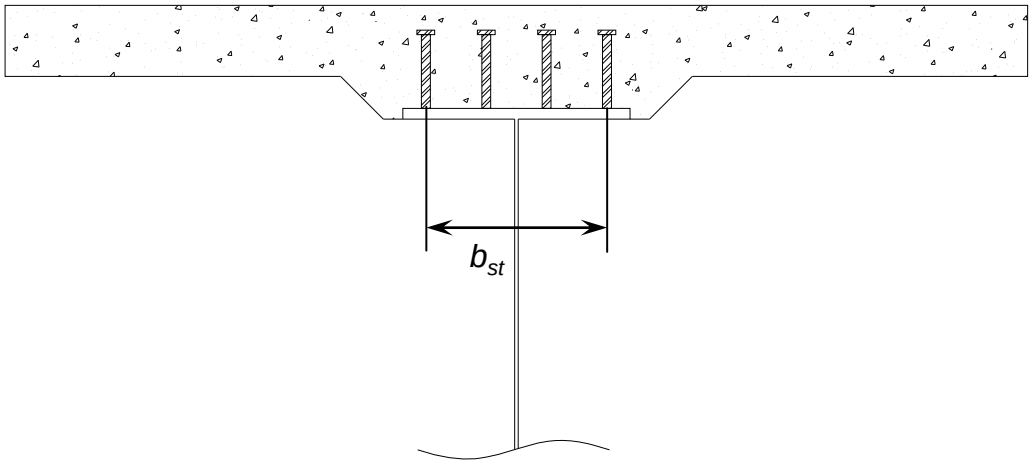

Figure 6.24: Effective Width of Compression Strut

7. REHABILITATION OF END PANELS

7.1 General

The Manual for Bridge Evaluation (AASHTO 2011) is used by bridge engineers to perform load rating of existing bridges. When the load rating factor is greater than 1.0, the bridges are deemed safe and no further action is required. However, when the load rating factor is less than 1.0, the bridges must be strengthened to maintain current vehicular loading. Otherwise, vehicular loading on the bridge must be restricted.

Many bridges have been recently reevaluated. Results showed that some bridges had a rating factor much smaller than 1.0 due to the deficiency in shear strength in the end panels, where the shear strength was determined based on the shear buckling strength per AASHTO Specifications (2014) without taking advantage of any partial tension-field action and composite slab effect. However, it was shown in Chapter 5 that end panels could provide a considerable amount of post-buckling strength due to these two factors.

It is believed that using the proposed Eq. (6.33) will eliminate many cases of unnecessary shear strengthening. If the reevaluated load rating analyses with this equation show that some bridges still have a rating factor smaller than 1.0 due to the shear deficiency in the end panels, then these panels need to be reinforced. However, rehabilitation of the plate girder end panels may be a challenging task to design engineers. Therefore, guidelines are needed to rehabilitate plate girder end panels. In this Chapter, available rehabilitation schemes will be reviewed and an alternative rehabilitation scheme will be proposed.

7.2 Basler's Scheme

One of the well-known methods to rehabilitating end panels is adding another pair of stiffeners, or end stiffeners, at the end of the girder (Basler 1961a). Therefore, two pairs of stiffeners (a pair of bearing stiffeners and a pair of end stiffeners) at or near the support will resist the horizontal component of the tension-field action force (see Figure 7.1). Basler developed an equation for the required end stiffener area by assuming that

the tension-field stress would act at an inclination of 45 degrees and be uniformly distributed over the entire girder depth (see Figure 7.2). Then, both vertical and horizontal components induced by the tension-field stresses are $(\tau - \tau_{cr})t_w$. By considering the shaded area in Figure 7.2 as a beam with a span of *D*, the maximum bending moment due to the horizontal component is $(\tau - \tau_{cr})t_w D^2/8$. Assuming this moment is resisted by a force couple in the bearing stiffener and end stiffener pairs, a maximum compressive force of $(\tau - \tau_{cr})t_w D^2/8e$ develops in the end stiffener pair. Equating the resisting force $A_e F_{ye}$ offered by the end stiffener pair with the above force leads to Eq. (7.1).

$$A_e = \frac{(\tau - \tau_{cr})DA_w}{8eF_{ye}} = \frac{(V - V_{cr})D}{8eF_{ye}} \tag{7.1}$$

where A_w (= Dt_w) is the web area and F_{ye} is the yield stress of the end stiffeners.

To evaluate the adequacy of Eq. (7.1), nonlinear finite element analyses were performed again using Model SG1-7 (see Table 6.4). For Eq. (7.1) to be valid, the end panel should have the same shear strength as if it was an interior panel.

Based on Eq. (6.33) with α=1, which corresponds to the ultimate shear strength of an interior panel (V_s^{int}) as specified by AASHTO Specifications (2014), the expected shear strength of the rehabilitated Model SG1-7 is 401 kips (V_s^{int} = 401 kips). The required area of end stiffener pair, A_e, from Eq. (7.1) is 8.2 in.^{2} by using the same yield stress as the bearing stiffeners of Model SG1-7 ($F_{ye} = F_{yb}$ =41.1 ksi). It was assumed that the end stiffeners have the same width as bearing stiffeners (b_{es}=b_b=14.75 in.). Dividing the end stiffener area by the total width of the end stiffeners (b_{es}) gives a thickness (t_{es}) of 0.56 in.

Guided by the following criterion for local buckling control of each end stiffener (AASHTO 2014),

$$\frac{b_{es} - t_w}{2t_{es}} \le 0.38\sqrt{\frac{E}{F_y}} \tag{7.2}$$

the required thickness t_{es} is about 0.7 in. Although AASHTO requires a thickness of 0.7 in., a thickness of 0.56 in. is assigned to Model SG1R-EP1 for the comparison purposes. Then, a thickness of 0.75 in. is assigned to Model SG1R-EP2 and the thickness continues to increase up to 3.0 in. for the remaining models [see Table 7.1(a)].

Figure 7.3(a) shows the finite element model of the rehabilitated Model SG1-7. Nonlinear finite element analyses were carried out with various areas of end stiffeners. If the end stiffener pair functions as an effective anchor for the end panel to achieve the same shear capacity as an interior panel, it was postulated that both end and interior panels would fail simultaneously.

Table 7.1(a) shows a summary with different end stiffener areas, while Figure 7.4 shows the failure mode associated with each. The end stiffener pair of SG1R-EP1, which was designed per Basler's recommendations, did not properly serve as an anchor and failed to achieve the expected shear strength (V_s^{int} = 401 kips). Note that the end panel shear strength without an end stiffener pair was 324 kips (see Model SG1-7 in Table 6.4), only 11% less than that of SG1R-EP1 with the end stiffener pair. As the end stiffener area increased, so did the end panel shear strength. Then, when the area of the end stiffener pair reached 29.50 in.^{2} (SG1R-EP5 in Table 7.1), the end panel reached a shear strength of 402 kips. In addition, the interior panel also experienced minor web buckling as shown in Figure 7.4. SG1R-EP6, which had an end stiffener area of 36.88 in.^{2}, reached an ultimate shear strength of 408 kips and showed the expected behavior with both end and interior panels failing simultaneously (see Figure 7.4). Increasing the end stiffener area further did not increase the ultimate shear strength, as the shear strength and failure mode of SG1R-EP7 were almost the same as in SG1R-EP6. Therefore, it can be concluded from Table 7.1 and Figure 7.4 that Basler's recommendation for the required end stiffener area to have a full tension-field action is non-conservative.

7.3 Eurocode 3 Design Provision

A similar approach has been adopted in Eurocode 3 (2006). Section 9.3 of EN 1993-1-5 (2006) notes that the end stiffener pair can be considered as rigid and the full tension-field action can develope if the bearing and end stiffener pairs each have a cross

sectional area of at least $4Dt_w^2/e$, where e is the center-to-center distance between the stiffener pairs and $e > 0.1D$.

$$A_e \text{ and } A_b \geq \frac{4Dt_w^2}{e} \tag{7.3a}$$

$$e > 0.1D \tag{7.3b}$$

where A_e and A_b are the cross section areas of the end stiffener pair and the bearing stiffener pair, respectively. Following Eq. (7.3), A_e and A_b should be greater than 3.3 in.^{2} and e should be greater than 5.3 in. to provide full tension-field action for Model SG1-7. In the parametric study to follow, e was set at 5.5 in. as shown in Table 7.1(b). For a given total width (b_{es} in Figure 7.1) of the end stiffener pair of 14.75 in., the required thickness ($t_{es} = 0.224\,\text{in.}$) was too small based on Eq. (7.2). Following the local buckling criterion of Eq. (7.2), a minimum thickness of 0.75 in. was assigned to Model SG1-EP8. The remaining four models had increasing stiffener thicknesses, with SG1R-EP11 having a stiffener area of almost nine times that required by Eurocode 3. The area of the bearing stiffener pair remained the same as in the original model (Model SG1-7).

The last column in Table 7.1(b) summarizes the predicted shear strength and Figure 7.5 shows the associated failure modes. Although SG1R-EP9 and 10 had areas which were more than 3 times that required by Eurocode 3, both models did not achieve full tension-field action. The same observation was made by Alinia et al. (2009b) for the use of end stiffeners, and they commented that the minimum required area of end stiffener pair specified in Eurocode 3 was non-conservative. SG1R-EP10, which had an end stiffener area equal to 6.7 times that required by Eurocode 3, successfully achieved full tension-field action; it was able to achieve the expected shear strength of 401 kips and showed the expected failure mode.

The parametric study presented above showed that both the Basler and Eurocode 3 schemes of adding end stiffener pair may not be effective in mobilizing the full tension-field action in the end panels, unless a very large cross sectional area of end stiffener pairs is used. An alternate scheme is presented in the next section.

7.4 Proposed Scheme 1

To develop tension-field action in the end panels, the boundary members must provide enough flexural strength to serve as an anchor. Also, as presented in Section 6.3, the tension-band width in the web is directly related to the plastic hinge locations in the boundary members. That is, if the plastic hinge location along the bearing stiffeners can be shifted downward, the tension-band width in the web and the shear strength in the end panel will be increased.

One method of increasing the flexural strength of the vertical boundary members is to weld wing stiffeners to the bearing stiffeners and both flanges. Figure 7.6(a) shows the rehabilitation scheme using the wing stiffeners and Figure 7.6(b) shows the effective section of the vertical boundary. Note that when end stiffeners are used for rehabilitation, the end stiffeners are always in compression and, therefore, local buckling can be an issue. However, wing stiffeners are mainly in tension when a tension-field action develops.

Using the proposed scheme, nonlinear finite element analyses were performed. Using Model SG1-7 as the base model, the width of the wing stiffener was set to 5.5 in. and the wing stiffener thickness varied from 0.5 in. to 1.0 in. [see Table 7.2(a)]. Figure 7.3(b) shows the typical finite element model with wing stiffeners. Each wing stiffener was located at mid-width of each bearing stiffener. A plot of the applied load versus girder mid-span deflection from analysis on Model SG1R-W1 is shown in Figure 7.7. The maximum load achieved was 394 kips at a mid-span deflection of 1.37 in., as shown in Table 7.2(a). To compare the ultimate shear strength from the nonlinear finite element analysis with the shear strength predicted by Eq. (6.33), the parameter α is also presented in Table 7.2(a). As wing stiffener thickness increased from 0.5 in. to 1.0 in., M_{pb} increased from 964 kip-in. to 1,640 kip-in.

As seen in Table 7.2(a), the predicted shear strengths correlate very well with the results from nonlinear finite element analysis. Model SG1R-W1 with an α value of 0.92 showed a prediction of about 3% lower than the analysis result. Model SG1R-W2 with an α value of 1.0 had a predicted shear strength which is almost the same as that from nonlinear finite element analysis. Since Model SG1R-W2 reaches the ultimate

shear strength of an interior panel, Model SG1R-W3 showed the same result as SG1R-W2.

Figure 7.8 shows the failure modes. Interestingly, all failure modes were almost the same and the use of very thick wing stiffeners is unnecessary. Both the end and interior panels achieved their ultimate shear strengths at about the same time. Therefore, the addition of wing stiffeners is very effective in allowing the bearing stiffener pair to function as an anchor.

To further validate the effectiveness of the wing stiffener concept, a parametric study using Model SG2-92 (see Table 6.5) as the base model was performed. Note that Model SG2-92 is expected to have an ultimate shear strength of 273 kips with $\alpha=1$, which corresponds to that of an interior panel with tension-field action. Table 7.2(b) provides a summary of the models, while Figure 7.9 shows the corresponding failure modes. Similar trends can be observed. Compared to the shear strength obtained from the nonlinear finite element analysis, the predicted strength from Eq. (6.33) was underestimated by about 7% in Model SG2R-W1. Model SG2R-W1 had already achieved the ultimate shear strength of the interior panel based on the nonlinear finite element analysis. Thus, SG2R-W1, 2, 3, and 4 achieved almost the same strength and the same failure modes as shown in Figure 7.9.

From the results presented above, it is clear that adding wing stiffeners very effectively mobilizes tension-field action in the end panels. The proposed shear strength equation [Eq. (6.33)] provides a very accurate and yet slightly conservative estimate of the actual shear strength.

Design Procedure

Design of wing stiffeners can be performed by using α determined in Chapter 6. The design procedure follows:

(1) Given the required shear (V_u), solve Eq. (6.33) for the required α. For example, if the required α equals 0.8, it means 80% of the full tension-field action is needed.

(2) Determine the required M_{pb} by substituting the required α into Eq. (6.36). At this stage, one may assume $M_{pm}=M_{pf}$. If the calculated M_{pb} is greater than

M_{pf}, the assumption is correct. If not, let $M_{pm} = M_{pb}$ to solve the required M_{pb}.

(3) Size the wing stiffeners such that the plastic moment of the effective section shown in Figure 7.6(b) is at least equal to M_{pb}.

Taking Model SG2-92 as an example, assume the required shear strength is 240 kips. Note that $C = 0.25$, $\alpha = 0.59$, $(d_0 / D) = 0.5$, $V_p = 328$ kips, and the nominal shear strength (V_n) per AASHTO is 82.9 kips before rehabilitation (see Table 6.5 for details). Therefore, based on Eq. (6.33), the shear strength of the end panel before rehabilitation is

$$V_s = V_p \left[C + \alpha \frac{0.87(1-C)}{\sqrt{1+(d_0/D)^2}} \right] = 195 \text{ kips} \tag{7.4}$$

Step (1): Compute required partial tension-field action coefficient, α.

Given the shear demand, solve Eq. (6.33) for the required α.

$$328 \left[0.25 + \alpha \left(\frac{0.87(1-0.25)}{\sqrt{1+(0.5)^2}} \right) \right] > 240 \text{ kips} \tag{7.5}$$

Solving Eq. (7.5) gives a required α value of 0.83.

Step (2): Determine the required M_{pb}.

Assuming $M_{pm} = M_{pf} = 94.8$ kips-in. and using Eq. (6.36),

$$\begin{aligned} \alpha = 0.83 &= \frac{2.8\left(\sqrt{M_{pf} + M_{pm}} + \sqrt{M_{pb} + M_{pm}}\right)}{D\sqrt{t_w F_{yw}(1-C)}} \\ &= \frac{2.8\left(\sqrt{94.8 + 94.8} + \sqrt{M_{pb} + 94.8}\right)}{52.5\sqrt{0.1875(57.4)(1-0.25)}} \end{aligned} \tag{7.6}$$

Therefore, the required M_{pb} is 832 kips-in.

Step (3): Size wing stiffeners.

Figure 7.10 shows the effective section of the vertical boundary member. For simplicity, assume that the effective section has the same yield stress as the bearing

stiffeners F_y (= 41.1 ksi). Dividing the required M_{pb} by F_y gives the required plastic section modulus (Z_{xr}):

$$Z_{xr} = \frac{M_{pb}}{F_y} = 20.2 \text{ in.}^3 \tag{7.7}$$

Starting with a trial width of the wing stiffeners (b_{ws}) as 5.5 in., the required thickness of the wing stiffeners (t_{ws}) can be computed as follows. The total area of the section is

$$A = 0.188(4 + 0.5 + 1.96) + 1.0(12.94 - 0.188) + 2(5.5)t_{ws} = 14 + 11t_{ws} \tag{7.8}$$

Assuming the plastic neutral axis is located within the bearing stiffeners, the plastic neutral axis is

$$d_{PNA} = \frac{\left[\frac{A}{2} - t_w\left(e - \frac{t_b}{2}\right)\right]}{b_b} = \frac{\left[\frac{14 + 11t_{ws}}{2} - 0.188\left(4 - \frac{1}{2}\right)\right]}{12.94} = 0.49 + 0.43t_{ws} \tag{7.9}$$

If d_{PNA} is less than 1.0 in., the plastic neutral axis would be in the bearing stiffeners. In other words, t_{ws} should be less than 1.2 in. to satisfy the assumed plastic neutral axis location. Then, the plastic section modulus (Z_y) of the effective section can be computed by summing up the first moments of area about the plastic neutral axis. The effective section is divided into 5 segments about the plastic neutral axis shown in Figure 7.10. Therefore, the plastic section modulus is

$$Z_y = \sum_i Z_i = \sum_i A_i \chi_i \tag{7.10}$$

where A_i is the area of each segment and χ_i is the moment arm from the plastic neutral axis. The plastic section modulus of each segment is

$$\begin{aligned} Z_1 &= t_w\left(e - \frac{t_b}{2}\right)\left(\frac{e - t_b/2}{2} + d_{PNA}\right) \\ &= 0.188(3.5)(1.75 + 0.49 + 0.42t_{ws}) = 1.47 + 0.28t_{ws} \end{aligned} \tag{7.11a}$$

$$Z_2 = (12.94)\left(\frac{(0.49 + 0.42t_{ws})^2}{2}\right) = 1.55 + 2.66t_{ws} + 1.14t_{ws}^2 \tag{7.11b}$$

$$Z_3 = (12.94)\left(\frac{(1.0 - 0.49 - 0.42t_{ws})^2}{2}\right) = 1.68 - 2.77t_{ws} + 1.14t_{ws}^2 \tag{7.11c}$$

$$Z_4 = (0.188)(1.964)\left(\frac{1.964}{2} + 1.0 - 0.49 - 0.42t_{ws}\right) = 0.55 - 0.16t_{ws} \qquad (7.11d)$$

$$Z_5 = 2\left[5.5(t_{ws})\left(\frac{5.5}{2} + 1.0 - 0.49 - 0.42t_{ws}\right)\right] = 35.86t_{ws} - 4.62t_{ws}^2 \qquad (7.11e)$$

Summing up the plastic section modulus of each segment gives

$$Z_y = \sum_i Z_i = 5.25 + 35.87t_{ws} - 2.34t_{ws}^2 \qquad (7.12)$$

Setting $Z_y = Z_{xr} = 20.2$ in.^{3}, Eq. (7.12) can be rewritten as

$$2.34t_{ws}^2 - 35.87t_{ws} + 14.95 = 0 \qquad (7.13)$$

Solving Eq. (7.13) gives the required thickness of the wing stiffeners.

$$\begin{aligned} t_{ws} &= \frac{35.87 \pm \sqrt{35.87^2 - 4(2.34)(14.95)}}{2(2.34)} \\ &= \frac{35.87 \pm 33.86}{4.68} = 0.43 \text{ in. or } 14.90 \text{ in.} \end{aligned} \qquad (7.14)$$

Therefore, the required wing stiffener thickness is 0.43 in. Use 0.5 in. thick wing stiffeners. Note that wing stiffeners are tension members, and therefore, there is no need to check for local buckling.

7.5 Proposed Scheme 2

Although rehabilitation of plate girder end panels were discussed and one scheme was proposed in Section 7.4, a more practical rehabilitation scheme is to add another pair of stiffeners in the end panels. To avoid field welding in rehabilitation, a pair of angles can be fastened to the web by bolting (see Figure 7.12). The effectiveness of this scheme was investigated by finite element analysis in this section. To simplify the modeling, it was assumed that bolting was as effective as welding. Thus, the model similar to that in Figure 7.13 was analyzed. It is shown in the figure that the original end panel is divided into two subpanels, with Subpanel 1 serving as the new end panel.

From the rehabilitation design point of view, it is necessary to determine the location of the added stiffeners. One approach is to locate the stiffeners closer to the bearing stiffeners to increase the shear resistance (e.g., for C =1.0). An alternative approach is to add the stiffeners to divide the original end panels into two equal

subpanels. For practical design, it will be shown in the following that the latter approach is more effective and recommended.

Models SG1 and SG2 with three different width-depth ratios (0.5, 1.0, and 1.5) were considered. For approach 1, stiffeners were added at a distance of 10.5 in. away from the bearing stiffeners such that the new end panels have a width-depth ratio of 0.2. Table 7.3 summarize the six models analyzed. Figure 7.14 and Figure 7.15 present the failure modes and the relationships between the applied load and mid-span deflection of SG1 and SG2 series, respectively. Table 7.4 summarizes the ultimate shear strengths before and after the addition of stiffeners. With the addition of stiffeners, the increase in shear strengths varied from 14% to 40%. However, as shown in the figures, the new end panel (subpanel 1) experienced buckling. If the new end panel had a plastic shear capacity ($= 0.58F_{yw}A_w$), the new end panel should have remained undamaged at that load level and only the new interior panel (subpanel 2) would buckle. In other words, it was expected with this rehabilitation approach that the ultimate shear strength of each finite element model should have been governed by the new interior panel.

Based on AASHTO Specifications (2014), the shear strengths (V_{AASHTO}) of the new interior panels were computed and are summarized in Table 7.5. It is obvious from the table that the ultimate shear strengths from the finite element analysis (V_{FEM}) do not reach those predicted by the AASTHO Specifications. This is due to the fact that new end panel (subpanel 1) does not have sufficient strength to provide the anchor mechanism. Increasing the stiffener thickness from 0.5 in. to 1.0 in. only increases the ultimate strength slightly (see Table 7.6).

Next, consider approach 2. By relocating the additional stiffeners to the mid-width of the original end panels, the width-depth ratios of the new end panel (subpanel 1) and the new interior panel (subpanel 2) are the same. Since the shear strength of subpanel 1 is usually less than that of subpanel 2, Eq. (6.33) can be used to compute the shear strength of the new end panel. A total of 14 models were investigated to demonstrate the effectiveness of this approach. Table 7.7 summarizes the details of these models. Figure 7.16 and Figure 7.17 show the failure modes of Models SG1 and SG2 series. As expected, new end panel experienced buckling for all finite element models. Therefore, the proposed equation [Eq. (6.33)] can be used to predict the

ultimate shear strength. Figure 7.18 presents the relationship between applied load and mid-span deflection of the rehabilitated models, while Table 7.8 summarizes the ultimate shear strengths before and after the rehabilitation. It is observed from Table 7.4 and Table 7.8 that adding vertical stiffeners in the mid-width of the original end panel is more effective in increasing the ultimate shear strength.

The predicted shear strengths by using Eq. (6.33) are also compared with the results from the finite element analyses in Table 7.9. The predicted ultimate shear strengths generally correlate well with the results from the finite element analyses. The mean ratios of FEM to the prediction before and after rehabilitation are 1.03 and 0.97, respectively, with a standard deviation of 0.04 and 0.06. Therefore, adding stiffeners in the mid-width of the original end panel is recommended for rehabilitation.

The accuracy of using Eq. (6.33) to predict the shear strength is evaluated in Figure 7.19, where a total of 28 cases (14 from before rehabilitation and 14 from after rehabilitation of Models SG1 and SG2 series, see Table 7.8) are presented. It is noted that Eq. (6.33) tends to overestimate the shear strength by up to approximately 15% when the width-depth ratio is less than 0.5. Therefore, Eq. (6.33) is applicable only when the width-depth rati is no less than 0.5.

Table 7.1: Effect of End Stiffener Area (Based on Model SG1-7)

(a) Basler's Approach

Model No.	t_{es} (in.)	b_{es} (in.)	t_b (in.)	b_b (in.)	A_e (in.^{2})	A_b (in.^{2})	e (in)	V_{FEM} (kips)
SG1R-EP1	0.56	14.75	1.0	14.75	8.26	14.75	4.0	361
SG1R-EP2	0.75				11.06			368
SG1R-EP3	1.0				14.75			380
SG1R-EP4	1.5				22.13			391
SG1R-EP5	2.0				29.50			402
SG1R-EP6	2.5				36.88			408
SG1R-EP7	3.0				44.25			409

(b) Eurocode 3 Approach

Model No.	t_{es} (in.)	b_{es} (in.)	t_b (in.)	b_b (in.)	A_e (in.^{2})	A_b (in.^{2})	e (in)	V_{FEM} (kips)
SG1R-EP8	0.75	14.75	1.0	14.75	11.06	14.75	5.5	389
SG1R-EP9	1.0				14.75			396
SG1R-EP10	1.5				22.13			402
SG1R-EP11	2.0				29.50			403

Table 7.2: Effect of Wing Stiffeners

(a) Based on Model SG1-7[d]

Model No.	t_{ws} (in.)	b_{ws} (in.)	M_{pf} [a] (kip-in.)	M_{pb} [b] (kip-in.)	α [c]	V_{FEM} (kips)	$V_{prediction}$ (kips)
SG1R-W1	0.5	5.5	147	964	0.92	394	384
SG1R-W2	0.75			1,307	1.00	400	401
SG1R-W3	1.0			1,640	1.08	401	401

(b) Based on Model SG2-92[e]

Model No.	t_{ws} (in.)	b_{ws} (in.)	M_{pf} (kip-in.)	M_{pb} (kip-in.)	α	V_{FEM} (kips)	$V_{prediction}$ (kips)
SG2R-W1	0.5	5.5	95	929	0.86	265	247
SG2R-W2	0.75			1,268	0.95	267	265
SG2R-W3	0.9			1,465	1.00	268	274
SG2R-W4	1.0			1,594	1.03	267	274

[a] from Eq. (6.39)
[b] from Eq. (6.40)
[c] from Eq. (6.36)
[d] see Table 6.4
[e] see Table 6.5

Table 7.3: Width-Depth Ratios of Panels (Approach 1)

Model No.	Width-Depth Ratio		
	before Rehabilitation	after Rehabilitation	
	End Panel	Subpanel 1 (New End)	Subpanel 2 (New Interior)
SG1-RS1	0.5	0.2	0.3
SG1-RS2	1.0		0.8
SG1-RS3	1.5		1.3
SG2-RS1	0.5		0.3
SG2-RS2	1.0		0.8
SG2-RS3	1.5		1.3

Table 7.4: Comparison of Shear Strength before and after Rehabilitation (Approach 1)

Model No.	Plastic Shear Strength (kips), V_{BR}	Ultimate Shear Strength (kips)		$\frac{V_{AR}}{V_{BR}}$
		before Rehabilitation, V_{BR}	after Rehabilitation, V_{AR}	
SG1-RS1	459.0	324.3	416.3	1.28
SG1-RS2		238.2	289.5	1.22
SG1-RS3		207.8	237.5	1.14
SG2-RS1	327.7	201.6	282.5	1.40
SG2-RS2		149.1	192.7	1.29
SG2-RS3		128.3	152.4	1.19

Table 7.5: Comparison of Subpanel 2 Shear Strength (Approach 1)

Model No.	V_{FEM} (kips)	V_{AASHTO} (kips)	$\frac{V_{FEM}}{V_{AASHTO}}$
SG1-RS1	416.3	452.2	0.92
SG1-RS2	289.5	344.1	0.84
SG1-RS3	237.5	272.9	0.87
SG2-RS1	282.5	306.6	0.92
SG2-RS2	192.7	236.8	0.81
SG2-RS3	152.4	186.6	0.82

Table 7.6: Effect of Stiffener Thickness on Shear Strengths (Approach 1)

Model No.	Ultimate Shear Strength (kips)		$\frac{V_{AR}^{t=1.0}}{V_{AR}^{t=0.5}}$
	Stiffener Thickness = 0.5 in.	Stiffener Thickness = 1.0 in.	
	$V_{AR}^{t=0.5}$	$V_{AR}^{t=1.0}$	
SG1-RS1	416.3	425.3	1.02
SG1-RS2	289.5	296.1	1.02
SG1-RS3	237.5	241.9	1.02
SG2-RS1	282.5	286.4	1.01
SG2-RS2	192.7	200.7	1.04
SG2-RS3	152.4	157.5	1.03

Table 7.7: Width-Depth Ratios of Panels (Approach 2)

Model No.	Width-Depth Ratio		
	before Rehabilitation	after Rehabilitation	
	End Panel	Subpanel 1 (New End)	Subpanel 2 (New Interior)
SG1-RSM1	0.5	0.25	0.25
SG1-RSM2	0.6	0.3	0.3
SG1-RSM3	0.7	0.35	0.35
SG1-RSM4	0.8	0.4	0.4
SG1-RSM5	0.9	0.45	0.45
SG1-RSM6	1.0	0.5	0.5
SG1-RSM7	1.5	0.75	0.75
SG2-RSM1	0.5	0.25	0.25
SG2-RSM2	0.6	0.3	0.3
SG2-RSM3	0.7	0.35	0.35
SG2-RSM4	0.8	0.4	0.4
SG2-RSM5	0.9	0.45	0.45
SG2-RSM6	1.0	0.5	0.5
SG2-RSM7	1.5	0.75	0.75

Table 7.8: Comparison of Shear Strength (Approach 2)

Model No.	Plastic Shear Strength (kips), V_{BR}	Ultimate Shear Strength (kips)		$\frac{V_{AR}}{V_{BR}}$
		before Rehabilitation, V_{BR}	after Rehabilitation, V_{AR}	
SG1-RSM1	459.0	324.3	433.7	1.34
SG1-RSM2		297.5	412.0	1.38
SG1-RSM3		277.6	388.3	1.4
SG1-RSM4		260.5	364.9	1.4
SG1-RSM5		247.1	336.9	1.36
SG1-RSM6		238.2	323.2	1.36
SG1-RSM7		207.8	270.0	1.30
SG2-RSM1	327.7	201.6	291.8	1.45
SG2-RSM2		186.1	267.4	1.44
SG2-RSM3		175.8	251.7	1.43
SG2-RSM4		164.8	228.9	1.39
SG2-RSM5		156.1	221.7	1.42
SG2-RSM6		149.1	202.2	1.36
SG2-RSM7		128.3	169.8	1.32

Table 7.9: Comparison of Shear Strength Predicted by FEM and Eq. (6.33)

Model No.	before Rehabilitation				after Rehabilitation			
	$\frac{d_o}{D}$	V_{FEM} (kips)	V_{pred} (kips)	$\frac{V_{FEM}}{V_{pred}}$	$\frac{d_o}{D}$	V_{FEM} (kips)	V_{pred} (kips)	$\frac{V_{FEM}}{V_{pred}}$
SG1-RSM1	0.5	324.3	333.8	0.97	0.25	433.7	459.0	0.94
SG1-RSM2	0.6	297.5	300.2	0.99	0.3	412.0	459.0	0.90
SG1-RSM3	0.7	277.6	278.8	1.00	0.35	388.3	441.9	0.88
SG1-RSM4	0.8	260.5	262.8	0.99	0.4	364.9	396.0	0.92
SG1-RSM5	0.9	247.1	249.5	0.99	0.45	336.9	359.9	0.94
SG1-RSM6	1.0	238.2	237.8	1.00	0.5	323.2	333.8	0.97
SG1-RSM7	1.5	207.8	192.6	1.08	0.75	270.0	270.4	1.00
SG2-RSM1	0.5	201.6	195.5	1.03	0.25	291.8	319.0	0.91
SG2-RSM2	0.6	186.1	179.9	1.03	0.3	267.4	278.9	0.96
SG2-RSM3	0.7	175.8	168.6	1.04	0.35	251.7	244.3	1.03
SG2-RSM4	0.8	164.8	159.2	1.04	0.4	228.9	221.8	1.03
SG2-RSM5	0.9	156.1	150.9	1.03	0.45	221.7	206.6	1.07
SG2-RSM6	1.0	149.1	143.4	1.04	0.5	202.2	195.5	1.03
SG2-RSM7	1.5	128.3	114.2	1.12	0.75	169.8	163.7	1.04
Average				1.03				0.97
Standard Deviation				0.04				0.06

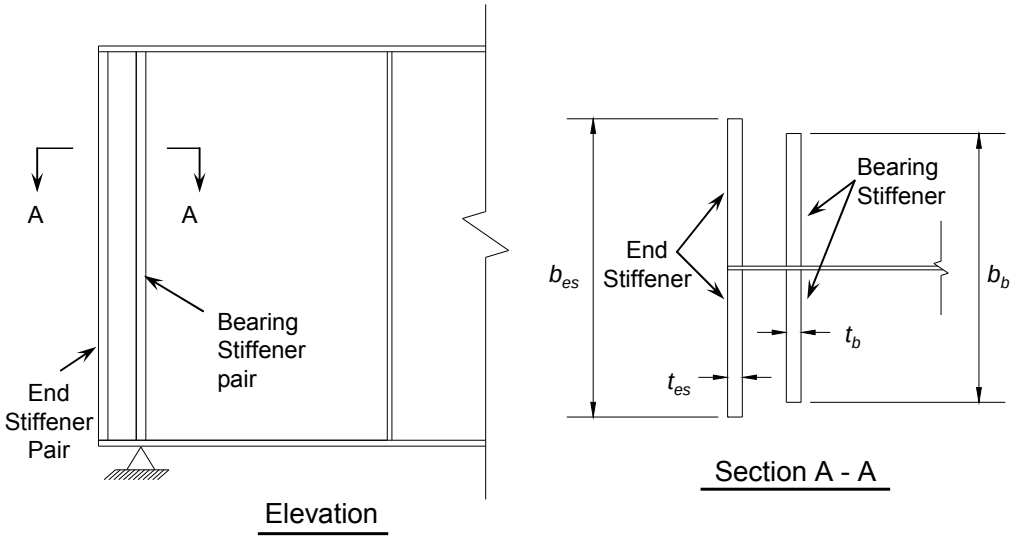

Figure 7.1: Configuration of End Stiffeners

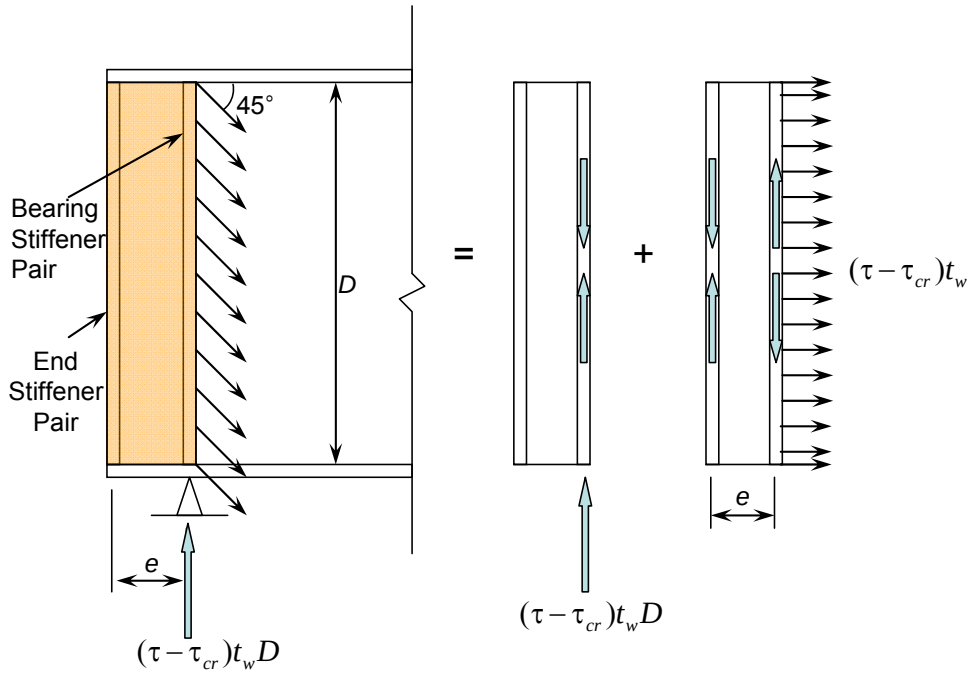

Figure 7.2: Basler's Model for End Stiffeners (adapted from Basler 1961a)

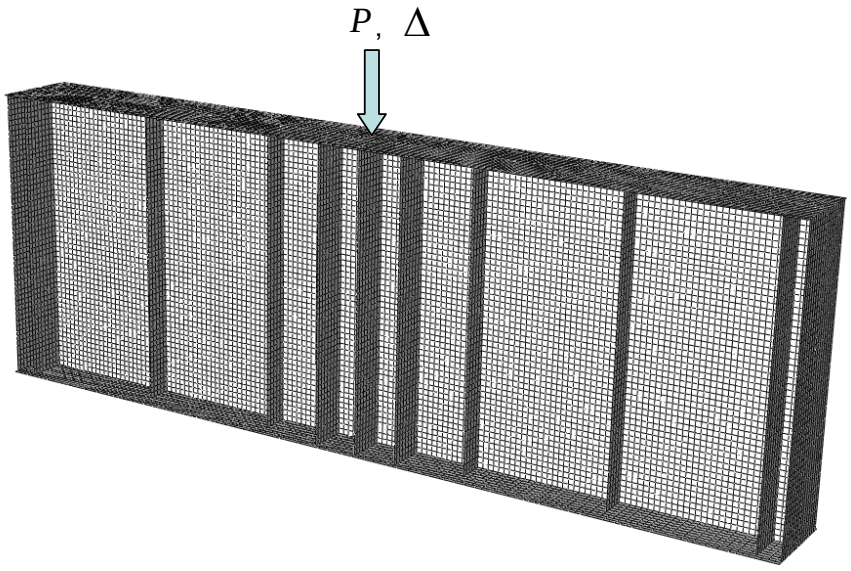

(a) Model with End Stiffeners

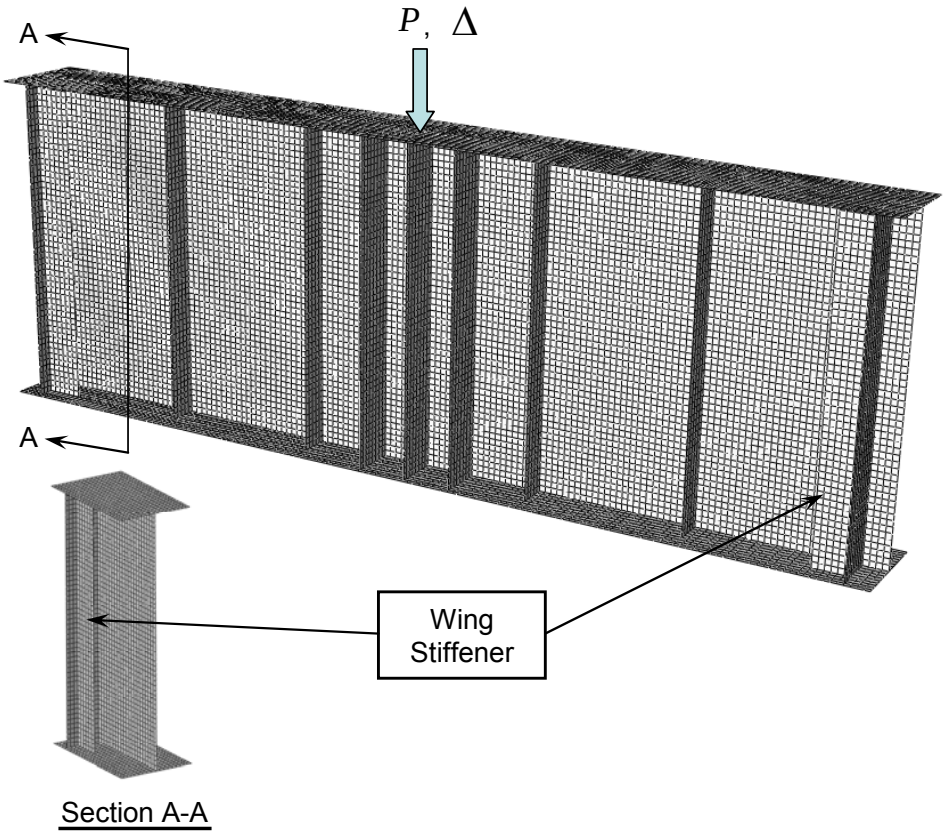

(b) Model with Wing Stiffeners

Figure 7.3: Rehabilitated Model SG1: Finite Element Models

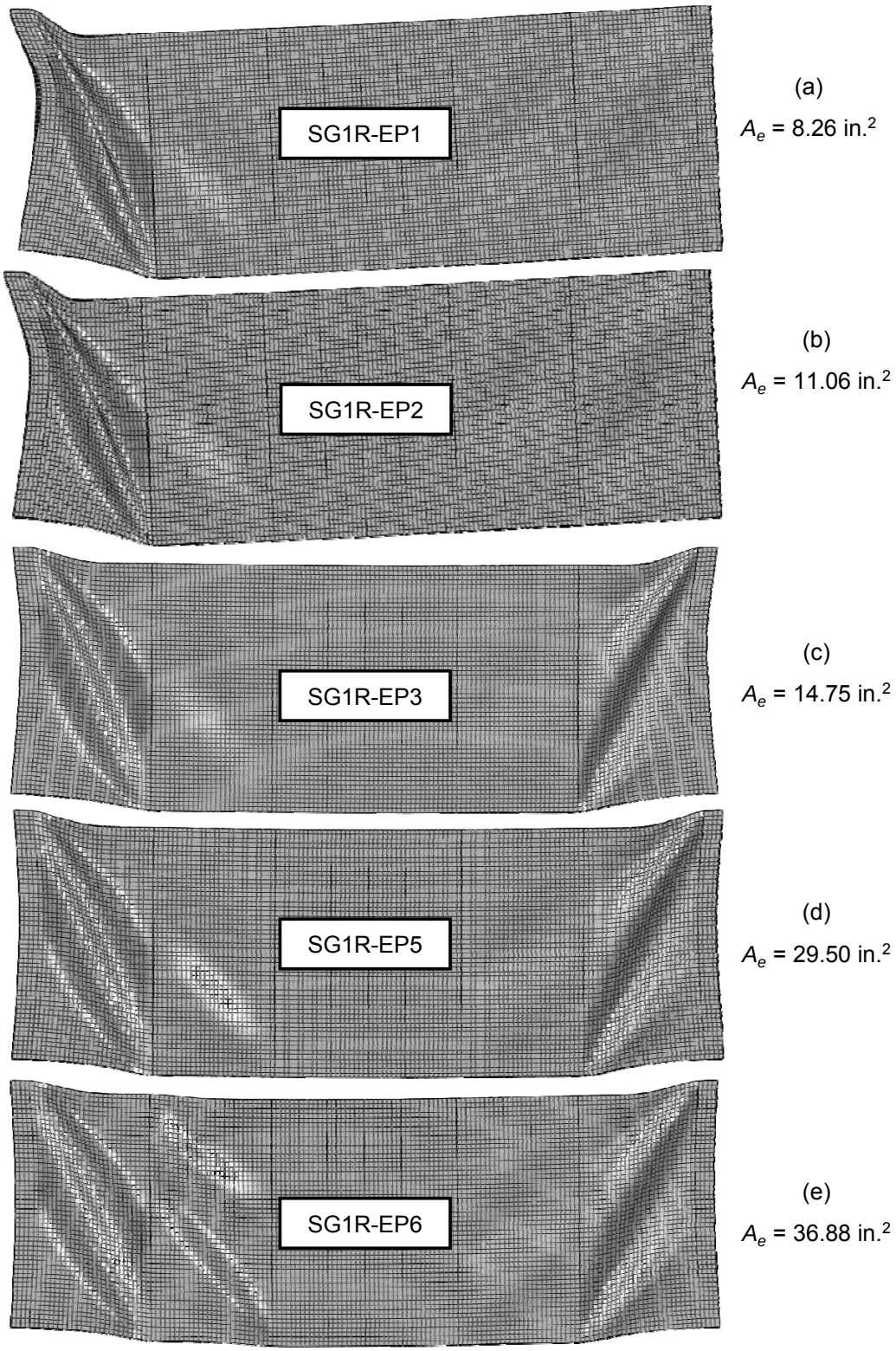

Figure 7.4: Basler's Scheme: Failure Mode as a Function of End Stiffener Area

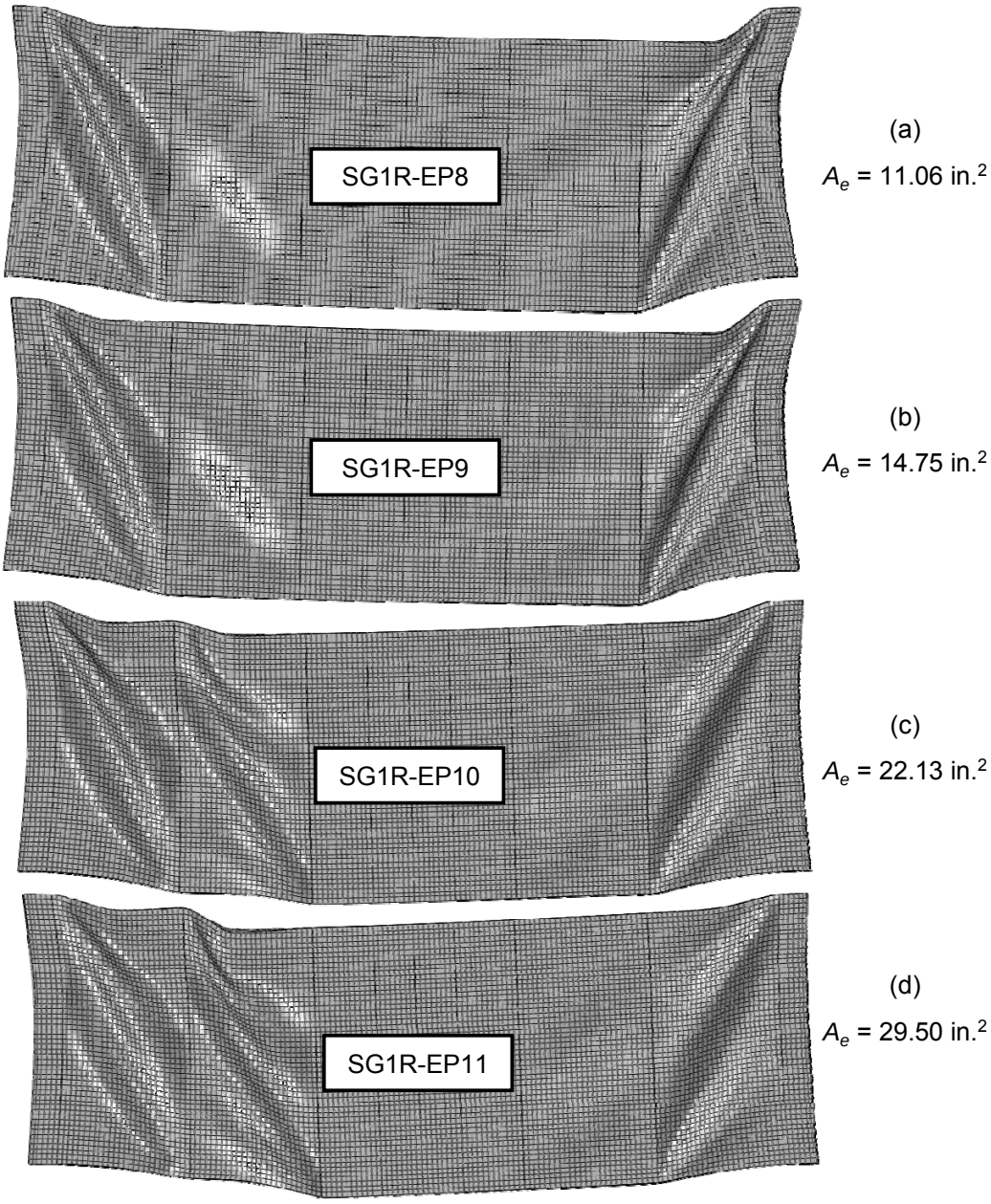

Figure 7.5: Eurocode 3 Scheme: Failure Mode as a Function of End Stiffener Area

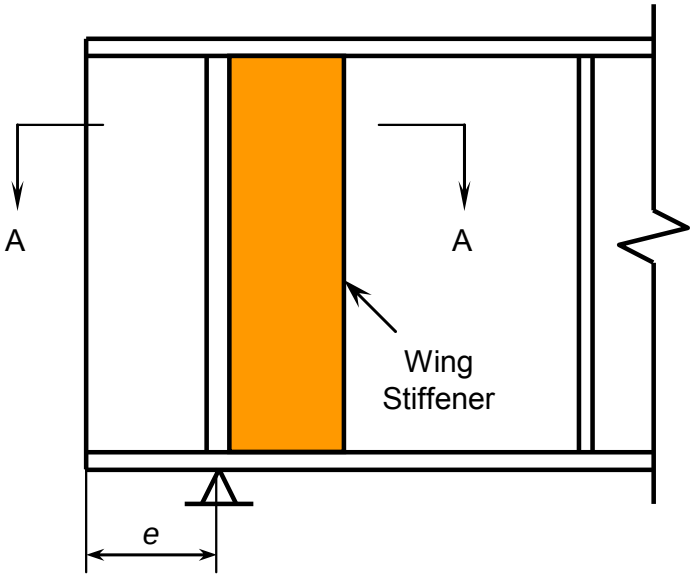

(a) Elevation

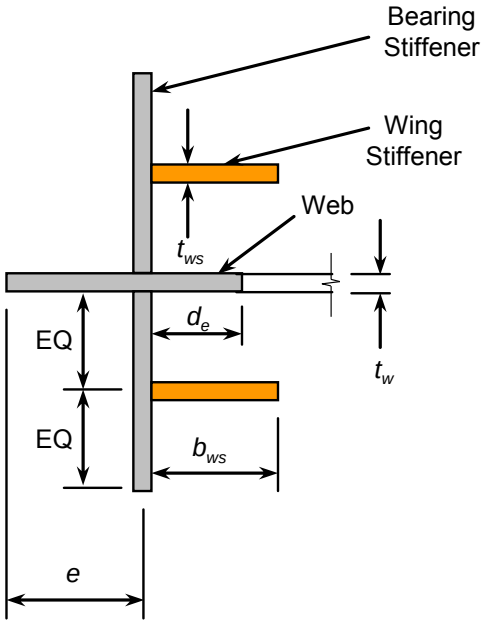

(b) Section A-A (Effective Section)

Figure 7.6: Wing Stiffener Rehabilitation Scheme for End Panel

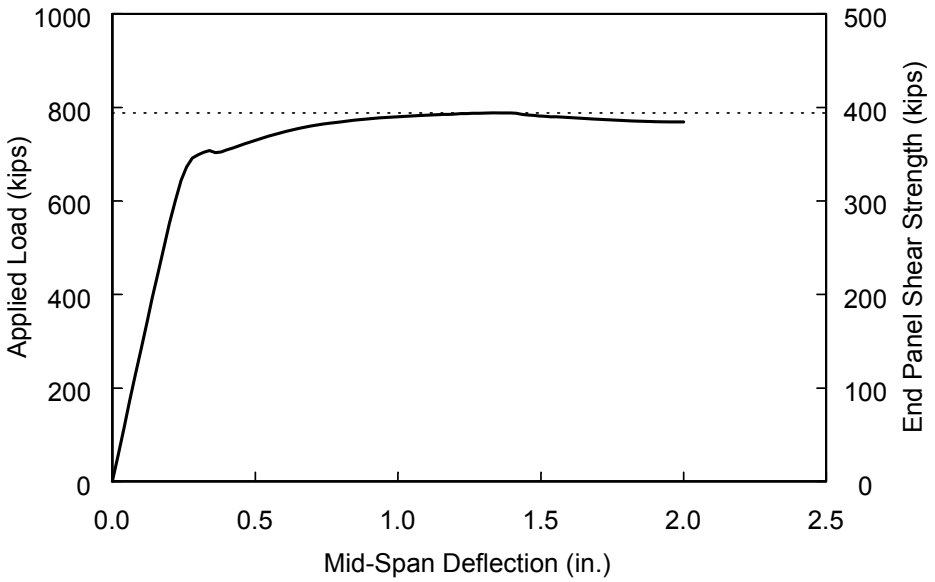

Figure 7.7: Model SG1R-W1: Applied Load versus Mid-Span Deflection

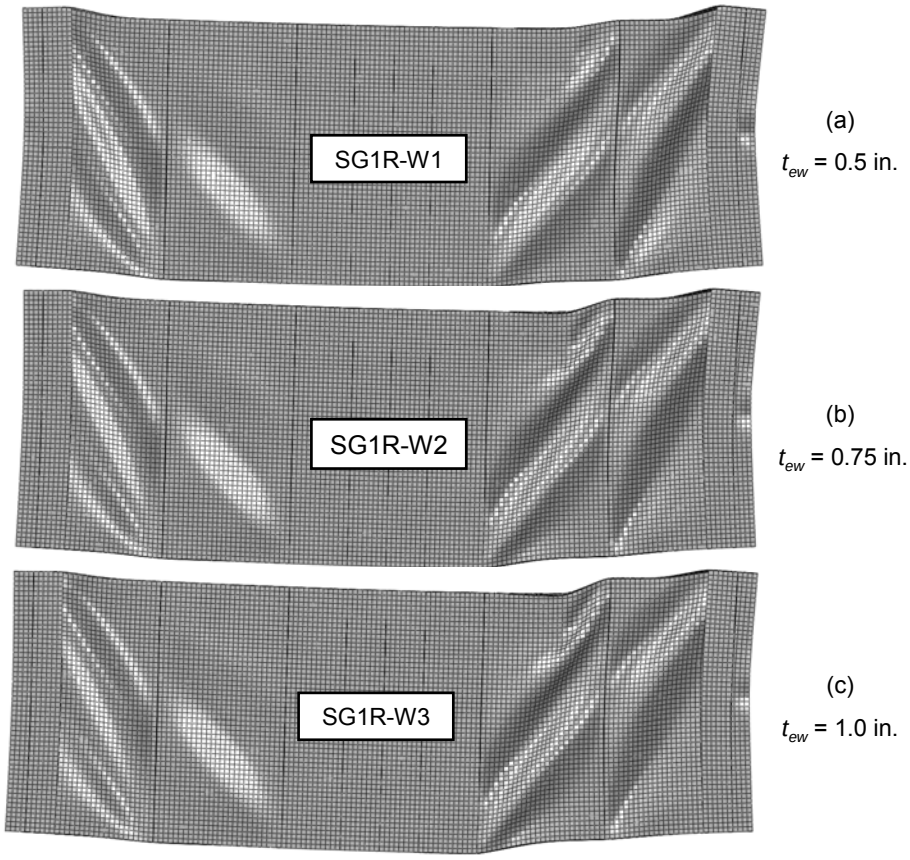

Figure 7.8: Wing Stiffener Rehabilitation Scheme: Failure Modes of SG1 Series

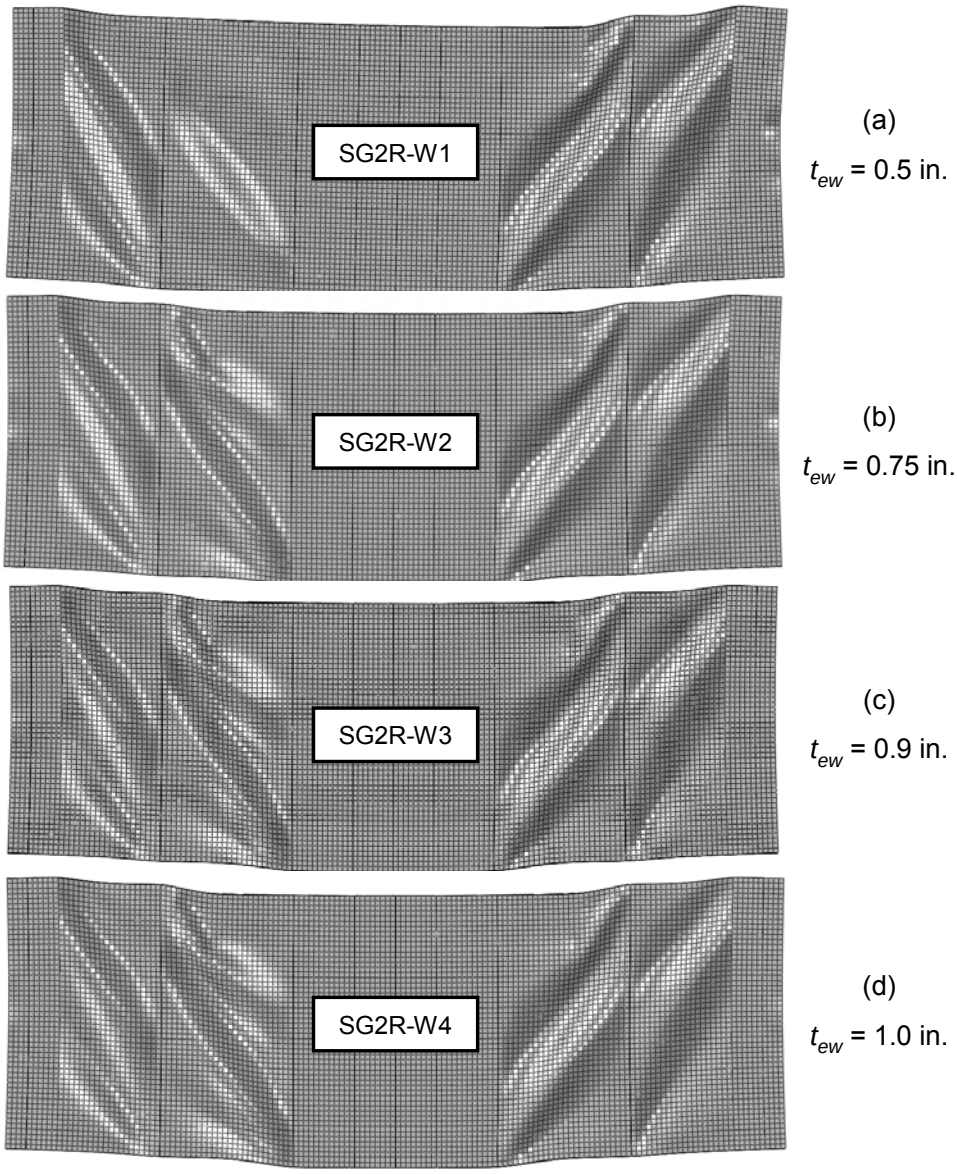

Figure 7.9: Wing Stiffener Rehabilitation Scheme: Failure Modes of SG2 Series

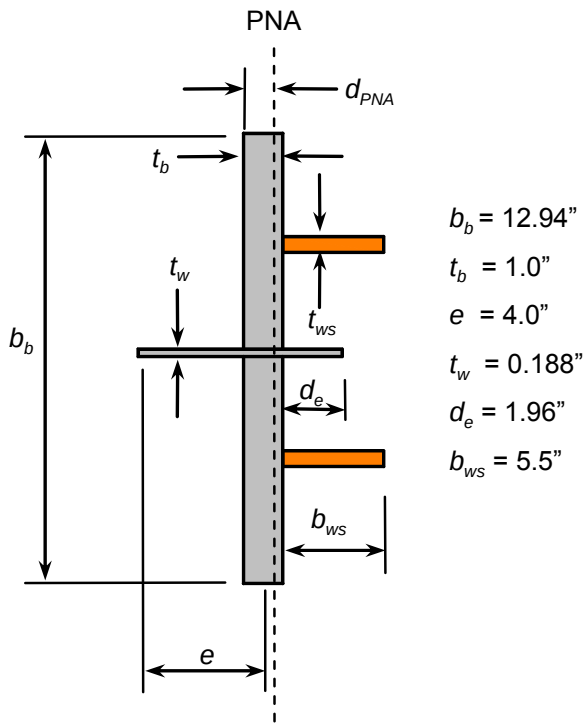

Figure 7.10: Example Calculation of M_{pb}

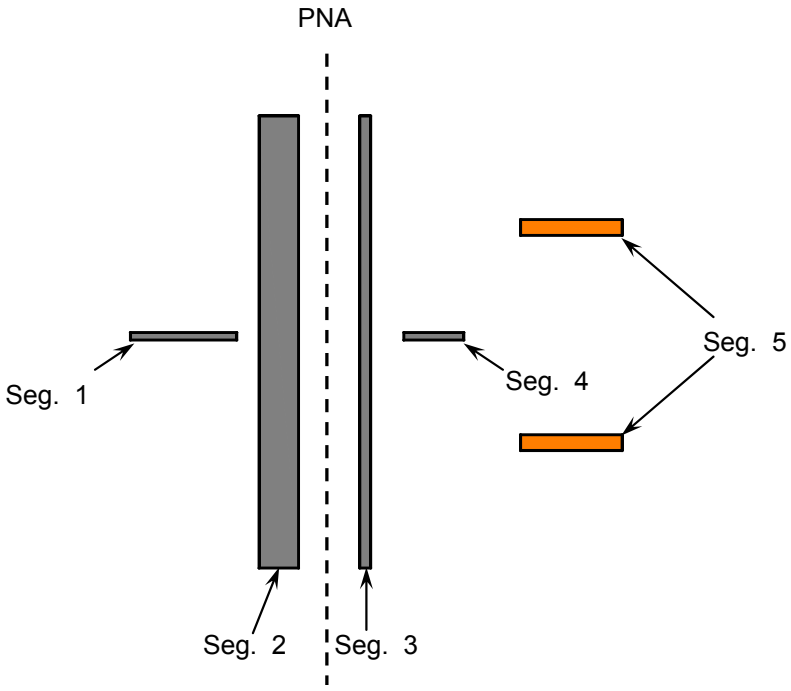

Figure 7.11: Components of M_{pb}

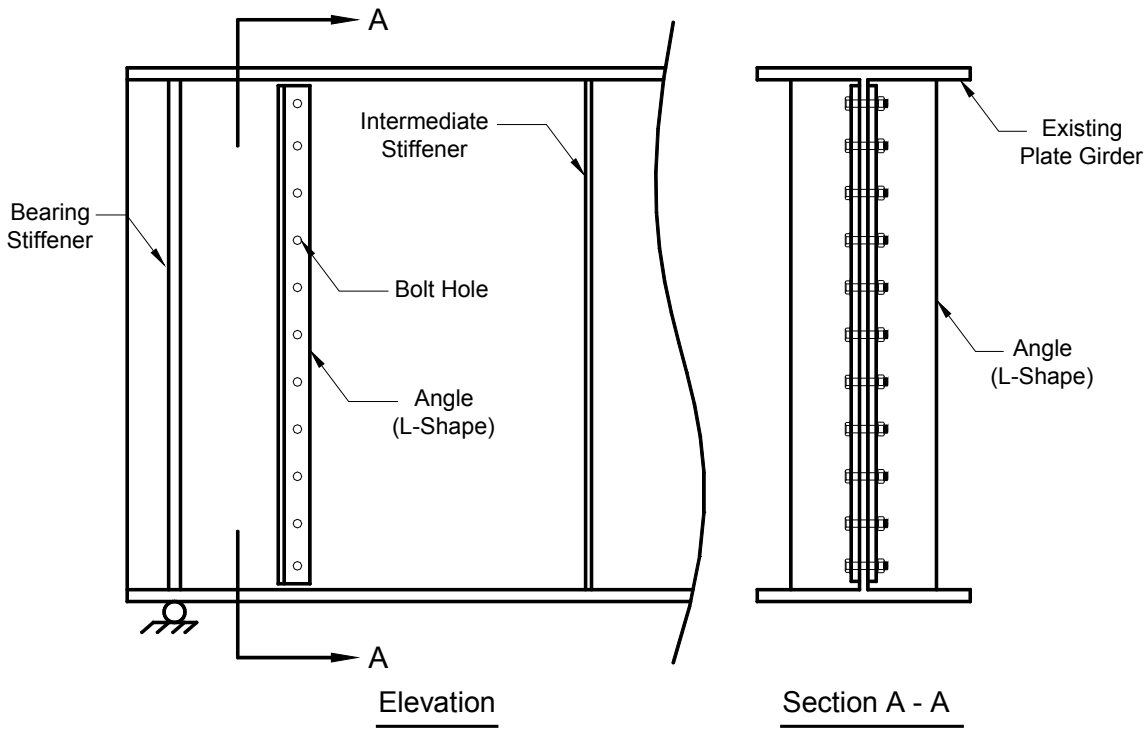

Figure 7.12: Rehabilitation Scheme with Bolted Angles

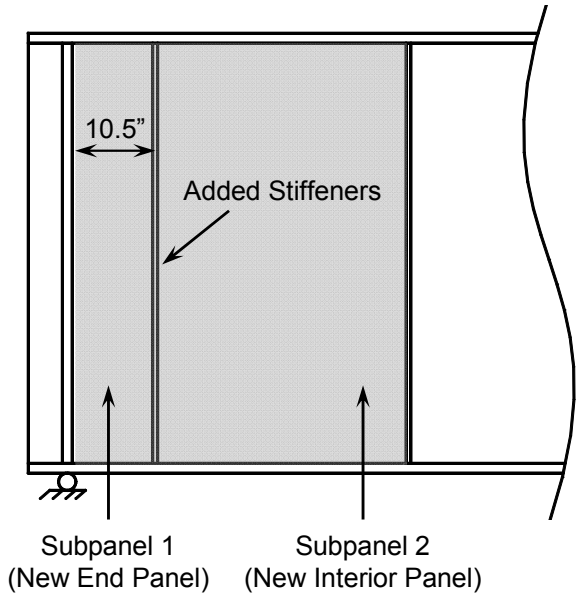

Note: The shaded area represents original end panel.

Figure 7.13: Subpanels 1 and 2

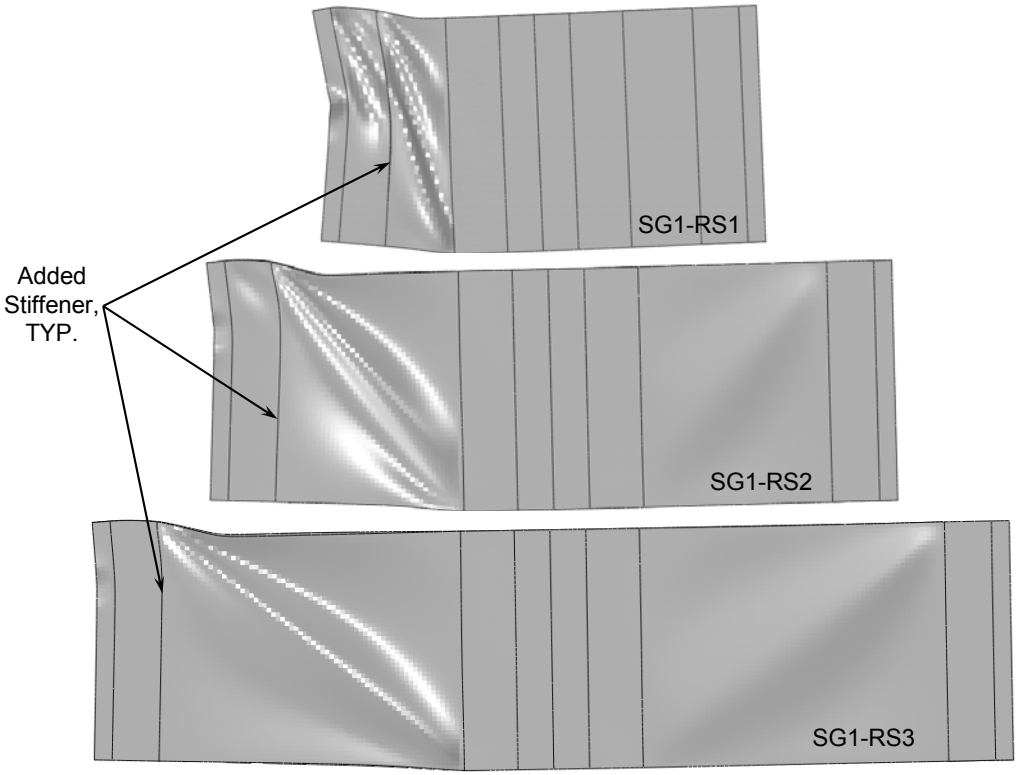

(a) Failure Mode

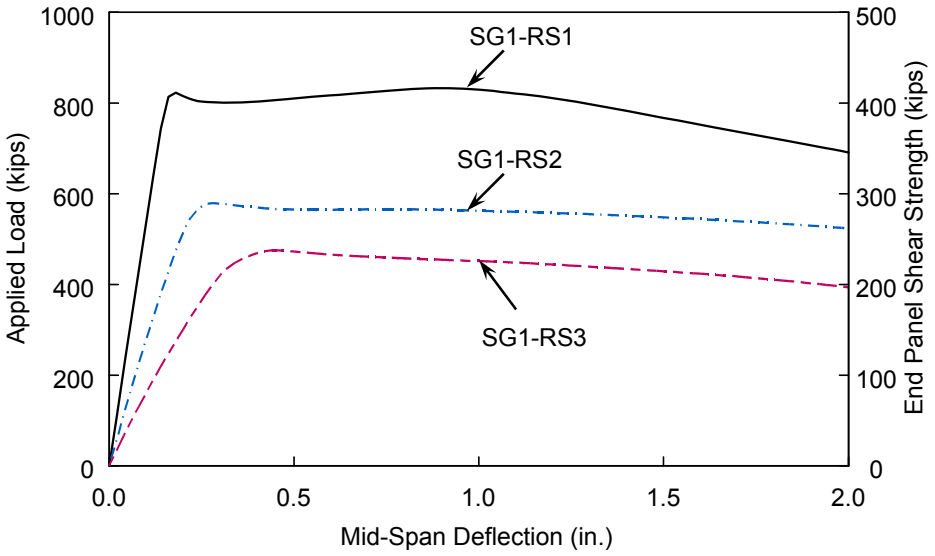

(b) Applied Load versus Mid-Span Deflection

Figure 7.14: SG1 Series (Approach 1)

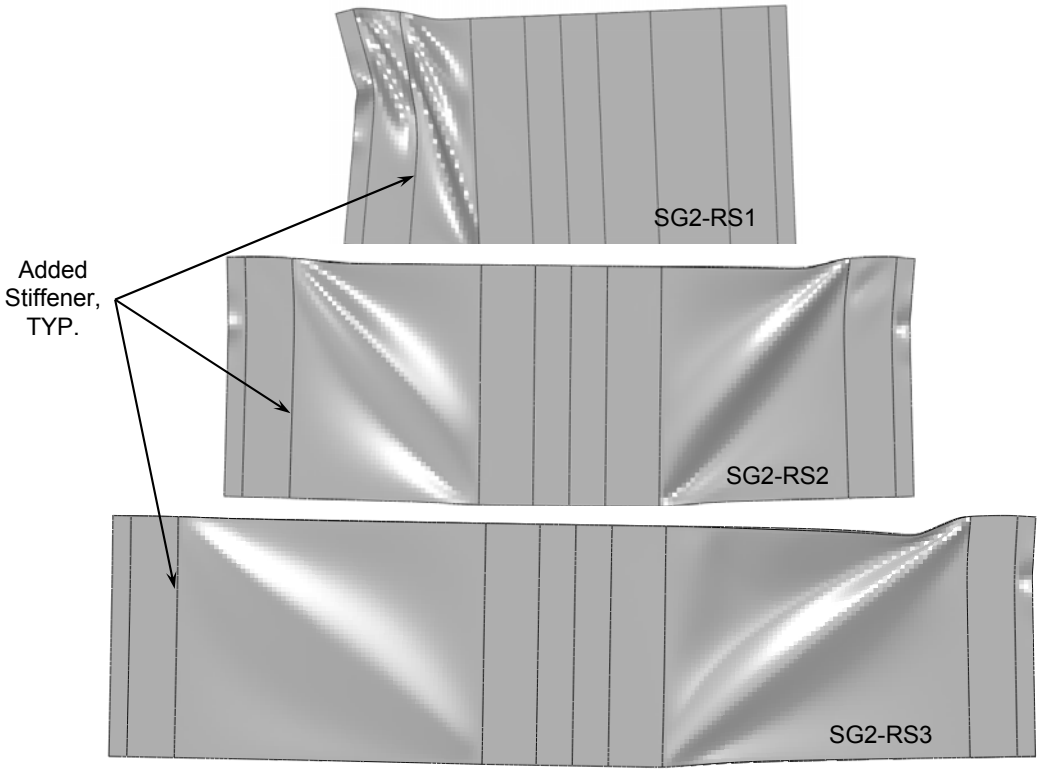

(a) Failure Mode

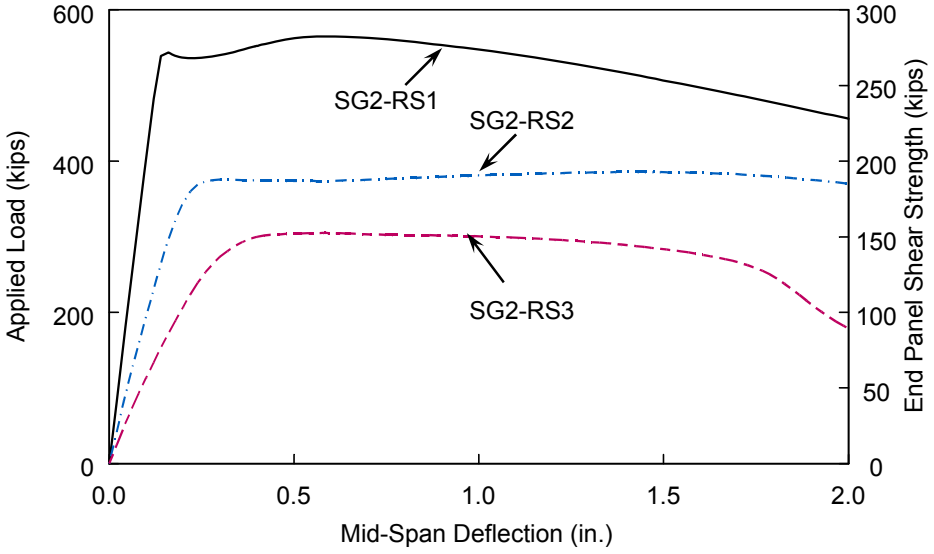

(b) Applied Load versus Mid-Span Deflection

Figure 7.15: SG2 Series (Approach 1)

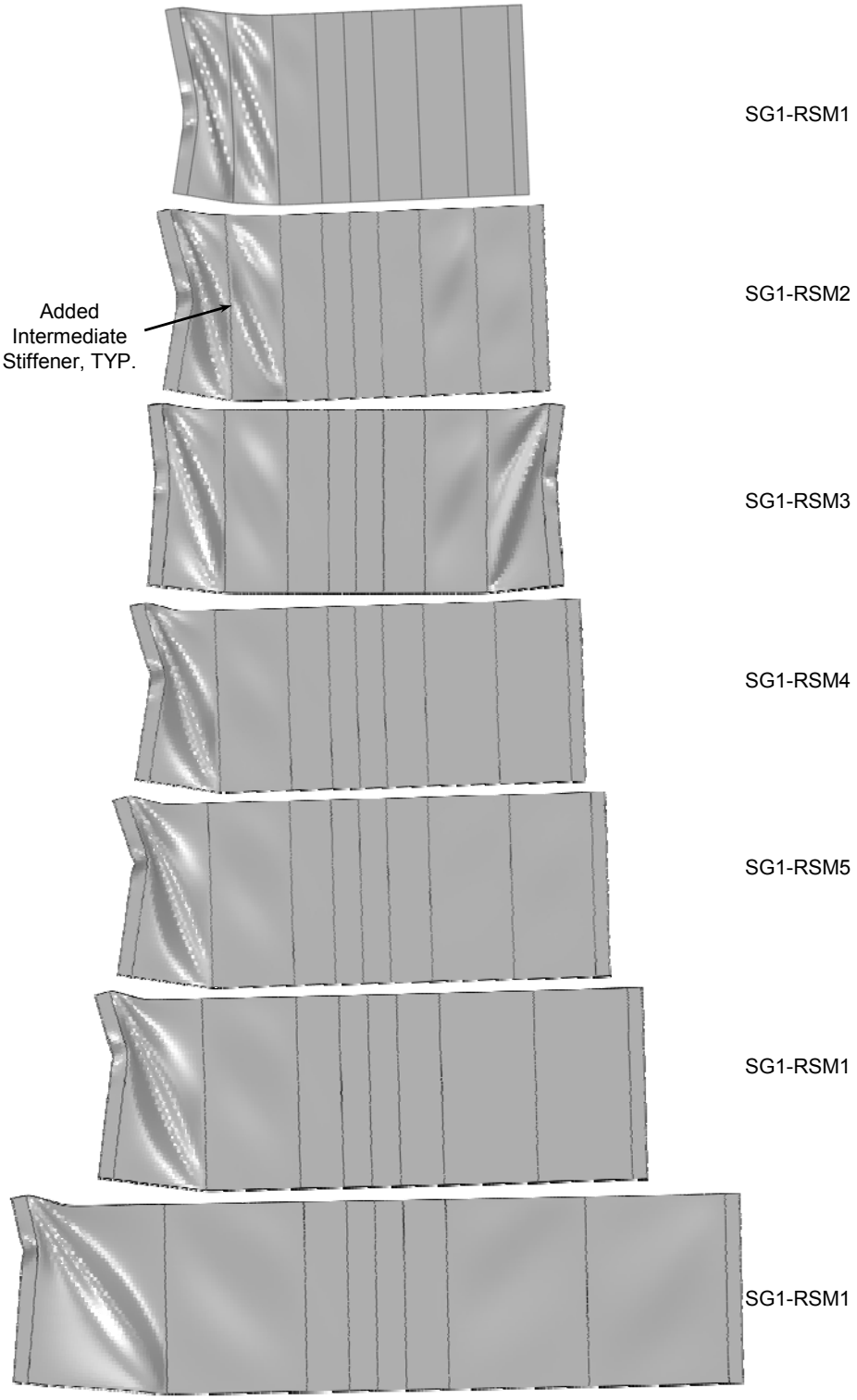

(a) SG1 Series (after Rehabilitation)

Figure 7.16: Failure Mode (Approach 2)

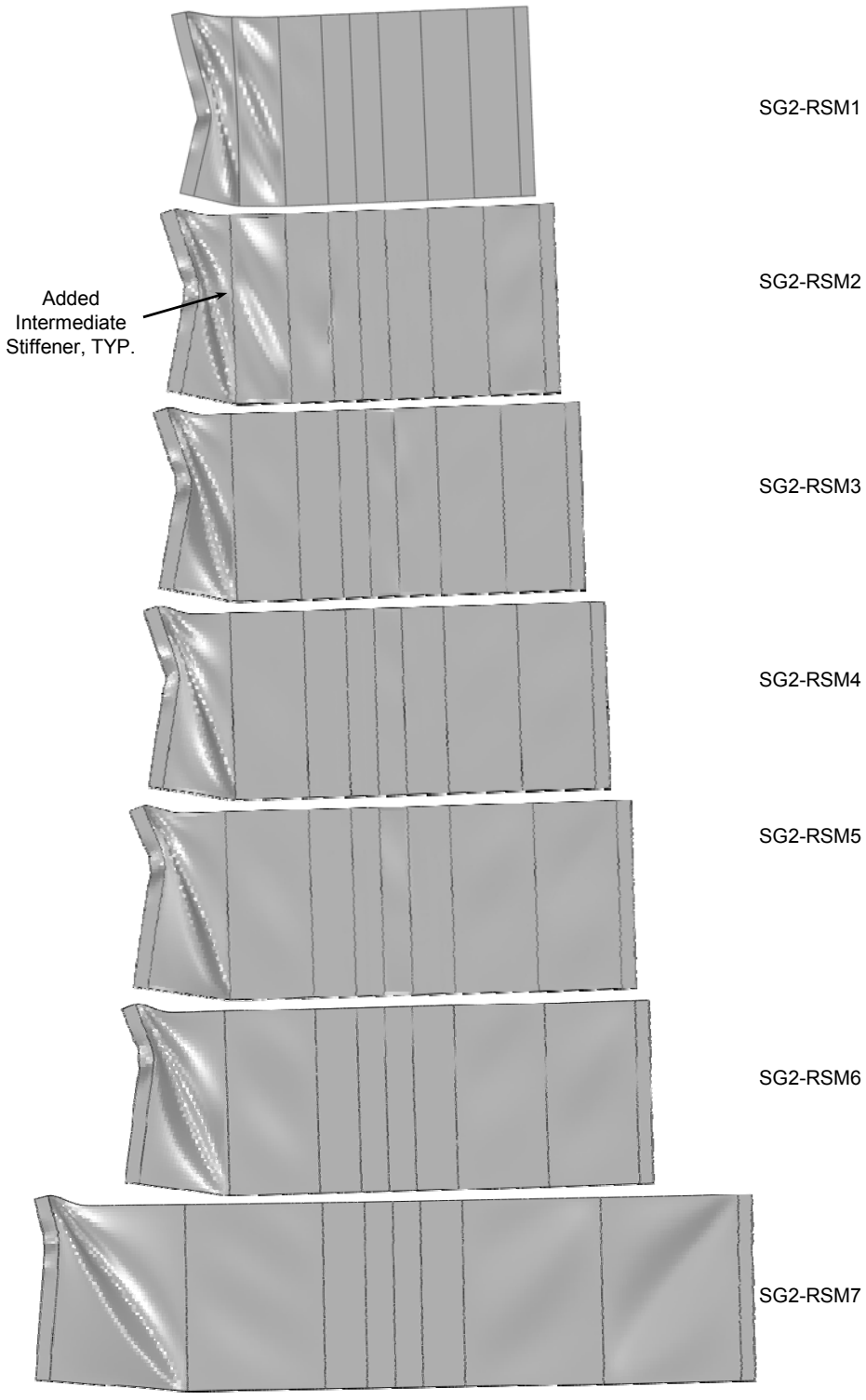

(b) SG2 Series (after Rehabilitation)

Figure 7.17: Failure Mode (Approach 2) (continued)

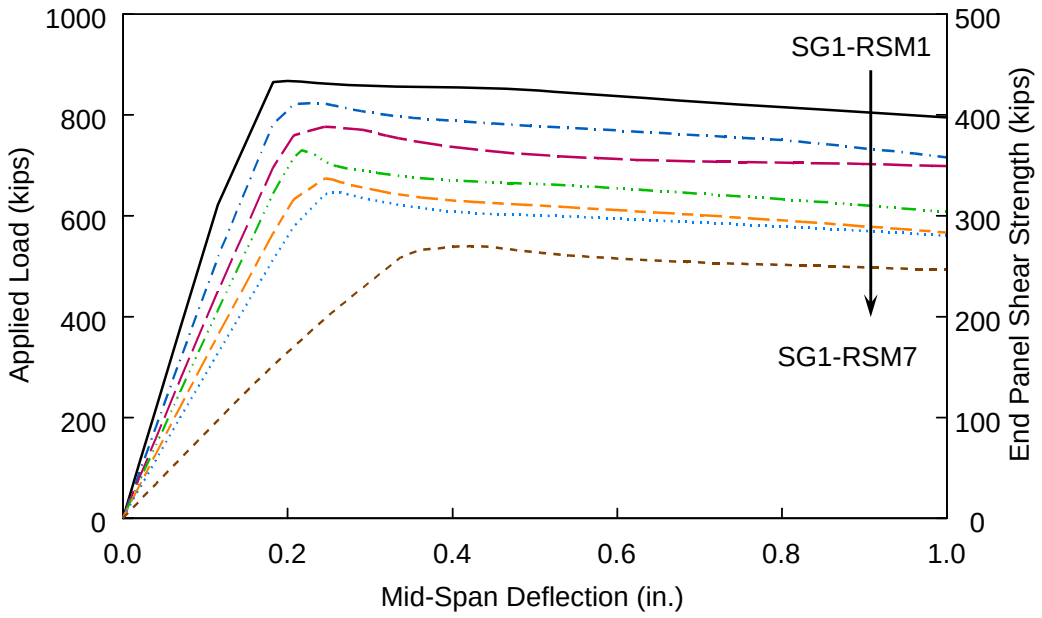

(a) SG1 Series

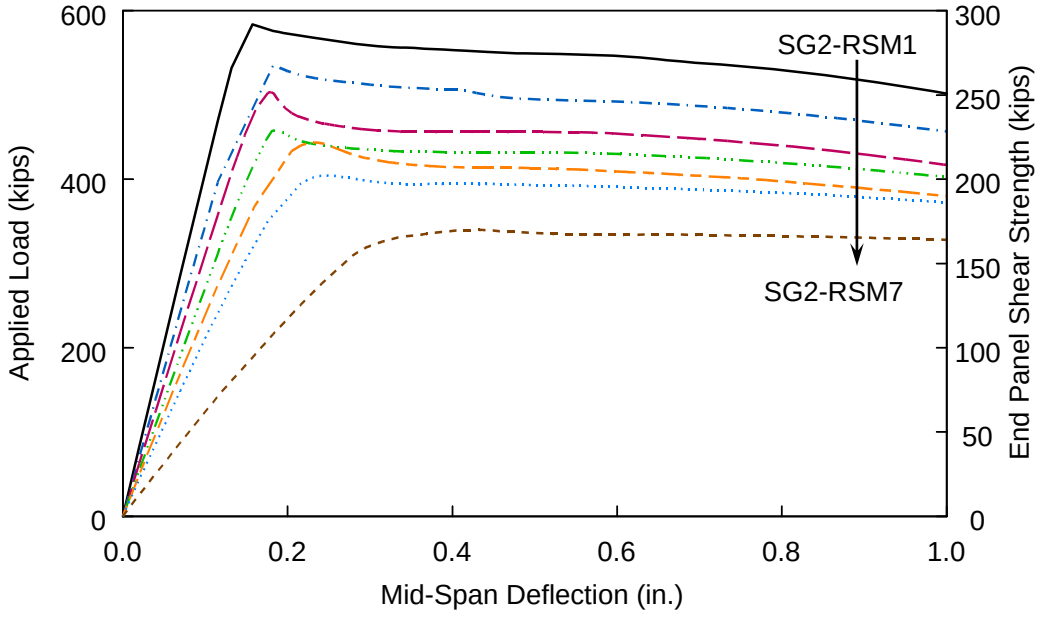

(b) SG2 Series

Figure 7.18: Applied Load versus Mid-Span Deflection (Approach 2)

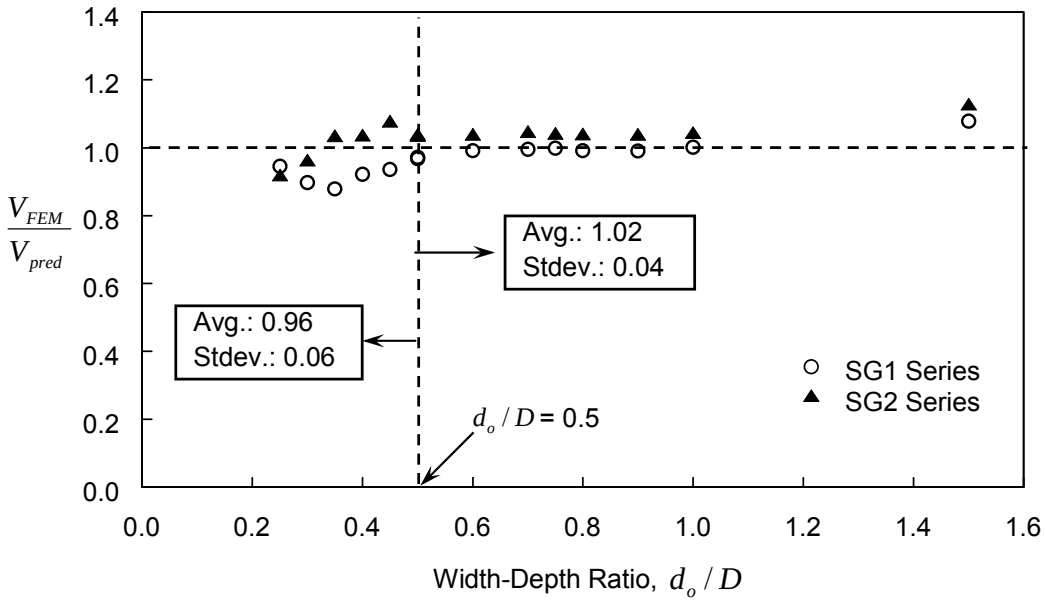

Figure 7.19: Effect of Width-Depth Ratio on Shear Strength of End Panels

8. TEST PROGRAM (PHASE 2)

8.1 Test Program

8.1.1 General

Continuing the Phase 1 tests, another four test specimens were fabricated and tested. The specimens were designated as Specimens SG3, SG4, CG3, and CG4. Specimens CG3 and CG4 were nominally identical to Specimens SG3 and SG4, except that the former incorporated concrete slabs.

8.1.2 Configuration and Fabrication of Test Specimensl

Table 8.1 shows the dimensions of three sample steel bridge girders provided by the California Department of Transportation (Caltrans) for the Phase 2 test program. Table 8.2 shows the specimen dimensions used in testing to represent the sample bridge girders. Depth-to-thickness ratio of 138 was used for all specimens, while the panel width-to-depth ratios of 1.5 and 0.75 were used for Specimen SG3 and SG4, respectively. The actual plate thicknesses of the specimens were measured and are summarized in Table 8.3.

The girders of Specimens CG3 and CG4 were nominally identical to those of Specimens SG3 and SG4, respectively, with the exception that the composite girder specimens included the headed shear studs welded to the top flanges of steel girder specimens to incorporate a concrete slab. The total slab thickness (t_c) and haunch depth (d_h) are shown in Table 8.2. Figure 8.2 and Figure 8.3 show the size of the shear studs, the geometry of concrete slab, and the steel reinforcement layout for these two composite specimens.

8.1.3 Material Properties

ASTM A36 steel was specified for all steel plates including the flanges, web, and intermediate and bearing stiffeners of the specimens. Tensile coupons were cut from the same plates for material testing. Average values of the measured mechanical properties of the component plates are summarized in Table 8.4.

Grade 40 longitudinal reinforcement (No. 4 and No. 5 for Specimens CG3 and CG4) with a minimum yield strength of 40 ksi and a minimum ultimate strength of 70 ksi was used. Due to the availiabity issues, Grade 60 transverse reinforcement was used for No. 6 rebars. Three samples of each size of reinforcement were tested. The average values of the measured mechanical properties are also summarized in Table 8.5.

A design concrete compressive strength of 4,000 psi was specified for the concrete slab. A total of 21 cylinders were cast and cured under the same conditions as the test specimens to obtain the compressive and split tensile strengths of the concrete. Each three-cylinder set was tested for compressive strength on the 7^{th}, 14^{th}, 21^{st}, 28^{th}, and 32^{nd} day (day of testing for CG4), while another three-cylinder set was tested for splitting tensile strength on the day of testing for each composite specimen. Although Specimen CG3 was tested on the 25^{th} day of the concrete cast, the concrete cylinder was tested on the 28^{th} day due to the laboratory schedule. However, it is believed that the difference should be minor. Table 8.6 summarizes the average values of compressive and splitting tensile strengths from testing.

Type B headed shear stud connectors made from ASTM A108 material with a minimum yield strength of 51 ksi and a minimum ultimate strength of 65 ksi was used for the interconnection of steel girder to concrete slab.

8.1.4 Initial Geometrical Imperfections

Initial geometrical imperfections of the steel girders were measured before testing. The measured web minimum and maximum imperfection values of each panel are also summarized in Table 8.7.

8.1.5 Test Setup, Loading Procedure, and Instrumentation

The configuration of steel girder specimens (Specimens SG3 and SG4) is shown in Figure 8.1 for Specimens SG3 and SG4. Specimen SG3 has a width-depth ratio of 1.5, which is the upper limit per AASHTO Specifications (2014). Speimen SG4 is the same as Specimen SG3 except that additional intermediate stiffeners were incorporated to make the width-depth ratio be half of Specimen SG3. Figure 8.2 and Figure 8.3 show the overall configuration of Specimens CG3 and CG4. The figures also provide the size of the shear studs, the geometry of the concrete slab, and the steel reinforcement layout.

Since Phase 2 test specimens had the same overall specimen length, the same test setup scheme of Phase 1 test program was used. That is, each specimen was simply supported and monotonically loaded to the top flange through a W36×302 loading beam at mid-span of the specimen. See Chapter 2 for the details of the test setup.

Test specimens were instrumented with a combination of displacement transducers, strain gage rosettes, and uni-axial strain gages to measure global and local responses at specific locations. One displacement transducer measured vertical displacement at the mid-span of each specimen and was used as the feedback sensor for actuator control. Strain gage rosettes measured the principal strains on the web panel, while uni-axial strain gages monitored the strains of flanges and bearing stiffeners. Load cells mounted on the actuators measured applied load. The instrumentation plan for each specimen is provided in Appendix A.

8.2 Test Results

8.2.1 Specimen SG3

Figure 8.4 shows the test setup prior to testing. The relationship between the applied load and mid-span deflection is shown in Figure 8.5. The theoretical stiffness computed from Eq. (2.1) is also shown in the figure.

Figure 8.6 shows the test specimen at event *A*, which corresponds to the AASHTO nominal shear strength for end panels. Minor web buckling was observed at this event. When the maximum applied load was achieved (event *B*), web buckling became significant (see Figure 8.7). After event B, the strength degraded slowly and plastic hinges formed in the bearing stiffeners and both flanges as observed in Phase 1 test specimens. The deformed shape at event *C* is shown in Figure 8.8. The front and back sides of the east end panel after the specimen was unloaded and intrumetation removed are shown in Figure 8.9. The observed plastic hinge locations are also marked in the figure.

8.2.2 Specimen SG4

A plot of the applied load versus mid-span deflection is shown in Figure 8.10. The theoretical stiffness is well matched with the inistiall stiffeness from the test.

Figure 8.11 and Figure 8.12 show the deformed shape of the specime at events *A* and *B*, respectively. Minor web buckling was first observed at event *A* and became significant at event *B*. A close-up view of both end panels at event *B* in Figure 8.12 shows that the east end panel has more significant web local buckling. The load dropped with the significant web buckling of the east end panel, but the load started increasing again with the significant buckling of the west end panel (see Figure 8.13). Then, the applied load dropped again before the specimen resisted more load and achieved the maximum load. After achieving the maximum load at event *D*, the load slowly degraded with the deformation in the flanges and bearing stiffeners. Figure 8.14 shows the deformed shape at event *D*. It is obvious from the figure that the boundary members also experienced a large deformation. Eventually, the east end panel failed with plastic hinges formed in the flanges and bearing stiffeners. The deformed shape at event *E* is shown in Figure 8.15.

The failure modes included plastic hinge formation on the boundary members and web buckling on the front and back sides of the east end panel as shown in Figure 8.16. Figure 8.17 shows the failure modes of both Specimens SG3 and SG4. The failure modes are very similar to those of Phase 1 Specimens (SG1 and SG2) as shown in Figure 3.15.

8.2.3 Specimen CG3

Specimen CG3 was nominally identical to Specimen SG3, except that it incorporated a concrete slab. Figure 8.18 shows the relationship between applied load and mid-span deflection.

Specimen CG3 showed similar behavior to Specimen SG3. Figure 8.19 shows the deformed shape at event *A* when minor web buckling developed in both end panels. Then minor yielding in the end panels was observed at a mid-span deflection of 0.2 in. Figure 8.20 shows the web buckling pattern at a mid-span defection of 0.3 in. Damage in the concrete slab was not visible and the specimen was able to resist more loads. Eventually, the specimen reached the maximum applied load (= 697 kips) at a mid-span deflection of 1.14 in. Figure 8.21 shows the buckling pattern at event *B*. The shear crack on the concrete slab caused a loss of load resistance. As the mid-span deflection

increased, the cracks widened. The failure mode of the specimen at event *C* (Δ = 2.5 in.) is shown in Figure 8.22. The crack patterns are also summarized in Figure 8.23. At the completion of testing, concrete crushing at the top surface of the concrete slab is shown in Figure 8.24(a). Figure 8.24 (b) shows the yielding pattern as a result of tension-field formation along the panel diagonal in the web and plastic hinges developed in the flanges and bearing stiffeners.

8.2.4 Specimen CG4

Specimen CG4 was nominally identical to Specimen SG4, except that CG4 incorporated a concrete slab. Figure 8.25 shows the relationship between applied load and mid-span deflection. Since actuators reached its capacity during the test, it was decided to add steel mounting plates (11.64 kips) on the top of the concrete slab near the mid-span of the specimen to fail the specimen. Considering this additional weight, the expected global response is also plotted in the figure.

At event *A*, web buckling was very minor in both end panels. The measured web out-of-plane deformation was about 0.063 in. in both end panels. Figure 8.26 shows the deformed shape at event *A*. The amplitude of web buckling grew rapidly and the measured out-of-plane deformation was 0.375 in. in both end panels at a mid-span deflection of 0.2 in. After this point, the stiffness softened, web buckling became significant, and yielding due to the tension-field formation occurred in both end panels. Also note that two interior web panels experienced buckling at a mid-span deflection of 0.35 in. Figure 8.27 shows the web local buckling and the associated yielding pattern at a mid-span deflection of 0.4 in. At this event, flexural concrete cracks were also observed. The number of cracks increased as the mid-span deflection increased. The buckling pattern at the maximum load (= 890 kips) is shown in Figure 8.28. Figure 8.29 shows the concrete crack patterns observed during the test. Figure 8.30 shows the failure mode of the specimen at event *C*. Plastic hinges that developed in flanges and bearing stiffeners are also marked in the figure.

8.2.5 Recorded Local Responses

Figure 8.31 shows the locations of the displacement transducers that measured the web out-of-plane deformations. L2, L3, and L4 were installed on the back side of the

east end panel, while L5, L6, L7 were placed on the back side of the west end panel. All displacement transducers were located at the mid-width of the panel. L2 and L5 were located at the distance of 11 in. away from the top flange, while L4 and L7 were placed at the same distance from the bottom flange. L3 and L6 were installed near the mid-height of the panels. Figure 8.32 to Figure 8.35 show the web out-of-plane deformation of each test specimen. The expected buckling load predicted per the AASHTO Specifications (2014) is also presented in the figure.

Figure 8.36 shows the locations and orientations of the strain gage rosettes for all specimens. All strain gage rosettes were installed on the back side of the panel web. From the rosette data, principal strains and directions were computed. Figure 8.37 plots the principal tensile strains across the panel diagonal of both east and west end panels at the ultimate load (Event *B*). The horizontal reference line in the figure represents the strain value corresponding to the tension-field stress (σ_t) proposed by Basler (1961a).

The principal tensile strains recorded at five middle strain gage rosettes in each panel are beyond the strain corresponding to the tension-field stress. Table 8.8 and Table 8.9 summarize the principal tensile directions of five middle strain gage rosettes of each section at ultimate load (Event *B*). The recorded principal angles varied but most of them were within ± 10° of the angle of the panel diagonal (34° for Specimens SG3 and CG3, and 53° for Specimens SG4 and CG4) with respect to the flange.

8.2.6 Comparison of Test Results

Table 8.10 summarizes the end panel shear strengths based on both AASHTO Specifications (2014) and experimental results. The shear overstrengths for each specimen, computed as the ratio of the experimental strength to the AASHTO nominal strength, are listed in the last column of the table. As observed from Phase 1 test results, the AASHTO Specifications (2014) are very conservative in calculating the shear strength of the end panels. Figure 8.38 summarizes the measured plastic hinge locations in the top flange and bearing stiffeners for each test specimens after completing the tests.

Figure 8.39 shows the relationship between the normalized ultimate shear strength and the web depth-to-thickness ratio. The curves were constructed based on the actual web yield stress from the coupon tests. It is found that the actual shear strengths of

Phase 2 test specimens were slightly higher than theAASHTO-predicted strengths of the interior panel, which consider full tension-field action. It should be noted that the boundary members (flanges and bearing stiffeners) in these specimens provided high flexural strength such that the coefficient, α, in the proposed Eq. (6.33) is greater than 1.0. Therefore, the shear strengths of Specimens SG3 and SG4 are very close to the shear strengths of the panels considering full tension-field action.

In Phase 1 tests, the increase in shear strength due to the contribution from concrete slab was about 12% for composite Specimens CG1 and CG2. In Phase 2 tests, however, the increase in shear strength due to the contribution from concrete slab was significantly higher and was about 61% in Specimen CG3 and 63% in CG4. This is expected as, for a given concrete slab, the composite action effect is more significant on shallower than deeper steel girders.

Table 8.1: Sample Caltrans Steel Bridge Girder Dimensions

Bridge No.	Section			Width-Depth Ratio, d_0/D	Depth-Thickness Ratio, D/t_w
	Top Flange (in.)	Web (in.)	Bottom Flange (in.)		
42-0246R	10×5/8	42×5/16	18×1	0.86	134
50-0316 (Spans 2&3)	12×1	45×5/16	20×1-1/8	0.71	144
50-0316 (Spans 1&4)	12×5/8	45×5/16	20×7/8	0.80	144

Table 8.2: Specimen Dimensions

Spec. No.	Width-Depth Ratio, d_0/D	Depth-Thickness Ratio, D/t_w	Web Depth, D (in.)	Top and Bottom Flanges		Total Slab Thickness (t_c)/ Haunch Depth (d_h) (in.)	Scale Factor
				Thickness, t_f (in.)	Width, b_f (in.)		
SG3	1.5	138	43	1.0	18.0	No Slab	1
CG3						8.25 / 2.75	
SG4	0.75	138	43	1.0	18.0	No Slab	1
CG4						8.25 / 2.75	

Table 8.3: Steel Plate Thicknesses

Specimen No.	Component	Nominal Thickness (in.)	Measured Thickness (in.)
SG3 / CG3 SG4 / CG4	Flanges	1.00	1.006
	Web	0.3125	0.305
SG3 / CG3 SG4 / CG4	Bearing Stiffener	1.00	1.006
	Intermediate Stiffener	0.5	0.486

Table 8.4: Average Mechanical Properties of Steel Plates

Specimen No.	Steel Grade	Component / Heat Number	Yield Stress (ksi)	Tensile Strength (ksi)	Elongation (%)
SG3, CG3, SG4, CG4	A36	Flanges / 7N615	45.6 (47.7)[a]	71.5 (63.5)	27.2[b] (28)[c]
		Web / 919696	36.9 (45.1)	60.7 (64.5)	38.1[b] (24)[c]
		Bearing Stiffener / 7N615r	45.6 (47.7)	71.5 (63.5)	27.2[b] (28)[c]
		Intermediate Stiffener / 918573	40.1 (46.6)	64.2 (65.0)	30.4[b] (24)[c]

Note:

a. Values in parentheses are based on Certified Mill Test Reports, others from tensile coupon tests at UCSD.

b. Elongation is based on 2 in. gage length.

c. Elongation is based on 8 in. gage length.

Table 8.5: Average Mechanical Properties of Steel Reinforcements

Bar Size	Yield Stress (ksi)	Tensile Strength (ksi)
No. 4	45.9	67.4
No. 5	47.2	71.6
No. 6	64.6	93.3

Table 8.6: Average Mechanical Properties of Concrete

Curing Period (Days)	Compressive Strength, f'_c (ksi)	Splitting Tensile Strength, f_t (ksi)
7	3.45	NA
14	4.19	NA
21	4.48	NA
28	4.80	0.47
32	5.07	0.43

Table 8.7: Measured Initial Web Imperfections (in.)

Measured Initial Imperfections		Specimen No.			
		SG3	SG4	CG3	CG4
Panel 1	Min.	-0.0625	-0.0372	0.0000	0.0000
	Max.	0.1875	0.2123	0.2377	0.2311
Panel 2	Min.	NA	0.0000	NA	-0.0495
	Max.	NA	0.2188	NA	0.2064
Panel 3	Min.	NA	-0.0551	NA	-0.0625
	Max.	NA	0.1624	NA	0.1624
Panel 4	Min.	0.0000	0.0000	0.0000	-0.1123
	Max.	0.3125	0.2500	0.3125	0.2874

Table 8.8: Prinicipal Strain Direction at Ultimate Load (Steel Plate Girders)

Specimen No.		Rosette Number	Panel Diagonal Angle (degree)	Principal Tensile Strain Angle (degree)
SG3	East Panel 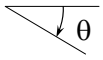	R05	34	40
		R04		37
		R03		56
		R02		67
		R01		56
	West Panel 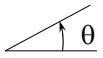	R06		37
		R07		45
		R08		50
		R09		52
		R10		49
SG4	East Panel 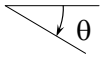	R05	53	37
		R04		48
		R03		NA
		R02		53
		R01		57
	West Panel 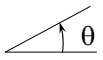	R08		48
		R09		20
		R10		NA
		R11		50
		R12		54

Table 8.9: Prinicipal Strain Direction at Ultimate Load (Composite Plate Girders)

Specimen No.		Rosette Number	Panel Diagonal Angle (degree)	Principal Tensile Strain Angle (degree)
CG3	East Panel 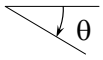	R05	34	38
		R04		40
		R03		22
		R02		36
		R01		32
	West Panel 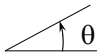	R06		33
		R07		34
		R08		16
		R09		31
		R10		31
CG4	East Panel 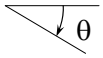	R05	53	48
		R04		19
		R03		49
		R02		48
		R01		52
	West Panel 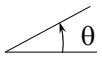	R08		51
		R09		44
		R10		47
		R11		51
		R12		53

Table 8.10: Comparison of End Panel Shear Strengths

Specimen No.	AASHTO Predicted Nominal Strength (kips)	Experimental Shear Strength (kips)	Shear Overstrength
SG3	135.4	212.1	1.57
CG3		348.6	2.57
SG4	241.6	279.0	1.15
CG4		445.4	1.84

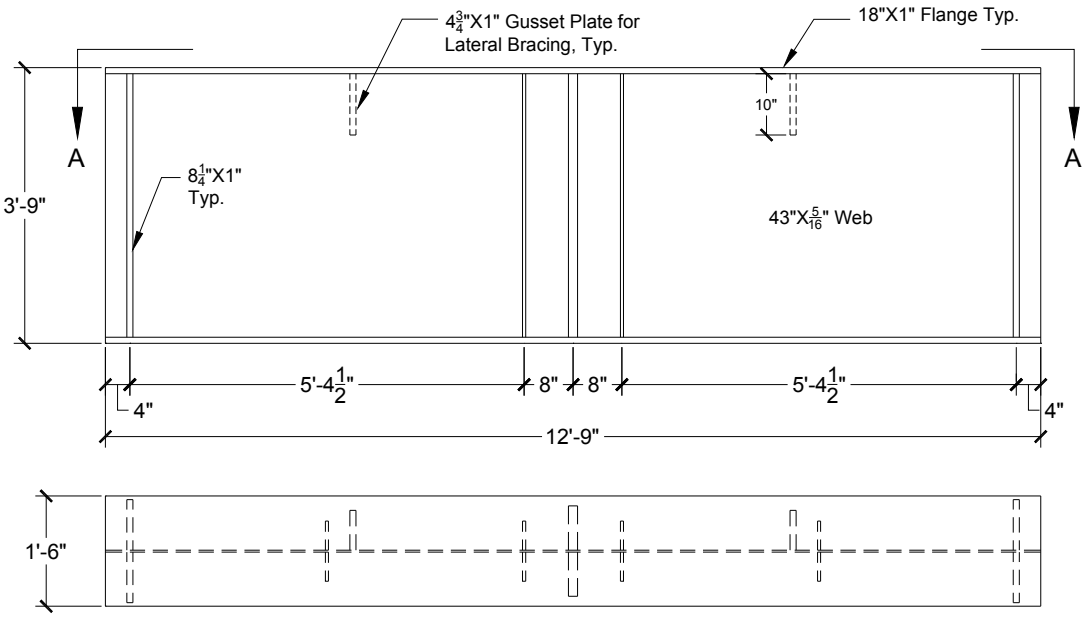

View A - A

(a) Specimen SG3

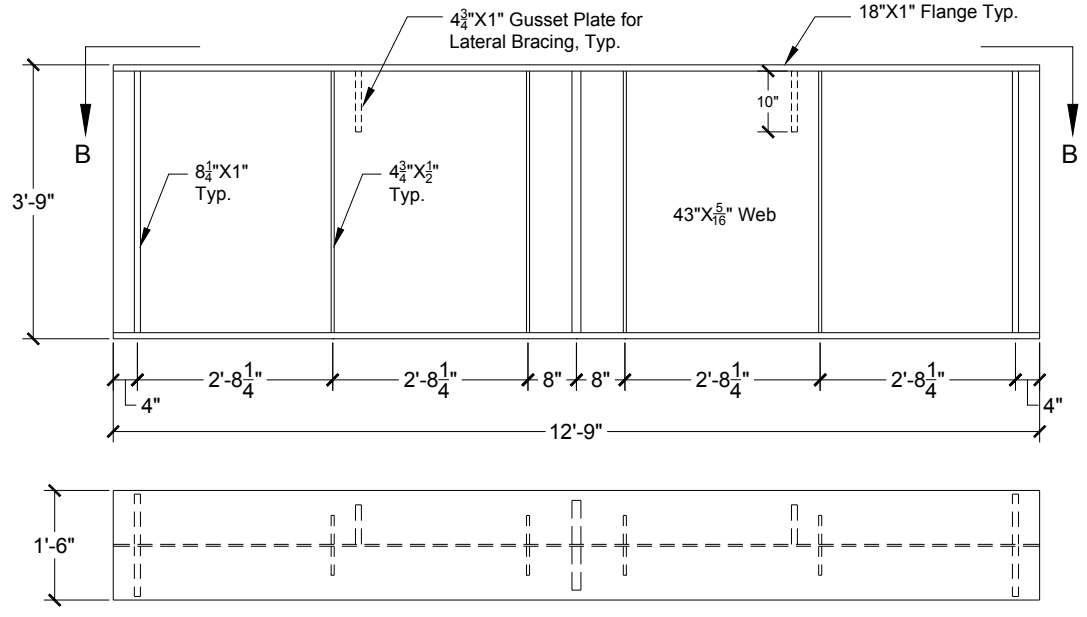

View B - B

(b) Specimen SG4

Figure 8.1: Configuration of Steel Girder Test Specimens

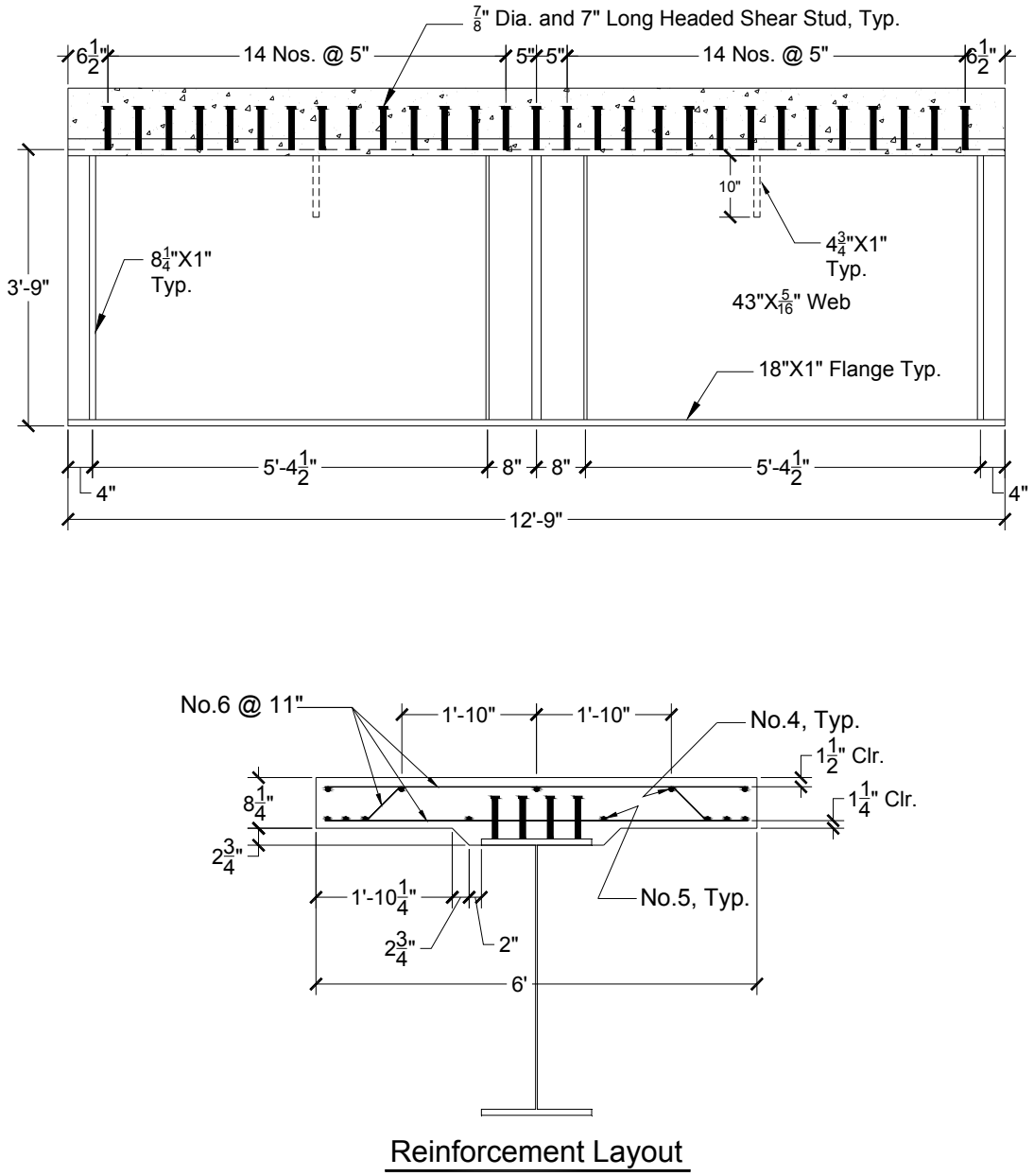

Figure 8.2: Specimen CG3: Configuration of Composite Girder Test Specimens

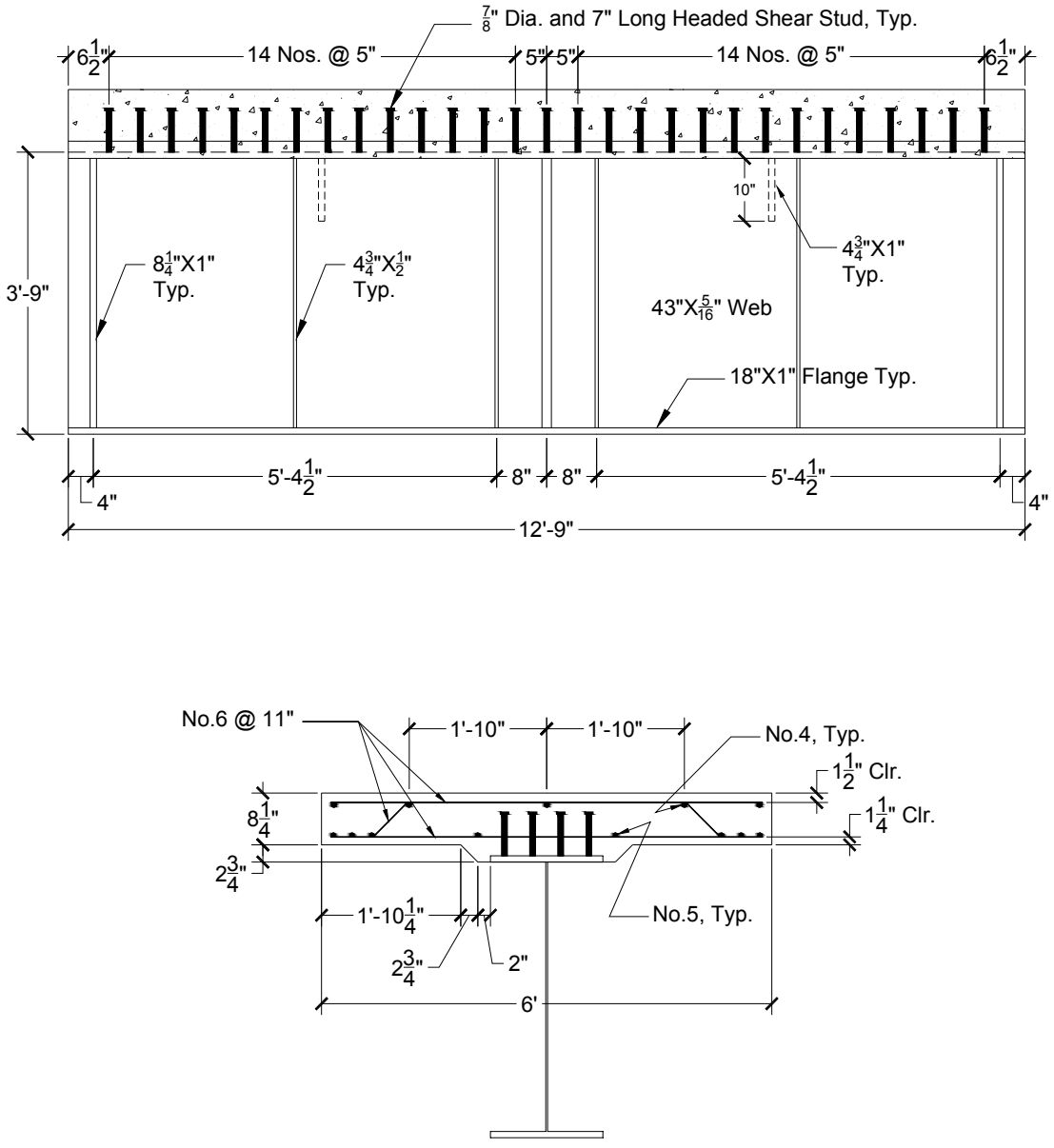

Figure 8.3: Specimen CG4: Configuration of Composite Girder Test Specimens

(a) Front View

(b) Side View

Figure 8.4: Specimen SG3 Test Setup

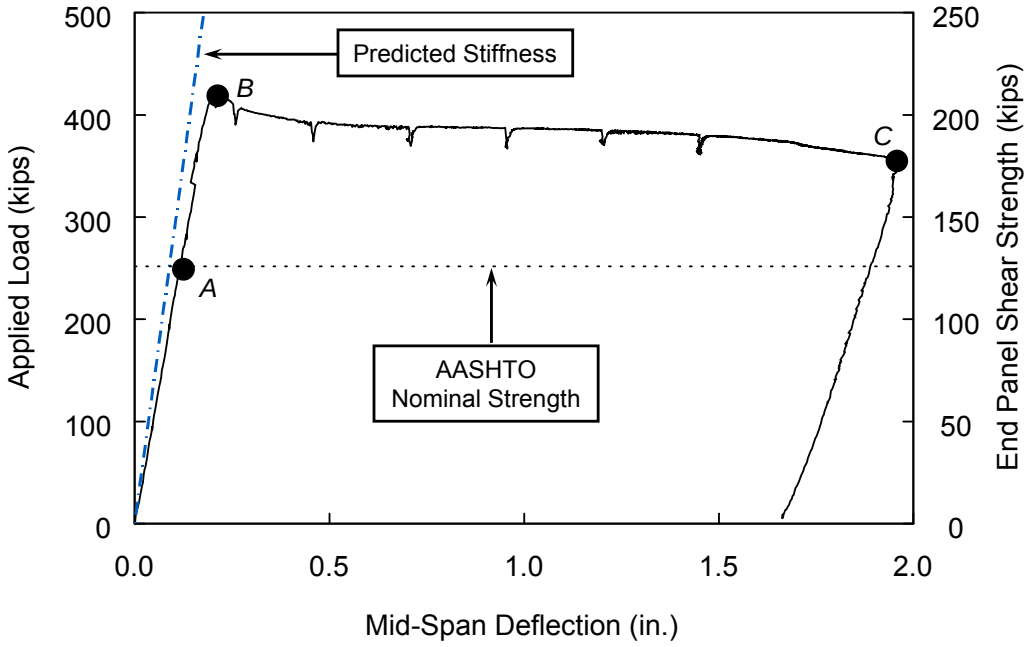

Figure 8.5: Specimen SG3 Applied Load versus Mid-Span Deflection

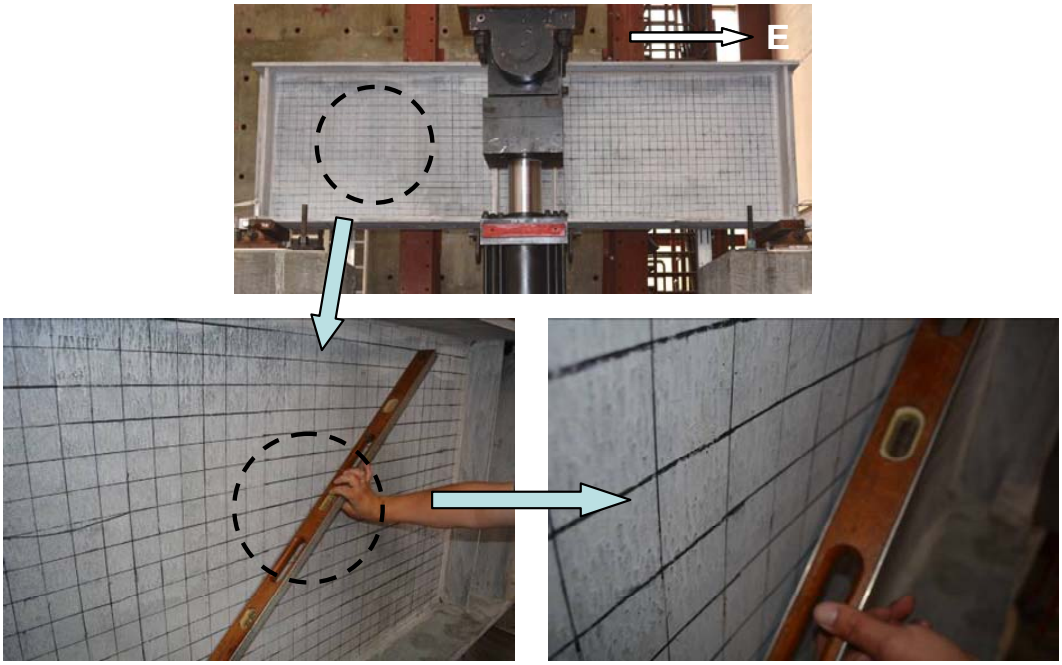

Figure 8.6: Specimen SG3: Web Local Buckling at Event *A*

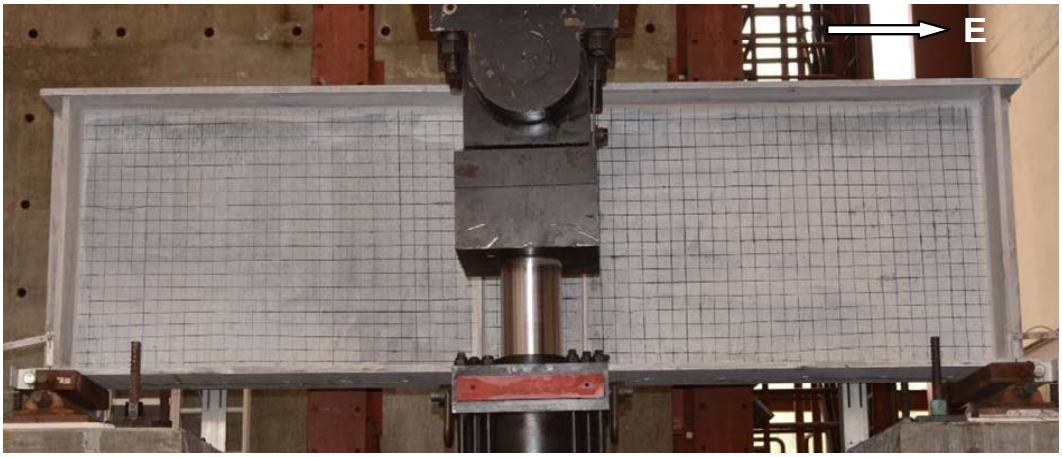

(a) Overall View

(b) West End Panel

(c) East End Panel

Figure 8.7: Specimen SG3: Web Local Buckling at Event *B*

Figure 8.8: Specimen SG3: Failure Mode at Event *C*

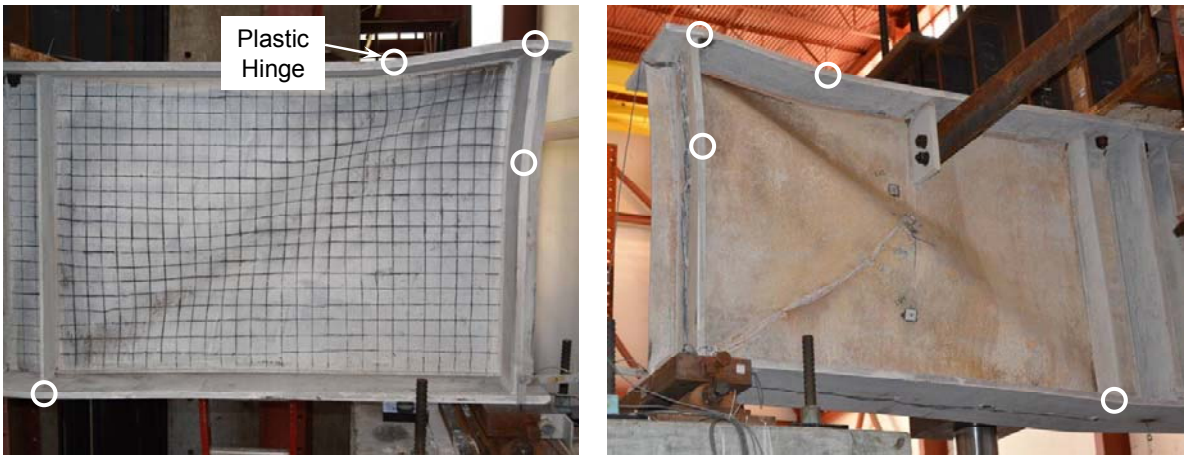

(a) Front Side (b) Back Side

Figure 8.9: Specimen SG3: Failure Mode after Completion of Test (East End Panel)

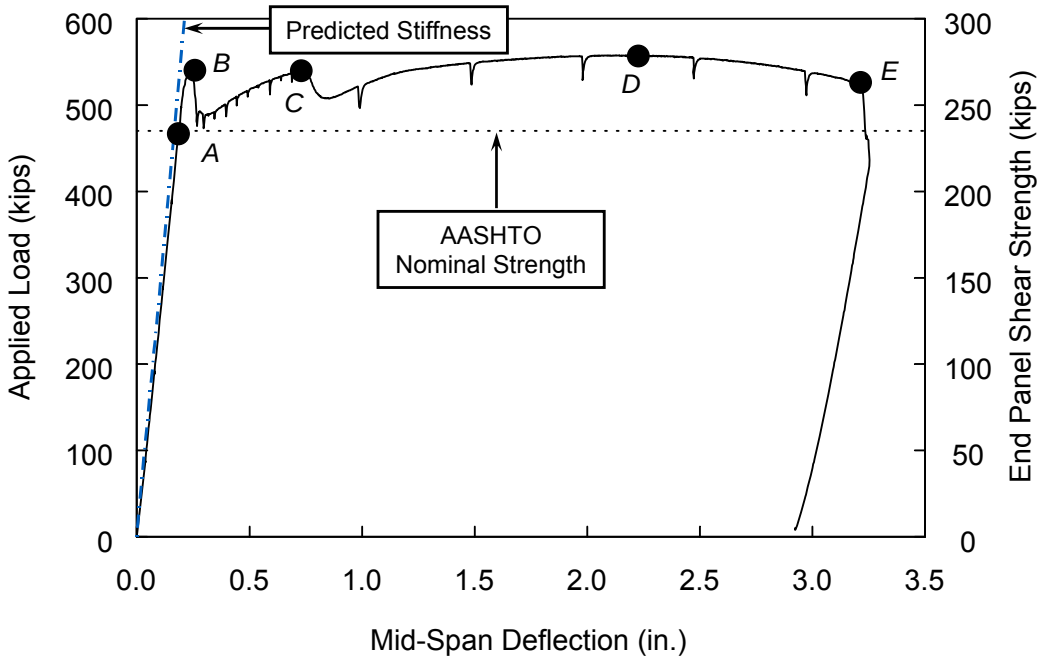

Figure 8.10: Specimen SG4: Applied Load versus Mid-Span Deflection

Figure 8.11: Specimen SG4: Web Local Buckling at Event *A*

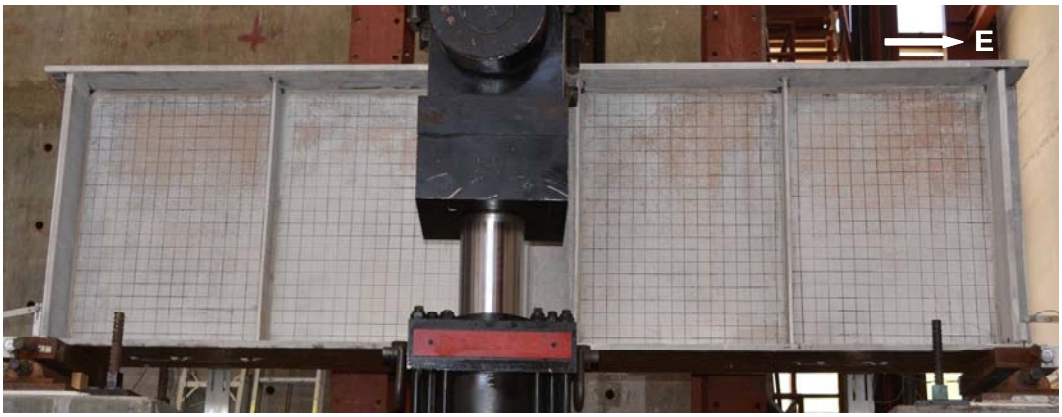

(a) Overall View

(b) West End Panel

(c) East End Panel

Figure 8.12: Specimen SG4: Web Local Buckling at Event *B*

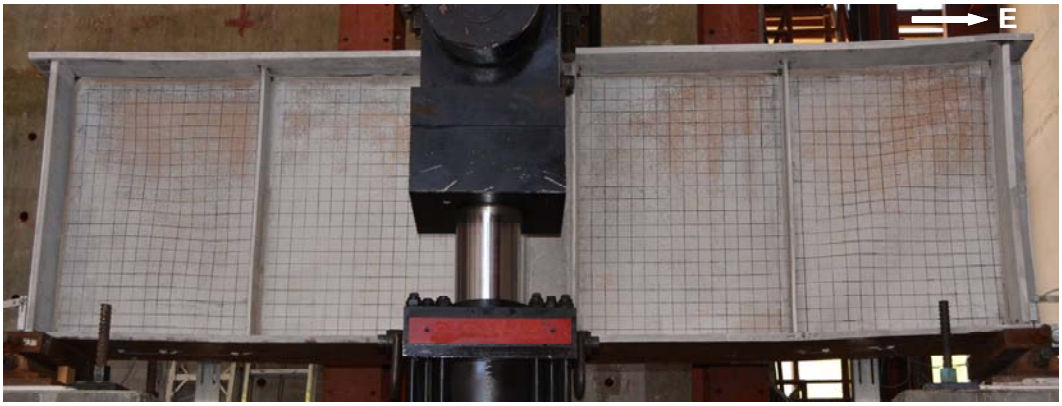

(a) Overall View

(b) West End Panel

(c) East End Panel

Figure 8.13: Specimen SG4: Deformed Shape at Event *C*

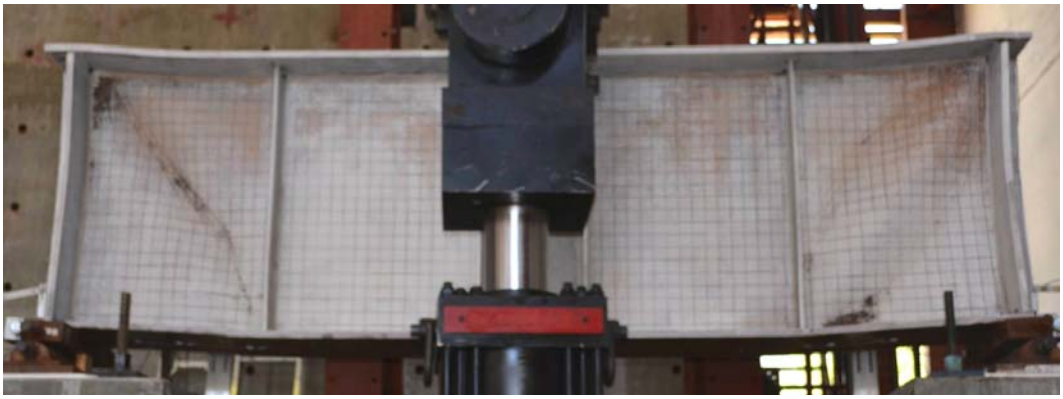

Figure 8.14: Specimen SG4: Deformed Shape at Event *D*

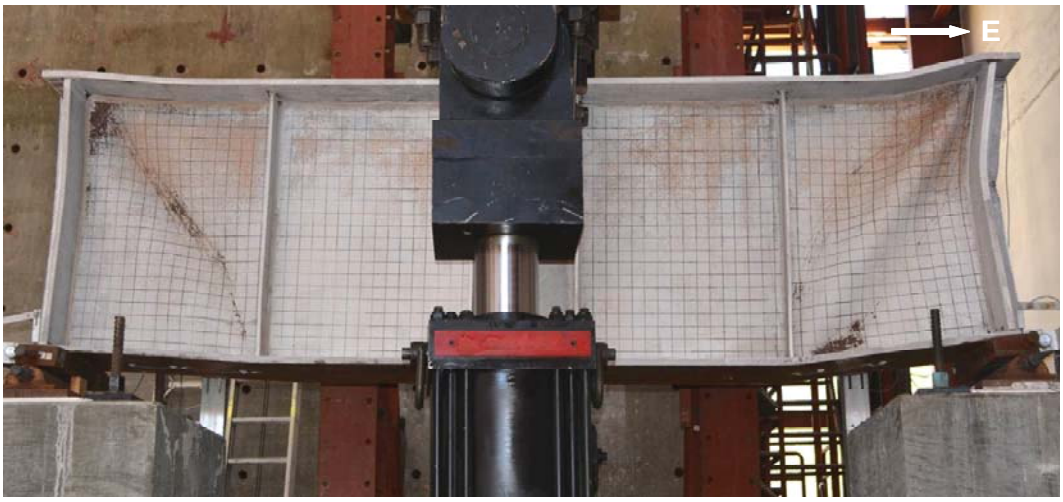

Figure 8.15: Specimen SG4: Failure Mode at Event *E*

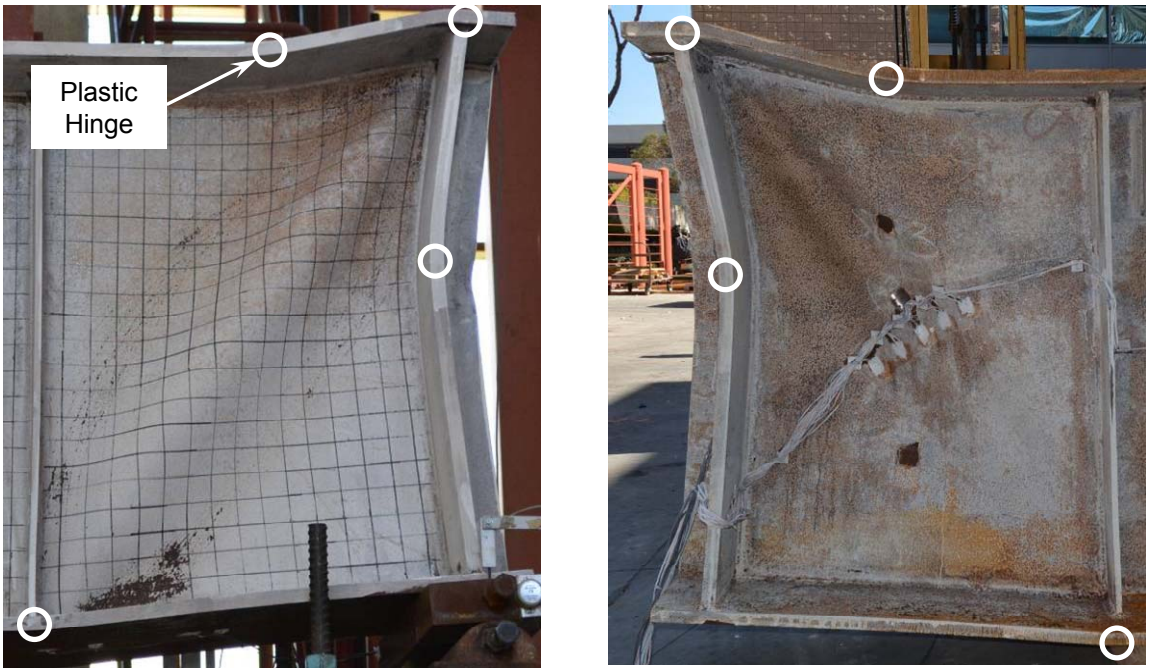

(a) Front Side (b) Back Side

Figure 8.16: Specimen SG4: Failure Mode after Completion of Test (East End Panel)

Figure 8.17: Failure Modes of SG1 and SG2

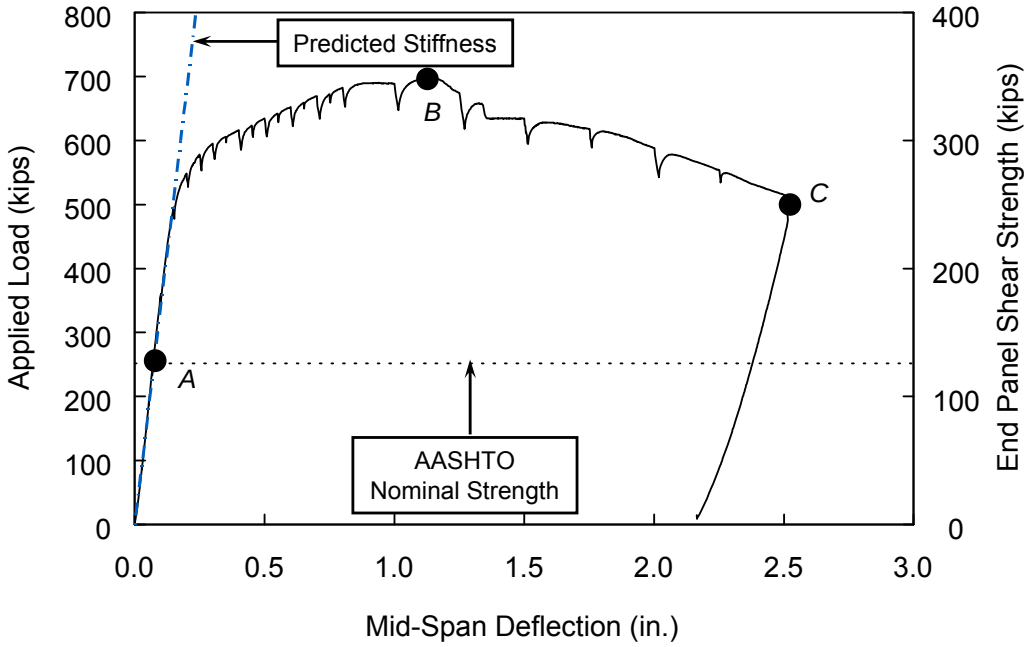

Figure 8.18: Specimen CG3: Applied Load versus Mid-Span Deflection

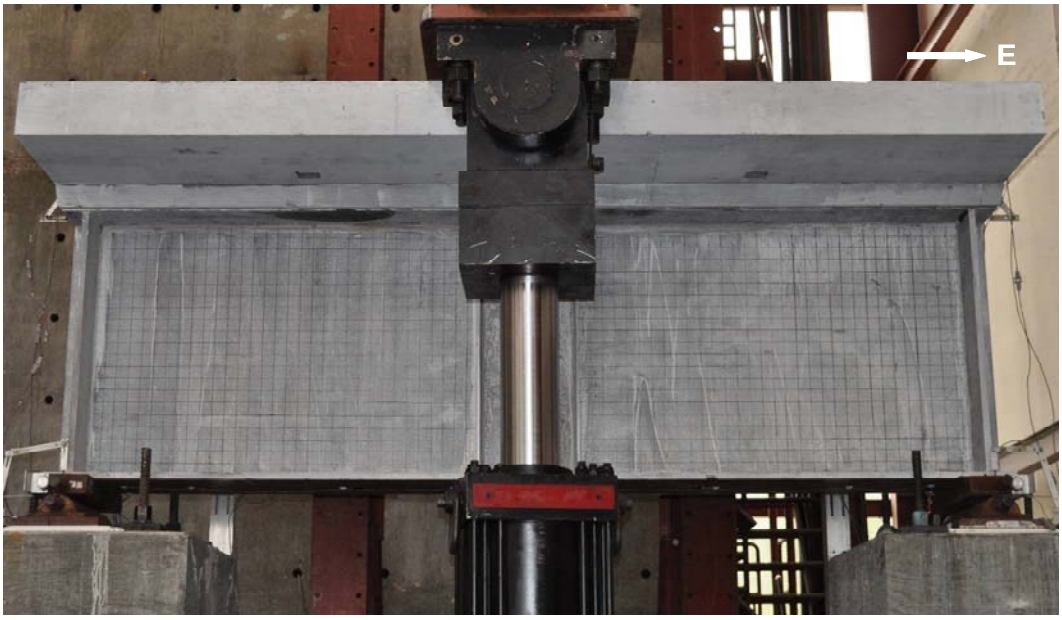

Figure 8.19: Specimen CG3: Overall View at Event *A*

Figure 8.20: Specimen CG3: Web Yielding pattern at $\Delta = 0.3$ in.

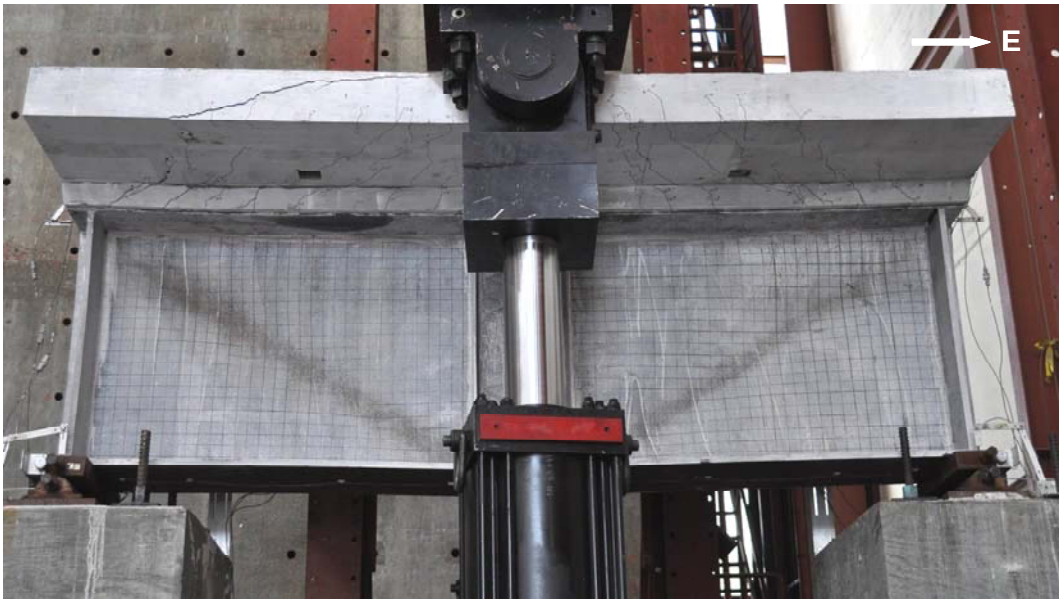

Figure 8.21: Specimen CG3: Deformed Shape at Event *B* (Maximum Load)

Figure 8.22: Specimen CG3: Failure Mode at Event *C*

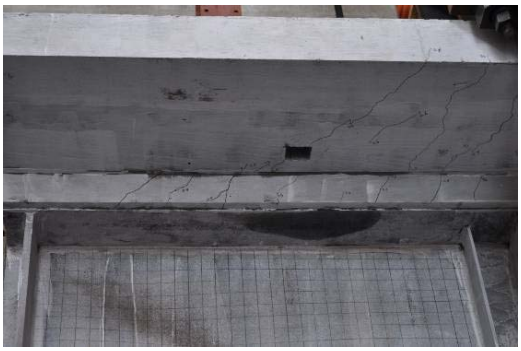

(a) at Δ = 0.6 in. (Event *B*)

(b) at Δ = 1.2 in.

(c) at Δ = 1.5 in.

(d) at Δ = 2.0 in.

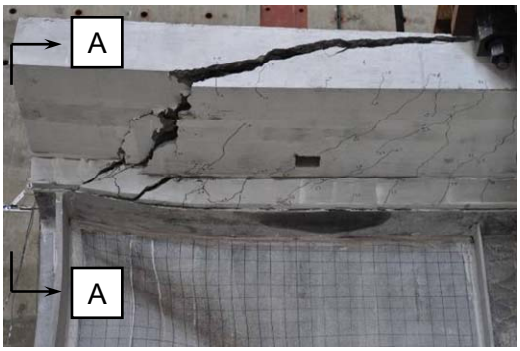

(e) at Δ=2.5 in.

(f) End View A - A

Figure 8.23: Specimen CG3: Propagation Concrete Slab Cracks

(a) Concrete Crushing

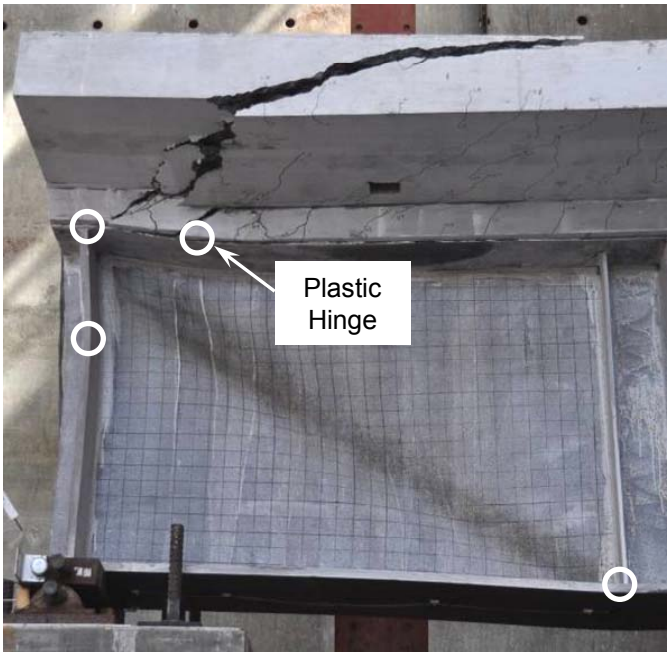

(b) Front Side of West End Panel

Figure 8.24: Specimen CG3: Failure Mode after Completion of Test

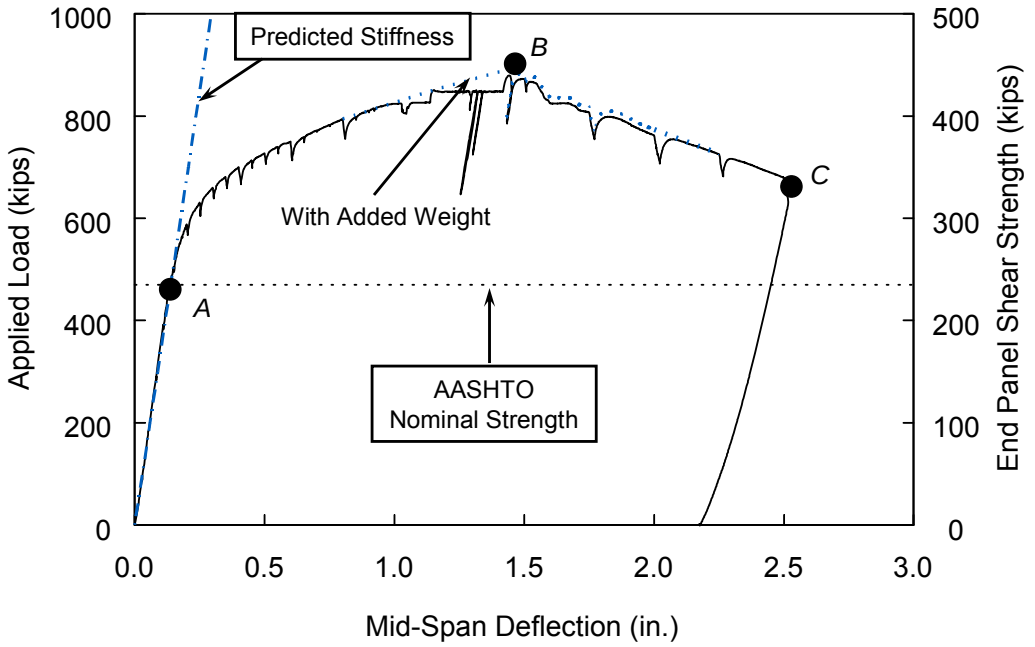

Figure 8.25: Specimen CG4: Applied Load versus Mid-Span Deflection

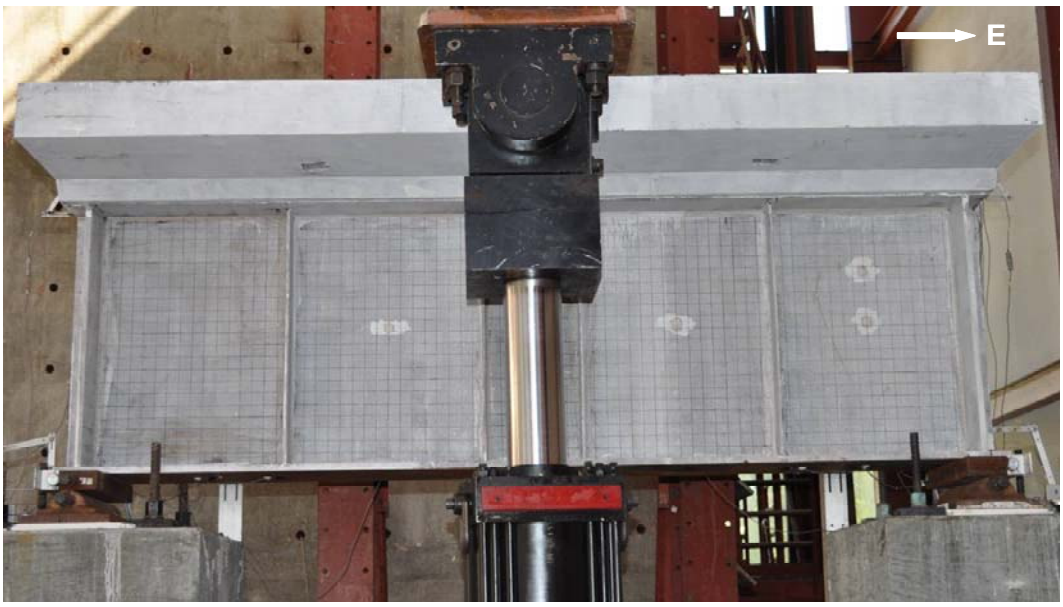

Figure 8.26: Specimen CG4: Overall View at Event *A*

(a) Overall View

(b) West End Panel

(c) East End Panel

Figure 8.27: Specimen CG4: Web Local Buckling and Yielding Patterns at $\Delta = 0.4$ in

Figure 8.28: Specimen CG4: Yielding Pattern at Event *B*

(a) at Δ = 0.4 in.

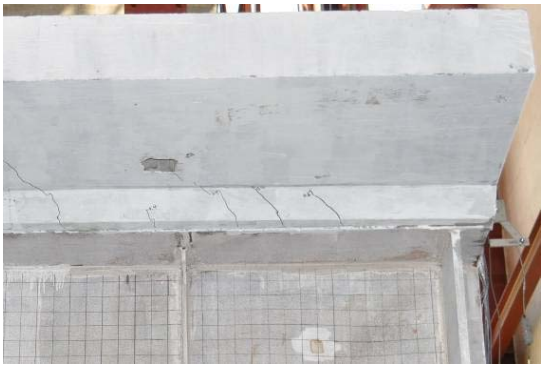

(b) at Δ = 0.6 in.

(c) at Δ = 1.0 in.

(d) at Δ = 1.75 in.

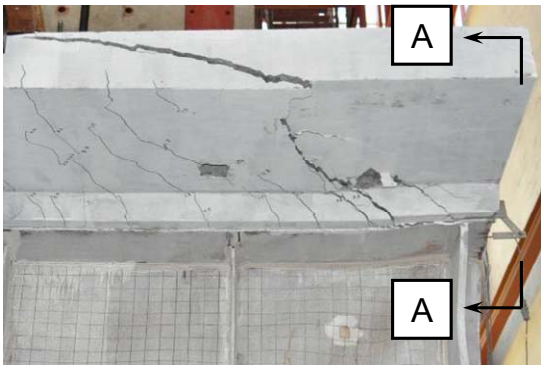

(e) at Δ = 2.5 in.

(f) End View A - A

Figure 8.29: Specimen CG4: Concrete Slab Crack Propagation

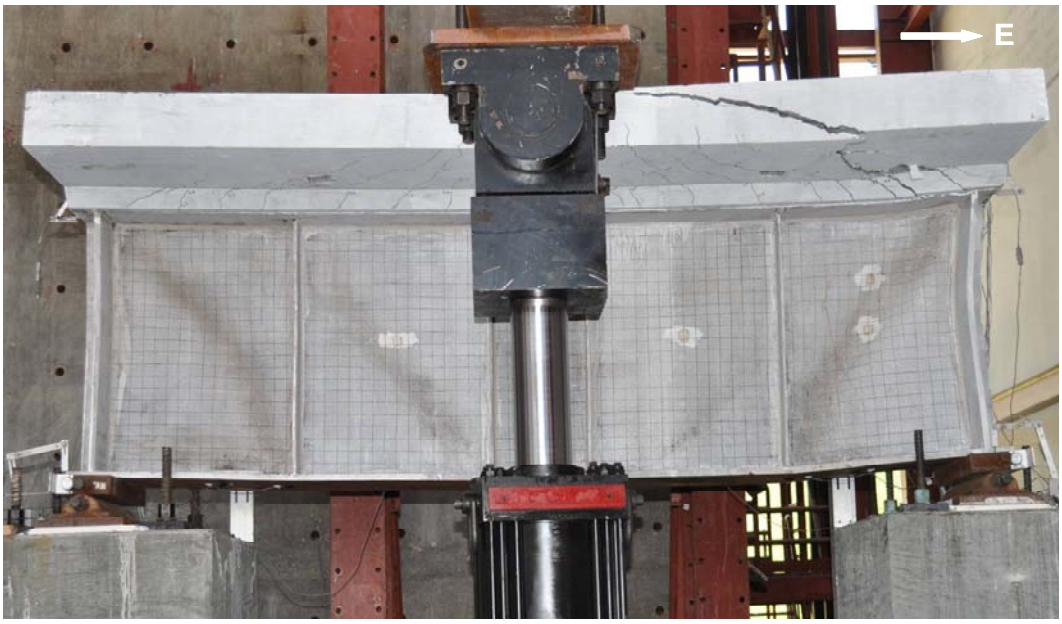

(a) Overall View

(b) Front Side of East End Panel

Figure 8.30: Specimen CG4: Failure Mode at Event *C*

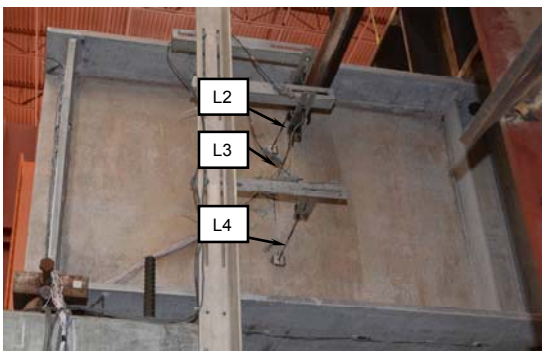

(a) East End Panel

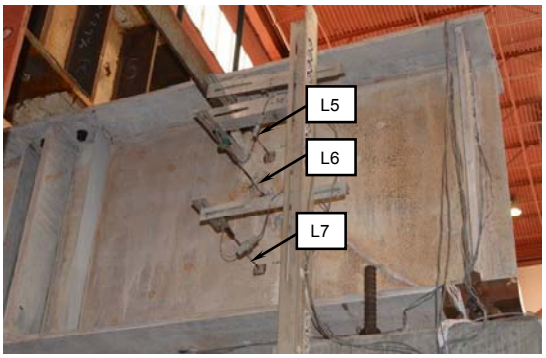

(b) West End Panel

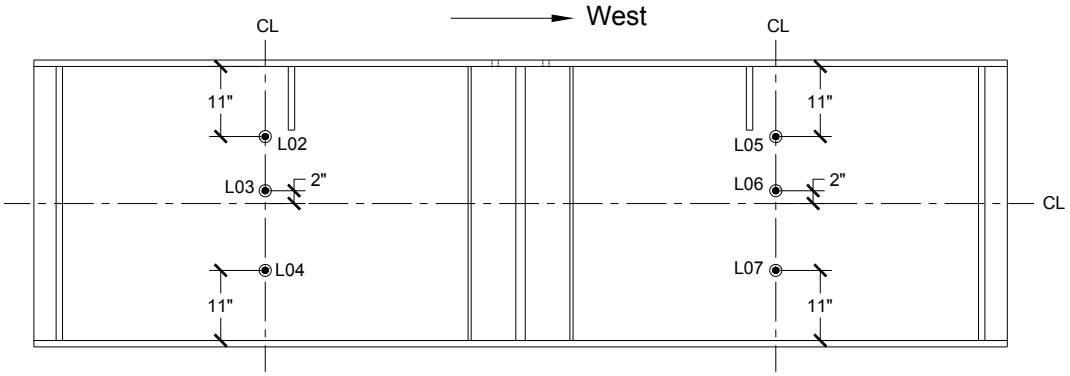

(c) Locations of Displacement Transducers

Figure 8.31: Specimen SG3: Locations of Displacement Transducers (Back Side)

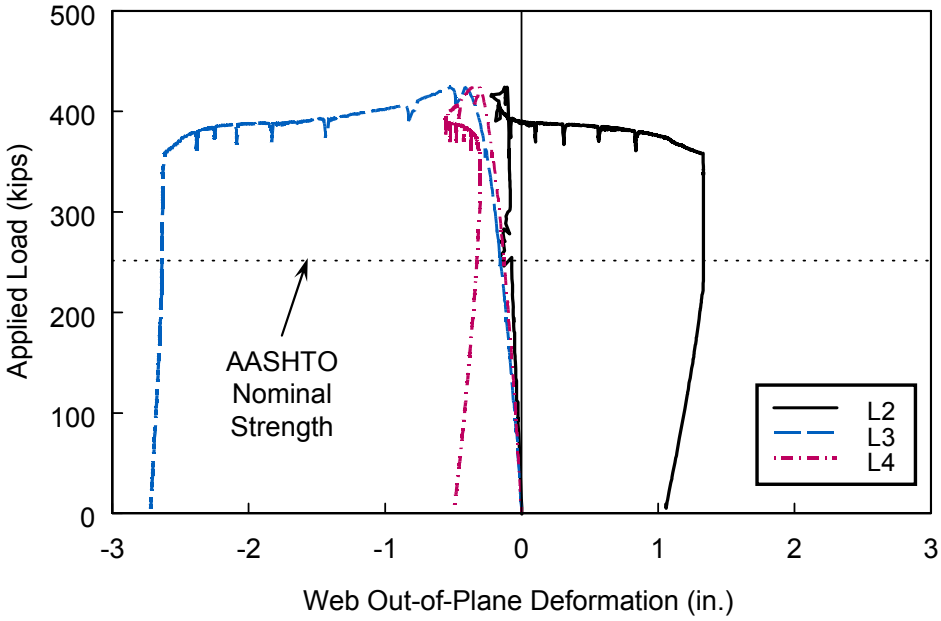

(a) East End Panel

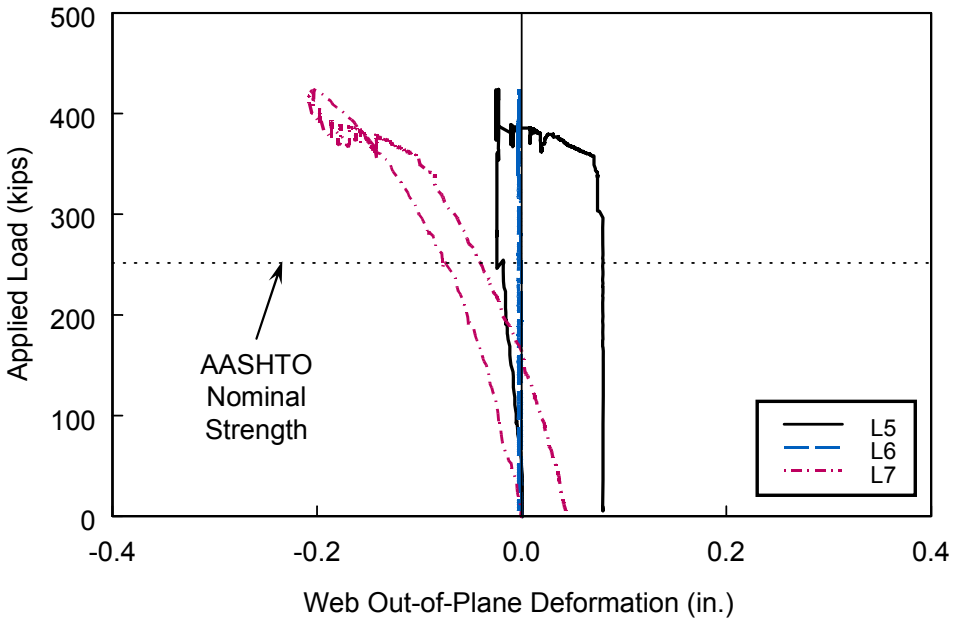

(b) West End Panel

Figure 8.32: Specimen SG3: Web Out-of-Plane Deformation

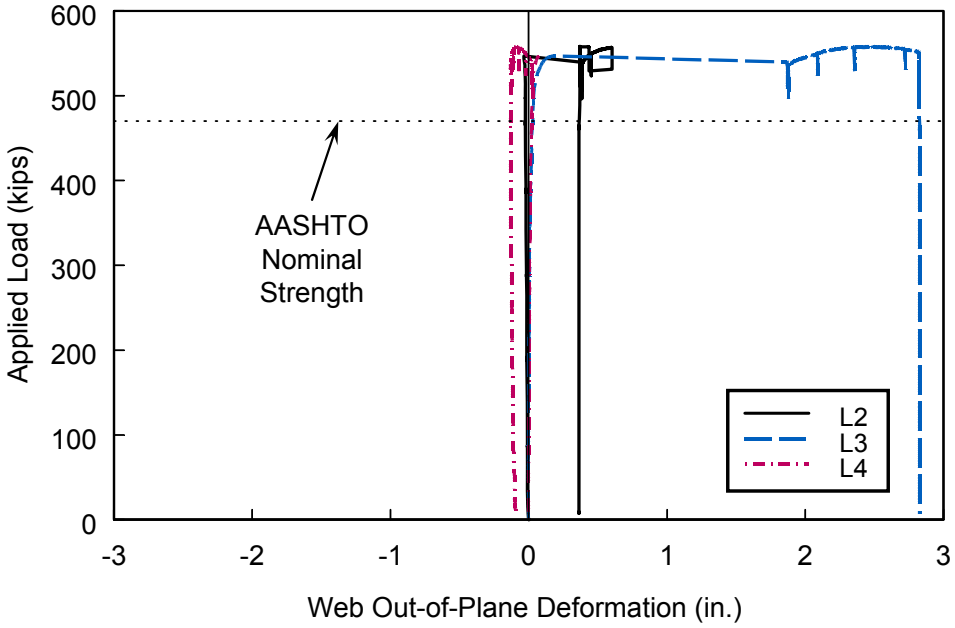

(a) East End Panel

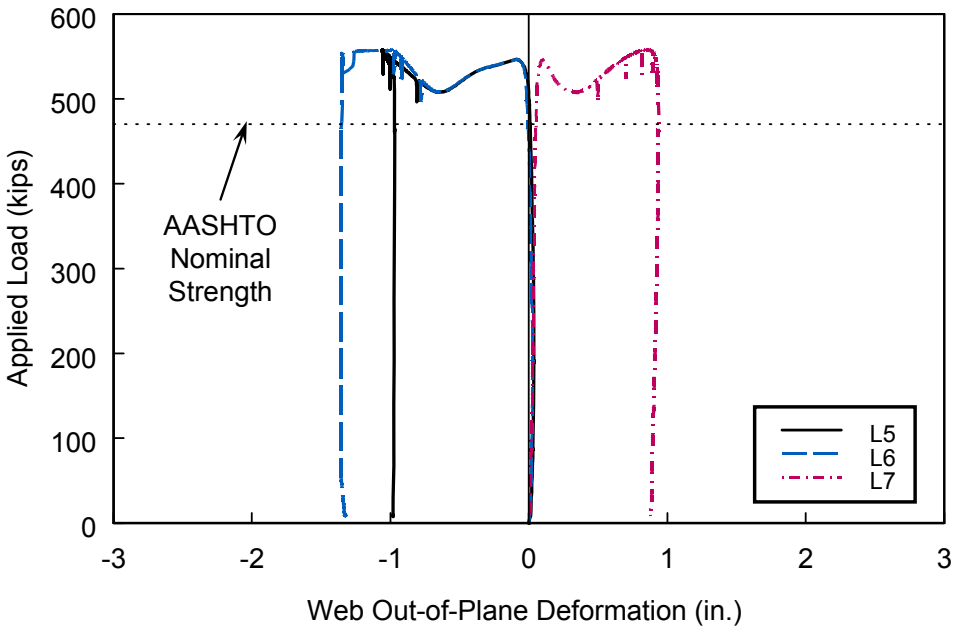

(b) West End Panel

Figure 8.33: Specimen SG4: Web Out-of-Plane Deformation

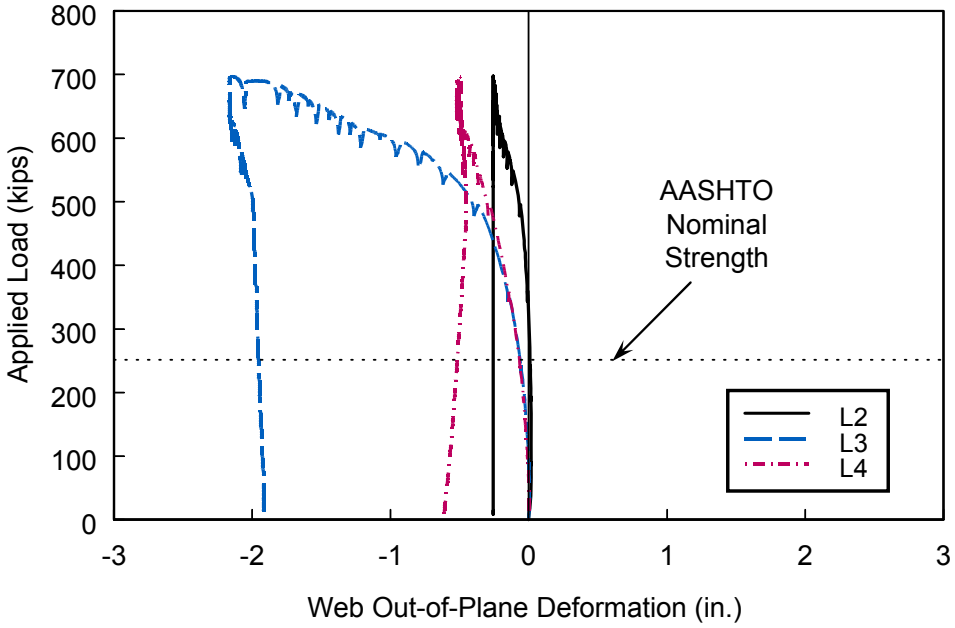

(a) East End Panel

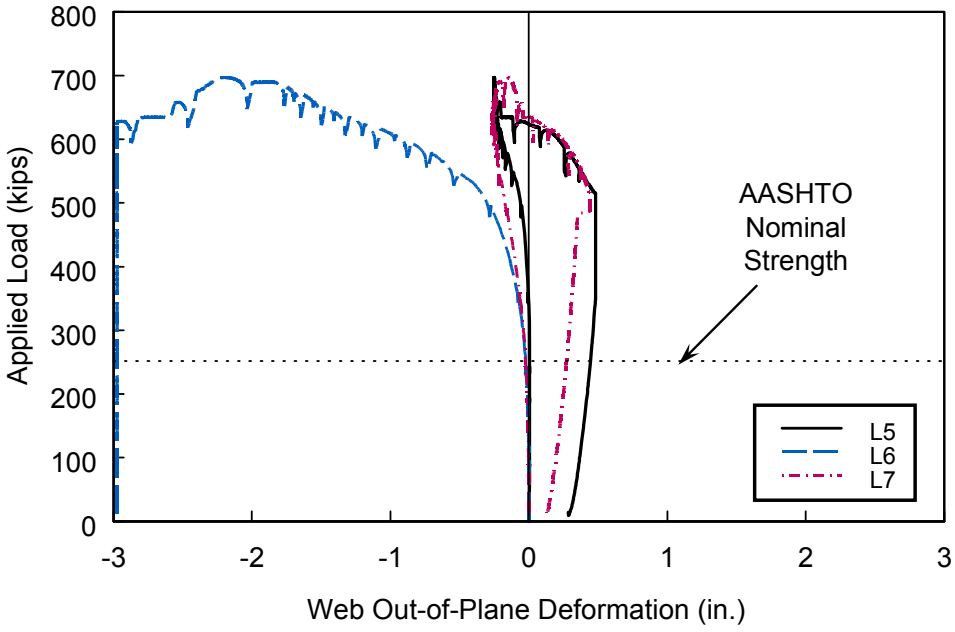

(b) West End Panel

Figure 8.34: Specimen CG3 Web Out-of-Plane Deformation

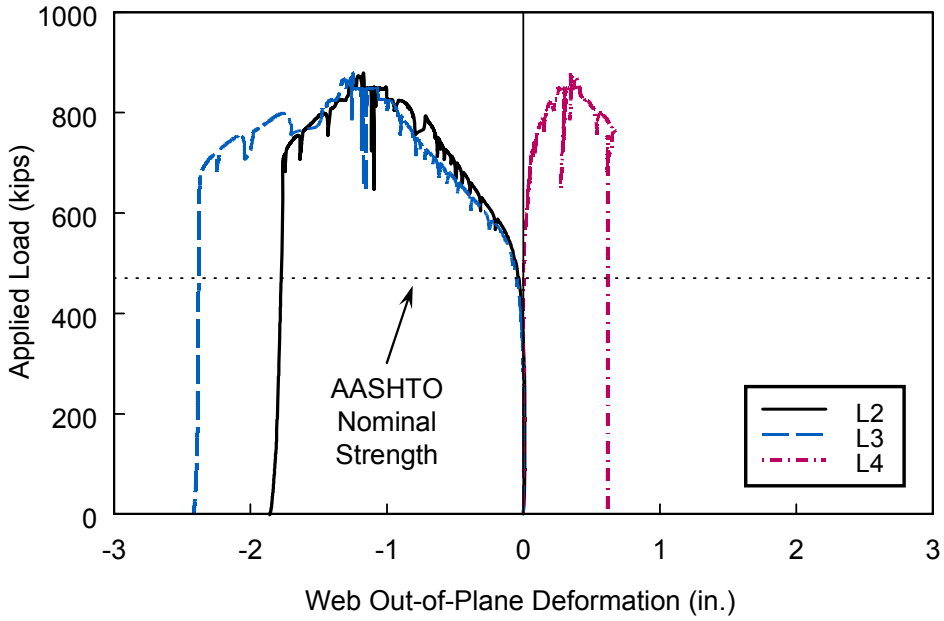

(a) East End Panel

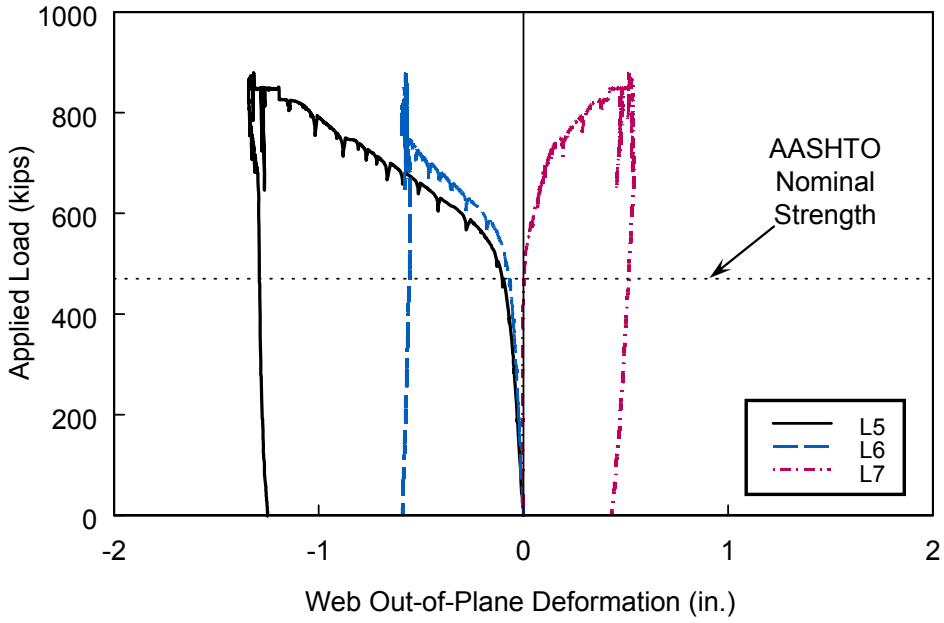

(b) West End Panel

Figure 8.35: Specimen CG4 Web Out-of-Plane Deformation

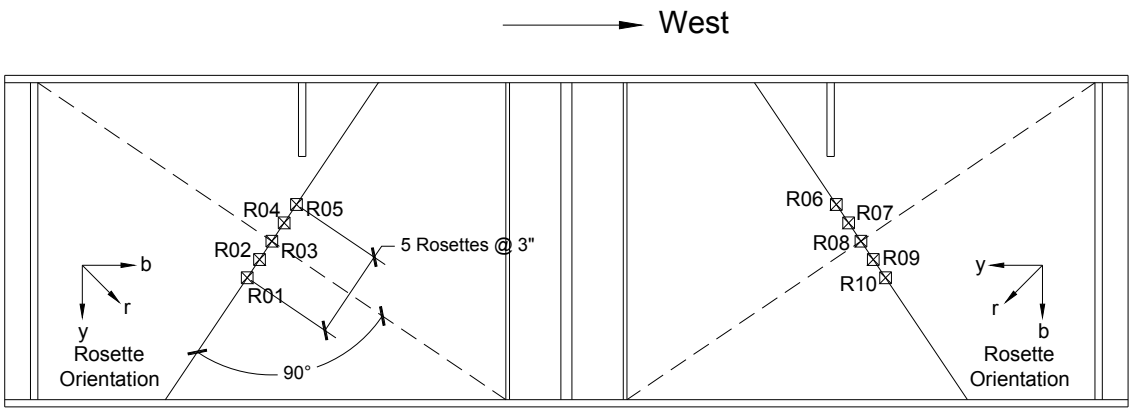

(a) Specimens SG3 and CG3

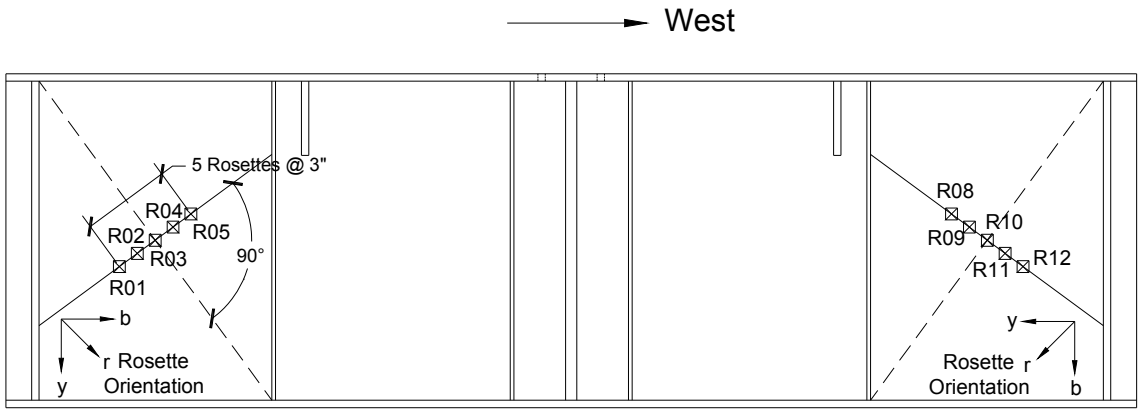

(b) Specimens SG4 and CG4

Figure 8.36: Locations of Strain Rosettes in End Panels (Back Side)

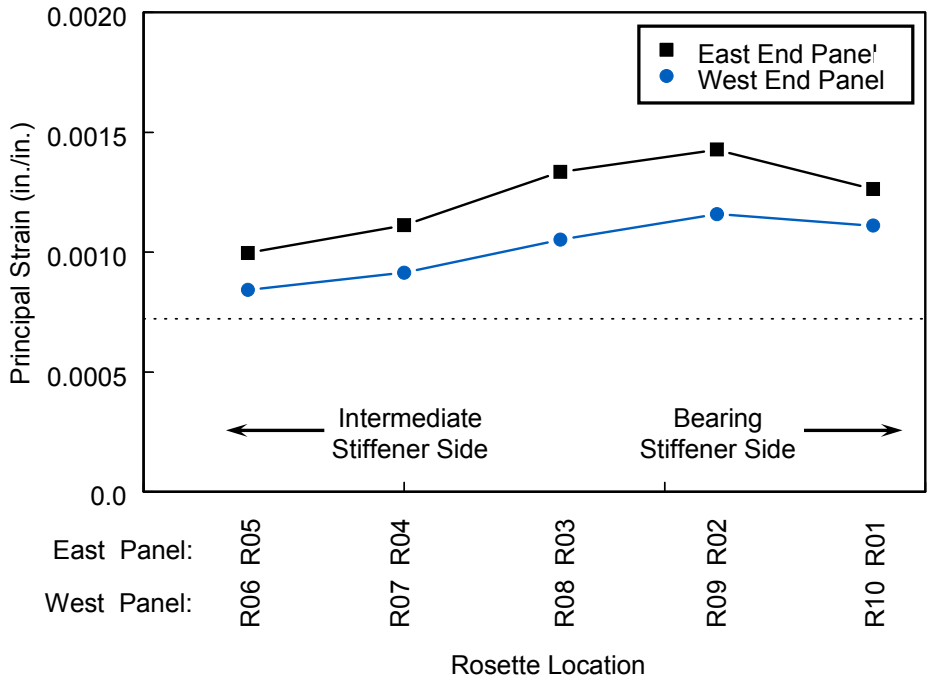

(a) Specimen SG3

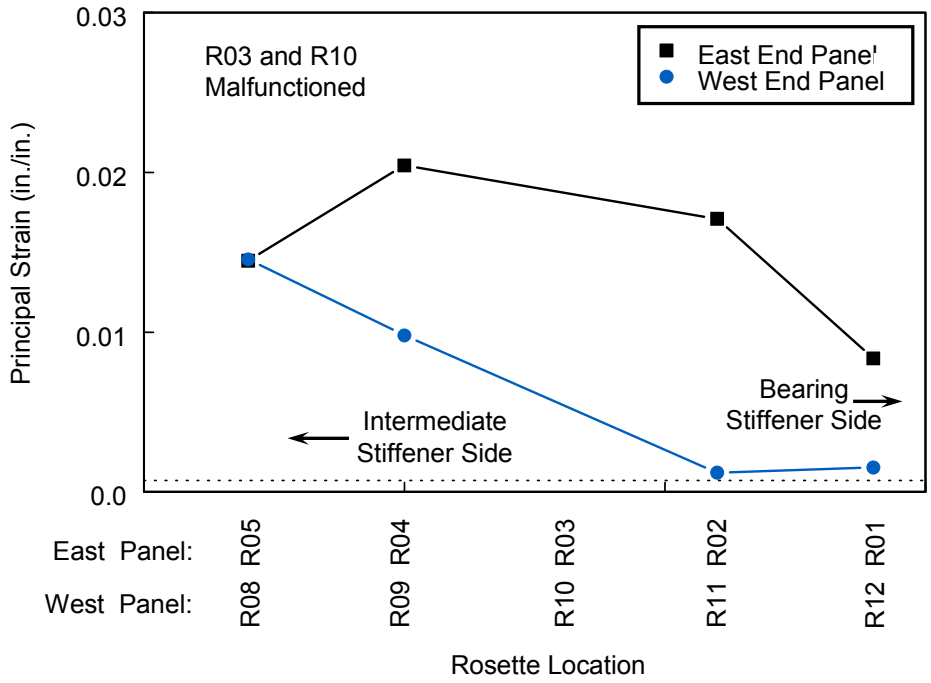

(b) Specimen SG4

Figure 8.37: Principal Strains across Panel Diagonals at Maximum Load

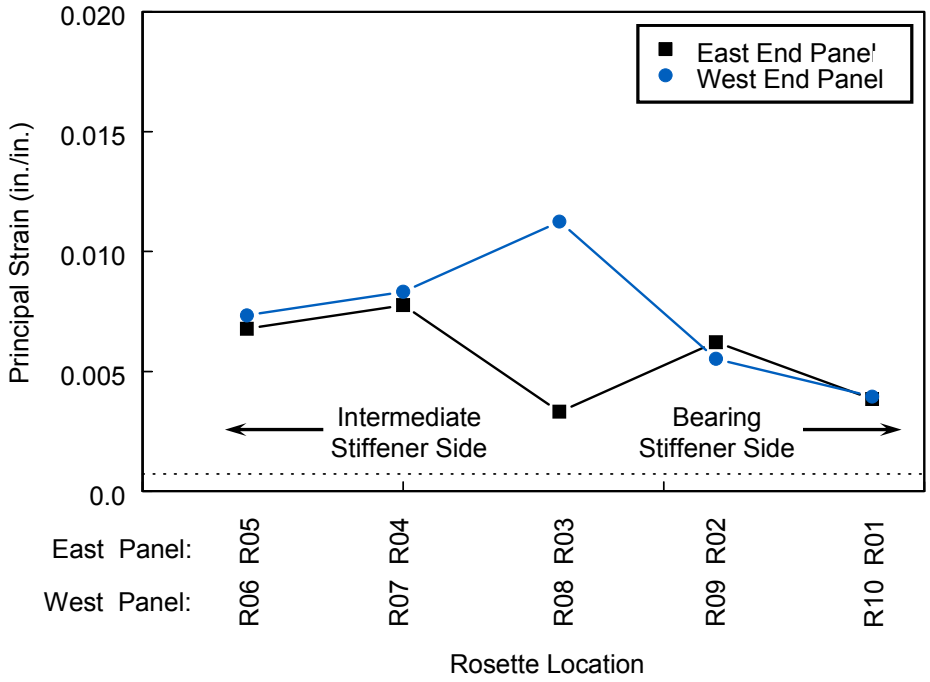

(c) Specimen CG3

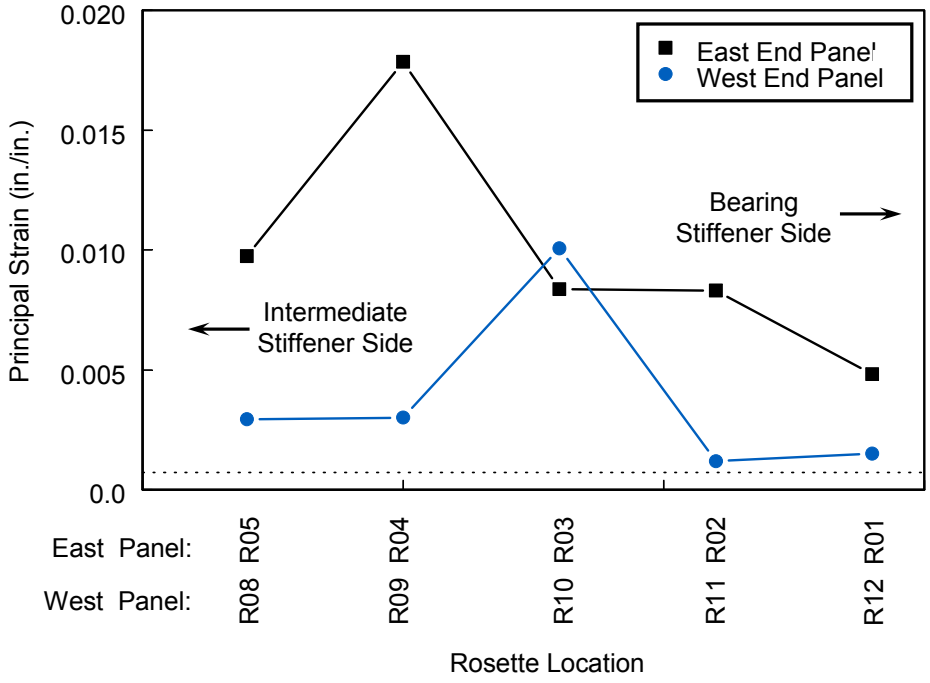

(d) Specimen CG4

Figure 3.34: Principal Strains across Panel Diagonals at Maximum Load (continued)

Specimen No.	*a* (in.)	*b* (in.)
SG3	20.13	15.25
CG3	17.5	15.0
SG4	15.5	18.5
CG4	14.25	17.5

Figure 8.38: Measured Plastic Hinge Locations

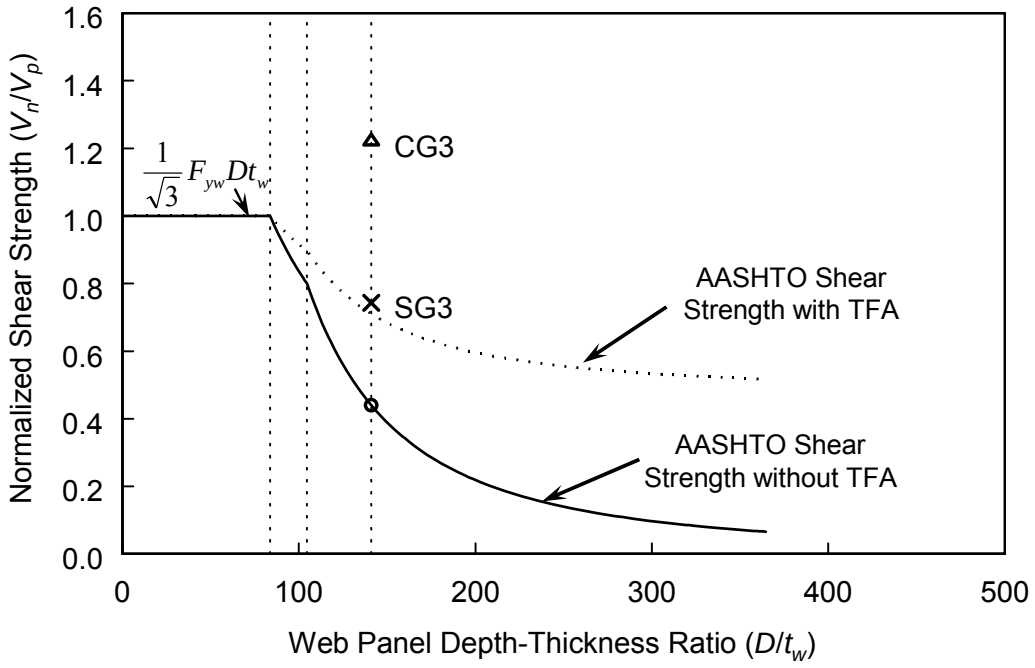

(a) Specimens SG3 and CG3

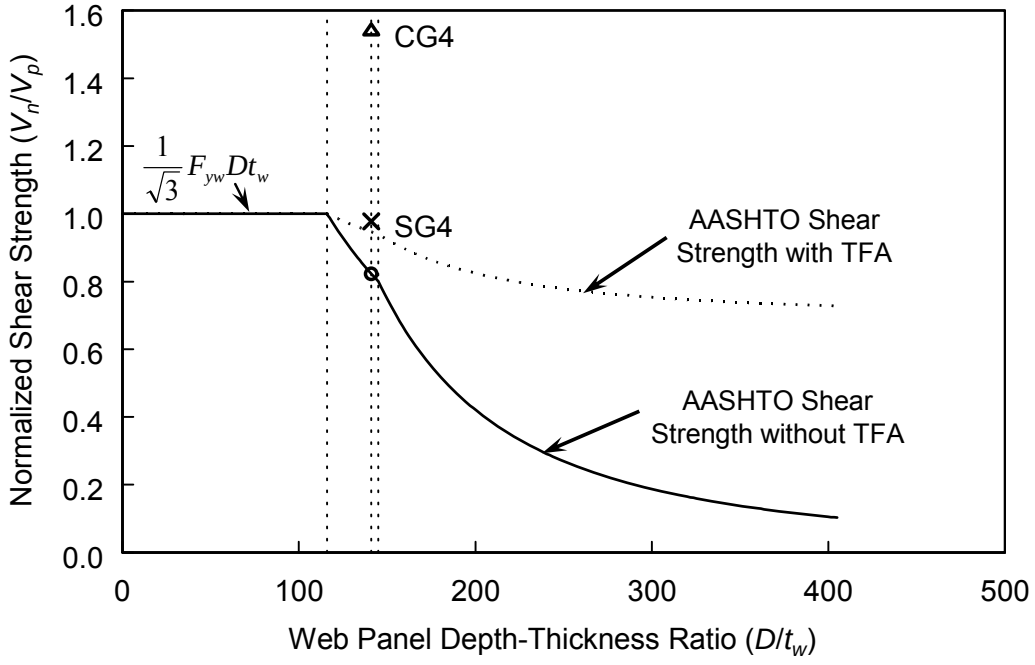

(b) Specimens SG4 and CG4

Figure 8.39: Comparison between Test Results and AASHTO Nominal Shear Strengths

9. ANALYTICAL STUDY OF TEST SPECIMENS (PHASE 2)

9.1 Nonlinear Finite Element Analysis

9.1.1 General

Standard 3-D shell elements (S4R) were used to model steel plate girder specimens (Specimens SG3 and SG4), while the eight-node linear brick elements (C3D8R) were used to model the concrete slab for Specimens CG3 and CG4. The steel reinforcement and shear studs were modeled with two-node linear beam elements (B31). True stress and strain were calculated from the engineering stress and strain from the coupon test results and used to describe the nonlinear behavior of the materials (see Chapter 4). A simply supported boundary condition was used, and the lateral bracing was simulated by preventing the lateral movement of the bracing locations. Also, the measured plate thicknesses shown in Table 8.3 were used in the finite element models. Residual stresses were not considered, but initial geometrical imperfections were incorporated in the analysis.

9.1.2 Steel Plate Girder Specimens (SG3 and SG4)

Figure 9.1 shows the typical finite element model. Figure 9.2 and Figure 9.3 show the buckling patterns of Specimens SG3 and SG4 from both testing and finite element analysis. The corresponding load-deflection curves are compared in Figure 9.4. As shown in the figures, the finite element analysis could reasonablely simulate the behavior of both specimens. The buckling patterns of the test specimens and finite element models were very similar, and the load-deflection curves between the two were also similar. Although the maximum load was achieved at a larger mid-span deflection, the value of the maximum load from the finite element analysis is very close to the one from the test results. The ratios of ultimate shear strength from experimental testing to that from finite element analysis are 1.00 for both specimens (see Table 9.1).

Figure 9.5 compares the plastic hinge locations formed in the top flange and bearing stiffeners. Plastic hinge locations (*a* and *b*) from experimental testing and finite

element analysis are summarized in the corresponding table. As shown in the figure and table, the plastic hinges formed in similar locations.

9.1.3 Composite Plate Girder Specimens (CG3 and CG4)

The correlation between the predicted and experimental responses for the steel-concrete composite girder specimens is provided in Figure 9.6. The response from Model CG3 is very close to that from Specimen CG3 up to the maximum load. After reaching the maximum load, Model CG3 showed a load drop of about 1-kip and the analysis was stopped due to the convergence issues [see Figure 9.6(a)]. Model CG4 showed a little soft behavior in the second branch (nonlinear region) and the analysis was stopped at a deflection of about 1.0 in. due to the convergence issues. For this reason, the buckling patterns of Specimens CG3 and CG4 from both testing and finite element analysis were compared at were compared at this displacement level as shown in Figure 9.7 and Figure 9.8. The ratios of ultimate shear strengths obtained form the experiments to those of finite element analyses are 0.99 and 1.08 for Specimens CG3 and CG4, respectively (see Table 9.1).

9.2 Comparison of Test Results with Predictive Equation

The predicted shear strengths of the specimens were calculated by using the proposed Eq. (6.33) for steel girder specimens (Specimens SG3 and SG4). Table 9.2 compares the shear strengths from tests, finite element analysis, and prediction from Eq. (6.33). Since the calculated α is greater than 1.0 for both specimens, the coefficient α of 1.0 is adopted for both calculations. Therefore, the calculated shear strength from Eq. (6.33) provides the same prediction for the case of interior panels with tension-field action per AASHTO Specifications (2014). The ratios of the shear strengths from the predictive equation to those from the tests are 0.95 for both Specimens SG3 and SG4.

Table 9.3 summarizes the shear strengths for composite girder specimens (Specimens CG3 and CG4). The predicted shear strengths for both specimens were still too conservative compared to the results from both tests and finite element analyses. The ratios of the shear strengths from the predictive equation to those from the tests are

0.71 for both Specimens CG3 and CG4. The conservatism is mainly from Eq. (6.48) for predicting the contribution from concrete slab.

9.3 Modification of Predictive Equation for Concrete Shear Strength

In developing Eq. (6.48), it was assumed that only one compression strut developed as shown in Figure 6.23. Because shear connectors were much more closely space in Phase 2 specimens, multiple compression struts could be developed. Figure 9.9(b) and Figure 9.10(b) show that the major cracks occurred between the two observed plastic hinges.

For CG3, Figure 9.9(c) shows four rows of shear connectors existed between plastic hinges. The "effective" compression strut can be assumed to run from points *A* and *B*. The strut angle is

$$\phi = \tan^{-1}\left(\frac{h_s}{S_h}\right) \tag{9.1}$$

where h_s is the stud height and S_h is the distance between the bearing stiffeners and the first row of shear connectors to the right of the interior plastic hinge as shown in Figure 9.9(c). The horizontal component of the compression force in the strut is limited by the shear strength of the shear connectors, which can be computed as nQ_n, with n = number of shear connectors between the plastic hinges and Q_n = nominal shear resistance of a single shear connector. According to AISC Specificatios (2010), Q_n is determined as:

$$Q_n = 0.5A_{sa}\sqrt{f_c^{'}E_c} \le R_g R_p A_{sa} F_u \tag{9.2}$$

where A_{sa} = cross-sectional area of the shear stud, $f_c^{'}$ = concrete compressive strength, E_c = modulus of elasticity of concrete, F_u = the specified minimum tensile strength, and the values of R_g and R_p are 1.0 and 0.75, respectively, when the studs are welded directly to the steel girder. Then, the vertical component of the effective compression strut force is the vertical shear resisted by the concrete slab:

$$V_c = nQ_n \tan\phi \tag{9.3}$$

By applying the above procedure to CG4, Figure 9.10(c) shows the effective compression strut. This procedure results in a ϕ value of 17.3° and 21.7° for CG3 and CG4, respectively, which correlate well with the observed crack angles in Figure 9.9(a) and Figure 9.10(a). The calculated V_c and the total shear resistances are suumarized in Table 9.4. The ratios of the shear strengths from the modified prediction to those from the tests are 0.99 and 0.91 for Specimens CG3 and CG4, respectively.

Note that Eq. (6.48) was developed on the basis that compression failure of the concrete strut is the limit state, while Eq. (9.3) for a composite slab with closely spaced shear connectors used the shear strength of the connectors as the limit state. Further study is needed to establish a criterion in judging which limit state would govern the shear strength of concrete slab (V_c).

Table 9.1: Shear Strength Comparison between FEM and Experiments

Specimen No.	Panel Shear Strength, V (kips)		V_{TEST} / V_{FEM}
	FEM Result, V_{FEM}	Test Result, V_{TEST}	
SG3	211.3	212.1	1.00
SG4	277.9	279.0	1.00
CG3	351.4	348.6	0.99
CG4	411.5	445.4	1.08

Table 9.2: Shear Strength Comparison (Steel Girder Specimens)

Specimen No..	α	Shear Strength, V_s (kips)		
		Test	FEM	Prediction [Eq. (6.33)]
SG3	1.0	212.1	211.3	200.6
SG4	1.0	279.0	277.9	266.2

Table 9.3: Shear Strength Comparison (Composite Girder Specimens)

Specimen No.	Test (kips)	FEM (kips)	Prediction (kips)		
			V_s [Eq. (6.33)]	V_c [Eq. (6.48)]	V_n (= V_s+V_c) [Eq. (6.43)]
CG3	348.6	351.4	200.6	48.1	248.7
CG4	445.4	411.5	266.2	50.1	316.3

Table 9.4: Comparison of Shear Strength between Modified Prediction and Test Results

Specimen No.	Test (kips)	Prediction (kips)			$\frac{\text{Prediction}}{\text{Test}}$
		V_s [Eq. (6.33)]	V_c [Eq. (9.3)]	V_n (= V_s+V_c) [Eq. (6.43)]	
CG3	348.6	200.6	146.0	346.6	0.99
CG4	445.4	266.2	139.9	406.1	0.91

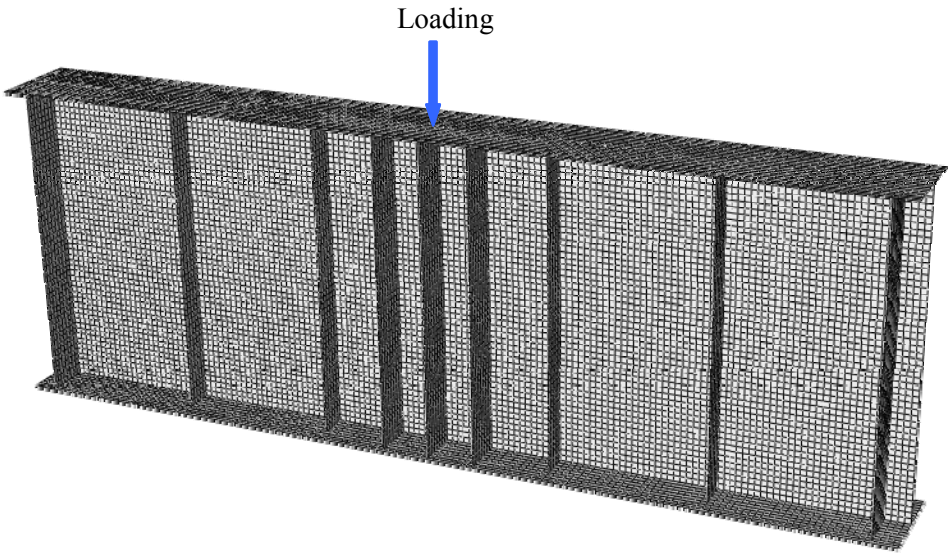

Figure 9.1: Specimen SG3: Typical Finite Element Model and Mesh

(a) Experiment

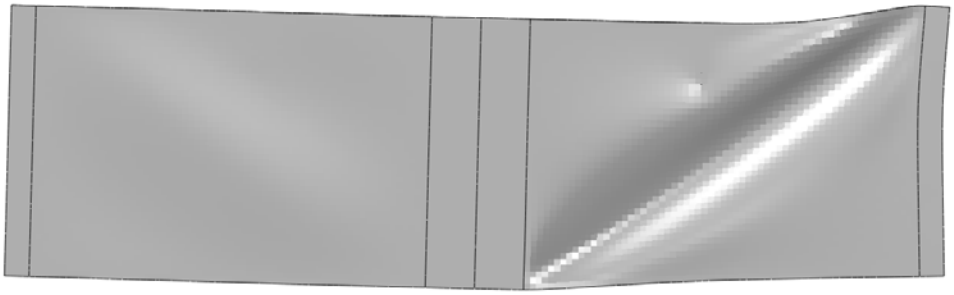

(b) Finite Element Analysis

Figure 9.2 Comparison of Buckling Pattern of Specimen SG3

(a) Experiment

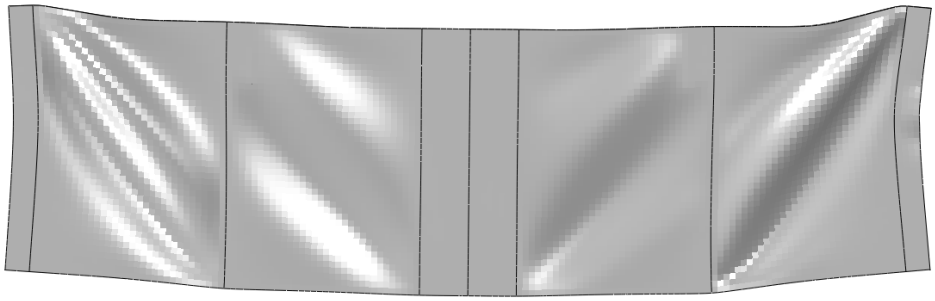

(b) Finite Element Analysis

Figure 9.3 Comparison of Buckling Pattern of Specimen SG4

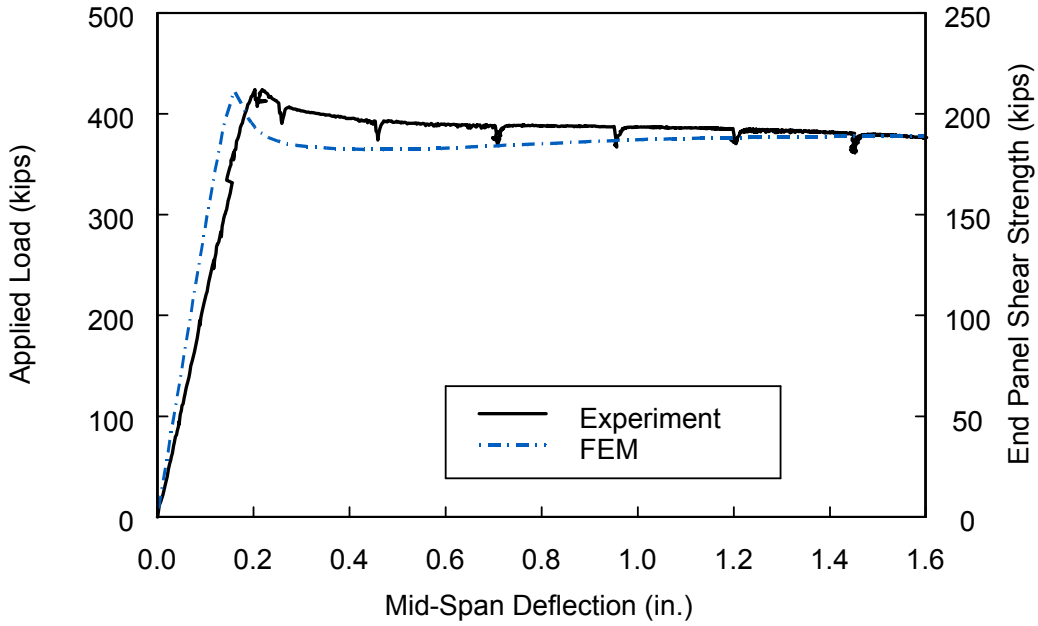

(a) Specimen SG3

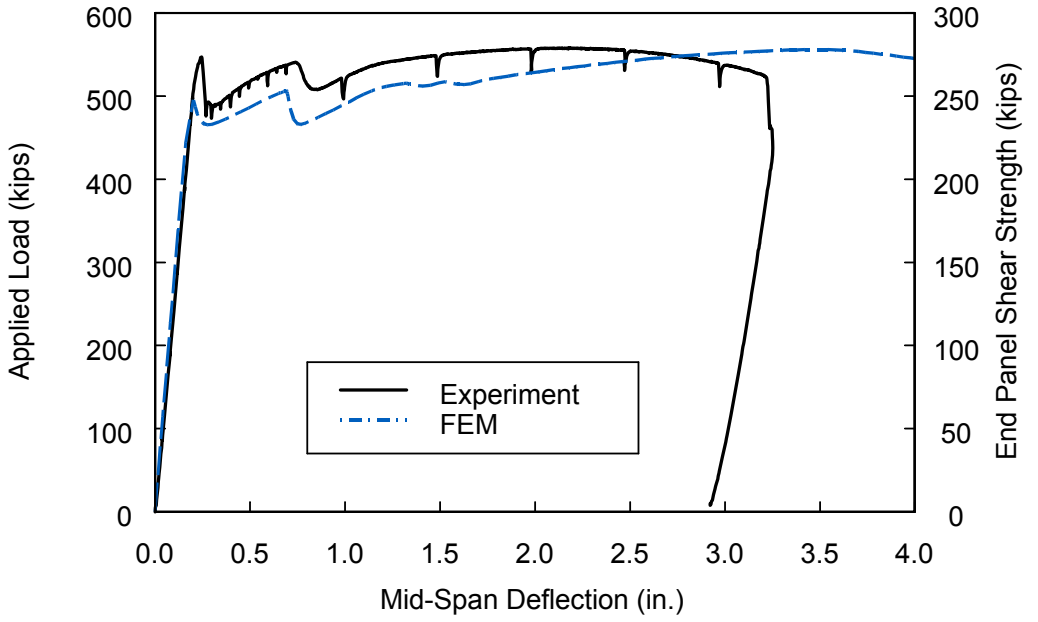

(b) Specimen SG4

Figure 9.4: Correlation between Test Results and FEM Analyses

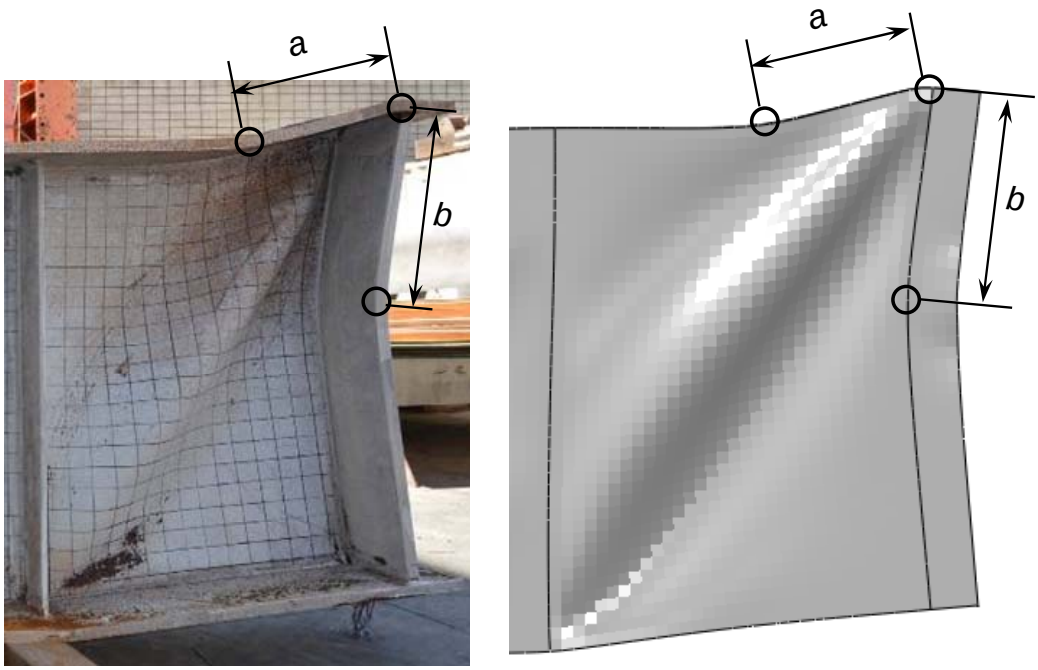

Specimen No.	*a* (in.)		*b* (in.)	
	Test	FEM	Test	FEM
SG3	20.1	19.2	15.3	15.0
SG4	15.5	14.1	18.5	17.0

Figure 9.5: Comparison of Plastic Hinge Locations

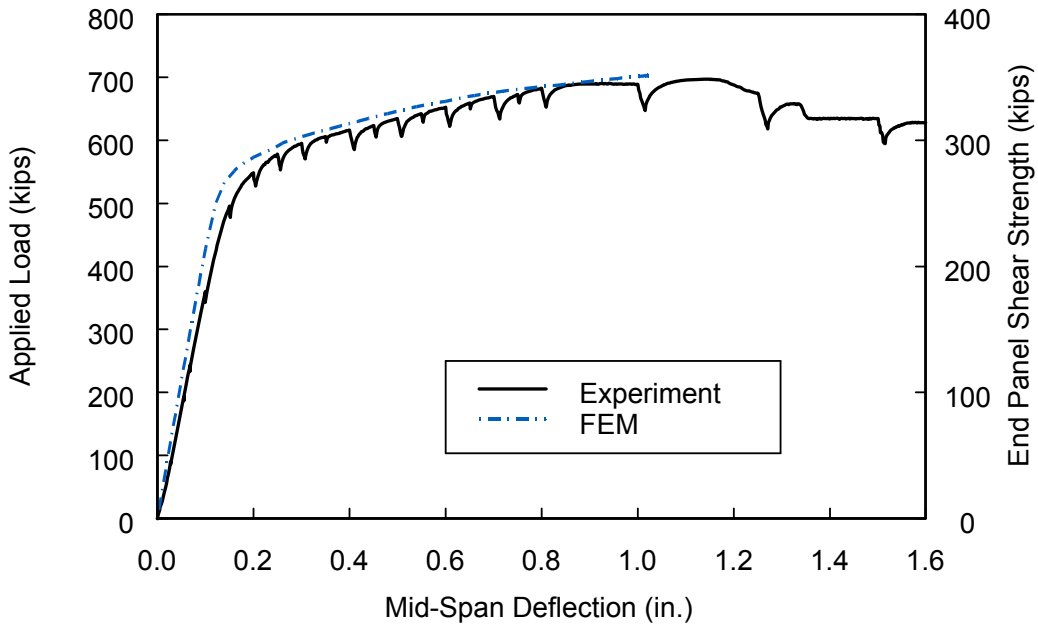

(a) Specimen CG3

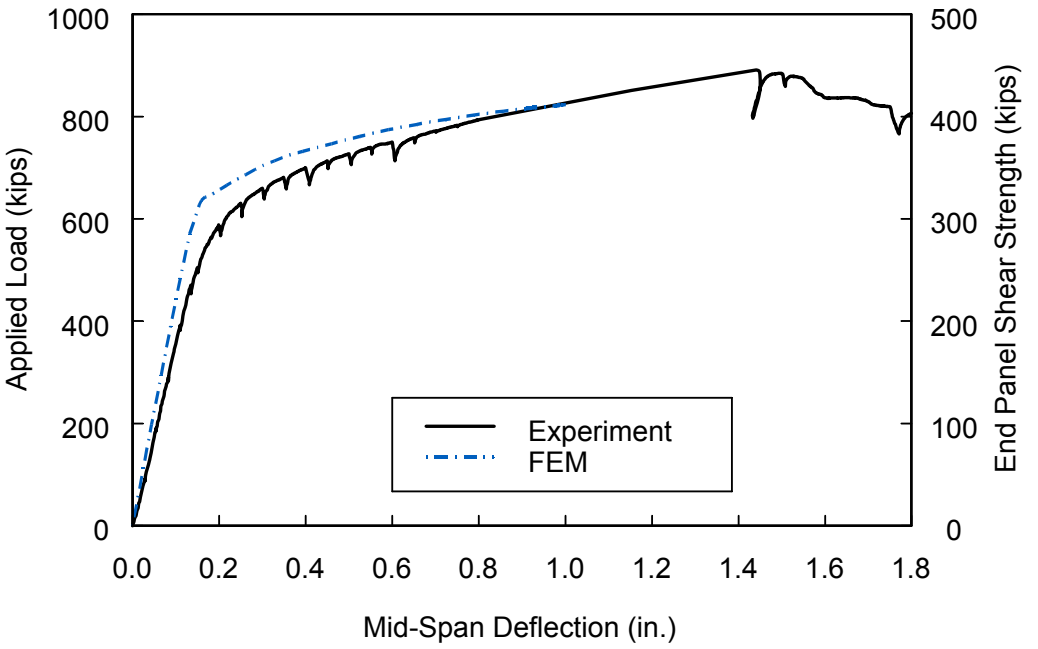

(b) Specimen CG4

Figure 9.6: Correlation between Test Results and FEM Analyses (CG3 and CG4)

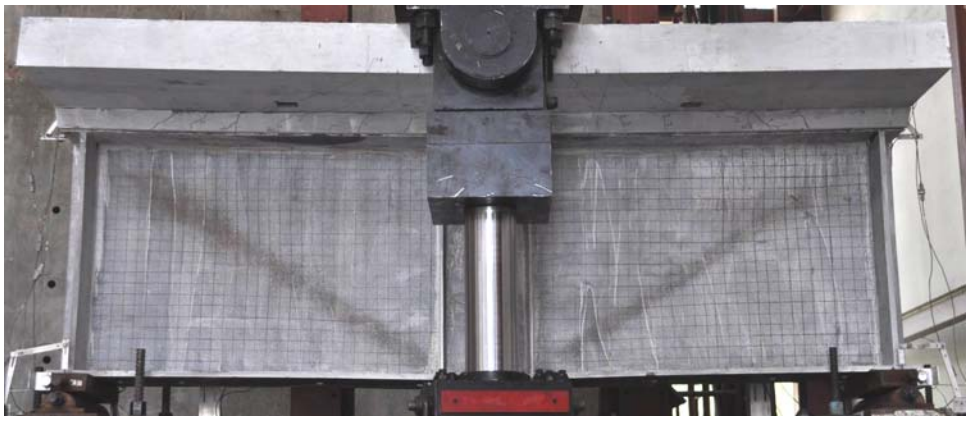

(a) Experiment

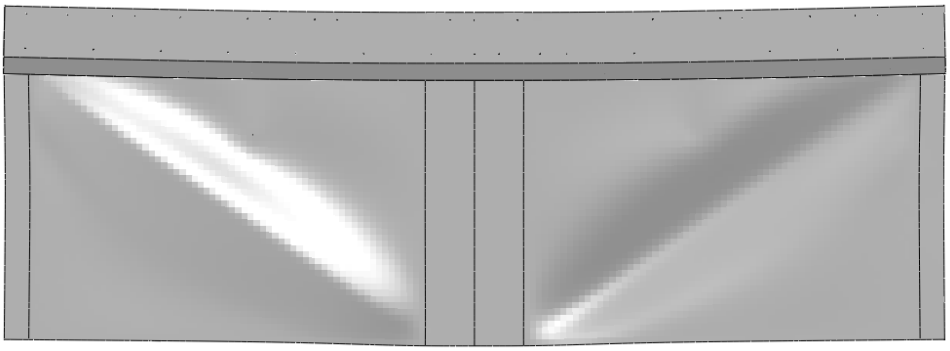

(b) Finite Element Analysis

Figure 9.7 Comparison of Buckling Pattern of Specimen CG3 (at 1.0 in. Disp.)

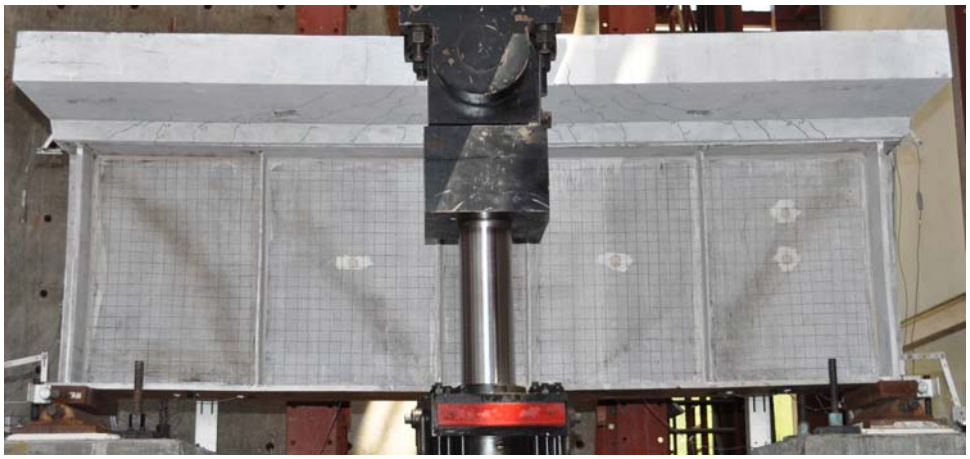

(a) Experiment

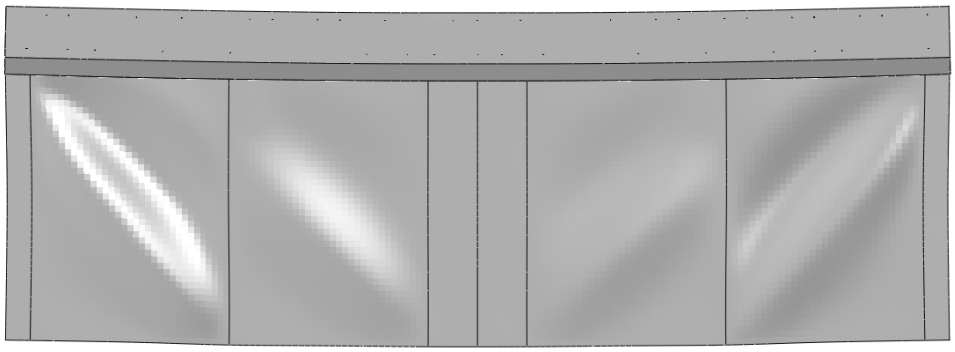

(b) Finite Element Analysis

Figure 9.8 Comparison of Buckling Pattern of Specimen CG4 (at 1.0 in. Disp.)

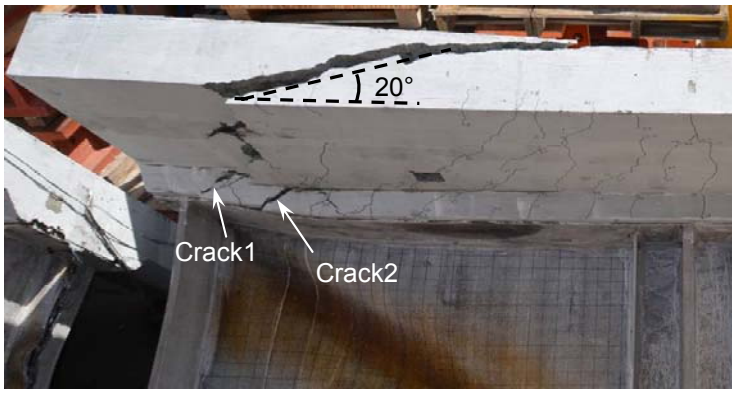

(a) Crack Angle

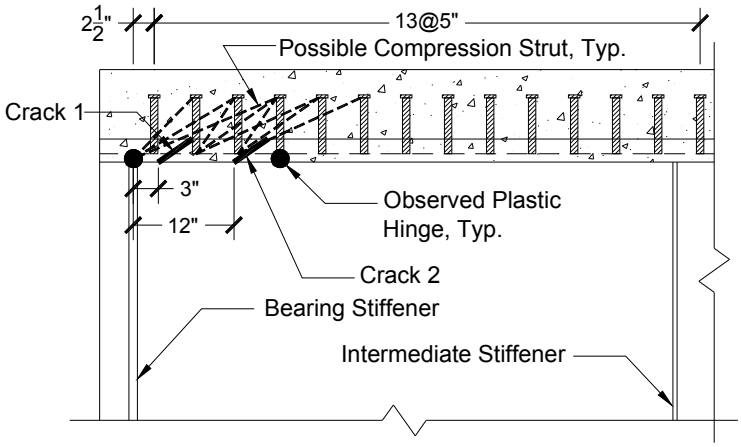

(b) Possible Formation of Compression Struts

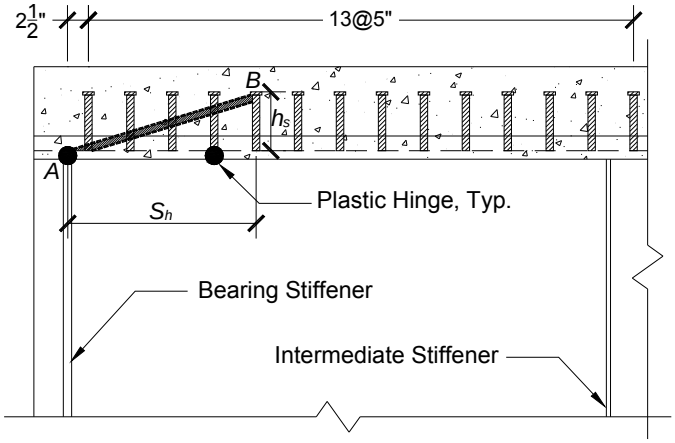

(c) Effective Compression Strut

Figure 9.9: Assumed Compression Strut (Specimen CG3)

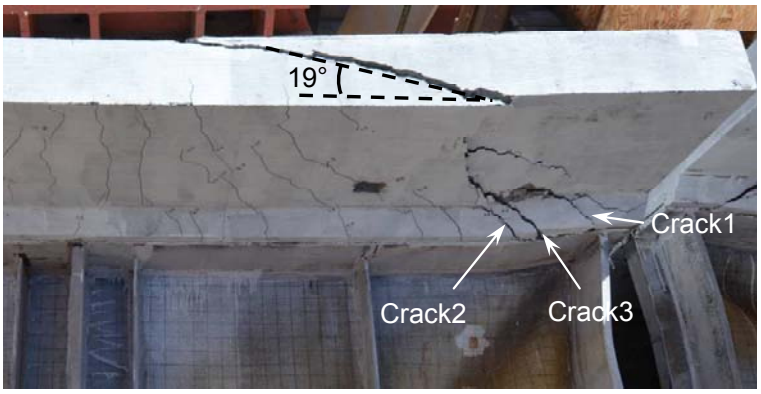

(a) Crack Angle

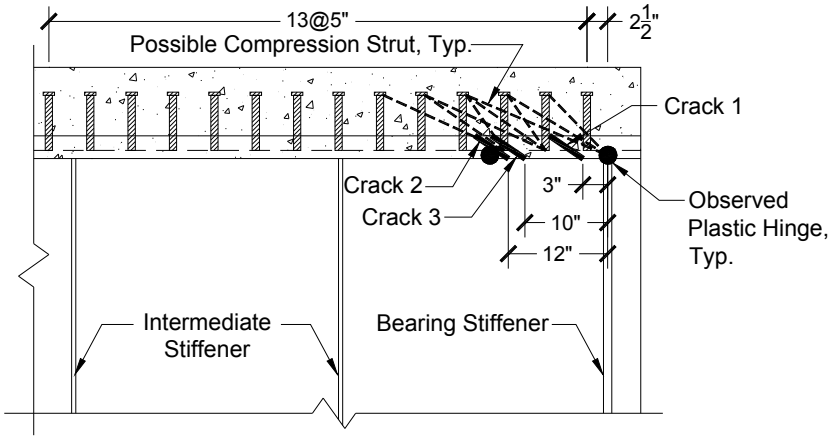

(b) Possible Formation of Compression Struts

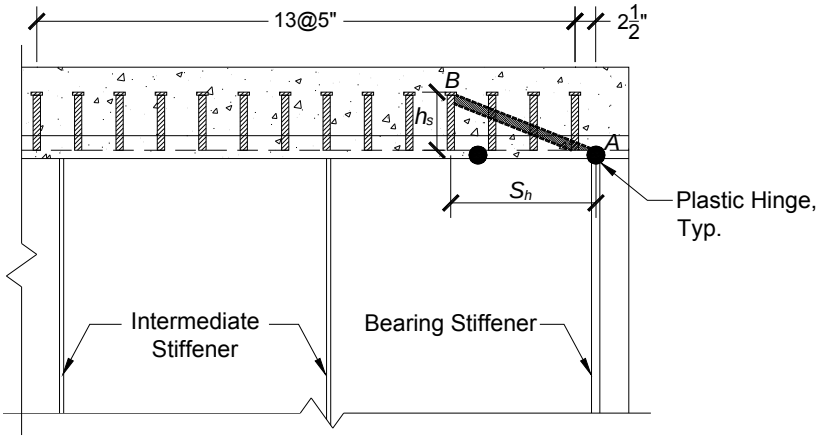

(c) Effective Compression Strut

Figure 9.10: Assumed Compression Strut (Specimen CG4)

10. NUMERICAL PARAMETRIC STUDY

10.1 General

Since the results of nonlinear finite element analyses correlated well with the test results, additional numerical study with ABAQUS was carried out to further investigate the behavior of plate girder end panels. In this chapter, the effects of longitudinal stiffener, small flange areas, large width-depth ratios, noncompact web, and unequal top and bottom flanges are examined.

10.2 Effect of Longitudinal Stiffener

Longitudinal stiffeners are frequently used in existing highway bridge girders. The primary function of longitudinal stiffeners is to control lateral web deflections, and hence the longitudinal stiffeners can serve as a simple support. As a result, two subpanels are simply supported and each subpanel would develop its own shear strength. By summing up the shear strengths from each subpanel, the ultimate shear strength of the entire panel with longitudinal stiffener can be determined. Cooper (1966) also assumed that each subpanel develops its own tension field after buckling based on the observation from the experimental testing conducted by Fielding and Cooper (1965).

A study by Rockey and Leggett (1962) showed that the optimum location of a longitudinal stiffener under pure bending is at about 0.2 of the web depth (0.2D) from the compressive flange, while its optimum location under pure shear is at mid-depth (0.5D), respectively. For combined shear and bending, the longitudinal stiffener should be located between 0.2D and 0.5D (Salmon and Johnson, 1996). With those two longitudinal stiffener locations, nonlinear finite element analyses with longitudinal stiffeners added in Models SG1 and SG2 were carried out to investigate the effect of the longitudinal stiffener.

Figure 10.1 shows the finite element models with two different placements of longitudinal stiffeners. The longitudinal stiffeners were added to both sides of the web and extended to the ends of the girder. The same material properties and thicknesses from the flanges of each specimen were used for the longitudinal stiffeners. Table 10.1

summarizes the shear strength of each subpanel and the entire shear strength of the end panels. For example, subpanel 1 in Model SG1LS02 has a depth-thickness ratio of 42, which falls in the shear yield zone with a shear yield strength ($V_y = 0.58A_wF_{yw}$) of 91.8 kips. However, subpanel 2 falls in the elastic buckling zone where the proposed equation [Eq. (6.33)] was used to calculate the shear strength. The calculated α value from Eq. (6.36) was 0.862 and the shear strength from Eq. (6.33) was 297.4 kips. Summing up the shear strength of each subpanel gives an ultimate shear strength ($V_{prediction}$) of 362 kips. This calculation slightly overestimates the shear strengthresult from FEM (see Figure 10.2). However, the ultimate shear strengths predicted by this procedure for the other models (Models SG2LS02, SG1LS05, and SG2LS05) correlate well but with a slight conservatism as shown in Figure 10.3 through Figure 10.5. Therefore, the proposed Eq. (6.36) provides either close or somewhat conservative shear strength when longitudinal stiffeners are used.

Note from the buckling patterns (Figure 10.2 through Figure 10.5) that subpanels 1 and 2 tend to develop the same tension-field angle which is the diagonal direction of the larger subpanel (subpanel 2 in this case). This trend was also observed in Cooper's testing (see Figure 10.6), although he assumed the tension field angle would always be the diagonal in each subpanel.

10.3 Effect of Small Flange Areas

For an interior panel to be qualified for a tension-field action, AASHTO Specifications (2014) require that the flange area be sufficiently large:

$$V_n = V_p\left[C + \frac{0.87(1-C)}{\sqrt{1+(d_0/D)^2}}\right] \qquad \text{for } \frac{2Dt_w}{(b_{fc}t_{fc}+b_{ft}t_{ft})} \le 2.5 \qquad (10.1)$$

When Eq. (10.1) is violated, the AASHOTO Specifications provide the following equation to account for the partial tension-field action:

$$V_n = V_p\left[C + \frac{0.87(1-C)}{\sqrt{1+(d_0/D)^2}+(d_0/D)}\right] \qquad \text{for } \frac{2Dt_w}{(b_{fc}t_{fc}+b_{ft}t_{ft})} > 2.5 \qquad (10.2)$$

That is, the AASHTO Specifications provide two shear strength equations for the interior panels, depending on whether sufficient flange areas are provided. For end panels,

however, the proposed Eq. (6.33) explicitly considers the effect of small flanges in the form of M_{pf} in Eq. (6.36). To check the adequacy of Eq. (6.33) when small flanges are used, an additional six ABAQUS models, which were variations of Specimens SG1 and SG2, were created and analyzed (see Table 10.2). From Specimen SG1, the flange thickness and the width were taken as 0.5 in. and 8 in., respectively, such that the following web-to-flange area ratio is 3.28 which is larger than 2.5. This ratio is applied to three different width-depth ratios (0.5, 1.0, and 1.5) as shown in Models SG1-1, -2, and -3 in Table 10.2. Similarly, Models SG2-1, -2, and -3 were modified from Specimen SG2. The flange thickness and width used for the models are also presented in Table 10.2. The ultimate shear strengths of FEM and prediction [i.e., Eq. (6.33)] are compared in Table 10.3. The average shear strength ratio of prediction to FEM is 0.9 with a standard deviation of 0.03. Figure 10.7 plots the results to compare the ultimate shear strengths of prediction and FEM. The proposed equation still provides an accurate and slightly conservative estimate of the actual shear strength.

10.4 Effect of Noncompact Web

A noncompact web is a web that experiences inelastic buckling. Since Specimen SG4 had the noncompact web, the plastic hinge locations per the proposed equation were different than the actual hinge locations, although the predicted ultimate shear strength is still close to the test result due to the limit of $\alpha\,(\leq 1.0)$. To further investigate the effect of a noncompact web, three finite element models per each test specimen were modeled by varing the web thicknesses. For Specimens SG1 with a web yield stress of 60.3 ksi and a width-depth ratio of 0.5, the depth-thickness ratios should be between 123 and 154 to be classified as a noncompact web. Table 10.4 summarizes the range of the depth-thickness ratios required for a noncomapc web in each test specimen. The depth-thickness ratios for SG1 series of models were selected to vary from 130 to 150. See Table 10.5 for the selected depth-thickness ratios for the other finite element models. The ultimate shear strengths of finite element analyses, predictions per Eq. (6.33), and AASHTO Specifications are also summarized in the table.

Figure 10.8 presents the predicted shear strengths per Eq. (6.33) and AASHTO Specifications, normalized by FEM results. It is noted from Figure 10.8(a) that the

proposed equation overestimates the ultimate shear strength by approximately 16%. However, Figure 10.8(b) shows that the proposed equation provides a very accurate estimation of the ultimate shear strength. The average ratio of the prediction to FEM is 1.00 with a standard deviation of 0.02. Since the proposed equation provides either a close or slightly nonconservative estimation when a noncompact web is used, the resistance factor (ϕ) may need to be determined separately.

10.5 Effect of Unequal Top and Bottom Flanges

Highway steel plate girder bridges often have top and bottom flanges of different dimensions. In Chapter 6, the ultimate shear strength of plate girder end panels was derived, assuming that both the top and bottom flanges have the same dimensions and steel grade.

Considering different top and bottom flanges, Eqs. (6.16) and (6.19) can be rewritten as:

$$V_{ps} = \frac{\left(M_{pf}^{t} + M_{pm}\right)}{a} + \frac{(D-b)\left(M_{pb} + M_{pm}\right)}{bd_0} + \frac{\left(M_{pf}^{b} + M_{pb}\right)}{d_0} + \left(\frac{a\sigma_t t_w \sin^2\theta}{2}\right) - \left(\frac{b\sigma_t t_w \cos^2\theta (D-b)}{2d_0}\right) + b\sigma_t t_w \sin\theta\cos\theta - \frac{\sigma_t t_w b^2 \cos^2\theta}{2d_0} \tag{10.3}$$

$$a = \sqrt{\frac{2(M_{pf}^{t} + M_{pm})}{\sigma_t t_w \sin^2\theta}} \tag{10.4a}$$

$$b = \sqrt{\frac{2(M_{pb} + M_{pm})}{\sigma_t t_w \cos^2\theta}} \tag{10.4b}$$

where M_{pf}^{t} and M_{pf}^{b} are the plastic moments of top and bottom flanges, respectively. Substituting Eq. (10.4) into Eq. (10.3), the post buckling strength (V_{ps}) is:

$$V_{ps} = \sigma_t t_w \sin\theta(a\sin\theta + b\cos\theta) + \frac{M_{pf}^{b} + M_{pb}}{d_0} - \frac{\sigma_t t_w b^2}{2d_0}\cos^2\theta \tag{10.5}$$

Therefore, summing up the beam action shear buckling strength (V_{cr}) and post-buckling strength (V_{ps}) gives the ultimate shear strength of an end panel with unequal top and bottom flanges.

$$V_s = \sigma_t t_w \sin\theta(a\sin\theta + b\cos\theta) + \frac{M_{pf}^b + M_{pb}}{d_0} - \frac{\sigma_t t_w b^2}{2d_0}\cos^2\theta + \tau_{cr} D t_w \qquad (10.6)$$

Substituting Eq. (10.4b) into the third term of Eq. (10.6) gives

$$V_s = \sigma_t t_w \sin\theta(a\sin\theta + b\cos\theta) + \frac{M_{pf}^b - M_{pm}}{d_0} + \tau_{cr} D t_w \qquad (10.7)$$

The second term on right-hand side of Eq. (10.7) is the additional shear capacitiy when the difference between top and bottom flange sizes is considered.

Consider two cases as in Section 6.6: weak flange and weak bearing stiffeners.

Case 1: $M_{pf}^t \le M_{pb}$ (weak flange)

In this case, M_{pm} equals to M_{pf}^t. Then, Eq. (10.7) becomes

$$V_s = \sigma_t t_w \sin\theta(a\sin\theta + b\cos\theta) + \frac{M_{pf}^b - M_{pf}^t}{d_0} + \tau_{cr} D t_w \qquad (10.8)$$

It is readily shown that the second term on right-hand side of Eq. (10.8) vanishes when top and bottom flanges are identical and, thus, Eq. (10.8) reduces to Eq. (6.24).

Case 2: $M_{pf} > M_{pb}$ (weak bearing stiffeners)

In this case, M_{pm} equals to M_{pb} and Eq. (10.7) becomes

$$V_s = \sigma_t t_w \sin\theta(a\sin\theta + b\cos\theta) + \frac{M_{pf}^b - M_{pb}}{d_0} + \tau_{cr} D t_w \qquad (10.9)$$

The additional shear capacity terms, $\left(M_{pf}^b - M_{pf}^t\right)/d_0$ for Case 1 or $\left(M_{pf}^b - M_{pb}\right)/d_0$ for Case 2 is generally small when compared with the remaining two terms in either Eq. (10.8) or Eq. (10.9). Therefore, by ignoring the additional shear terms, the proposed Eq. (6.33) is still applicable for cases with unequal top and bottom flanges. That is, the proposed equation essentially considers the size of the top flange only.

To validate that the proposed equation still can be used for unequal top and bottom flanges, additional finite element analyses were carried out based on Models SG1 and SG2. Table 10.6 summarizes the top and bottom flange dimensions as well as the

ultimate shear strengths from both finite element analyses and the prediction per Eq. (6.33). The ultimate shear strengths are compared in Figure 10.9. The prediction provides a good correlation with the finite element analysis results and, therefore, it is concluded that the proposed equation is valid for both equal and unequal top and bottom flanges.

Table 10.1: Effect of Longitudinal Stiffener

(a) Longitudinal Stiffener at 0.2D

Model No.	Subpanel	Subpanel Shear Strength	$V_{prediction}$ (kip)	V_{FEM} (kip)
SG1LS02	1	91.8*	389.2	371.0
	2	297.4		
SG2LS02	1	65.5*	242.2	260.1
	2	176.7		

* Based on shear yielding (= $0.58A_wF_{yw}$); others based on Eq. (6.33).

(b) Longitudinal Stiffener at 0.5D

Model No.	Subpanel	Subpanel Shear Strength	$V_{prediction}$ (kip)	V_{FEM} (kip)
SG1LS05	1	201.7	403.4	414.6
	2	201.7		
SG2LS05	1	66.3	252.6	286.8
	2	66.3		

Table 10.2: Parameters of FEM Models with Small Flange Areas

Model No.	Web Yield Stress, F_y (ksi)	Depth-Thk. Ratio, D/t_w	Width-Depth Ratio, d_0/D	Web Depth, D (in.)	Beam Flanges		$\frac{2Dt_w}{(b_{fc}t_{fc}+b_{ft}t_{ft})}$
					Thickness, t_f (in.)	Width, b_f (in.)	
SG1-1	60.3	210	0.5	52.5	0.5	8	3.28
SG1-2			1.0				
SG1-3			1.5				
SG2-1	57.4	280	0.5		0.56	6	2.93
SG2-2			1.0				
SG2-3			1.5				

Table 10.3: Effect of Small Flange Area on Ultimate Shear Strength

Model No.	FEM (kips)	Eq. (6.33) (kips)	$\frac{\text{Eq. (6.33)}}{\text{FEM}}$
SG1-1	308.8	287.1	0.93
SG1-2	222.0	203.2	0.92
SG1-3	191.0	166.5	0.87
SG2-1	191.8	170.3	0.89
SG2-2	134.4	124.7	0.93
SG2-3	115.5	99.8	0.86
Average	–		0.90
STDEV	–		0.03

Table 10.4: Ranges of Depth-Thickness Ratio for a Noncompact Web

Specimen No.	Web Yield Stress (ksi)	Width-Depth Ratio	Range of Depth-Thickness Ratio for Noncompact Web
SG1	60.3	0.5	123−154
SG2	57.4	0.5	126−157
SG3	36.9	1.5	84−106
SG4	36.9	0.75	117−146

Table 10.5: Effect of Noncompact Web

(a) Based on Models SG1 and SG2

Model No.	Depth-Thickness Ratio	Shear Strength (kips)			$\frac{\text{Eq. (6.33)}}{\text{FEM}}$
		FEM	Eq. (6.33)	AASHTO	
SG1SR1	130	638.6	732.4	700.5	1.15
SG1SR2	140	578.5	669.8	604.0	1.16
SG1SR3	150	527.0	615.2	526.2	1.17
SG2SR1	130	591.6	700.9	683.5	1.18
SG2SR2	140	546.8	640.8	589.3	1.17
SG2SR3	150	500.9	580.7	513.3	1.16
Average	–				1.16
STDEV	–				0.01

(b) Based on Models SG3 and SG4

Model No.	Depth-Thickness Ratio	Shear Strength (kips)			$\frac{\text{Eq. (6.33)}}{\text{FEM}}$
		FEM	Eq. (6.33)	AASHTO	
SG3SR1	85	449.0	463.4	462.2	1.03
SG3SR2	95	392.7	392.5	370.0	1.00
SG3SR3	105	339.7	338.6	302.9	1.00
SG4SR1	120	322.0	327.3	321.6	1.02
SG4SR2	130	298.2	295.2	274.0	0.99
SG4SR3	140	278.6	268.6	236.3	0.96
Average	–				1.00
STDEV	–				0.02

Table 10.6: Effect of Unequal Top and Bottom Flanges

(a) Based on Model SG1

Model No.	Flange Width (in.)		Top and Bottom Flange Thickness (in.)	Shear Strength (kips)		$\frac{\text{Eq. (6.33)}}{\text{FEM}}$
	Top Flange	Bottom Flange		FEM	Eq. (6.33)	
SG1UTB1	16	16	0.75	324.3	333.8	1.03
SG1UTB2	14			322.0	327.9	1.02
SG1UTB3	12			320.6	320.4	1.00
SG1UTB4	10			318.9	312.4	0.98
Average	–					1.01
STDEV	–					0.02

(b) Based on Model SG2

Model No.	Flange Width (in.)		Top and Bottom Flange Thickness (in.)	Shear Strength (kips)		$\frac{\text{Eq. (6.33)}}{\text{FEM}}$
	Top Flange	Bottom Flange		FEM	Eq. (6.33)	
SG2UTB1	14	14	0.625	201.0	195.5	0.97
SG2UTB2	12			200.2	190.8	0.95
SG2UTB3	10			198.4	184.6	0.93
Average	–					0.95
STDEV	–					0.02

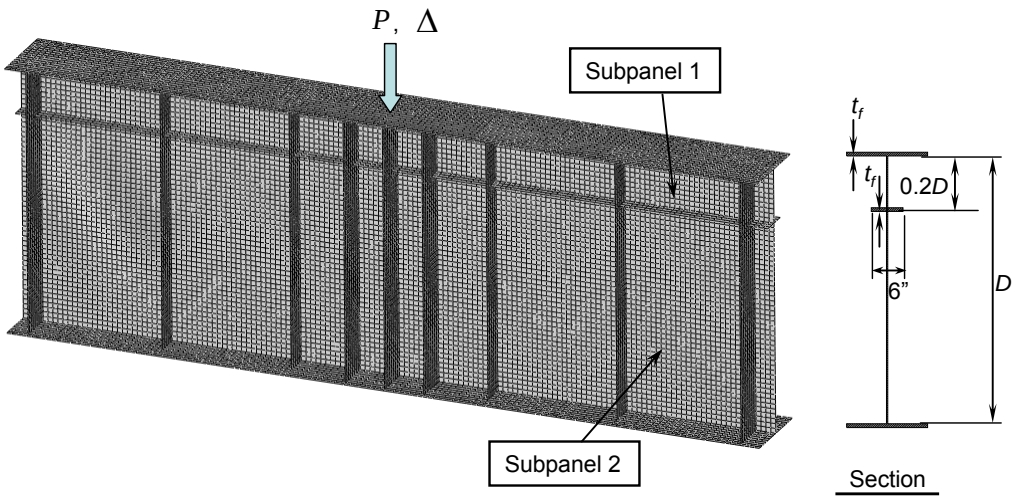

(a) Longitudinal Stiffeners at 0.2*D*

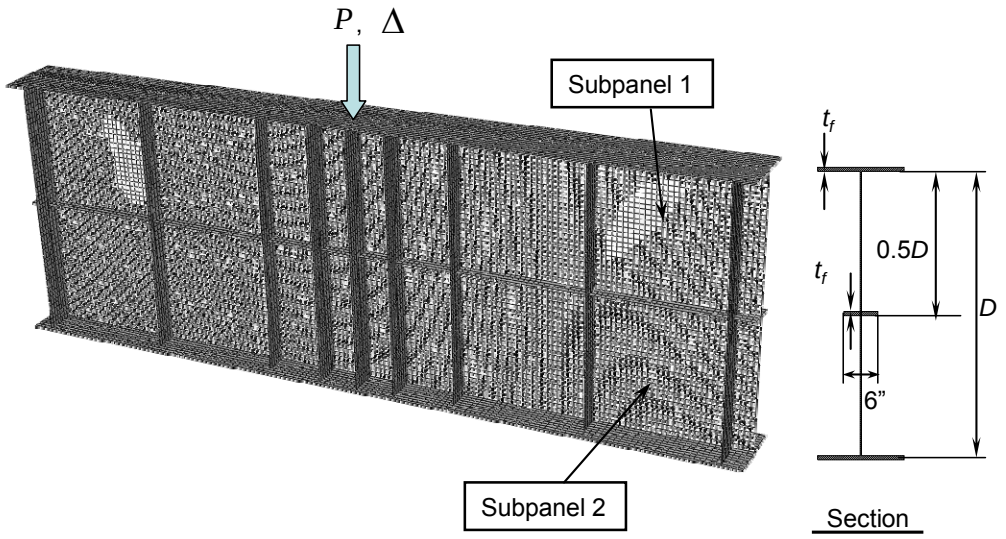

(b) Longitudinal Stiffeners at 0.5*D*

Figure 10.1: Finite Element Models with Different Longitudinal Stiffener Locations

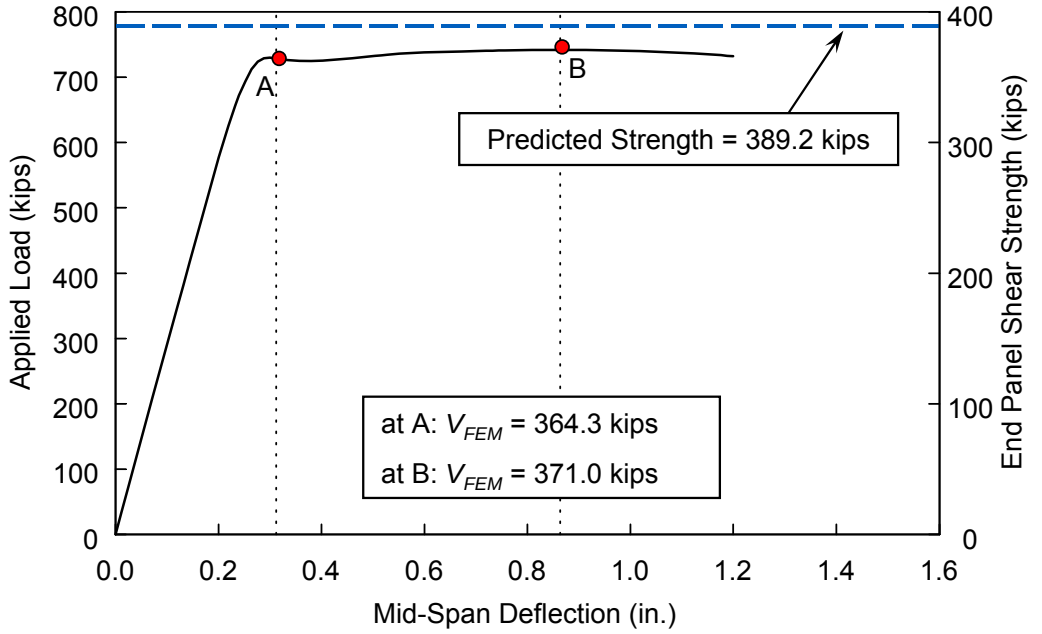

(a) Global Response

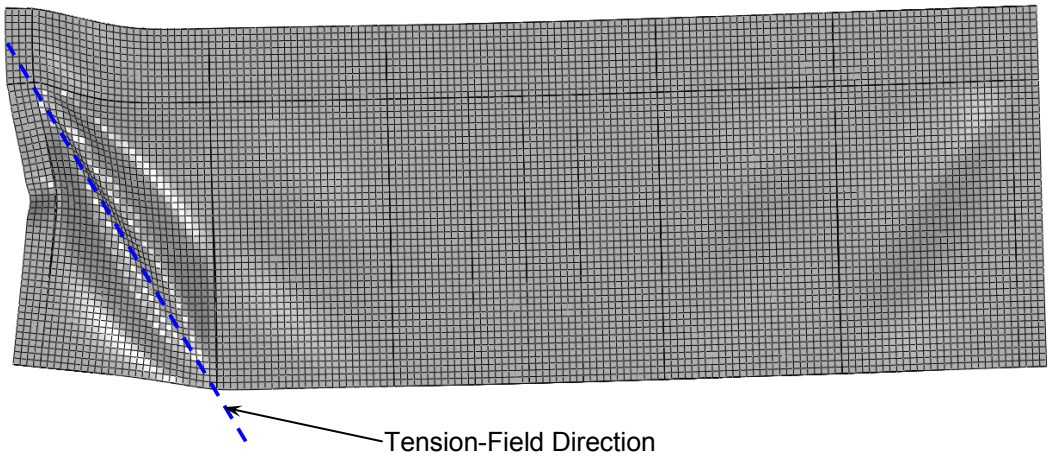

(b) Buckling Pattern

Figure 10.2: SG1LS02: Effect of Longitudinal Stiffener

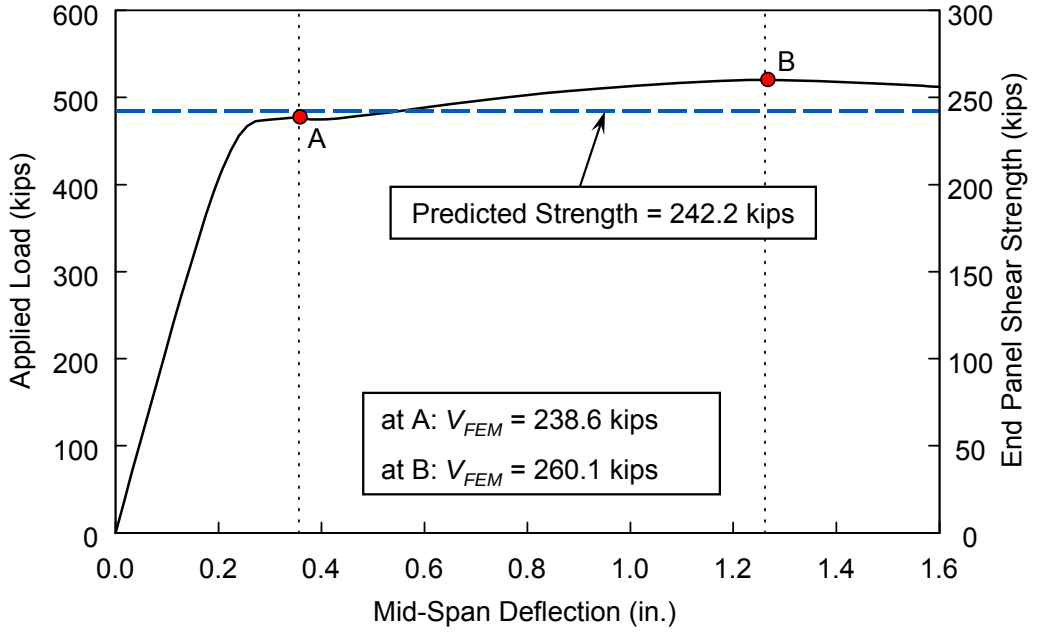

(a) Global Response

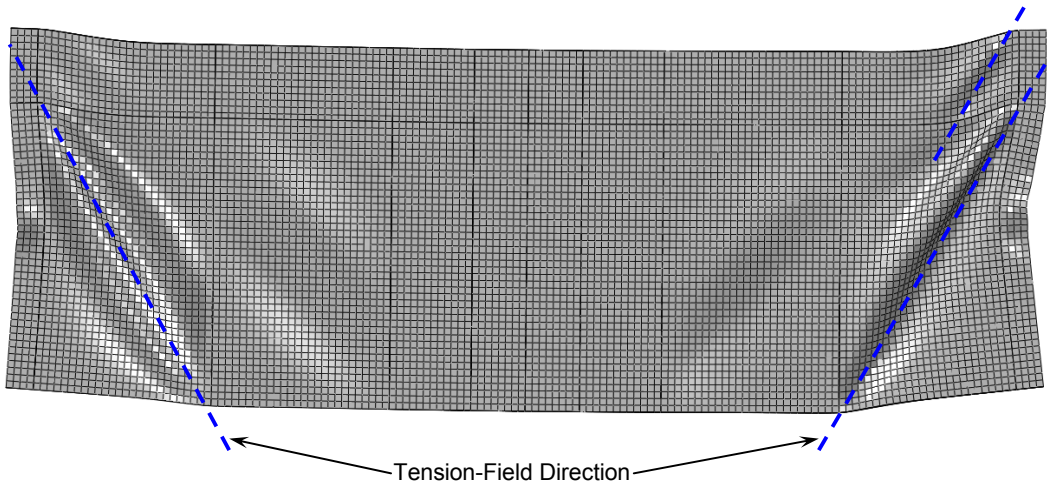

(b) Buckling Pattern

Figure 10.3: SG2LS02: Effect of Longitudinal Stiffener

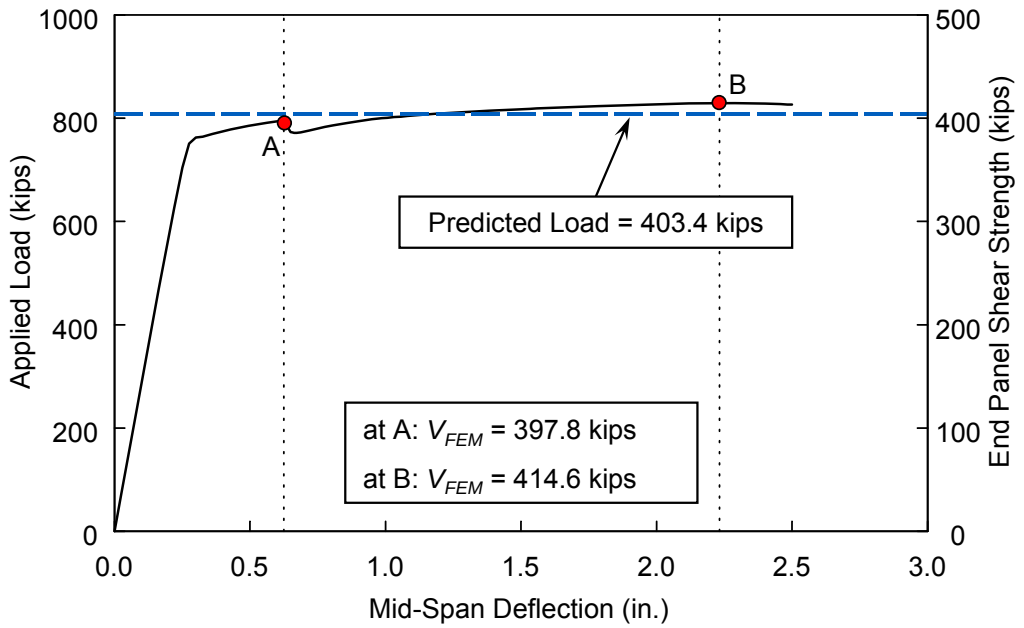

(a) Global Response

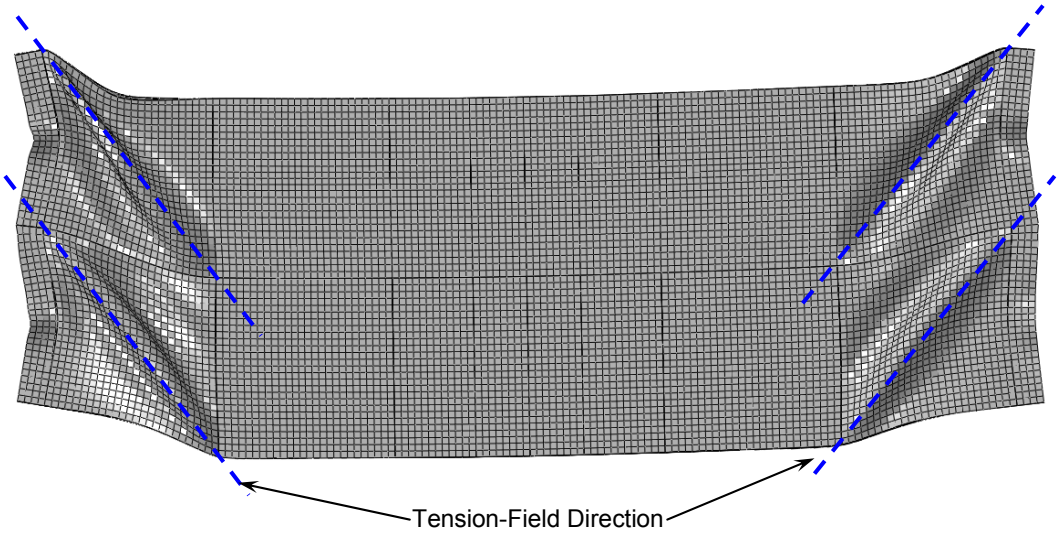

(b) Buckling Pattern

Figure 10.4: SG1LS05: Effect of Longitudinal Stiffener

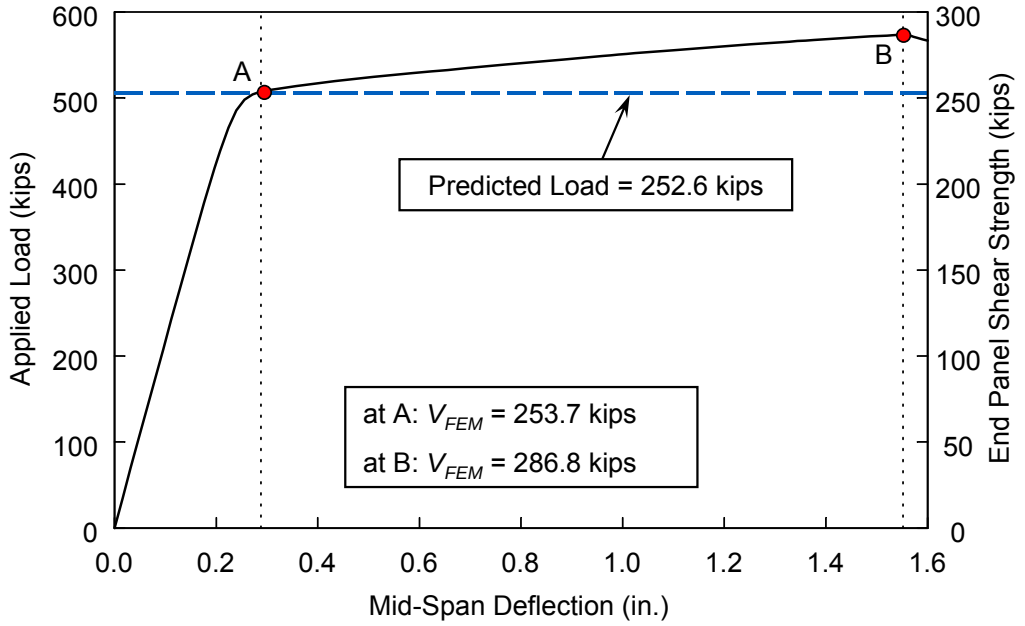

(a) Global Response

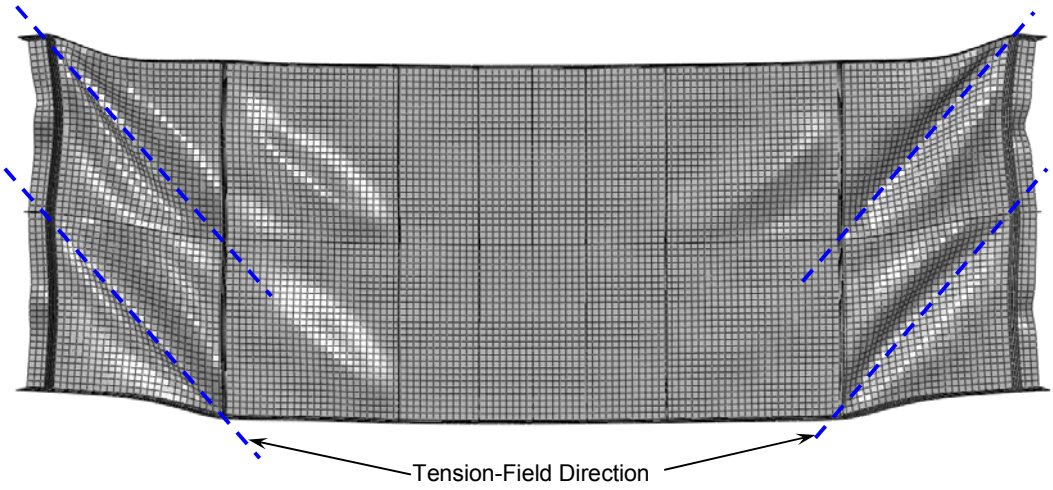

(b) Buckling Pattern

Figure 10.5: SG2LS05: Effect of Longitudinal Stiffener

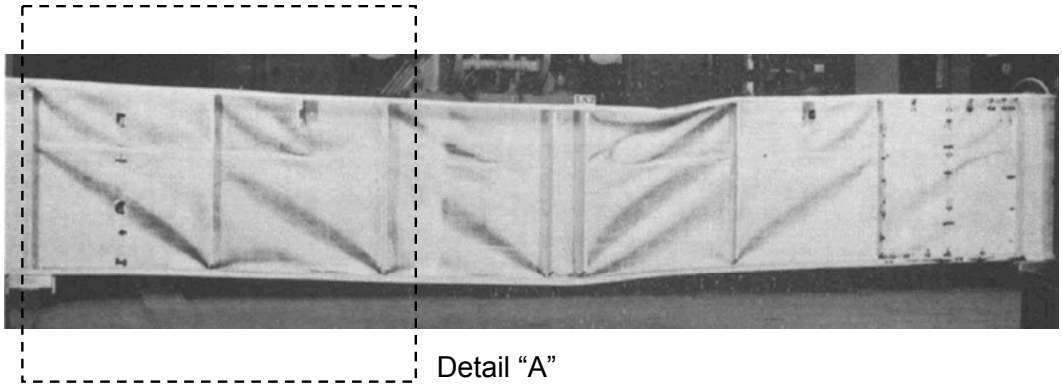

(a) Overall Deformed Shape

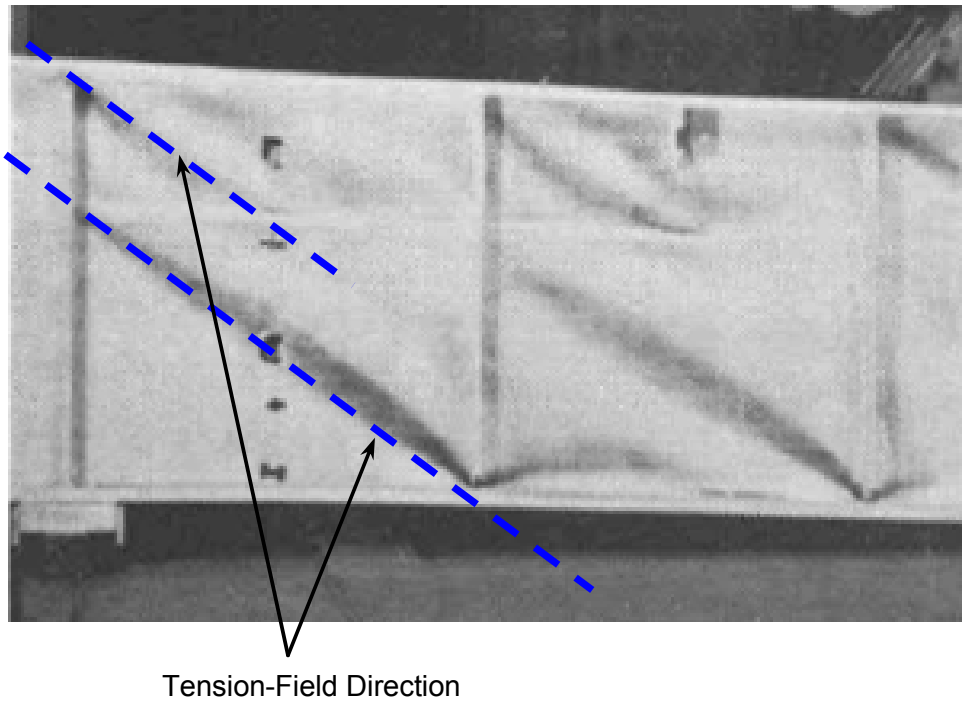

(b) Detail “A”

Figure 10.6: Girder LS2 after Testing (adopted from Cooper, 1966)

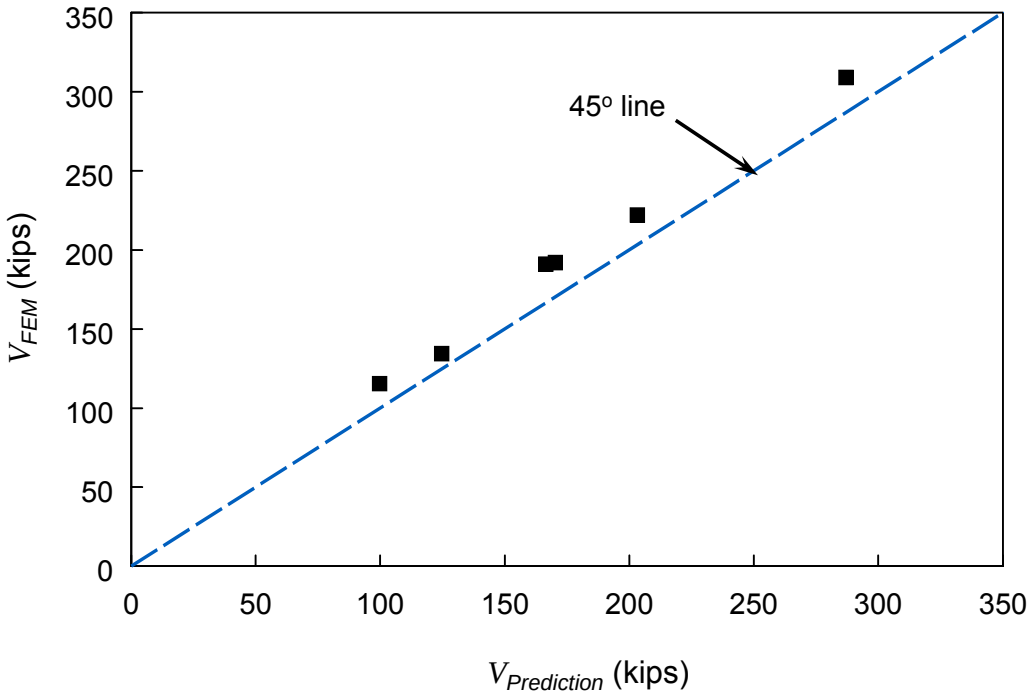

Figure 10.7: Coimparison of Shear Strengths of Plate Girders with Small Flange Area

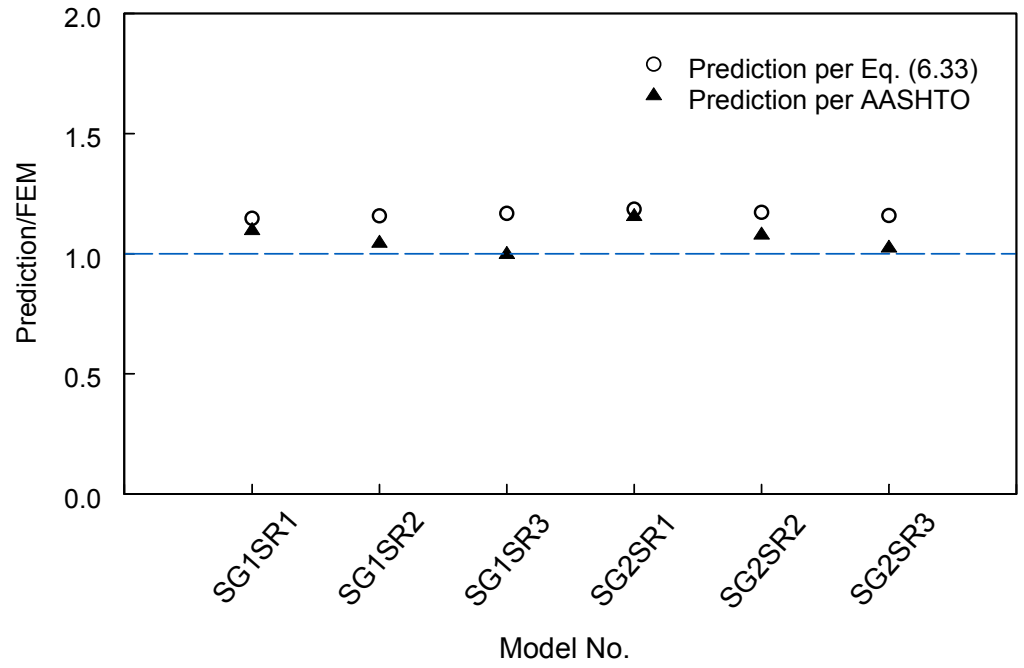

(a) Model Series of SG1 and SG2

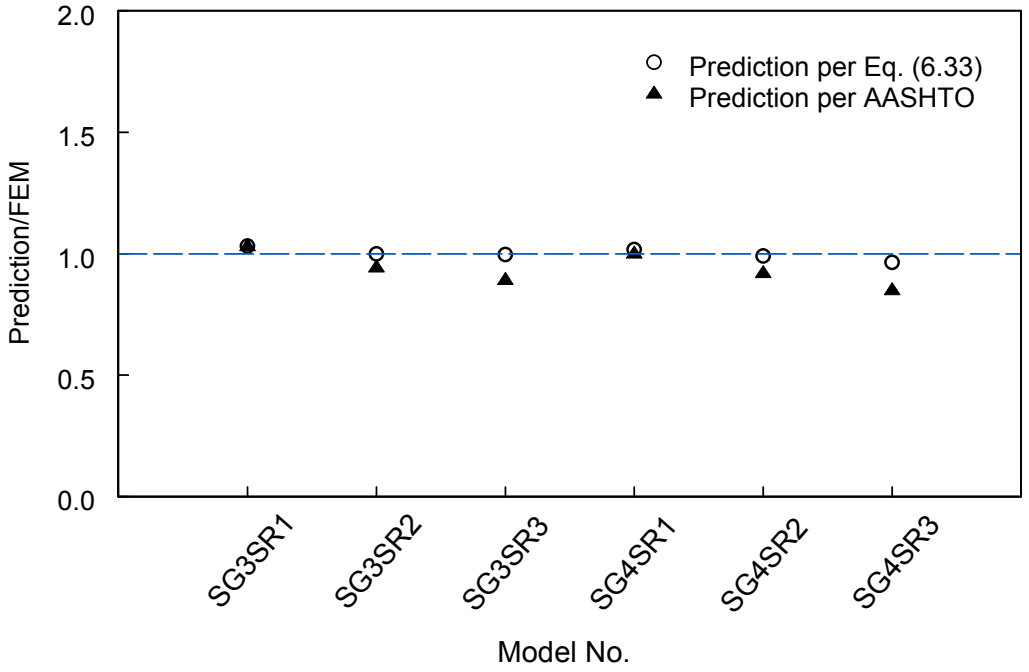

(b) Model Series of SG3 and SG4

Figure 10.8: Shear Strength Comparison of Plate Girder End Panel with Noncompact Web

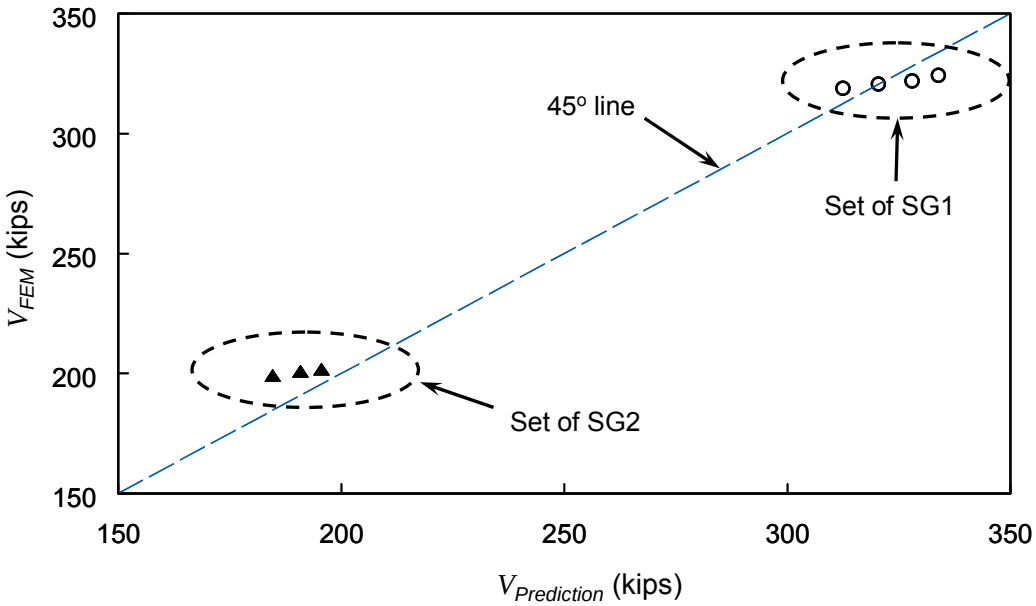

Figure 10.9: Shear Strength Comparison of Plate Girder End Panel with Unequal Top and Bottom Flanges

11. RESISTANCE FACTOR FOR THE PROPOSED SHEAR STRENGTH EQUATION

The resistance factor, ϕ, for the proposed shear strength in Eq. (6.33) is computed as follows (SSRC 2010):

$$\phi = \rho_R e^{-\beta \alpha_R V_R} \tag{11.1}$$

where

$$\rho_R = \rho_G \rho_M \rho_P \tag{11.2}$$

ρ_R is the bias coefficient for the resistance, i.e., the mean value of the ratio of the measured resistance to the nominal resistance, and the remaining terms are defined as follows:

ρ_G : bias coefficient for the cross-sectional geometry

ρ_M : bias coefficient for the material property

ρ_P : bias coefficient for the design equation

V_R : coefficient of variation associated with ρ_R $\left(= \sqrt{V_G V_M V_P}\right)$

β : Reliability index taken as 3.0

α_R : coefficient of separation taken as 0.55

Kennedy and Gad Aly (1980) statistically determined the coefficient of the geometry (ρ_G) and the associated coefficient of variation (V_G) which are 1.015 and 0.013, respectively. Those values were also used in White and Barker (2008) to develop the resistance factor. Cooper et al. (1978), Kennedy and Gad Aly (1980), and White and Barker (2008) used a bias coefficient for the material properties (ρ_M) of 1.10 with an associated coefficient of variation (V_M) of 0.110. Thus, Eq. (11.1) can be re-written as:

$$\phi = 1.015(1.10)\rho_P e^{-(3)(0.55)\sqrt{(0.013)(0.110)V_P}} \tag{11.3}$$

Where

$$\rho_P = \text{mean}\left(\frac{\text{Measured Strength}}{\text{Predicted Strength per Eq. (6.33)}}\right) \tag{11.4}$$

$$V_P = \frac{\text{standard deviation } (\sigma_p)}{\text{mean value } (\rho_p)} \tag{11.5}$$

ρ_P and V_P are the bias coefficient for the design equation and the associated coefficient of variation.

Based on the available test results of steel girder specimens (SG series: SG1 to SG4, EPS series: EPS1-1 to EPS 8-13 in Table 6.3), the values of ρ_P and V_P are computed and listed in Table 11.1. From Eq. (11.3), the calculated ϕ value is 1.136, which is larger than 1.0. It implies that Eq. (6.33) is somewhat conservative. For design purposes, a value of 1.0 can be used.

Table 11.1: Resistance Factor Based on Physical Tests

Specimen No.	Shear Strength (kips)		Test/Prediction
	Test	Prediction	
SG1	315.3	328.9	0.959
SG2	190.3	188.5	1.010
SG3	212.1	200.6	1.057
SG4	279.0	266.2	1.048
EPS1-1	8.4	8.4	1.000
EPS1-2	9.0	9.7	0.928
EPS4-3	12.9	13.2	0.977
EPS2-4	8.9	9.2	0.967
EPS2-5	9.2	10.3	0.893
EPS3-6	11.6	10.2	1.137
EPS3-7	13.7	12.3	1.114
EPS5-8	8.2	7.9	1.038
EPS5-9	8.6	8.1	1.062
EPS6-10	8.9	8.5	1.047
EPS7-11	7.1	5.9	1.203
EPS7-12	5.6	5.4	1.037
EPS8-13	4.8	4.3	1.116
		Avg. (ρ_P)	1.035
		Stdev. (σ_P)	0.079
		V_P	0.077

12. SUMMARY AND CONCLUSIONS

Welded steel plate girders, usually characterized by having very deep sections, have been widely used for bridge construction. This economically efficient structural form typically comprises a very slender web which can easily buckle in shear. Therefore, the slender web is usually stiffened with transverse stiffeners. In early 1960s, Basler studied the shear capacity of stiffened web panels and quantified their post-buckling strength due to the tension-field action. This concept was adopted in AASHTO Specifications in 1973, which allowed post-buckling strength due to the tension-field action for both interior and end panels. When the 1986 AASHTO Interim Specifications were released, however, tension-field action for end panels was not permitted. This also applies to the AISC Specification (2014) for building construction. This change negatively impacts the load rating of many steel plate girder bridges built before 1973. The main objective of this research was to evaluate the actual shear strength of end panels through experimental and analytical investigations and to develop reliable shear strength equations.

The testing program consisted of two phases. In Phase 1, two large-size steel plate girders and two steel-concrete composite girders were fabricated and each specimen consisted of two end panels and two interior panels with a panel width-to-depth ratio of 0.5. Two different depth-to-thickness ratios (210 and 280) were considered. During testing of two steel girder specimens, out-of-plane deformations of the web rapidly increased once the shear buckling load predicted by AASHTO Specifications (2014) was achieved. But the end panels were able to resist much higher shear force after the shear buckling load was reached, indicating that a tension-field action took place in the web.

Testing showed that the collapse mechanism in the end panels involved the development of four plastic hinges (see Figure 3.8): one in the top flange, one in the bearing stiffener pair, one at the junction of the top flange and bearing stiffener pair, and one at the junction of the bottom flange and first intermediate stiffener(s). The recorded principal tensile strains at ultimate load were close to or beyond the strain value corresponding to the tension-field stress proposed by Basler [Eq. (1.10)]. In addition,

the angles of the principal tensile strains were generally within ±10° of the panel diagonal angle with respect to the flange. The addition of a concrete slab further increased the shear capacity of the end panels, but to a lesser extent. Two composite girder specimens showed about 12% higher shear strength than their steel counterparts.

Finite element analyses predicted very well the actual behaviors of the test specimens. Then a series of parametric studies was conducted to evaluate the effects of the following parameters: flange and bearing stiffener thicknesses, panel depth-to-thickness ratio, panel width-to-depth ratio, concrete slab width, and end shear stud spacing. The plastic hinge locations in the top flange and bearing stiffeners directly affected the width of the tension-field band and, thus, the post-buckling strength. The analyses also confirmed that some portion of the web needed to be included in the calculation of plastic moments for the top flange and bearing stiffener pair; these two flexural strengths affected the plastic hinge locations. The effect of concrete slab width was insignificant; testing also showed that the effective width of the concrete slab was close to the top flange width of the steel girder.

Analytical studies were then conducted to evaluate the shear strength of the plate girder end panels. A plastic analysis with virtual work was used to derive the post-buckling shear strength. This model led to a predictive equation [Eq. (6.33)], which included a partial tension-field action factor α [Eq. (6.36)]. To determine α, plastic moments of the girder top flange and the bearing stiffener pair were needed; an effective depth of the web was proposed for this purpose. Results from 15 experimental tests (13 small-scale specimens and 2 large-size specimens tested in Phase 1 of this program) and 99 finite element analyses correlated very well with the proposed equation. In addition, a strut-and-tie model (see Section 6.9) was developed to include the shear strength contribution from the concrete slab.

When the end panels of an existing steel plate girder bridge require retrofit due to a deficiency in shear resistance, one scheme, originally proposed by Basler (1961a) that adds another pair of end stiffeners next to the bearing stiffeners (see Figure 7.2), was investigated. Finite element simulations of two design procedures, one proposed by Basler and another one that has been adopted in Eurocode 3 (2006), were found to be non-conservative and not effective. Alternate rehabilitation schemes that either (1) add

a pair of wing stiffeners (see Figure 7. 6) welded to the bearing stiffeners and flanges and flanges to increase the flexural strengths of these boundary elements, or (2) add another pair of stiffeners in the mid-width of existing end panels panels (see Figure 7.12) were proposed. For the first approach, finite element analysis showed that the proposed retrofit scheme effectively shifts the plastic hinge in the bearing stiffener pair downward, widens the tension-field band and, thus, increases the shear strength. A design procedure and an example are provided (see Section 7.5). The other approach is using a pair of angles fastened to the web by bolting in the mid-width of the existing end panels. The effectiveness of this approach is also verified by finite element analysis. For this approach, finite element analysis showed that placing the new stiffeners at the midspan of the original end panel, not placing them very close to the bearing stiffeners, was more effective. The proposed Eq. (6.33) can be used to predict the shear strength of the rehabilitated end panel. The proposed equation is valid when the width-to-depth ratio is not less than 0.5.

Phase 2 test specimens (two steel and two composite plate girders) had a panel width-to-depth ratio of 0.75 and 1.5, and had a much lower depth-to-thickness ratio (= 138). The behaviors and failure modes of these shallower test specimens were very similar to those of Phase 1. Tension-field action could be developed in these specimens and the actual shear strengths were much higher than those predicted by the AASHTO Specifications (2014). The ultimate shear strengths from testing were also compared with those predicted by the proposed shear strength equations developed in the Phase 1 study. The predicted shear strengths of the steel specimens correlated well with those from testing. However, the concrete slab resisted more shear than that predicted by the proposed equation. It was observed that using more closely spaced shear connectors, as was the case in Phase 2 spcimens, required the strut-and-tie model to be adjusted to account for the different failure mechanism (see Section 9.3).

Nonlinear finite element analyses were also conducted to investigate the effects of longitudinal stiffeners, small flange areas, noncompact web, and unequal top and bottom flanges on the shear strength of end panels. When longtidunial stiffeners are used, the total shear strength of the end panel can be calculated by summing up the shear strengths of subpanels with the proposed shear strength equation. To calculate the shear strength

with tension-field action in the interior panels, the AASHTO Specifications (2014) provide two equations based on the flange area relative to the toal cross-sectional area. For end panel applications, the proposed shear strength equation automatically considers the effect of flange area and, thus, a separate shear strength equation is not needed. The proposed shear strength equation also applies to the case of equal or unequal top and bottom flanges. When a noncompact web is used, the proposed shear strength equation provides either close or slightly nonconservative estimate of the shear strength.

Based on 17 test results (4 large-size specimens and 13 small-scale specimens), the resistance factor was statistically determined. The calculated resistance factor was larger than 1.0, which implies that the proposed equation is somewhat conservative. For design purposes, it is recommended that a value of 1.0 be used.

REFERENCES

(1) AASHTO. (1973). *Standard Specifications for Highway Bridges,* 11th Ed., American Association of State Highway Officials, Washington, D.C.

(2) AASHTO. (1977). *Standard Specifications for Highway Bridges,* 12th Ed., American Association of State Highway Officials, Washington, D.C.

(3) AASHTO. (2014). AASHTO *LRFD Bridge Design Specifications,* American Association of State Highway and Transportation Officials, Washington, D.C.

(4) AASHTO. (2011). *Manual for Bridge Evaluation,* 2nd Ed., American Association of State Highway and Transportation Officials, Washington, D.C.

(5) ABAQUS. (2011). *ABAQUS Standard User's Manual*, *Version 6.11*, Dassault Systèmes. Providence, RI.

(6) ACI. (2005). *Building Code Requirements for Structural Concrete and Commentary. ACI 318-05,* American Concrete Institute, Farmington Hills, Michigan.

(7) ACI. (2008). *Building Code Requirements for Structural Concrete and Commentary. ACI 318-08,* American Concrete Institute, Farmington Hills, Michigan.

(8) AISC. (2010). *Specification for Structural Steel Buildings. ANSI/AISC 341-10,* American Institute of Steel Construction, Chicago, IL.

(9) Ajam, W. M. A. (1986). "Finite element study of the post-buckling behaviour of plate girder panels under shear load." *Ph.D Thesis*, Concordia Univ., Montreal, Quebec, Canada.

(10) Alinia, M. M., Hahashi, H. R., and Khorram, A. (2009a). "Nonlinearity in the postbuckling behaviour of thin steel shear panels." *Thin-Walled Structures*, 47, pp. 412-420.

(11) Alinia, M. M., Shakiba, M., and Hahashi, H. R. (2009b). "Shear failure characteristics of steel plate girders." *Thin-Walled Structures*, 47, pp. 1498-1506.

(12) Allison, R. W., Johnson, R. P., and May, I. M. (1982). "Tension field action in composite plate girdersr." *Proc*., *Inst*. *Civ*. *Eng*., 73(2), pp. 255-276.

(13) AWS D1.1. (2000). *Structural Welding Code-Steel,* American Welding Society, Miami, Florida.

(14) Baskar, K., Shanmugam, N. E., and Thevendran, V. (2002). "Finite-element analysis of steel-concrete composite plate girder." *J. Struct. Eng*., ASCE, 128(9), pp. 1158-1168.

(15) Basler, K. (1961a). "Strength of plate girders in shear." *J. Struct. Div.,* ASCE, 87(7), pp. 151-181.

(16) Basler, K. (1961b). "Strength of plate girders under combined bending and shear." *J. Struct. Div.,* ASCE, 87(2), pp. 181-197.

(17) Basler, K., Yen, B. T., Muller, J. A., and Thürlimann, B. (1960). "Web buckling tests on welded plate girders." *Welding Research Council Bulletin,* No. 64.

(18) Chern, C., and Ostapenko, A. (1969). "Ultimate strength of plate girder under shear" *Friz Engineering Laboratory Report No. 328.7*, Lehigh Univ. Bethehem, PA.

(19) Cooper, P. B. (1966). "Static strength of longitudinally stiffened plate girders" *Friz Engineering Laboratory Report No. 304.9*, Lehigh Univ. Bethehem, PA.

(20) Cooper, P. B., Galambos, T. V., and Ravindra, M. K. _1978_. "LRFD criteria for plate girders." *J. Struct. Div*., 104(9), pp. 1389–1407.

(21) Darehshouri, S. F., Shanmugam, N. E., and Osman, S. A. (2012). "Collapse behavior of composite plate girders loaded in shear." *J. Struct. Eng.,* ASCE, 138(3), pp. 318-326.

(22) CEN. (2006). Eurocode 3: *Design of Steel Structures - Part 1-5: General Rules - Plated Structural Elements.,* EN 1993-1-5, European Committee for Standarization, Brussels, Belgium.

(23) Fujii, T. (1971) "A comparison between theoretical values and experimental results for the ultimate shear strength of plate girders." *IABSE Volume-Band 11*, *Colloquium*, *Design of Plate and Box Girders for Ultimate Strength*, London, pp. 161-171.

(24) Herzog, M. (1974). "Ultimate strength of plate girders from tests." *J. Strut. Div*., ASCE, 100(5), pp. 849-864.

(25) Höglund, T. (1971). "Simply supported thin plate plate I-girders without web stiffeners subjected to distributed transverse load." *IABSE*, *Colloquium*, *Design of Plate and Box Girders for Ultimate Strength*, London

(26) Höglund, T. (1997). "Shear buckling resistance of steel and aluminum plate girders." *Thin-Walled Structures,* 29(1-4), pp. 13-30.

(27) Horne, M. R., and Grayson, W. R (1983). "Parametric finite element study of transverse stiffeners for webs in shear." *Proc*., *Michael R. Horne Conf*., L. J. Morris, ed., Granada Publishing, London, pp. 329-341.

(28) Huslid, J. M., and Rockey, K. C. (1979). "The influence of end post rigidity on the collapse behaviour of plate girders." *Proc*., *Inst*. *Civ*. *Eng*., 67(2), pp. 285-312.

(29) Karthik, M. M., and Mander, J. B. (2011). "Stress-block parameters for unconfined and confined concrete based on a unified stress-strain model." *J. Struct. Eng.,* ASCE, *137*(2), pp. 270-273.

(30) Kennedy, D. J. L., and Gad Aly, M. (1980). "Limit states design of steel structures—Performance factors." *Can. J. Civ. Eng*., 7(1), pp. 45–77.

(31) Kent, D. C., and Park, R. (1971). "Flexural members with confined concrete." *J. Struct. Div., Proc*., ASCE, 97(ST7), pp. 1969-1990.

(32) Komatsu, S. (1971) "Ultimate strength of stiffened plate girders subjected to shear." *IABSE Volume-Band 11*, *Colloquium*, *Design of Plate and Box Girders for Ultimate Strength*, London, pp. 49-65.

(33) Kuhn, P. (1956). *Stresses in Aircraft and Shell Structures,* McGraw-Hill, New York.

(34) Lee, S. C., and Yoo, C. H. (1998). "Strength of plate girder web panels under pure shear." *J. Struct. Eng*., ASCE, 124(2), pp. 184-194.

(35) Lee, S. C., and Yoo, C. H. (1999). "Experimental study on ultimate shear strength of web panels." *J*. *Struct*. *Eng.,* ASCE*,* 125(8), pp. 838-846.

(36) Liang, Q. Q., Uy, B., Bradford, M. A., and Ronagh, H. (2005). "Strength analysis of steel-concrete composite beams in combined bending and shear." *J*. *Struct*. *Eng.,* ASCE*,* 131(10), pp. 1593-1600.

(37) Marsh, C., Ajam, W., and Ha, H. K. (1988). "Finite Element Analysis of postbuckled shear webs." *J. Struct. Eng*., ASCE, 114(7), pp. 1571-1587.

(38) Neal B. G. (1985). *The plastic methods of structural analysis*, 3rd Ed., Chapman and Hall, New York.

(39) Nie, J., Xiao, Y., and Chen, L. (2004). "Experimental studies on shear strength of steel-concrete composite beams." *J*. *Struct*. *Eng.,* ASCE*,* 130(8), pp. 1206-1213.

(40) Popovics, S. (1973). "A numerical approach to the complete stress-strain curves of concrete." *Cement and Concrete Research*, 3(5), pp. 583-599.

(41) Porter, D. M., Rockey, K. C., and Evans, H. R. (1975). "The collapse behaviour of plate girders loaded in shear." *The Structural Engineer,* 53(8), pp. 313-325.

(42) Real, E., Mirambell, E., and Estrada, I. (2007). "Shear response of stainless steel plate girders." *Engineering Structures*, 29(7), pp. 1626-1640.

(43) Rockey, K. C., and Leggett, D. M. A. (1962). "The buckling of a plate girder web under pure bending when reinforced by a single longitudinal stiffener." *Proc Inst. Civ. Eng.*, Vol. 21

(44) Rockey, K. C., and Skaloud, M. (1972). "The ultimate load behaviour of plate girders loaded in shear." *The Structural Engineer*, 50(1), pp. 29-48.

(45) Salmon, C. G., Johnson, J. E. (1996). *Steel Structures-Design and Behavior*, 4th Ed., Prentice Hall, New Jersey.

(46) Safar, S. S. (2013). "Shear strength of end web panels." *Thin-Walled Structures,* 67, pp. 101-109.

(47) Shanmugam, N. E., and Baskar, K. (2003). "Steel-concrete composite plate girders subject to shear loading." *J. Struct. Eng.*, ASCE, 129(9), pp. 1230-1242.

(48) SSRC. (2010). *Guide to Stability Design Criteria for Metal Structures*, 6th Ed., Edited by Ronald D. Ziemian, Wiley, New York.

(49) Stanway, G. S., Champman, J. C., and Dowling, P. J (1993). "Behaviour of a web plate in shear with an intermediate stiffener." *Proc., Inst. Civ. Eng.*, 116(1), pp. 54-68.

(50) Thorenfeldt, E., Tomaszewicz, A., and Jensen, J. J. (1987). "Mechanical properties of high-strength concrete and application in design." *Proc. of the Symposium on Utilization of High-Strength Concrete,* Tapir, Trondheim, Norway, pp. 149-159.

(51) Timoshenko, S. P., Gere, J. M. (1961). *Theory of Elastic Stability*, 2nd Ed., McGraw-Hill, New York.

(52) Tsai, W. T. (1988). "Uniaxial compression stress-strain relation of concrete." *J. Struct. Eng.*, 114(9), pp. 2133-2136.

(53) Wagner, H. (1931). "Flat sheet metal girder with very thin metal web." *Tech. Notes. 604-606,* National Advisory Committee on Aeronautics (NACA), Washington, D.C.

(54) White, D. W., Barker, M. G. (2008). "Shear resistance of transversely stiffened steel I-girders." *J. Struct. Eng.,* ASCE, 134(9), pp. 1425-1436.

(55) Wilson, J. M. (1886). "On specifications for strength of iron bridges." *Trans.* ASCE, Vol. 15, Part I, pp. 401-403, 489-490.

(56) Yen, B. T., and Basler, K. (1962). "Results of an investigation of plate girders" *Friz Engineering Laboratory Report No. 251.25*, Lehigh Univ. Bethehem, PA.

(57) Yoo, C. H., and Lee, S. C. (2006). "Mechanics of web panel post-buckling behavior in shear." *J. Struct. Eng.*, ASCE, 132(10), pp. 1580-1589.

APPENDIX A. INSTRUMENTATION

A1 Displacement Transducers

A1.1 Specimens SG1 and SG2

The locations of displacement transducers for Specimens SG1 and SG2 are shown in Figures A.1 and A.2, respectively. Displacement transducer L1 measured the girder mid-span vertical deflection and was used as the feedback sensor for actuator control. L2 through L9 measured web out-of-plane deformation. L10 through L21 measured top flange deformation along half of the end panel width in the region of plastic hinge formation. L22 through L31 measured deformations along half of the length of the bearing stiffeners. L32 through L41 measured bottom flange deformation. L42 through L49 measured the average shear deformation of the panels.

A1.2 Specimens CG1 and CG2

The locations of displacement transducers for Specimens CG1 and CG2 are shown in Figures A.3 and A.4, respectively. These specimens had an arrangement of displacement transducers similar to their steel girder counterparts, except that the transducers on top and bottom flanges of the steel girder were removed and two displacement transducers (L28 and L29) where added to measure the slip between the concrete slab and steel girder (see Figures A.3 and A.4).

A1.3 Specimens SG3 and SG4

The locations of displacement transducers for Specimens SG3 and SG4 are shown in Figures A.5 and A.6, respectively. These specimens had a similar arrangement of displacement transducers to Specimens SG1 and SG2. However, the displacement transducers on bearing stiffeners and flanges were removed.

A1.4 Specimens CG3 and CG4

Figures A.7 and A.8 show the locations of displacement transducers for Specimens SG3 and SG4, respectively.

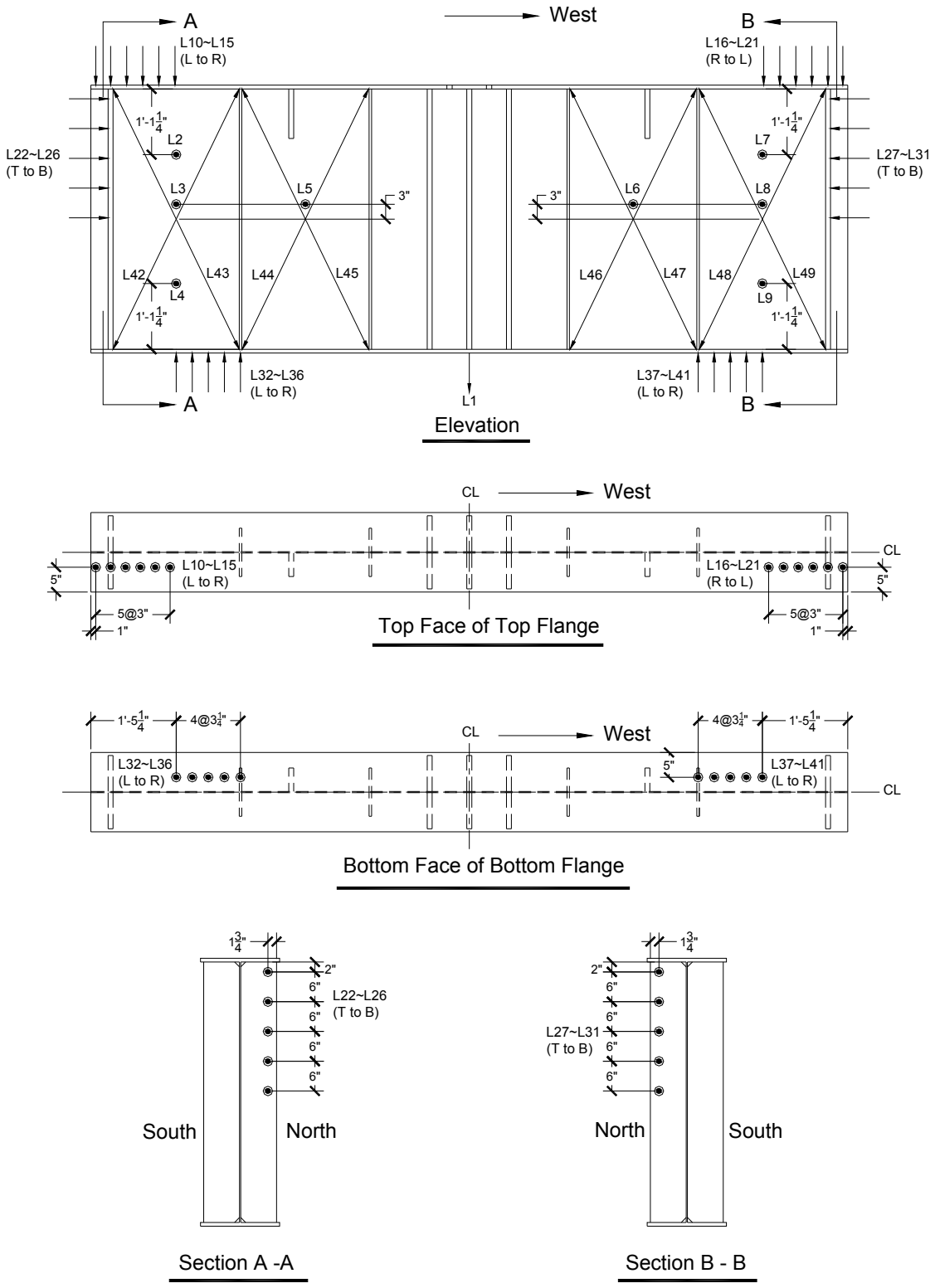

Figure A.1: Specimen SG1: Displacement Transducers

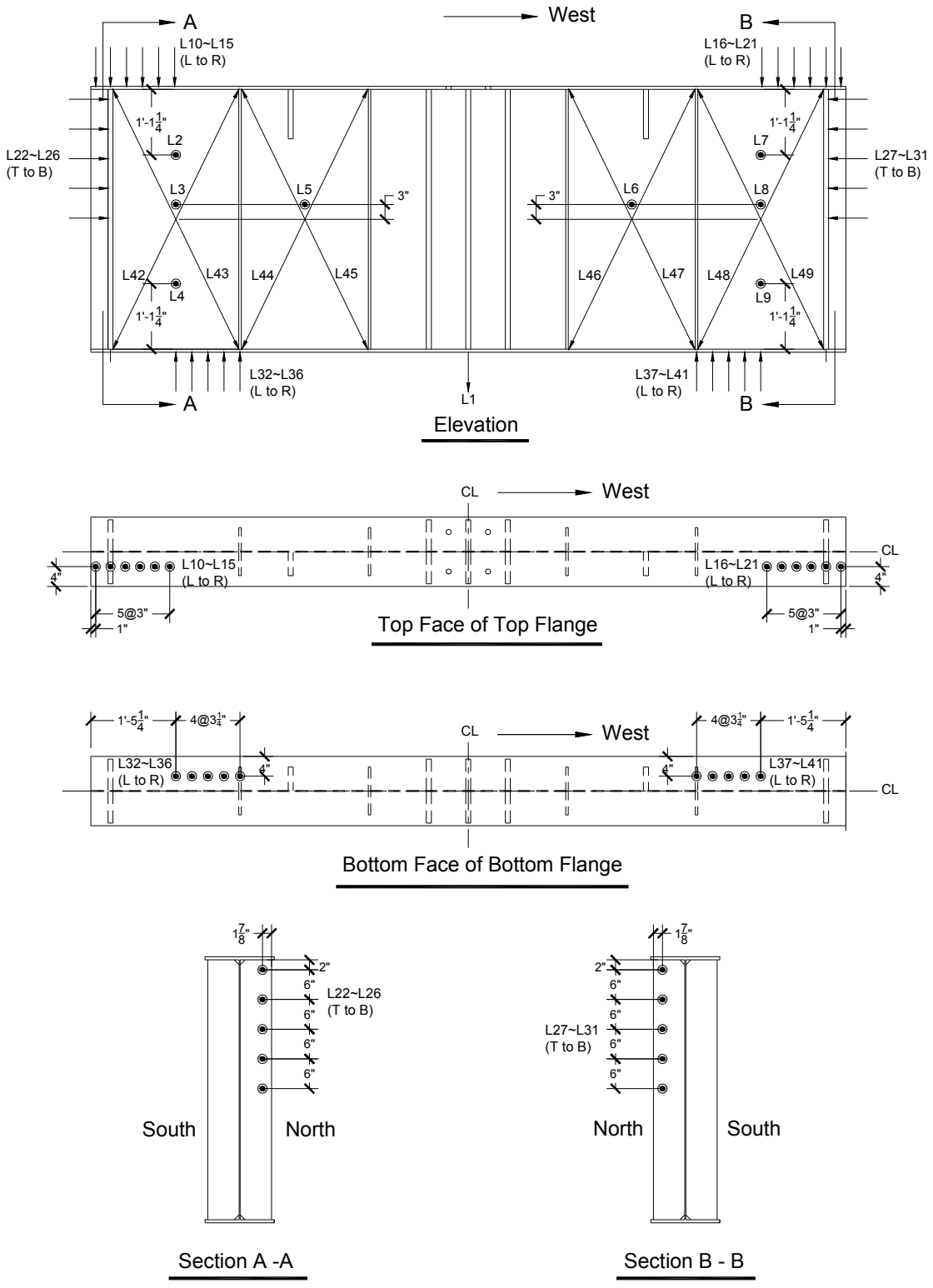

Figure A.2: Specimen SG2: Displacement Transducers

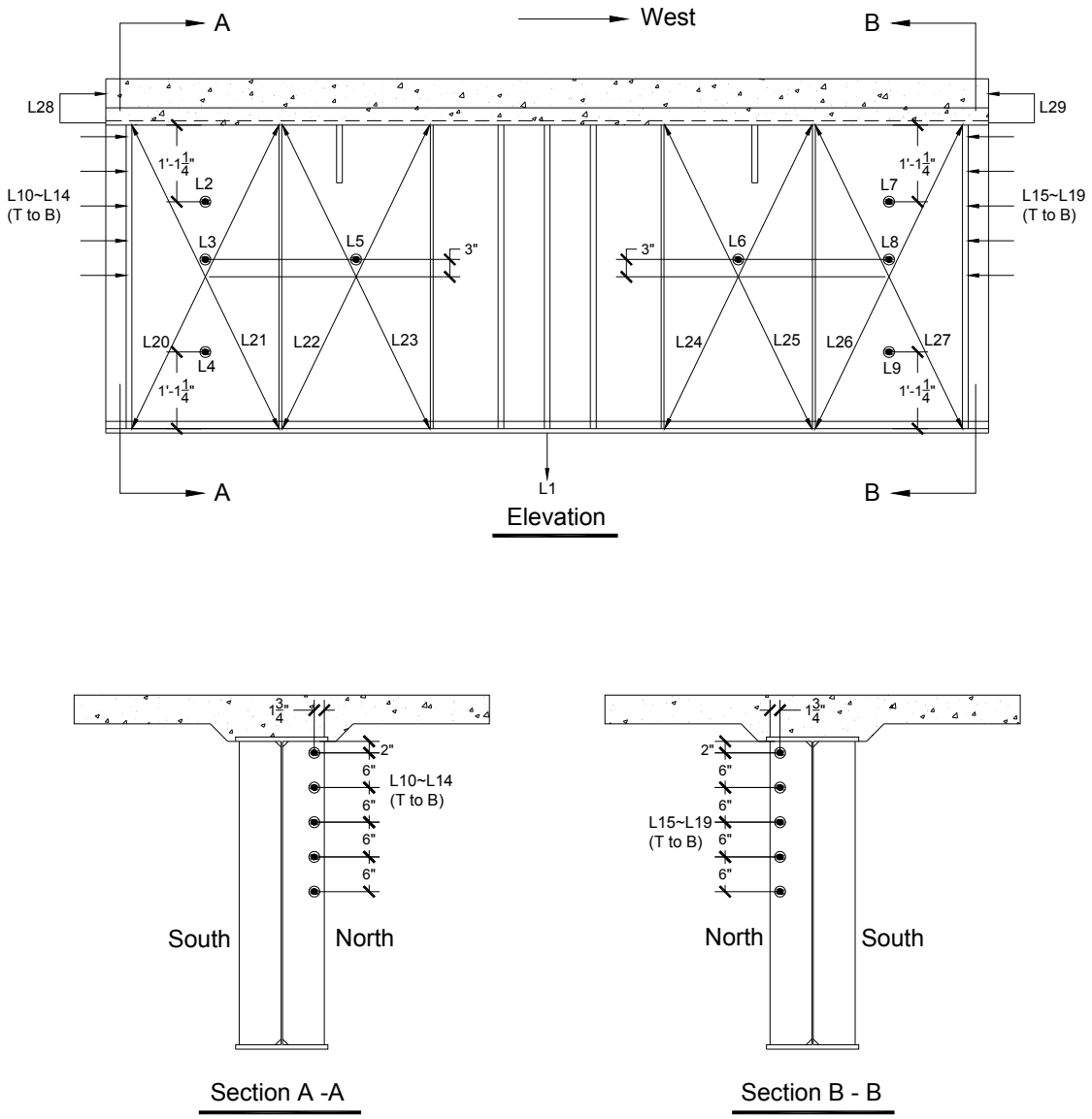

Figure A.3: Specimen CG1: Displacement Transducers

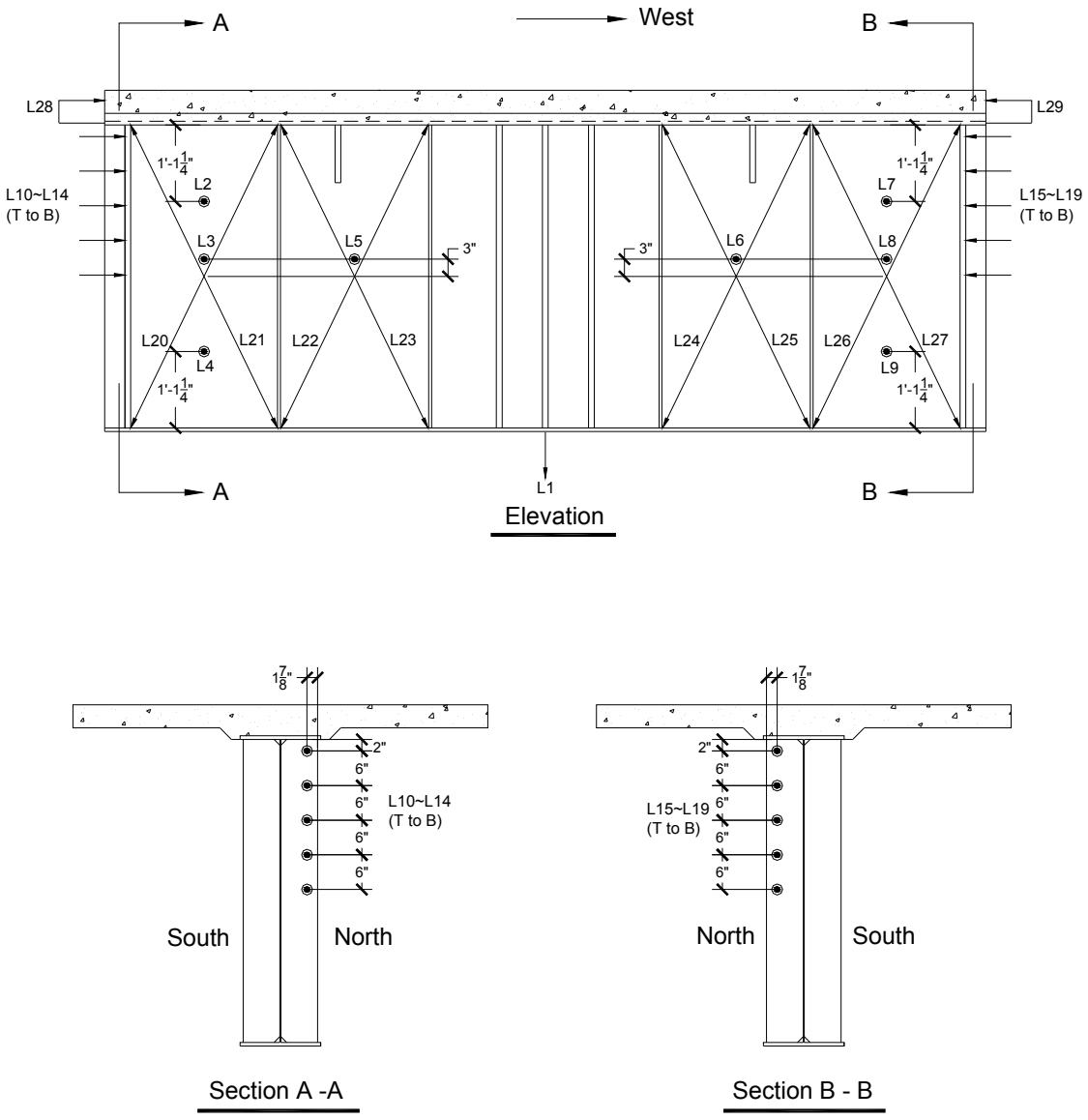

Figure A.4: Specimen CG2: Displacement Transducers

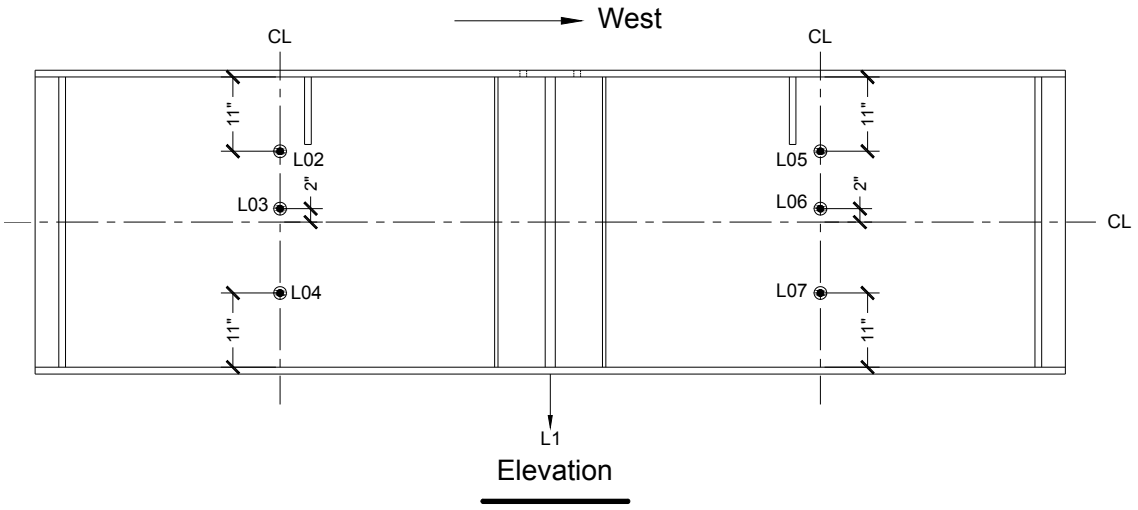

Figure A.5: Specimen SG3: Displacement Transducers

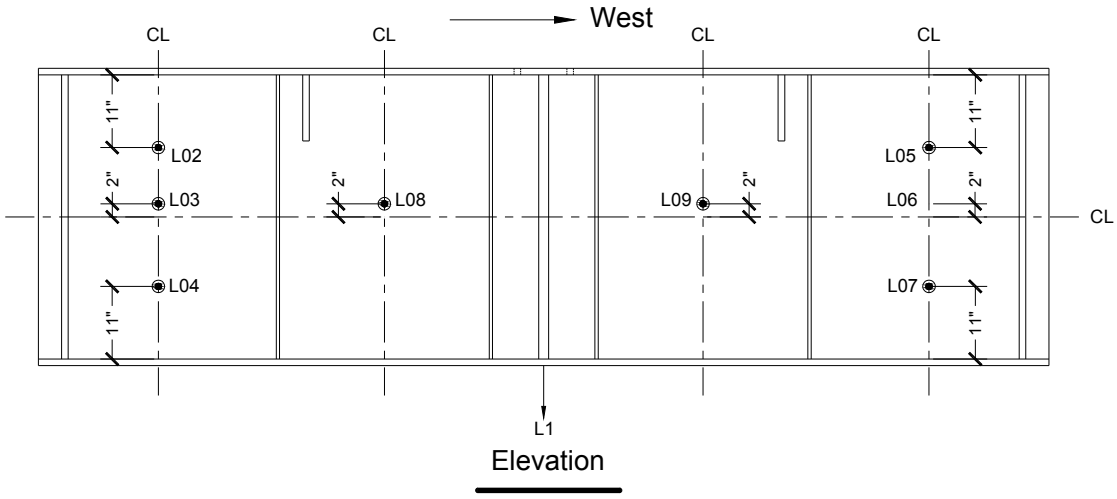

Figure A.6: Specimen SG4: Displacement Transducers

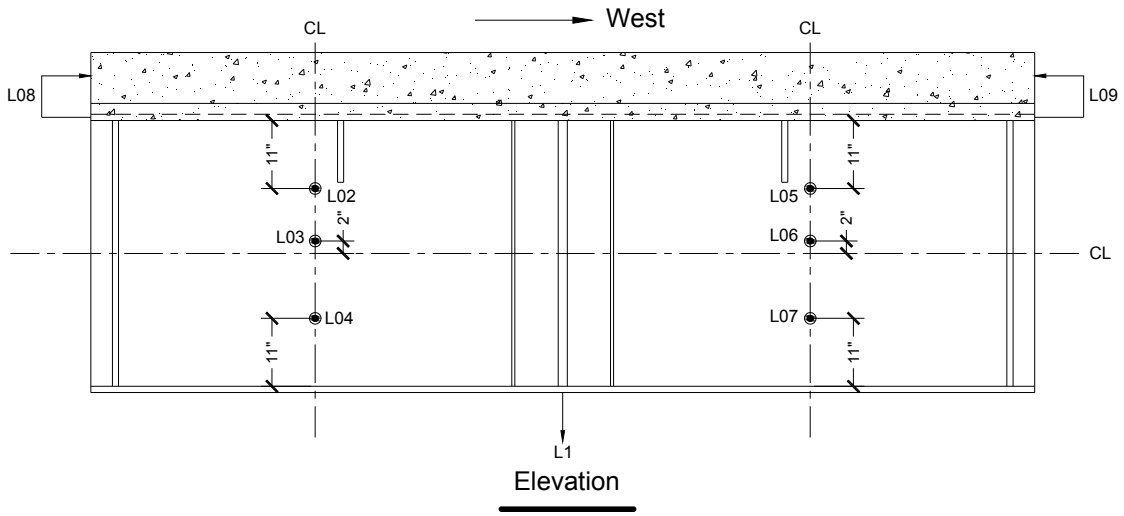

Figure A.7: Specimen CG3: Displacement Transducers

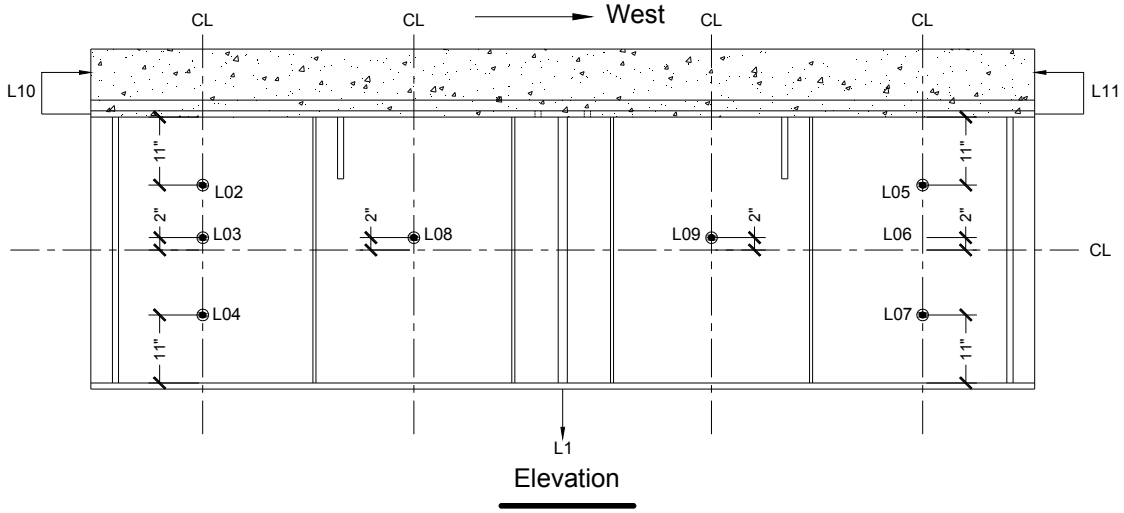

Figure A.8: Specimen CG4: Displacement Transducers

A2. Strain Gages

A number of strain rosettes and uniaxial strain gages were installed on the specimens. The layouts of the gages are shown in Figure A.9 to Figure A.16. The strain gages labeled in parentheses represent gages on back side of the specimens.

The strain gage rosettes consist of three individual strain gage elements oriented precisely 45° apart. The strain gage rosettes were installed on the web panels to measure the principal strains and directions. In all end panels excluding the West end panel of Specimen SG1, a group of strain gage rosettes were placed 3 in. apart along a line perpendicular to and intersecting the midpoint of the panel diagonal (see Figures A.9 through A.16).

Uniaxial strain gages were used to measure the strains at the specific locations. Most uniaxial strain gages were installed on the flanges and bearing stiffeners near plastic hinge locations. In Specimens SG2, CG1, and CG2, uniaxial strain gages were placed back-to-back on the bearing stiffeners to measure both flexural and axial strains.

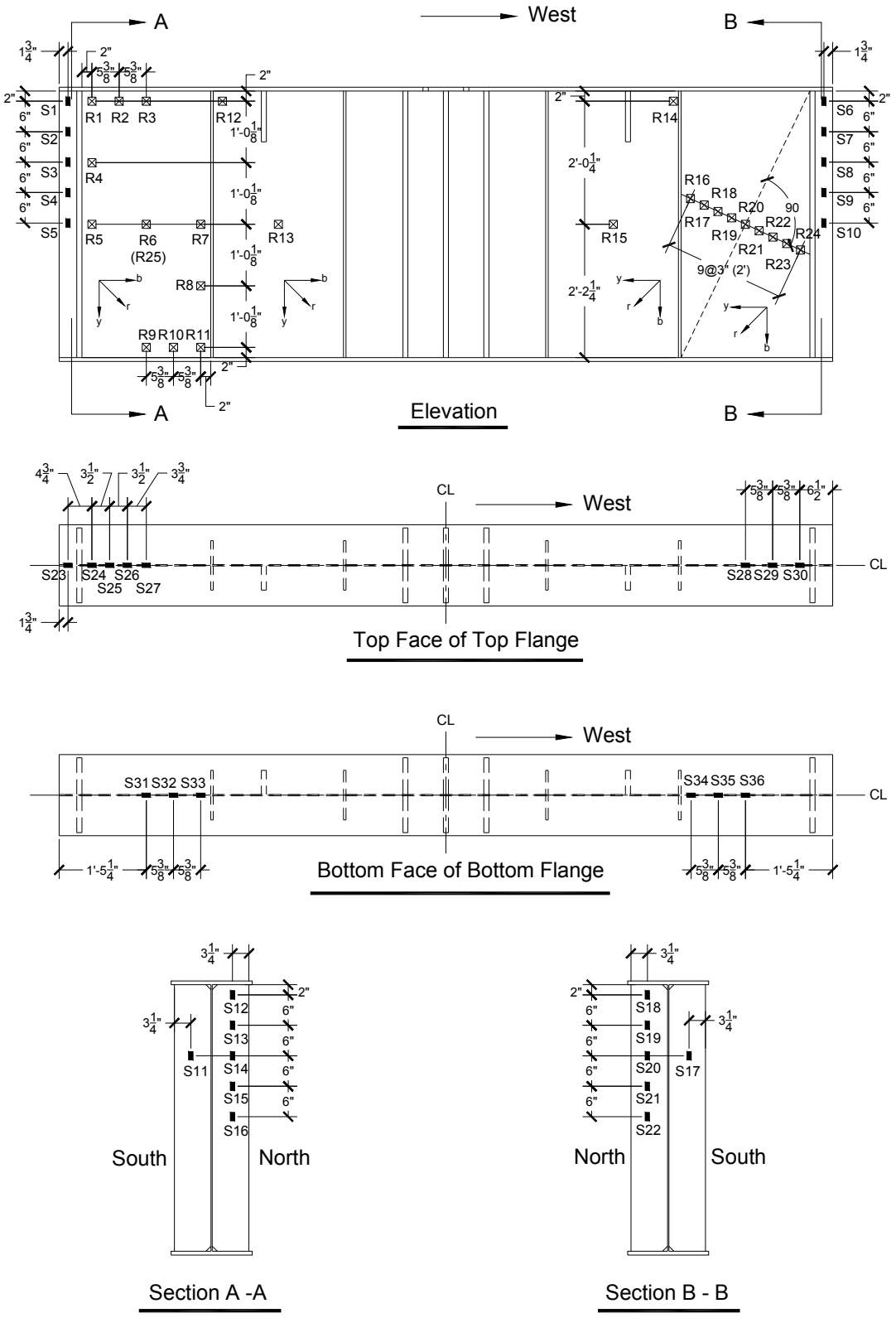

Figure A.9: Specimen SG1: Strain Gage and Rosette Locations

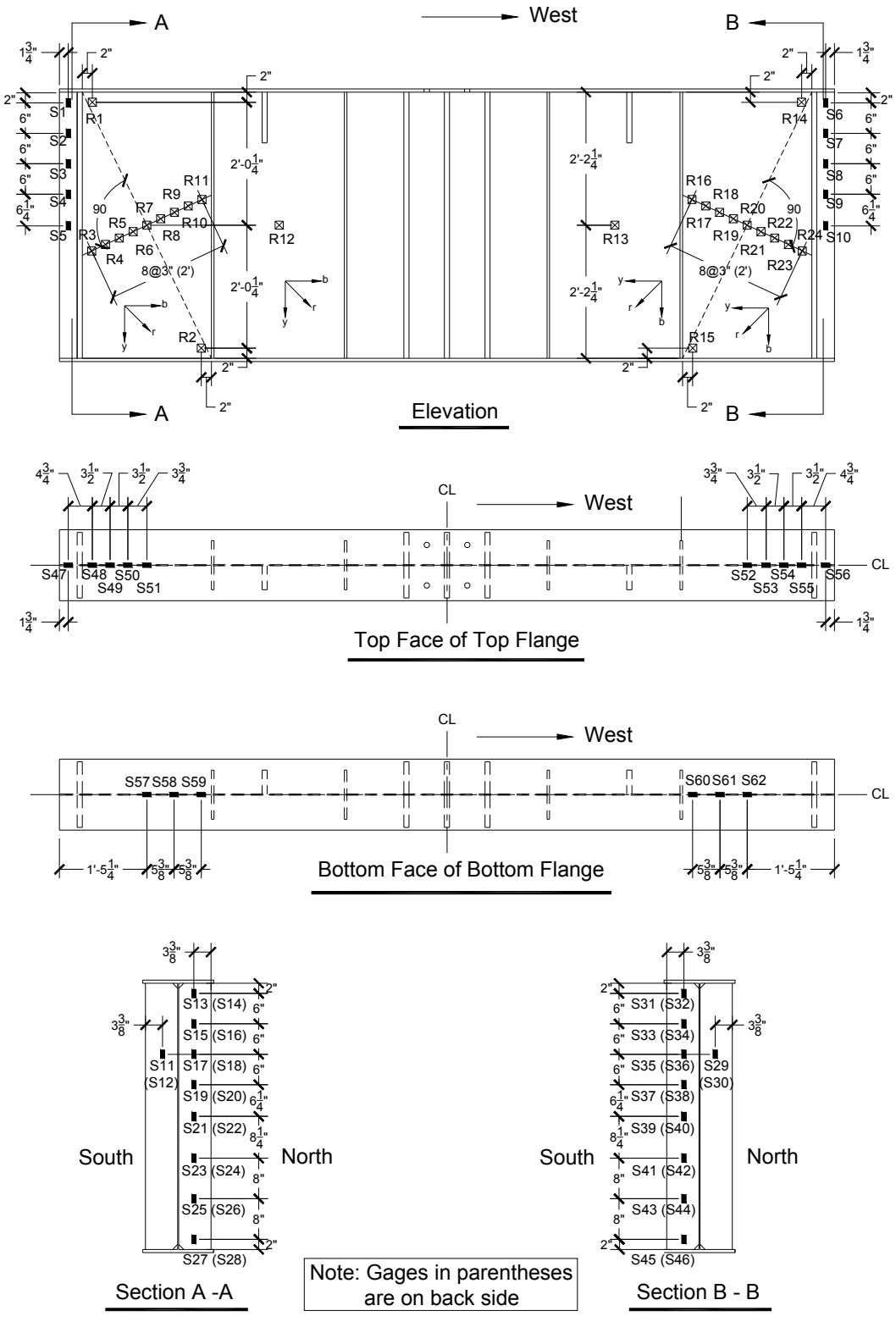

Figure A.10: Specimen SG2: Strain Gage and Rosette Locations

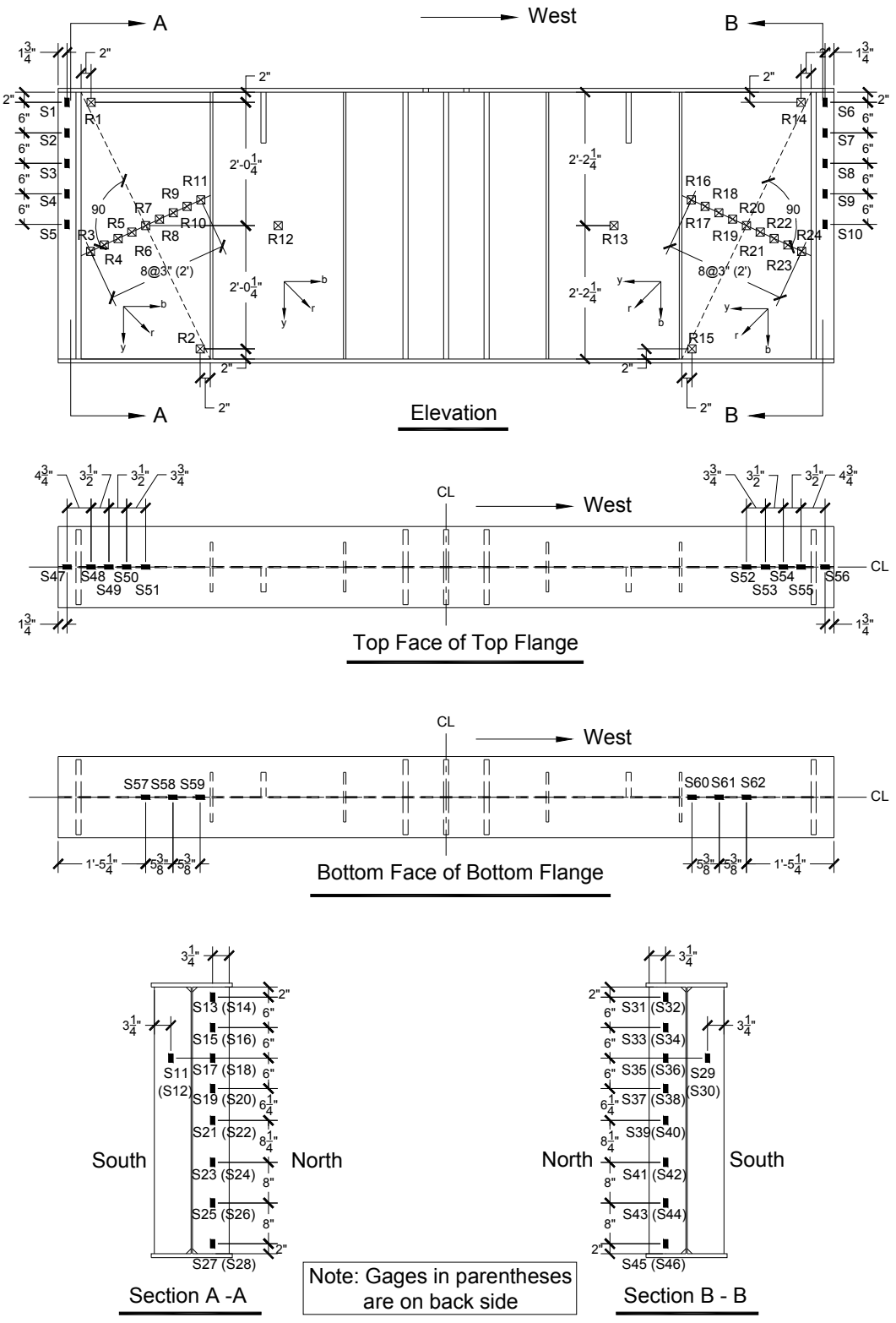

Figure A.11: Specimen CG1: Strain Gage and Rosette Locations

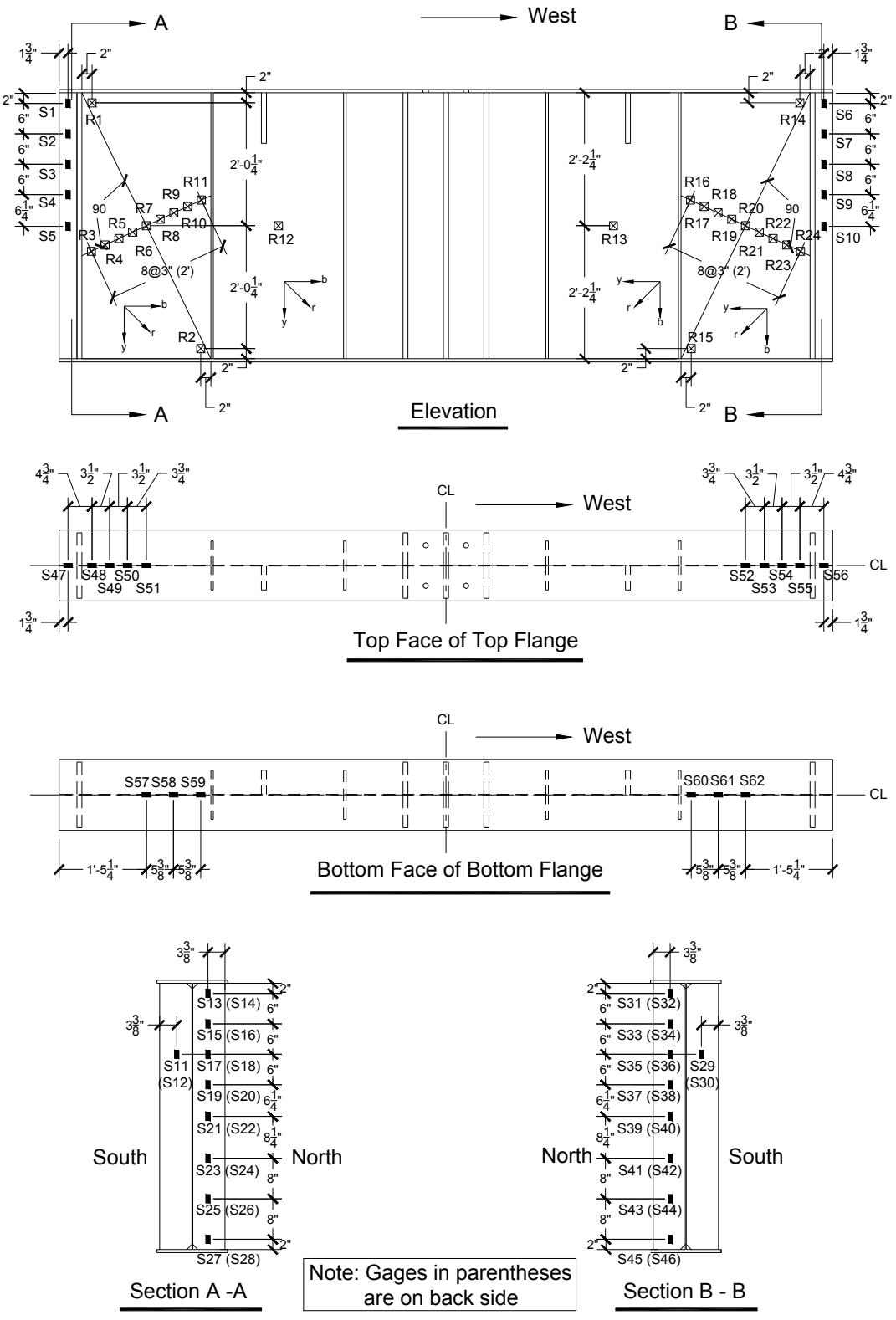

Figure A.12: Specimen CG2: Strain Gage and Rosette Locations

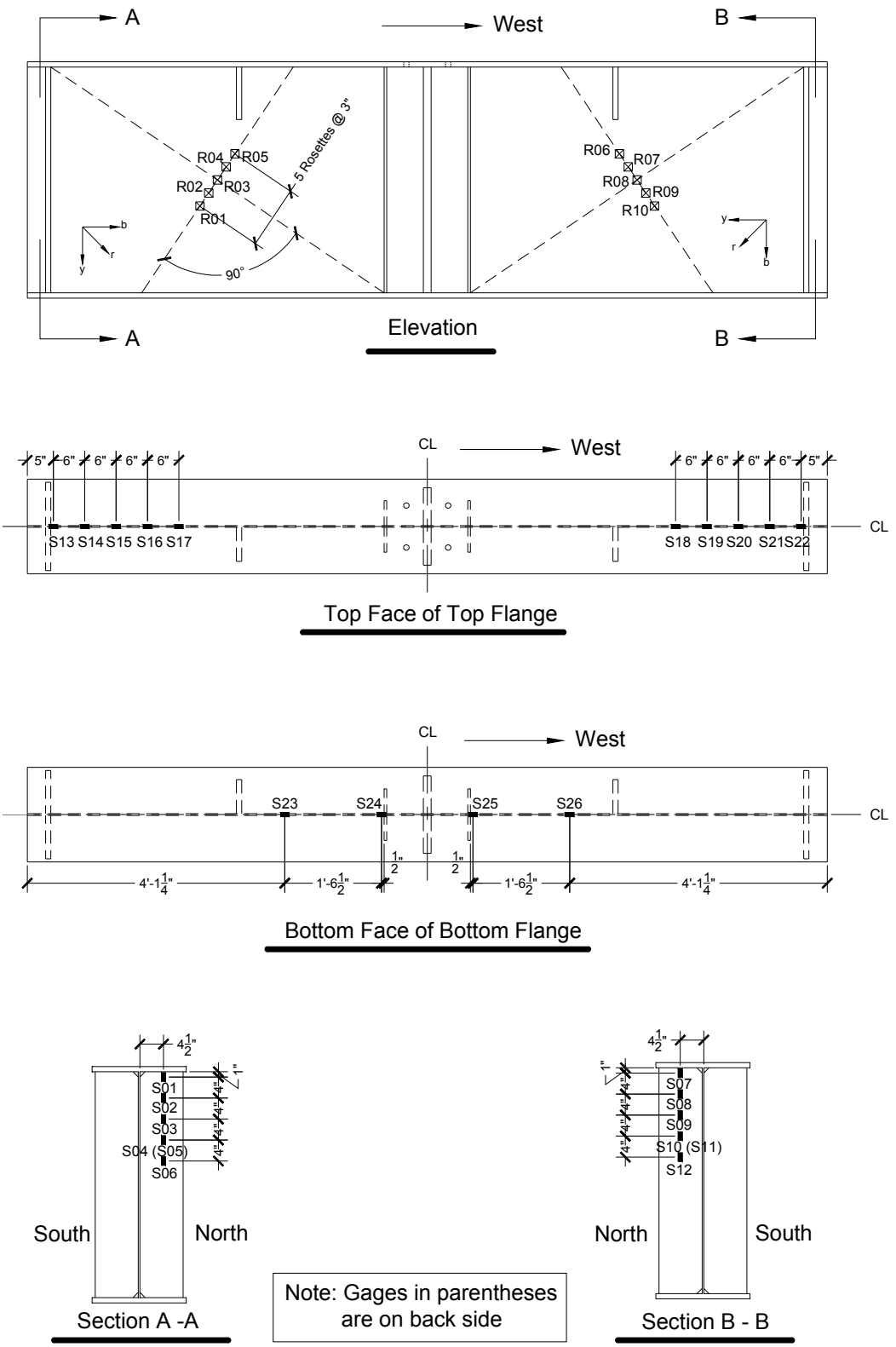

Figure A.13: Specimen SG3: Strain Gage and Rosette Locations

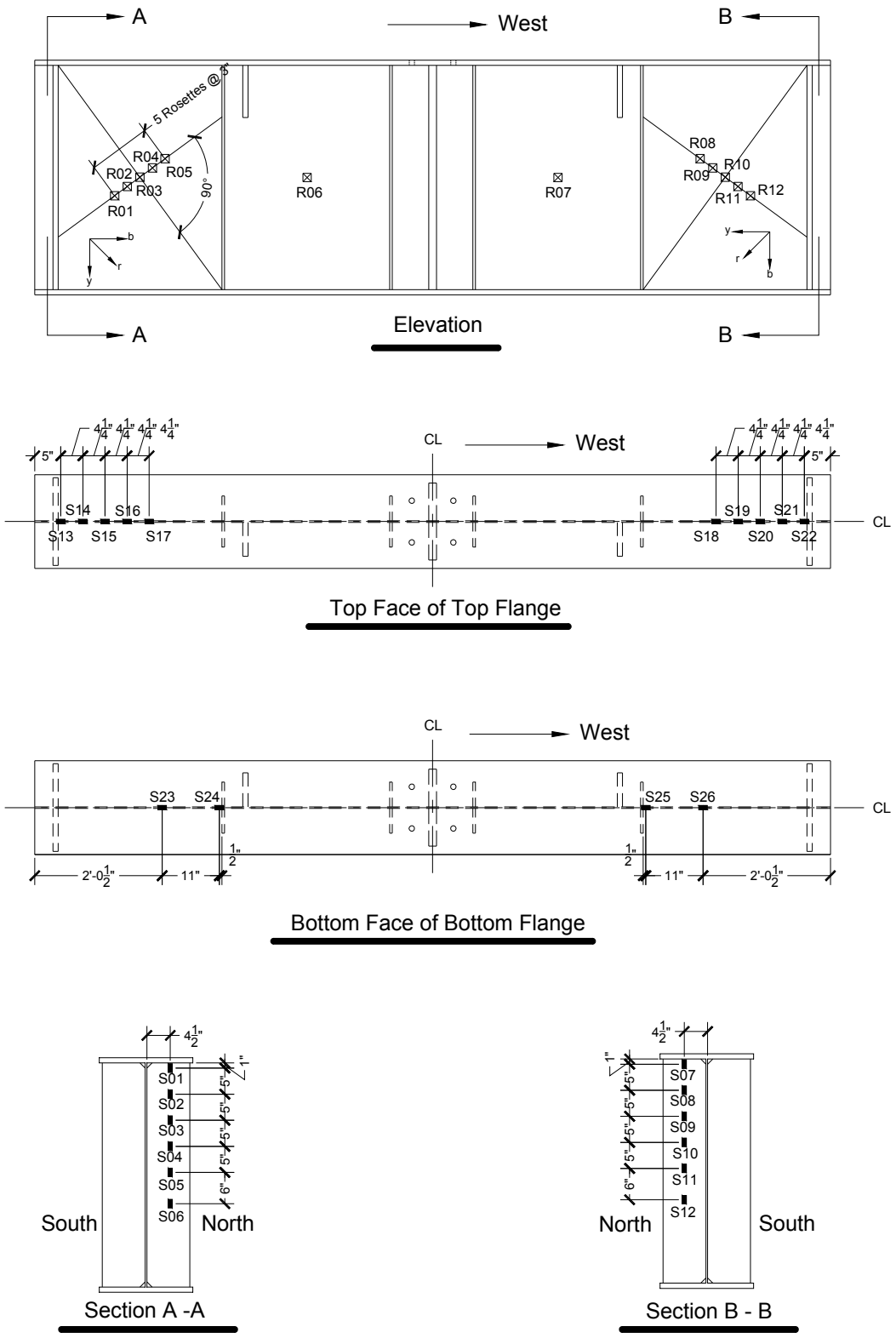

Figure A.14: Specimen SG4: Strain Gage and Rosette Locations

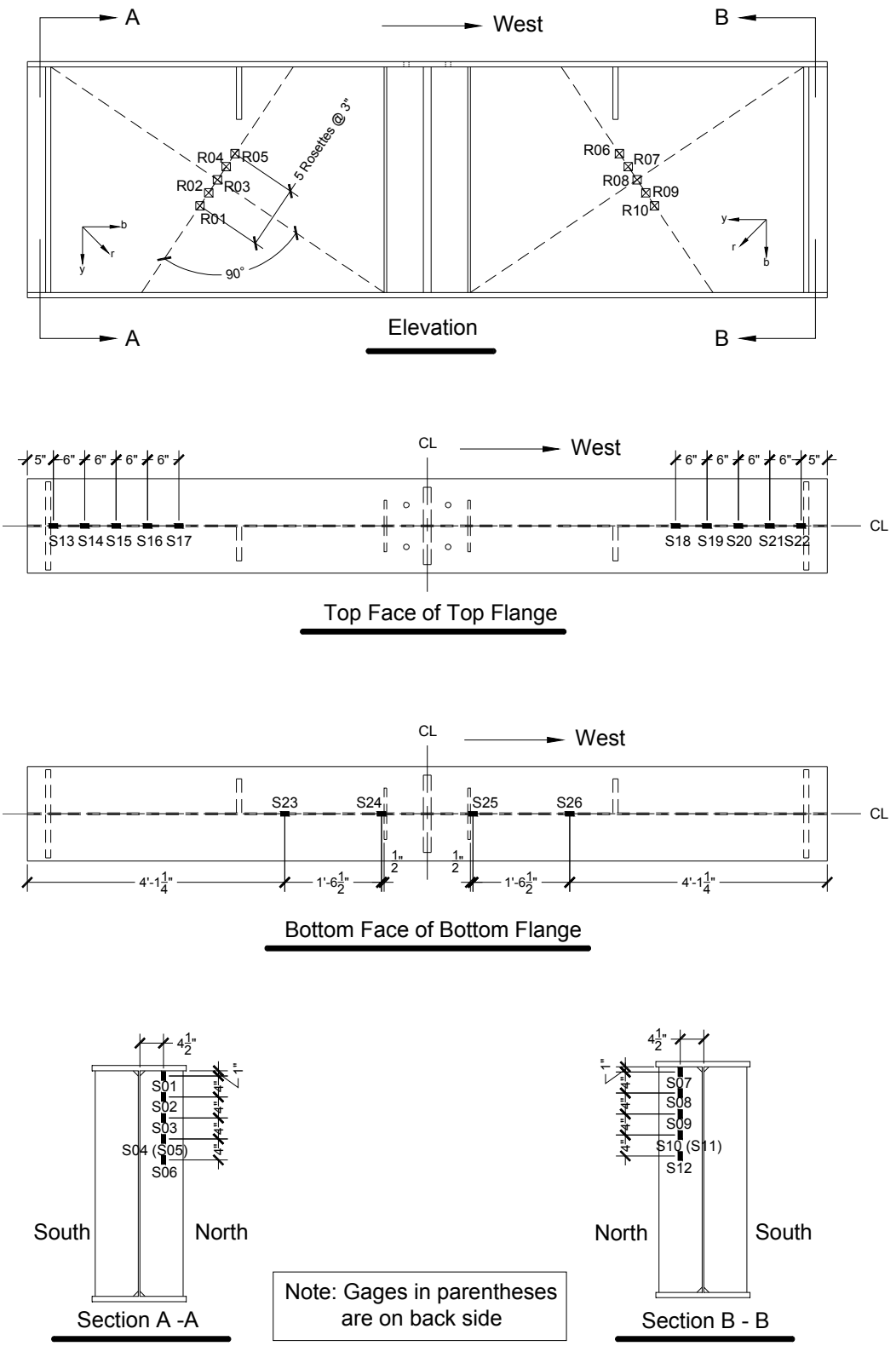

Figure A.15: Specimen CG3: Strain Gage and Rosette Locations

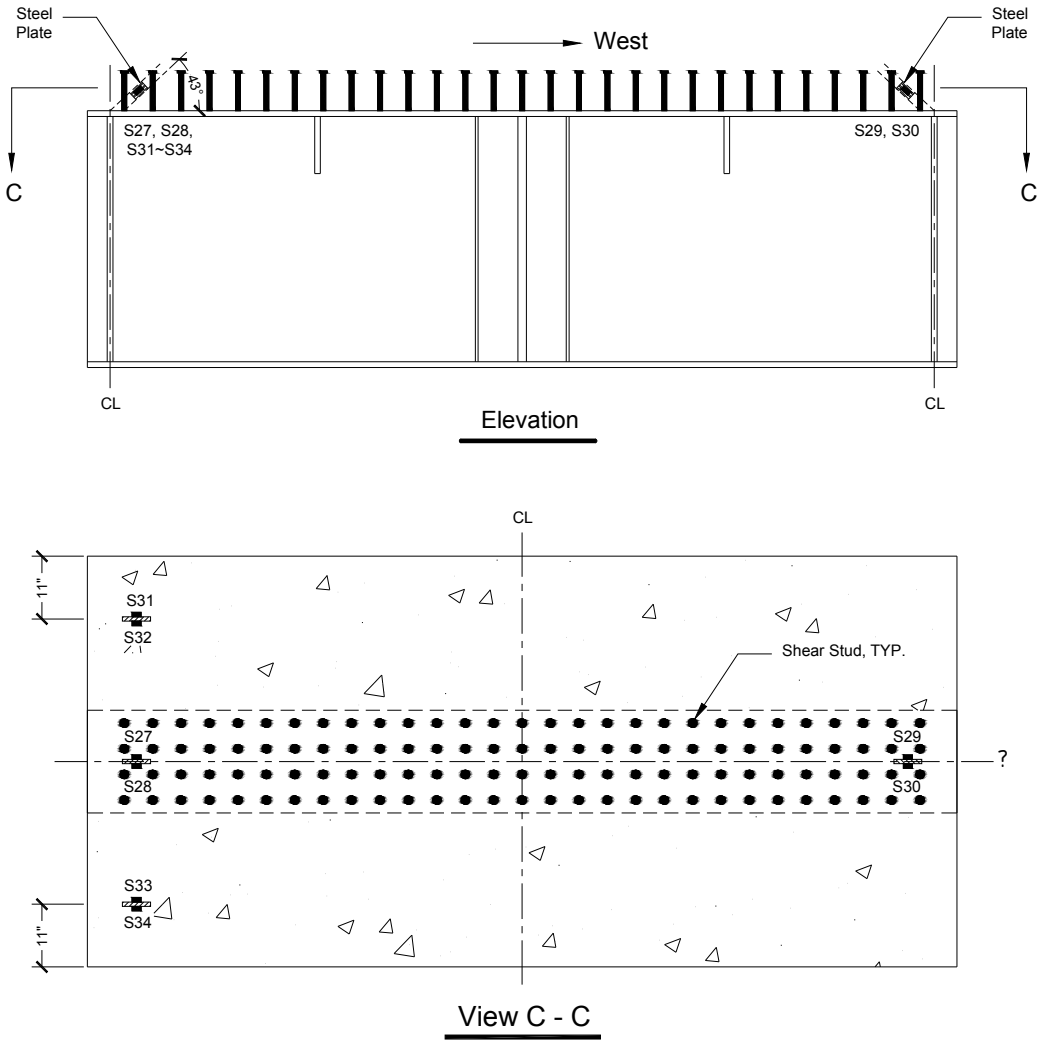

Figure A.15: Specimen CG3: Strain Gage and Rosette Locations (continued)

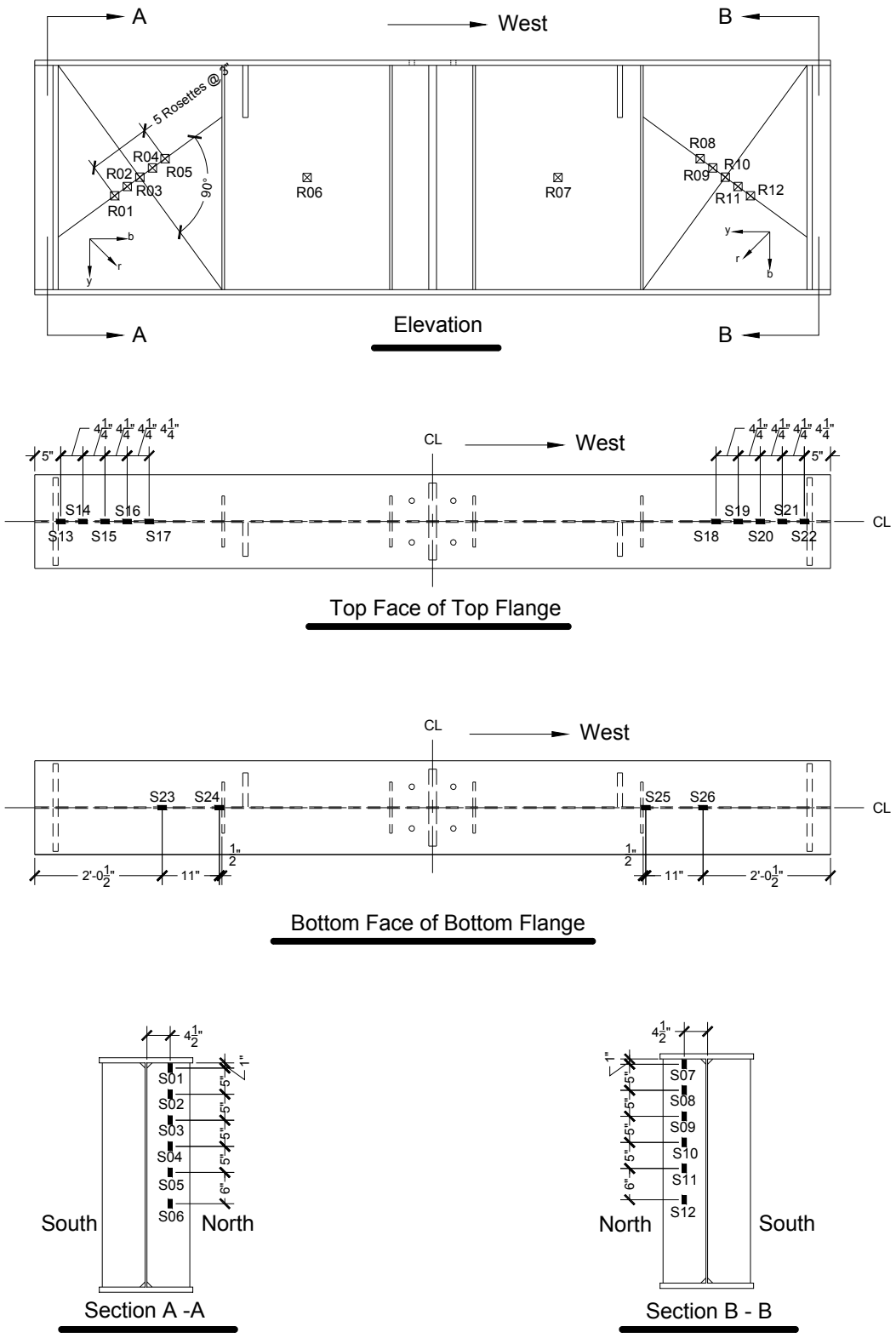

Figure A.16: Specimen CG4: Strain Gage and Rosette Locations

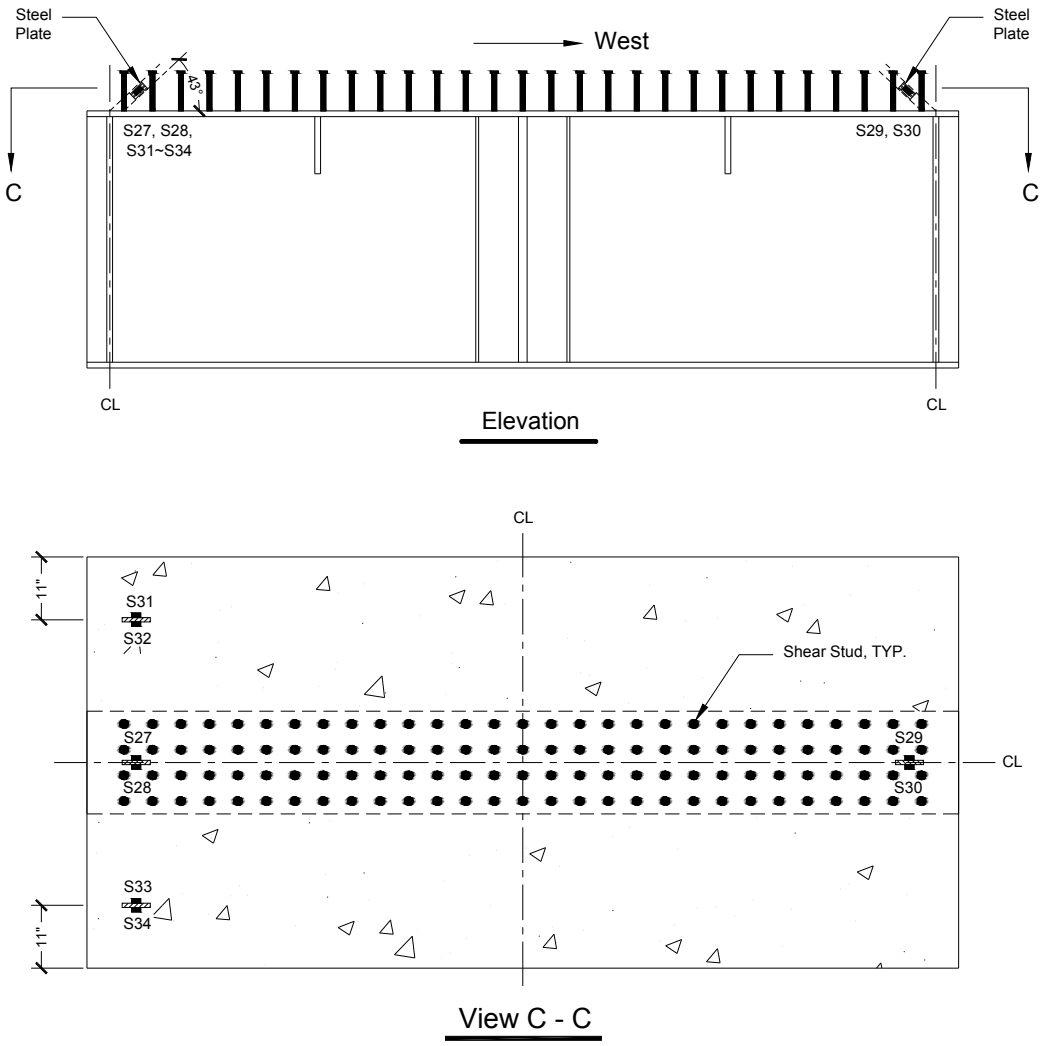

Figure A.16: Specimen CG4: Strain Gage and Rosette Locations (continued)

APPENDIX B. PLOTS OF DEFORMATION AND STRAIN

B1. Deformation Plots

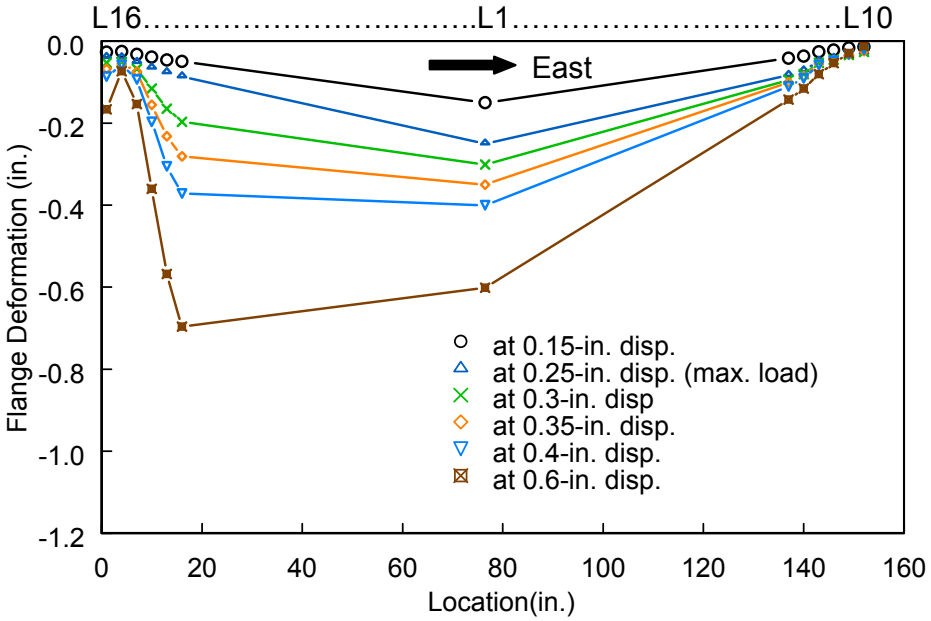

(a) Top Flange Deformation (in.)

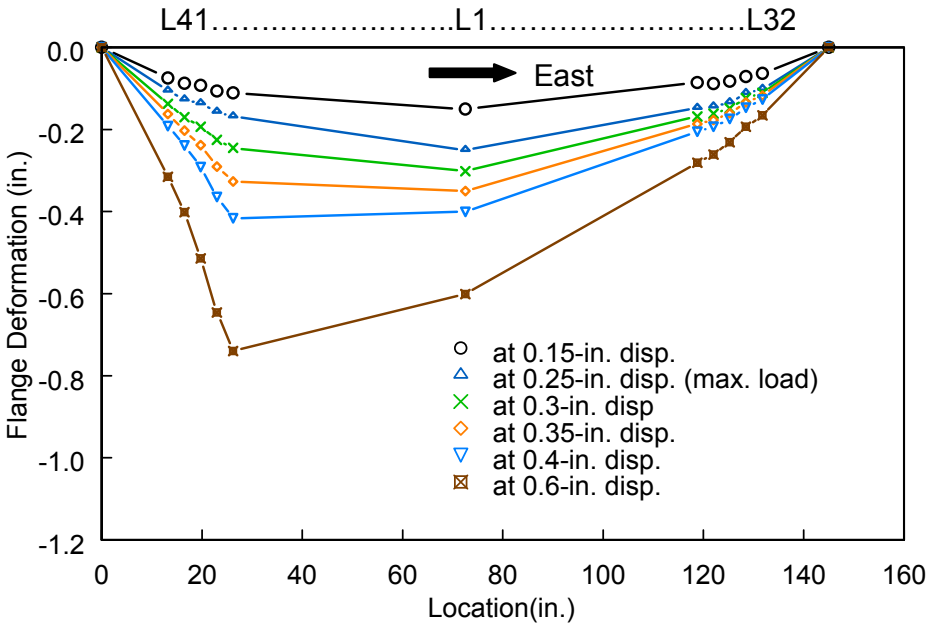

(b) Bottom Flange Deformation (in.)

Figure B.1: Specimen SG1: Flange Deformation

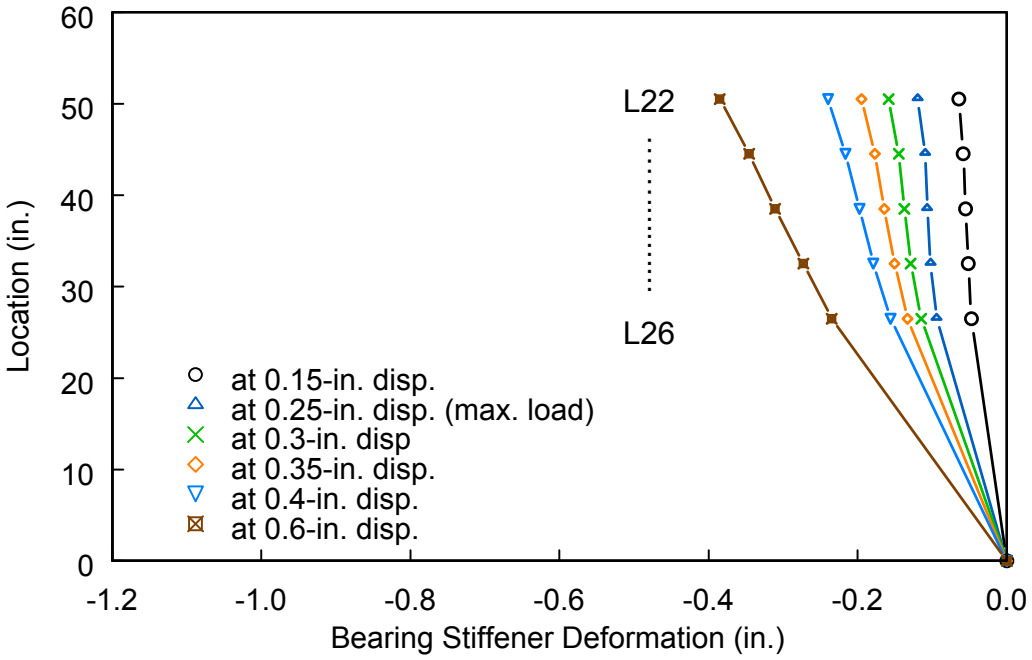

(a) East Side

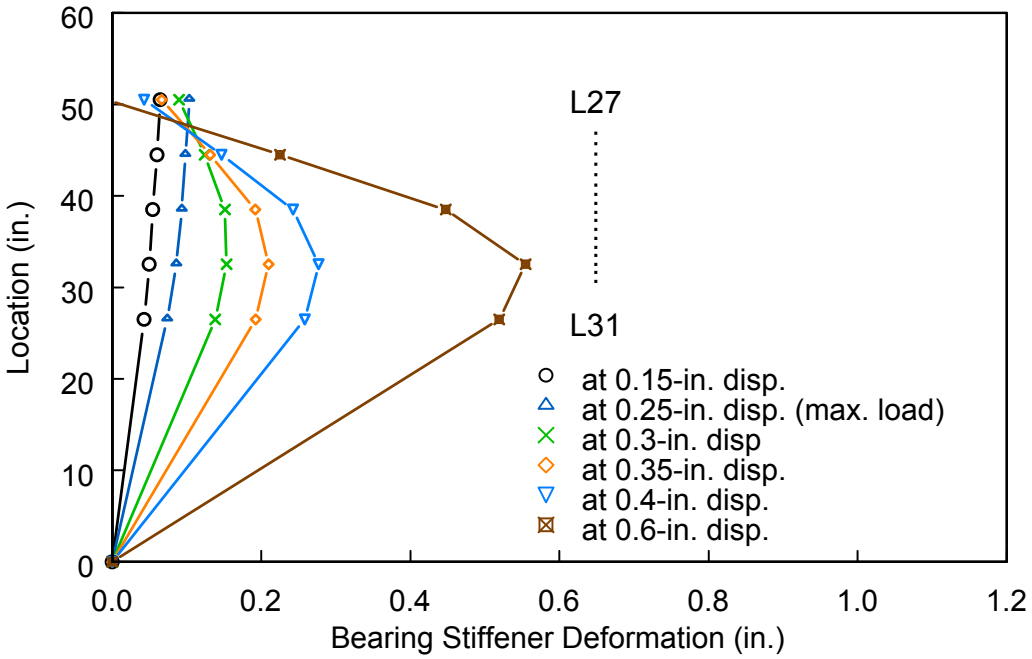

(b) West Side

Figure B.2: Specimen SG1: Bearing Stiffener Deformation

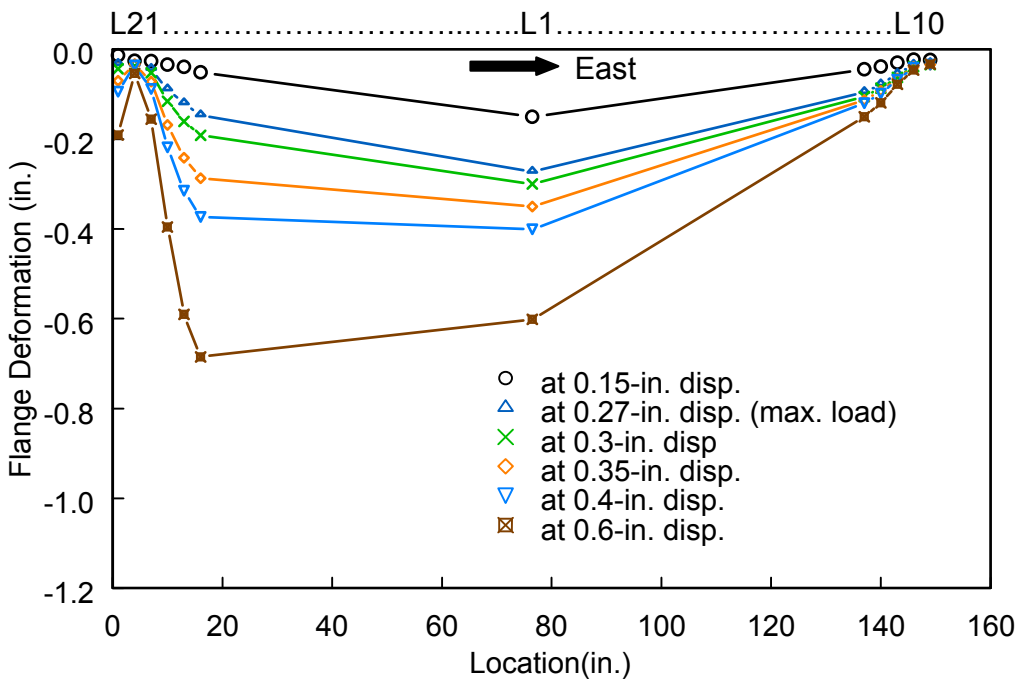

(a) Top Flange Deformation (in.)

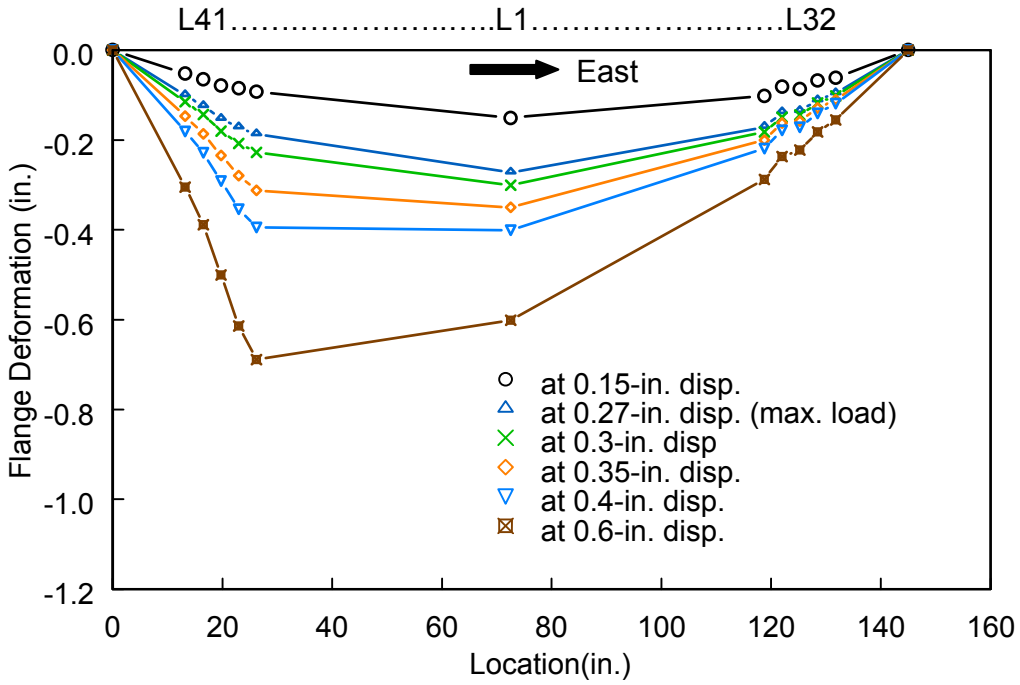

(b) Bottom Flange Deformation (in.)

Figure B.3: Specimen SG2: Flange Deformation

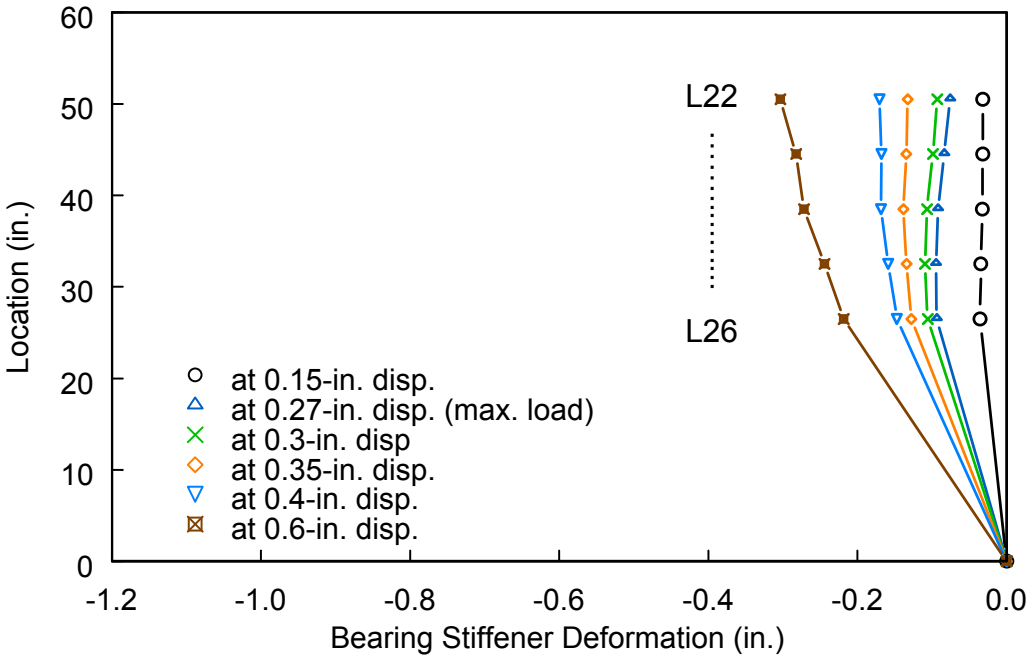

(a) East Side

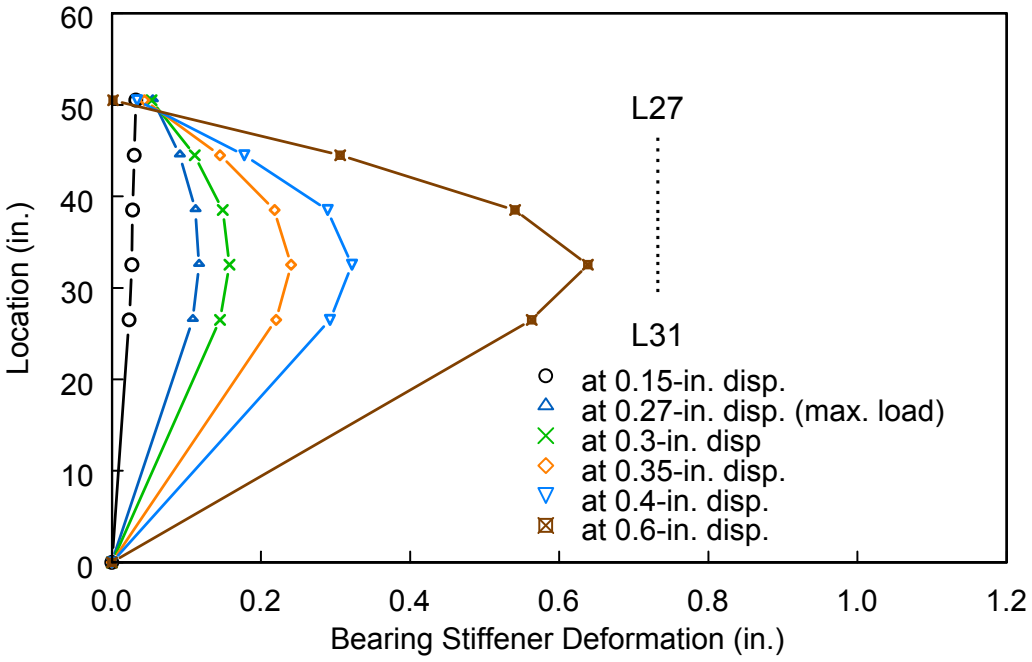

(b) West Side

Figure B.4: Specimen SG2: Bearing Stiffener Deformation

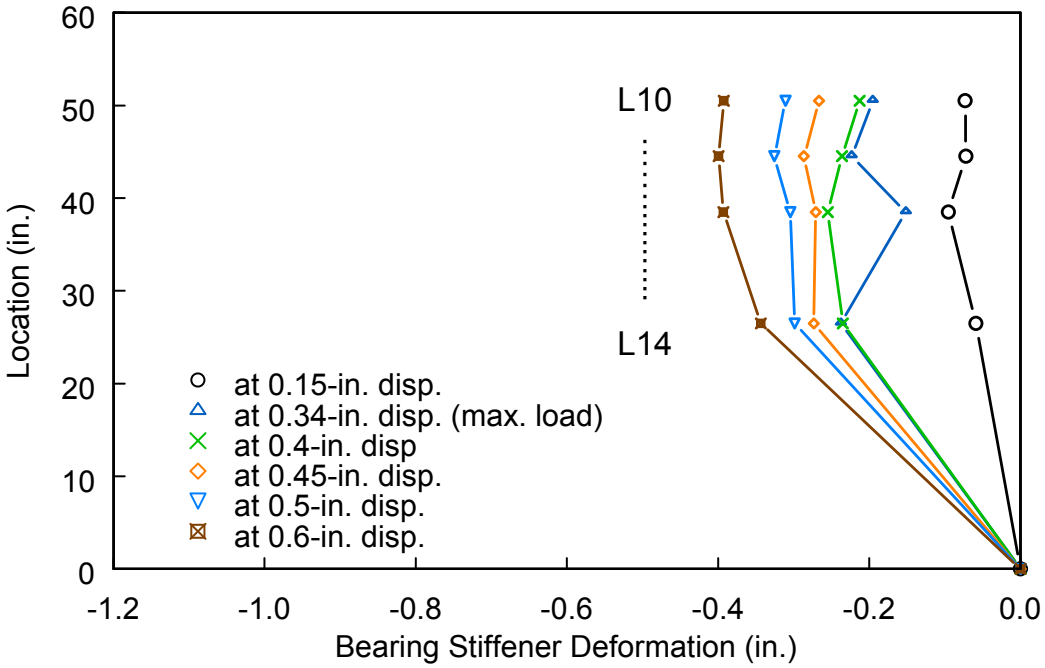

(a) East Side

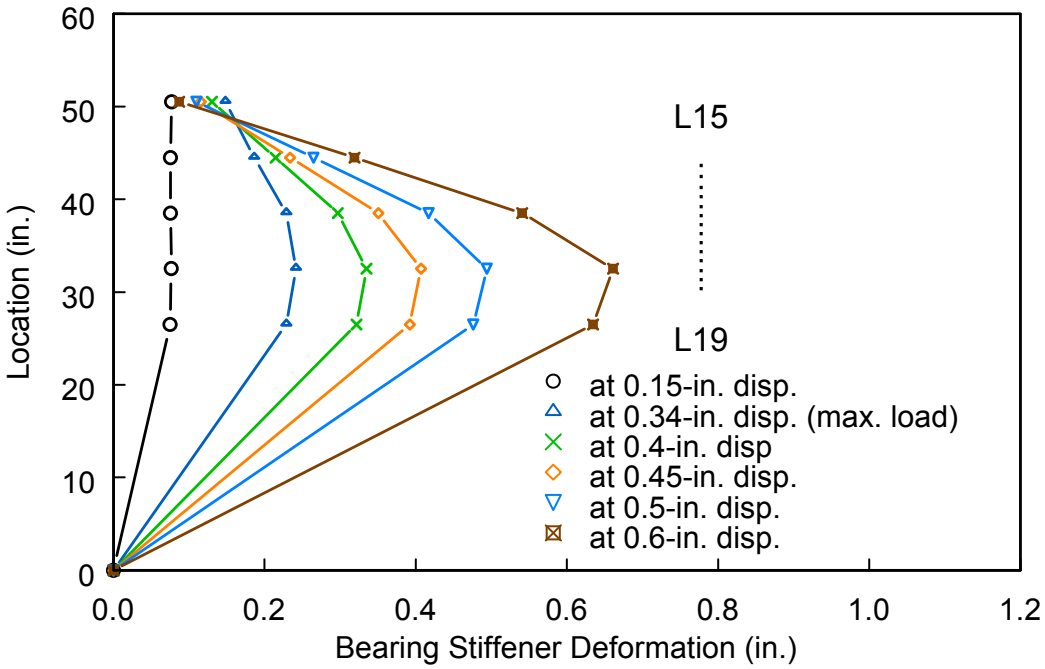

(b) West Side

Figure B.5: Specimen CG1: Bearing Stiffener Deformation

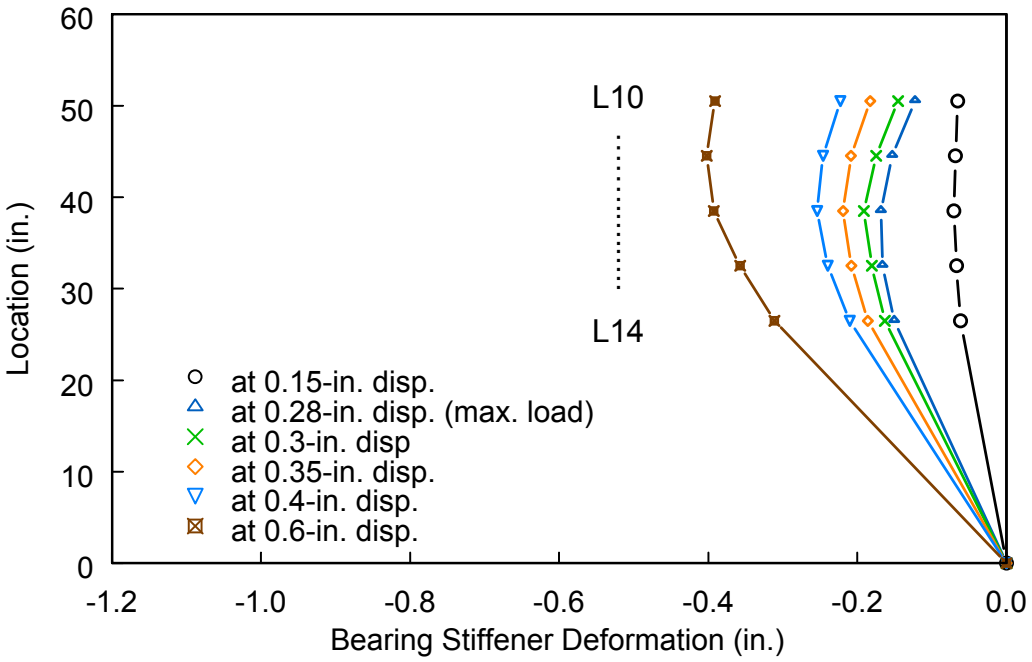

(a) East Side

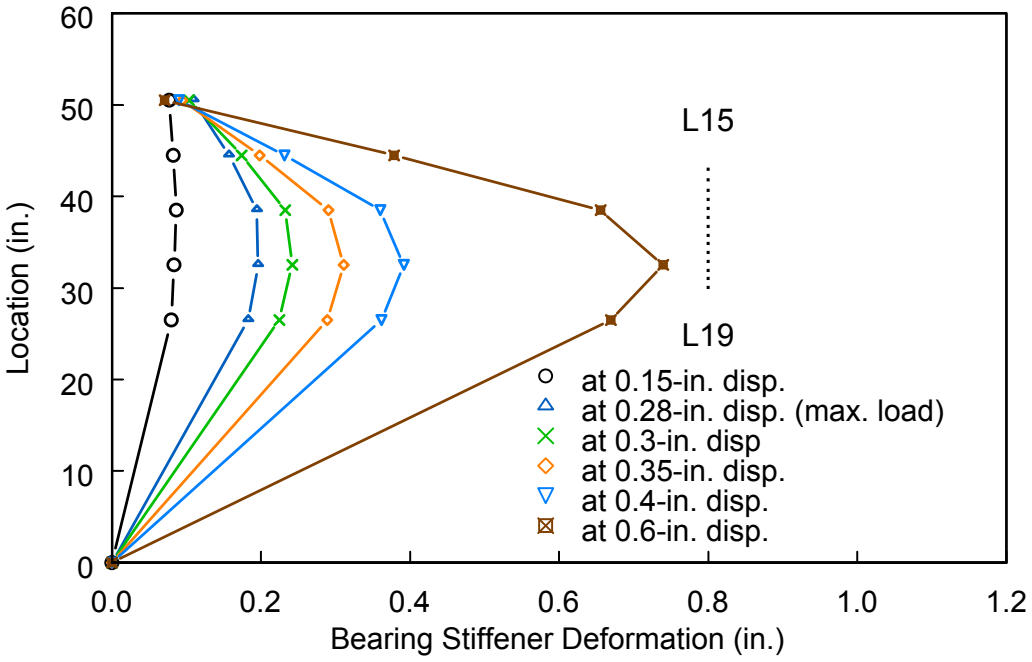

(b) West Side

Figure B.6: Specimen CG2: Bearing Stiffener Deformation

B2. Strain Plots

B2. 1 Principal Strain Plots in Web Panels

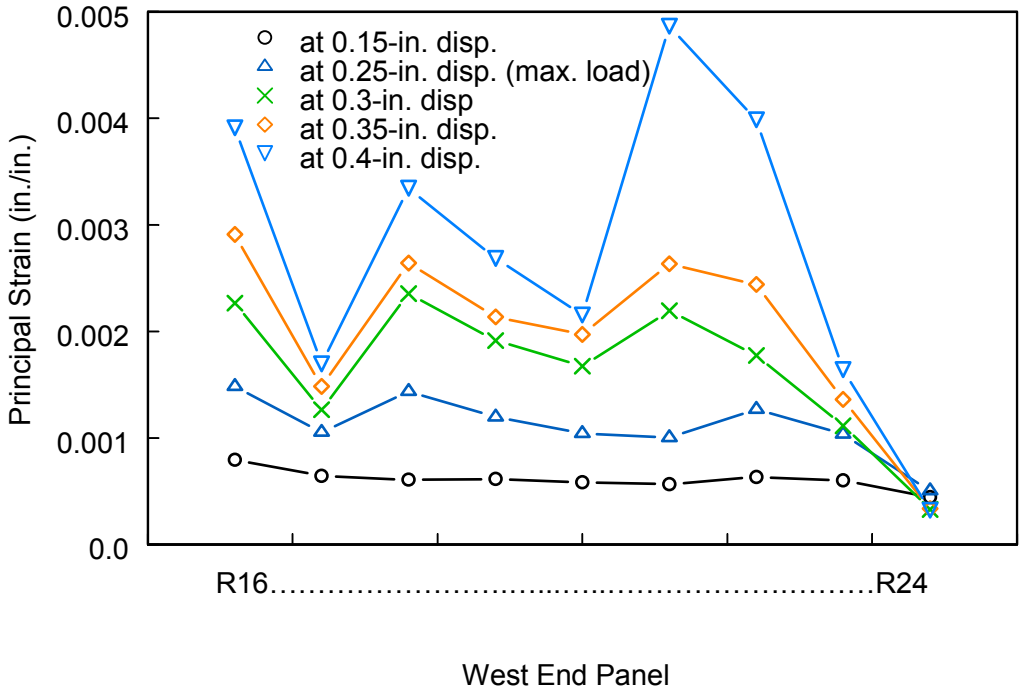

Figure B.7: Specimen SG1: Principal Strain

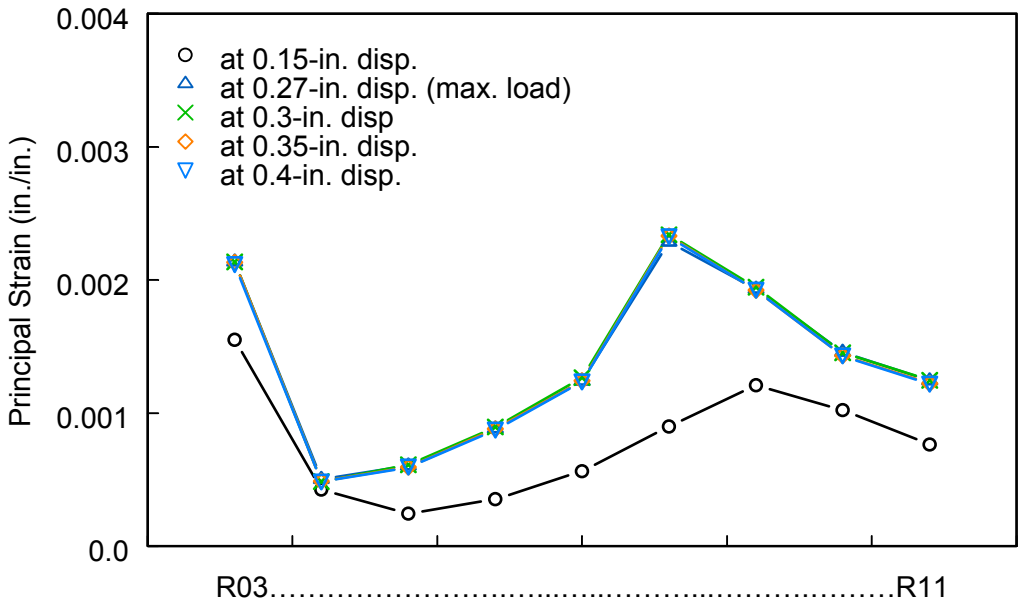

(a) East End Panel

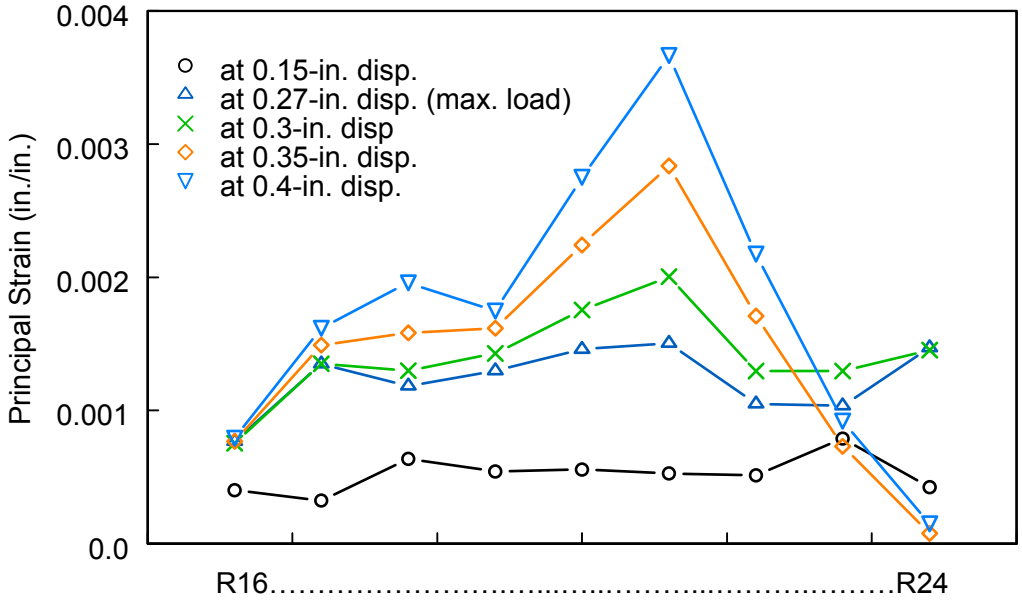

(b) West End Panel

Figure B.8: Specimen SG2: Principal Strain

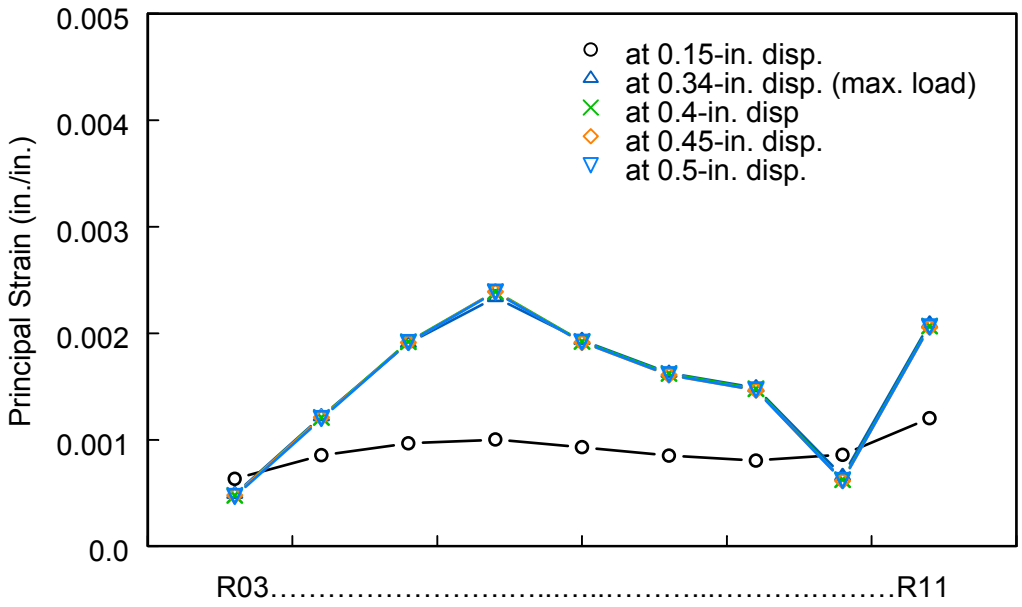

(a) East End Panel

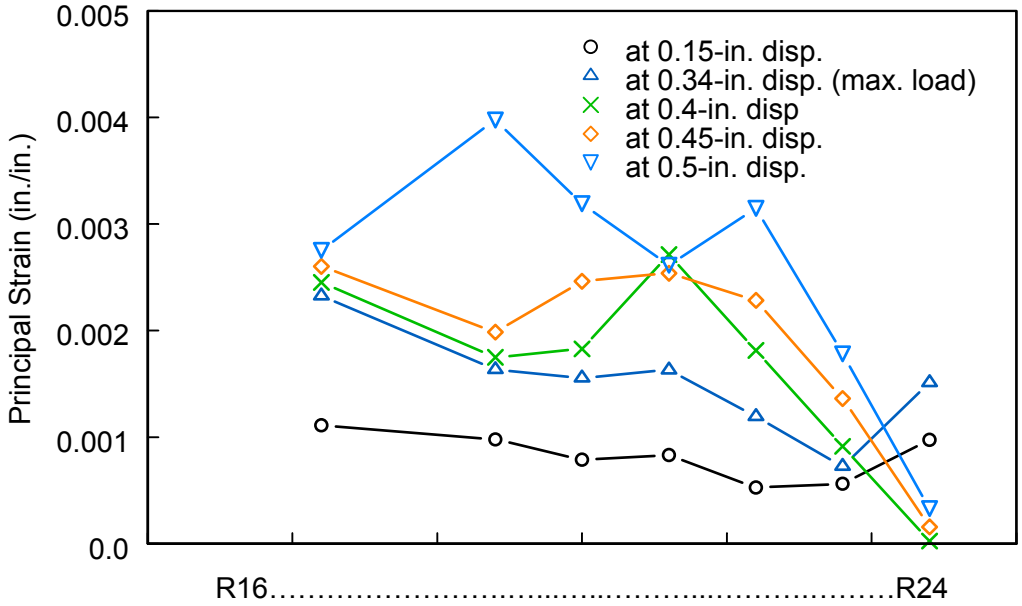

(b) West End Panel

Figure B.9: Specimen CG1: Principal Strain

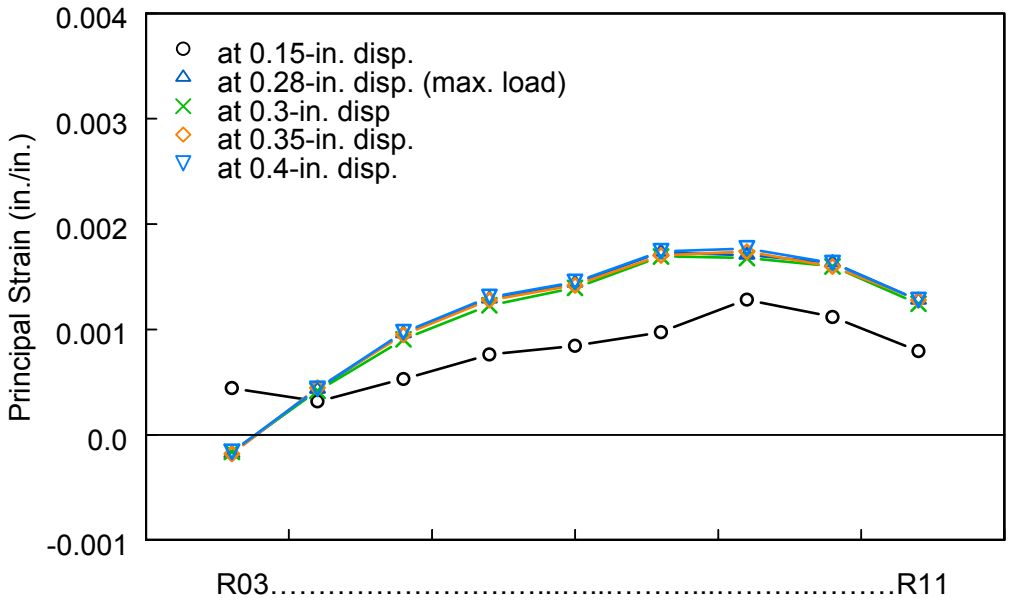

(a) East End Panel

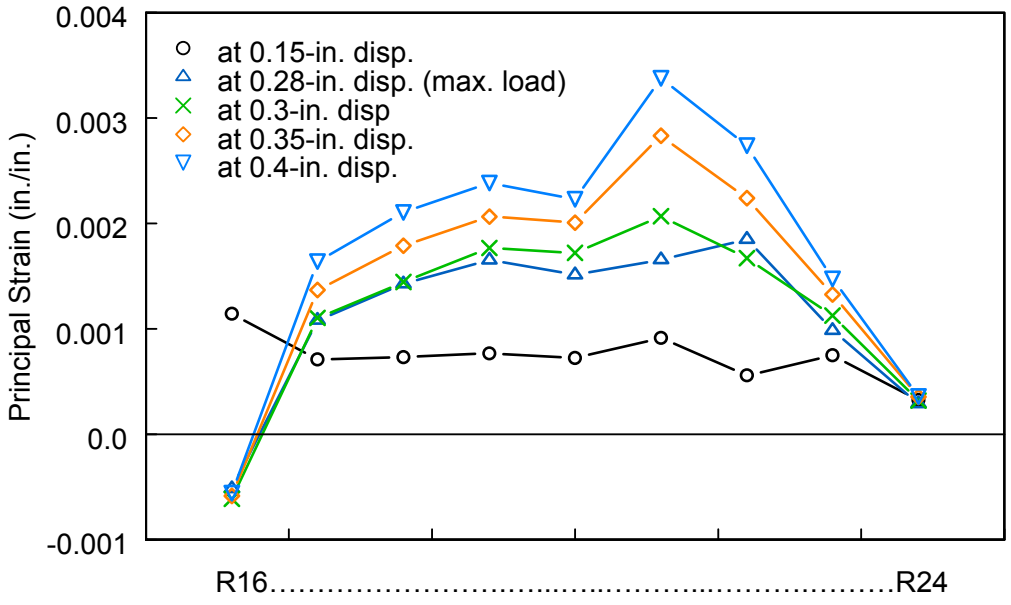

(b) West End Panel

Figure B.10: Specimen CG2: Principal Strain

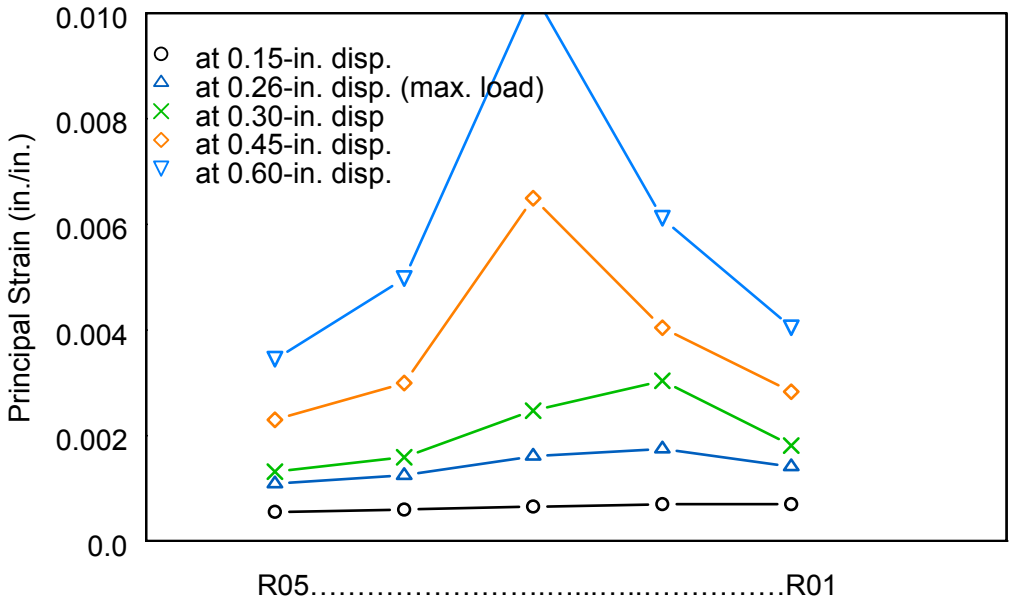

(a) East End Panel

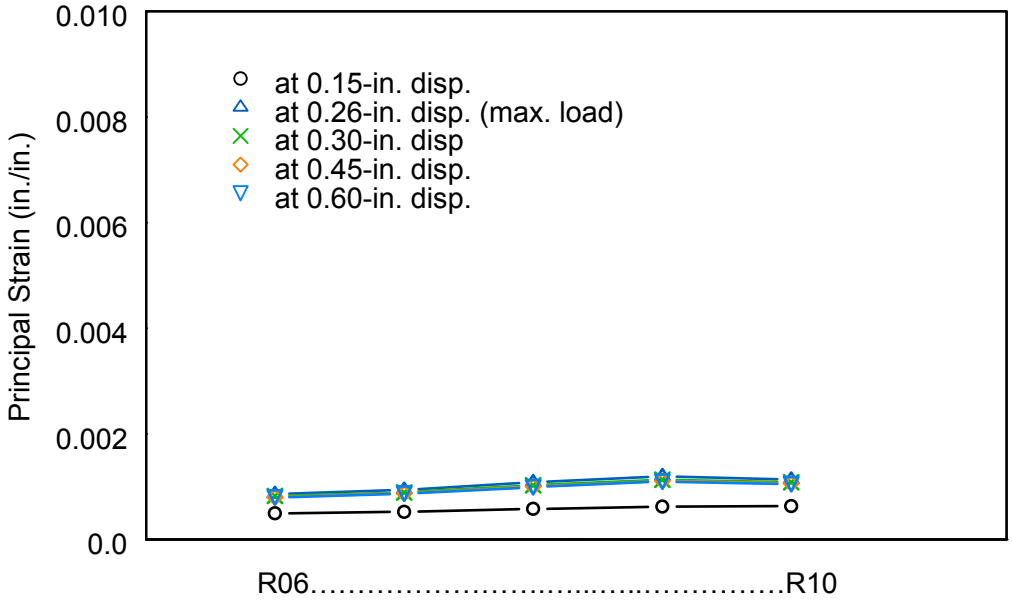

(b) West End Panel

Figure B.11: Specimen SG3: Principal Strain

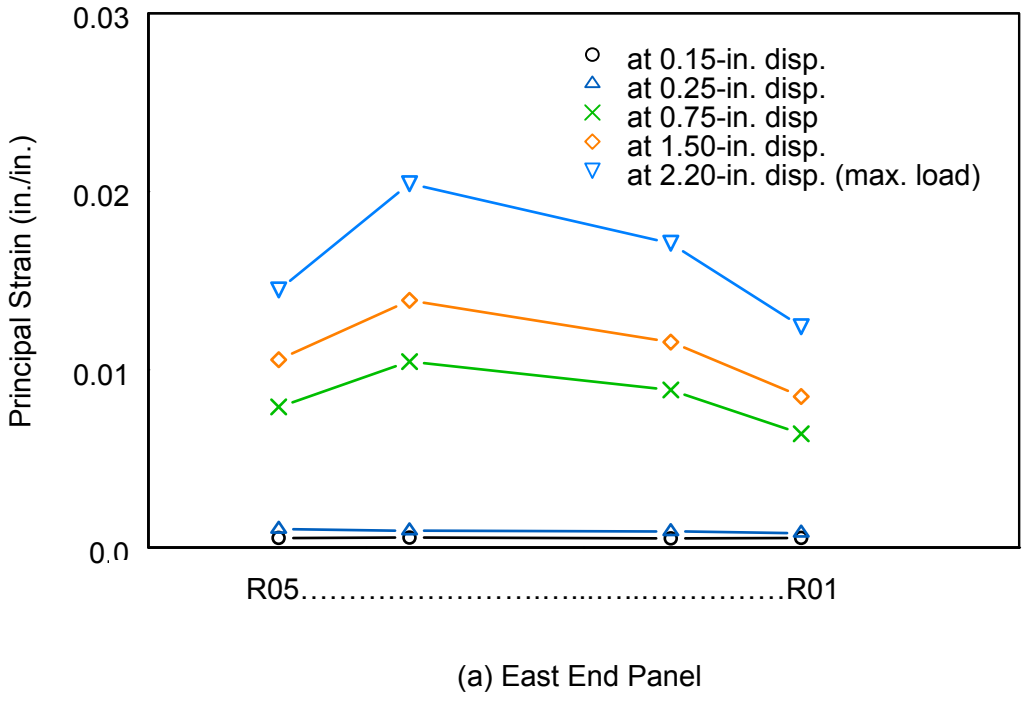

(a) East End Panel

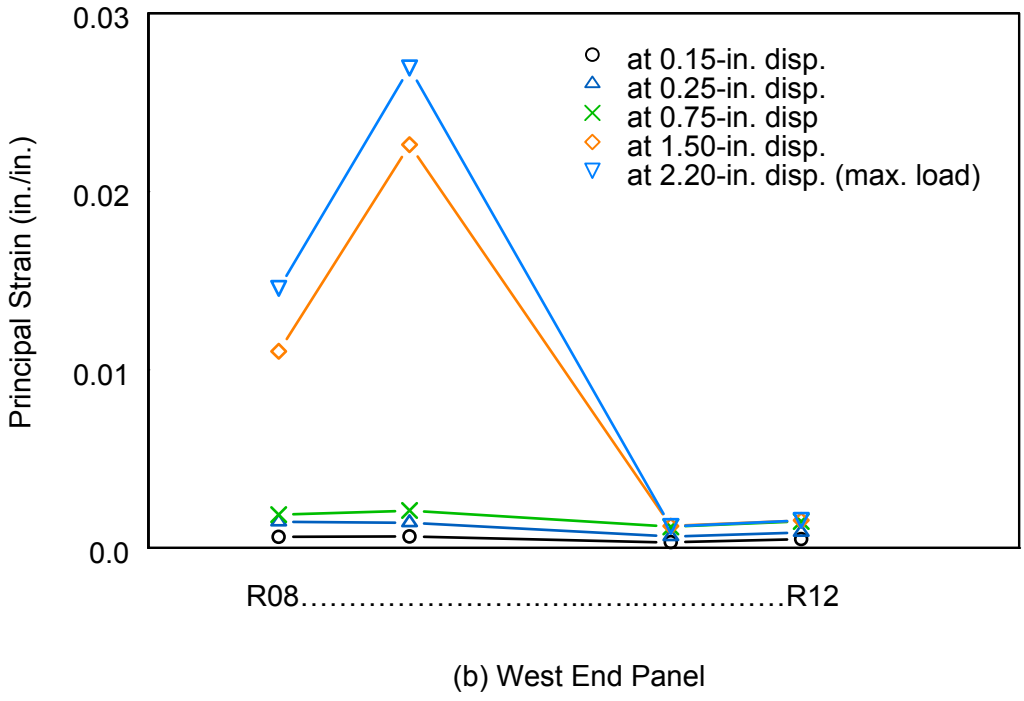

(b) West End Panel

Figure B.12: Specimen SG4: Principal Strain

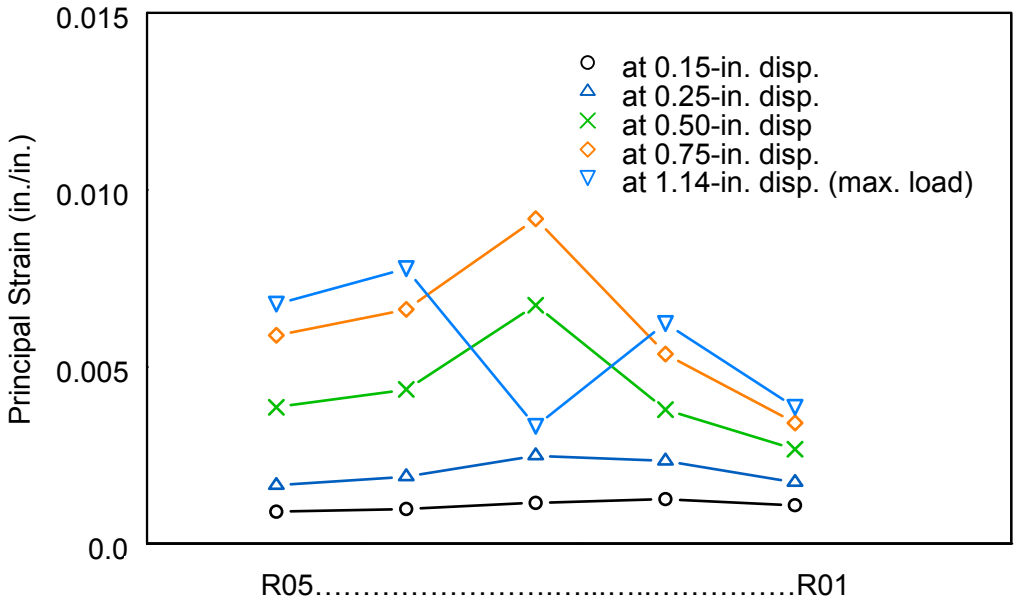

(a) East End Panel

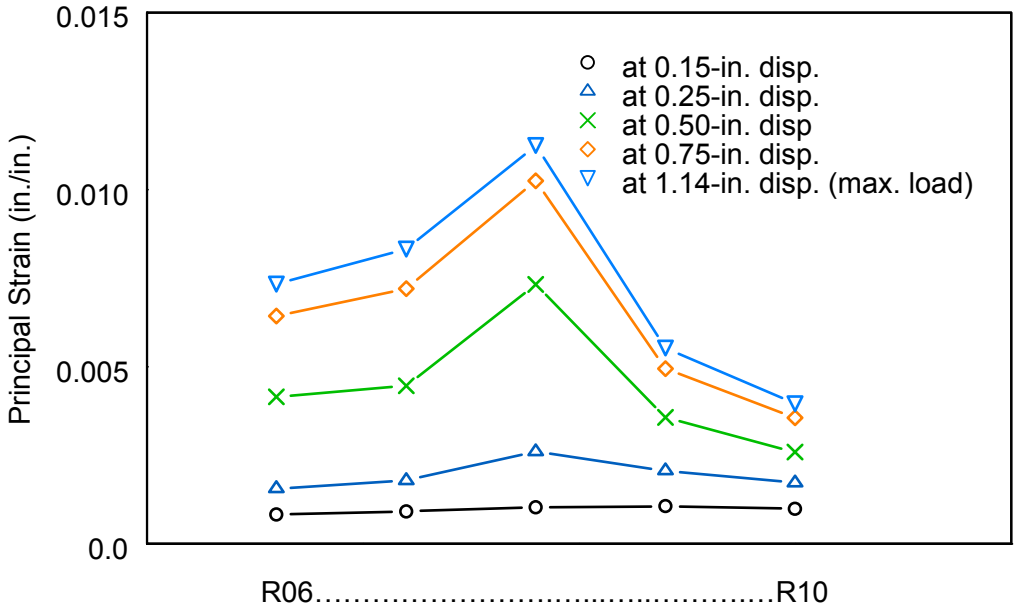

(b) West End Panel

Figure B.13: Specimen CG3: Principal Strain

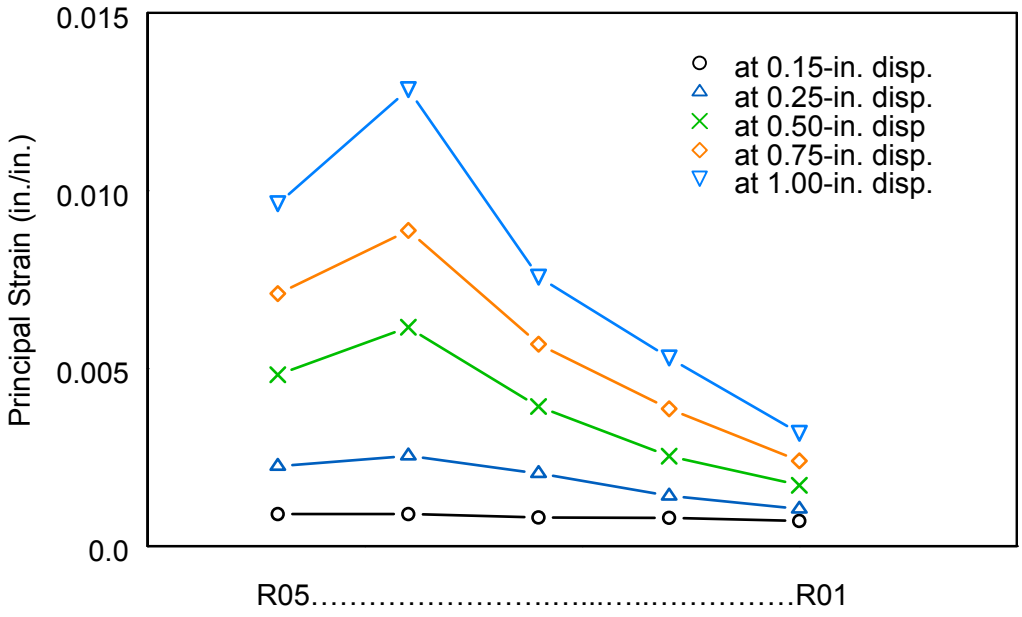

(a) East End Panel

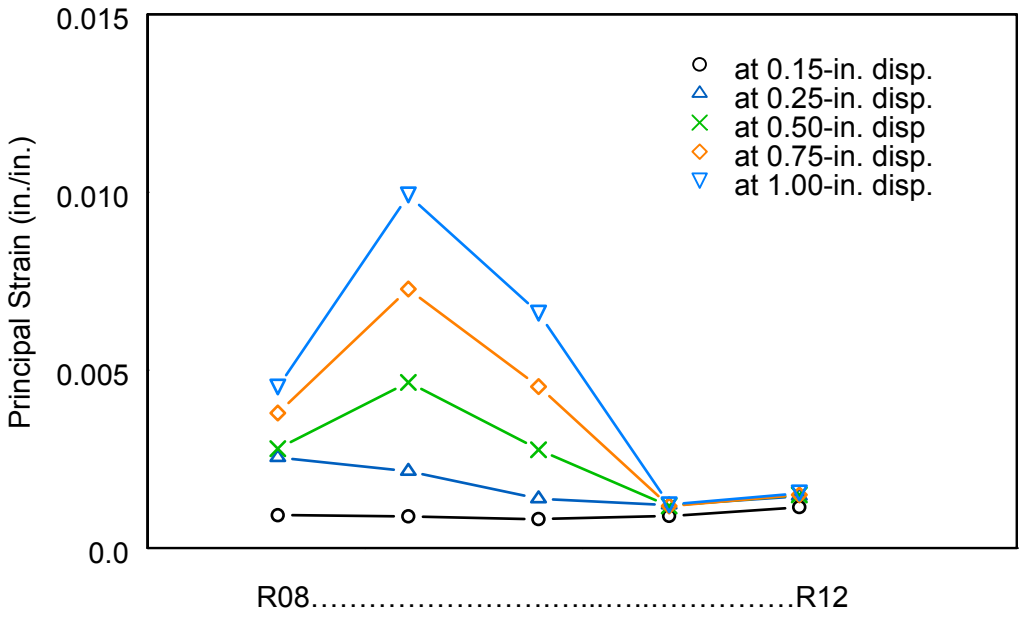

(b) West End Panel

Figure B.14: Specimen CG4: Principal Strain

B2. 2 Strain Plots in Extended Webs and Bearing Stiffeners

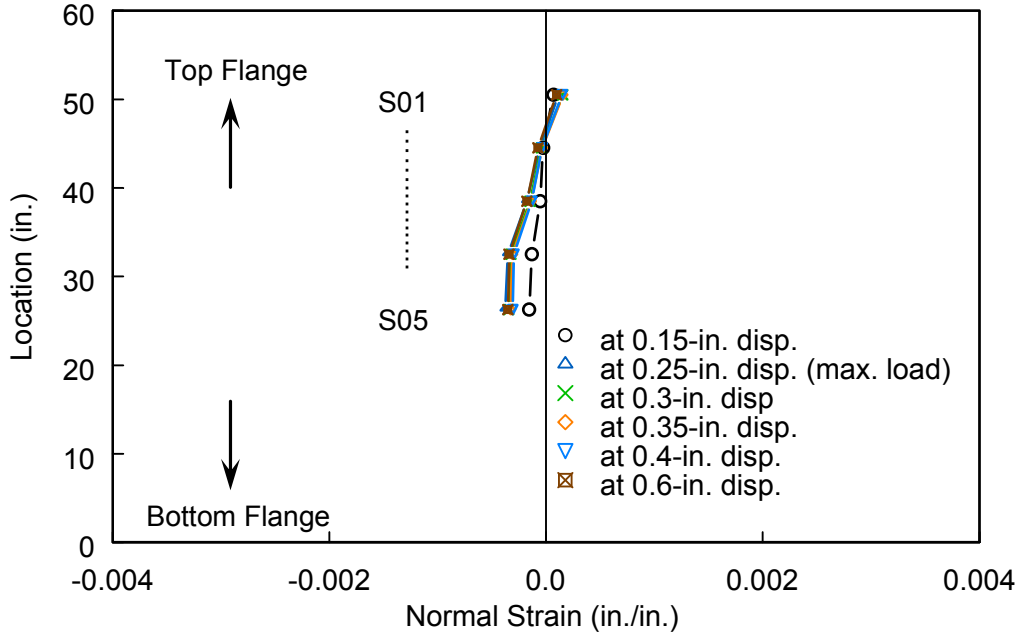

(a) East Side

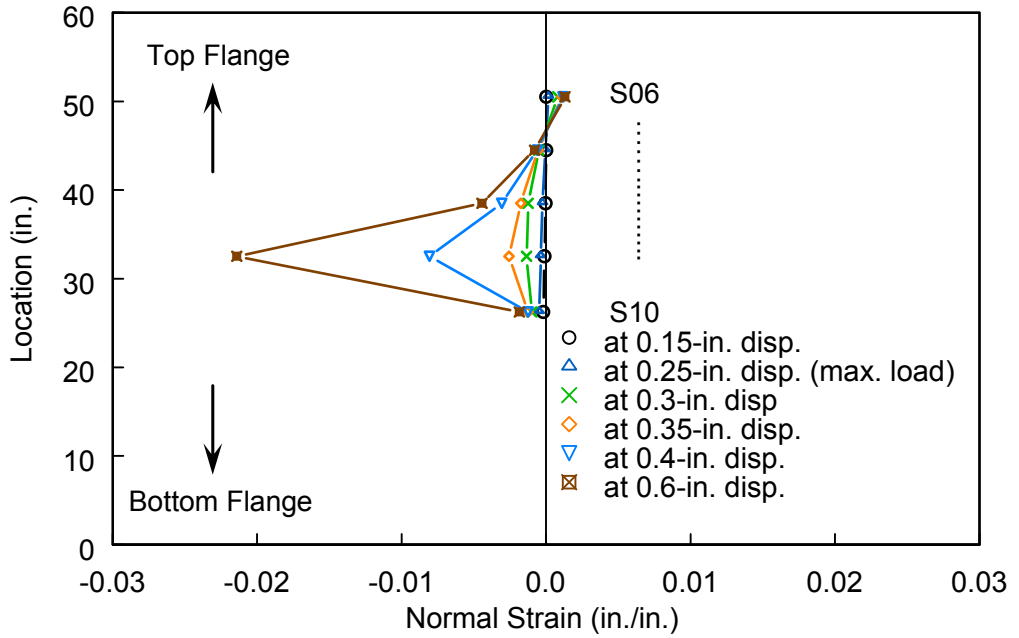

(b) West Side

Figure B.15: Specimen SG1: Strain Profiles in Extended Web

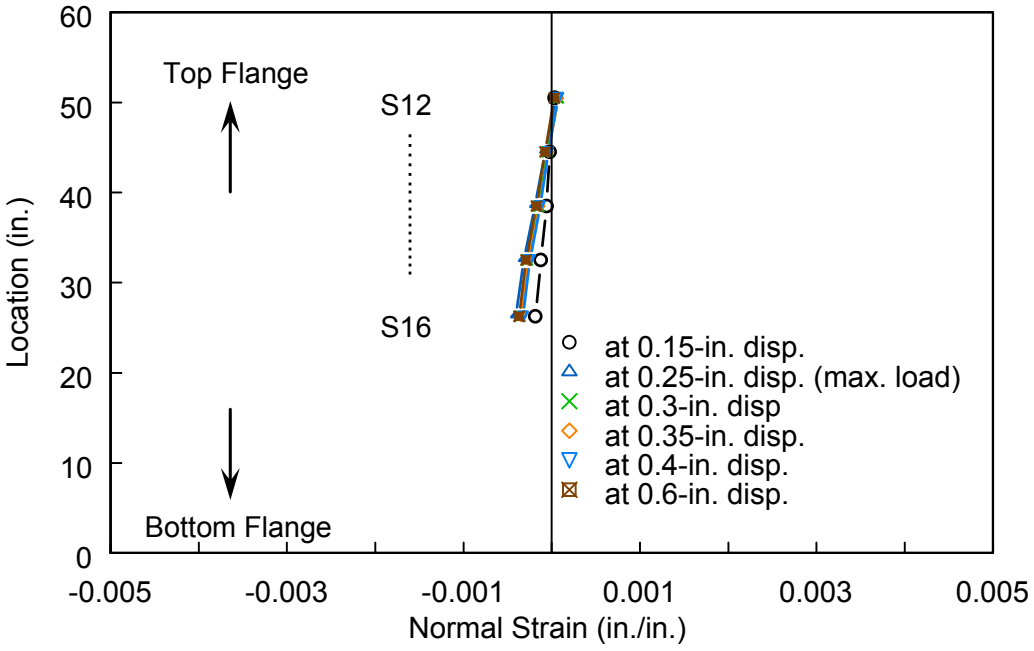

(a) East Side

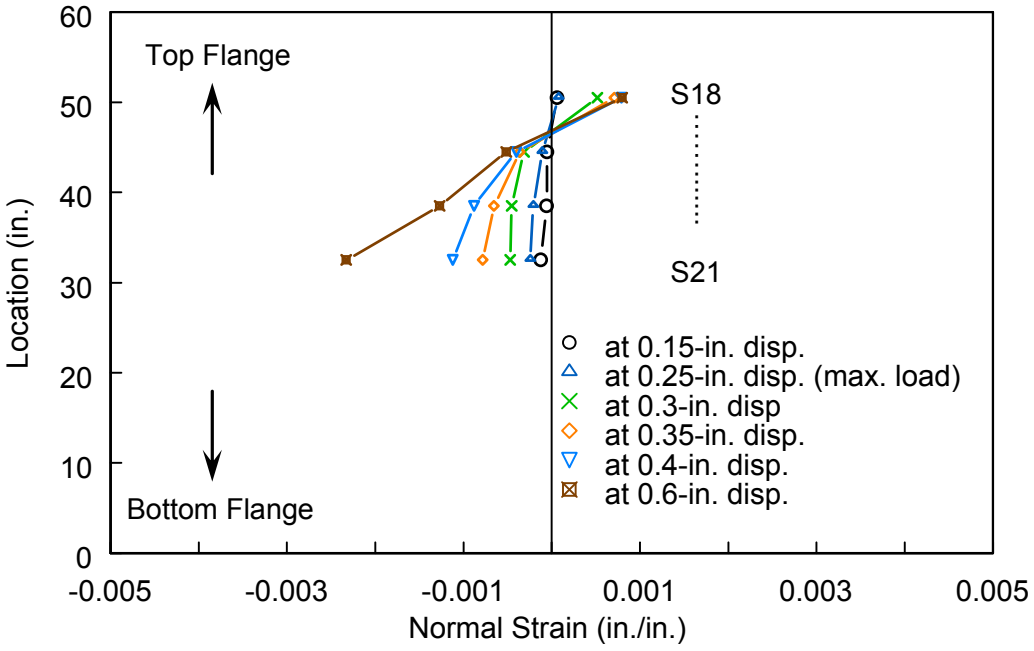

(b) West Side

Figure B.16: Specimen SG1: Strain Profiles in Bearing Stiffener

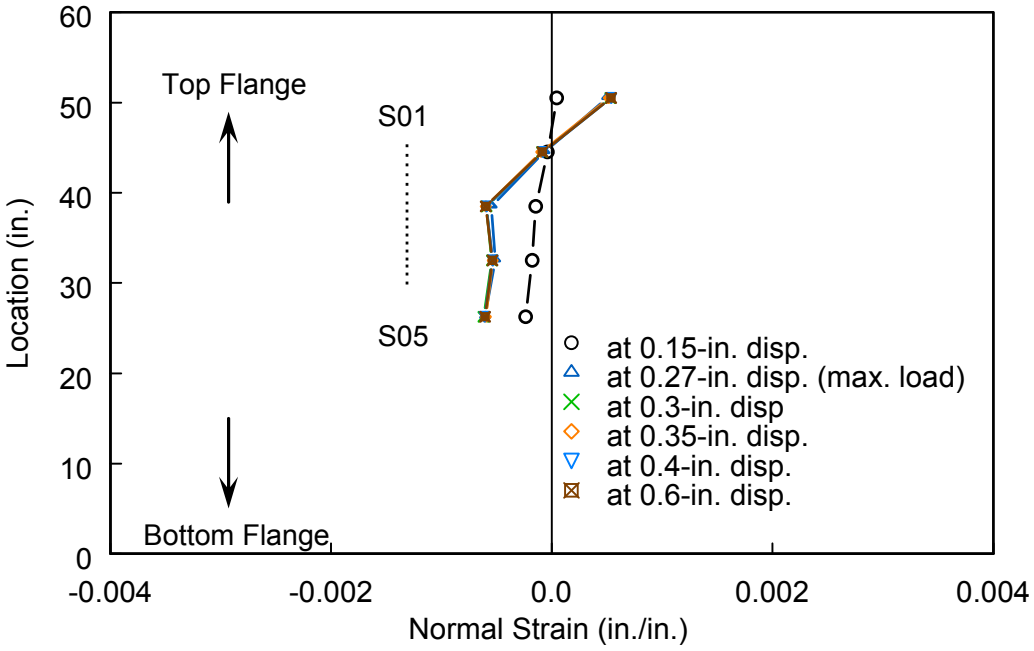

(a) East Side

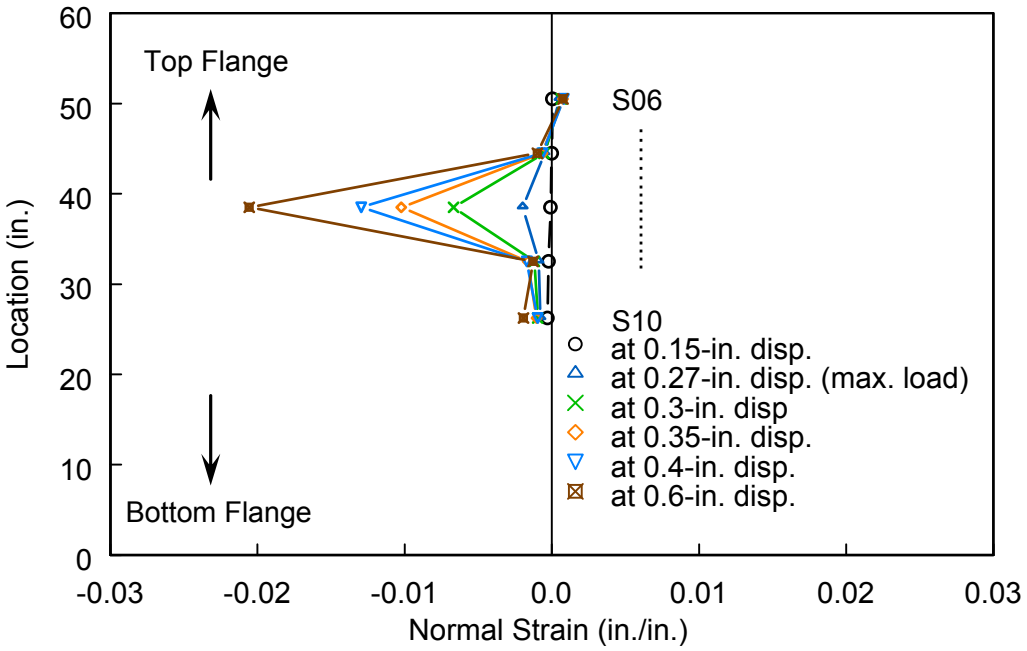

(b) West Side

Figure B.17: Specimen SG2: Strain Profiles in Extended Web

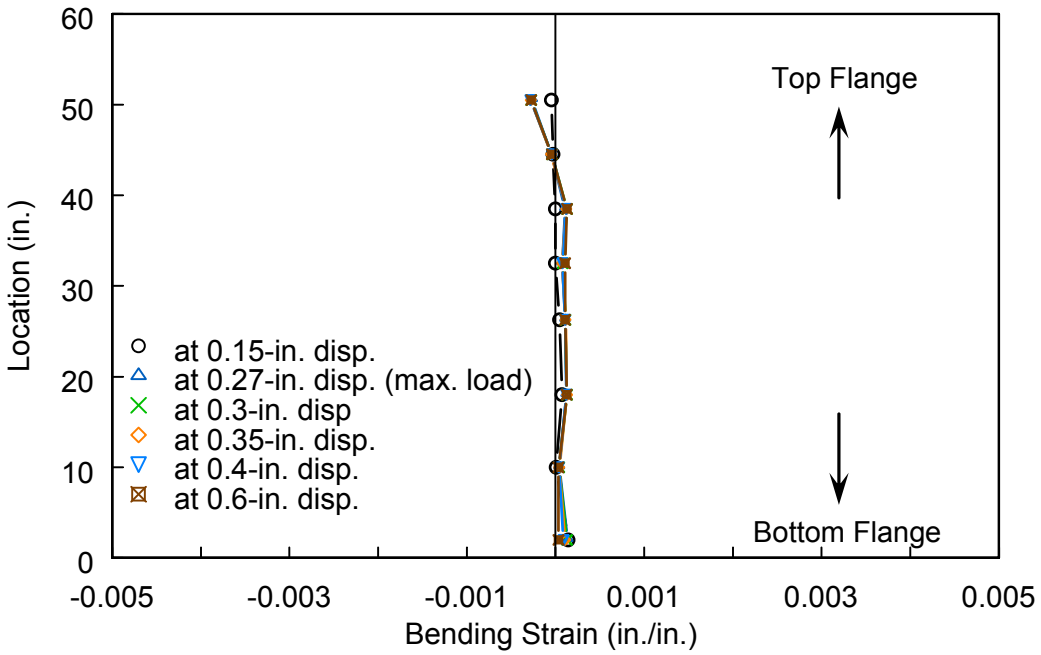

(a) Bending Strain Profiles

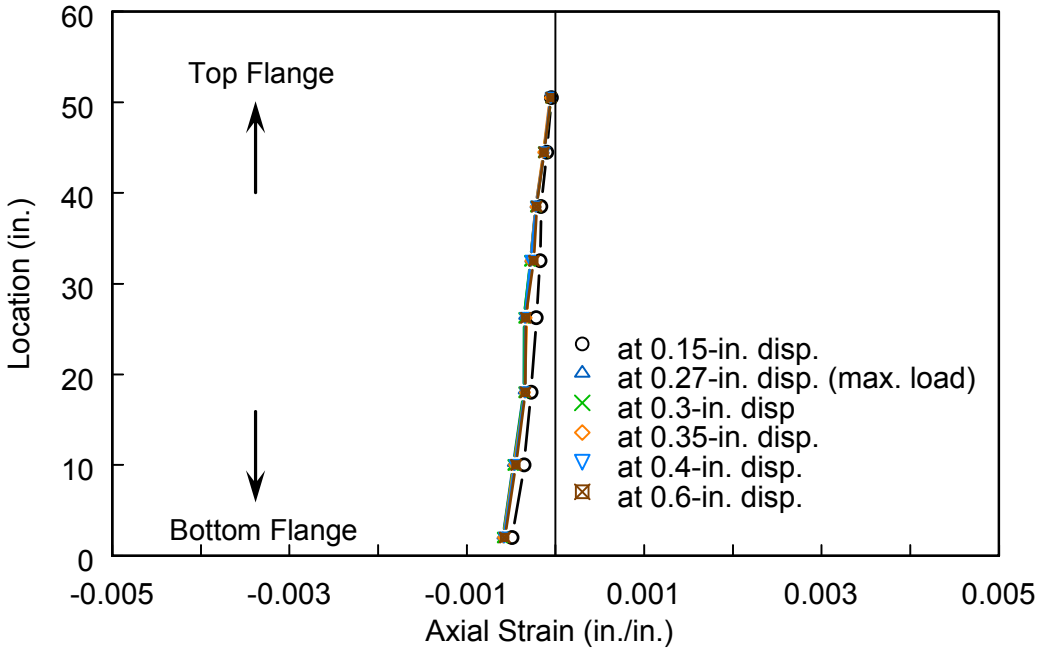

(b) Axial Strain Profiles

Figure B.18: Specimen SG2: Strain Profiles in Bearing Stiffener (East Side)

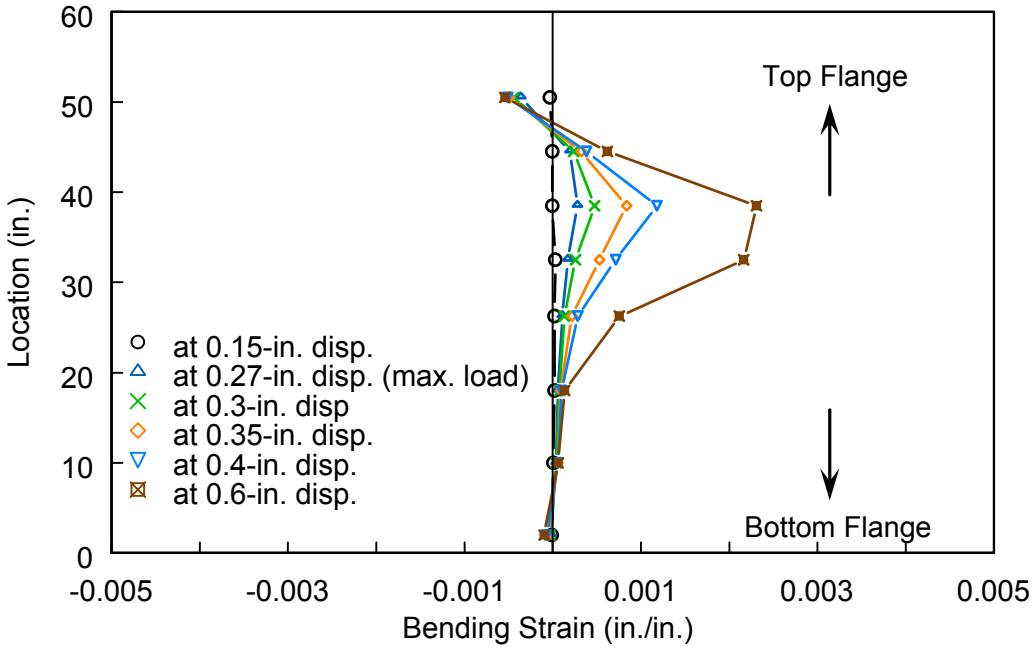

(a) Bending Strain Profiles

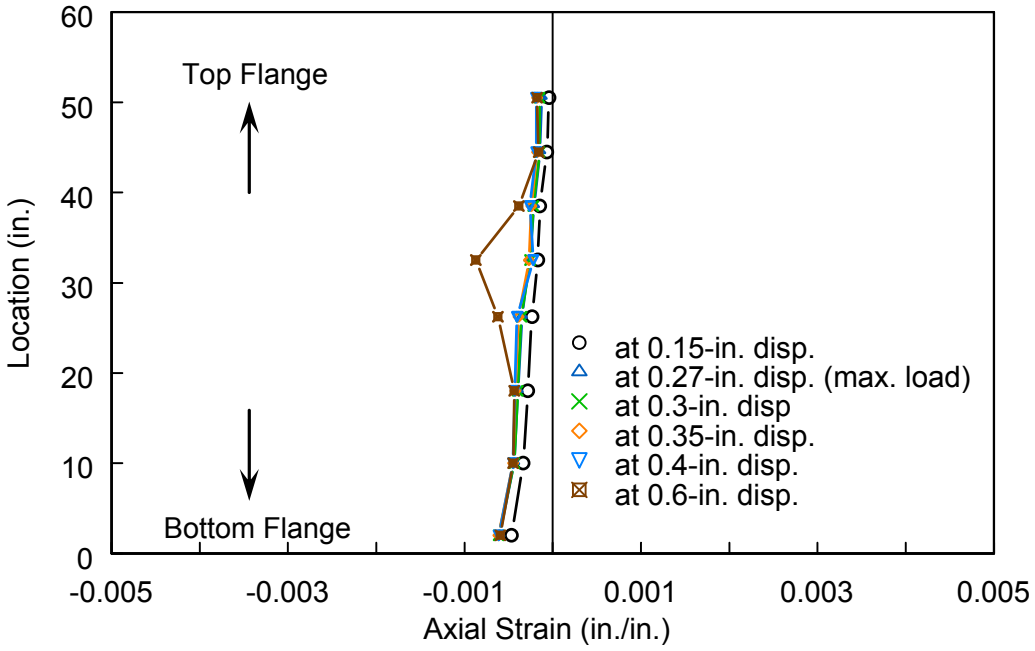

(b) Axial Strain Profiles

Figure B.19: Specimen SG2: Strain Profiles in Bearing Stiffener (West Side)

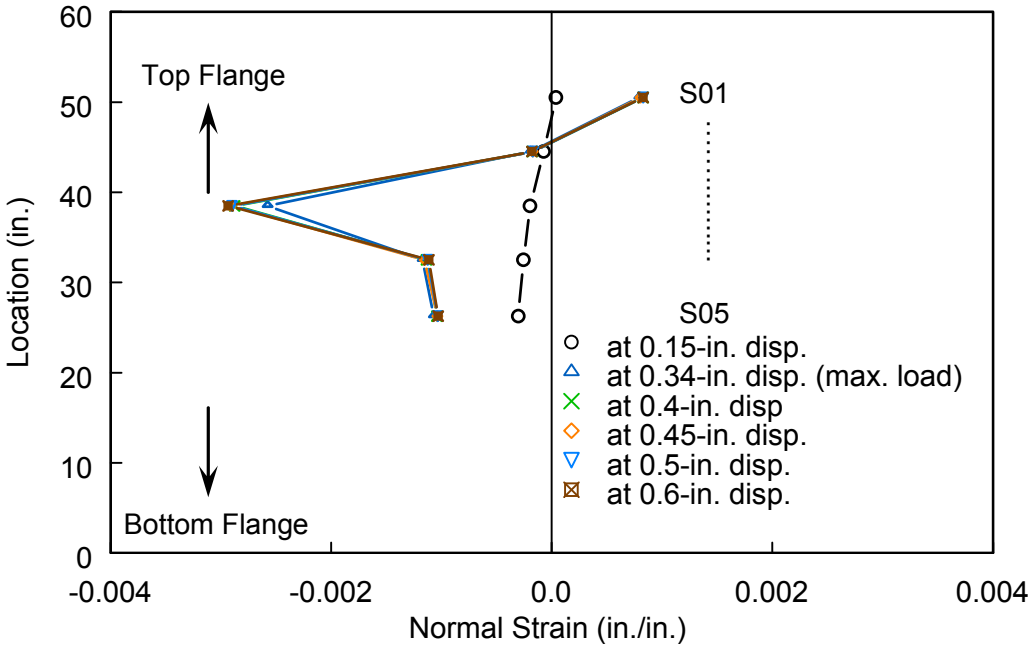

(a) East Side

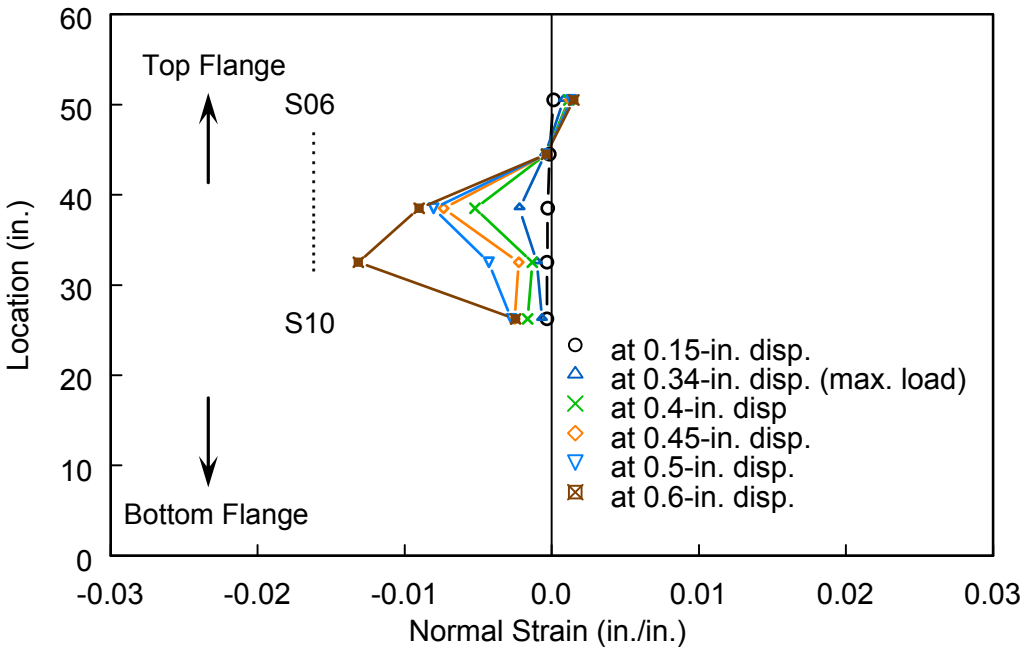

(b) West Side

Figure B.20: Specimen CG1: Strain Profiles in Extended Web

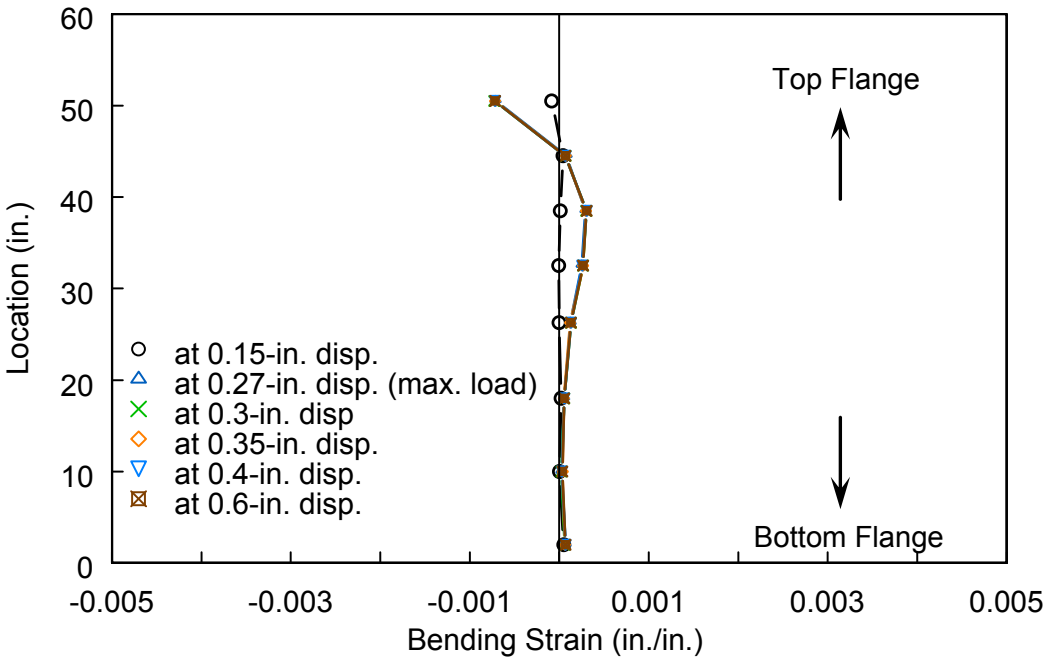

(a) Bending Strain Profiles

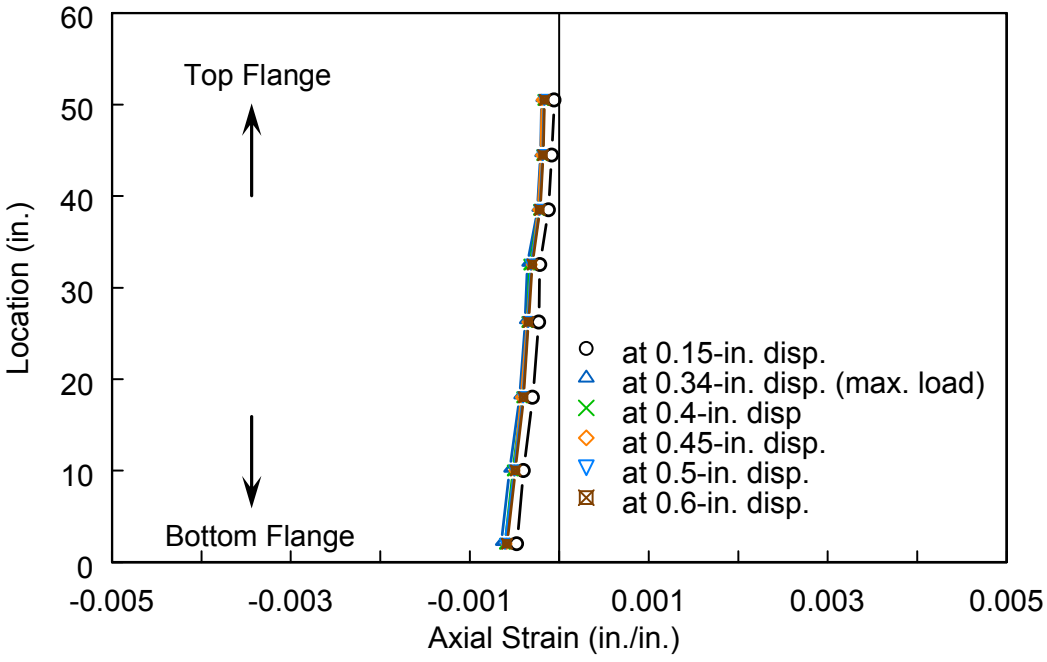

(b) Axial Strain Profiles

Figure B.21: Specimen CG1: Strain Profiles in Bearing Stiffener (East Side)

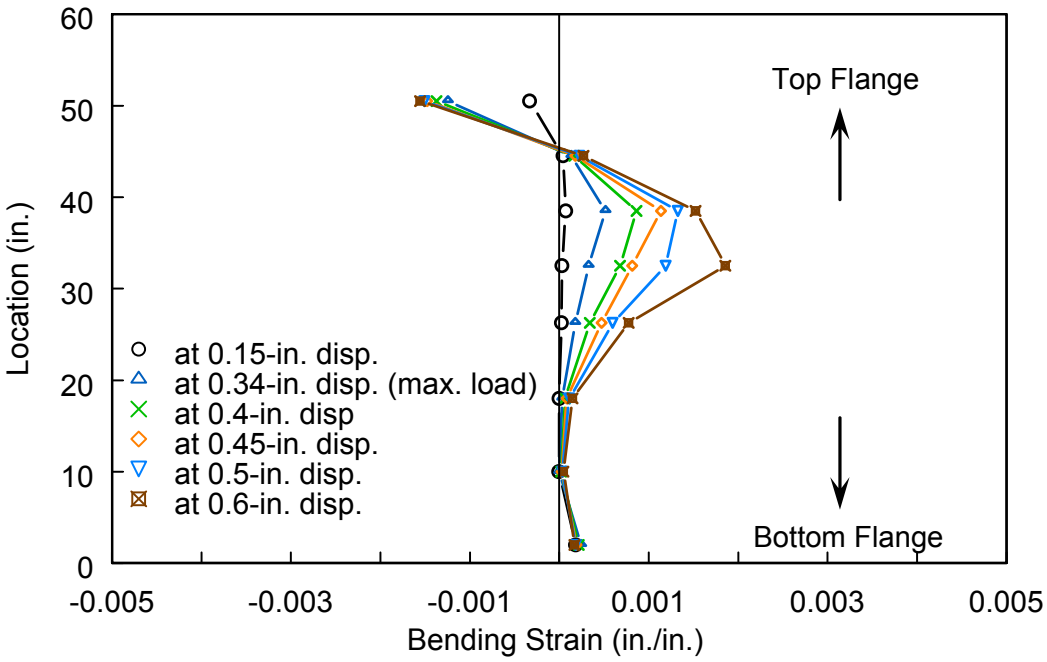

(a) Bending Strain Profiles

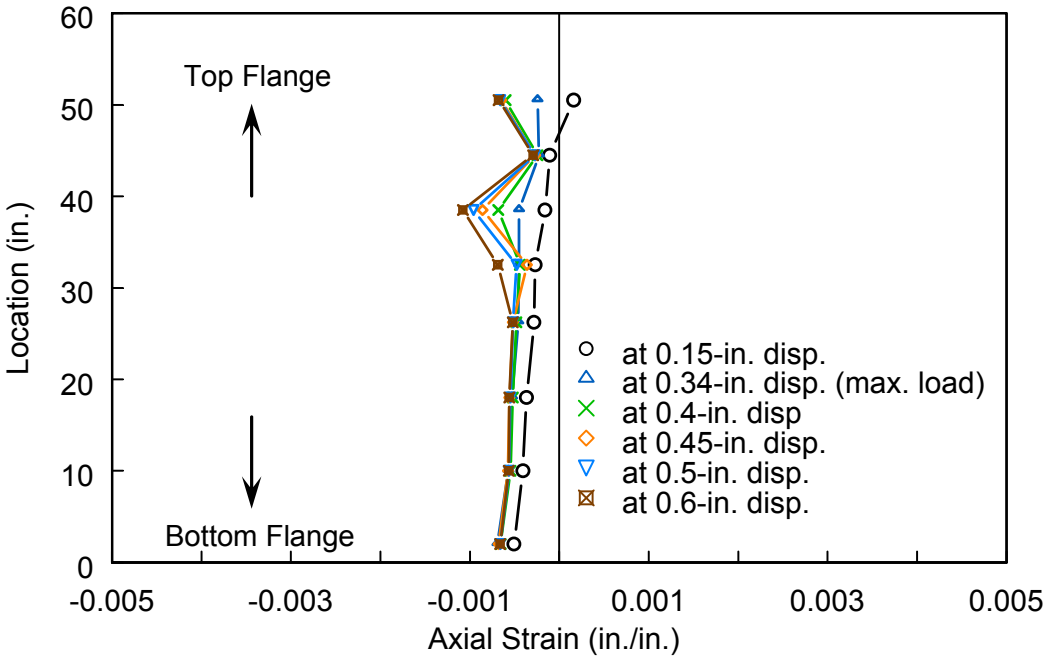

(b) Axial Strain Profiles

Figure B.22: Specimen CG1: Strain Profiles in Bearing Stiffener (West Side)

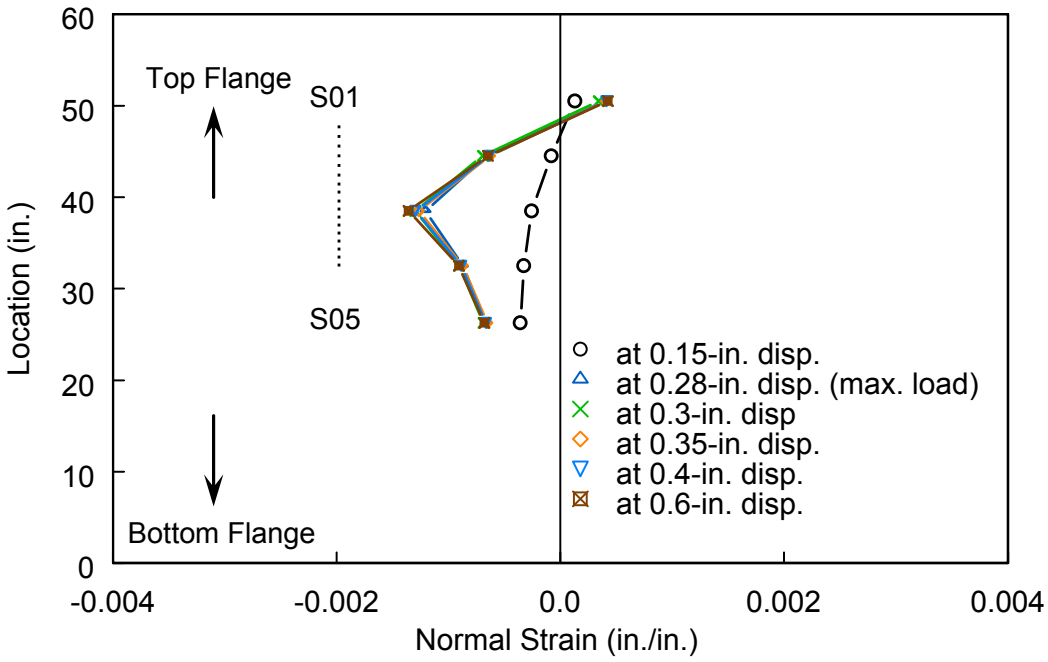

(a) East Side

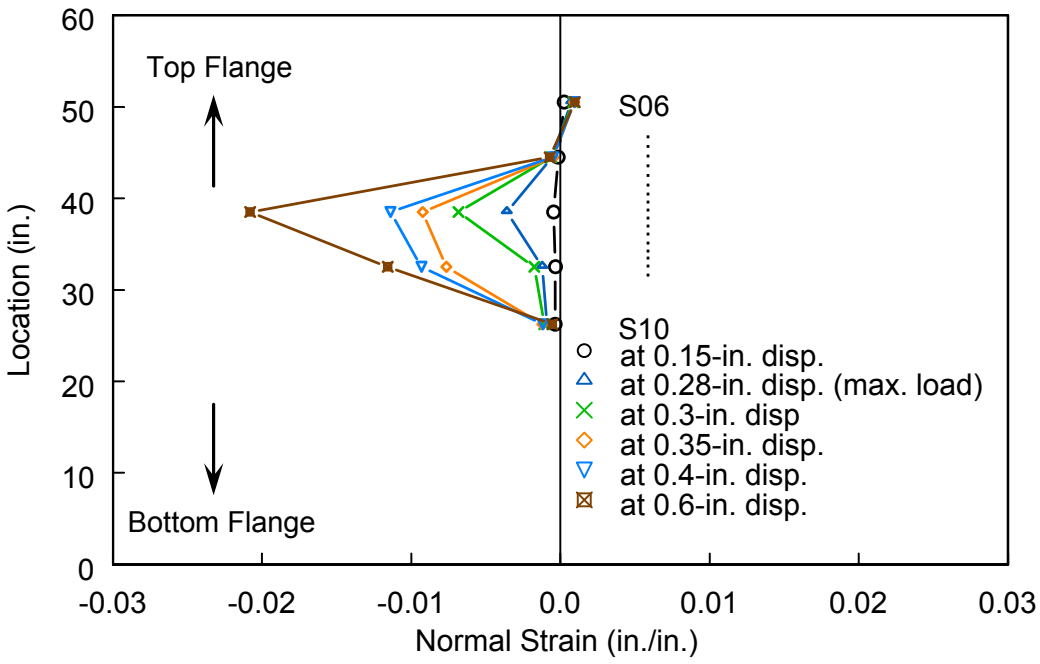

(b) West Side

Figure B.23: Specimen CG2: Strain Profiles in Extended Web

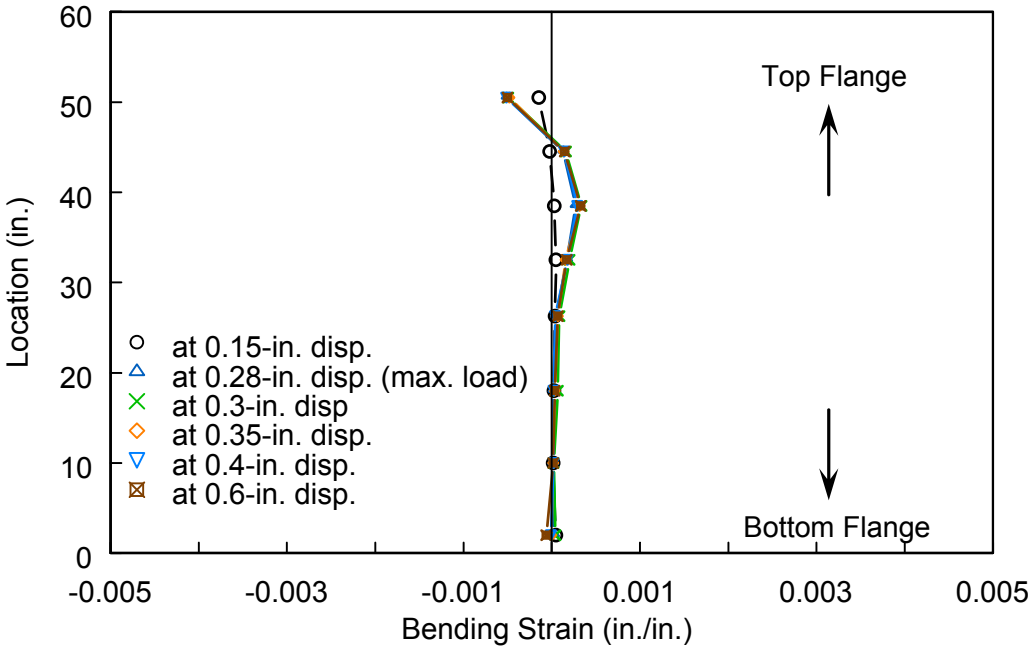

(a) Bending Strain Profiles

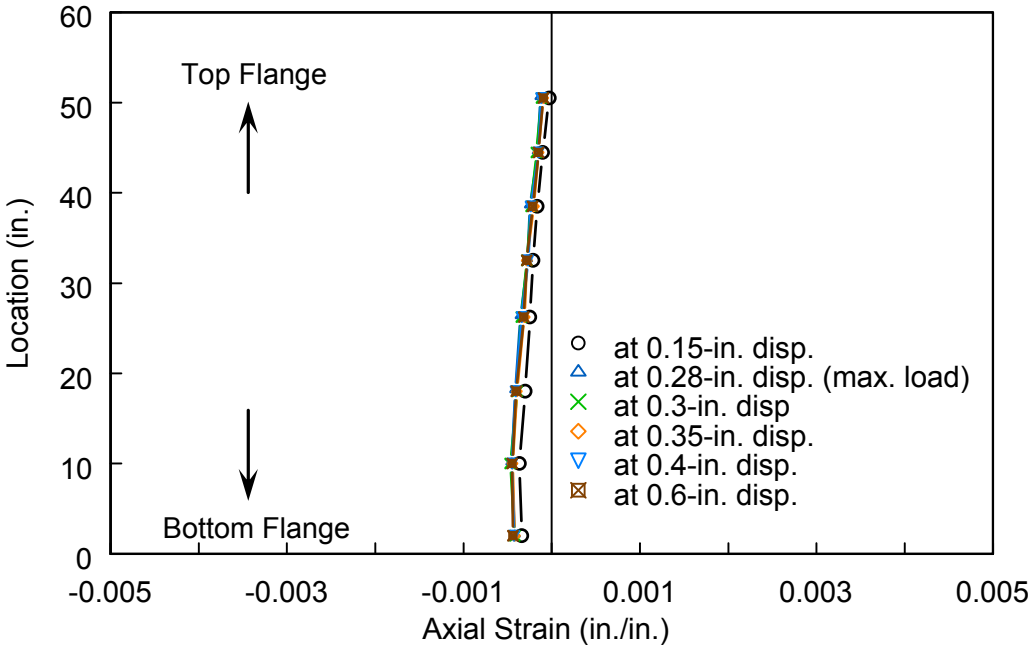

(b) Axial Strain Profiles

Figure B.24: Specimen CG2: Strain Profiles in Bearing Stiffener (East Side)

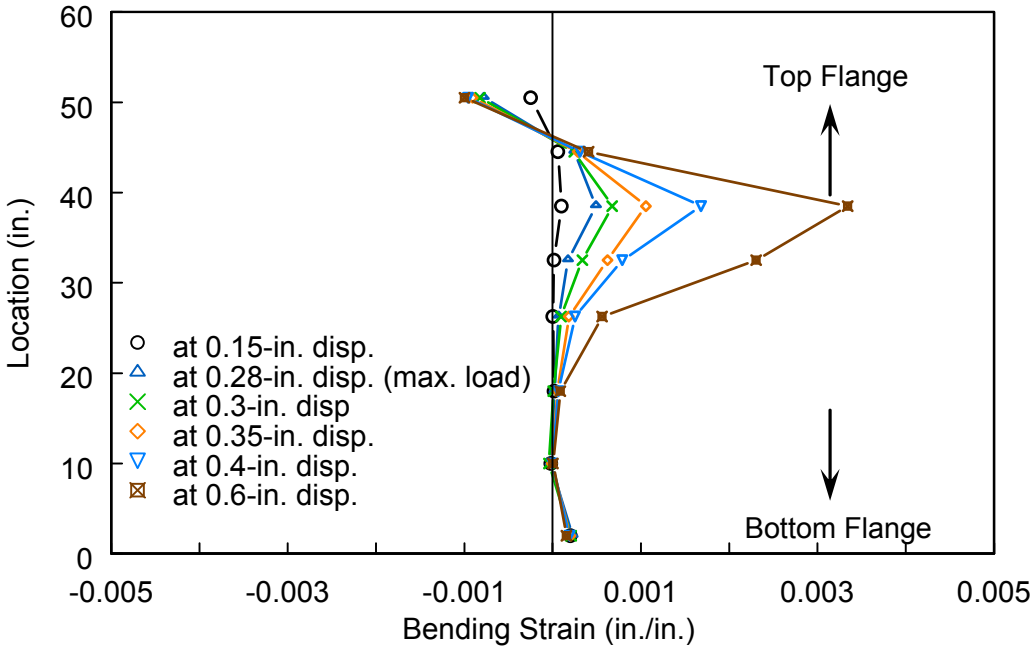

(a) Bending Strain Profiles

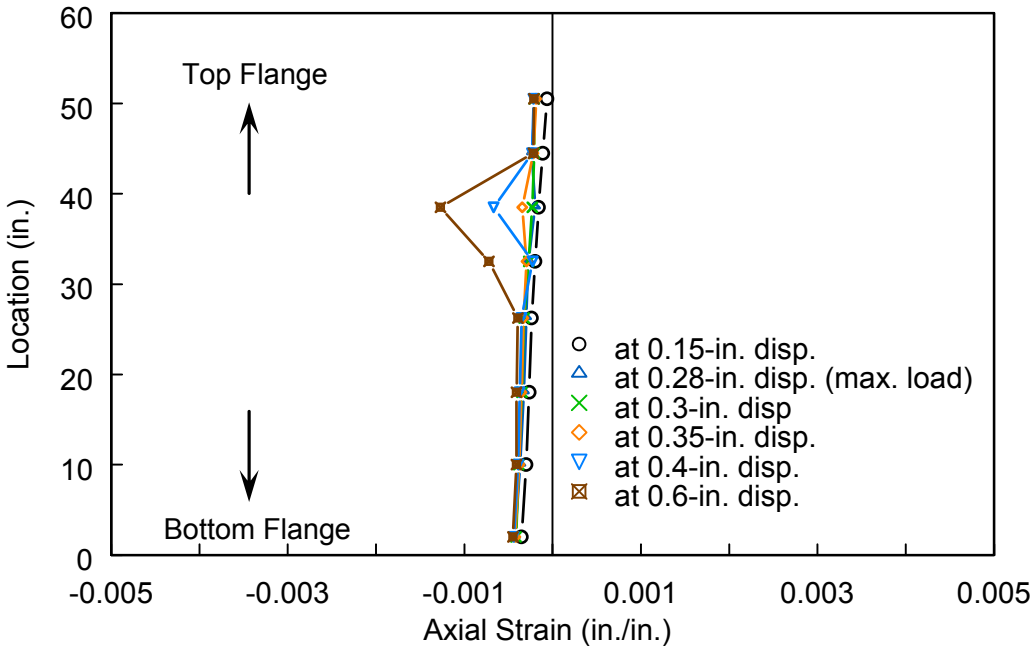

(b) Axial Strain Profiles

Figure B.25: Specimen CG2: Strain Profiles in Bearing Stiffener (West Side)

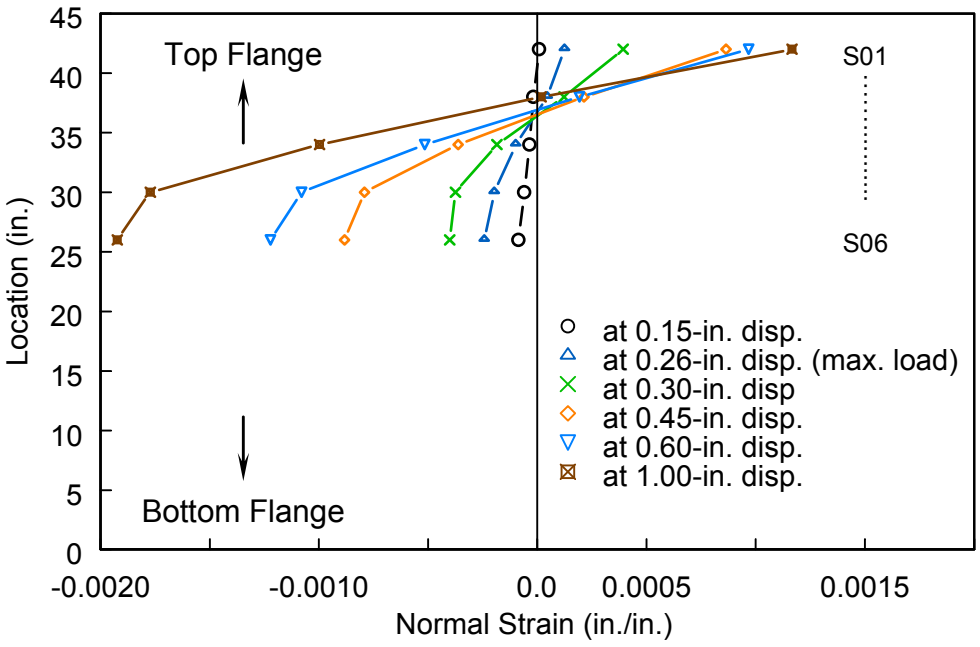

(a) East Side

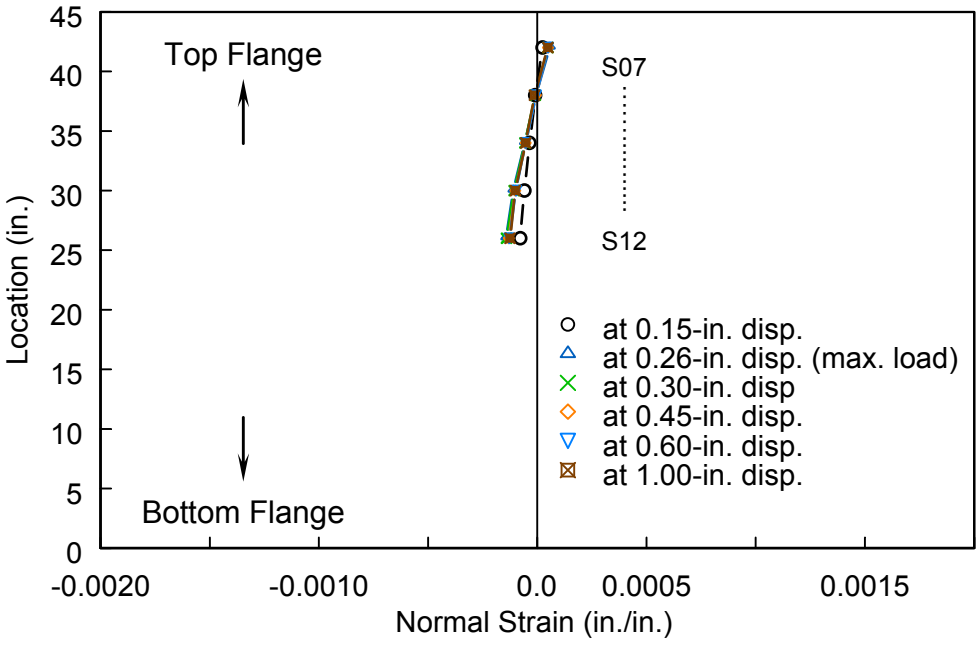

(b) West Side

Figure B.26: Specimen SG3: Strain Profiles in Bearing Stiffener

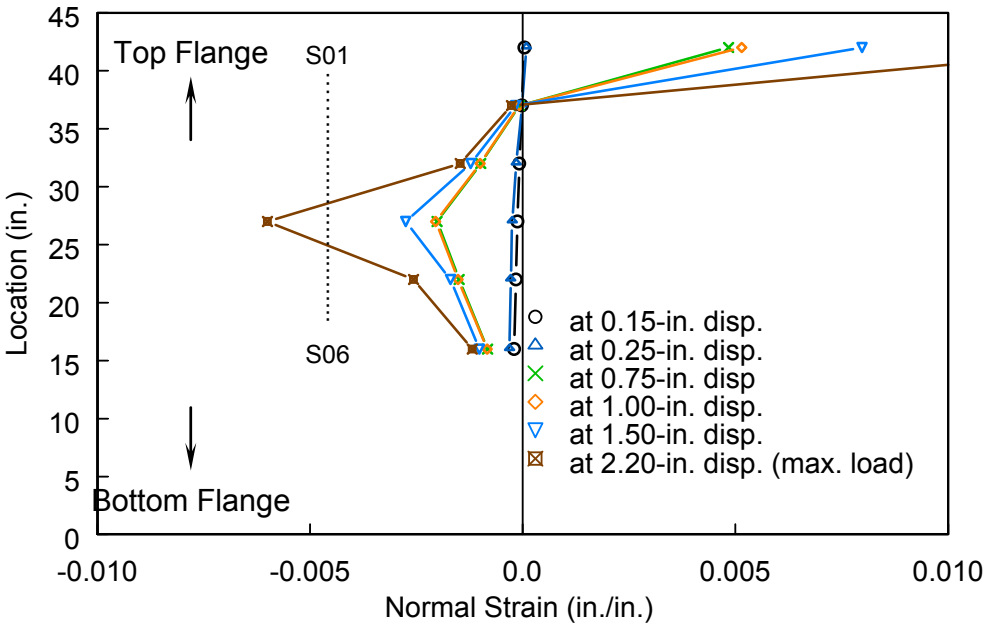

(a) East Side

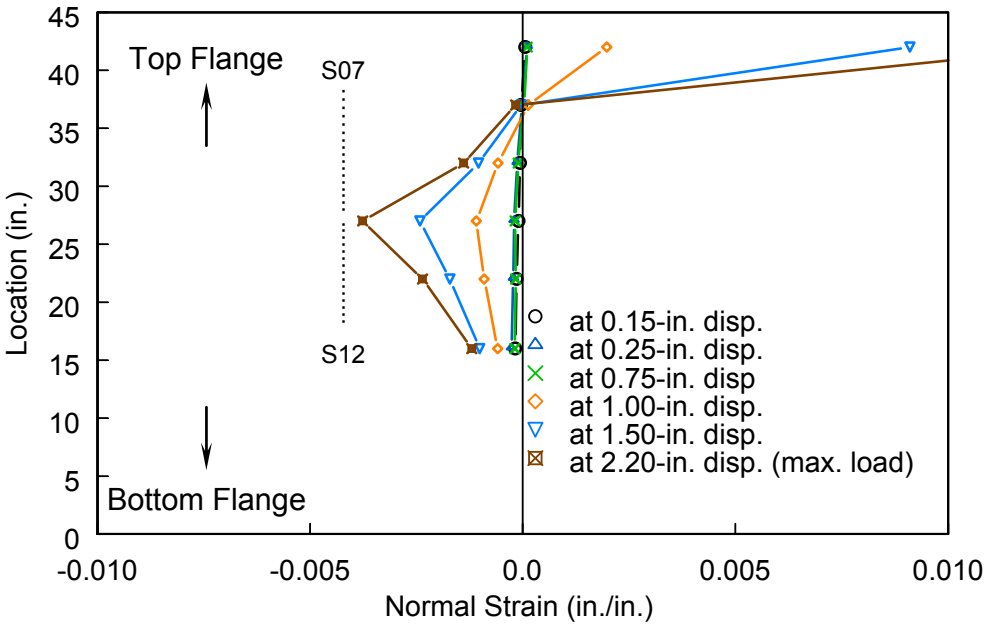

(b) West Side

Figure B.27: Specimen SG4: Strain Profiles in Bearing Stiffener

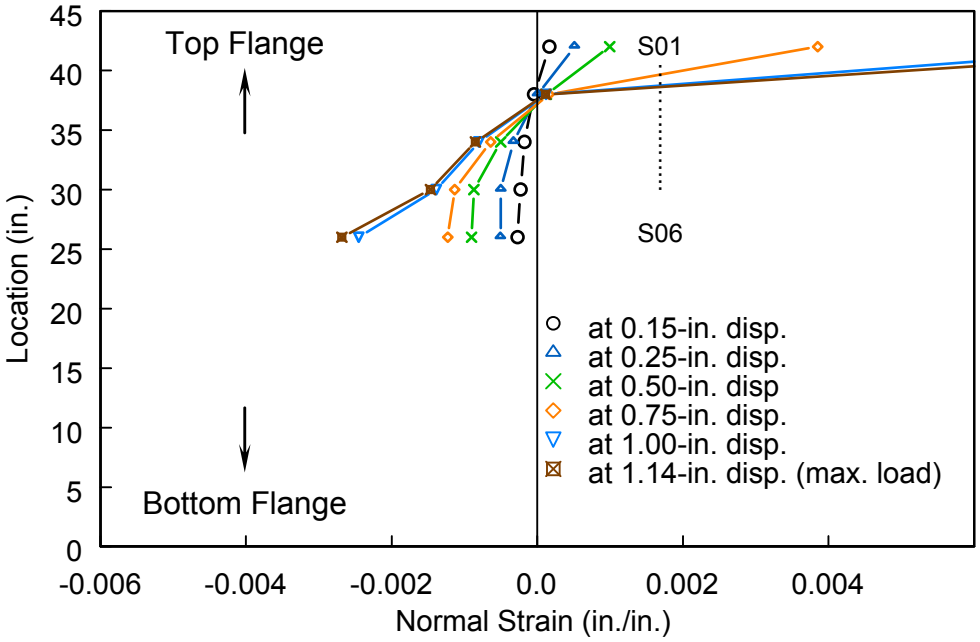

(a) East Side

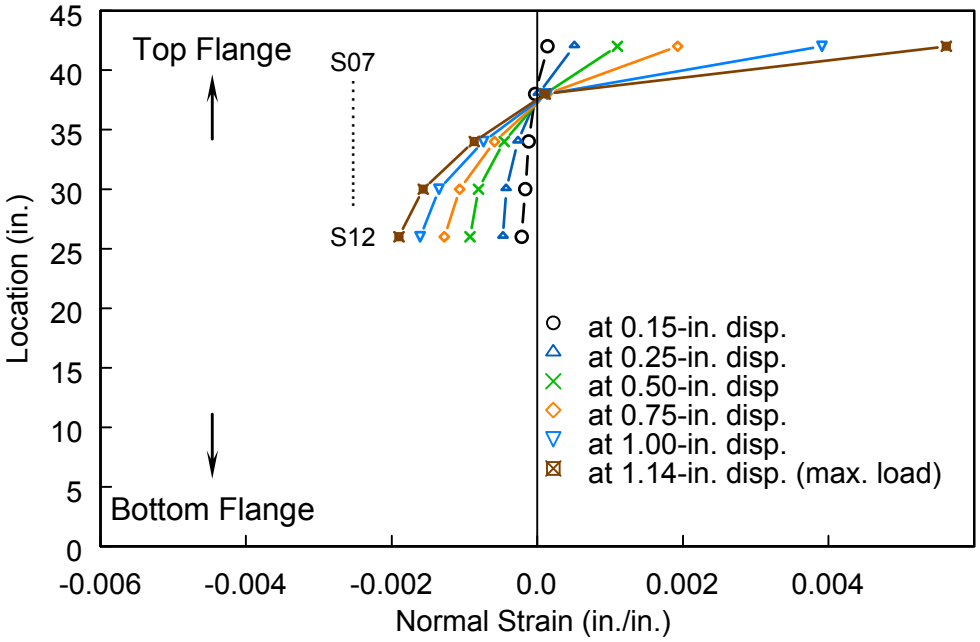

(b) West Side

Figure B.28: Specimen CG3: Strain Profiles in Bearing Stiffener

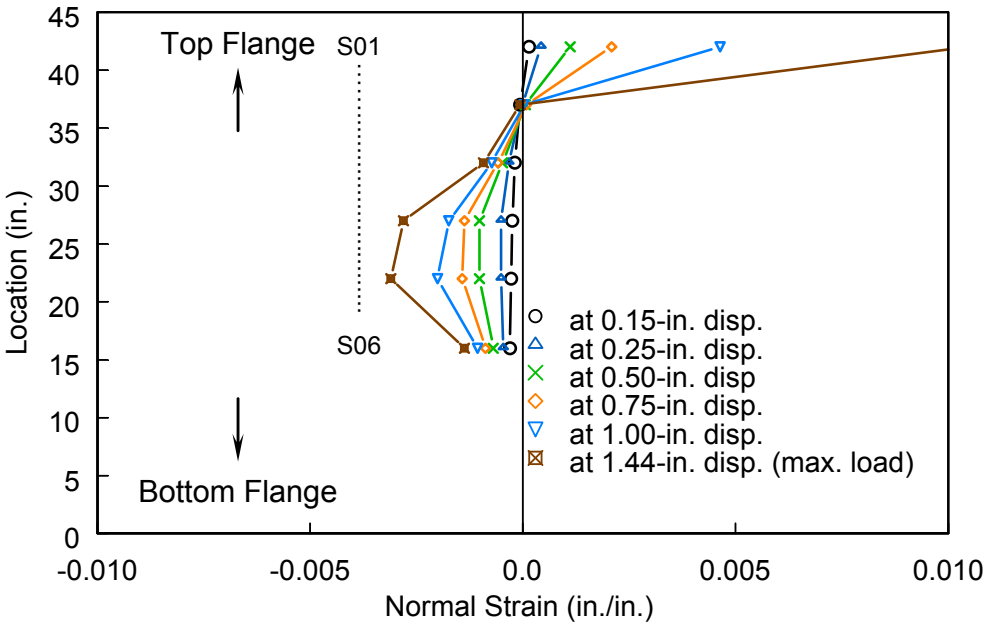

(a) East Side

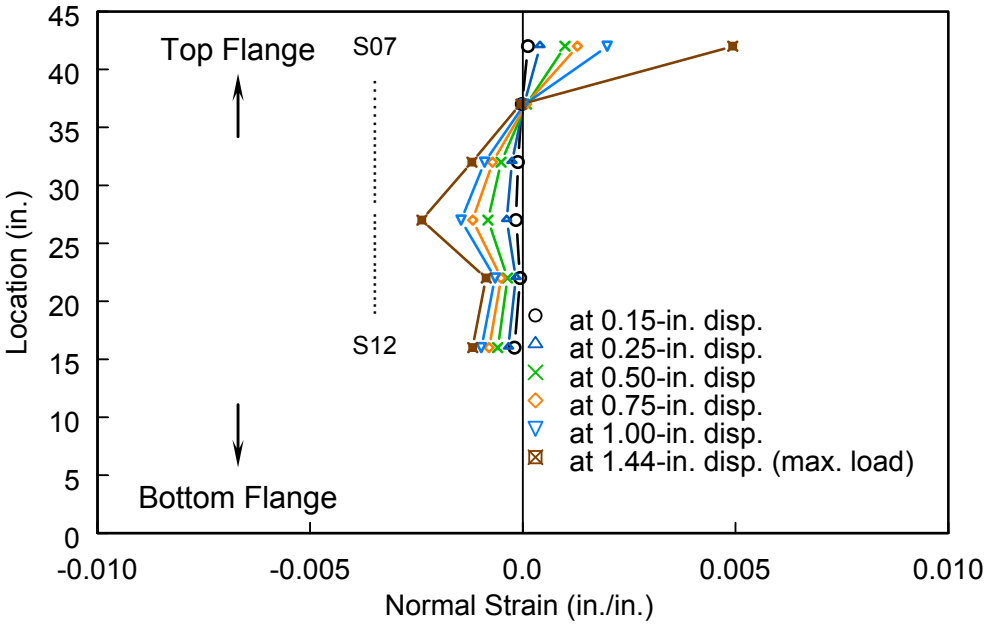

(b) West Side

Figure B.29: Specimen CG4: Strain Profiles in Bearing Stiffener

B2. 3 Strain Plots in Steel Girder Flanges

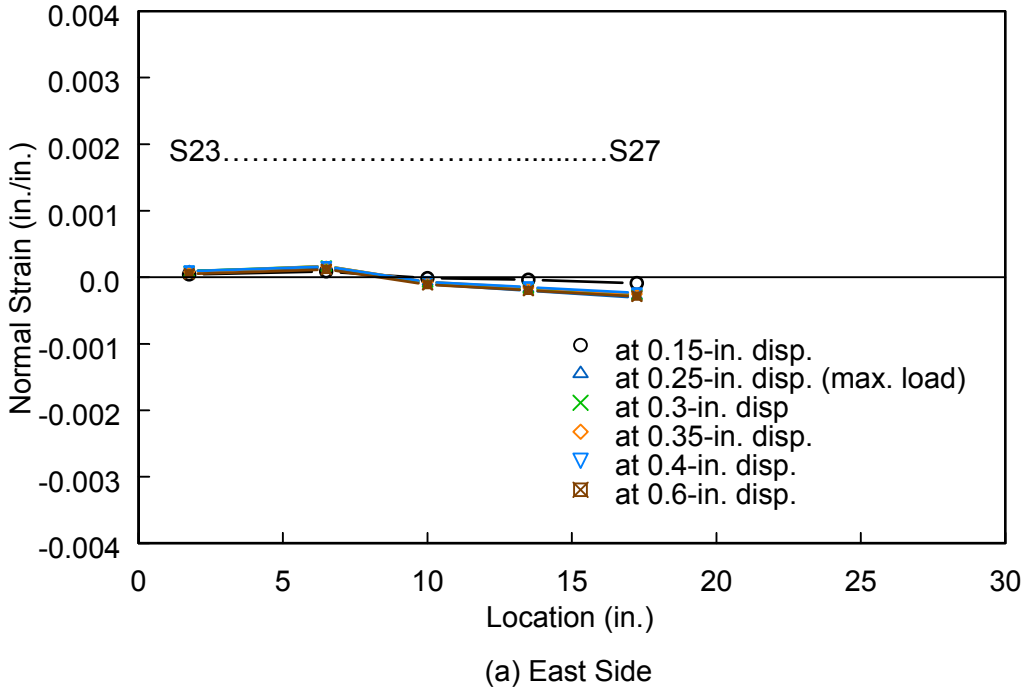

(a) East Side

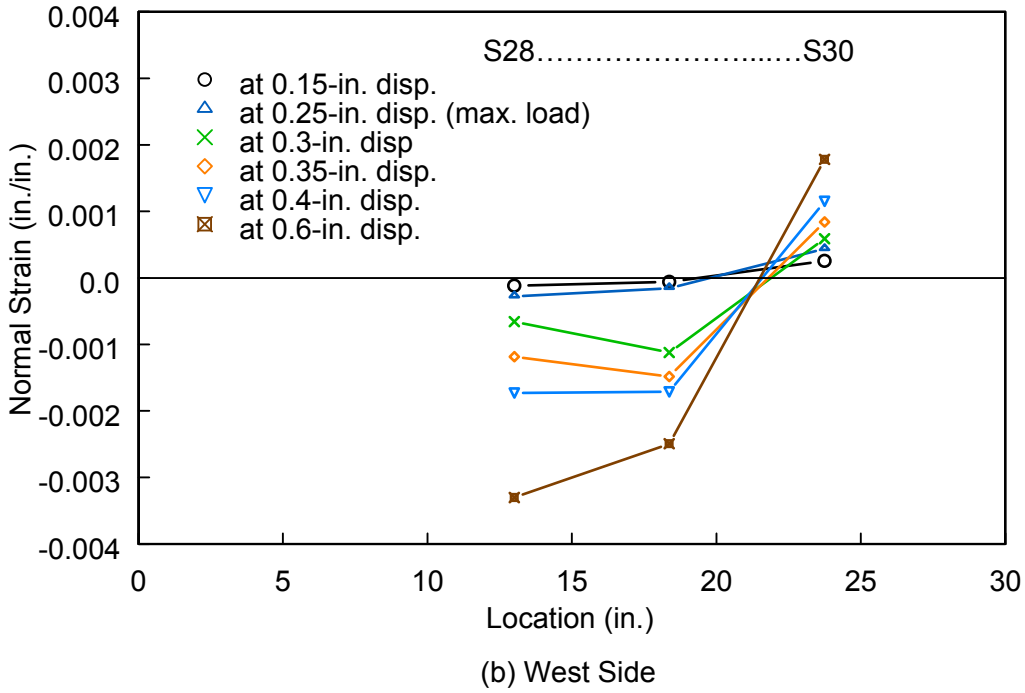

(b) West Side

Figure B.30: Specimen SG1: Strain Profiles in Compression Flange (Top Flange)

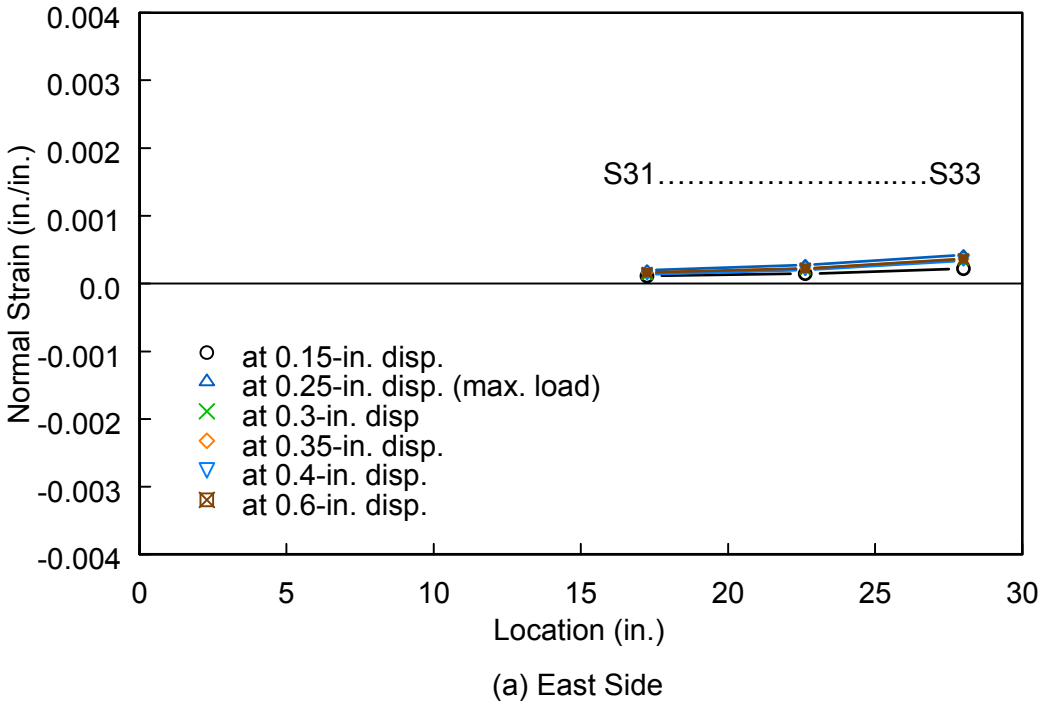

(a) East Side

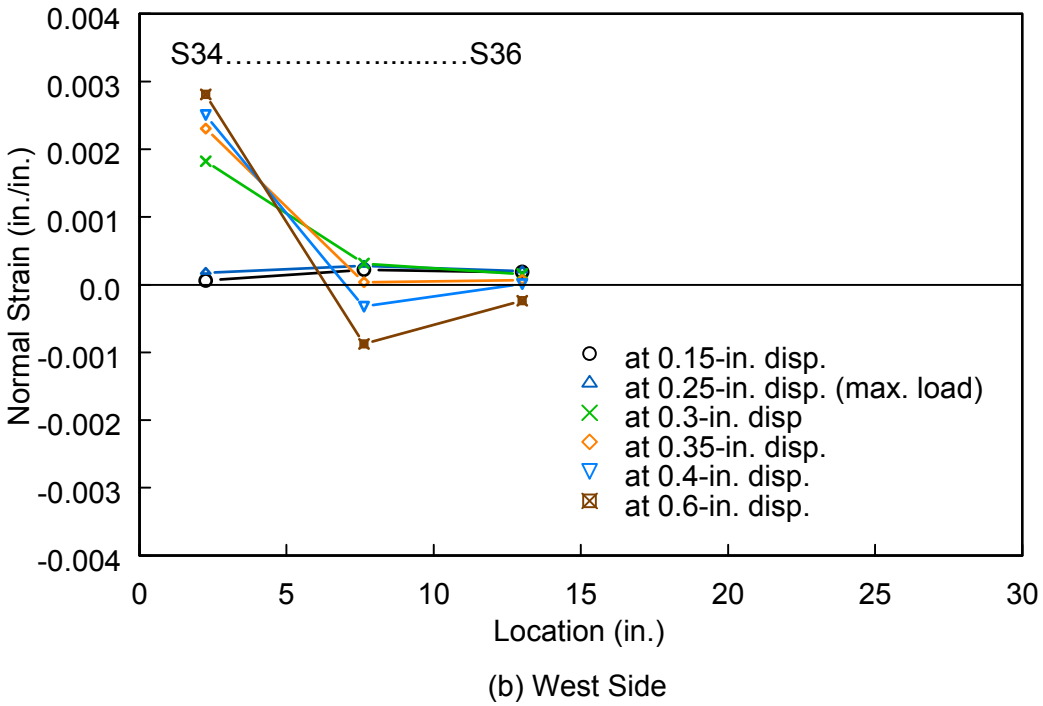

(b) West Side

Figure B.31: Specimen SG1: Strain Profiles in Tension Flange (Bottom Flange)

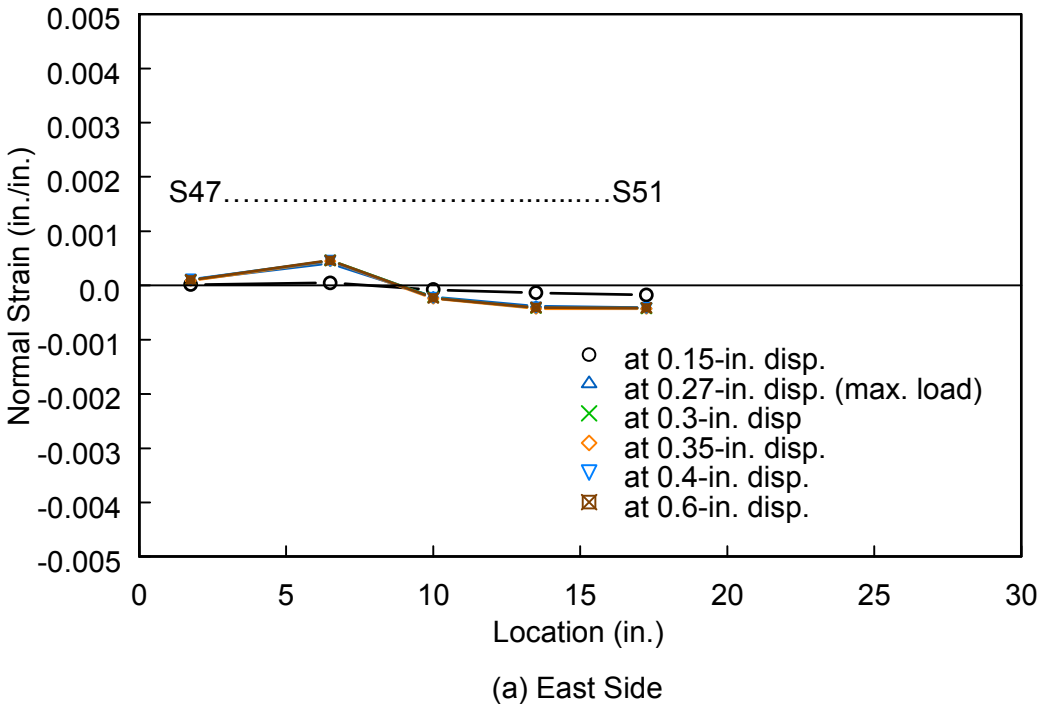

(a) East Side

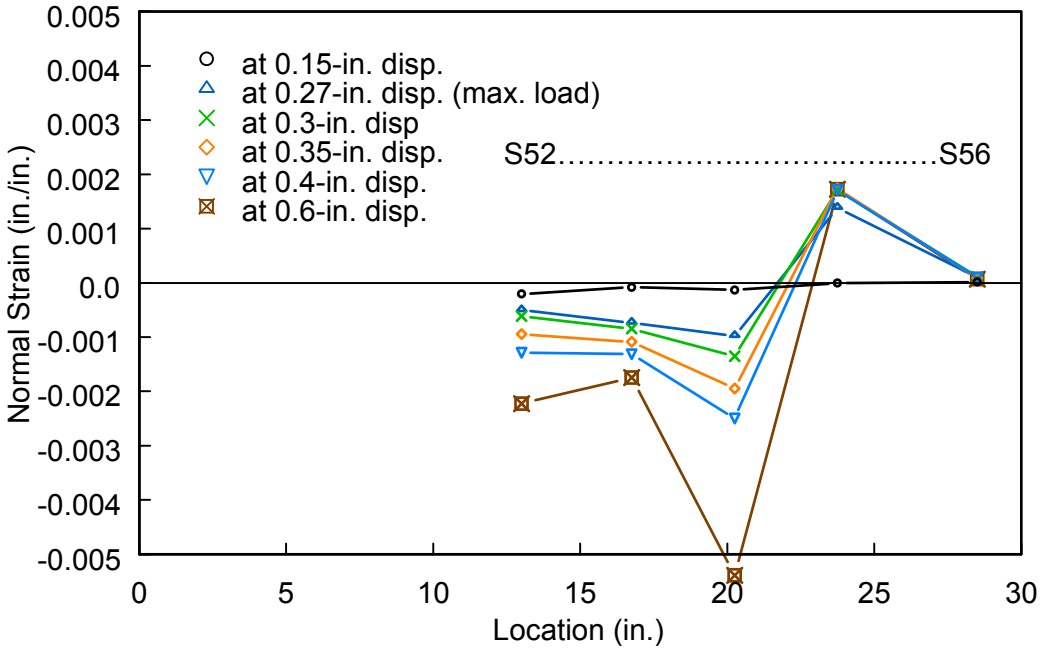

(b) West Side

Figure B.32: Specimen SG2: Strain Profiles in Compression Flange (Top Flange)

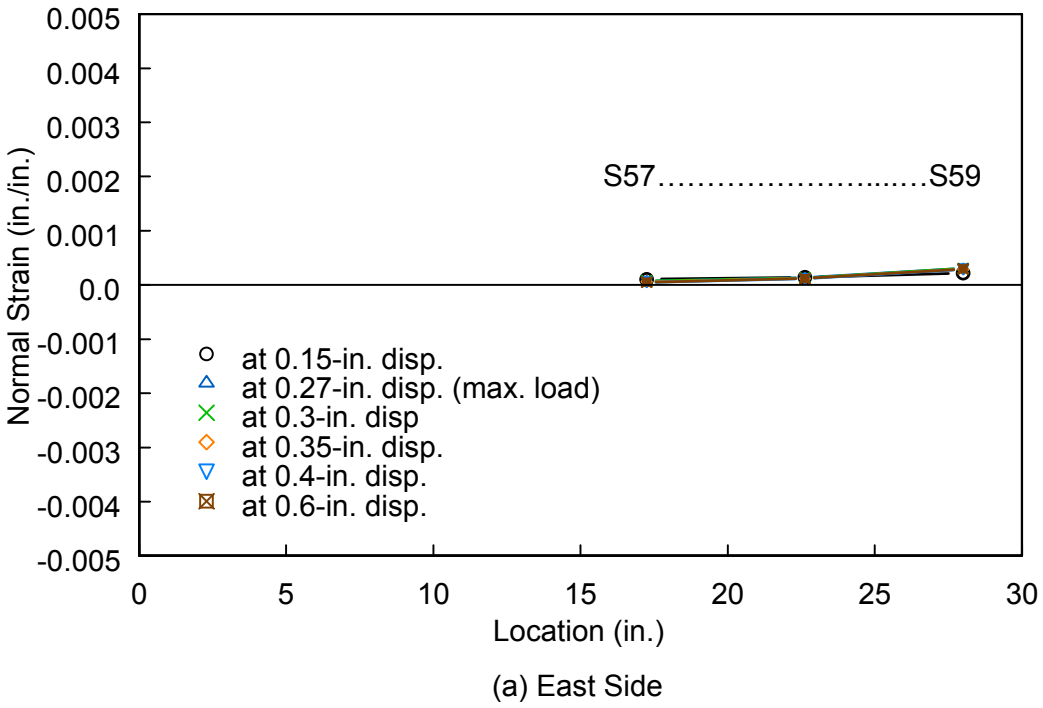

(a) East Side

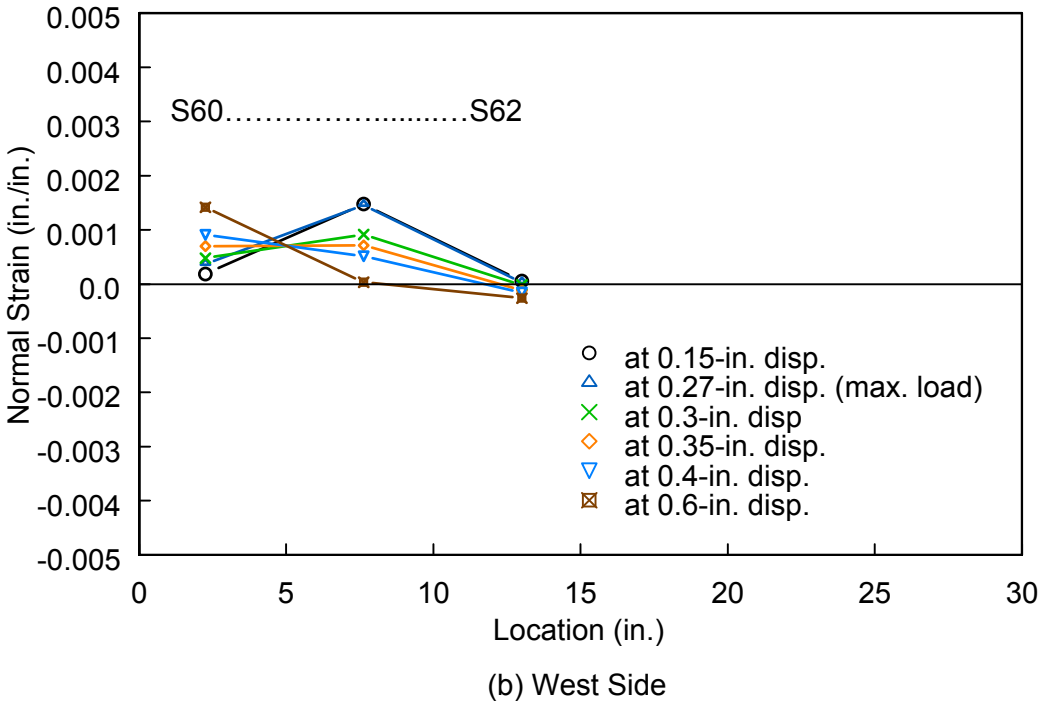

(b) West Side

Figure B.33: Specimen SG2: Strain Profiles in Tension Flange (Bottom Flange)

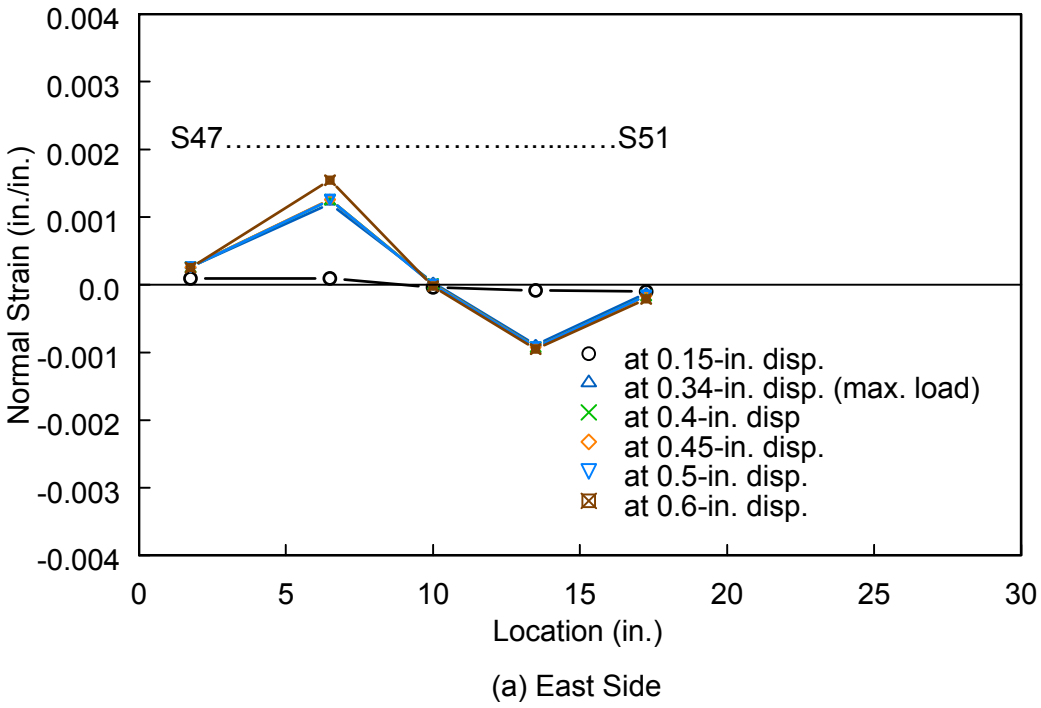

(a) East Side

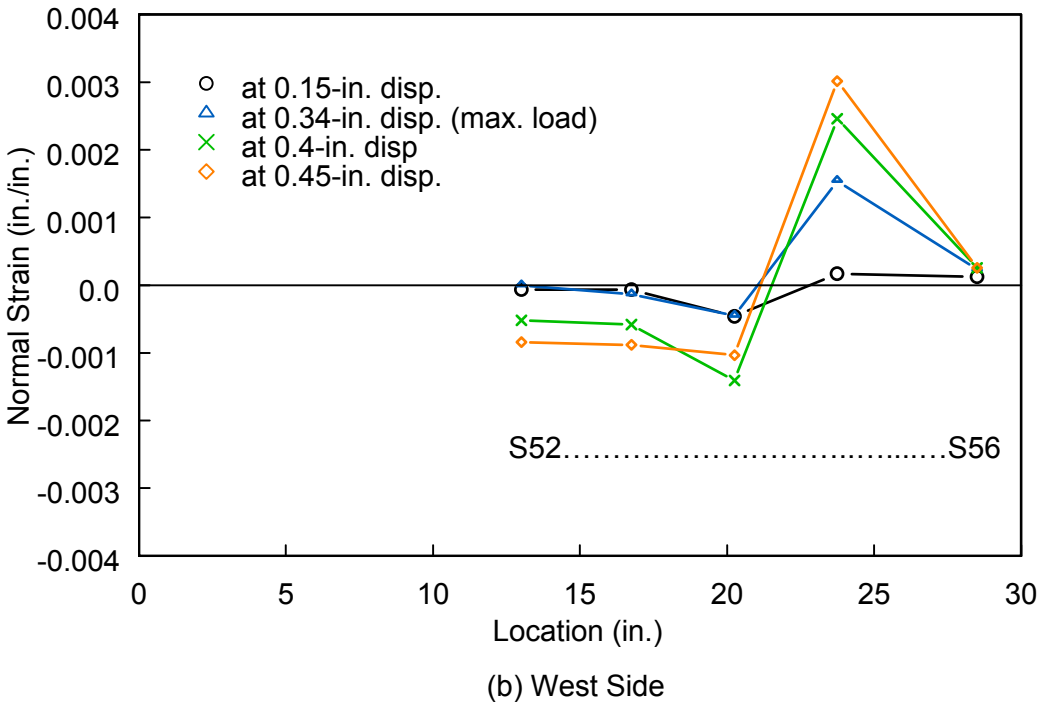

(b) West Side

Figure B.34: Specimen CG1: Strain Profiles in Compression Flange (Top Flange)

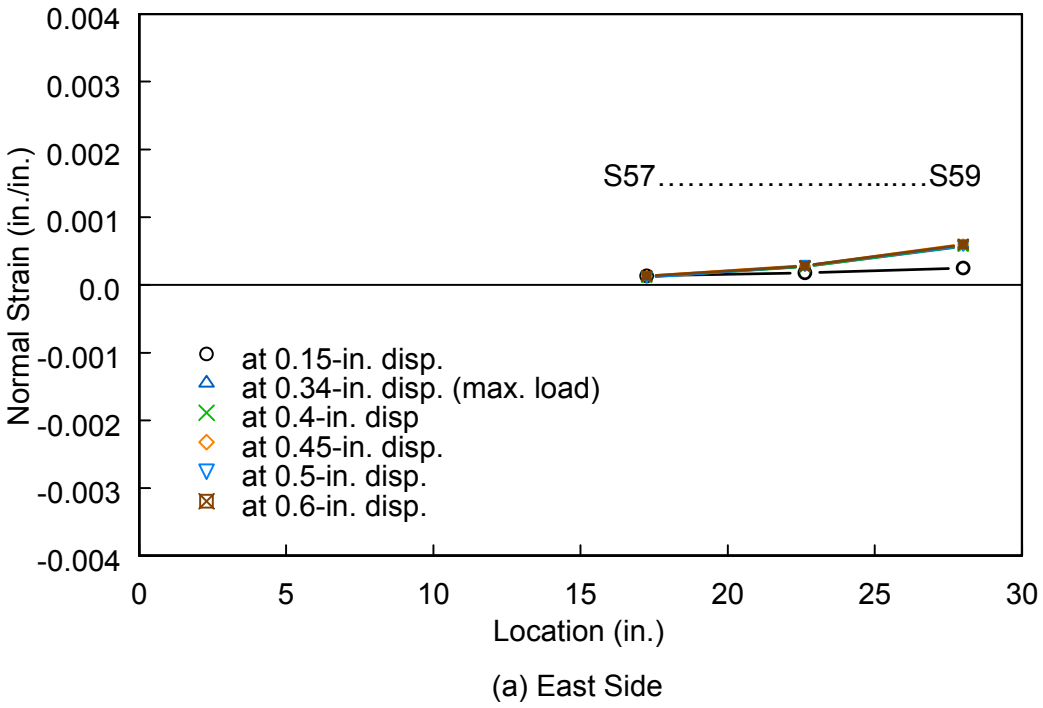

(a) East Side

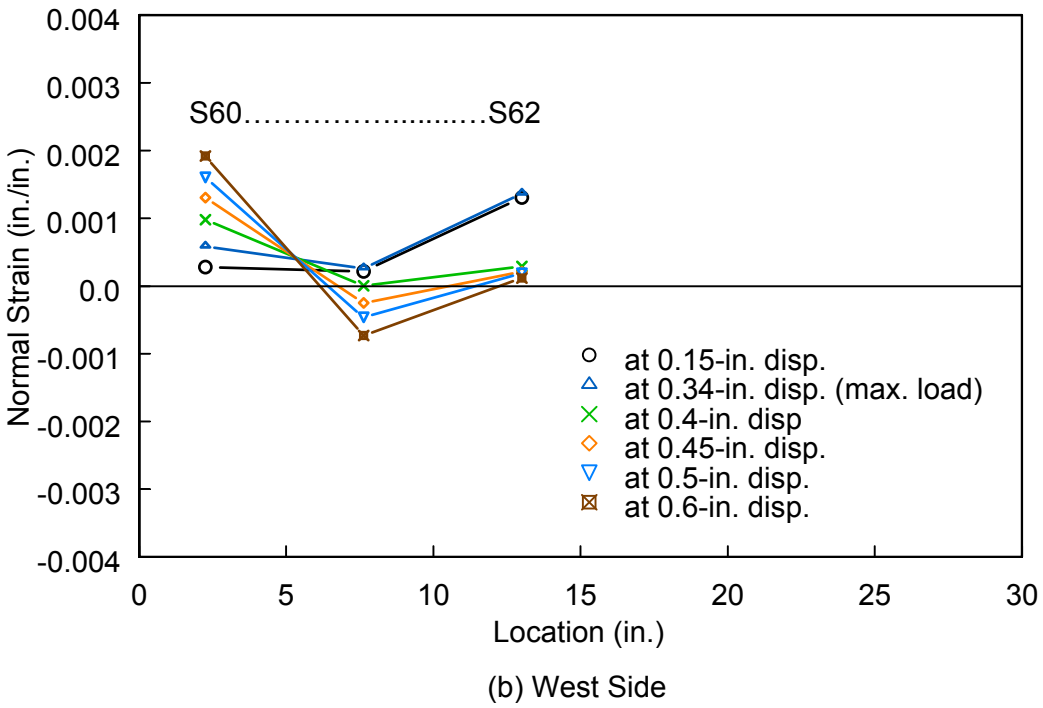

(b) West Side

Figure B.35: Specimen CG1: Strain Profiles in Tension Flange (Bottom Flange)

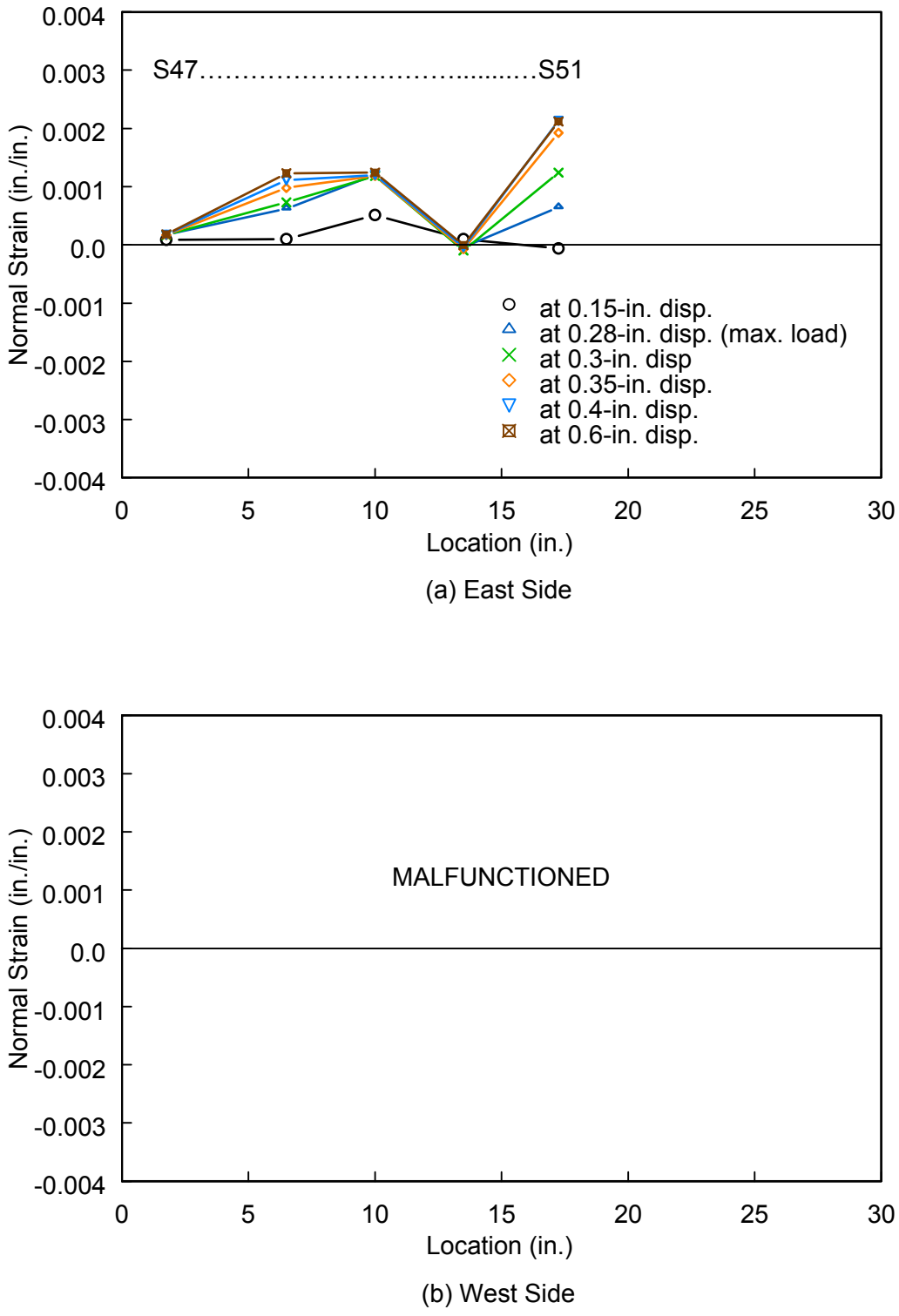

Figure B.36: Specimen CG2: Strain Profiles in Compression Flange (Top Flange)

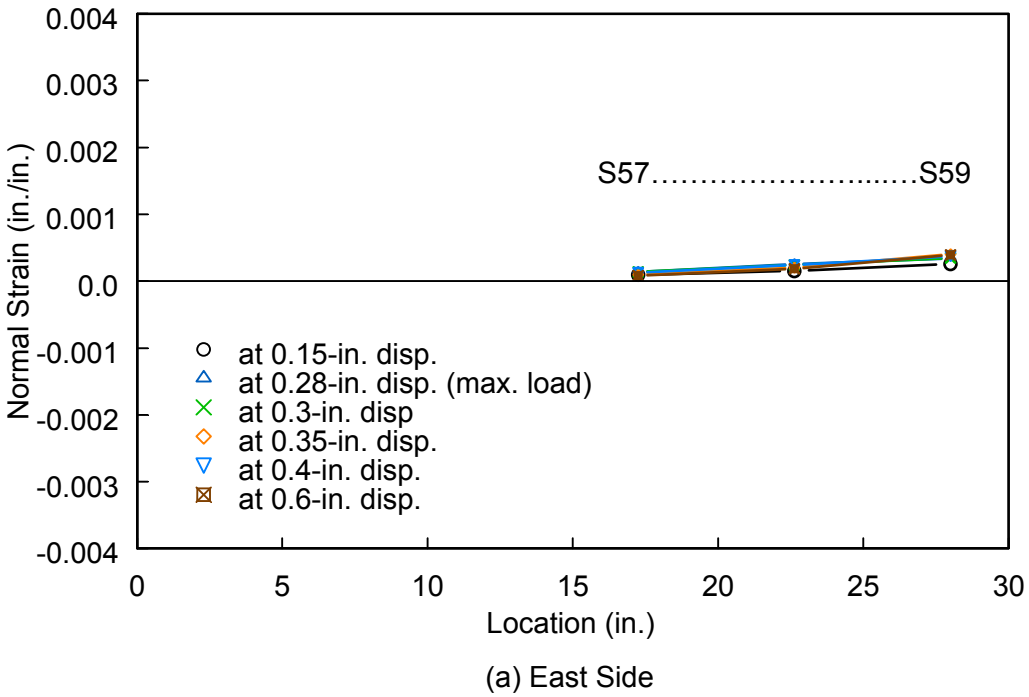

(a) East Side

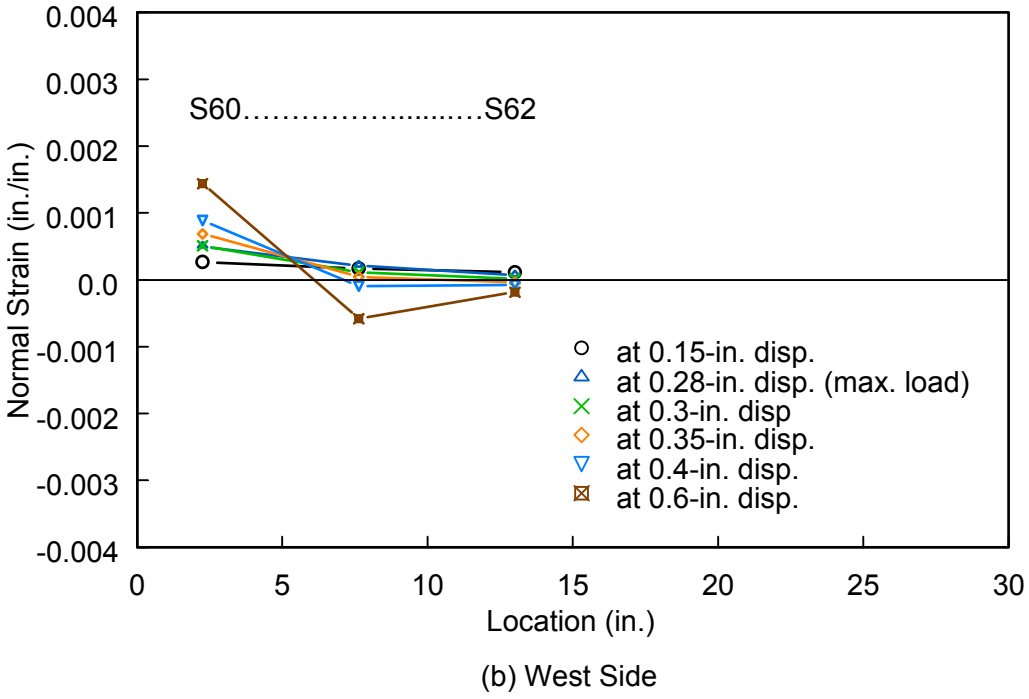

(b) West Side

Figure B.37: Specimen CG2: Strain Profiles in Tension Flange (Bottom Flange)

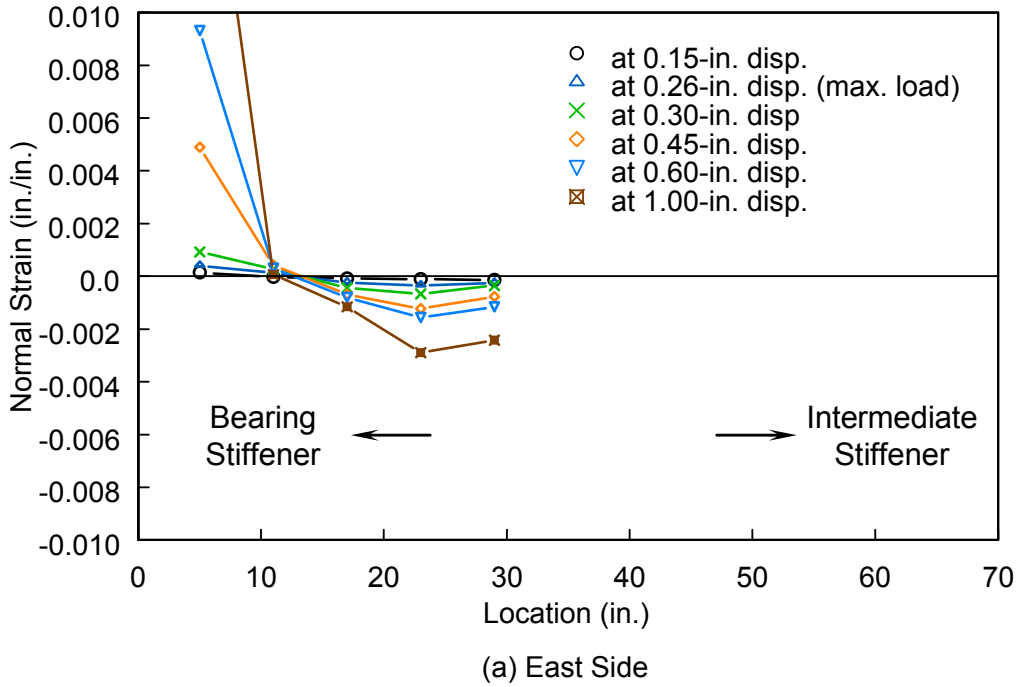

(a) East Side

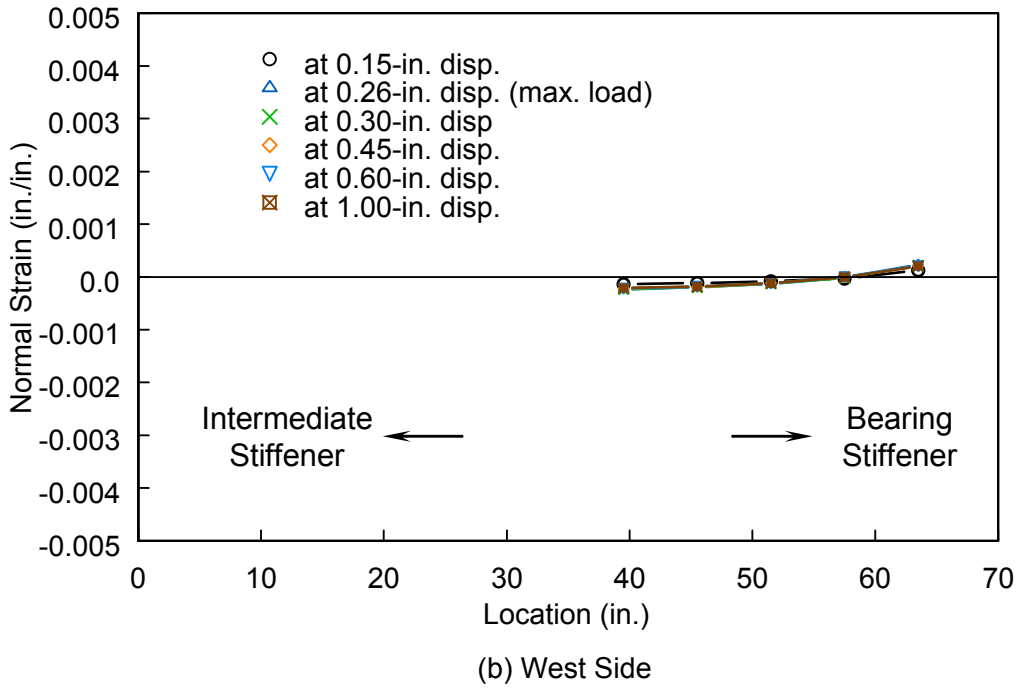

(b) West Side

Figure B.38: Specimen SG3: Strain Profiles in Compression Flange (Top Flange)

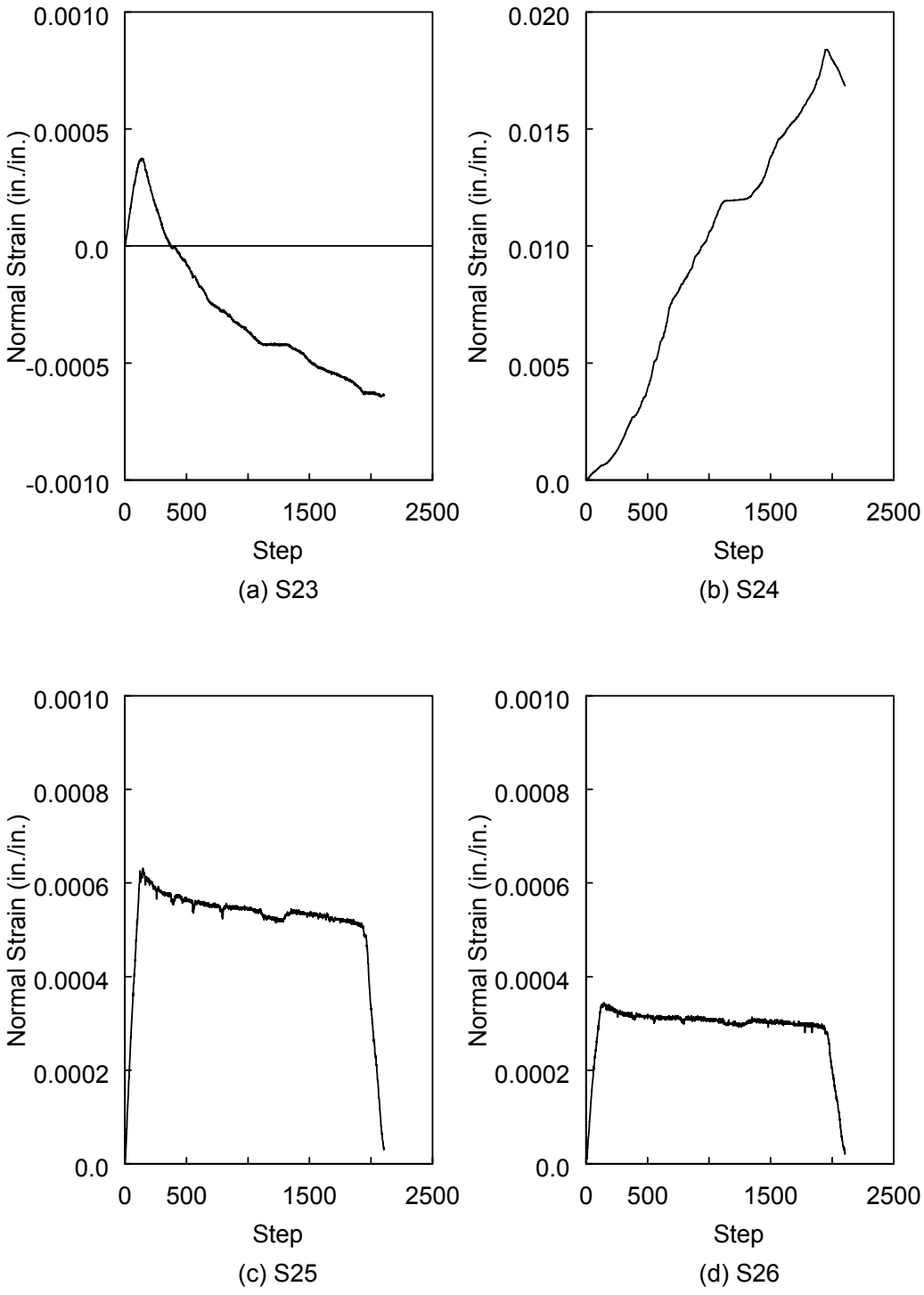

Figure B.39: Specimen SG3: Strain Profiles in Tension Flange (Bottom Flange)

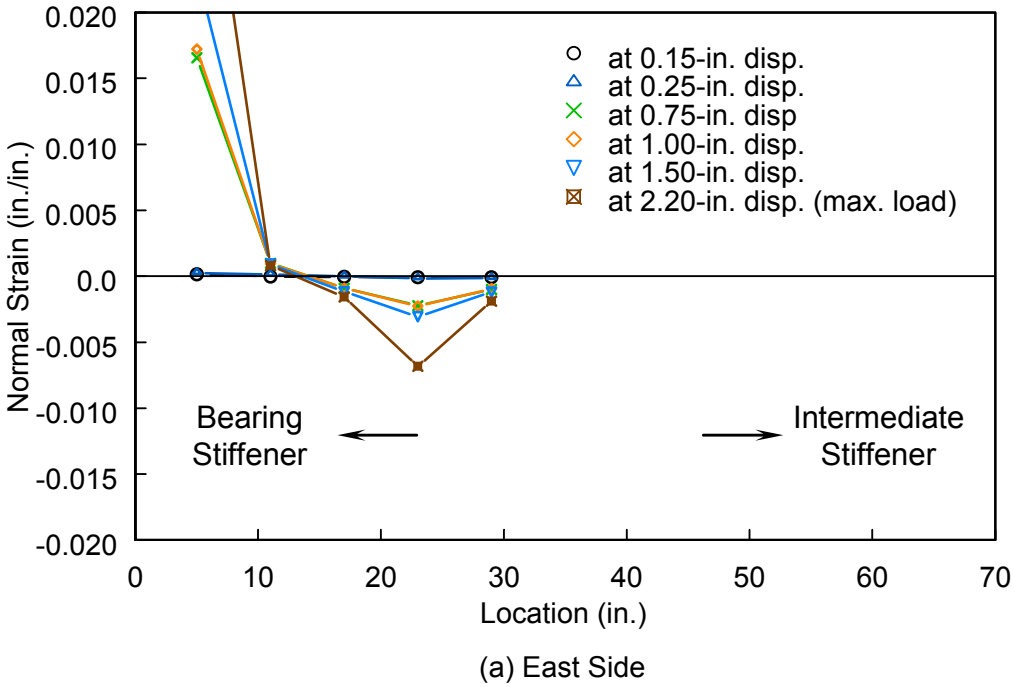

(a) East Side

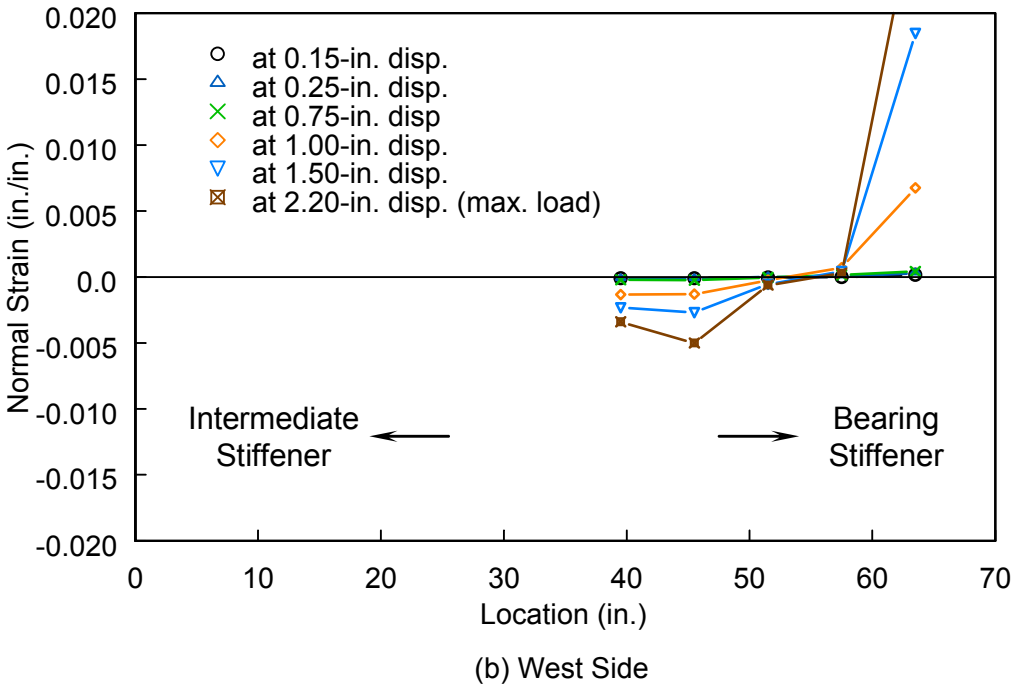

(b) West Side

Figure B.40: Specimen SG4: Strain Profiles in Compression Flange (Top Flange)

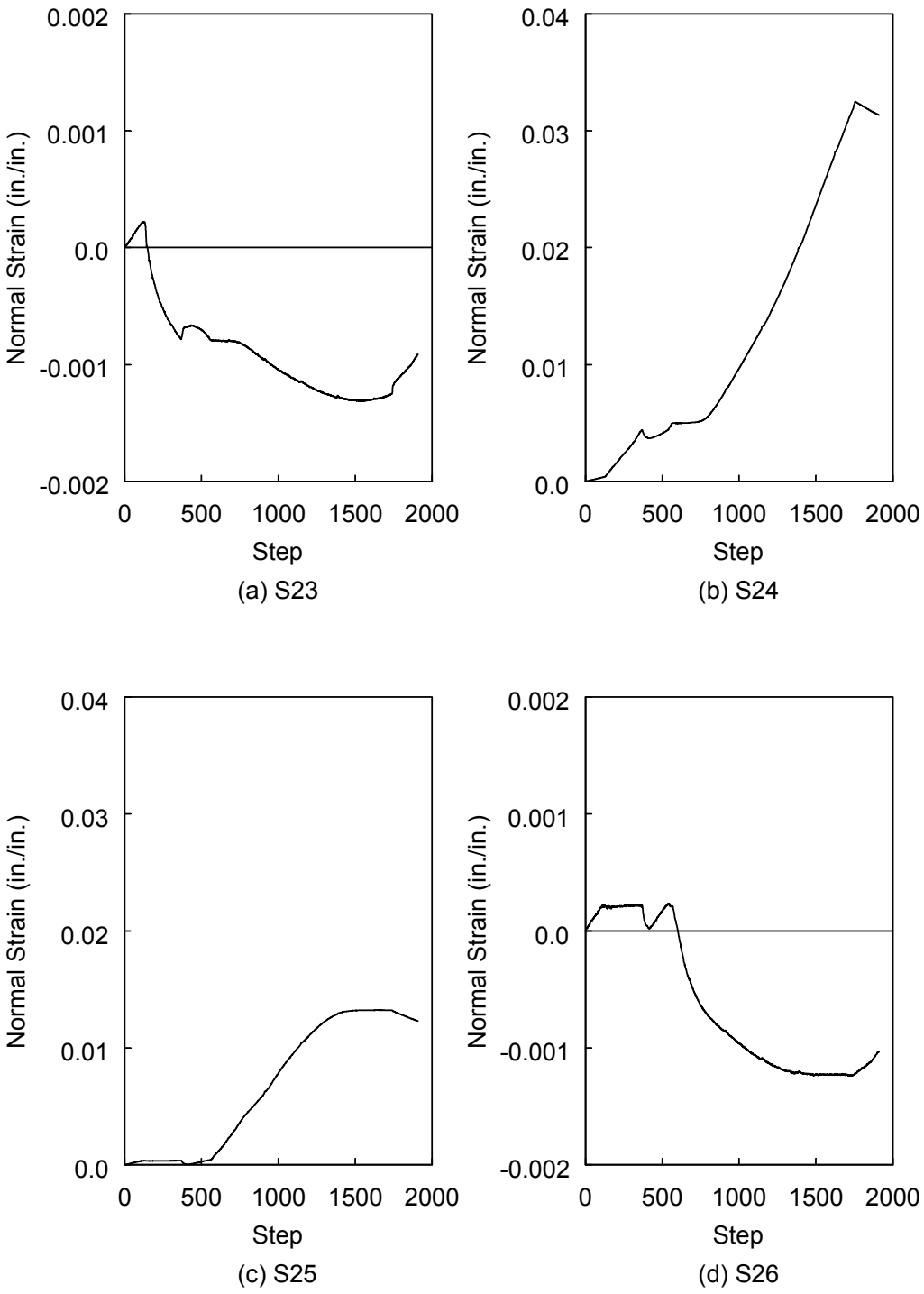

Figure B.41: Specimen SG4: Strain Profiles in Tension Flange (Bottom Flange)

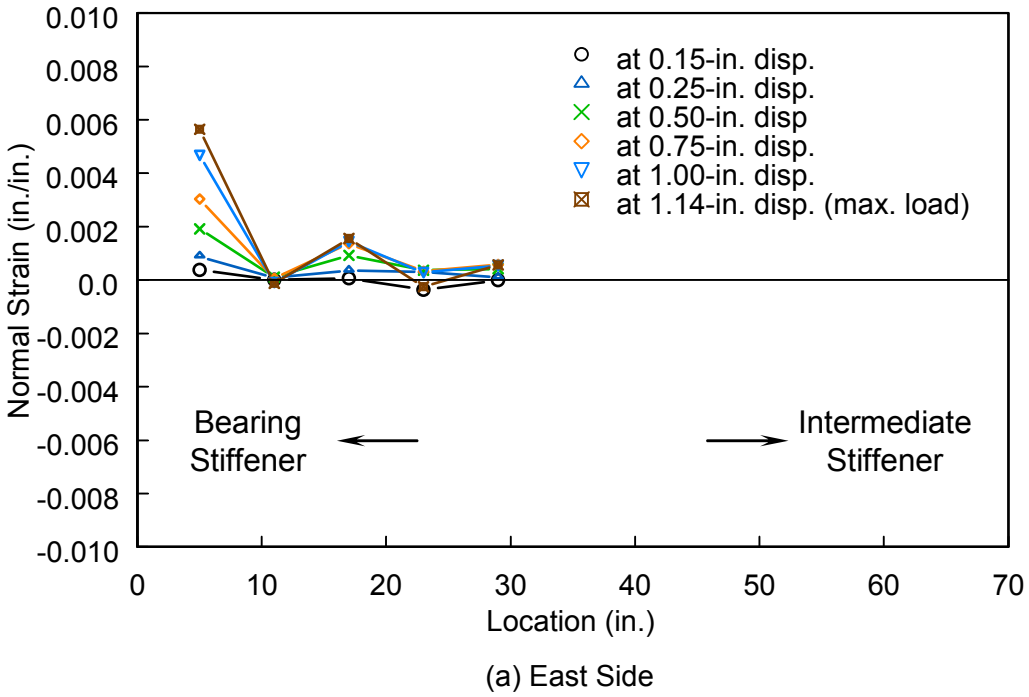

(a) East Side

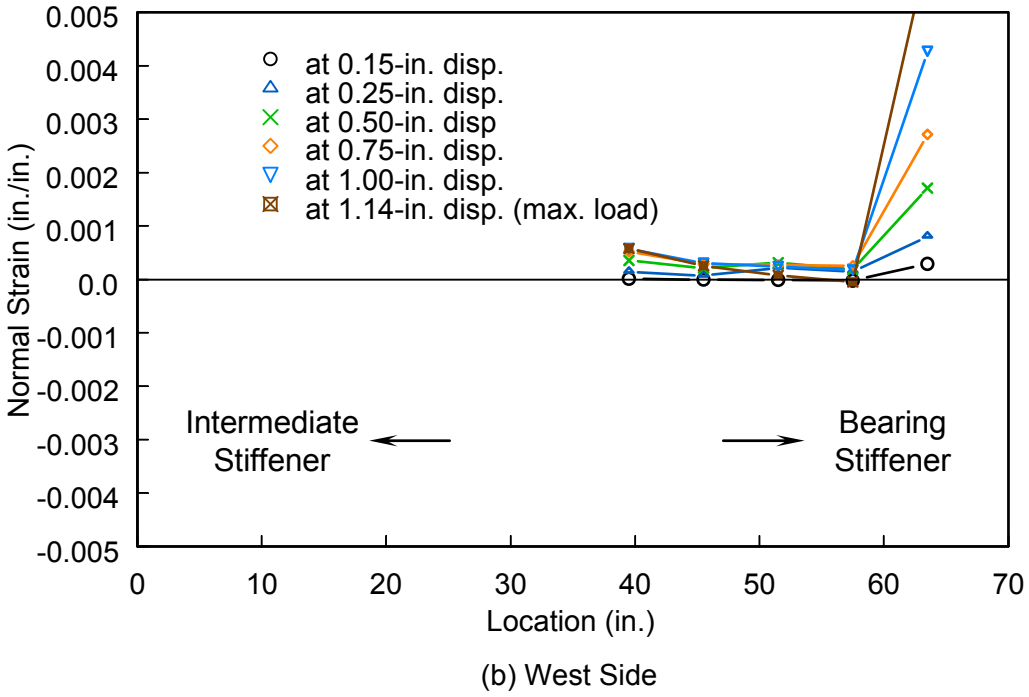

(b) West Side

Figure B.42: Specimen CG3: Strain Profiles in Compression Flange (Top Flange)

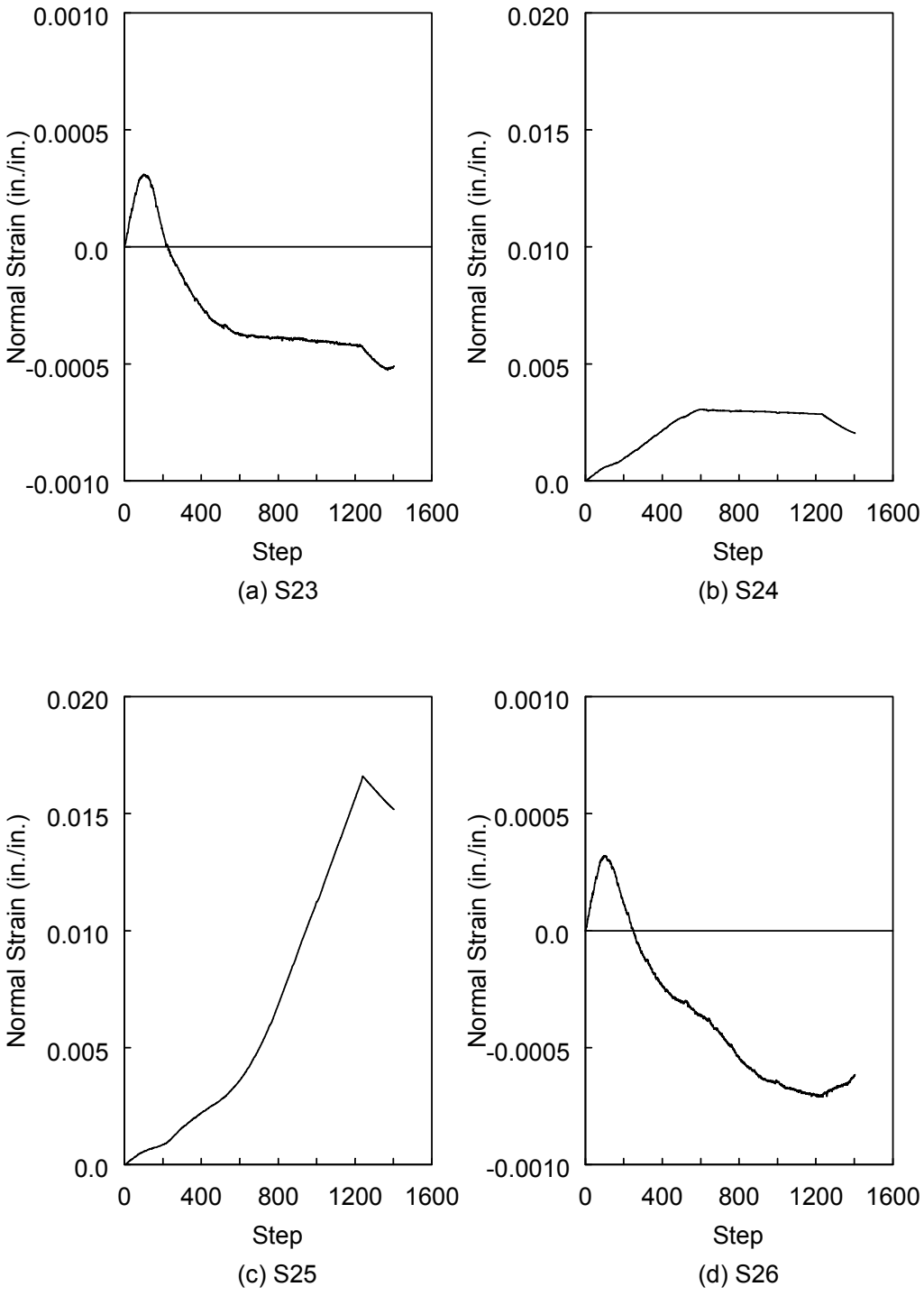

Figure B.43: Specimen CG3: Strain Profiles in Tension Flange (Bottom Flange)

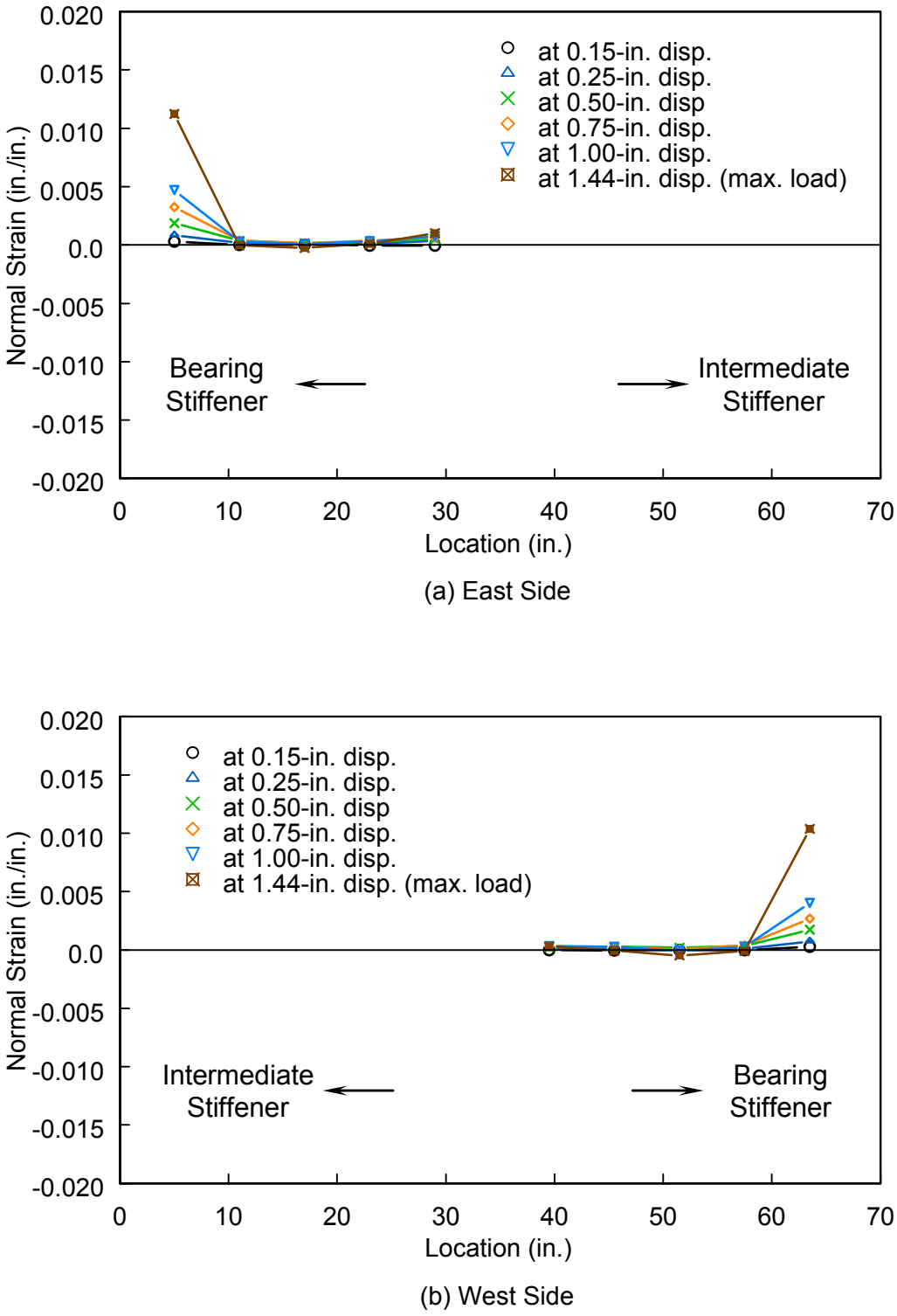

Figure B.44: Specimen CG4: Strain Profiles in Compression Flange (Top Flange)

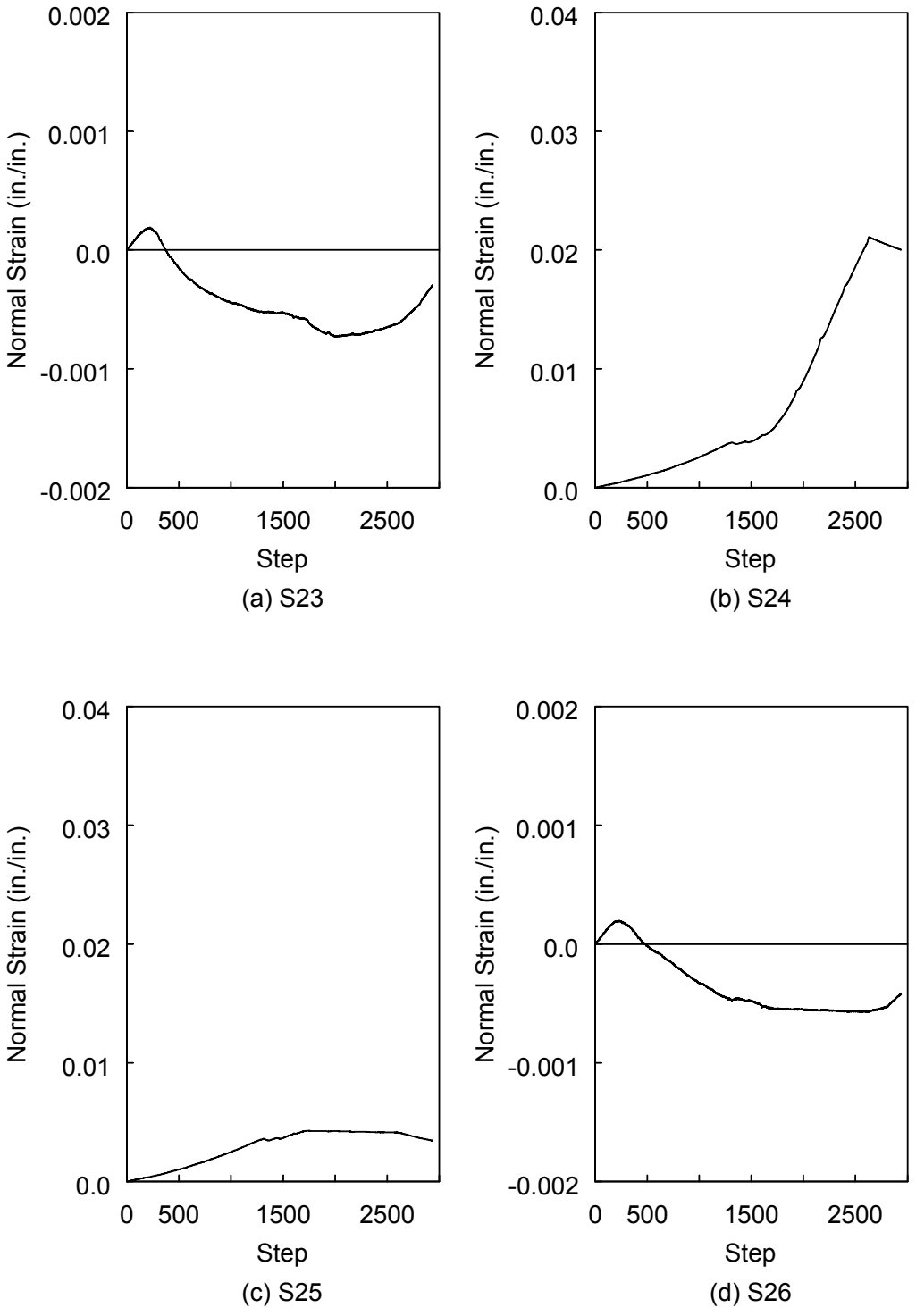

Figure B.45: Specimen CG4: Strain Profiles in Tension Flange (Bottom Flange)

B2. 4 Strain Plots in Concrete Deck

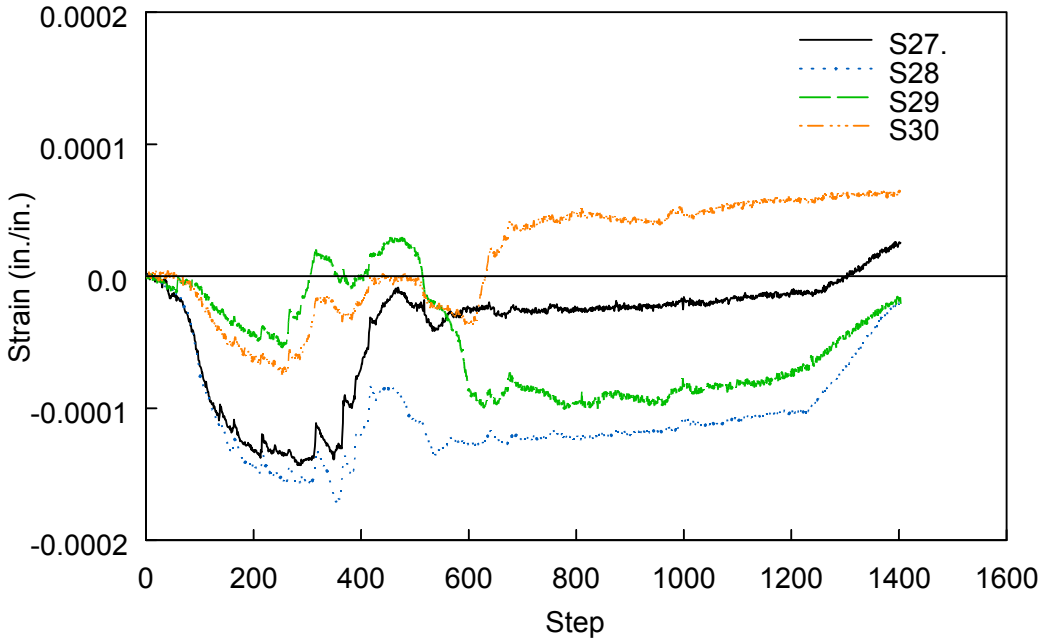

(a) S27 through S30

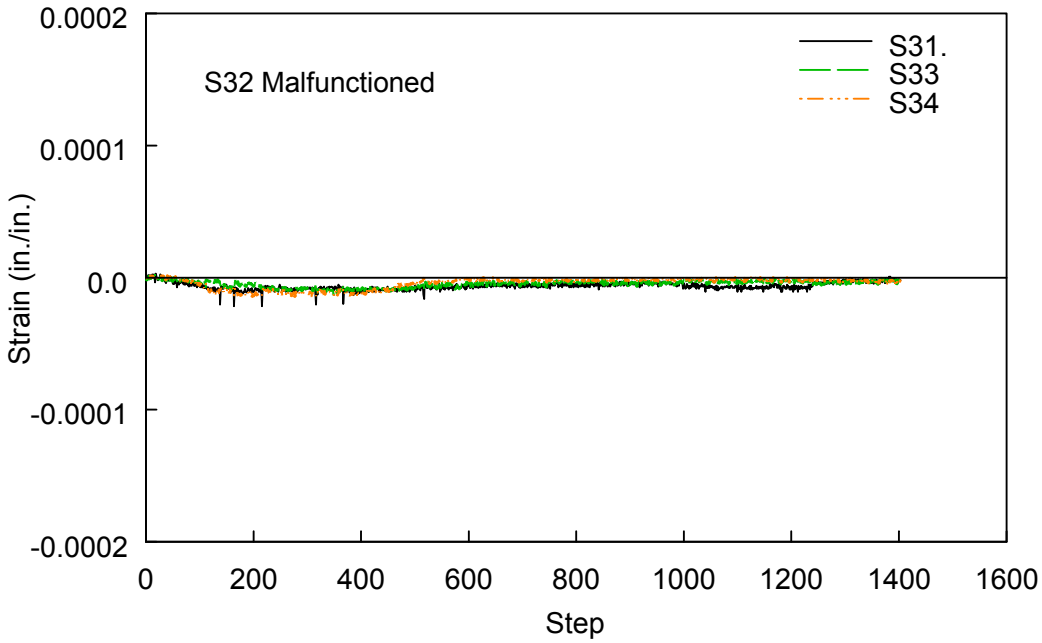

(b) S31 through S34

Figure B.46: Specimen CG3

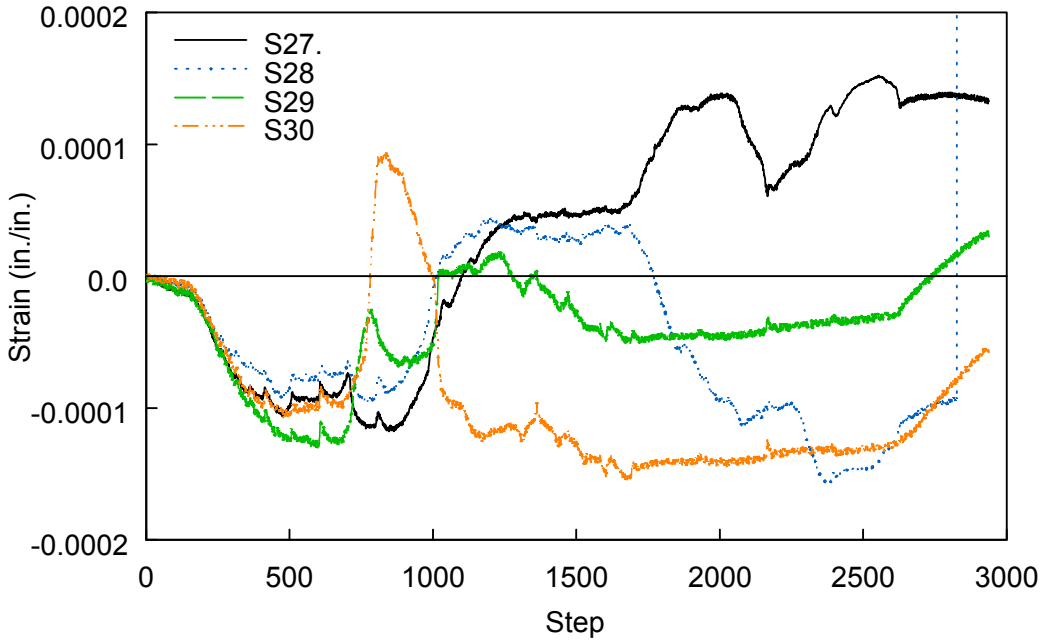

(a) S27 through S30

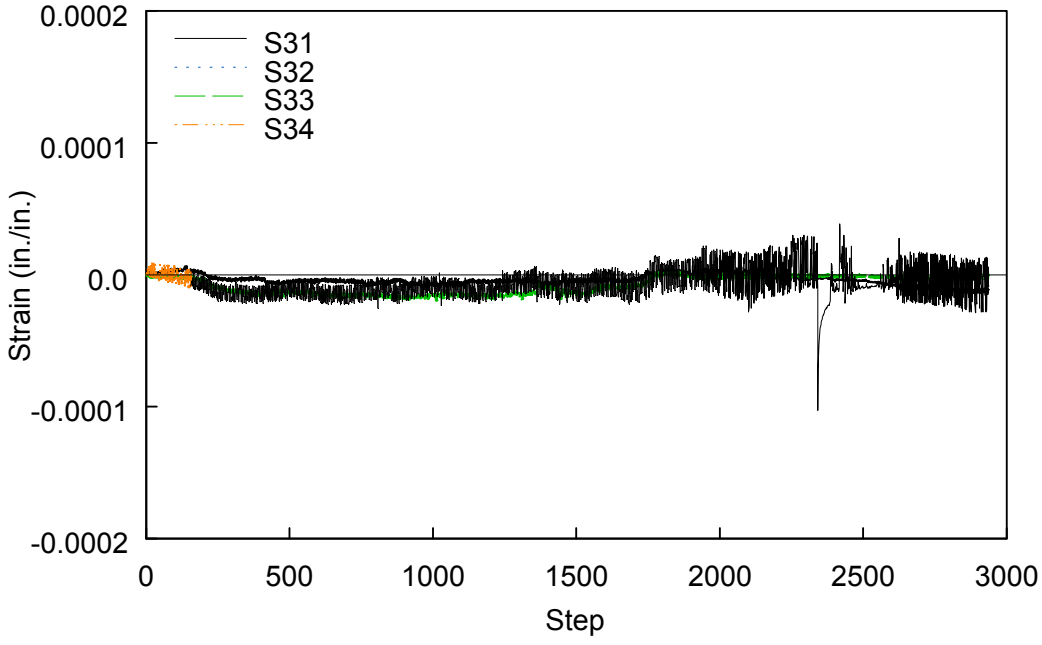

(b) S31 through S34

Figure B.47: Specimen CG4